# DECOMPOSITION AND ITS EFFECTS ON MECHANICAL PROPERTIES IN AL-ZN-MG-CU ALLOYS

A Thesis
Presented to
The Academic Faculty

by

Justin Lamb

In Partial Fulfillment
of the Requirements for the Degree
Doctorate of Philosophy in the
School of Materials Science and Engineering

Georgia Institute of Technology
MAY 2016

Copyright © Justin Lamb 2016

# DECOMPOSITION AND ITS EFFECTS ON MECHANCIAL PROPERTIES IN AL-ZN-MG-CU ALLOYS

Approved by:


Dr. Thomas H. J. Sanders Jr., Advisor
School of Materials Science & Engineering
*Georgia Institute of Technology*

Dr. Naresh Thadhani
School of Materials Science & Engineering
*Georgia Institute of Technology*

Dr. Arum M. Gokhale, Professor
School of Materials Science & Engineering
*Georgia Institute of Technology*

Dr. Preet Singh, Professor
School of Materials Science & Engineering
*Georgia Institute of Technology*

Mr. Victor Dangerfield
Research & Development
*The Universal Alloy Corporation*



Date Approved: December 2, 2015

*Who hath measured the waters in the hollow of his hand, and meted out heaven with the span, and comprehended the dust of the earth in a measure, and weighed the mountains in scales, and the hills in a balance?*

- *Isaiah 40:12*

# ACKNOWLEDGEMENTS

It would be amiss not to foremost express my gratitude towards Dr. Thomas H. J. Sanders Jr for introducing me to the wide world of aluminum and for giving a farmer's boy from Appalachia a chance. I also wish to thank Vic Dangerfield for his continuous support and insight during the course of my tenure at Georgia Tech as well as the Universal Alloy Corporation. To the Universal Alloy Corporation in general, I feel obligated to express my sincerest appreciation for their time and support of my research. This includes, but is not limited to: Chip Poth, Mike Colt, Hailey Jesequel, Ben Gagen, Mario Pacheco, Mike Wilson, Charles Johnson, and Jeremy Senn.

I would also like to thank my lab mates: Ricky Whlelchel, Judy Dickson, and Peter Chamberlain for their assistance and general their general tomfoolery over the course of my time at Georgia Tech. I should also mention Peter Marshall for his various contributions.

I would also like to acknowledge Dr. Tim Langan at Surface Treatment Technologies, Todd Walters at the Georgia Tech Institute for Electronics and Nanotechnology, and Dr. Thomas Dorin for their insight and support in preforming the TEM portion of this work. I would also like to thank Bill Krumme at Vista Metals for his help verifying alloy compositions.

Last, but certainly not least, I would like to thank my family for their support during the past few years. Without their constant prayers and support, I'm unsure as to whether I would have ever made it to this point.

# TABLE OF CONTENTS

# LIST OF TABLES

PART I – A REVIEW OF LITERATURE

Page



PART II – THE QUARTERNARY AL-ZN-MG-CU SYSTEM

Page

PART III – RESEARCH ON REGISTERED 7XXX-SERIES ALUMINUM ALLOYS

Page



APPENDICES

Page

# LIST OF FIGURES

PART I – A REVIEW OF LITERATURE

Page

PART II – THE QUARTERNARY AL-ZN-MG-CU SYSTEM

Page

PART III – RESEARCH ON REGISTERED 7XXX-SERIES ALUMINUM ALLOYS

Page

APPENDICES

Page

# LIST OF SYMBOLS AND ABBREVIATIONS

A ..... Constant

at.% ..... Atomic Percent

β ..... Constant

$C_s$ ..... Concentration in the Solid

C{t} ..... Time Dependent Constant

$\bar{C}_x$ ..... Mean Concentration of x in the Matrix

$\dot{\varepsilon}$ ..... Strain Rate

$f_s$ ..... Fraction Solidified

$f_x$ ..... Fractional Distance Across the Dendrite Arm

G .....Gas Constant (extrusion modeling)

γ ..... Energy of Migrating Grain Boundary

J .....Mechanical Equivalent of Heat

k ..... Partitioning Coefficient

L ..... Billet Length

n ..... Constant

$P_Z$ ..... Zener Drag

Q ..... Activation Energy

$Q_D$ ..... Hot Deformation Activation Energy

R ..... Gas Constant

r ..... Radius

σ ..... Stress

T ..... Temperature

ΔT ..... Change in Temperature

t ..... time

$V_B$ ..... Ram Velocity

$V_v$ ..... Volume Fraction

wt.% ..... Weight Percent

Z ..... Zener-Hollomon Parameter

AA ..... Artificial Aging

BFTEM ..... Bright Field Transmission Electron Microscope

CDF ..... Composite Dark Field

DC ..... Direct Chill (Casting)

DFZ ..... Dispersoid Free Zone

DSC ..... Differential Scanning Calorimetry

HRB ..... Rockwell Hardness (B-scale)

HRTEM ..... High Resolution Transmission Electron Microscope

NA ..... Natural Aging

PFZ ..... Precipitate Free Zone

REX ..... Recrystallization

SADS ..... Select Area Diffraction Patterns

SAXS ..... Small Angle X-Ray Scattering

SEM ..... Scanning Electron Microscope

SHT ..... Solution Heat Treatment

TEM ..... Transmission Electron Microscope

VRC ..... Vacancy Rich Cluster(s)

# SUMMARY

The effects of variations in composition on the decomposition process in Al-Zn-Mg-Cu alloys (i.e. – 7xxx-series aluminum alloy) were studied emphasizing their effect on mechanical properties. Several experimental quaternary alloys were studied to compare their behavior with commercial 7xxx-series alloys. The investigation included studies on the effects of natural aging, artificial aging, quench sensitivity, precipitate free zone formation, and homogenization. Additionally, "true aging" curves (i.e. – hardness/strength vs. conductivity) were presented in order to visualize and quantify the entire precipitation process.

It is obvious that fluctuations in the main alloying elements/processing parameters can alter the precipitation process, but the purpose of this work was to quantify those changes using standard industrial techniques. It was found that natural aging was detrimental for strength in the T6 temper for alloys containing more than 1.0 wt.% Cu, and was shown to alter the coarsening kinetics in the over-aged condition (T7). Conversely, for alloys with Cu contents less than 0.5% natural aging was shown to be beneficial for strength. Altering the Zn:Mg ratio was also shown to effect natural aging response of an alloy in addition to introducing additional precipitation processes (T-phase). Therefore, this work is a blueprint for advanced alloy manufacturing that allows for the rapid production of new alloys and tempers by narrowing the research focus depending on an alloy's composition.

# CHAPTER 1

# INTRODUCTION

Precipitation hardenable aluminum alloys were first discovered by Wilm [1] in 1911 while studying the Al-Cu system and were later characterized by Merica, Waltenburg, and Scott [2] in 1919. These early Al-Cu alloys were almost immediately commercialized for Zeppelin frames and components during World War I, and have remained an essential building material in the aerospace industry ever since [3].

The precipitation hardenable 7xxx-series of aluminum alloys, which are based on either the ternary Al-Zn-Mg or the quaternary Al-Zn-Mg-Cu systems, are extensively utilized for structural components in aerospace applications due to their high specific strength. Aluminum alloy 7075, one of the first modern aerospace 7xxx-series aluminum alloys, was developed by the Japanese company Sumintomo Metals in 1936, and the application of 7075 on the Mitsubishi A6M Zero fighter plane revolutionized the aerospace industry [4], [5]. The alloy was later reversed-engineered by ally forces after chemical analysis was performed on A6M wreckage recovered during World War II and rebranded as ESD (extra super duralumin). During the war several variants of ESD were developed in the UK and USA with the modern version of 7075 (then known as 75S) introduced by Alcoa in 1943, and was made famous by its inclusion on the B-29 Flying Fortress [5]. The alloy was registered with the Aluminum Association in 1954, and alongside other 7xxx-series alloys has become one of the cornerstone materials of the aerospace industry [6]. An in-depth history on the development of other 7xxx-series alloys stemming from 7075 (7050, 7178, 7079, 7001) is given by Hunsicker [7].

The documented main hardening phases in 7xxx-series alloys are: GP zones (type I and type II), η', and η ($MgZn_2$); however, the decomposition process of 7xxx-series aluminum alloys is complex. Research suggests the decomposition process is controlled

by a myriad of factors including: the Zn:Mg ratio, the (Zn+Cu):Mg ratio, the solution heat treatment (SHT), the plastic deformation process, the natural aging time, and the artificial aging practice. The large number of factors leads to a complex precipitation process, which can best be thought of as a series of "sub-precipitation sequences."

The goal of this work is to attempt to characterize and quantify the effects of these factors on the decomposition process, and how they affect the mechanical properties of 7xxx-series alloys. For this work a series of experimental Al-Zn-Mg-Cu alloys were studied alongside a series of registered, but more complex, 7xxx-series alloys including: 7136, 7050, 7075, 7150, 7178, and variations of these commercial alloys.

### 1.1 References


[1] A. Wilm, "Metallurgical invesitgations of aluminum alloys containing magneisum," *Metallurgie*, vol. 8, p. 225, 1911.

[2] P. D. Merica, R. G. Waltenberg, and H. Scott, "Heat treatment of Duralumin," *Sci. Pap.*, pp. 271–315, 1919.

[3] M. E. Fine, "Precipitation hardening of aluminum alloys," *Metall. Trans. A*, vol. 6, no. April, pp. 625–630, 1975.

[4] JAA, "Chronology," *Japan Aluminum Assocatiation*, 2002. [Online]. Available: http://www.aluminum.or.jp/basic/alumi-sangyo/hf00.html.

[5] I. J. Polmear, "Aluminium alloys – a century of age hardening," *Mater. Forum*, vol. 28, pp. 1–14, 2004.

[6] The Aluminum Association, *International Alloy Designations and Chemical Composition Limits for Wrought Aluminum and Wrought Aluminum Alloys*. Arlington, VA, 2009.

[7] H. Y. Hunsicker, "Development of Al-Zn-Mg-Cu alloys for aircraft," in *Proc. Rosehain Centenary Conf. on the Contribution of Physical Metallurgy to Engineering Practice*, 1976, pp. 359–376.

# PART I

# A REVIEW OF LITERATURE

# CHAPTER 2

# INTRODUCTION

The precipitation process in Al-Zn-Mg-Cu (7xxx-series) alloys is highly complex consisting of both homogenous and heterogeneous nucleation and growth sections depending on the various processing parameters. For example, the precipitation process most referenced for 7xxx-series alloys is:

$$\alpha_{ssss} \rightarrow GP\ zones \rightarrow \eta' \rightarrow \eta\ (MgZn_2)$$

The precipitation of GP-zones at room temperature is essentially a homogenous process that takes place a room temperature, while the transformation of GP-zones to η' and η is a heterogeneous process. However, a quick review of current literature reveals this an incomplete description as the role of vacancy rich clusters (VRC) and dislocations are ignored. Furthermore, two distinct types of Guinier-Preston zones (GP-I and GP-II zones) are known to occur, but the delineation of the two is negated above.

Processing parameters such as solution heat treatment, stretching, and aging are also known to alter the precipitation process in 7xxx-series alloys. For instance, quickly heating/slowly quenching an alloy above the GP-solvus temperature is known to make the following heterogeneous nucleation process dominate:

$$\alpha_{ssss} \rightarrow \eta' \rightarrow \eta\ (MgZn_2)$$

Likewise, processing steps like stretching are known to cause the direct heterogeneous precipitation of η on dislocations. The composition of a 7xxx-series alloy can also alter the precipitation process via several methods including changing the morphology and composition of the precipitates. For example, Cu additions are known to change the morphology of GP-zones and raise the GP-zone solvus temperature.

Therefore, it is evident that understanding how various factors affect the precipitation process is vital in understanding the effects of decomposition on an alloy's

mechanical properties. However, due the complexity of the 7xxx-series system the exact mechanisms governing the decomposition process are still of some debate (an in-depth review of the various observed precipitations processes and their components is presented later in *Chapter 6 – The Precipitation Process*). The following section is an in-depth literature review of the complex decomposition process in 7xxx-series aluminum alloys and the various factors that affect it. It is divided into five chapters roughly following a typical processing procedure for a 7xxx-series alloy (see Figure 1). Chapters 3-5 pertain to the solidification (casting), the homogenization, and the extrusions processes, respectively, because these steps in production can have far reaching effects on the mechanical behavior of Al-Zn-Mg-Cu alloys. Chapter 6 covers the precipitation process in the general order of decomposition (i.e. – VRC → GP Zones → η' → η), with Chapter 7 detailing how the precipitation process can be altered by various post plastic deformation procedures (ex – artificial aging).

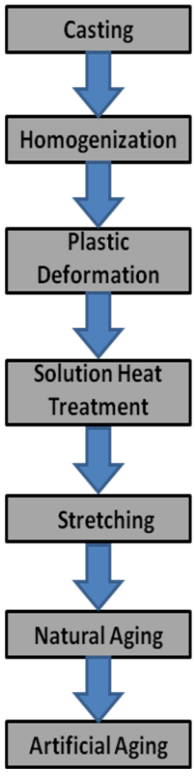


Figure 1 – *The typical processing procedure for a 7xxx-series aluminum alloy*

# CHAPTER 3

# SOLIDIFICATION OF AL-ZN-MG-CU ALLOYS

The following chapter is an overview of the solidification process and casting techniques which are relevant to this work. Gravity and direct chill casting are covered as well as the effects of cooling rate and grain refiners. The as-cast structures of 7xxx-series alloys are reviewed and common solidification complications are briefly discussed. A comprehensive table of solid solubilities for various elements in aluminum can be found in Appendix A. It should be noted that terms "ingots" and "billets" refer to the as-cast materials intended for rolling and extruding, respectively.

## 3.1 An Overview of the Casting Procedure

Aluminum alloy billets are prepared by melting and mixing virgin aluminum, aluminum scrap, and various alloying additions. The main concern during the casting process is ensuring a thorough mixture of the constituents together; however, effectively filtering and degassing the metal to remove dross, oxides, other non-metallic impurities, and hydrogen is also extremely important for commercial alloys [1].

### 3.1.1 Gravity Casting

Gravity casting is a form of permanent mold casting in which molten metal is poured into a preheated mold coated with a refractory material, which prevents the metal from sticking to the mold [2], [3]. The pouring procedure is critically important in gravity casting. Pouring should take place at the lowest possible position with respect to the mold and the stream of molten aluminum should be continuous and steady [4]. This helps minimize turbulence, oxide generation, and subsequent entrapment as well as lowers the need for further degassing. It should also be noted that frequent skimming of the metal oxide layer that forms between the molten aluminum and the air is required to ensure quality casts. The process is simple, however, complications such as hot tearing

and porosity plague gravity casting. Therefore, gravity casting is typically not used for the production of billets.

### 3.1.2 Direct Chill Casting

The need for uniform billet structures lead to the development of direct chill (DC) casting [1], [5]. The DC casting process, which is usually carried out vertically as seen in Figure 2, is a semi-continuous process in which molten aluminum is poured into a fixed, water-cooled mold with a retractable base. The process of solidification in the DC casting occurs in two stages. First, molten metal is solidified in the mold which is water cooled forming a shell into which the remaining molten aluminum can be poured. When the solidified shell is strong enough to contain the molten aluminum, the shell is then lowered at a constant rate while being continuously sprayed with water, which allows for a uniform billet structure to be obtained [6]. Compared to gravity casting, DC casting offers uniform grain structures and smooth billet surfaces that can be adequately control by varying the rate of heat flow from the billet [1].

Modeling the direct chill casting process has been the focus of a great deal of research. Models have been proposed by Mortensen [6], Drezet and Rappaz [7], and Fjaer and Mo [8] among others. The complex boundary conditions and liquid behavior of the molten aluminum, however, make the problem highly complex and beyond the scope of this review.

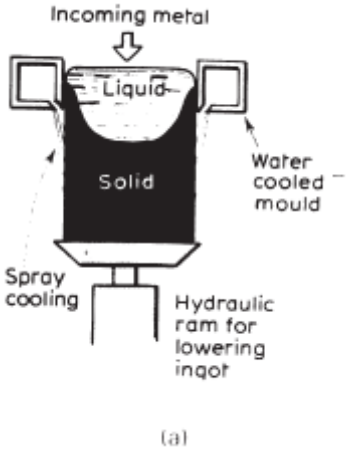


Figure 2 – *Schematic of a direct chill processes* [1].

### 3.2 Cooling Rate

Thanaboonsobut and Sanders [9] showed that the cooling rate from the melt is an important variable in the casting process that can be manipulated to optimize the grain structure of wrought aluminum alloys. Furthermore, it was shown by Thanaboonsobut and Sanders [9] that the grain size; the type, size, number density, and distribution of constituent particles; and the amount of dispersoid forming elements (i.e. – Zr, Cr, Mn, etc.) retained in supersaturated solid solution are all influenced by the cooling rate. Generally speaking, increasing the cooling rate generates more grain boundaries and promotes a more homogeneous distribution of constituent particles [10]. This is due to the fact that increased cooling rates result in higher undercoolings, which subsequently leads to faster nucleation and growth rates resulting in a finer microstructure. The effects of cooling rate have been the focus of a great deal of research that are summarized in [11].

It should be noted that there is research to suggest that the cooling rate from melt may play a critical role in determining the recrystallization resistance of an aluminum alloy during solution heat treatment (SHT) [9], [12]. It was shown that at critical cooling rates constituent alpha-particles (AlFeMnSi) in AA6013 reached the critical size for particle stimulated nucleation (PSN) as predicted by the Humphreys and Kalu [9], [13]

model. This is illustrated in Figure 3 where the volume fraction of recrystallized grains initially increases with cooling rate, and then upon reaching a critical cooling rate begins to decrease. Thanaboonsobut and Sanders [9] explained that at low cooling rates the size of alpha constituent particles in AA6013 are large, while their number density is low. Likewise, as the cooling rate increases the particles increase in number density, but become too small for PSN. Therefore, it is important that a constant cooling rate be utilized in order to be able to distinguish the effects of composition that could otherwise be masked by varying cooling rates.

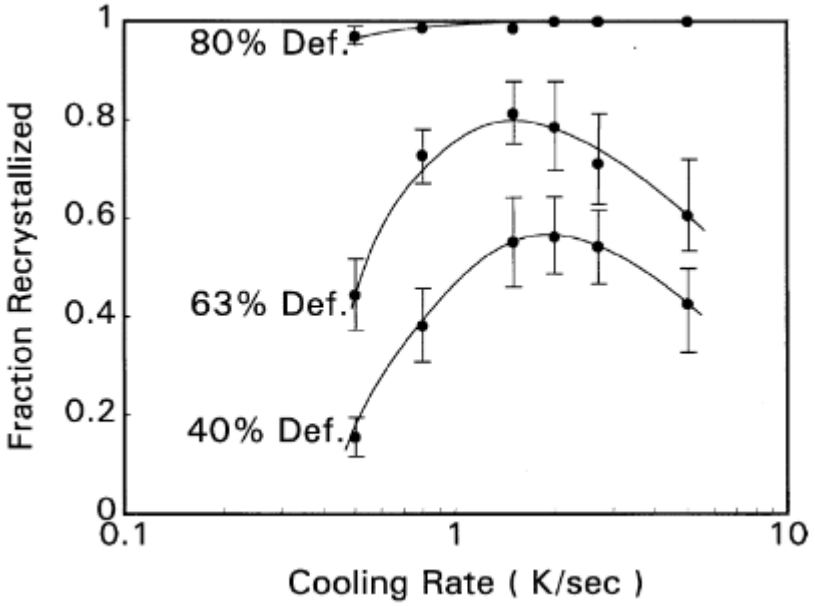


Figure 3 – *Plot of the volume fraction of recrystallized grains as a function of cooling rate for three levels of deformation* [9].

### 3.3 Grain Refinement

Grain refiners, such as Al-Ti-B or Al-Ti-C, are often utilized in commercial 7xxx-series alloys to promote fine, equiaxed grain structures [10]. Grain refiners reduce segregation and hot cracking propensity (solidification cracking) in the as-cast structure as well as promote better responses to plastic deformation steps and surface finishing techniques [14]–[16].

The vast majority of grain refining applications utilize Al-Ti-B master alloys, which form soluble $Al_3Ti$ particles and insoluble $TiB_2$ particles [10], [17]. Al-Ti-B master alloys have shown to be highly effective in refining grains in moderate amounts, and are insensitive to cooling rate [10]. However, excess amounts of grain refiners lead to a number of quality problems due to the tendency of the refiners to agglomerate. With respect to billets, the adverse effects of superfluous Al-Ti-B grain refining are often seen in the internal cracking of extrusion billets [10], [18]. Several alloying additions, including Zn, Mg, and Cu, are known to improve the efficiency of Al-Ti-B grain refiners; however, Pourkia *et al.* [10] states that the exact reasons for this are unknown, but it may be related to the ability of Zn, Mg, and Cu to lower the activity of Zr (see below).

### 3.3.1 The Chromium and Zirconium Equivalences

Dispersoid forming elements such as Zr and Cr are often effective grain refiners as they can act as nucleation sites for the Al-matrix and pin grain boundaries [10], [19], [20]. Unfortunately, $CrAl_7$ primary crystals, which often form during the casting of aluminum alloys like 7075, can grow large enough to become a significant defect in the final wrought microstructure and decrease fracture toughness [21]. This phenomena, which essentially stems from the melt being held at a temperature just above the peritectic in the L + $Al_7Cr$ phase field via a process described in [21], is not easily controlled. Even keeping the Cr-levels to the minimum required level (0.18 wt.% in 7075) is not sufficient to avoid the formation of the primary Cr-crystals due to a concept called the chromium equivalence.

The chromium equivalence, which was first described by Steele and Collins [22] in 1959, says that primary Cr-crystals form even at relatively low Cr-levels due to other alloying elements such as Ti, Mn, Fe, and V contributing to their formation [21]. The original chromium equivalence equation presented by Steele and Collins [22] can be seen in Equation 1, which states that primary Cr-crystals will form if the wt.% of Cr in

addition to the relative contributions of Ti, Mn, and Fe (all in wt.%) is greater than 0.244 wt.%:

$$Cr + 0.797\ Ti + 0.090\ Mn + 0.142\ Fe \geq 0.244 \quad (1)$$

However, the chromium equivalence has since been updated with Beerntsen [21] presenting a new form of the equation to include vanadium, V, which can been seen in Equation 2:

$$Cr + 2.03\ V + 0.54\ Ti + 0.24\ Mn + 0.055\ Fe \geq 0.236 \quad (2)$$

Where again Cr, V, Ti, Mn, and Fe represent their composition in the alloy in question in wt.%.

Similarly, Zr can also form a primary crystal as Beerntsen [21] showed for AA2219 and a 705x-type alloy containing Zr. This "zirconium equivalence" is given by Equation 3:

$$Zr + 0.2\ Ti + 0.02\ V \geq 0.14 \quad (3)$$

Where Zr, Ti, and V represent their respective composition in wt.%. Interestingly, Beernsten [21] found that Zr and Cr played little to no role in the formation of the other's primary crystal. The effects of these "equivalences" must be taken into account, especially in the recasting of aluminum alloys where impurity levels (i.e. – Fe, Si, etc.) are known to rise.

The effects of dispersoids on the Al-Zn-Mg-Cu microstructure will be discussed further in *Chapter 4 – The Homogenization of Al-Zn-Mg-Cu Alloys.* However, it is worth mentioning that research has shown that Al-Ti-B additions to Zr-containing alloys have proven less effective in refining grains. This has been attributed to the coating of $Al_3Ti$ and $TiB_2$ particles by $ZrB_2$, which decreases the effectiveness of $TiB_2$ to act as a nucleation site for α-aluminum [10].

### 3.4 The As-Cast Structure

The high solute content of 7xxx-series aluminum alloys leads to a plethora of phases in the as-cast structure [23]; however, the most commonly observed phases in the

as-cast structure of Al-Zn-Mg-Cu alloys are η ($MgZn_2$), T (Al-Mg-Cu), S (Al-Mg-Cu), and θ ($Al_2Cu$) [10], [17]–[20], [24], [25]. The as-cast structure of an aluminum alloy is usually highly cored due to nonequilibrium cooling conditions [26]. The consequences of a cored microstructure are that the primary phase is nonuniform in composition and that low-melting temperature phases (i.e. – nonequilibrium eutectic) can be present. Increasing the alloy content, or the larger the freezing range of an alloy (i.e. – the larger the difference between the liquidus and the solidus), increases the amount of nonequilibrium eutectic present in the as-cast structure [26]. An example of the segregation caused by a cored microstructure can be seen in Figures 4 and 5. The as-cast microstructure is dendritic in nature with various primary and secondary dendrites easily distinguishable.

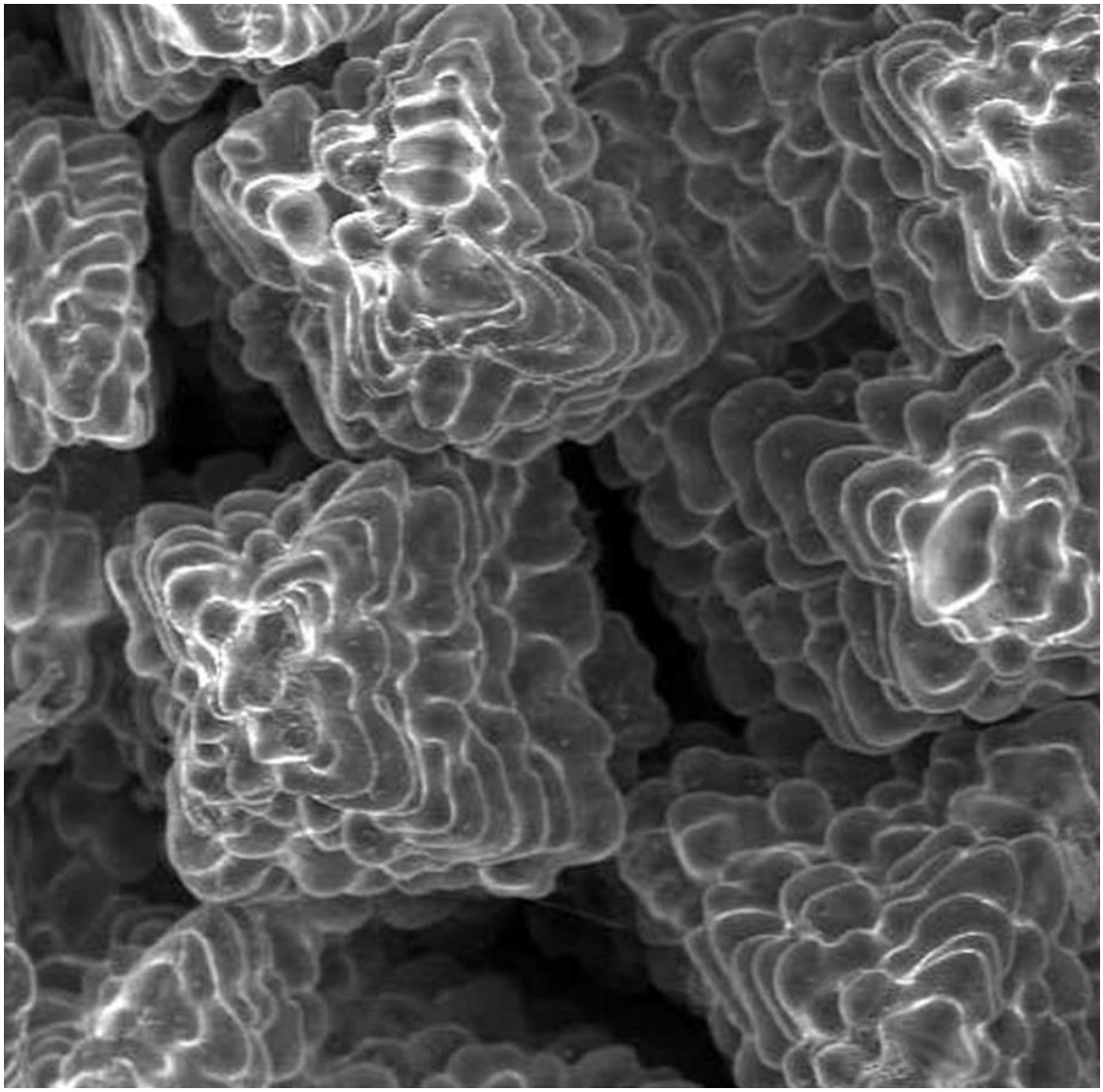

Figure 4 – *Micrograph of typical dendritic structures* [27].

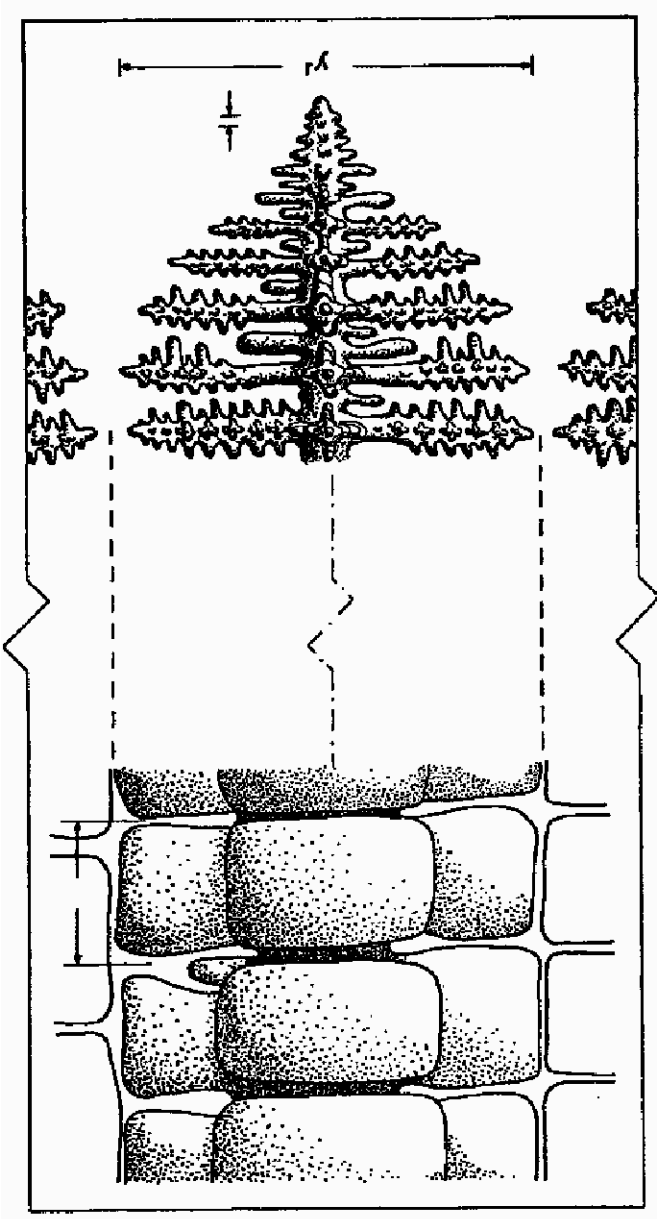

Figure 5 – *Schematic of typical dendritic structure displaying primary, secondary, and ternary dendrites* [27].

### 3.5 Solidification Complications

Macrosegregation, which is a non-uniform chemical composition over a 'large' distance, is a major defect that can occur in semi-continuous direct-chill casting [28]. The defect is extremely deleterious due to the fact that it is largely unaffected by subsequent heat treatments (i.e. – homogenization). This typically leads to the scrapping of billets, which is a costly and energy consuming process. An in-depth literature review

on the mechanisms controlling macrosegreagtion as well as how it is typically controlled in the industrial process is provided by Nadell *et al.* [28] and Fleming *et al*. [29]–[31].

Solidification cracking occurs via grain boundary separation in the presence of film-like constituents during the solidification process [16]. The severity of solidification cracking in 7xxx-series alloys can be directly correlated to the temperature difference, $\Delta T$, between the liquidus and solidus. Kim *et al*. [16] notes that the larger the value of $\Delta T$ the higher the susceptibility to solidification cracking, and further states that Mn and Zr alloying additions decrease an alloy's susceptibility. It should also be noted, however, that Cr and Cu additions tend to increase a 7xxx-series susceptibility to solidification cracking.

Cold cracking (see Figure 6) is a major issues in non-stress relieved aluminum billets due to the residual stresses left over from the casting process [8]. Therefore, aluminum billets are stress relieved following the casting procedure. The stress relief process typically sees a billet heated to a sub-homogenization temperature and held there for several hours before being air cooled back to room temperature.

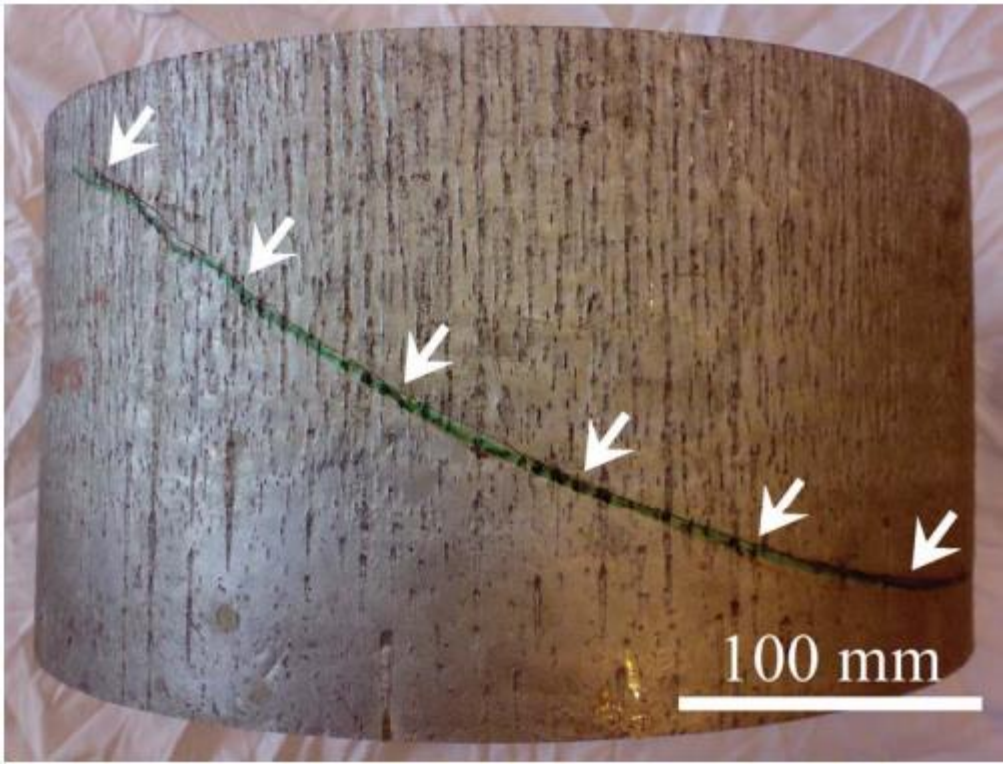


Figure 6 – *Photograph showing an example of a cold crack in a DC cast 7xxx-series billet* [32].

### 3.6 Summary

An overview of the casting of aluminum alloys, specifically Al-Zn-Mg-Cu alloys, was presented. The two casting methods used for this work, gravity and DC casting, were covered as well as the morphology of common as-cast structures. Common casting defects were also briefly reviewed. It is important to understand the effects of different casting types, as well as the possible defects associated with them, as they can have far reaching effects on the final properties of aluminum alloys as well as their subsequent processing. Therefore, understanding the as-cast microstructure is an integral part in truly discerning the effects of compositional variations in 7xxx-series alloys.

### 3.7 References

[1] I. J. Polmear, *Light Metals*. Arnold, 1995.

[2] E. P. Degarmo, J. T. Black, and R. A. Kohser, *Materials and Processes in Manufacturing*, 9th ed. 2003.

[3] S. Kalpakjan and S. Schmid, *Manufactoring Engineering and Techonology*, 5th ed. Pearson, 2006.

[4] J. R. Davis, *Aluminum and Aluminum Alloys*. ASM International, 1993.

[5] V. S. Zolotorevsky, N. A. Belov, and M. V. Glazoff, *Casting Aluminum Alloys*. Pittsburgh, 2007.

[6] D. Mortensen, "A mathematical model of the heat and fluid flows in direct-chill casting of aluminum sheet ingots and billets," *Metall. Mater. Trans. B*, vol. 30, pp. 119–133, 1999.

[7] J.-M. Drezet and M. Rappaz, "Modeling of ingot distortions during direct chill casting of aluminum alloys," *Metall. Mater. Trans. A*, vol. 27, pp. 3214–3225, 1996.

[8] H. G. Fjaer and A. Mo, "ALSPEN - a mathematical model for thermal stresses in direct chill casting of aluminum billets," *Metall. Trans. B*, vol. 21, pp. 1049–1061, 1990.

[9] B. Thanaboonsombut and T. H. Sanders Jr., "The effect of cooling rate from the melt on the recrystallization behavior of aluminum alloy 6013," *Metall. Mater. Trans. A*, vol. 28, pp. 2137–2142, 1997.

[10] N. Pourkia, M. Emamy, H. Farhangi, and S. H. Seyed Ebrahimi, "The effect of Ti and Zr elements and cooling rate on the microstructure and tensile properties of a new developed super high-strength aluminum alloy," *Mater. Sci. Eng. A*, vol. 527, pp. 5318–5325, 2010.

[11] E. Lavernia, G. Rai, and N. J. Grant, "Rapid solidification processing of 7xxx aluminium alloys: a review," *Mater. Sci. Eng.*, vol. 79, pp. 211–221, 1986.

[12] P. N. Anyalebechi, T. N. Rouns, and R. E. Sanders Jr., "Effects of cooling cate and grain refining on constituent phase particle size in as-cast 3004 alloy," in *Light Metals 1991*, 1990, pp. 21–850.

[13] F. J. Humphreys and P. N. Kalu, "Annealing processes: recovery, recrystallization, and grian growth," in *Risu National Laboratory*, 1986, pp. 385–390.

[14] Y. Birol, "The performance of Al-Ti-C grain refiners in twin-roll casting of aluminum foilstock," *J. Alloys Compd.*, vol. 430, pp. 179–187, 2007.

[15] L. Yu, X. Liu, Z. Wang, and X. Bian, "Grain refinement of A356 alloy by AlTiC/AlTiB master alloys," *J. Mater. Sci. Lett.*, vol. 40, pp. 3865–3867, 2005.

[16] H. T. Kim and S. W. Nam, "Solidification cracking susceptibility of high strength aluminum alloy weldment," *Scr. Mater.*, vol. 34, no. 7, pp. 1139–1145, 1996.

[17] J. E. Hatch, *Aluminum: Properties and Physical Metallurgy*. ASM, 1984.

[18] T. Sheppard, *Extrusion of Aluminium Alloys*. Kluwer Academic Publishers Group, 1999.

[19] X. M. Li and M. J. Starink, "Identification and analysis of intermetallic phases in overaged Zr-containing and Cr-containing Al-Zn-Mg-Cu alloys," *J. Alloys Compd.*, vol. 509, pp. 471–476, 2011.

[20] S. H. Seyed Ebrahimi, M. Emamy, N. Pourkia, and H. R. Lashgari, "The microstructure, hardness, and tensile properties of a new super high strength aluminum alloy with Zr addition," *Mater. Des.*, vol. 31, pp. 4450–4456, 2010.

[21] D. J. Beerntsen, "Effect of vanadium and zirconium on the formation of CrAl7 primary crystals in 7075 aluminum alloy," *Metall. Trans. B*, vol. 8, pp. 687–688, 1977.

[22] L. E. Steele and D. L. W. Collins, "Giant chromium intermetallics in commercial Al-Zn-Mg-Cu alloys," *J. Inst. Met.*, vol. 88, pp. 260–265, 1959.

[23] C. Mondal and A. K. Mukhopadhyay, "On the nature of T (Al2Mg3Zn3) and S (Al2CuMg) phases present in as-cast and annealed 7055 aluminum alloy," *Mater. Sci. Eng. A*, vol. 391, pp. 367–376, 2005.

[24] L. Hai, C. Dahu, W. Zhixiu, and Z. Ziqiao, "High-pressue homogenization treatment of Al-Zn-Mg-Cu aluminum alloy," *J. Mater. Sci.*, vol. 43, pp. 1583–1586, 2008.

[25] K. Chen, H. Liu, Z. Zhang, S. Li, and R. I. Todd, "The improvement of constituent dissolution and mechanical properties of 7055 aluminum alloy by stepped heat treatments," *J. Mater. Process. Technol.*, vol. 142, no. 1, pp. 190–196, Nov. 2003.

[26] J. P. Schaffer, A. Saxena, S. D. Antolovich, T. H. Sanders Jr., and S. B. Warner, *The Science and Design of Engineering Materials*. Atlanta, GA: WCB/McGraw-Hill, 1999.

[27] W. Kurz and D. J. Fisher, *Fundamental of Solidifcation*. CRC Press, 1998.

[28] R. Nadella, D. G. Eskin, Q. Du, and L. Katgerman, "Macrosegregation in direct-chill casting of aluminum alloys," *Prog. Mater. Sci.*, vol. 53, pp. 421–480, 2008.

[29] M. C. Flemings and G. E. Nereo, "Macrosegregation part 1," *AIME Met. Soc. Trans.*, vol. 239, no. 9, pp. 1449–1461, 1967.

[30] M. C. Flemings, R. Mehrabian, and G. E. Nereo, “Macrosegregation part 2,” *Trans. Met. Soc. AIME*, vol. 242, no. 1, pp. 41–49, 1968.

[31] M. C. Flemings and G. E. Nereo, “Macrosegregation part 3,” *Trans. Met. Soc. AIME*, vol. 242, no. 1, pp. 50–55, 1968.

[32] M. Lalpoor, D. G. Eskin, D. Ruvalcaba, H. G. Fjaer, A. Ten Cate, N. Ontijt, and L. Katgerman, “Cold cracking in DC-cast high strength aluminum alloy ingots; an intrinsic problem intensified by casting process parameters,” *Mater. Sci. Eng. A*, vol. 528, pp. 2831–2842, 2011.

# CHAPTER 4

# THE HOMOGENIZATION OF AL-ZN-MG-CU ALLOYS

The processing of 7xxx-series aluminum alloys includes a wide range of thermo-mechanical treatments including homogenization. Homogenization, which is carried out after the casting process, serves to remove micro-segregation from the as-cast structure as well as dissolve large soluble phases that form during solidification. However, the homogenization process serves other important functions such as increasing the workability of the ingot, and controlling the precipitation, growth, and dispersion of dispersoids [1]–[3].

For high solute 7xxx-series alloys like 7136 (8.4-9.4 wt.% Zn, 1.8-2.5 wt.% Mg, 1.9-2.5 wt.% Cu) and 7055 (7.6-8.4 wt.% Zn, 1.8-2.3 wt.% Mg, 2.0-2.6 wt.% Cu), a large number of constituent particles often remain in the alloy after conventional processing due to the proximity of these alloys to the solid-solubility limit of the Al-Zn-Mg-Cu system [4]–[7]. Therefore, non-conventional processing steps are utilized to give these alloys the desired properties (i.e. – mechanical strength, corrosion resistance, fracture toughness, etc.), including complex multi-step homogenization treatments [8].

The following is a brief overview on the homogenization of 7xxx-series alloys including the governing diffusion mechanisms, dispersoid precipitation and growth, and the effects of multi-stage homogenization treatments. It is important to note that due to the highly proprietary nature of homogenization that only single-step homogenization treatments where used in this work. Extrusions provided by the Universal Alloy Corporation (UAC) were homogenized prior to delivery at the Georgia Institute of Technology (GT).

### 4.1 Mechanisms Governing Homogenization

The as-cast microstructure is often characterized by the presence of large intermetallic particles that were rejected to the interdendritic regions during solidification and the presence of micro-segregation across the dendrite cell [3]. Homogenization aims to dissolve the large intermetallic phases into solution as well as decrease the degree of micro-segregation. Therefore, in order to quantify the homogenization process a clear understanding of the diffusion process is essential.

Consider the flow of atoms between two atomic planes, A and B, separated by a distance b in one direction x. The number of atoms in each plane can be given by Equation 4:

$$n_x = c_x b \tag{4}$$

Where $c_x$ is the concentration of diffusion atoms in plane x. Likewise, the number of jumps per unit time by one atom is given by $pv_v$, where p is the probability of any one jump in the x direction and $v_v$ is the mean frequency with which an atom leaves a site. Therefore, the number of atoms leaving plane A and arriving at B in a unit of time is $p_x v_j c_1 b$, and the number of atoms leaving B and arriving at A is given by $p_x v_j c_2 b$. The net gain of atoms at B is therefore given by Equation 5:

$$J_x = p_x v_j b(c_1 - c_2) \tag{5}$$

Where $J_x$ is the flux of the diffusing atoms. Sheppard [3] states that by setting $c_1 - c_2 = -b(dc/dx)$ this flux becomes identical to Fick's First law given by Equation 6.

$$J_x = -p_x v_j b^2 (dc/dx) = -D(dc/dx) \tag{6}$$

Where D is the diffusion coefficient, which for fcc lattices where $b = a/\sqrt{2}$ is taken to be equal to $(1/12)v_j a^2$ [3].

Sheppard [3] points out that while there are many conceivable transport mechanisms for atomic movement in aluminum, the continual migration of vacancies is the most likely. Atomic diffusion via vacancy migration depends on two factors: the

probability that a site is vacant, and the probability that an atom has the required activation energy to make the jump.

Fricke [9] states that the diffusion coefficient D varies with temperature according to the Arrhenius relation:

$$D = D_0 \exp\left(\frac{-Q}{RT}\right) \tag{7}$$

Where T is the absolute temperature, R is the universal gas constant, Q is the activation for diffusion, and $D_0$ is known as the frequency factor. It should be noted that when expanded (see Shepard [3]) $D_0$ contains a frequency factor, *f*, which is related to the probability of an atom jumping back to its previous position. For FCC lattices, *f* is taken as 0.80 [3].

The temperature at which a particular alloy is homogenized is dictated by a number of factors including: the incipient melting temperature, the precipitation and coarsening kinetics of dispersoids, and intermetallic SHT temperature. More in-depth literature on temperature selection can be found here: [3], [10]. Likewise, several factors contribute to the time required to homogenize a 7xxx-series alloy including the size of the dendrites, and the diffusion rates of the alloyed elements (see Table 1). Once a temperature and time have been established, the homogenization treatment can be customized for various purposes like dispersoid precipitation using Equation 8.

$$\frac{t_1}{t_2} = exp\left[\frac{-Q}{R}\left(\frac{1}{T_1} - \frac{1}{T_2}\right)\right] \tag{8}$$

Where $t_1$ and $t_2$ are times, $T_1$ and $T_2$ are absolute temperatures, Q is the activation energy for a given element or alloy, and R is the universal gas constant. Equation 8 allows an equivalent temperature and time for homogenization to be calculated given the alloy will not experience incipient melting or disperoid coarsening. For example if an alloy was originally homogenized at 470°C (878°F) for 24 hours, but there was a desire to lower the homogenization temperature to 450°C (842°F) then Equation 8 could be used to show the alloy would need be at 450°C for 42.1 hours to have the same equivalent time.

Table 1 – *Diffusion coefficients for various elements in aluminum at 470°C (878°F)* [3], [9]–[11].

| Element | $D_0$ ($m^2/s$) | Q (kJ/mol) | D ($m^2/s$) |
|---|---|---|---|
| **Silicon (Si)** | 9.00E-05 | 125.60 | 1.33E-13 |
| **Iron (Fe)** | 4.10E-15 | 58.60 | 3.11E-19 |
| **Copper (Cu)** | 2.90E-05 | 125.60 | 4.29E-14 |
| **Manganese (Mn)** | 2.20E-05 | 121.40 | 6.43E-14 |
| **Magnesium (Mg)** | 1.10E-04 | 117.20 | 6.34E-13 |
| **Chromium (Cr)** | 3.00E-11 | 62.80 | 1.15E-15 |
| **Nickel (Ni)** | 4.40E-04 | 145.69 | 2.52E-14 |
| **Zinc (Zn)** | 1.10E-05 | 93.70 | 2.85E-12 |
| **Titanium (Ti)** | 1.12E-01 | 260.51 | 5.43E-20 |
| **Zirconium (Zr)** | 7.28E-02 | 347.00 | 8.58E-19 |
| **Silver (Ag)** | 1.30E-05 | 116.75 | 8.06E-14 |
| **Vanadium (V)** | 1.60E00 | 302.96 | 8.05E-22 |
| **Gallium (Ga)** | 3.10E-06 | 100.00 | 2.89E-13 |
| **Germanium (Ge)** | 3.20E-07 | 83.70 | 4.19E-13 |
| **Cadmium (Cd)** | 3.20E-08 | 62.80 | 1.23E-12 |
| **Hydrogen (H)** | 2.10E-05 | 11.00 | 1.23E-08 |
| **Helium (He)** | 3.00E-04 | 155.00 | 3.82E-15 |
| **Lithium (Li)** | 4.50E-04 | 138.00 | 8.98E-14 |
| **Beryllium (Be)** | 5.20E-03 | 167.00 | 9.49E-15 |
| **Cobalt (Co)** | 4.60E-02 | 176.00 | 1.96E-14 |
| **Indium (In)** | 1.20-E05 | 117.00 | 7.16E-14 |
| **Tin (sn)** | 2.50E-05 | 121.00 | 7.81E-14 |
| **Uranium (U)** | 1.00E-05 | 117.00 | 5.97E-14 |
| **Plutonium (Pu)** | 7.20E05 | 318.00 | 3.20E-17 |

The diffusion process occurring during homogenization was illustrated by Fan *et al.* [12] in an Al-6.31wt.%Zn-2.33Mg-1.7Cu-0.12Zr-0.09Fe-0.05Si experimental alloy. It was shown that the as-cast structure of said alloy consisted chiefly of S- ($Al_2CuMg$), T- ($Al_2Mg_3Zn_3$), and η-phase ($MgZn_2$); however, the segregation of solute that occurred during solidification lead to a high concentration of η along the inter-dendritic (eutectic) regions with an extended composition range of $Mg(Zn, Cu, Al)_2$. During the homogenization process (460°C for 24 hours), it was observed that because of the slow diffusion velocity of Cu compared to Zn and Mg there existed a gradual diffusion transformation of η to S-phase in the inter-dendritic channels [12]. The driving force for this transformation was stated as being the supersaturation of Cu left behind by the

diffusing Zn and Mg. Following nucleation, S-phase coarsened gradually along the pre-existing η-phase until the transformation was complete. Fan *et al.* [12] hypothesized that the reaction was probably controlled by the diffusion of Cu and Zn between Al-matrix and η-phase boundary. Upon completion of the η to S-phase transformation, S-phase began to decrease in volume fraction until it begins to go fully into solution, which starts to occur after 12 hours at 460°C [12].

## 4.2 Common Dispersoids in 7xxx-Series Alloys

In addition to removing micro-segregation and dissolving large, soluble intermetallic particles, homogenization is also utilized to precipitate out a fine dispersion of dispersoids. These dispersoids inhibit recrystallization (REX) during subsequent plastic deformation (i.e. – extrusion, rolling, etc.) and solution heat treatment (SHT). The four main alloying elements that form dispersoids in 7xxx-series alloys are zirconium (Zr), manganese (Mn), scandium (Sc), and chromium (Cr). It should also be noted that dispersoids directly affect the quench sensitivity of 7xxx-series aluminum alloys during SHT as they are, along with grain boundaries, the primary precipitation sites for heterogeneous nucleation [13], [14].

### 4.2.1 Zirconium (Zr)

Nes [15] states that for high strength 7xxx-series alloys that small additions of Zr have a profound effect on recrystallization resistance, mechanical properties, stress corrosion cracking resistance, and quench sensitivity. The addition of Zr generally creates spherical, metastable, coherent dispersoids with an $Al_3Zr$ composition [16], [17]. Although, in some cases fan-shaped particles, rod-like particles in the <100> planes, and/or plates on the {100} planes have been shown to exist [15]. Zr dispersoids have been shown to primarily nucleate heterogeneously on sub-grain boundaries and dislocations [15].

The Al-Zr phase diagram (see Figure 7) is a peritectic for small alloying additions, and therefore Zr tends to segregate towards the center of the dendrite structure

during solidification [18]. This segregation during solidification leads to an insufficient Zr concentration in the inderdentric channels creating a dispersoid free zone (DFZ) [19]. This can be shown by simple Schiel equation model (see Equation 9) as can be seen in Figure 8 [20]:

$$C_s = k\text{C}_{Zr}(1-f_s)^{(k-1)} \quad (9)$$

Where k is the portioning coefficient, $\text{C}_{Zr}$ is the mean concentration of Zr in the matrix, and $f_s$ is the fraction of metal solidified. The following assumptions were made in the calculations presented in Figure 8: the alloy was 7136, k was taken to be 1.4 (see Robson [18]), and $\text{C}_{Zr}$ was taken as 0.11 wt.%. Additionally, $f_s$ was assumed to increase linearly from 0-1 (1-D growth model), which meant it could be replaced by $f_x$ (the fractional distance across the dendrite arm).

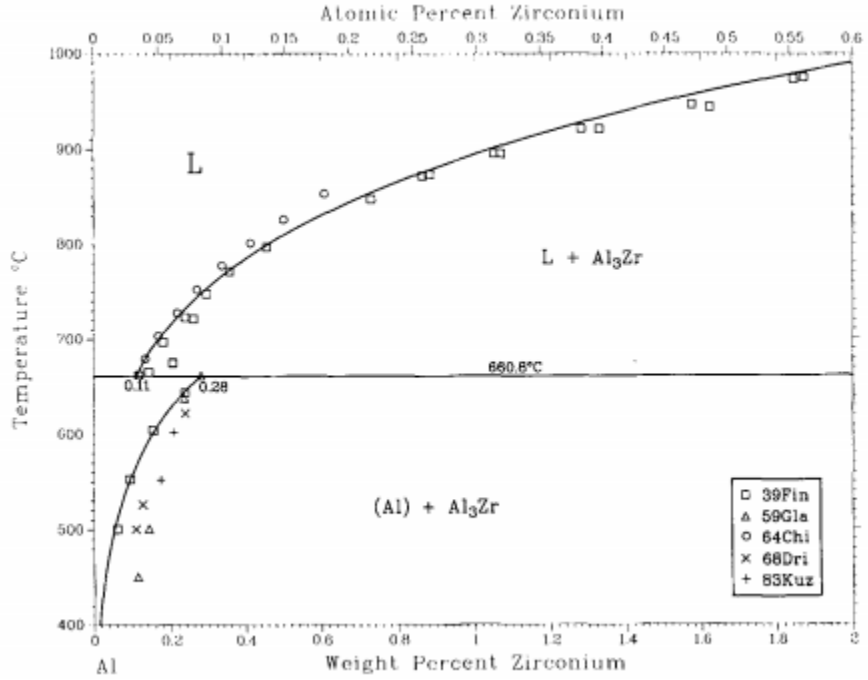


Figure 7 – *The aluminum-rich section of the aluminum-zirconium phase diagram* [21].

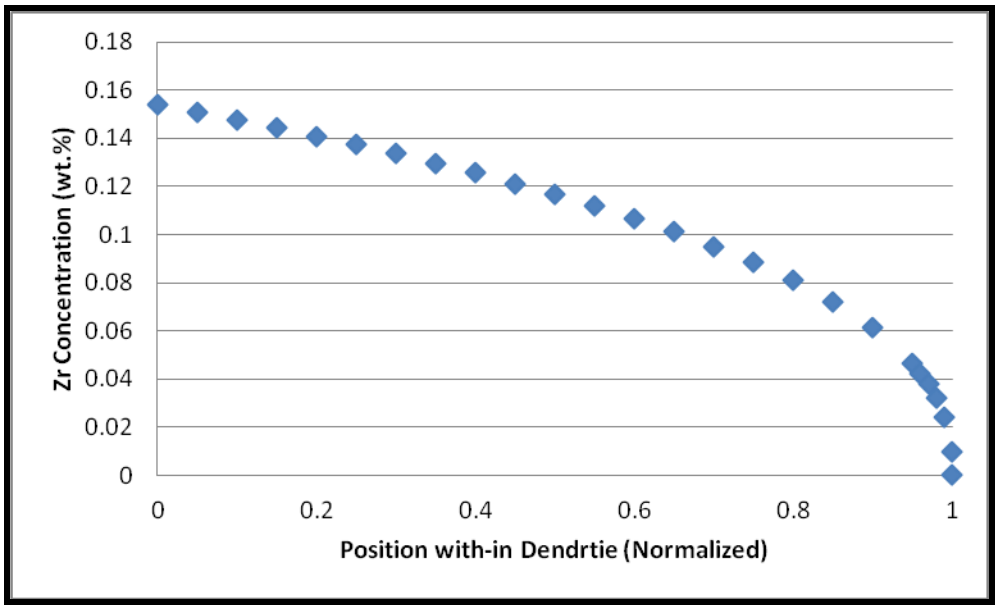


Figure 8 – *Estimation of Zr in solidified 7136. k was estimated as 1.4 and $C_{Zr}$ was taken to be 0.11wt.%. Note: position "0" is taken as the center of the dendrite and postion "1" is taken as the interdendritic region.*

The interdendrtic regions are populated by large Fr and Si rich consitutent particles, which serve as catalysts and nucleation sites for REX [17]. Once a grain begins to REX, it is only stopped when the migrating REX front encounters a sufficent number of dispersoids to become pinned by the Zener drag effect [22], [23]. The Zener drag effect for coherent particles assuming a random spatial correlation between the boundaries and the dispersoids is given by [1]:

$$P_z = \frac{3V_v\gamma}{r} \tag{10}$$

Where $V_v$ is the local volume fraction of dispersoids, r is the particle radius, and $\gamma$ is the energy of the migrating grain boundary. Therefore, there exists a criticl value of $V_v/r$ that will overcome the driving force of the migrataing boundary. It is evident that this value can be increased most easliy by increasing the local volume fraction of dispersoids or reducing their radius. However, volume fraction is often fixed based on alloy composition, so smaller dispersoids are typically disired. Nes [15] gives the radius of Zr dispersoids as 20 to 60 nm, thus explaining their effectivness as REX inhibitors.

Homogenization temperature, which provides the driving force for dispersoid precipiation and growth, is therefore crtical. At high homogenization temperatures (i..e. – 475-490°C), the solubility and the diffusion rate of Zr in Al are high. This leads to a low $V_v$ of dispersoids with a large radius, both of which are detrimental to the final product with respect to REX. However, various contradictions [15], [24]–[26] around apprioate first step temperatures appear to suggest it is an alloy specific property. For example, Lu *et al.* [27] showed there was no apprecible level of Zr disperoid precipiation below 450°C for 7150, but Deng *et al*. [26] showed apprecible dispersoid precipiation at 400°C for 7085. While care is often taken to avoid dispersoid coarsening, tt has been shown that once Zr dispersoids were fully precipitated their growth was relatively slow [15], [28].

Zr additions have also been shown to reduce grain size [29], [30]. This was attributed to the fact that Zr dispersoids can act as hetergenous nucleation sites for the aluminum matrix as well as η-phase. This reduction in grain size allows for a more uniform microstructure, which also aids in the homogenization process.

### 4.2.2 Manganese (Mn)

Mn additions, which generally range in the 0.0-0.8 wt.% range, to 7xxx-series alloys can result in the formation of Al-Mn-Cu and Al-Mn-Fe dispersoids [31], [32]. The Al-Mn binary system is a eutectic as opposed to the peritectic Al-Zr system. This means the Mn concentrations in the as-cast structure are higher in the inter-dendritic channels rather than the center of the dendrites [32]–[34].

### 4.2.3 Scandium (Sc)

Small additions of Sc cause $Al_3Sc$ dispersoids to precipitate out of the aluminum solid solution from the melt leading to an increase in mechanical properties, weldability, and REX resistance [35], [36]. The $Al_3Sc$ dispersoid is a stable heterogeneous particle with a $L1_2$ FCC structure and a melting point of 1266°C (2311°F) [35]. The maximum solubility of Sc in Al at 660°C (1220°F) is approximately 0.38 wt.% [37]. Sc-dispersoids

precipitate much more rapidly and homogenously than Zr-dispersoids, but are known to also coarsen at a faster rate [35].

The effects of Sc are further enhanced with the addition of Zr to form the complex $Al_3(Zr_xSc_{1-x})$ dispersoid [38]. Yongdong *et al*. [36] showed that Sc additions had little to no effect in normal alloying quantities without the addition of Zr. It was suggested that this was due to the tendency of Sc to substitute for Al in the Al-Zr unit cell, and it was noted that Sc often stays in solid solution without the presence of Zr. Therefore, it could be stated that Sc additions help "nucleate" α-Al rather than its on dispersoid in normal alloying quantities. Riddle and Sanders [35] showed that Sc additions did improve REX resistance in Al-Sc-Zr-Mg alloys. It was shown that the $Al_3(Zr_xSc_{1-x})$ dispersoid displayed a nucleation rate similar to that $Al_3Sc$, but did not coarsen as rapidly increasing its effectiveness [35], [38].

Sc additions have also been shown to greatly improve the resistance of 7xxx-series alloys to SCC [37]. This observation is consistent with the inhibition of REX by the presence of the $Al_3(Zr_xSc_{1-x})$ dispersoid. However, the use of Sc in commercial 7xxx-series alloys has been limited due to its scarcity and therefore cost.

### 4.2.4 Chromium (Cr)

The Al-Mg-Cr dispersoid, also known as E-phase, is precipitated out of solid solution during homogenization when Cr additions up to 0.3 wt.% are made to 7xxx-series alloys [31]. E-phase is typically on the order of 0.02 to 0.5 μm in size with an extended composition range. Staley [31] reported the composition of E-phase as $Al_{12}Mg_2Cr$ whereas Li and Starink [39] and Lim *et al.* [13] reported it as $Al_{18}Mg_3Cr_2$ and $Al_{18}Mg_2Cr_3$, respectively.

Concerns over quench sensitivity and REX have led the replacement of Cr in modern 7xxx-series alloys with Zr, particularly for thick product applications [39], [40]. However, Li *et al.* [39] showed that Cr-containing alloys like Zn, Mg, Cu contents similar

to 7075 displayed smaller volume fraction of course intermetallic particles (i.e. – S-phase and $Al_7Cu_2Fe$) than Zr-containing alloys like 7050.

### 4.3 The Effects of Multi-Step Homogenization Treatments

Multi-step homogenization processes are typically required in modern 7xxx-series alloys like 7136 and 7055. The first step(s) usually aims to precipitate out a fine dispersion of dispersoids, and the later steps aim to dissolve equilibrium phases and coarse intermetallics back into solution to increase workability [3], [27], [41]. Single-step homogenization processes typically are inadequate at dissolving all the equilibrium phases in modern alloys like 7055 due their composition being close to the solid solubility limit of the Al-Zn-Mg-Cu system [42].

Chen *et al.* [42] showed that stepped homogenization treatments (ex. – 455°C for 24 hours followed by 490°C for 50 hours) in 7055 allowed for almost complete dissolution of S-, T-, and η-phase without localized melting. This was attributed to the dissolution of η-phase, which has a melting temperature of approximately 475°C (887°F), during the first homogenization step. The melting temperatures of the quasi-binary T- and S-phase eutectics have been reported as 489°C (912°F) and 518°C (964°F), respectively [43].

With respect to dispersoid nucleation and growth, especially the $Al_3Zr$ dispersoid, a great deal of research has gone into optimizing the homogenization process. Models [32], [18], [19], [44], [45] have been constructed that effectively describe this process in modern 7xxx-series alloys. These models are beyond the scope of this review since dispersoid optimization will largely be ignored, but each follows a similar pattern. First, the distribution of Zr atoms (or other dispersoid forming elements) are calculated using the Schiel equation. These local concentrations are then plugged into a nucleation model. Once dispersoid particles have been "nucleated," these particles are subjected to rigorous growth/shrinkage analysis. The objective of each model is then to maximize the Zener drag effect.

Table 2 displays a comparison of several single- and multi-step homogenization treatments found in literature. The homogenizations listed in Table 2 had varying effects due to alloy composition and other processing parameters. The table is only meant to serve as a general guide to homogenization treatments.

Table 2 – *Various single-step and multi-step homogenization procedures found in literature. It should be noted that all compositions are in wt.% and an Al-bal. is assumed* [3], [8], [32], [18], [46], [29], [47], [26].

| Alloy | Step 1 | Step 2 | Step 3 | Lead Author |
|---|---|---|---|---|
| 7055 | 470°C-50 hrs | 478°C-50 hrs | - | Chen |
| 7055 | 455°C-24 hrs | 490°C-50 hrs | - | Chen |
| 7085 | 400°C-12 hrs | 470°C-12 hrs | - | Deng |
| 12Zn-3.3Mg-2.5Cu-0.3Zr | 450°C-24 hrs | - | - | S. Ebrahimi |
| 7020 | 470°C-24 hrs | - | - | Eivani |
| 12Zn-3.5Mg-3.0Cu-0.14Zr | 450°C-96 hrs | 460°C-128 hrs | - | Hai |
| 7050, 7075 | 250°C-24 hrs | 470°C-24 hrs | - | Ou |
| 7050 | 418°C-5 hrs | 475°C-24 hrs | - | Robson |
| Unspecified | 200°C-2 hrs | 460°C-4 hrs | 475°C-12 hrs | Sheppard |

### 4.4 Summary

The basic mechanisms governing the homogenization process were covered as well as the effects of common dispersoids. While homogenization treatments for 7xxx-series alloys are often complex and considered highly proprietary, they can have far

reaching effects on an alloy's final properties. Therefore, any systematic compositional study needs to begin with characterizing the homogenization process.

## 4.5 References


[1] J. T. Staley, "Properties related to fracture toughness," *Am. Soc. Test. Mater.*, p. 71, 1976.

[2] I. J. Polmear, *Light Metals*. Arnold, 1995.

[3] T. Sheppard, *Extrusion of Aluminium Alloys*. Kluwer Academic Publishers Group, 1999.

[4] T. S. Srivatsan, S. Anand, S. Sriram, and V. K. Vasudevan, "The high-cycle fatigue and fracture behavior of aluminum alloy 7055," *Mater. Sci. Eng. A*, vol. 281, pp. 292–304, 2000.

[5] J. Champlin, J. Zakrajsek, T. S. Srivatsan, P. C. Lam, and M. Manoharan, "Influence of notch severity on the impact fracture behavior of aluminum alloy 7055," *Mater. Des.*, vol. 20, pp. 331–341, 1999.

[6] T. S. Srivatsan and V. K. Vasudevan, "Temperature and the ductility, deformation, and fracture of Al 7055," *J. Met.*, vol. 1, pp. 42–45, 1999.

[7] The Aluminum Association, *International Alloy Designations and Chemical Composition Limits for Wrought Aluminum and Wrought Aluminum Alloys*. Arlington, VA, 2009.

[8] L. Hai, C. Dahu, W. Zhixiu, and Z. Ziqiao, "High-pressue homogenization treatment of Al-Zn-Mg-Cu aluminum alloy," *J. Mater. Sci.*, vol. 43, pp. 1583–1586, 2008.

[9] W. G. Fricke Jr., "Correlation between frequency factor and activation energy for diffusion in aluminum alloys," *Scr. Metall.*, vol. 6, pp. 1139–1144, 1972.

[10] J. E. Hatch, *Aluminum: Properties and Physical Metallurgy*. ASM, 1984.

[11] J. Dickson, L. Zhou, a. Paz y Puente, M. Fu, D. D. Keiser, and Y. H. Sohn, "Interdiffusion and reaction between Zr and Al alloys from 425° to 625 °C," *Intermetallics*, pp. 1–9, Feb. 2014.

[12] X. Fan, D. Jiang, Q. Meng, and L. Zhong, "The microstructural evolution of an Al-Zn-Mg-Cu alloy during homogenization," *Mater. Lett.*, vol. 60, pp. 1475–1479, 2006.

[13] S. Lim, S. Yun, and S. Nam, “Improved quench sensitivity in modified aluminum alloy 7175 for thick forging applications,” *Mater. Sci. Eng. A*, vol. 371, no. 1–2, pp. 82–90, Apr. 2004.

[14] K. G. Kent, “The effect of quench rate on the microstructure and stress corrosion resistance of a weldable Al-Zn-Mg alloy,” *J. Inst. Met.*, vol. 97, pp. 127–128, 1969.

[15] E. Nes, “Precipitation of the metastable cubic Al3Zr-phase in subperitectic Al-Zr alloys,” *Acta Metall.*, vol. 20, pp. 499–506, 1972.

[16] H. P. Degischer, G. Rumplmair, W. Lacom, and F. Kutner, “Distribution of Al3Zr precipitates in AlZn4.5Mg,” in *Proc. Int. Electron Microscopy*, 1984, pp. 753–754.

[17] O. Engler, E. Sachot, J. C. Ehrstrom, A. Reeves, and R. Shahani, “Recrystallization and texture in hot deformed aluminum alloy 7010 thick plates,” *Mater. Sci. Technol.*, vol. 12, pp. 717–729, 1996.

[18] J. D. Robson, “Optimizing the homogenization of zirconium containing commercial aluminium alloys using a novel process model,” *Mater. Sci. Eng. A*, vol. 338, pp. 219–229, 2002.

[19] J. D. Robson and P. B. Prangnell, “Dispersoid precipitation and process modelling in zirconium containing commerical aluminum alloys,” *Acta Mater.*, vol. 49, pp. 599–613, 2001.

[20] E. Scheil, “Bemerkugen zur schichtkristallbildung,” *Zeitchrift fuer Met.*, vol. 34, pp. 70–72, 1942.

[21] J. L. Murray, A. Peruzzi, and J. P. Abriata, “The Al-Zr (aluminum-zirconium) system,” *J. Phase Equilibria*, vol. 13, pp. 277–291, 1992.

[22] C. S. Smith, “Grains, phase, and interphase: an interpretation of the microstructure,” *Trans. Met. Soc. AIME*, vol. 175, pp. 15–51, 1948.

[23] E. E. Underwood, *Quantitative Stereology*. Addison-Wesley, 1970.

[24] X. Fan, D. Jiang, Q. Meng, B. Zhang, and T. Wang, “Evolution of eutectic structures in Al-Zn-Mg-Cu alloys during heat treatment,” *Trans. Met. Soc. AIME*, vol. 16, pp. 577–581, 2006.

[25] Y. Deng, Z. Yin, and F. Cong, “Intermetallic phase evolution of 7050 aluminum alloy during homogenization,” *Intermetallics*, vol. 26, pp. 114–121, 2012.

[26] Y. D. Li and W. L. Wu, “Microstructural evolution of Al-Zn-Mg-Cu alloy during homogenization,” *J. Mater. Sci.*, vol. 46, pp. 875–881, 2011.

[27] X. Lü, E. Guo, P. Rometsch, and L. Wang, “Effect of one-step and two-step homogenization treatments on distribution of Al3Zr dispersoids in commercial AA7150 aluminium alloy,” *Trans. Nonferrous Met. Soc. China*, vol. 22, no. 11, pp. 2645–2651, Nov. 2012.

[28] M. S. Zedalis and M. E. Fine, “Precipitation and ostwald ripening in dilute Al base-Zr-V alloys,” *Metall. Trans. A*, vol. 17, pp. 2187–2198, 1986.

[29] S. H. Seyed Ebrahimi, M. Emamy, N. Pourkia, and H. R. Lashgari, “The microstructure, hardness, and tensile properties of a new super high strength aluminum alloy with Zr addition,” *Mater. Des.*, vol. 31, pp. 4450–4456, 2010.

[30] N. Pourkia, M. Emamy, H. Farhangi, and S. H. Seyed Ebrahimi, “The effect of Ti and Zr elements and cooling rate on the microstructure and tensile properties of a new developed super high-strength aluminum alloy,” *Mater. Sci. Eng. A*, vol. 527, pp. 5318–5325, 2010.

[31] J. T. Staley, “Microstructure and toughness of high-strength aluminum alloys,” in *Properties Related to Fracture Toughness*, 1976, pp. 71–96.

[32] A. R. Eivani, H. Ahmed, J. Zhou, and J. Duszczyk, “An experimental and theoretical investigation of the formation of Zr-containing dispersoids in Al-4.5Zn-1Mg aluminum alloys,” *Mater. Sci. Eng. A*, vol. 527, pp. 2418–2430, 2010.

[33] U. M. Iqbal and V. S. S. Kumar, “Effect of process parameters on micriostructure and mechanical properties on severe plastic deformation process of AA7075-T6 aluminum alloy,” *Adv. Mater. Res.*, vol. 622–623, pp. 705–709, 2013.

[34] J. Murray, A. Peruzzi, and J. P. Abriata, “Alloy Phase Diagrams,” in *ASM Handbook*, 1992, pp. 2.4–2.56.

[35] Y. W. Riddle and T. H. Sanders, “A study of coarsening, recrystallization, and morphology of microstructure in Al-Sc-(Zr)-(Mg) alloys,” *Metall. Mater. Trans. A*, vol. 35, pp. 341–350, 2004.

[36] H. Yongdong, Z. Xinming, and C. Zhiqiang, “Effect of minor Sc and Zr addition on grain refinement of as-cast Al-Zn-Mg-Cu alloys,” *China Foundary*, vol. 6, pp. 214–218, 2009.

[37] A. K. Mukhopadhyay, “Microstructure and properties of high strength aluminium alloys for structural applications,” *Trans. Indian Inst. Met.*, vol. 62, no. 2, pp. 113–122, 2009.

[38] Y. W. Riddle, “Al3(Sc1-xZr) dispersoids in aluminum alloys: coarsening and recrystallization control,” Georgia Instititute of Technology, 2000.

[39] X. M. Li and M. J. Starink, “Identification and analysis of intermetallic phases in overaged Zr-containing and Cr-containing Al-Zn-Mg-Cu alloys,” *J. Alloys Compd.*, vol. 509, pp. 471–476, 2011.

[40] A. K. Mukhopadhyay, Q. B. Yang, and S. R. Singh, “The influence of zirconium on the early stages of aging of a ternary Al-Zn-Mg alloy,” *Acta Metall.*, vol. 42, no. 9, pp. 3083–3091, 1994.

[41] S. Liu, J. You, X. Zhang, Y. Deng, and Y. Yuan, “Influence of cooling rate after homogenization on the flow behavior of aluminum alloy 7050 under hot compression,” *Mater. Sci. Eng. A*, vol. 527, no. 4–5, pp. 1200–1205, Feb. 2010.

[42] K. Chen, H. Liu, Z. Zhang, S. Li, and R. I. Todd, “The improvement of constituent dissolution and mechanical properties of 7055 aluminum alloy by stepped heat treatments,” *J. Mater. Process. Technol.*, vol. 142, no. 1, pp. 190–196, Nov. 2003.

[43] The Aluminium Development Association, *Equilibrium Diagrams of Aluminium Alloy Systems*. London: The Aluminium Development Association, 1961.

[44] J. D. Robson and P. B. Prangnell, “Modelling Al3Zr dispersoid precipitation in multicomponent aluminium alloys,” *Mater. Sci. Eng. A*, vol. 352, pp. 240–250, 2003.

[45] J. D. Robson, “A new model for prediction of dispersoid precipitation in aluminium alloys containing zirconium and scandium,” *Acta Mater.*, vol. 52, pp. 1409–1421, 2004.

[46] K. Chen, H. Liu, Z. Zhang, S. Li, and R. I. Todd, “The improvement of constituent dissolution and mechanical properties of 7055 aluminum alloy by stepped heat treatments,” vol. 142, pp. 190–196, 2003.

[47] B. Ou, J. Yang, and M. Wei, “Effect of homogenization and aging treatment on mechanical properties and stress-corrosion cracking of 7050 alloys,” *Metall. Mater. Trans. A*, 2007.

# CHAPTER 5

# PLASTIC DEFORMATION OF WROUGHT ALUMINUM ALLOYS: EXTRUSION AND ROLLING

The following chapter is a brief overview of two highly complex plastic deformation processes: extrusion and rolling. More in depth analysis of each plastic deformation process covered in this chapter can be found elsewhere: [1]–[7]. The topics of recrystallization (REX), recovery, and grain growth are also briefly covered.

## 5.1 Extrusion of Aluminum Alloys

Extrusion is a complex thermos-mechanical plastic deformation process involving interactions between the processing variables and the extruded material's high temperature properties. During the extrusion process a billet is forced through a die opening with a smaller cross-sectional area via indirect compression [8]. Sheppard [1], [9] showed that extrusion is a thermally activated process involving mass transfer. The chief processing variables in the extrusion process are the extrusion ratio (R), the ram speed (V), and the extrusion temperature (T) [8]. With respect to extrudability, it has been shown that 7xxx-series become harder to extrude with increasing amounts of Zn, Mg, and Cu [10].

### 5.1.1 Direct versus Indirect Extrusions

The two most common types of aluminum extrusion are the direct and indirect methods. In a direct extrusion, a billet is placed in a container and pushed through a die opening by the ram pressure [1], [8]. This process can be seen schematically in Figure 9. The direction of metal within a direct extrusion is the same as that of the ram with the billet sliding relative to the container walls.

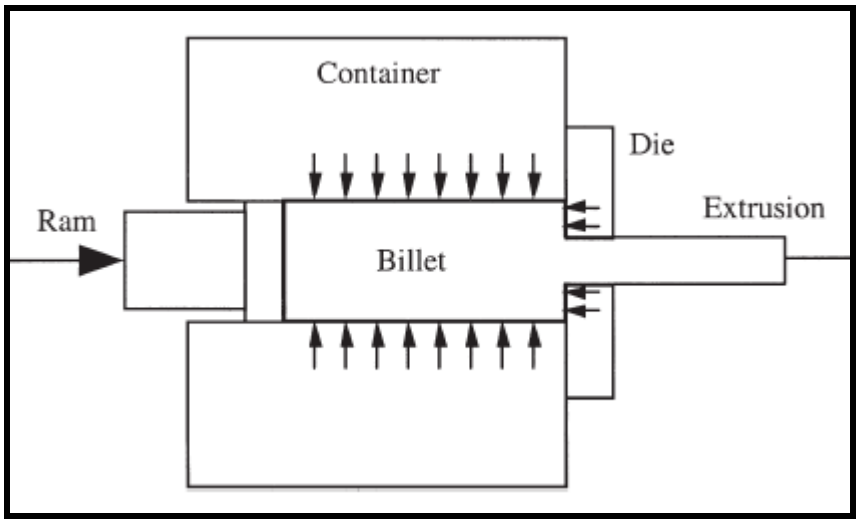


Figure 9 – *Schematic detailing the direct extrusion process* [8]. *Note – the arrows represent the various pressures on the billet during the extrusion process.*

Conversely, in the indirect extrusion method the die moves relative to the container (i.e. – the container is fixed) [1], [8]. Therefore, there is no displacement between the billet and the container. The indirect extrusion method, which is detailed in Figure 10, is characterized by the relative absence of friction between the billet surface and the container. Variations in flow patterns and pressure-displacement curves for direct versus indirect extrusions can be seen in Figures 11 and 12, respectively. Generally for aerospace applications, the indirect method produces a higher quality product as it reduces the likelihood of REX issues.

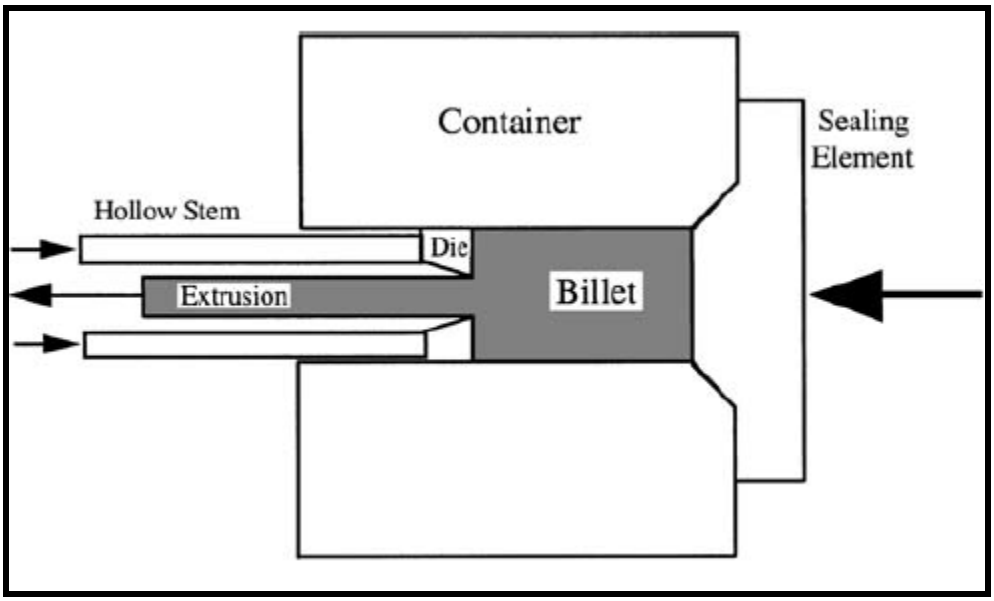


Figure 10 – *Schematic detailing the indirect extrusion process* [8].

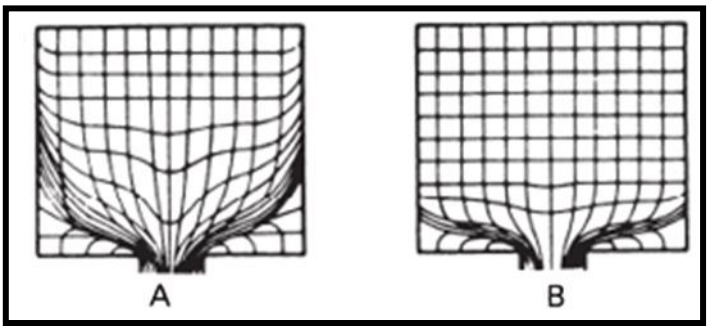


Figure 11 – *Schematic detailing the flow patterns for (a) a direct and (b) an indirect extrusion process* [8].

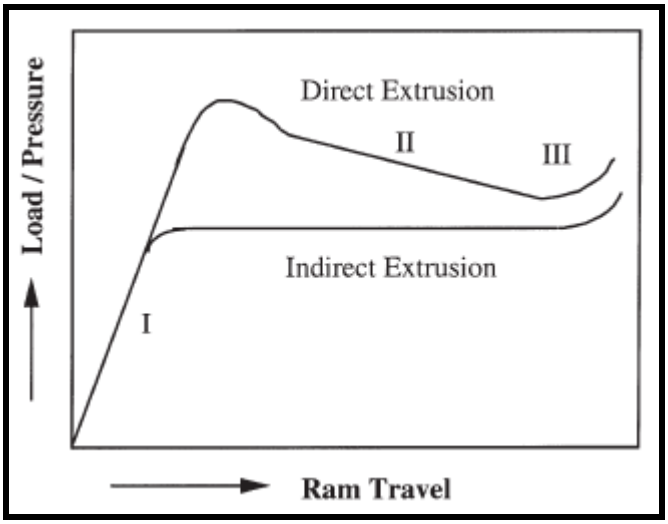


Figure 12 – *Variation of load or pressure with ram travel for both direct and indirect extrusions processes* [8]. *The steady-state region (II) is the most important region of interest as the final extruded product comes from this region.*

### 5.1.2 Extrusion Ratio

The extrusion ratio, R, is defined as the ratio of the initial cross-sectional area ($A_0$) of the billet to the final cross-sectional area of the extrude ($A_f$) and is given by Equation 11 [11]:

$$R = \frac{A_0}{A_f} \tag{11}$$

The extrusion ratio can also be directly correlated to the dead meatal zone angle inside a billet via Equation 12 as shown schematically in Figure 13 [8]:

$$\alpha = f(R, \bar{\sigma}, m, m') \tag{12}$$

Where $\bar{\sigma}$ is the flow stress, m is the friction factor between the billet and container interface, and m' is the friction factor between the flowing metal and die-bearing interface.

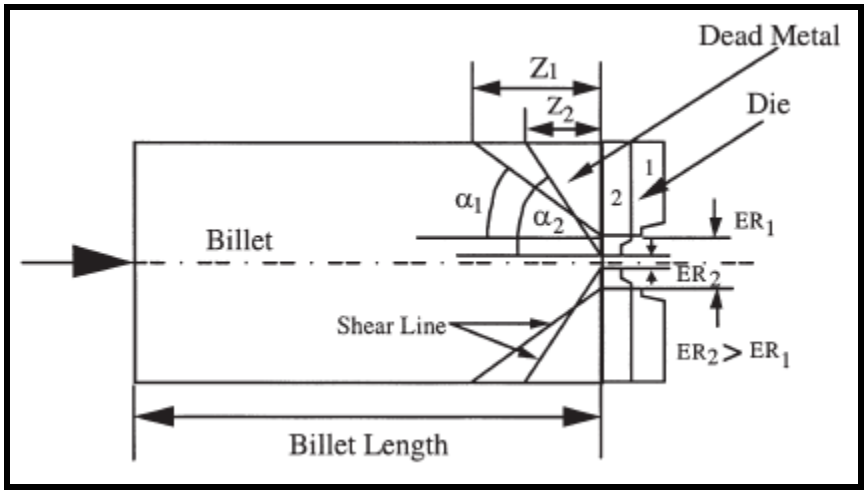


Figure 13 – *Relationship between the extrusion ratio and the dead metal zone angle* [8].

### 5.1.3 Strain Rate

The strain rate, $\dot{\varepsilon}$, is not constant during the extrusion process as it varies from point to point throughout the deformation zone; however, it is possible to define an average value for strain rate in order to model the extrusion [9]. The Feltham definition of strain rate is commonly used and is given by Equation 13:

$$\dot{\varepsilon} = \frac{6V_B D_B^2 \ln(R) \tan \omega}{D_B^3 - D_E^3} \quad (13)$$

Where

$$\omega = 54.1 + 3.45 \ln R \quad (14)$$

In equations 13 and 14 R is the extrusion ratio, $D_B$ is the grain size in the billet, $D_E$ is the grain size in the extrusion, and $V_B$ is the ram velocity.

### 5.1.4 Extrusion Temperature

The energy dissipated during the extrusion of an aluminum billet is converted to thermal energy resulting in a rise in temperature in both the transverse and perpendicular directions with respect to the ram. However, it was shown by Sheppard and Wood [12] that any transverse plan in the billet can be assumed to be at a uniform temperature at any time during the extrusion process. They showed that temperature rise during the extrusion process could be given by Equation 15:

$$\Delta T = \frac{0.95 L V_B \, t J^{-1} - \Delta T_D \, C\{t\}}{C_l\{t\}} \quad (15)$$

Where L is the billet length, $V_B$ is the ram velocity, t is the time after commencement of the ram stroke, J is the mechanical equivalent of heat, $\Delta T_D$ is the temperature differential between the billet and the container, and C{t} and $C_l${t} are time dependent constants.

The temperature distributions of aluminum alloy 6603 billets under various loading, tooling, and handling conditions was detailed by Johannes *et al.* [13]. Johannes *et al.* [13] used analytical solutions to heat transfer problems and finite element analysis to show that for aluminum billets of conventional dimensions radial thermal gradients are halved in tens of seconds, longitudinal thermal gradients are halved in hundreds of seconds, and the temperature difference between a billet and air is halved in thousands of seconds. These thermal gradients are important to understand as temperature is the most important measurable parameter in the extrusion process due to its relative contribution to the Zener-Hollomon parameter (see *5.1.5 Temperature Compensated Strain Rate*).

### 5.1.5 Temperature Compensated Strain Rate

The relationship between peak stress (or steady state stress), strain rate, and temperature during the hot plastic deformation of metallic materials can be expressed via the Zener-Hollomon parameter, Z (i.e. – the temperature compensated strain rate), and is given by Equation 16 [14]:

$$Z = \dot{\varepsilon}\, exp\left(\frac{Q_D}{GT}\right) = A_1 \sigma^{n_1} \tag{16}$$

Where $A_1$ and $n_1$ are constants, σ is the stress, $\dot{\varepsilon}$ is the strain rate, $Q_D$ the hot deformation activation energy (see Table 3), G is the gas constant, and T is the absolute temperature. However, the power law version of Z (Equation 3-6) breaks down at high stresses. Z can also be given by Equation 17, which conversely breaks down at low stresses [15].

$$Z = A_2\, exp(\beta\sigma) \tag{17}$$

It should be noted that $A_2$ and β are constants. A more general form of Z, which is applicable over a wide temperature range, was proposed by Sellars and McTegart [16] and is given by Equation 18:

$$Z = A(\sinh \alpha\sigma)^n \tag{18}$$

Where A and n are constants; α is the stress multiplier and is also an adjustable parameter given by Equation 19:

$$\alpha = \frac{\beta}{n} \approx \frac{\beta}{n_1} \tag{19}$$

As can be seen in Equation 18, the peak stress is directly related to Z. The coefficients A, α, and n can be determined via multiple regression analysis of data obtained from tension, compression, and torsions tests [1]; a selection of these constants from literature can be seen in Table 3.

Table 3 – *Z constants for several 7xxx-series alloys* [1], [17]. *Note – SHT = solution heat treated.*

| Alloy | Source | Condition | $Q_D$ (kJ/mol) | α | n | lnA |
|---|---|---|---|---|---|---|
| **Pure Al** | Li *et al.* | - | 142 | - | - | - |
| **7012** | Li *et al.* | SHT | 200-230 | - | - | - |
| **7012** | Li *et al.* | Aged | 141-162 | - | - | - |
| **7075** | Li *et al.* | SHT | 300-400 | - | - | - |
| **7075** | Li *et al.* | Aged | 143-156 | - | - | - |
| **7075** | Sheppard | - | 129.4 | 0.0141 | 5.41 | 20.75 |
| **7050** | Li *et al.* | - | 256.6 | - | - | - |
| **7050** | Sheppard | - | 151.5 | 0.0269 | 2.86 | 22.85 |
| **7056** | Li *et al.* | - | 244.64 | - | - | - |
| **7150** | Li *et al.* | - | 229.75 | - | - | - |
| **7150** | Sheppard | - | 158.8 | 0.013 | 6.1 | 29.2 |

As can be seen in Table 3, the hot deformation activation energies for solution heat-treated (SHT) alloys are higher than aged or air-cooled homogenized alloys. This is because dislocations can be pinned by solute atoms in solid solution, which increases the stress required to move the dislocation. There is also an added component of friction drag that must be accounted for when determining the activation energy of dislocation moving through a solid solution [15]. This is important to note because the rolling ingots used in this work were water-quenched after being homogenized instead of air-cooled, which makes their microstructures more like that of a SHT'ed alloy instead of atypical homogenized billet or ingot.

The importance of Z, however, lies in the fact that it can often be directly correlated to an alloy's final properties in terms of strength, fatigue resistance, and even corrosion resistance as it has a direct influence over an alloy's final microstructure [1], [8], [12], [18]. Therefore, it is important to understand the contributions of texture to an alloy's final properties, so the effects of compositional variations can be clearly delineated.

### 5.2 Rolling of Aluminum Alloys

Aluminum plate and sheet are produced via the reduction of cast ingots by rolling. Rolling is a deformation process in which ingots are passed through one or more pairs of rollers to obtain a desired thickness [19]. The difference between the initial and final thickness of a rolled product is called the draft, d, and is given by Equation 20:

$$d = t_0 - t_f \tag{20}$$

Where $t_0$ and $t_f$ are the initial and final thickness, respectively. A schematic of a typical rolling process can be seen in Figure 14. Typically, a rolled product is considered a "plate" if the product is at least 6.3 mm (0.75 in) thick [7]. If the product is between 6.3mm (0.75 in) and 0.20 mm (0.008 in), the product is considered "sheet." Anything rolled aluminum product thinner than 0.20 mm is considered "foil" [7].

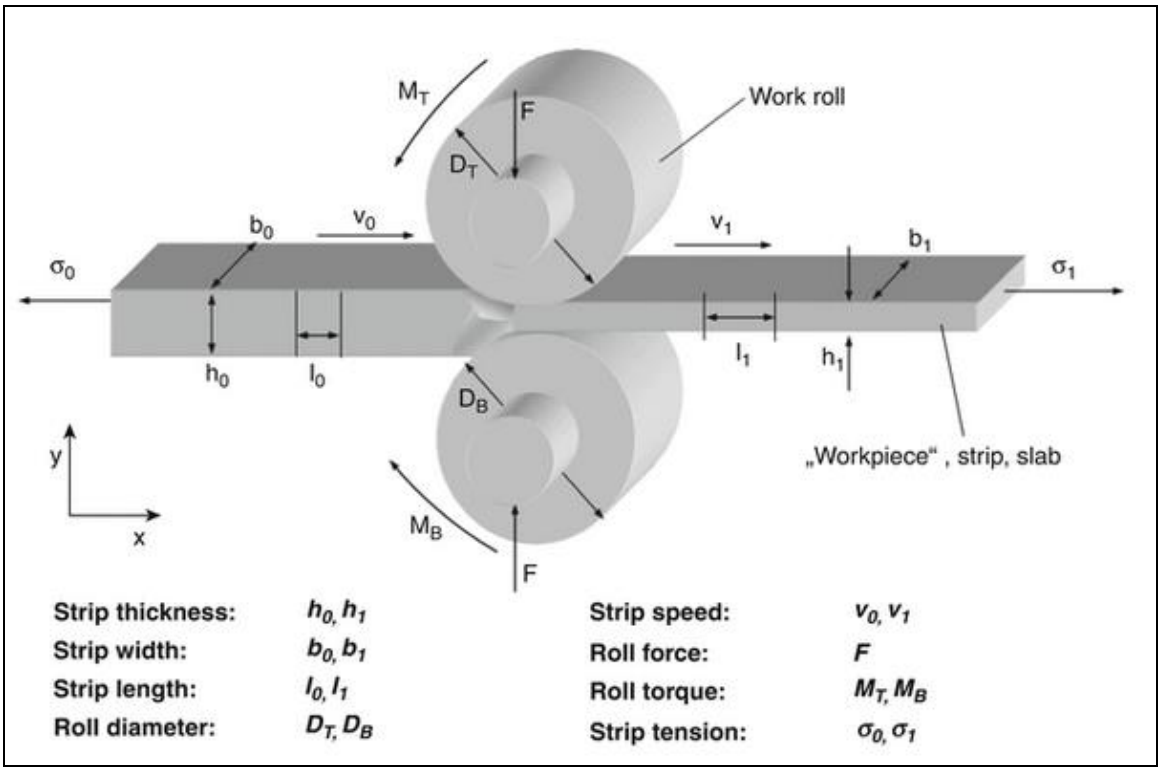


Figure 14 – *Principles of rolling and nomenclature of important variables* [20].

Like extrusion, rolling is typically a 'hot' operation that breaks down the as-cast microstructure resulting in elongated grains in the rolling direction [21]. Hot rolling also welds pores left the casting process creating a "denser, stronger metal" [7]. The degree

of work in the wrought structure is often initially uneven varying greatly from the surface to the center. For example, a thick plate may have a wrought grain structure near the surface, but may have a grain structure in the center that closely resembles the ingot's grain structure. Uniformity of plate can be accomplished can be increased via increasing the reduction percentage or by pre-forging the ingot, although care must be taken not to REX the product [21]. Between passes aluminum alloys typically experience static restoration via recovery or static REX [22]. Petkovic *et al.* [23] showed that there is a critical strain for static REX to occur, and therefore care must be taken in determining deformation procedures in order to avoid REX the product.

Aluminum product can also be "cold" rolled. Cold rolling refers to the rolling of ingots/plates/sheet/foils at temperatures low enough for stain-hardening to occur [7]. Cold rolling breaks and offsets the lattice planes thereby increasing the number of dislocations. These dislocations in turn resistive further lattice movement, which increases the material's strength. Cold rolled products typically have a better surface finish than hot rolled products, and therefore cold rolling can also be used as a secondary operation if surface finish is a concern [7].

### 5.3 Recrystallization, Recovery, and Grain Growth

The microstructural alterations that occur during deformation, solution heat treatment, and/or annealing of aluminum alloys are referred to as recrystallization, recovery, and grain growth. Humphreys [24] states it is important to understand that the three distinct processes may occur in tandem or independently of each other depending on various metallurgical and processing factors. For example, Sheppard [9] notes that the softening mechanism for high stacking fault energy materials (like aluminum) during the extrusion process is dynamic recovery, which can be subsequently followed by static REX. The following is a brief overview of all three processes; however, more in-depth analysis can be found in: [1], [5], [18], [23]–[28].

### 5.3.1 Recrystallization (REX)

Recrystallization as defined by Doherty *et al*. [27] is "the formation of a new grain structure in a deformed material by the formation and migration of high angle grain boundaries (i.e. – boundaries with a misorientation greater than 10-15°) driven by the stored energy of deformation." REX has been shown to adversely affect strength and fracture toughness while increasing ductility. The degree of REX grains in a microstructure is influenced by the distribution and morphology of second phase particles in the matrix. For example, the addition of dispersoid forming elements (ex. – Cr, Mn, Zr, Sc, etc.) have proven effect in inhibiting REX [22], [29], [30]. REX can be sub-divided into two main categories: dynamic and static REX.

The term dynamic REX refers to the REX of deformed grains during the deformation process [27]. Conversely, static REX refers to REX that occurs after the deformation process, typically during the SHT cycle and/or on the runout table. The mechanisms for each form of REX are similar, and they are both thermally activated process that only occur above a critical temperature [27]. The critical temperature for REX is dependent on the deformation percentage and the initial grain size. For example, increasing the deformation percentage of a microstructure increases the stored energy, which aids in the migration of high angle grain boundaries. Likewise, smaller grains are more prone to REX since grain boundaries often act as nucleation sites for REX.

Typically, high stacking fault energy materials like aluminum do not dynamically REX under normal extrusion conditions. However, Sun *et al.* [28] observed dynamic REX in 7075 at elevated extrusion temperatures. The dynamic REX grains grew with increasing temperature and decreasing strain rate, which is a typical characteristic of dynamic REX.

With respect to REX it should be noted that often times there is a microstructural gradient within an extrusion with equiaxed REX grains present on the surface and a wrought fibered structure in the core of the extrusion. This is attributed to the increase in

stored energy near the surface regions compared to the center of the extrusion, which provides the energy needed to overcome the Zener drag effect during SHT [10].

### 5.3.2 Recovery

In contrast to REX, recovery does not involve the movement of high angle grain boundaries [27]. Instead, recovery involves the rearrangement or the removal of defects in the crystal structure to reduce excess free energy. Hatch [5] states that during recovery dislocations are rearranged into a cellular sub-grain structure, and that this process is sometimes referred to as polygonization. Recovery is a continuous process during the SHT (or annealing) cycle that occurs until the sub-grain boundaries are completely free of dislocation tangles. During the recovery process, Hatch [5] notes that the sub-grain size will gradually increase as well. It has been shown that the sub-grain size of an aluminum alloy is a function of Z as shown in Equation 21 [9]:

$$d^{-m} = x + y \ln Z \tag{21}$$

Where x and y are material constants. Sun *et al.* [28] showed that for 7075 extruded below 350°C (662°F) that only dynamic recovery occurred; however at extrusion temperatures above 350°C local dynamic REX was observed. Sun *et al*. [28] also noted that the number of secondary phase particles in the aluminum matrix decreased with increasing deformation temperature; the secondary phase particles tend to hinder sub-grain boundary movement, but promote dislocation absorption and rotation of the sub-grain structure both of which aid continuous recovery. While the removal of defects can decrease the strength of an aluminum alloy (while at the same time increasing its ductility), it can increase the electrical conductivity of the alloy by increasing the mean-free path of electrons [27].

### 5.3.3 Grain Growth

The competing process of grain growth is a process by which neighboring grains are consumed by each other in an attempt to reduce excess free energy [5]. Grain growth can be beneficial or detrimental pending the intended application. For instance, at room

temperature many metals exhibit a Hall-Patch behavior (i.e. – small grain sizes means a higher yield stress), but at high temperatures the smaller the grains the greater the tendency of the metal to creep. This is due to the disordered nature of grain boundaries acting as "super-highways" for vacancies allowing them rapidly diffuse through the matrix [26], [31]. Grain growth can be hindered by dispersoids via Zener pinning much like a migrating REX grain boundary [26].

## 5.4 Summary

The plastic deformation processes of extrusion and rolling were briefly covered as well as the competing processes of REX, recovery, and grain growth. Both plastic deformation processes will be utilized in this work, although exact processing parameters may not be given. However, it is important to comprehend the effects each plastic deformation process can have on the mechanical properties and microstructure of an aluminum alloy. Similarly, a knowledge of the basic effects of REX, recovery, and grain growth in aluminum alloys is paramount in distinguishing and characterizing compositional effects from microstructural effects on an alloy's final properties.

## 5.5 References


[1] T. Sheppard, *Extrusion of Aluminium Alloys*. Kluwer Academic Publishers Group, 1999.

[2] G. E. Dieter, H. A. Kuhn, and S. L. Semiatin, *Handbook of Workability and Process Design*. ASM, 2003.

[3] J. G. Kaufman, *Introduction to Aluminum Alloys and Tempers*. ASM, 2000.

[4] J. Hirsch, B. Skrotzki, and G. Gottstein, *Aluminum Alloys: Their Physical and Mechanical Properties*. Aachen, Germany: International Conference on Aluminum Alloys, 2008.

[5] J. E. Hatch, *Aluminum: Properties and Physical Metallurgy*. ASM, 1984.

[6] H. J. McQueen, S. Spigarelli, M. E. Kassner, and E. Evangelista, *Hot Deformation and Processing of Aluminum Alloys*. CRC Press, 2011.

[7] The Aluminum Association, *Rolling Aluminum: From the Mine through the Mill*. Aluminum Association, 1990.

[8] P. K. Saha, *Aluminum Extrusion Technology*. Metals Park, Ohio: ASM, 2000.

[9] T. Sheppard, "The modern extrusion process: temperature and speed," in *Modern Extrusion: plant, tooling, processing, and products*, University of Aston - Birmingham, 1980.

[10] S. H. Seyed Ebrahimi, M. Emamy, N. Pourkia, and H. R. Lashgari, "The microstructure, hardness, and tensile properties of a new super high strength aluminum alloy with Zr addition," *Mater. Des.*, vol. 31, pp. 4450–4456, 2010.

[11] T. Udomphol, "Extrusion." Suranaree University of Technology, 2007.

[12] T. Sheppard and E. P. Wood, "Effect of section geometry on extrudability of Al-Cu-Mn alloy," *Met. Technol.*, vol. 7, pp. 58–66, 1980.

[13] V. I. Johannes and C. W. Jowett, "Temperature distribution in aluminum extrsuion billets," in *Six International Aluminum Extrusion Technology Seminar*, 1996.

[14] C. Zener and J. H. Hollomon, "Effect of strain rate upon plastic flow of steel," *J. Appl. Phys.*, vol. 15, no. 1, pp. 22–32, 1944.

[15] H. Zhang, N. Jin, and J. Chen, "Hot deformation behavior of Al-Zn-Mg-Cu-Zr aluminum alloys during compression at elevated temperature," *Trans. Nonferrous Met. Soc. China*, vol. 21, no. 3, pp. 437–442, Mar. 2011.

[16] C. M. Sellars and W. J. McTegart, "On the mechanisms of hot deformation," *Acta Metall.*, vol. 14, no. 3, pp. 1136–1138, 1966.

[17] Y. D. Li and W. L. Wu, "Microstructural evolution of Al-Zn-Mg-Cu alloy during homogenization," *J. Mater. Sci.*, vol. 46, pp. 875–881, 2011.

[18] T. Sheppard, N. Parson, and M. Zaidi, "Dynamic recrystallization in Al-7Mg alloy," *Met. Sci.*, vol. 17, no. 10, pp. 481–490, 1983.

[19] E. P. Degarmo, J. T. Black, and R. A. Kohser, *Materials and Processes in Manufacturing*, 9th ed. 2003.

[20] K. Karhausen and H. Pawelski, "Mechanics and friction in metal rolling," in *Encyclopedia of Lubricants and Lubrication*, 2014, pp. 1122–1136.

[21] I. J. Polmear, *Light Metals*. Arnold, 1995.

[22] R. Ranganathan, “Recrystallization resistance in aluminum alloys containing zirconium,” Georgia Institute of Technology, 1991.

[23] R. A. Petkovic, M. J. Luton, and J. J. Jonas, “Recovery and recrystallization of polycrystalline copper after hot working,” *Acta Metall.*, vol. 27, pp. 1633–1648, 1979.

[24] F. J. Humphreys, “A unified theory of recovery, recrystallization and grain growth, based on the stability and growth of cellular microstructures - I. the basic model,” *Acta Mater.*, vol. 45, pp. 4231–4240, 1997.

[25] F. J. Humphreys and P. N. Kalu, “Annealing processes: recovery, recrystallization, and grian growth,” in *Risu National Laboratory*, 1986, pp. 385–390.

[26] F. J. Humphreys and M. Hatherly, *Recrystallization and Related Annealing Phenomena*. Elsevier, 1995.

[27] R. D. Doherty, D. a. Hughes, F. J. Humphreys, J. J. Jonas, D. J. Jensen, M. E. Kassner, W. E. King, T. R. McNelley, H. J. McQueen, and A. D. Rollett, “Current issues in recrystallization: a review,” *Mater. Sci. Eng. A*, vol. 238, pp. 219–274, Nov. 1997.

[28] Z.-C. Sun, L.-S. Zheng, and H. Yang, “Softening mechanism and microstructure evolution of as-extruded 7075 aluminum alloy during hot deformation,” *Mater. Charact.*, vol. 90, pp. 71–80, Apr. 2014.

[29] Y. W. Riddle and T. H. Sanders, “A study of coarsening, recrystallization, and morphology of microstructure in Al-Sc-(Zr)-(Mg) alloys,” *Metall. Mater. Trans. A*, vol. 35, pp. 341–350, 2004.

[30] K. C. Kim and S. W. Nam, “Effects of Mn-dispersoids on the fatigue mechanism in an Al–Zn–Mg alloy,” *Mater. Sci. Eng. A*, vol. 244, pp. 257–262, 1998.

[31] J. P. Schaffer, A. Saxena, S. D. Antolovich, T. H. Sanders Jr., and S. B. Warner, *The Science and Design of Engineering Materials*. Atlanta, GA: WCB/McGraw-Hill, 1999.

# CHAPTER 6

# THE PRECIPITATION PROCESS

The following is an in-depth literature review on the complex precipitation process of Al-Zn-Mg-Cu alloys. Numerous precipitates are discussed including vacancy rich clusters (VRC) and Guinier-Preston (GP) zones. It should be pointed out that GP-zones in 7xxx-series alloys can be subdivided into two types: spherical Mg-rich GP-I zones, and lenticular Zn-rich GP-II zones.

The precipitation process most often reported for 7xxx-series alloys follows the sequence:

$$\alpha_{ssss} \rightarrow \text{VRC/GP Zones} \rightarrow \eta' \rightarrow \eta$$

However, there appears to be a variety of additional "sub-precipitation sequences" that can occur depending on compositional and processing factors:

| | |
|---|---|
| $\alpha_{ssss} \rightarrow$ VRC $\rightarrow$ GP - II $\rightarrow \eta' \rightarrow \eta$ ($MgZn_2$) | P1 |
| $\alpha_{ssss} \rightarrow$ GP – I $\rightarrow$ Solid Solution | P2 |
| $\alpha_{ssss} \rightarrow$ GP – I $\rightarrow$ ? $\rightarrow \eta$ | P3 |
| $\alpha_{ssss} \rightarrow \eta' \rightarrow \eta$ | P4 |
| $\alpha_{ssss} \rightarrow$ Dislocations $\rightarrow \eta$ | P5 |
| $\alpha_{ssss} \rightarrow$ GP – I (small) $\rightarrow \eta' \rightarrow \eta$ | P6 |

Understanding these factors and the contributions of P1-P6 is important because they control the microstructure and alloy properties. However, the complexity of the 7xxx-series system suggests the precipitation sequences above and the exact mechanisms governing the precipitation process are still open for discussion.

## 6.1 Vacancy Rich Clusters

The existence of vacancy rich clusters (VRC) has been verified by certain 'resistivity anomalies' often observed during the isothermal aging of 7xxx-series alloys [1], [2]. These resistivity anomalies are the initial decrease and subsequent increase in the conductivity of solid solutions during the aging process. It has been shown to be

directly correlated to the size and density of VRCs in the matrix and governed by Equation 22:

$$p = \frac{m}{ne^2 <\tau>} \tag{22}$$

Where

$$<\tau> = \frac{1}{4\pi} \int_{S_F} \frac{d\Omega_k}{|\tau(k)|^{-1}} \tag{23}$$

It is important to note that *p* is the resistivity, <τ> is the relaxation time averaged over the incident wave vectors, τ(k) is the relaxation time, *m* is the mass of the solute atoms, and *n* is the number of solute atoms. Equations 22 and 23 are explained in more detail in [2].

Luiggi *et al*. [2] showed that small clusters containing less than 100 atoms explained semi-quantitatively the resistivity anomaly and states that "isotropic scattering allows the definition of an excess of resistivity per atom in a cluster, which is calculated as a function of its size and compactness." However, eventually VRCs reach a critical size and the resistivity reaches maximum at which point it is speculated VRC begin to transform into GP zones. This behavior is illustrated in Figures 15 and 16.

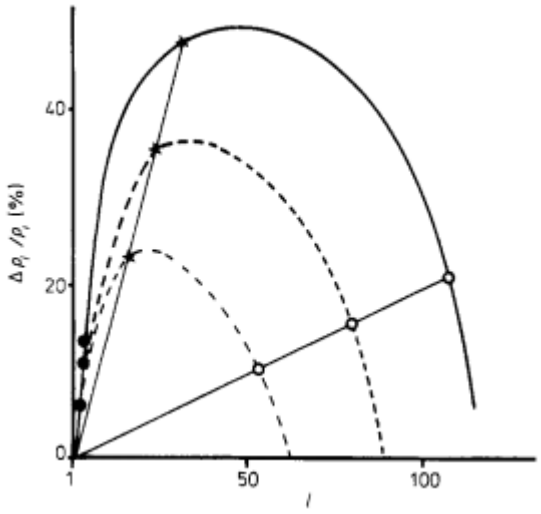


Figure 15 – *Relative resistivity per solute atom of a cluster containing $4p^2C_C = l$ zinc atoms; ●, p = 1; *, p = 2; ○, p = 3; curves of equal cluster composition —, $C_C$ = 100%; ---, $C_C$ = 75%; - - -, $C_C$ = 50%* [2].

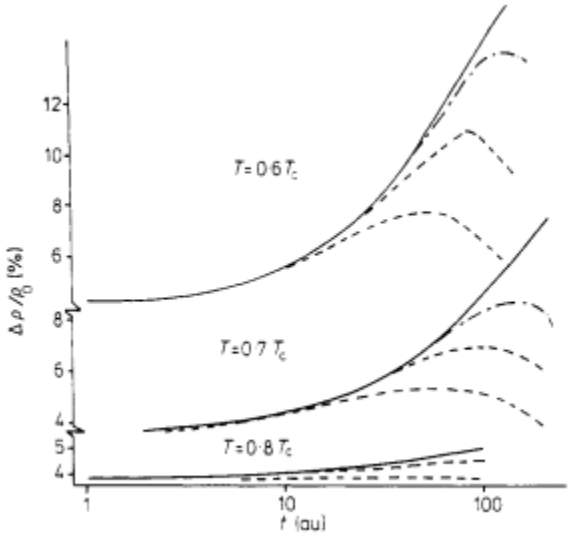


Figure 16 - *Theoretical isothermal resistivity variation for an Al-10%Zn alloy at different temperature ratios $T/T_c$: summed contributions of clusters of less than x atoms:●—●, x = 33; ---, x = 23; - - -, x = 16; —, total contribution. It should be noted that $T_C$ represents the top of the coherent miscibility gap for the $\alpha_R$' metastable phase, and therefore $0.6T_c \approx 25°C$ (77°F) and $0.8T_C \approx 125°C$ (257°F)* [2].

In fact, the importance VRC appears to be their role as the precursor to GP-II zones [1], [3]–[7]. This role appears to be well substantiated by literature in that GP-II zones have been shown to be quench sensitive (i.e. – GP zones need a large excess of quench in vacancies to precipitate) [4], [8]–[11]. However, VRC appear to have little to no influence on the precipitation of GP-I zones during natural aging (NA) [4]. To date, VRC have not been observed, although Curratis *et al*. [12] did report the existence of Frank loops in an experimental Al-Zn-Mg alloy quenched from a SHT temperature greater than 490°C (914°F).

### 6.2 Guinier-Preston Zones

The process of GP-zone formation (i.e. – the process by which decomposition of the supersaturated solid solution takes place from room temperature to approximately 150°C) as well as their composition and structure has been the subject of a great deal of research [4], [13]–[15]. Ringer and Hono [16] have concluded that GP zones contain roughly equal concentrations of Mg and Zn. Furthermore, they noted that "the observed

zone shape and composition seem(ed) consistent with the atomic size effects expected from the fact that Zn and Mg are smaller and larger, respectively, than Al," and their conclusions are echoed by other authors [3], [16]–[19]. In work done on the characterization and formation of GP zones, Staley [1] states that at low heating rates GP zones will coarsen instead of dissolving away. These large GP zones can then act as nucleation sites for various precipitates thereby increasing the strength of an aluminum alloy.

It is widely accepted that there are two main types of GP zones classified as GP-I and GP-II zones [3]–[7], [13]. GP-I zones are Mg rich in nature and coherent with the aluminum matrix forming on the {001} planes. GP-I zones are reported to form over a wide range of temperatures from room temperature (RT) to 150°C (302°F), and appear to be independent of solution heat treatment (SHT) temperature [4], [13]. However, the main strengthening phase in 7xxx-series alloys, η', is not believed to form on GP-I zones except in rare cases [20]. Rather it is generally believed that upon heating above the GP-zone solvus temperature, GP-I zones either dissolve back into solution or transform directly into η [3], [4]. Figure 17 shows a bright field transmission electron microscope (BFTEM) image of GP-I zones while Figure 18 details a proposed anti-phase structure consistent with the diffuse spots from GP-I zones [3].

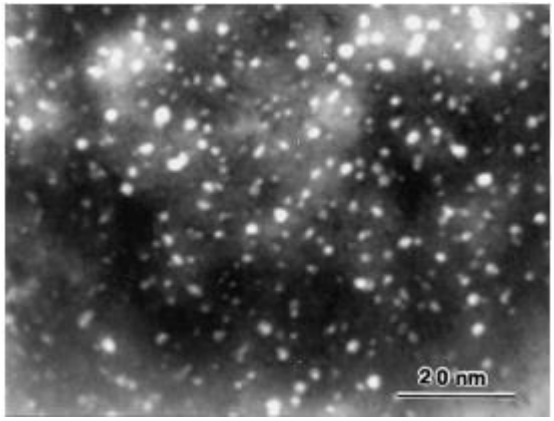


Figure 17 – *Bright-field TEM image of GP-I zones along the [001]-projection* [3].

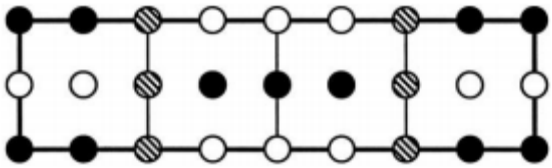

Figure 18 – *Projected anti-phase structure similar to CuAu(II) along [001] which is consistent with the diffuse spots from GP-I zones (cf. Fig. 3a [6]). Zn atoms are reprsented as filled circles, Mg (or Al) as open circles, and hatched circles represent disorderd sites.* [3].

GP-II zones, conversely, are Zn-rich in nature and are incoherent with the aluminum matrix forming on the {111} planes [3], [13]. Unlike GP-I zones, GP-II zones appear to form only at temperatures above 70°C (158°F) and are highly dependent on SHT temperature, which indicates a high dependence on quenched-in vacancies (i.e. – VRC) to precipitate [3], [13]. This transition from VRC to GP-II zones appears to take place at approximately 100°C (212°F), which correlates to the active mobility temperature of magnesium in aluminum (i.e. – the temperature at which there is significant vacancy motion to allow for the migration of Mg in the Al matrix) [3]. Therefore while GP-II zone precipitation can take place below 100°C in some cases, it is well documented that the large-scale precipitation of GP-II zones responsible for achieving maximum strength only occurs above this temperature.

The dependence of GP-II zones on the mobility of Mg via VRC is supported by their accepted structural model in which Zn atoms, which have an inter-row spacing 6-8% less than that of Al, are surrounded by Mg atoms, whose radius is 12% larger than that of Al [3]. In this model, Mg atoms produce a local lattice expansion, which relieves part of the strain from the contraction of the lattice created by the Zn-clusters. This model is further backed by high resolution transmission TEM (HRTEM) images along the $<110>_{Al}$ projections (see Figure 19 – 21). GP-II zones appear to be thin layers, 1-2 atoms thick and 3-5 nm wise on the {111} family of planes as widely reported [3].

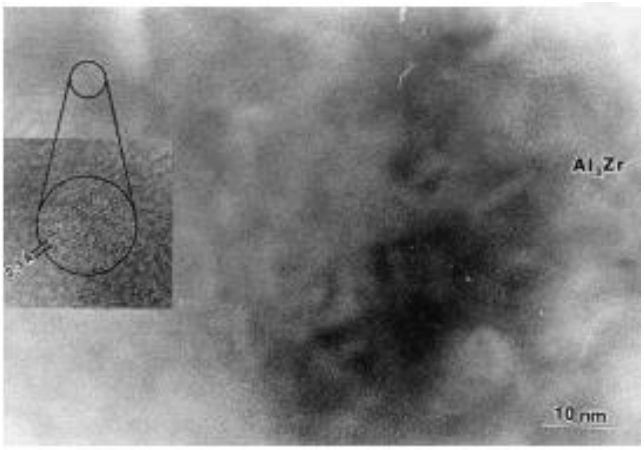


Figure 19 – *TEM image of GP-II zones in the [111] projections with insert showing the 0.23nm spacing* [3].

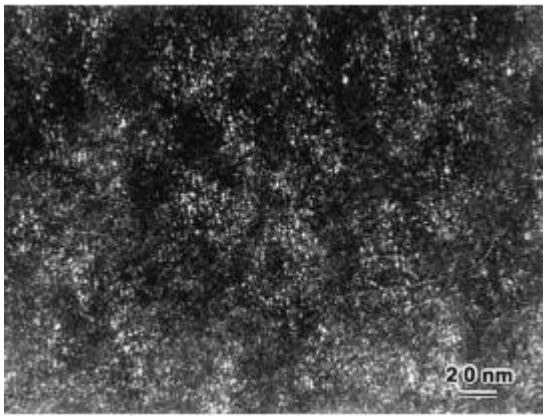


Figure 20 – *Composite dark field (CDF) image of GP-II zones taken with a diffuse (422)/3 spot near [111] projection showing a weak, irregular contrast* [3].

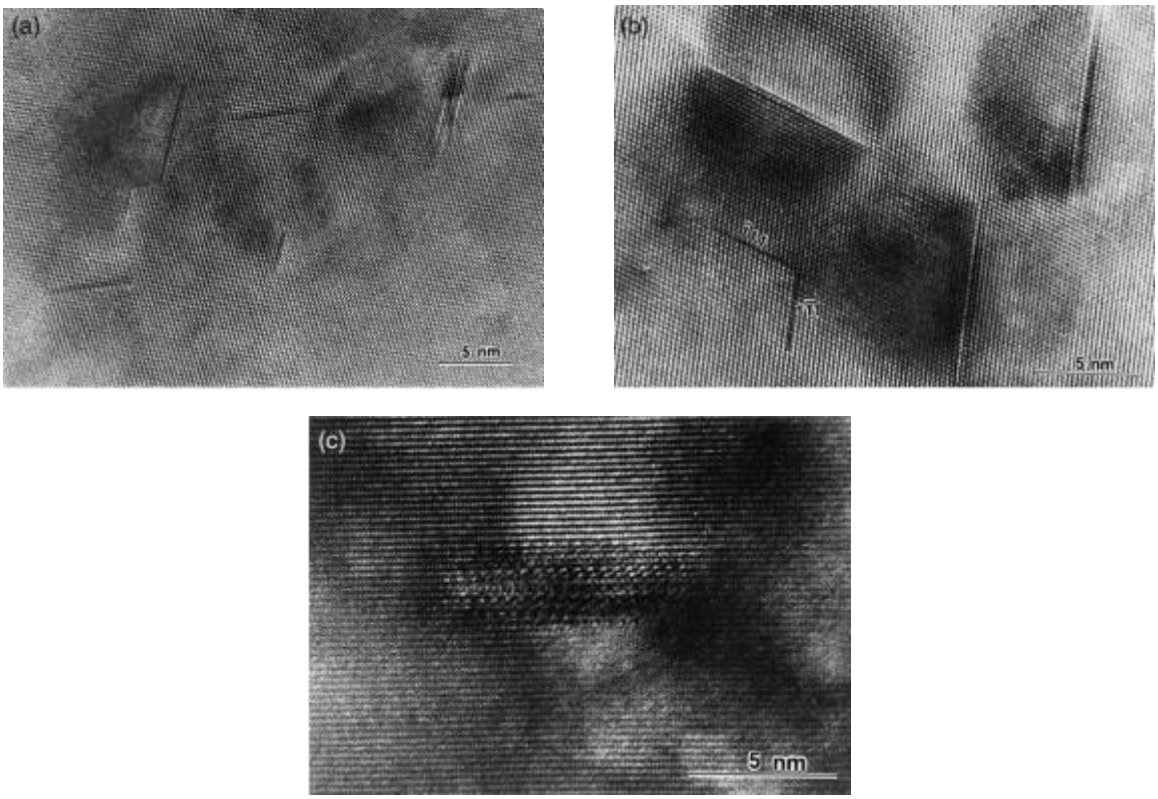


Figure 21 – *a.) and b.) HRTEM images in [110] projection, showing GP-II zones as {111} layers one to two atoms thick in two magnifications. Note the strain field on the sides of the zones; c.) thicker zone or precipitate on (111) plane, a possible transition stage in the formation of η'* [3].

It should be noted that work done by Chinh *et al.* [21] showed that Cu had a dramatic effect on the development and subsequent stabilization of GP zones (both type I and II) in 7xxx-series alloys, especially with respect to their size, shape, and composition. For example, Chinh et *al.* [21] observed that in Al-Zn-Mg alloy GP zones were mostly spherical in nature, but in Al-Zn-Mg-Cu alloys two distinct types of GP zones formed: spherical and ellipsoidal/plate-like. It was suggested that these morphological changes were caused by the stabilization of VRC by Cu, which increased the lattice strain. The strain induced by this morphological change (spherical to ellipsoidal) is known to assist the heterogeneous nucleation of η' [21]. This effect is evident by observations on Al-Zn-Mg alloys were η' is not evident in the microstructure after aging at low temperatures (i.e. – below 120°C), but is observed in Al-Zn-Mg-Cu alloys at relatively low aging

temperatures. These observations therefore suggest that GP-II zones directly transform into η' instead of reverting back to solid solution and re-precipitating [21].

### 6.3 The Metastable η'-Phase

It is well-established and universally accepted that the metastable η'-phase, $MgZn_2$ or $Mg(ZnCuAl)_2$, is the main hardening phase in 7xxx-series aluminum alloys in the T6 temper [1], [16], [17], [22]. Several models have been proposed for the structure of η', which is believed to be either hexagonal or pseudo-hexagonal in nature [23], [24]. η' is reported to be semi-coherent with the aluminum matrix with lattice parameters: a = 0.496 nm ≈ $[211]/2_{Al}$ and c = 1.4 nm ≈ $2[111]_{Al}$ [3]. These reported structural characteristics agree with the general consensus that the majority of η' precipitates nucleate on GP-II zones, and as previously mentioned, are the main structural phase found (along with GP zones) in the T6 temper. Selected area diffraction patterns (SADS) TEM images of η' can be seen below in Figures 22 – 25 [24].

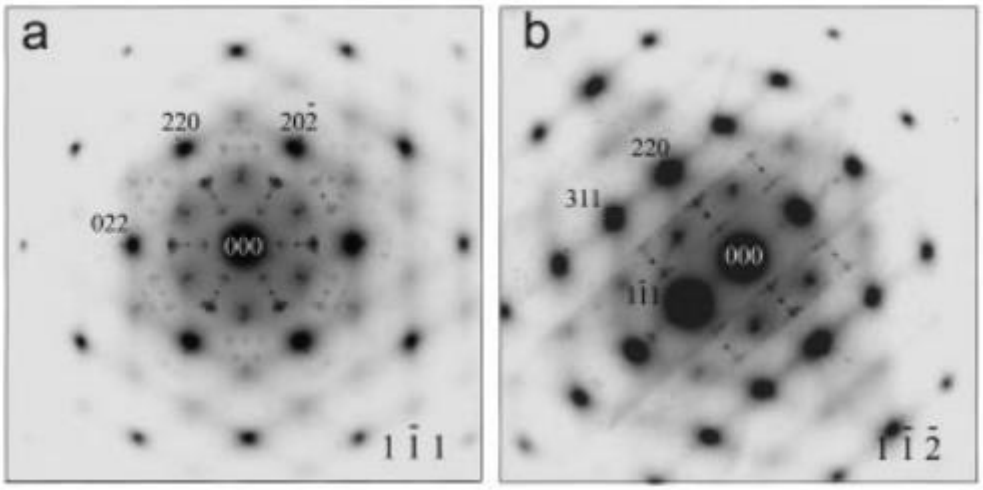


Figure 22 – *The SAD patterns of η' along a.) the [1-11] and b.) [11-2] axis of the aluminum matrix* [24].

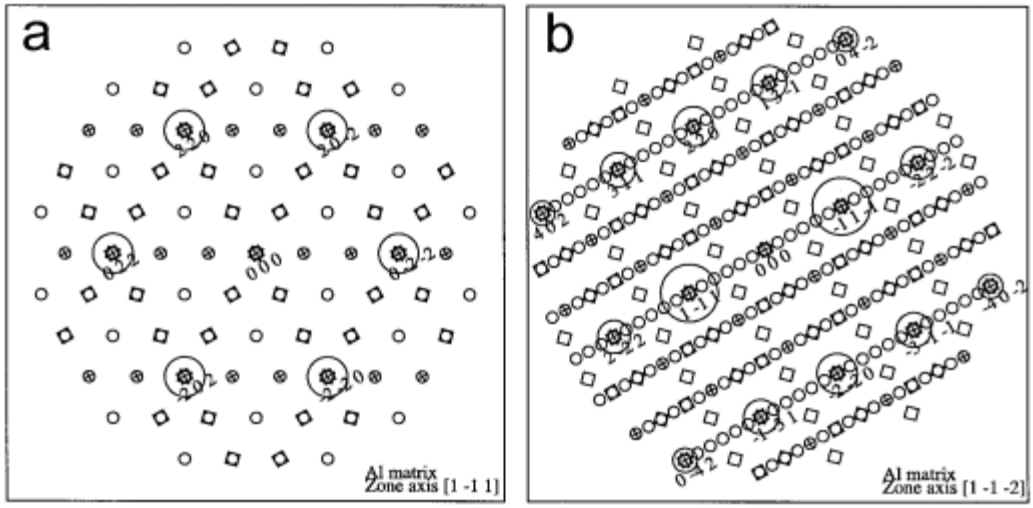


Figure 23 – *The simulated SADS pattern of η' and the aluminum matrix along a.) the [1-11] and b.) the [11-2] zone axis of the aluminum matrix. Diffraction spots from four orientations sets of precipitates are indicated by squares, diamonds, circles, and crosses respectively* [24].

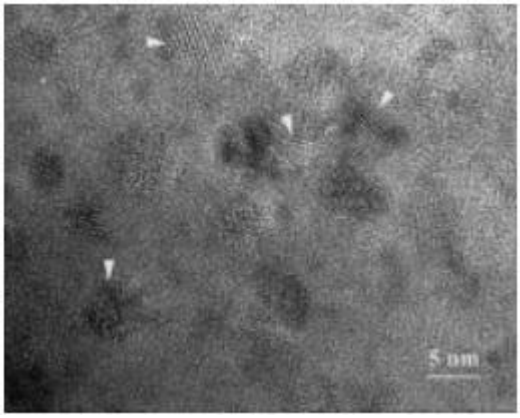


Figure 24 – *HRTEM image taken with the incident electron beam along the [111] zone axis of the aluminum matrix. This relatively low magnification image gives a global view of the distribution of the η' precipitates. Images of the η' precipitates are indicated by arrow heads* [24].

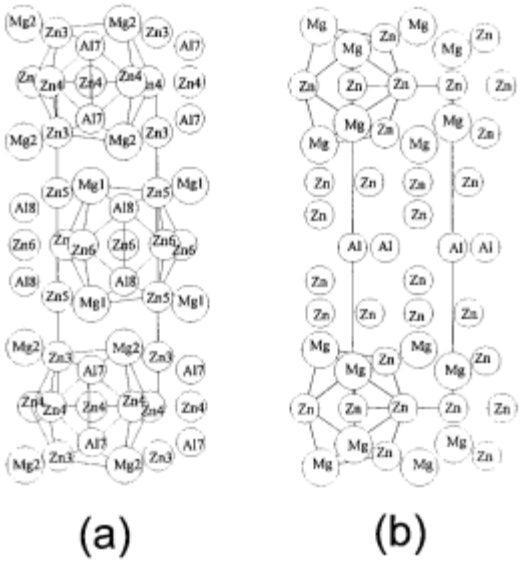


Figure 25 – *The [110] projection of a.) the new model of η' phase and b.) the Auld-Cousland model* [24].

The stability of η' seems to be dependent on a number of factors including heating rate [5], [25]. The effect of heating rate on the stability of η' can be seen in Figure 26. At 30°C/hour, the η' and η precipitation peaks are well separated, which is in direct contrast to the relative nature of the peaks when the heating rate is increased to 300°C/hour. Therefore, this DSC data suggests that at lower heating rates η' is more stable than at higher ramp rates. Deschamps *et al.* [5] demonstrated that an increased reversion of GP zones during high heating rates (i.e. - $T > T_{critical}$) results in a more difficult nucleation of η'. Therefore η' does not begin to nucleate until the alloy has reached a higher than normal temperature (i.e. – the nucleation temperature is as high as that of η' in Cu-free 7xxx-series alloys), which could result in the nucleation of η' with larger than normal radii. Therefore, it is possible because the larger radius that the η' precipitates begin to transform almost immediately to η [5].

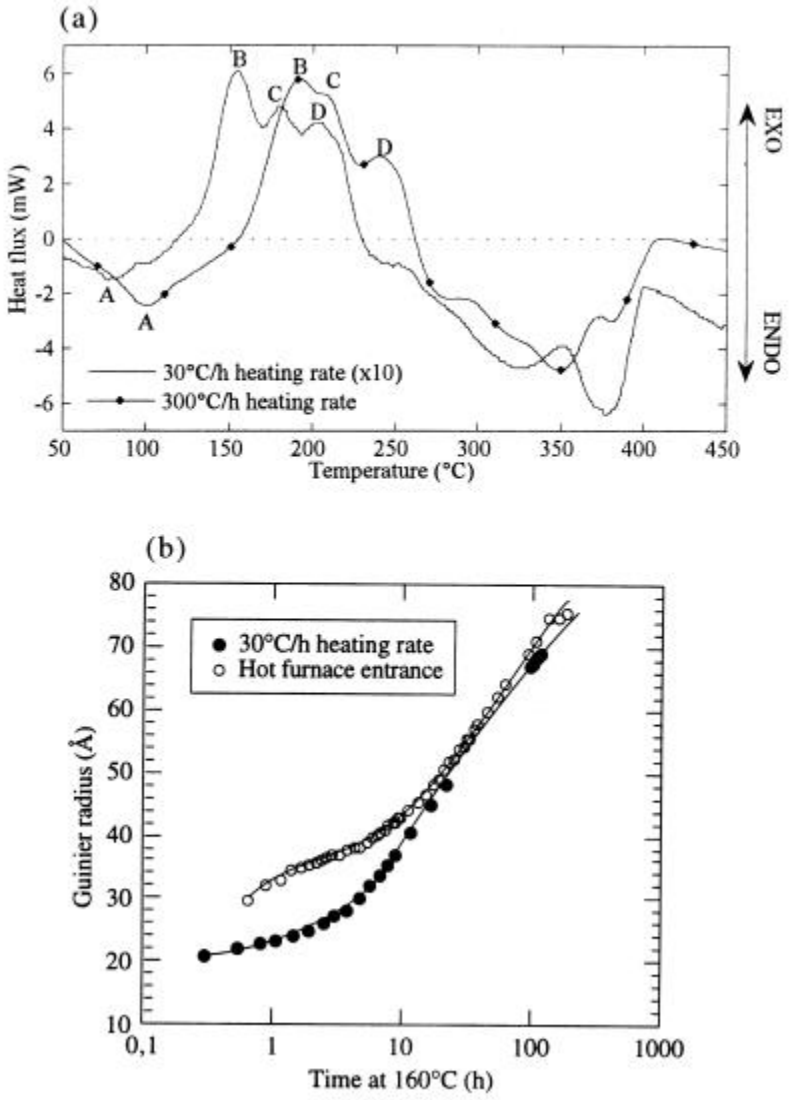


Figure 26 – *Influence of heating rate on the phase transformations during aging at 160°C (320°F): a.) DSC thermograms preformed after 3 days of natural aging at two different heating rates (the DSC signal is multiplied by a factor of 10 in the case of the 30°C/hour heating rate); b.) evolution of the Guinier radius during aging at 160°C as a function of the heating rate to the aging temperature investigated by in situ SAXS* [5].

### 6.4 The Stable η-Phase

The stable η-phase, $MgZn_2$, which is known to occur in up to nine crystallographic orientations designated $\eta_1$-$\eta_9$ with respect to the aluminum matrix, is believed to mainly heterogeneously nucleate on pre-existing η' rather than through dissolution and re-precipitation [26]–[28]. While this is the subject of some debate, it

appears to be a reasonable assumption for bulk η transformations. It should be mentioned, however, that the precipitation process leading to η-phase can be circumnavigated in some cases if the manufacturing process contains a deformation process, but this phenomenon will be discussed in further details in *Chapter 7 – Post Plastic Deformation Factors*.

Structurally, η is an equilibrium laves phase with a hexagonal close packed (HCP) structure (lattice parameters: a = 0.516-0.522 nm and c = 0.849-0.860 nm) [24], [29]. The classical Auld and Cousland model, which is based on chemistry and x-ray diffraction data, was the most accepted model for η for years, but recent developments have proved their model to be structurally inaccurate. Li et. al. [24] proposed a new model which can be seen below in Figure 27. It is important to remember that as the equilibrium phase in Al-Zn-Mg-X alloys, the size, shape, distribution, orientation, and composition of η directly correlate to the properties of 7xxx-series alloys in the T7 temper (i.e. – the over-aged temper).

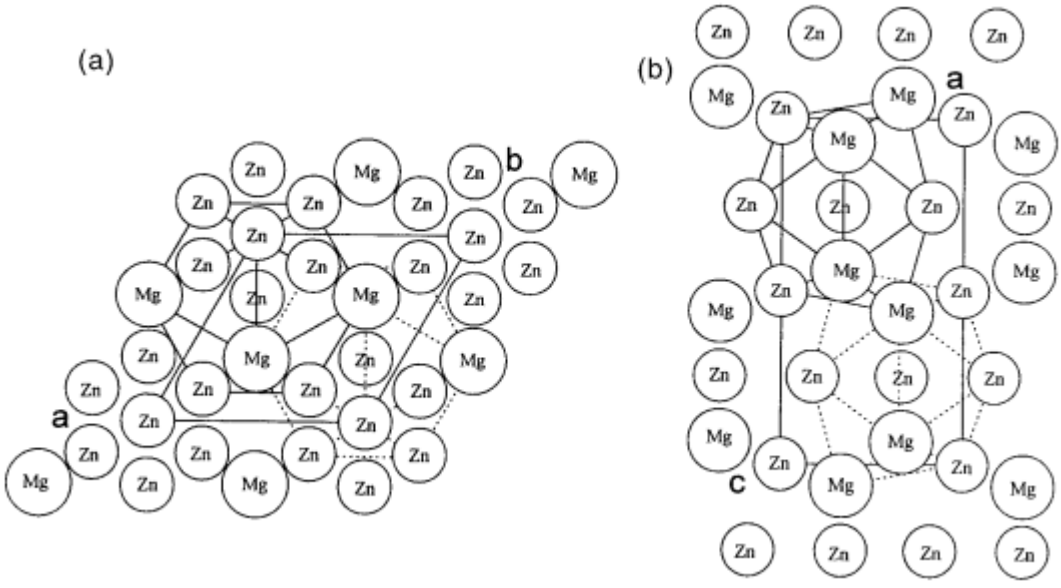


Figure 27 – *Structure projection of the η-phase along a.) the [001] and b.) the [110] axis in which shells of icosahedral clusters are outlined* [24].

### 6.5 Other Precipitates

T-phase, $(Al,Zn)_{49}Mg_{32}$, is a ternary intermetallic equilibrium phase that has been shown to precipitate our during the artificial aging of Al-Zn-Mg-Cu alloys via the following precipitation process [30]:

$$\alpha_{ssss} \rightarrow \alpha + T' \rightarrow \alpha + T \qquad P7$$

It is believed that the existence of this precipitation process can be directly linked to the Mg content of a 7xxx-series alloy as it only regularly appears in high Mg alloys [31]. T-phase has a cubic structure with a = 1.45 nm [29]. Generally, the precipitation of T-phase is considered detrimental to an alloy's properties and should be avoided due to corrosion and fracture toughness issues.

### 6.6 The Effects of the Zn:Mg Ratio and the Cu Content

To even the casual observer it is evident that perhaps the largest factor in determining the overall properties of a 7xxx-series alloy is composition. Upon reflection, it is evident that the Zn:Mg ratio and the Cu content, dictate the precipitation process of a 7xxx-series alloy more than any other contributing factor with respect to composition [32]. Sheppard [32] states that four main equilibrium precipitate particles can be distinguished from varying Zn:Mg ratios. It should be noted that the following Zn:Mg ratios are given with respect to wt.%:

Mg:Zn $\geq$ 6:1 – leads to the formation of $Al_8Mg_5$
6:1 $\geq$ Mg:Zn $\geq$ 3:7 – leads to the formation of $Al_2Zn_3Mg_3$
2:5 $\geq$ Mg:Zn $\geq$ 1:7 – leads to the formation of $MgZn_2$
Mg:Zn < 1:10 – leads to the formation of $Mg_2Zn_{11}$

These values can roughly be translated to the following at.% assuming that the alloys only contain Al, Zn, and Mg:

Mg:Zn $\geq$ 13.3:0.8 – leads to the formation of $Al_8Mg_5$
13.3:0.8 $\geq$ Mg:Zn $\geq$ 16.0:13.6 – leads to the formation of $Al_2Zn_3Mg_3$
9.3:10.0 $\geq$ Mg:Zn $\geq$ 5.3:13.8 – leads to the formation of $MgZn_2$
Mg:Zn < 2.5:9.3 – leads to the formation of $Mg_2Zn_{11}$

These four main groups can be seen graphically below in Figures 28 (wt.%) and 29 (at.%) with Figure 29 containing an overlay of the registered compositions of several common 7xxx-series alloys. It should be noted, however, that 7xxx-series alloys meant for aluminum extrusion generally fall within the $MgZn_2$ (η-phase) range. The composition ranges of several 7xxx-series alloys are plotted below in Figure 30 [33].

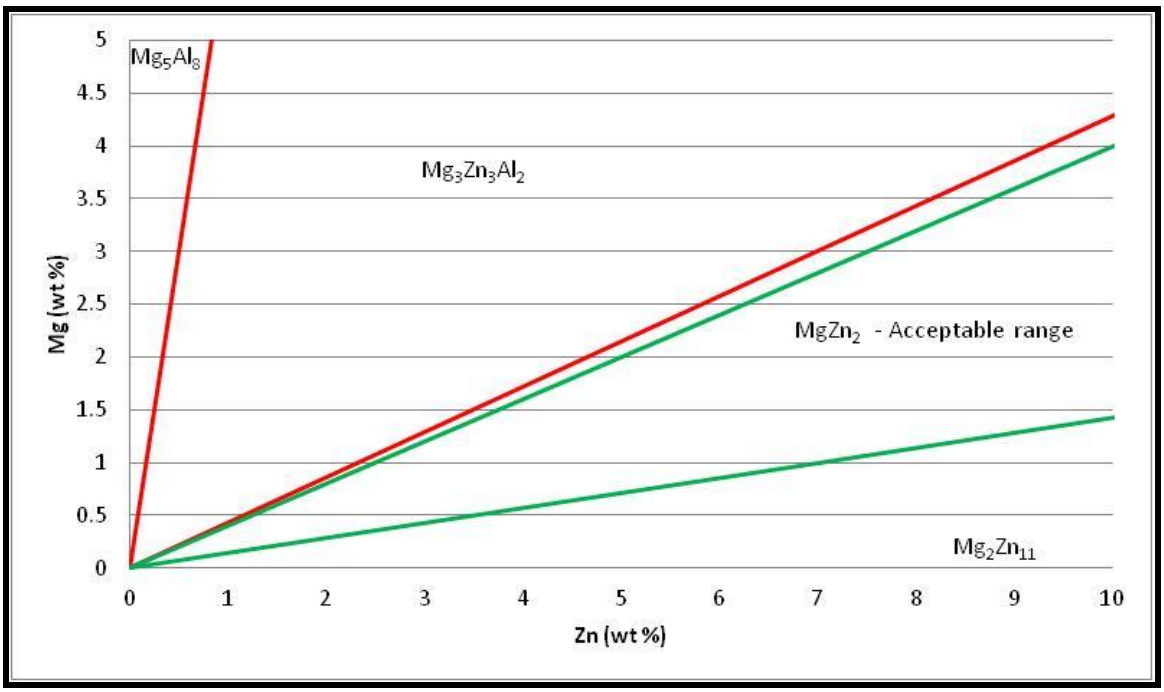


Figure 28 – *Graphical representation of the dominating hardening phase in Al-Zn-Mg alloys as a function of the Zn:Mg ratio in terms of weight percent* [32].

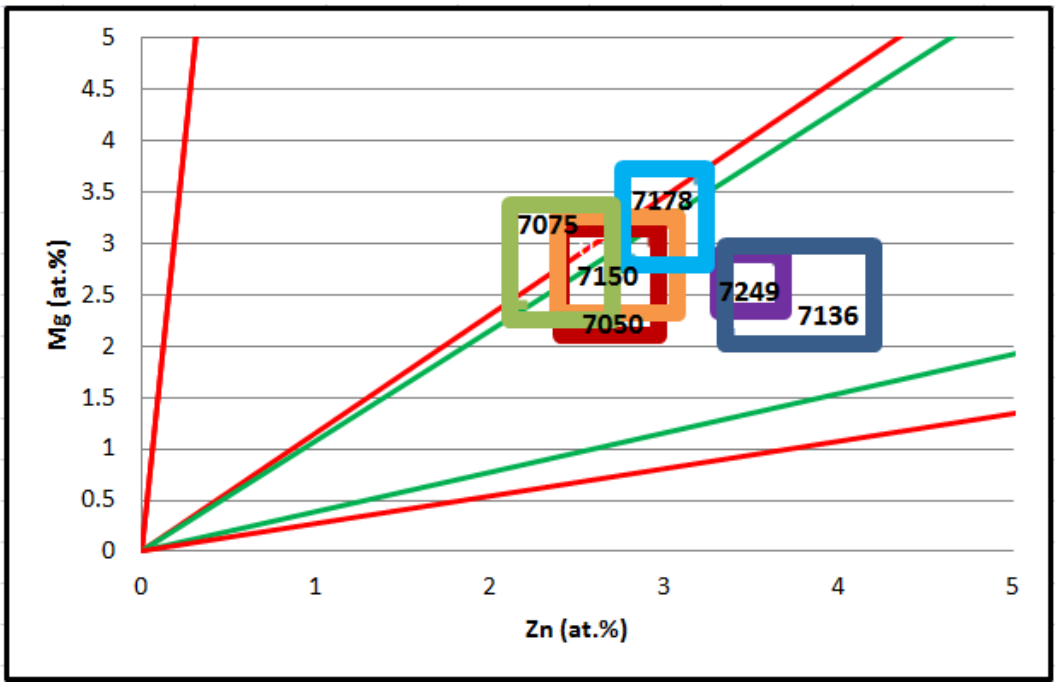


Figure 29 – *Graphical representation of the dominating hardening phases in Al-Zn-Mg alloys as a function of the Zn:Mg ratio in terms of atomic percent* [32], [33]. *Note – 7050 is the red box, 7075 is the green box, 7150 is the orange box, 7178 is the light blue box, 7249 is the purple bark, and 7136 is the navy box.*

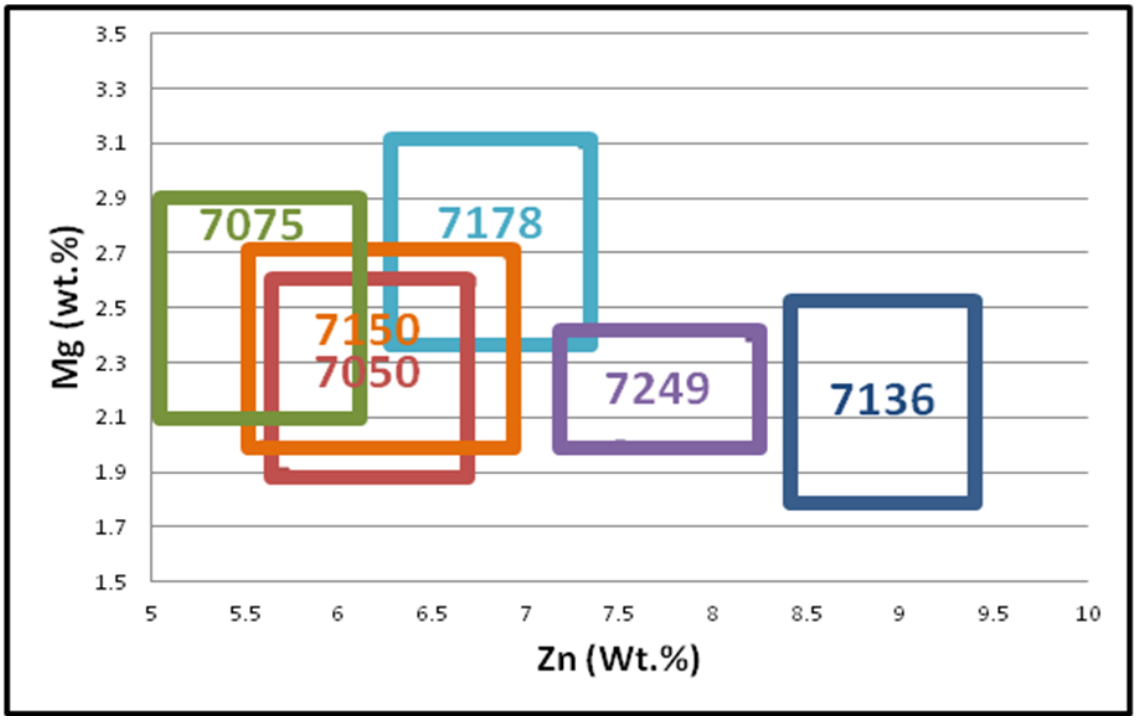


Figure 30 – *Graphical representation of common 7xxx-series alloys with respect to approximate registered composition ranges* [33].

Clinch *et al.* [4] provides a very detailed paper on the effect of the Zn:Mg ratio on the strength and toughness of 7xxx-series aluminum alloys. Clinch's work focused on five simple experimental compositions whose partial compositions can be seen below in Table 4. It should be noted that Clinch also added chromium (Cr) in addition to the ever-present silicon (Si) and iron (Fe) to act as a grain refiner. Clinch cast ingots approximately 250 mm x 180 mm x 35 mm in size via gravity casting into chilled molds. The blocks were then homogenized and cold rolled to a 60% total reduction. Clinch's samples then underwent a SHT at 475°C (887°F) for 1 hour prior to a water-quench. The samples where then aged by a two-step artificial age (105°C <221°F> for 6 hours followed by aging at 165°C <329°F>); however, Clinch neglected to stretch his experimental alloys.

Table 4 – *Compositions of the experimental 7xxx-series alloys investigated by Clinch* [4].

| **Alloy ID** | **Chemical Compositions at.% (wt.%)** | | | | | |
|---|---|---|---|---|---|---|
| | **Zn** | **Mg** | **Cu** | **Total Solute** | **Zn:Mg Ratio** | **Alloys** |
| **1** | 3.1 (7.8) | 1.5 (1.3) | 0.9 (2.0) | 5.8 | 2.1 | - |
| **2** | 3.0 (6.9) | 1.9 (1.7) | 0.9 (2.0) | 5.8 | 1.6 | - |
| **3** | 2.7 (6.3) | 2.1 (1.9) | 0.9 (2.0) | 5.7 | 1.3 | 7050 |
| **4** | 2.5 (5.9) | 2.3 (2.1) | 0.9 (2.0) | 5.7 | 1.1 | 7075 |
| **5** | 2.3 (5.5) | 2.5 (2.3) | 0.9 (2.0) | 5.7 | 0.9 | 7075 |

Clinch's work concluded that the Zn:Mg ratio has a considerable influence in determining the aging kinetics of 7xxx-series alloys of equivalent strength, both in terms of time taken to reach a T6 temper and the subsequent coarsening kinetics leading to a T7 temper [4]. Clinch's work proposed the following precipitation processes for 7xxx-series aluminum alloys [4]:

First Stage age at 105°C (T1): SSSS → GP-I/GP-II → η'

Second Stage age at 165°C (T2): GP-I → Solid Solution
SSSS → GP-II → η' → $\eta_2$
SSSS → η' → $\eta_2$
SSSS → $\eta_1$

Clinch's work suggests that the Zn:Mg ratio also effects the width of the precipitate free zones (PFZs) and therefore could ultimately affect the stress corrosion cracking (SCC) resistance of the alloy [4].

The finding of Clinch *et al.* [4] are echoed by Mukhopadhyay [29] who states the SCC resistance of a 7xxx-series alloy is affected by its (Zn+Cu):Mg ratio. Mukhopadyay states that SCC susceptibility tends to increase with increasing Zn+Mg contents in Al-Zn-Mg alloys, which usually have a Zn:Mg ratio of 6-7 wt.% to improve SCC resistance. In Al-Zn-Mg-Cu alloys, the Zn+Mg content typically falls in the 8-10 wt.% range with Cu contents typically ranging from 1-2.6 wt.% [29]. It was shown by Sarkar *et al.* [34] that increasing the Cu content in a 7xxx-series alloy from 1.0 to 2.1 wt.% slows down the SCC velocity by an order of magnitude. It must be noted as well that the highly corrosive T-phase has been shown to stabilize with lower Zn:Mg ratios and at elevated temperatures [29].

## 6.7 Summary

An overview of the complex precipitation process in 7xxx-series alloys and the compositional factors that affect it were presented. The importance of a variety of sub-precipitation sequences to the overall precipitation process was covered with emphasis placed on the formation of VRC and GP zones. Compositional factors were also presented and discussed.

## 6.8 References


[1] J. T. Staley, "Aging kinetics of aluminum alloy 7050," *Metall. Trans.*, vol. 5, pp. 929–932, 1974.

[2] N. Luiggi, J. P. Somon, and P. Guyot, "Residual resistivity of clusters in solid solutions," *J. Phys. F Met. Phys.*, vol. 10, pp. 865–872, 1980.

[3] L. . Berg, J. Gjønnes, V. Hansen, X. . Li, M. Knutson-Wedel, G. Waterloo, D. Schryvers, and L. Wallenberg, "GP-zones in Al–Zn–Mg alloys and their role in artificial aging," *Acta Mater.*, vol. 49, no. 17, pp. 3443–3451, 2001.

[4] M. R. Clinch, S. J. Harris, W. Hepples, N. J. H. Holroyd, M. J. Lawday, and B. Noble, “Influence of zinc to magnesium ratio and total solute content on the strength and toughness of 7xxx-series alloys,” *Mater. Sci. Forum*, vol. 519–521, pp. 339–344, 2006.

[5] A. Deschamps, F. Livet, and Y. Brechet, “Influence of predeformation on ageing in an Al-Zn-Mg Alloy-I: microstructure evolution and mechanical properties,” *Acta Mater.*, vol. 47, pp. 281–292, 1998.

[6] A. Deschamps and Y. Brechet, “Influence of predeformation on ageing in an Al-Zn-Mg Alloy - II: modeling precipitation kinetics and yield stress,” *Acta Mater.*, vol. 47, pp. 293–305, 1998.

[7] G. Waterloo, V. Hansen, J. Gjønnes, and S. R. Skjervold, “Effect of predeformation and preaging at room temperature in Al–Zn–Mg–(Cu , Zr) alloys,” *Mater. Sci. Eng.*, vol. 303, pp. 226–233, 2001.

[8] C. Panseri and T. Federighi, “Ischronal annealing of vacancies in aluminum,” *Philos. Mag.*, vol. 3, no. 35, pp. 1223–1240, 1958.

[9] J. D. Embury and R. B. Nicholson, “The nucleation of precipitates: the system Al-Zn-Mg,” *Acta Metall.*, vol. 13, pp. 403–417, 1965.

[10] Z. Katz and N. Z. Ryum, “Precipitation kinetics in Al-alloys,” *Scr. Metall.*, vol. 15, no. 3, pp. 265–268, 1980.

[11] N. Z. Ryum, “Precipitation kinetics in an Al-Zn-Mg alloy,” *Z. Met.*, vol. 66, pp. 338–344, 1975.

[12] P. Curratis, R. Kroggel, and R. Wolter, “Quenched-in dislocation loops in Al-Zn-Mg alloys,” *Mater. Sci. Forum*, vol. 13–14, pp. 475–482, 1987.

[13] H. Loffler, I. Kovacs, and J. Lendvai, “Decomposition processes in Al-Zn-Mg alloys,” *J. Mater. Sci.*, vol. 18, pp. 2215–2240, 1983.

[14] G. Dlubek, R. Krause, O. Brummer, and G. Plazaola, “Study of formation and reversion of guinier-preston zones in Al-4.5at%Zn-xat%Mg alloys by positrons,” *J. Mater. Sci.*, vol. 21, pp. 853–858, 1986.

[15] R. Ferragut, A. Somoza, and A. Dupasquier, “On the two-step ageing of a commercial Al-Zn-Mg Alloy: a study by positron lifetime spectroscopy,” *J. Phys. Condens. Matter*, vol. 8, pp. 8945–8952, 1996.

[16] S. P. Ringer and K. Hono, “Microstructural evolution and age-hardening in aluminum alloys: atom probe, field-ion microscopy, and transmission electron microscopy studies,” *Mater. Charact.*, vol. 44, pp. 101–103, 2000.

[17] T. H. Sanders Jr., R. R. Sawtell, J. T. Staley, R. J. Buccie, and A. B. Thakker, "Effect of microstructure on fatigue crack growth of 7xxx aluminum alloys under constant amplitude and spectrum loading," 1978.

[18] H. Schmalzried and V. Gerold, "Rontgenographische untersucugen urberdie ausartung einer aluminum-madnesiu-zink-legiergung," *Z. Met.*, vol. 49, pp. 291–301, 1957.

[19] P. N. Andler and R. Delasi, "Calorimeteric studies of 7000 series aluminum alloys - II: comparision of 7075, 7050, RX720," *Met. Trans. A*, vol. 8, pp. 1185–1190, 1977.

[20] G. Sha and A. Cerezo, "Early-stage precipitation in Al–Zn–Mg–Cu alloy (7050)," *Acta Mater.*, vol. 52, no. 15, pp. 4503–4516, Sep. 2004.

[21] N. Q. Chinh, J. Lendvai, D. H. Ping, and K. Hono, "The effect of Cu on mechanical and precipitation properties of Al–Zn–Mg alloys," *J. Alloys Compd.*, vol. 378, no. 1–2, pp. 52–60, Sep. 2004.

[22] R. Rangathan, "Recrystallization resistance in aluminum alloys containing zirconium," Georgia Institute of Technology, 1991.

[23] J. H. Auld and S. M. Cousland, "The structure of the metstable n' phase in aluminum-zinc-magnesium alloys," *J. Aust. Inst. Met.*, vol. 19, pp. 194–201, 1974.

[24] X. . Li, V. Hansen, J. Gjønnes, and L. . Wallenberg, "HREM study and structure modeling of the n' phase, the hardening precipitates in commerical Al-Zn-Mg alloys," *Acta Mater.*, vol. 47, no. 9, pp. 2651–2659, 1999.

[25] A. Deschamps and Y. Brechet, "Influence of quench and heating rates on the ageing response of an Al-Zn-Mg-(Zr) alloy," *Mater. Sci. Eng.*, vol. A251, pp. 200–207, 1998.

[26] J. Gjønnes and C. J. Simensen, "An electron microscope investigation of the mircostructures in an aluminum-zinc-magnesium alloy," *Acta Mater.*, vol. 18, pp. 871–890, 1970.

[27] H. Y. Hunsicker, "Development of Al-Zn-Mg-Cu alloys for aircraft," in *Proc. Rosehain Centenary Conf. on the Contribution of Physical Metallurgy to Engineering Practice*, 1976, pp. 359–376.

[28] A. Yamaoto, K. Minami, U. Ishihara, and H. Tsubakino, "Calorimetric and resistivity study on the formation and redissolution of precipitates in 7050 aluminum alloys," *Mater. Trans. JIM*, vol. 39, pp. 69–74, 1998.

[29] A. K. Mukhopadhyay, “Microstructure and properties of high strength aluminium alloys for structural applications,” *Trans. Indian Inst. Met.*, vol. 62, no. 2, pp. 113–122, 2009.

[30] J. Lendvai, “Precipitation and strengthening in aluminium alloys,” *Mater. Sci. Forum*, vol. 217–222, pp. 43–56, 1996.

[31] G. Sha and A. Cerezo, “Characterization of precipitates in an aged 7xxx series Al alloy,” *Surf. Interface Anal.*, vol. 36, pp. 564–568, 2004.

[32] T. Sheppard, *Extrusion of Aluminium Alloys*. Kluwer Academic Publishers Group, 1999.

[33] The Aluminum Association, *International Alloy Designations and Chemical Composition Limits for Wrought Aluminum and Wrought Aluminum Alloys*. Arlington, VA, 2009.

[34] B. Sarkar, M. Marek, and E. A. Stark Jr., “The effect of Cu content and heat treatment on the stress corrosion characteristics of Al-6Zn-2Mg-XCu alloys,” *Met. Mater. Trans. A.*, vol. 12, pp. 1939–1943, 1981.

# CHAPTER 7

# POST PLASTIC DEFORMATION FACTORS

Following the extrusion process, aluminum alloys are often subjected to a number of mechanical and thermo-mechanical treatments, which can affect their mechanical properties. The post-extrusion processing of 7xxx-series aluminum alloys often includes: solution heat treatment (SHT), a plastic deformation step (ex. – stretching), a natural aging (NA) period, and an artificial aging (AA) cycle. The following chapter briefly discusses the impacts of these procedures on the decomposition process in 7xxx-series alloys.

## 7.1 The Effects of Solution Heat Treatment and Stretching

SHT is an important step in the processing of all precipitation hardenable alloys systems. The purpose of SHT is to put the microstructure into one phase (i.e. – into solution), so the precipitation process can occur in a controlled manner [1], [2]. For 7xxx-series alloys the temperature at which this occurs if often times near the incipient melting point, which if reached could result in localized melting effectively forcing the alloy to be scrapped. Therefore, SHT is generally a tightly controlled process in the industrial setting. Chen *et al*. [3] provides a detailed study on the effects of several SHT on 7055 including dual-step SHT.

SHT also introduces a large vacancy concentration in to the aluminum matrix [4]. These vacancies act as nucleation sites during the aging process, especially for GP-II zones. Therefore, a good quench practice from SHT is required to trap the vacancies in the matrix. The quench sensitivity of an alloy is generally a direct result of the total solute, the dispersoid type, and the degree of recrystallization (REX) [2], [5], [6]. As mentioned in *Chapter 4 – The Homogenization of Al-Zn-Mg-Cu Alloys*, Cr-containing alloys like 7075 and 7178 often time display a high degree of quench sensitivity whereas

Zr-containing alloys like 7136 and 7055 do not [5], [7], [8]. The total amount of solute, especially with respect to the Zn, Mg, and Cu concentrations, has a direct correlation to the quench sensitivity of an alloy; for instance, an alloy with a high solute content will have a tendency to experience rapid decomposition during a slow quench resulting in the formation of equilibrium phases in the microstructure [9]. Research has shown that this could be attributed to the addition of Cu to an Al-Zn-Mg alloy and/or low magnesium contents (i.e. – a low Zn:Mg ratio) [8]–[11].

It has been well documented that dislocations, vacancies, and solute atoms appear to have dramatic effects on the decomposition process in Al-Zn-Mg-Cu alloys [12]–[14]. In the study of 7xxx-series alloys it is imperative that the effect of dislocations and vacancies on the decomposition process not be ignored as the industrial process of aluminum extrusion almost always involves a plastic deformation process (ex. – stretching) [7]. This plastic deformation step often introduces a large density of dislocations which can alter the precipitation process of the alloy either by the heterogeneous precipitation of η or by the modification of the precipitation kinetics [15]. With respect to the formation of η precipitates on dislocations, research suggests that the growth of these particles is much faster than their growth in the bulk material which leads to a large, coarse particle [16]. It has also been shown that the presence of these stretch-induced dislocations slows down the precipitation kinetics during low temperature aging (thus most affecting the formation of VRC and GP zones) due to the annihilation of quench-induced vacancies on said dislocations [16], [17]. This in turn leads to a decrease in η' which leads to a decrease in the strength of the alloys in the T6 temper. There is research, however, that suggest that subjecting a low copper, stretched alloy to natural aging prior to artificial aging should allow for some of the strength lost due to stretching to be regained [18].

## 7.2 Natural Aging

7xxx-series alloys are often subjected to a NA process either deliberately or inadvertently due to manufacturing constraints [7]. The effects of natural aging (NA) are often far-reaching even in the over-aged T7 condition. Therefore, it is paramount that the varying effects of NA period be well understood with respect to an alloy's final properties.

There is research to suggest that subjecting a low-Cu 7xxx-series alloy (ex. – 7108, 7030) to natural aging prior to an artificial heat treatment promotes the growth of a fine homogenous-like dispersion of GP-I zones [15], [18], [19]. In theory, the GP-I zones precipitated out during NA would be dissolved back into solution upon ramping to the artificial heat treatment temperature. Therefore, a fine dispersion of concentrated solute would exist that could act as nucleation sites for GP-II zones, which in turn would allow the alloy to undergo the preferred precipitation process. Waterloo *et al*. [18] and Deschamps *et al*. [15] reported that this practice allowed for some of the strength lost due to stretching (up to 20% when compared to non-stretched alloys) to be regained (up to 10%). However, their findings seem to suggest that the desired NA period may be highly alloy dependent with Waterloo reporting an optimum time of 24-58 hours for 7108 and Deschamps reporting an optimum time of 72 hours for 7030 [15], [18].

The effects of NA are not universally beneficial to 7xxx-series alloys. On the contrary, it appears that subjecting a high-Cu 7xxx-series alloys (i.e. – alloys with a Cu content approximately greater than 1 wt.%) to NA prior to artificial aging (AA) can be extremely detrimental to the strength of these alloys. This deleterious effects can be clearly seen in Figure 31 [2].

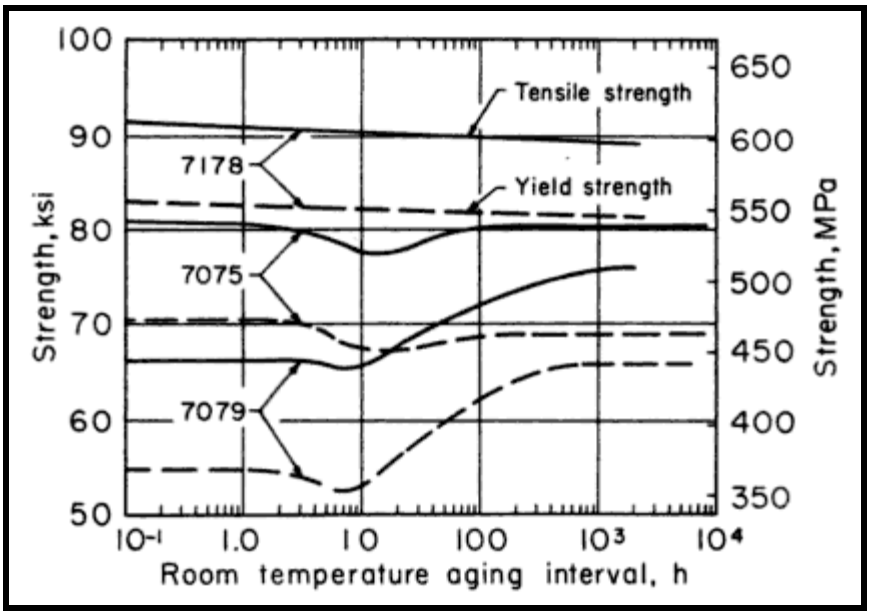


Figure 31 – *The effect of the time interval at room temperature between quenching and precipitation heat treating on the tensile and yield strengths of 7178-T6m 7075-T6, 7079-T6 alloy sheet. It should be noted that the following represent registered Cu composition ranges for the alloys plotted above: 7178 – 1.6-2.4 wt.%, 7075 – 1.2-2.0 wt.%, and 7079 – 0.4-0.8 wt.%* [2].

The decrease in strength is most likely due to the stabilization of GP-I zones that precipitate out during the NA process [20]. The effect of GP zone stabilization with increasing Cu content was first reported by Polmear [21] who observed an increase in the temperature range of zone stability with increase Cu content [22], [23]. Therefore, it appears reasonable that in high Cu alloys GP-I zones formed upon NA become stabilized and do not revert back into solution in time for GP-II zones to form, but rather precipitate directly to η as follows [24]:

$$\alpha_{ssss} \rightarrow \text{GP-I zones} \rightarrow \text{(possible SSSS?)} \rightarrow \text{Stable } \eta\ (MgZn_2)$$

While these findings may seem contradictory to some research, most notably that of Sha and Cerezo [25] who found that the precipitation of η' was possible on small GP-I zones (although the authors explicitly state that this is not the main precipitation process, but rather an anomaly), it becomes evident upon closer inspection that the size of the GP-I zones becomes a critical factor in this relatively undocumented precipitation sequence [26]. This size constraint coupled with the stabilizing effects of Cu seem to suggest that

the benefits of sparse GP-I to η' precipitation is not enough to overcome the effects of the widespread formation of η on GP-I zones.

### 7.3 Artificial Aging

The complexity of the Al-Zn-Mg-Cu precipitation process clearly indicates that a multi-step artificial heat treatment must be performed in order to optimize a 7xxx-series alloy. Generally, this is accomplished with a two-step aging heat treatment (100-130°C → 160+°C). The general mechanisms (as compiled from *Chapter 6 – The Precipitation Process*) taking place in these temperature ranges can be seen in Figure 32.

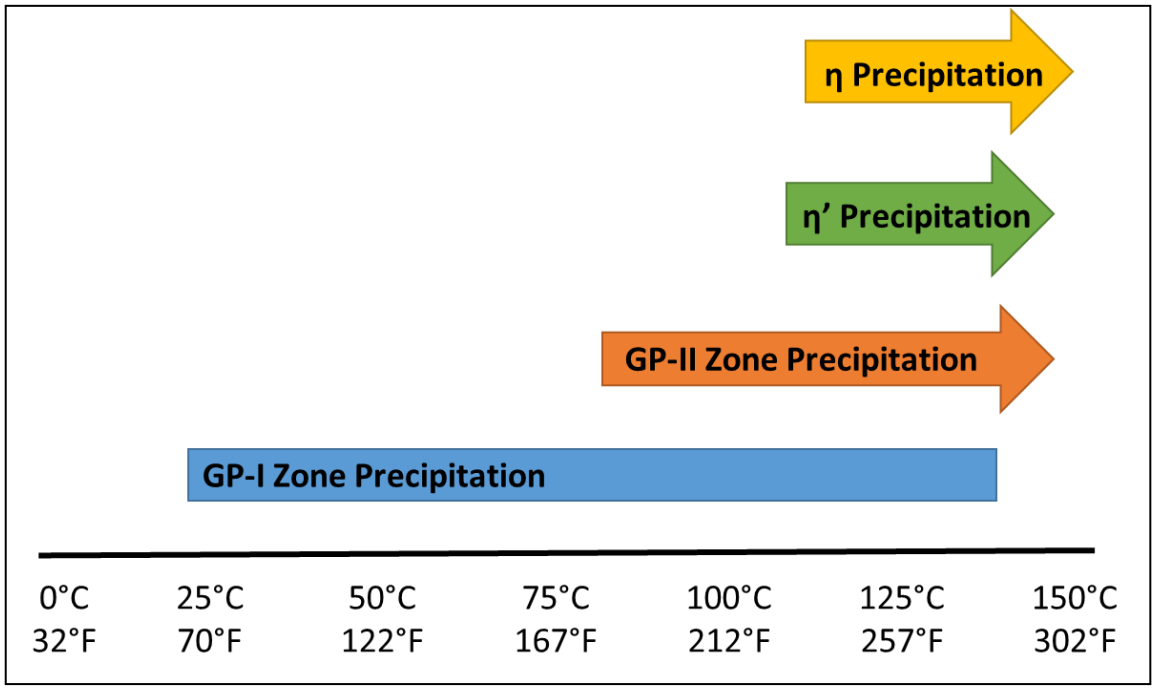


Figure 32 – *The effects of temperature on the precipitation process.*

In 1974, Cina [27] patented a three-step aging cycle he coined retrogression and re-aging (RRA), which he claimed offered comparable strength to T6 specimens and corrosion resistance comparable to T76 temper specimens. Typically, a RRA cycle is composed of three steps and can be seen below graphically in Figure 33 [28]:

| | |
|---|---|
| Step 1 | Pre-aging leading to an under-aged or T6 state. |
| Step 2 | Retrogression at a high temperature for a short duration. |
| Step 3 | Re-aging at temperatures similar to those for Step 1. |

It is important to note that the purpose of the retrogression step is to send the initially formed precipitates (i.e. – GP zones and η') back into solution. Research conducted by Xu *et al.* [28] demonstrated that not only are the RRA temperatures important, but that heating rate plays a large role as well. It was shown that that the RRA process for 7150 was optimized when a first step aging temperature of 60°C (140°F) was used and the heating rate to the second step aging temperature, 195°C (383°F), was approximately 5°C/min. Xu *et al*. [28] states this is due largely to the smaller potential difference between grain boundary precipitates and the matrix as well as a large volume fraction of precipitates in the matrix.

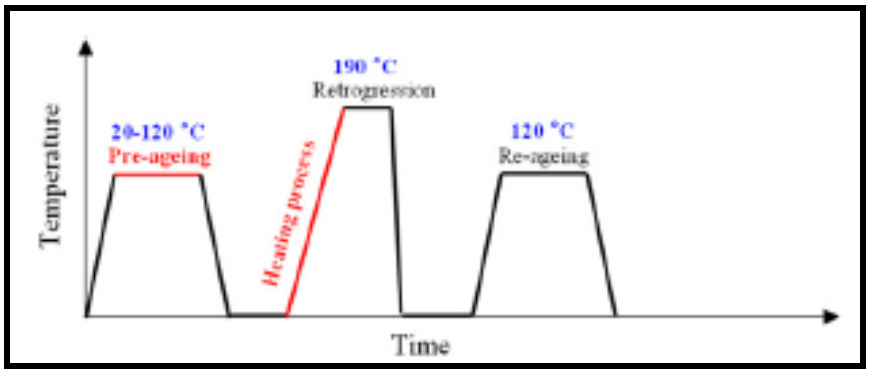


Figure 33 – *Schematic of RRA artifical aging procedure* [28].

Alcoa patent US 4.431,467 details a three step aging procedure for 7xxx-series aluminum alloys [29]. The three step aging procedure, which is stated to be effective particularly in the case of poorly quenched or thick aluminum products, patented by Staley and Sawtell [28] is as follows:

| | |
|---|---|
| Step 1: | 87.78-110°C (190-230°F) for 4-30 Hours |
| Step 2: | 110-126.67°C (230-260°F) for 4-30 Hours |
| Step 3: | 157.22-193.33°C (315-380°F) for 2-100 Hours |

Staley and Sawtell documented the results of multiple quench studies (see Table 5) that were subsequently subjected to the artificial heat treatment described above (see Figure 34). It was found that the three step aging procedure had no quantifiable effects on products that had experienced a proper quench, but tensile properties were improved for

poorly quenched samples. This was attributed to the growth of GP zones during the first, or "pre-age," step in between the large η precipitates that nucleated upon quench from SHT [28]. It should be noted that the GP-zones formed during the pre-aging step are most likely GP-I zones.

Table 5 – *Quench media and quench rates for various samples studied in US 4,431,467* [28].

| Sample | Quench Media | Quench Rate | |
|---|---|---|---|
| | | °C/sec | °F/sec |
| **I** | Water at 21°C | 1089 | 1960 |
| **II** | Water at 77°C | 370 | 666 |
| **III** | Water at 99°C | 39.10 | 70.30 |
| **IV** | Air Blast | 8.22 | 14.80 |
| **V** | Still Air | 1.90 | 3.42 |

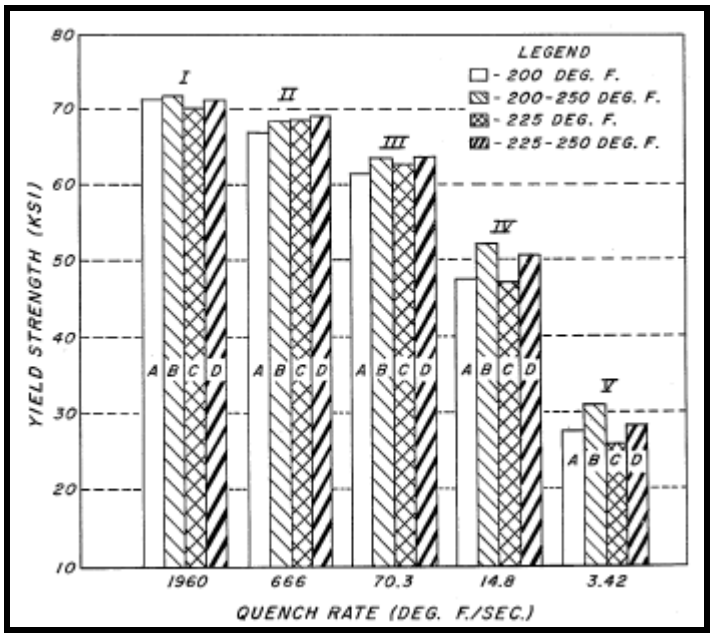


Figure 34 – *Tensile yield strength (KSI) versus quench rate (°F/sec) data from US 4,431,467* [28].

Buha *et al*. [29] describes a process known as "secondary aging" in which a 7xxx-series alloy is subjected to a natural aging or low temperature aging step (i.e. – RT to approximately 70°C) following a first step aging temperature of 130°C (266°F). The secondary aging treatment results in modified microstructure with more GP-II zones and

η’ precipitates, which increases fracture toughness and has a tensile strength comparable to a normal T6 treatment.

## 7.4 Summary

Several post process factors were discussed that could directly affect the mechanical properties and the decomposition process of 7xxx-series alloys. The effects of SHT and stretching were reviewed as were the basic principles of several industrial aging practices. In order to extract information on the effects of decomposition on mechanical properties these factors need to be well understood.

## 7.5 References


[1] C. Nowill, “Investigation of the quench and heating rate sensitivities of selected 7000 series aluminum alloys,” Worcester Polytechnic Institute, 2007.

[2] J. E. Hatch, *Aluminum: Properties and Physical Metallurgy*. ASM, 1984.

[3] K. Chen, H. Liu, Z. Zhang, S. Li, and R. I. Todd, “The improvement of constituent dissolution and mechanical properties of 7055 aluminum alloy by stepped heat treatments,” *J. Mater. Process. Technol.*, vol. 142, no. 1, pp. 190–196, Nov. 2003.

[4] A. Deschamps and Y. Brechet, “Nature and distribution of quenched-induced precipitation in an Al-Zn-Mg-Cu alloy,” *Scr. Mater.*, vol. 39, no. 11, pp. 1517–1522, 1998.

[5] S. Lim, S. Yun, and S. Nam, “Improved quench sensitivity in modified aluminum alloy 7175 for thick forging applications,” *Mater. Sci. Eng. A*, vol. 371, no. 1–2, pp. 82–90, Apr. 2004.

[6] S. D. Liu, X. M. Zhang, M. a. Chen, and J. H. You, “Influence of aging on quench sensitivity effect of 7055 aluminum alloy,” *Mater. Charact.*, vol. 59, no. 1, pp. 53–60, Jan. 2008.

[7] T. Sheppard, *Extrusion of Aluminium Alloys*. Kluwer Academic Publishers Group, 1999.

[8] A. Deschamps and Y. Brechet, “Influence of quench and heating rates on the ageing response of an Al-Zn-Mg-(Zr) alloy,” *Mater. Sci. Eng.*, vol. A251, pp. 200–207, 1998.

[9] A. J. Bryant, “The effect of composition upon the quench-sensitivity of some Al-Zn-Mg alloys,” *J. Inst. Met.*, vol. 94, pp. 94–99, 1966.

[10] C. Garcia-Cordovilla and E. Louis, “Investigation of the decomposition of the solid solution of a commerical Al-Zn-Mg alloy (7015), by means of DTA, hardness and conductivity measurements,” in *Thermal Analysis*, H. G. Wideman, Ed. Birkhauser Verlag, 1980, pp. 421–426.

[11] L. F. Mondolfo, *Aluminium Alloys: Structure and Properites*. London: Butterworths, 1976.

[12] H. Loffler, I. Kovacs, and J. Lendvai, “Decomposition processes in Al-Zn-Mg alloys,” *J. Mater. Sci.*, vol. 18, pp. 2215–2240, 1983.

[13] G. Dlubek, R. Krause, O. Brummer, and G. Plazaola, “Study of formation and reversion of guinier-preston zones in Al-4.5at%Zn-xat%Mg alloys by positrons,” *J. Mater. Sci.*, vol. 21, pp. 853–858, 1986.

[14] R. Ferragut, A. Somoza, and A. Dupasquier, “On the two-step ageing of a commercial Al-Zn-Mg Alloy: a study by positron lifetime spectroscopy,” *J. Phys. Condens. Matter*, vol. 8, pp. 8945–8952, 1996.

[15] A. Deschamps, F. Livet, and Y. Brechet, “Influence of predeformation on ageing in an Al-Zn-Mg Alloy-I: microstructure evolution and mechanical properties,” *Acta Mater.*, vol. 47, pp. 281–292, 1998.

[16] R. N. Allen and J. B. Vander Sande, “The oriented growth of precipitates on dislocations in Al-Zn-Mg,” *Acta Mater.*, vol. 28, no. 9, pp. 1185–1189, 1980.

[17] S. Cersesara and P. Fiorini, “Resistometric investigation of the ageing process after quenching and cold-work in Al-Zn-Mg alloys,” *Mater. Sci. Eng.*, vol. 10, pp. 205–210, 1972.

[18] G. Waterloo, V. Hansen, J. Gjønnes, and S. R. Skjervold, “Effect of predeformation and preaging at room temperature in Al–Zn–Mg–(Cu , Zr) alloys,” *Mater. Sci. Eng.*, vol. 303, pp. 226–233, 2001.

[19] A. Deschamps and Y. Brechet, “Influence of predeformation on ageing in an Al-Zn-Mg Alloy - II: modeling precipitation kinetics and yield stress,” *Acta Mater.*, vol. 47, pp. 293–305, 1998.

[20] J. Lamb, V. Dangerfield, and T. H. Sanders Jr., “The effect of natural aging on 7xxx-series alloys,” Canton, GA, 2013.

[21] I. J. Polmear, *Light Metals*. Arnold, 1995.

[22] J. T. Staley, “Aging kinetics of aluminum alloy 7050,” *Metall. Trans.*, vol. 5, pp. 929–932, 1974.

[23] H. Y. Hunsicker, “Development of Al-Zn-Mg-Cu alloys for aircraft,” in *Proc. Rosehain Centenary Conf. on the Contribution of Physical Metallurgy to Engineering Practice*, 1976, pp. 359–376.

[24] M. R. Clinch, S. J. Harris, W. Hepples, N. J. H. Holroyd, M. J. Lawday, and B. Noble, “Influence of zinc to magnesium ratio and total solute content on the strength and toughness of 7xxx-series alloys,” *Mater. Sci. Forum*, vol. 519–521, pp. 339–344, 2006.

[25] G. Sha and A. Cerezo, “Early-stage precipitation in Al–Zn–Mg–Cu alloy (7050),” *Acta Mater.*, vol. 52, no. 15, pp. 4503–4516, Sep. 2004.

[26] N. Q. Chinh, J. Lendvai, D. H. Ping, and K. Hono, “The effect of Cu on mechanical and precipitation properties of Al–Zn–Mg alloys,” *J. Alloys Compd.*, vol. 378, no. 1–2, pp. 52–60, Sep. 2004.

[27] B. Cina, “Retrogression and Reaging and the Role of Dislocations in the Stress Corrosion of 7000-Type Aluminum Alloys,” vol. 20, no. October, pp. 2087–2092, 1989.

[28] D. K. Xu, N. Birbilis, and P. A. Rometsch, “The effect of pre-ageing temperature and retrogression heating rate on the strength and corrosion behaviour of AA7150,” vol. 54, pp. 17–25, 2012.

[29] J. T. Staley and R. R. Sawtell, “Aging process for 7000 series aluminum base alloys,” US4,431,467, 1984.

# PART II

# THE QUARTERNARY AL-ZN-MG-CU SYSTEM

# CHAPTER 8

# INTRODUCTION

The crucial roles of the alloying elements Zn, Mg, and Cu in aluminum have been the subject of a great deal of research since the early 1900's, especially with respect to the decomposition process; however, the varying effects of compositional fluctuations on the decomposition process have yet to be fully understood [1], [2]. The following chapters seek to characterize and quantify the effects of various Zn:Mg ratios and Cu contents on the decomposition process in 7xxx-series aluminum alloys, and therefore their mechanical properties. Special attention was given to the production processes of homogenization and natural aging in addition to the effect of composition on the width of the precipitate free zones (PFZ) near grain boundaries.

The experimental alloys studied herein were cast, homogenized, and rolled at the Georgia Institute of Technology (GT). The composition of each alloy was verified by William Krumme at Vista Metal Corporation – Adairsville, GA (Vista-Adairsville) before being solution heat treated and stretched at the Universal Alloy Corporation – Canton, Ga (UAC-Canton). Various artificial and natural aging cycles were then utilized to fully understand the effects of composition and processing parameters on the decomposition process. These effects were then characterized and quantified using various metallurgical techniques including: optical microscopy (UAC-Canton), transmission electron microscopy (GT), differential scanning calorimetry (UAC-Canton), Rockwell hardness (GT), corrosion testing (UAC-Canton), and conductivity testing (UAC-Canton).

The following section is organized as follows: Chapter 9 covers the various materials and experimental procedures used; Chapter 10 details observations made during the casting and homogenization of the experimental alloys; and Chapter 11, likewise,

details observations made during the subsequent rolling, solution heat treatment, and stretching of the experimental alloys. Chapters 12 and 13 detail the effects of natural aging and artificial aging, respectively, while Chapter 14 seeks to correlate the width of the PFZ observed in the experimental alloys to their composition.

## 8.1 References


[1] W. Campbell and J. A. Mathews, "The alloys of aluminum," *J. Am. Chem. Soc.*, vol. 24, pp. 253–266, 1902.

[2] E. S. Shepard, "Aluminum-zinc alloys," *J. Am. Chem. Soc.*, vol. 8, pp. 504–512, 1905.

# CHAPTER 9

# MATERIALS AND EXPERIMENTAL PROCEDURE

In order to characterize and quantify the effects of decomposition on the mechanical properties of 7xxx-sereis alloys, a series of experimental Al-Zn-Mg-Cu alloys were cast at GT. The alloys, aptly referred to as GT1-8 herein, can be subdivided into two distinct groups: Group 1 (GT1-5) focuses on the effect of Cu-content with a semi-constant Zn:Mg ratios, and group 2 (GT6-8) focuses on the effects of varying Zn:Mg ratios with a semi-constant Cu-contents.

## 9.1 Materials

The average registered composition of aluminum alloy 7136 was used as an initial target for GT1 with respect to the Zn, Mg, and Cu contents [1]. The target compositions of experimental alloys GT2-8 were then delineated from GT1 in a systematic manner based on their intended purpose (i.e. – to study the effect of the Zn:Mg ratio or the effect of Cu-content), and can be seen in Table 6. The following raw materials were used to cast GT1-8:

- Aluminum Shot (99.9wt.% pure)
- Zinc Shot (99.9wt.% pure)
- Al-24wt.%Mg Master Alloy
- Al-33wt.%Cu Master Alloy

In order to avoid various complications, grain refiners, dispersoid forming elements, and other minor alloying additions were intentionally left out of the casts.

Table 6 – *Target compositions at.% (wt.%) for experimental alloys GT1-8.*

| Alloy | Zn | Mg | Cu |
|---|---|---|---|
| **GT1** | 4.00 (9.1) | 2.37 (2.0) | 1.00 (2.2) |
| **GT2** | 4.00 (9.1) | 2.37 (2.0) | 0.68 (1.5) |
| **GT3** | 4.00 (9.1) | 2.37 (2.0) | 0.45 (1.0) |
| **GT4** | 4.00 (9.1) | 2.37 (2.0) | 0.24 (0.5) |
| **GT5** | 4.00 (9.1) | 2.37 (2.0) | 0.00 (0.0) |
| **GT6** | 348 (7.9) | 3.08 (2.6) | 1.00 (2.2) |
| **GT7** | 3.28 (7.5) | 3.29 (2.8) | 1.00 (2.2) |
| **GT8** | 3.09 (7.1) | 4.68 (4.0) | 1.00 (2.2) |

As previously mentioned, experimental alloys GT1-8 can be subdivided into two categories. Figures 35 and 36 display the effects alloys GT1-5 and GT1, 6-8 are intended to study, respectively. It is believed that Cu-content plays a drastic role with respect to an alloy's response to natural aging (NA), and therefore alloys GT1-5 should help characterize and quantify these effects in a systematic manner. In a similar manner, it is believed that the dominate type of GP-zone is determined in part by the Zn:Mg ratio. Experimental alloys GT6-8 (along with GT1) seek validate and characterize these beliefs. Figure 37 shows how the target compositions for GT1-8 compare against each other.

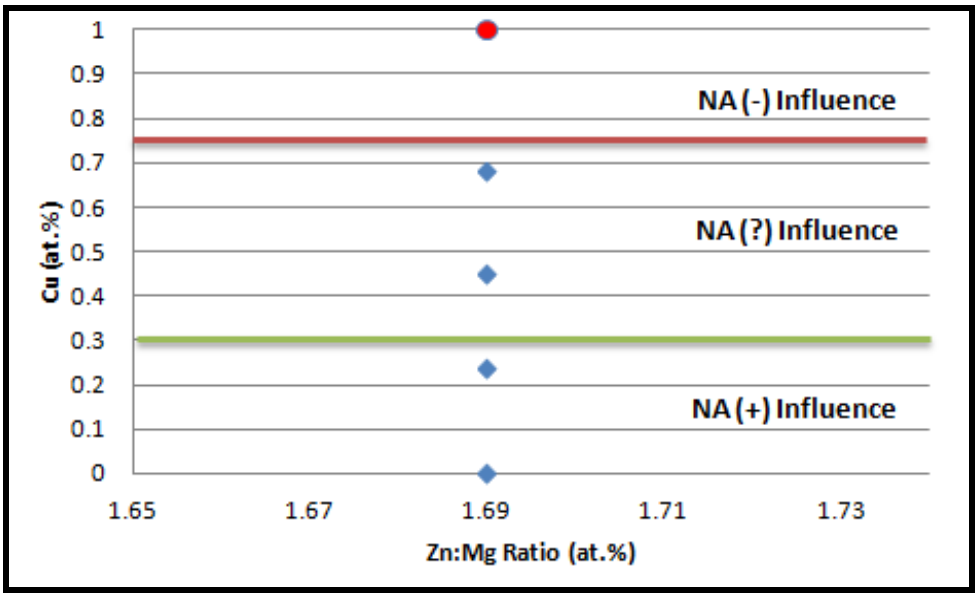


Figure 35 – *The target compositions for GT1-5. Note the red circle denotes the composition of GT1. The basis for the NA influence lines was covered in Part I of this document.*

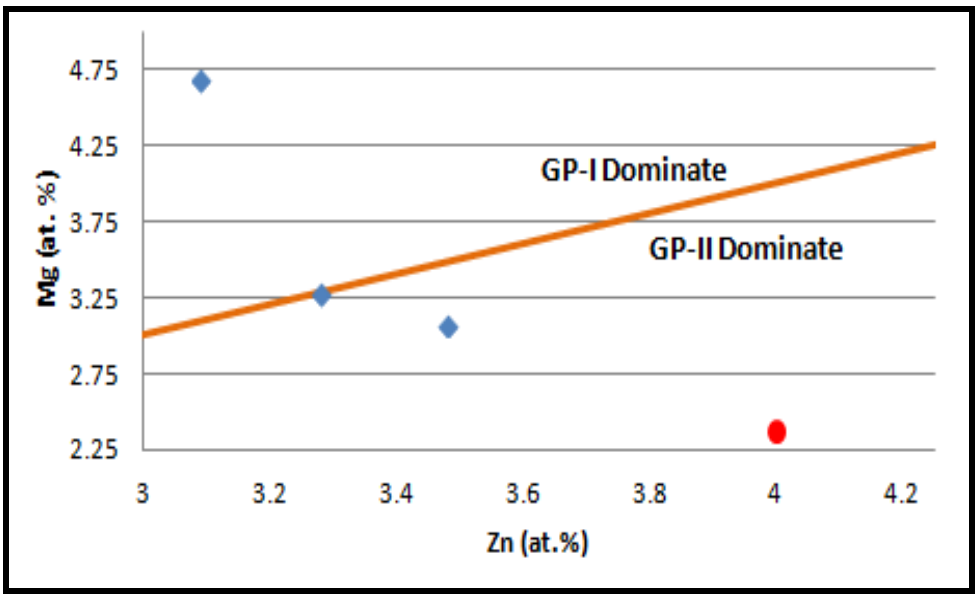


Figure 36 – *The target compositions for GT6-8. Note the red circle denotes the composition for GT1. The basis of the GP type domination line was covered in Part I of this document.*

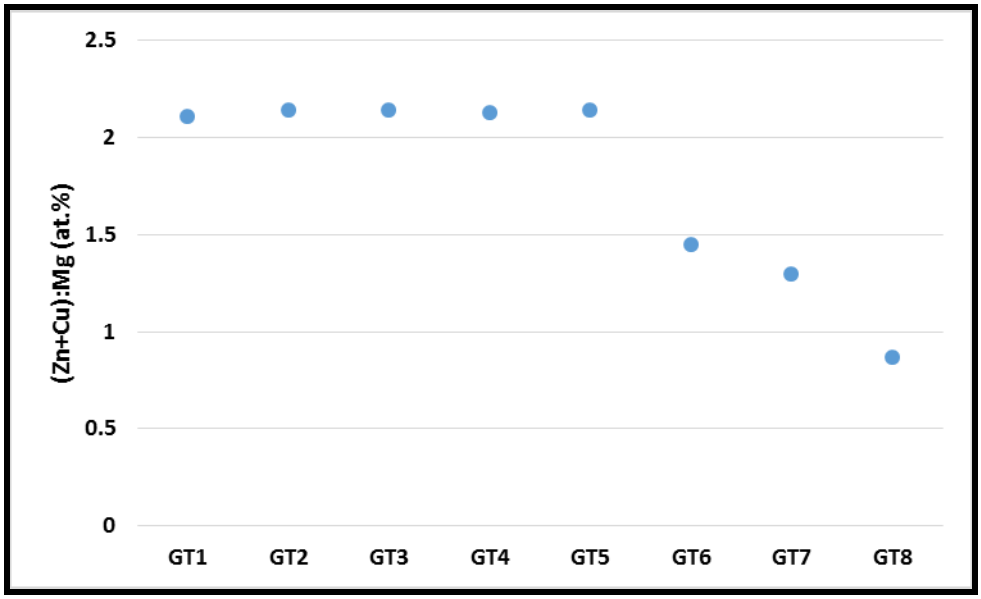


Figure 37 – *GT1-8 with respect to their target (Zn+Cu):Mg ratios (at.%).*

### 9.2 Casting Procedure

The book mold used for this work measures approximately 12.24 cm x 7.2 cm x 1.9 cm, and a 7136 ingot cast in the book mold weighs approximately 600 g. Therefore, casts of GT1-8 were planned for 600 g. Alloy composition verification was carried out by William Krumme at Vista-Adairsville using spark atomic emission spectrometry.

Experimental alloys GT1-8 were cast in two separate "runs" with alloys GT1-5 being cast first out of a master alloy (see below) and then GT6-8 being cast out of another master alloy.

### 9.2.1 GT1-5

To begin, six "Al-Zn-Mg master alloys" were gravity cast to use during the casting of GT1-5. These master alloys had approximately the composition of GT1 minus the copper (455.40g Al, 54.60g Zn, 50.00g Mg) as it has the lowest aluminum content of GT1-5. These six casts were then cut up and mixed to ensure a randomized and semi-constant Zn and Mg content. Subsequently, alloys GT1-5 were cast with small additions of Al shot and Al-Cu as necessary.

In accordance to the work done by Last [2] and Rangathan [3] with minor changes, the following steps were followed in the casting of GT1-5:

1. Pre-heat the furnace to 750°C (1382°F).
2. Add Al shot to the crucible and allow to melt.
3. Once molten, skim the top of the crucible and stir.
4. Allow furnace to reach 740°C (1364°F).
5. Skim the surface of the melt, add zinc shot, and then stir.
6. Allow furnace to sit at 750°C (1382°F) for 20 minutes.
7. Skim the surface of the melt, add Al-Mg master alloy, and then stir.
8. Allow the furnace to sit at 750°C (1382°F) for 20 minutes.
9. If molten, skim the surface, and then stir.
10. Allow melt to reach 740°C (1364°F).
11. Cast 'master' alloy.
12. Section the alloy and mix with other casts to ensure constant composition.
13. Pre-heat the furnace to 750°C (1382°F).
14. Add Al-Zn-Mg master alloy to the crucible and allow to melt.
15. Once molten, skim the surface, add Al-Cu master alloy, and stir.
16. Allow the furnace to sit at 750°C (1382°F) for 20 minutes.
17. If molten, skim the surface, and then stir.
18. Allow melt to reach 740°C (1364°F).
19. Cast final alloy.

It should also be noted that the book mold was preheated to 120°C (248°F) prior to casting to rid the mold of moisture, but was allowed to cool to RT prior to casting.

### 9.2.2 GT6-8

In order to produce GT6-8 a set of "master alloys" were gravity cast. These "master alloys" compositionally contained the final Al and Cu contents for each of the respected alloys and the minimum Zn and Mg contents found in the set. In a manner similar to the casting procedure for GT1-5, the master alloys were then cut up, randomized, and re-cast with appropriate Zn and Mg additions to produce GT6-8. The following casting procedure was used:

1. Pre-heat the furnace to 750°C (1382°F).
2. Add Al shot to the crucible and allow to melt.
3. Once molten, skim the top of the crucible and stir.
4. Allow furnace to reach 740°C (1364°F).
5. Skim the surface of the melt, add Zn shot, and then stir.
6. Allow the furnace to reach 740°C (1364°F).
7. Skim the surface of the melt, add Al-Cu master alloy, and then stir.
8. Allow the furnace to reach 740°C (1364°F).
9. Skim the surface of the melt, add Al-Mg master alloy, and then stir.
10. Allow furnace to sit at 750°C (1382°F) for 20 minutes.
11. If molten, skim the surface, and then stir.
12. Allow melt to reach 740°C (1364°F).
13. Cast 'master' alloy.
14. Section the alloy and mix with other cast to ensure constant composition.
15. Pre-heat the furnace to 750°C (1382°F).
16. Add Al-Zn-Mg-Cu master alloy to the crucible and allow to melt.
17. Once molten, skim the surface, add Zn shot, and stir.
18. Allow the furnace to sit at 750°C (1382°F) for 20 minutes.
19. Skim the surface of the melt, add Al-Mg master alloy, and then stir.
20. Allow the furnace to sit at 750°C (1382°F) for 20 minutes.
21. If molten, skim the surface, and then stir.
22. Allow melt to reach 740°C (1364°F).
23. Cast final alloy.

It should also be noted that the book mold was preheated to 120°C (248°F) prior to casting to rid the mold of moisture, but should be allowed to cool to RT prior to casting.

## 9.3 Homogenization

To determine the homogenization temperatures for alloys GT1-8, differential scanning calorimetry (DSC) scans were run on GT1-8 in the as-cast condition. The homogenization temperature was then determined by using the lowest onset melting

temperature in a set of alloys (i.e. – GT1-5 and GT6-8). Scans were run on a Pyris DSC 1 and a Pyris DSC 8000.

DSC samples were prepped by first core drilling a 0.635 cm (0.25 in) bar out of the end of the as-cast book mold. The bar was then cut via a high speed Leica saw into approximately 1 mm sections. The sections, subsequently, were ground using 400-600 grit paper to a height of 0.50 ± 0.05 mm. The samples were then cleaned with acetone before being mounted in a 10 μL aluminum pan. DSC scans were run against a reference (empty) 10 μL aluminum pan under argon at a rate of 20°C/min (68°F/min) from 50°C (122°F) to 515°C (959°F). The results were calculated using Pryis software.

The determination of the homogenization time was done using a Fick's Second Law estimation based off the average secondary dendrite arm spacing. Samples were mounted and polished according to the following polishing procedure using a Leica automatic polisher:

1. US 120 grit for approximately 30 seconds.
2. US 240 grit for 2 minutes.
3. US 400 grit for 2 minutes.
4. US 600 grit for 2 minutes.
5. US 800 grit for 2 minutes.
6. 9 μm diamond polish for 2 minutes and 30 seconds.
7. 3 μm diamond polish for 2 minutes and 30 seconds.
8. 1 μm diamond polish for 2 minutes and 30 seconds.
9. Colloidal silica polish for 1 minute.

Samples were etched using Keller's reagent (2-5% nitric acid, 1-5% hydrochloric acid, 0-5% hydrofluoric acid, water rem.) for approximately 20 seconds to reveal the dendritic microstructure. Approximately 50-75 measurements were taken per alloy using ImageJ software to determine the average dendrite arm spacing. The average arm spacing was plugged into Fick's second law (see Equation 24) to estimate the time needed for homogenization of alloys GT1-8 [4]:

$$\frac{\partial \varsigma}{\partial t} = D\frac{\partial^2 \varsigma}{\partial x^2} \tag{24}$$

Where ς is the concentration, D a diffusion coefficient, t the time in seconds, and x is the length of diffusion (i.e. – the dendritic arm spacing). A list of diffusion coefficients can be seen below in Table 7 (note – a more comprehensive list can be found in *Part I – Chapter 4 – The Homogenization of Al-Zn-Mg-Cu Alloys* in Table 1) . Solving Equation 24 for time (in hours) yields:

$$t = \frac{X^2}{3600D} \tag{25}$$

Were D is given by:

$$D = D_0 \exp\left(\frac{Q}{RT}\right) \tag{26}$$

It should be noted in Equations 25 and 26 that t is time, X is the average secondary dendritic arm spacing, D is the adjusted diffusion coefficient, R is the universal gas constant, T is the temperature, Q is the activation energy, and $D_0$ is the diffusion coefficient.

Table 7 – *Diffusion coefficients for common alloying elements found in 7xxx-series aluminum alloys. It should be noted that D is calculated from $D_o$ and Q and the homogenization temperature in Kelvin [30, 37, 38].*

| Element | $D_0$ ($m^2/s$) | Q (J/mol) |
|---|---|---|
| **Silicon (Si)** | 9.00E-05 | 125600 |
| **Iron (Fe)** | 4.10E-15 | 58600 |
| **Copper (Cu)** | 2.90E-05 | 125600 |
| **Manganese (Mn)** | 2.20E-05 | 121400 |
| **Magnesium (Mg)** | 1.10E-04 | 117200 |
| **Chromium (Cr)** | 3.00E-11 | 62800 |
| **Nickel (Ni)** | 4.40E-04 | 145690 |
| **Zinc (Zn)** | 1.10E-05 | 260510 |
| **Silver (Ag)** | 1.30E-05 | 116750 |
| **Vanadium (V)** | 1.60E-00 | 302960 |
| **Zirconium (Zr)** | 7.28E-02 | 240800 |
| **Titanium (Ti)** | 1.12E-01 | 260510 |

### 9.4 Rolling Procedure

Prior to rolling, alloys GT1-8 were milled to remove the liquation zone formed on the outer edge of the ingot. This operation was performed in order to prevent liquation cracks from forming during the rolling process, which can cause an ingot to splinter. This operation was found to be vitally important for GT6-8 due to their higher Mg content.

The ingots were then preheated to approximately 343°C (650°F) and allowed to soak at that temperature for 3 hours prior to rolling. The ingots were then rolled to approximately a 60% reduction over the course of three separate reduction steps. For example, the first step resulted in an overall reduction of approximately 20%, the second step resulted in an overall reduction of approximately 40%, and the third step reduced the alloy to the final reduction (i.e. – 60%). It should be noted that the ingots were allowed to reheat after each pass for 1 hour in order to regain some of the heat lost during the rolling process. Following the last reduction step, the alloys were water quenched and prepped for solution heat treatment (SHT).

### 9.5 Solution Heat Treatment, Stretching, and Aging

In order to determine the SHT temperature, differential scanning calorimetry (DSC) scans were performed on the material in the F-temper (i.e. – the as-rolled condition). The temperature was selected based off either the lowest onset melting temperature or the temperature at which the material was fully solutionized in the DSC. It should be noted that these temperatures can fluctuate based off the DSC scan ran, and therefore care must be taken to use the same scan rate for each sample. Once a SHT temperature was determined, the alloys were SHT at said temperature for 45 minutes to 1 hour pending final thickness. The alloys were then water quenched and subsequently stretched 1-2% using an MTS testing apparatus at UAC-Canton.

Experimental alloys GT1-8 were artificially aged at various temperatures in various furnaces over the course of this work: a Lindenburg box furance (GT) and two

Paragon furnaces with Sentry 2.0 controls (GT and UAC). In each furnace a "base" block of AA5083 was used to help regulate the temperature. In order to assure a constant temperature between experiments a thermocouple reader was used to independently measure the air temperature inside the furnace as well as the temperature of the "base" block. However, it should be noted that all furnaces have temperature gradients and the furnaces were never surveyed over the course of this work to determine their "working zones."

### 9.6 Rockwell Hardness and Conductivity

Samples were prepared for Rockwell hardness (B-scale) testing by milling the samples down to a 9/10 thicknesses (T/10). The test were then conducted using a series 500 Wilson Rockwell hardness tester according to ASTM E18-14 [5]. Generally, 15-30 measurements were made per sample in order to obtain a reasonable average and standard deviation. It should be noted that the tester's calibration was checked prior to each round of testing using a standard.

Conductivity measurements were also taken on a milled surface at T/10. Conductivity measurements were performed at UAC-Canton using a Verimet M4900C. Prior to measurement, the samples were allowed 30 minutes to equilibrate to the lab temperature at UAC-Canton. This step is important because temperature differences between the samples and the standards used to calibrate the conductivity meter can result in false conductivity measurements.

### 9.7 Differential Scanning Calorimetry

Differential scanning calorimetry (DSC) samples were prepared at UAC-Canton by core drilling the rolled alloys into 0.635 cm (0.25 in) rods. The rods were then sectioned and the resulting discs were ground to approximately 0.50 mm (0.019685 in) using US240 abrasive SiC paper. The samples were then cleaned with acetone before being weighed and encased in pure Al pans before being tested in a either a Pyris DSC 1

or a Perkin-Elmer DSC8000. The samples were scanned from 50°C (122°F) to 515°C (959°F) using a scan rate of 20°C/min.

Figure 38 displays a typical DSC scan on a 7xxx-series aluminum alloy and annotates the typical peaks observed. Excothermic reactions can be linked to precipitation/transformation events, and endothermic reactions can be linked to dissolution and melting events. Generally, low-temperature sharp endothermic melting peaks correlate to either T-phase (~470°C) or S-phase (~480°C) melting. Sharp endothermic peaks at lower temperatures generally correlate to REX event.

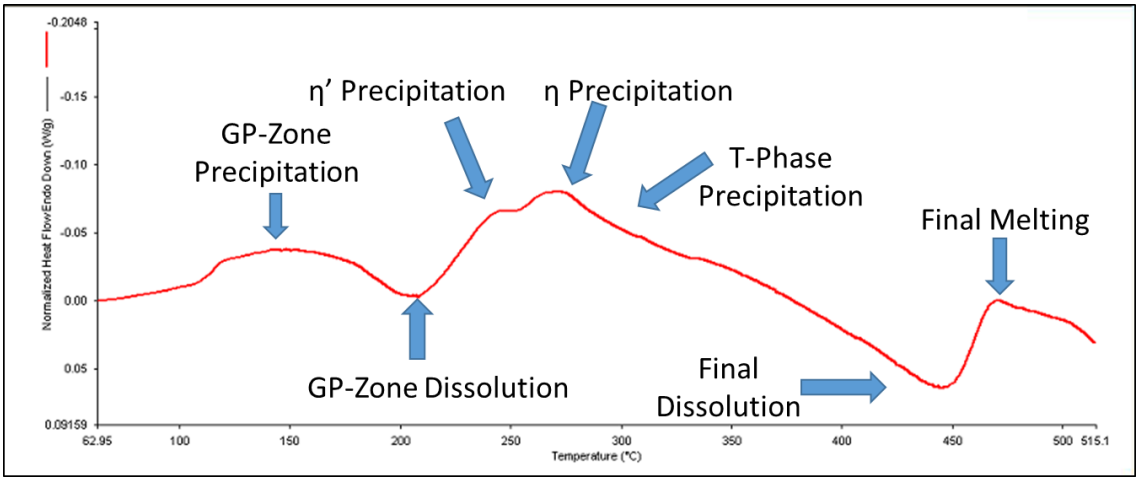


Figure 38 – *A general 7xxx-series aluminum alloy DSC curve annotating the various exothermic and endothermic peaks seen during the scan.*

### 9.8 Optical Microscopy

Samples prepared for optical microscopy were mounted and polished according the following polishing procedure using a Leica automatic polisher:

1. US 120 grit for approximately 30 seconds.
2. US 240 grit for 2 minutes.
3. US 400 grit for 2 minutes.
4. US 600 grit for 2 minutes.
5. US 800 grit for 2 minutes.
6. 9 µm diamond polish for 2 minutes and 30 seconds.
7. 3 µm diamond polish for 2 minutes and 30 seconds.
8. 1 µm diamond polish for 2 minutes and 30 seconds.
9. Colloidal silica polish for 1 minute.

The samples were washed with soap and water and then blow dried between each polishing step. The samples were then etched using a variety of etchants including Barker's Reagent, Kelley's Reagent, and phosphoric acid. The composition of the etchants used can be found in Appendix B.

### 9.9 Transmission Electron Microscopy

Numerous TEM samples were prepared over the course of this work at GT and Surface Treatment Technologies (ST2) by Tim Langan. It should be noted that while the exact method utilized by ST2 was not disclosed, the samples were jet-polished in a manner similar to that preformed at GT. TEM images were taken on a 100 KV Hitachi HT7700 with assistance from Todd Walters and Judy Dickson.

In order to prepare TEM samples at GT, GT1-8 (alongside samples of 7136 and 7075) were over-aged to a T73 temper (24 hours at 120°C followed by 24 hours at 160°C) prior to being machined into 0.635 cm DSC discs at UAC-Canton. The discs were then ground to approximately 0.50 mm using US240 SiC abrasive polishing paper. Subsequently, the disc were further ground to approximately 0.15 mm using US600 and then ground to approximately 0.05 mm using US800. The discs were then taken to GT were they were punched into 3 mm diameter disc, and jet-polished using a 75% methanol 25% nitric solution at -20°C (-4°F) to create TEM foils. Once the foils had been prepared, they were dipped in two beakers containing pure methanol 30 times each to clean each sample. The foils were then laid on coffee filters and gently blow dried.

### 9.10 Summary

The materials and methods utilized to study the decomposition process in 7xxx-series alloys were outlined. Once cast, experimental alloys GT1-8 were homogenized, rolled, solution heat treated, aged, and subsequently characterized using several methods including: optical microscopy, TEM, HRB, conductivity, and DSC. Alloying elements other than Zn, Mg, and Cu were ignored, including dispersoids. In some instances, analysis performed on registered 7xxx-series alloys is presented (ex – *Chapter 14 – The*

*Effect of Composition the Precipitate Free Zone*) in which case any deviations from the experimental procedure presented in this chapter are noted.

## 9.1 References


[1] The Aluminum Association, *International Alloy Designations and Chemical Composition Limits for Wrought Aluminum and Wrought Aluminum Alloys*. Arlington, VA, 2009.

[2] H. Last, "Precipitation of dispersoids in aluminum alloys," Georgia Institute of Technology, 1991.

[3] R. Rangathan, "Recrystallization resistance in aluminum alloys containing zirconium," Georgia Institute of Technology, 1991.

[4] T. Sheppard, *Extrusion of Aluminium Alloys*. Kluwer Academic Publishers Group, 1999.

[5] ASTM, "E18-14: standard test methods for Rockwell hardness of metallic materials." pp. 1–38, 2014.

# CHAPTER 10

# THE AS-CAST CONDITION AND HOMOGENIZATION

Experimental alloys GT1-11 were cast at GT. The alloys were cast and homogenized according the experimental procedure in Chapter 9. This chapter details the results of the casting and homogenization process as well as verification of the alloy compositions. Alloy composition verification was carried out by William Krumme (Vista-Adairsville).

It should be noted that this chapter contains information on three alloys, GT9-11, which were not covered in *Part II – Chapter 9 – Materials and Experimental Procedure*. This is because these three alloys were originally cast to be GT6-8, but due to an error during the casting process the alloys were not close to their target compositions. Still, the as-cast information they provided was deemed useful and was therefore included in this chapter. Subsequent chapters, however, will not contain information on GT9-11 as they did not survive the rolling process as a result of poor homogenization.

## 10.1 Verification of Alloy Composition

The compositions of GT1-11 were verified by William Krumme (Vista-Adairsville) and can be seen below in Table 8. Figure 39 gives a graphical representation of the experimental alloy compositions. It should be noted that the Fe and Si contents of these alloys are extremely low as are the contents of other impurities.

Table 8 – *Experimental alloy compositions (wt.%) as verified by Vista-Adairsville.*

| Alloy | Zn | Mg | Cu | Fe | Si | Other |
|---|---|---|---|---|---|---|
| **GT1** | 9.08 | 2.01 | 2.98 | 0.06 | 0.04 | 0.01 |
| **GT2** | 9.32 | 2.09 | 1.83 | 0.06 | 0.04 | 0.01 |
| **GT3** | 9.24 | 2.08 | 1.25 | 0.05 | 0.04 | 0.01 |
| **GT4** | 8.82 | 2.09 | 0.56 | 0.05 | 0.03 | 0.01 |
| **GT5** | 8.96 | 2.09 | 0.01 | 0.05 | 0.03 | 0.01 |
| **GT6** | 7.81 | 2.33 | 2.16 | 0.04 | 0.03 | 0.01 |
| **GT7** | 7.36 | 2.62 | 2.19 | 0.05 | 0.03 | 0.01 |
| **GT8** | 7.37 | 2.97 | 2.25 | 0.05 | 0.03 | 0.01 |
| **GT9** | 8.38 | 4.55 | 0.33 | 0.06 | 0.03 | 0.01 |
| **GT10** | 8.44 | 4.45 | 0.32 | 0.05 | 0.03 | 0.01 |
| **GT11** | 7.88 | 5.43 | 0.62 | 0.06 | 0.03 | 0.01 |

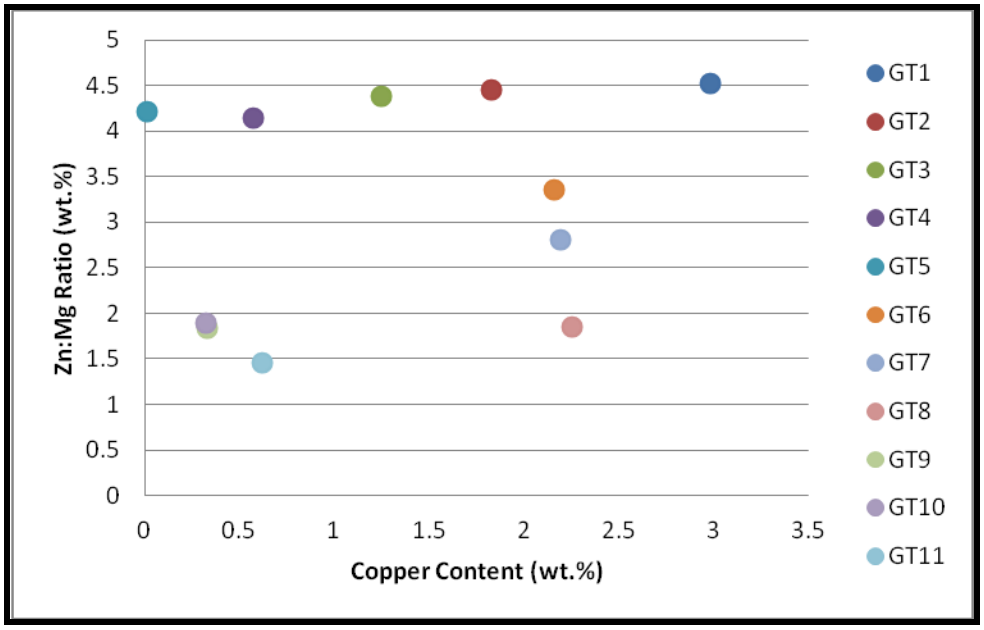


Figure 39 – *Copper contents versus the Zn:Mg ratios for experimental alloys GT1-11.*

### 10.2 The As-Cast Condition

Alloys GT1-11 were studied in the as-cast condition in order to determine the proper homogenization heat treatments for these alloys. Micrographs (see Figures 40 – 50) were taken in the longitudinal (casting) direction. These micrographs were then used to determine the average secondary dendrite arm spacing in the as-cast experimental alloys (see Table 9). These measurements were later used in conjunction with DSC to determine the homogenization for each alloy via a Fick's law estimation.

Table 9 – *Average secondary dendrite arm spacing (μm) with standard deviations for GT1-11. It should be noted the following averages are based off 50+ measurements.*

| Alloy | Dendritic Arm Spacing (μm) | Alloy | Dendritic Arm Spacing (μm) |
|---|---|---|---|
| GT1 | 34.43 ± 12.55 | GT7 | 32.93 ± 10.87 |
| GT2 | 31.82 ± 9.95 | GT8 | 41.83 ± 10.30 |
| GT3 | 38.33 ± 8.71 | GT9 | 46.42 ± 11.91 |
| GT4 | 35.67 ± 7.82 | GT10 | 35.88 ± 12.56 |
| GT5 | 24.78 ± 6.19 | GT11 | 34.35 ± 9.42 |
| GT6 | 50.52 ± 11.62 | | |

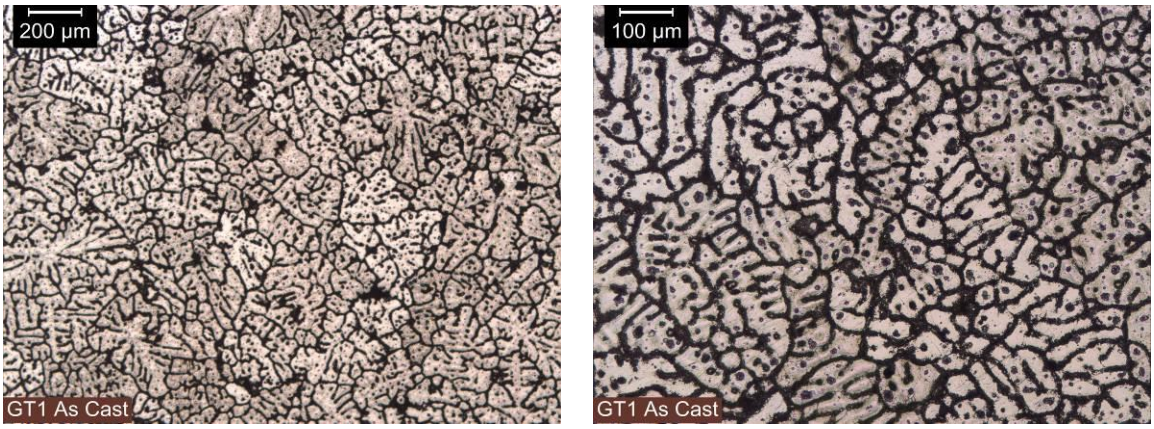

Figure 40 – *The as-cast microstructure of GT1 (Keller's reagent).*

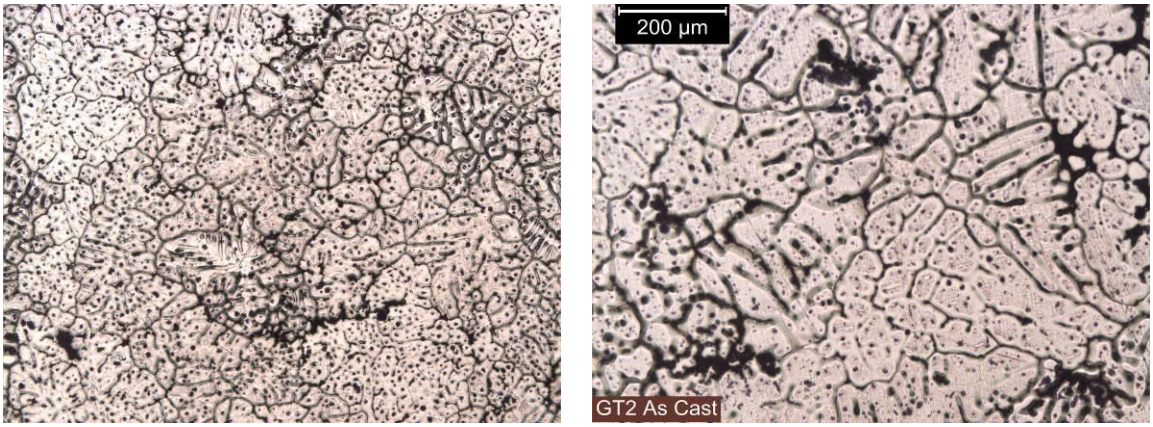

Figure 41 – *The as-cast microstructure of GT2 (Keller's reagent).*

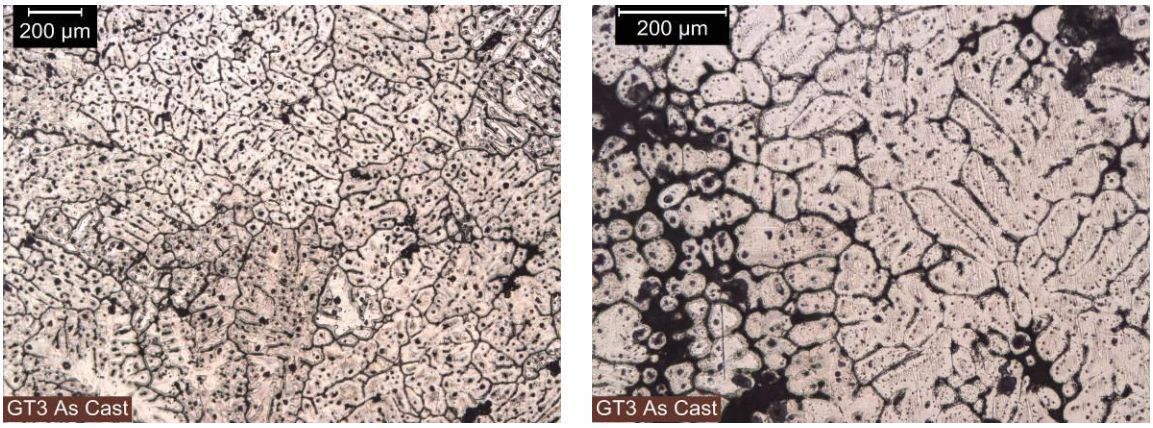

Figure 42 – *The as-cast microstructure of GT3 (Keller's reagent).*

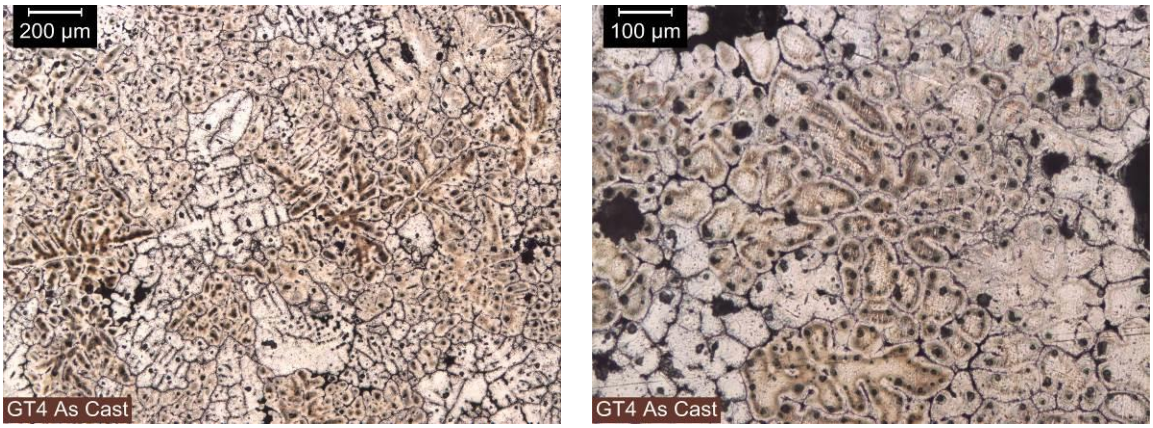

Figure 43 – *The as-cast microstructure of GT4 (Keller's reagent).*

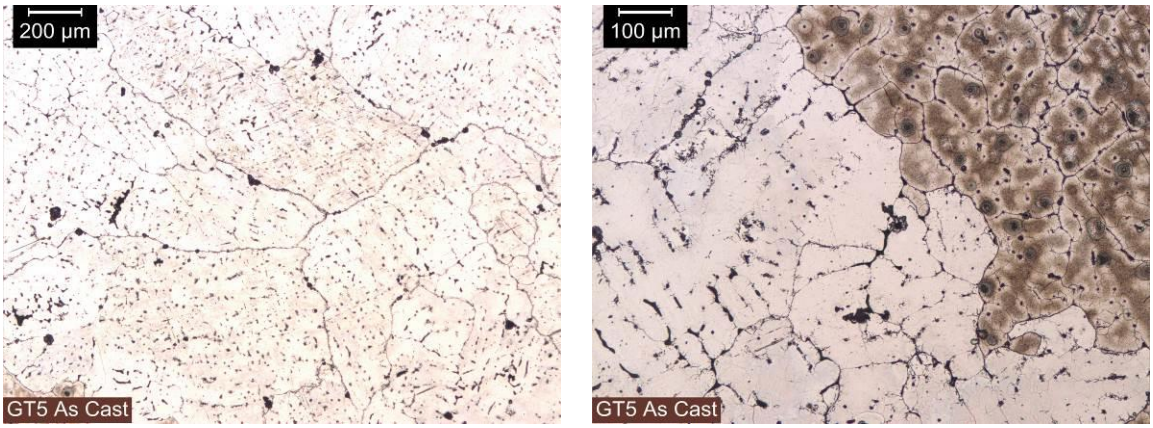

Figure 44 – *The as-cast microstructure of GT5 (Keller's reagent).*

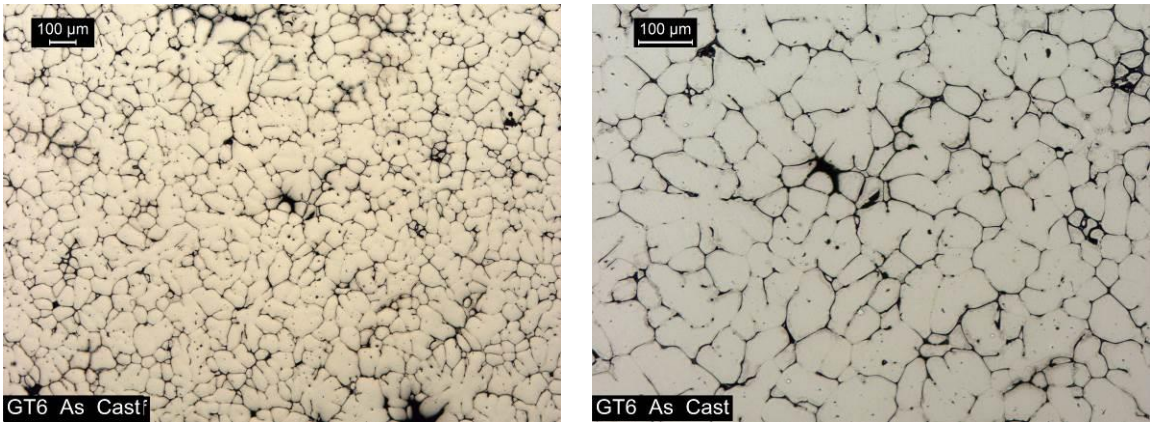

Figure 45 – *The as-cast microstructure of GT6 (phosphoric acid).*

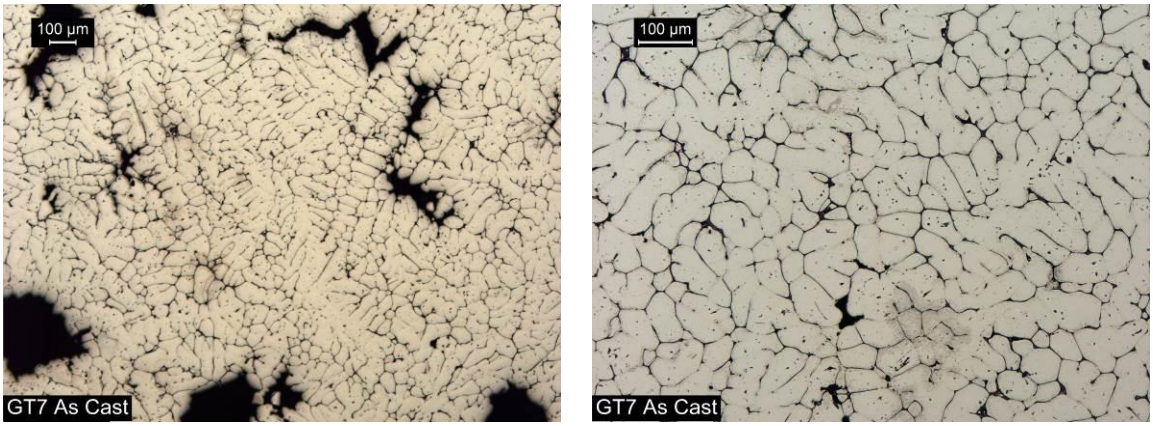

Figure 46 – *The as-cast microstructure of GT7 (phosphoric acid).*

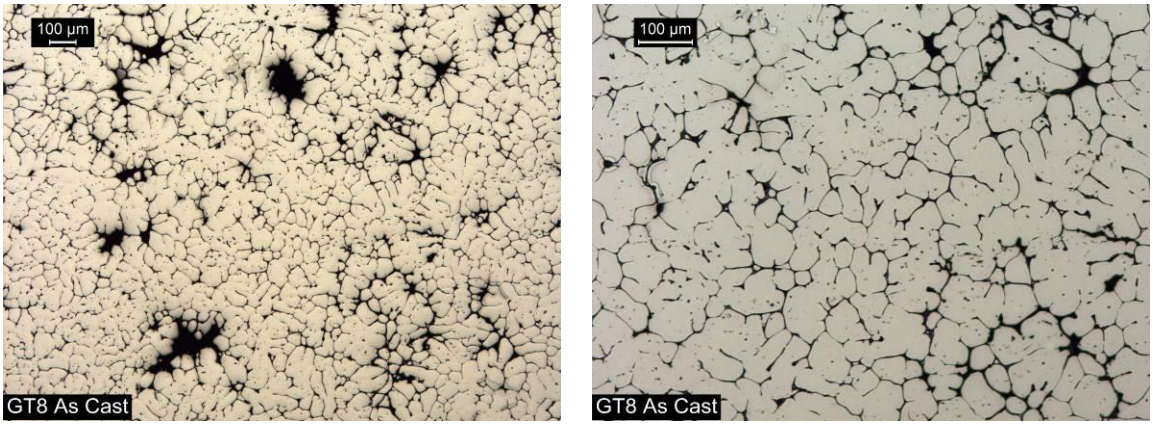

Figure 47 – *The as-cast microstructure of GT8 (phosphoric acid).*

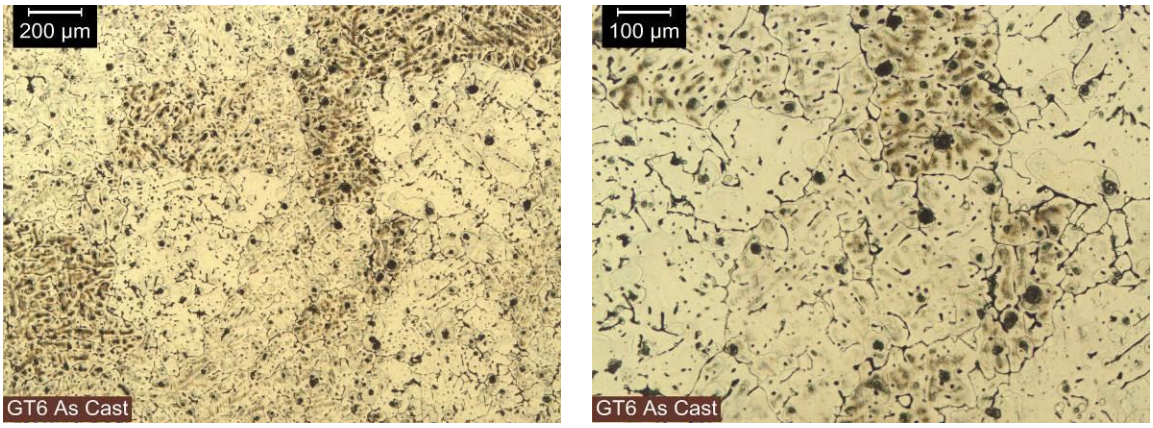


Figure 48 – *The as-cast microstructure of GT9 (phosphoric acid). Note: these micrographs were taken prior to the recasting of GT6, and are labeled as such.*

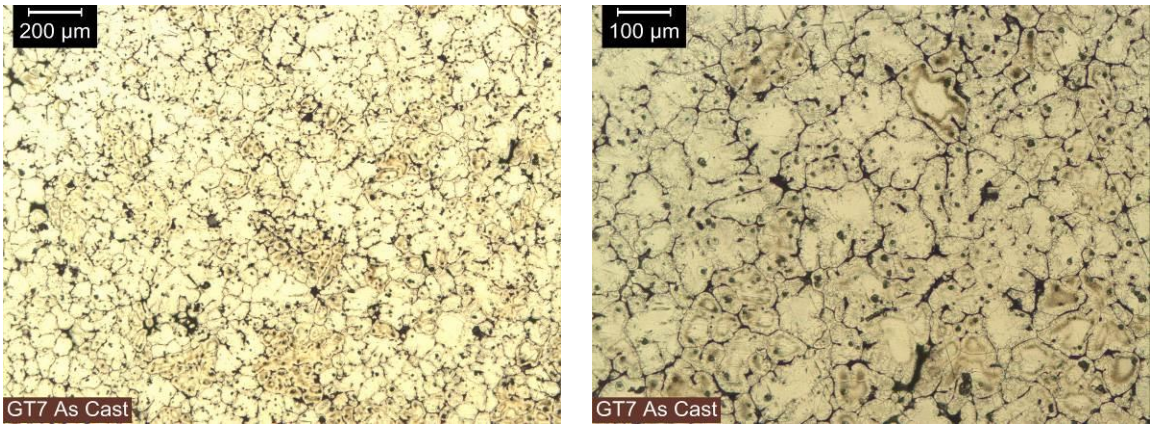


Figure 49 – *The as-cast microstructure of GT10 (phosphoric acid). Note: these micrographs were taken prior to the recasting of GT7, and are labeled as such.*

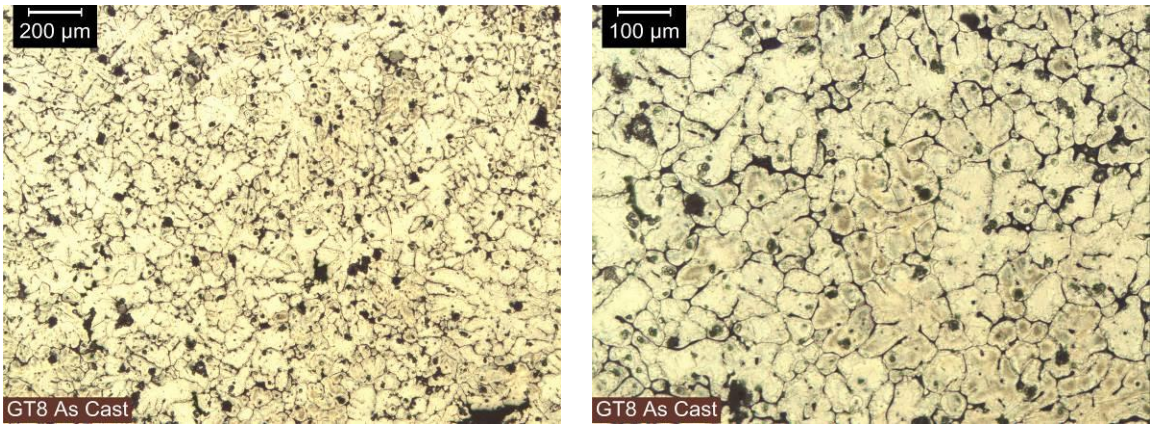


Figure 50 – *The as-cast microstructure of GT111 (phosphoric acid). Note: these micrographs were taken prior to the recasting of GT8, and are labeled as such.*

DSC scans on the experimental alloys were run using a Pyrius DSC 1 to determine their onset melting temperature (see Figures 51 – 53). The onset melting

temperatures can be seen graphically in Figures 54 – 56. With respect to alloys GT1-5 it was determined that as the copper content decreased (with a semi-constant Zn:Mg ratio) the onset melting temperature increased (i.e. – GT1 displayed the lowest onset melting temperature). This is not unexpected as it is well known that the two main common low-temperature melting phases often present in 7xxx-series alloys, S- and T-phase, both contain copper. Thus the results displayed above in Figure 54 were not unexpected.

GT6-8 displayed a linear increase in onset melting temperature with decreasing Zn:Mg ratios as can be seen in Figure 55, however the difference is slight and within standard error of the DSC (i.e. – the standard error of the Pyrius DSC 1 was taken to be ± 1°C). GT9-11 in comparison display a slightly different pattern which could be due to the different Cu levels of the alloys. It should be noted though that as Mg is increased, or Zn decreased, for a certain Cu level that the onset melting temperature appears to rise.

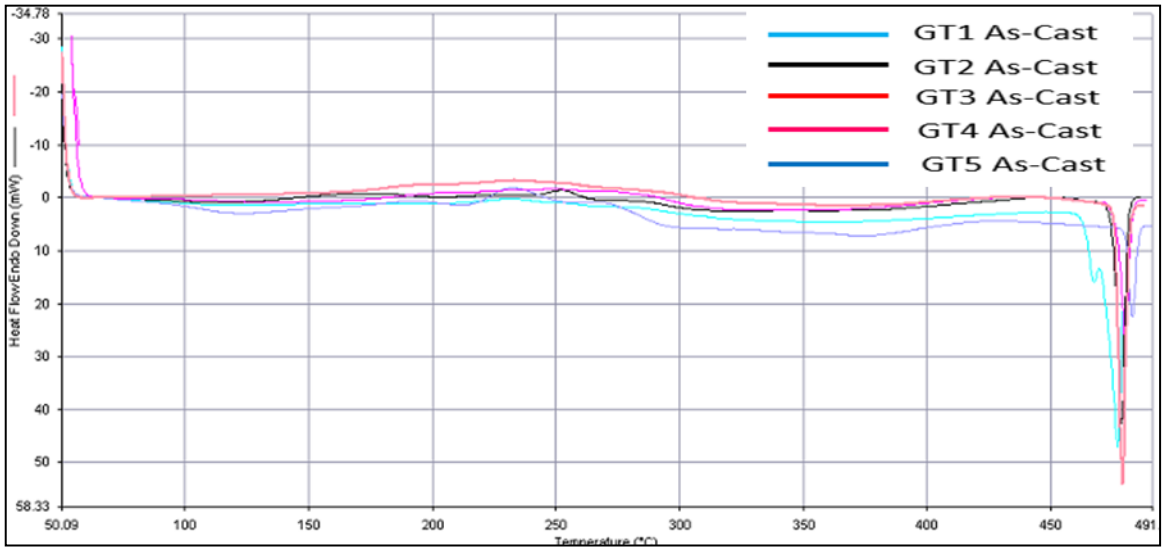


Figure 51 – *DSC scans of GT1-5 in the as-cast condition.*

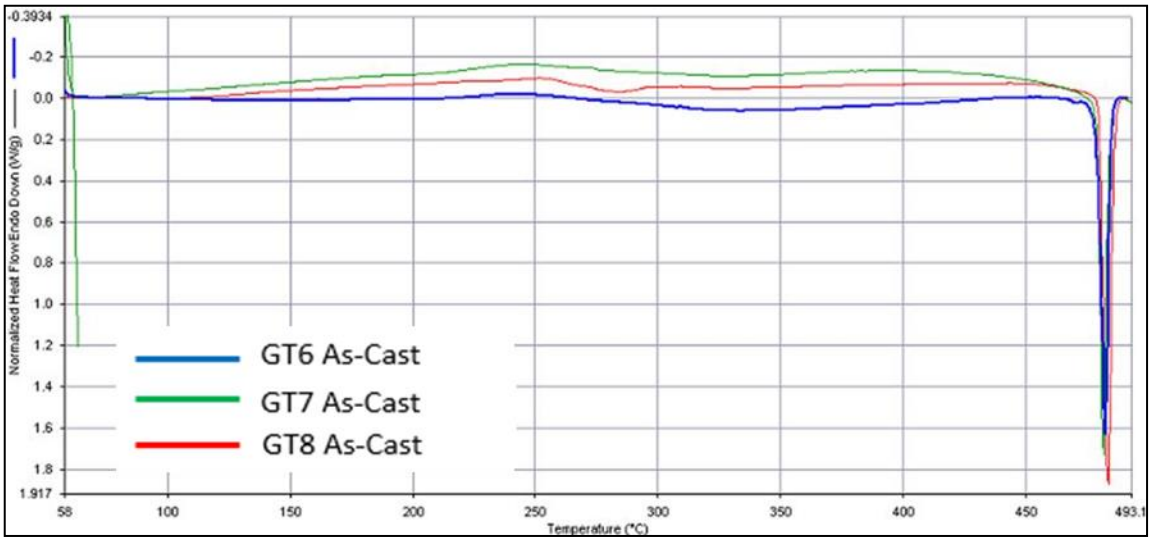


Figure 52 – *DSC scans of GT6-8 in the as-cast condition.*

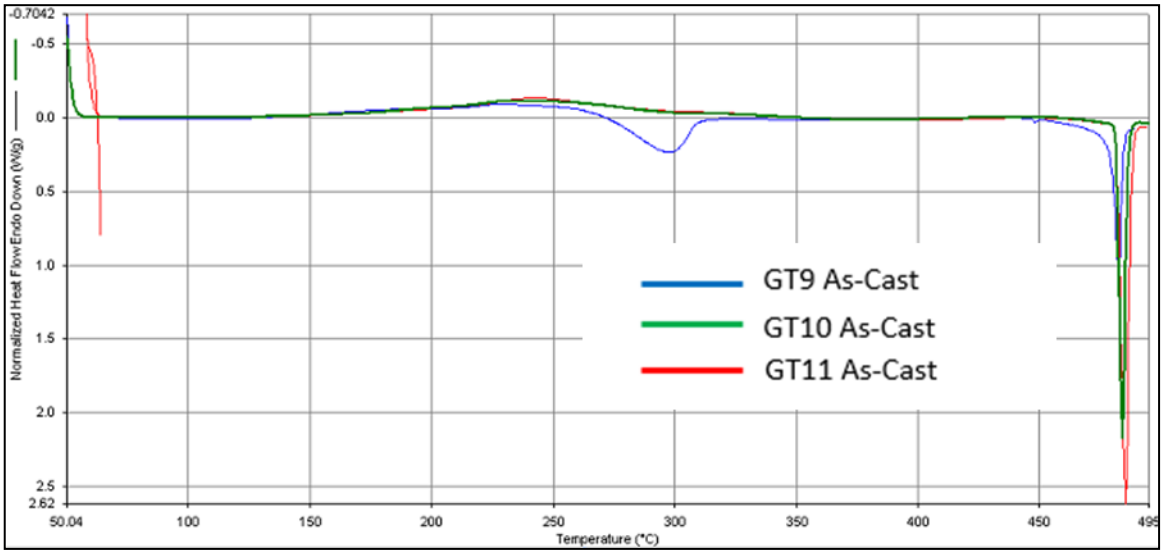


Figure 53 – *DSC scans of GT9-11 in the as-cast condition.*

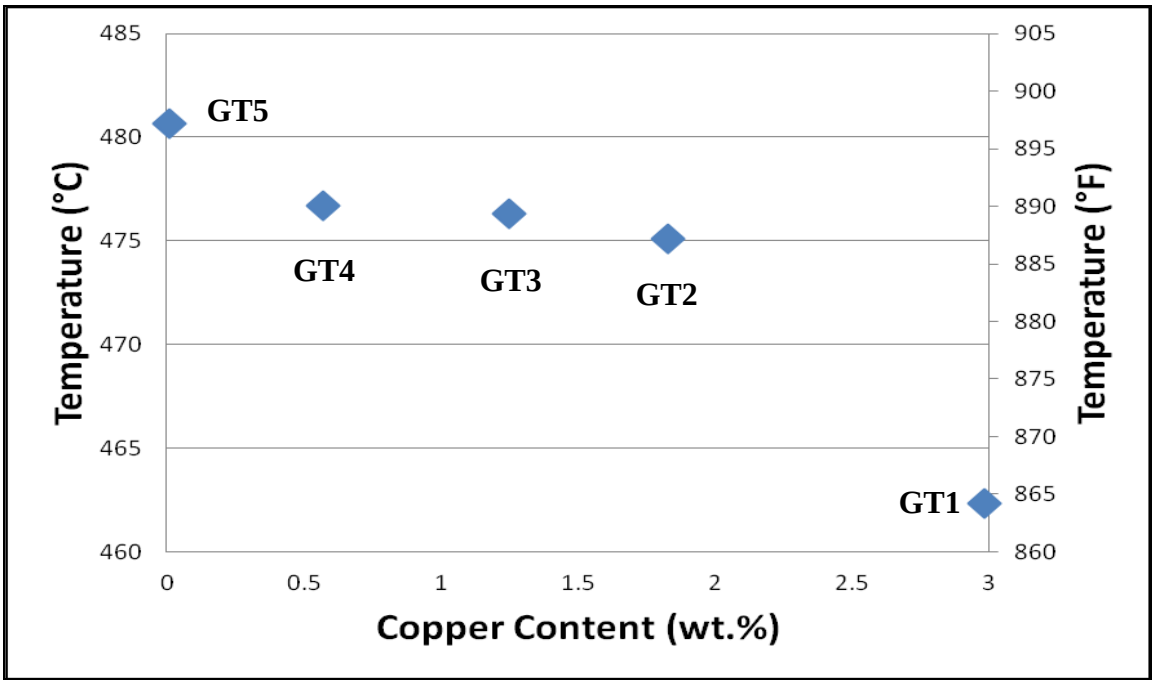


Figure 54 – *Onset melting data gathered by DSC on alloys GT1-5.*

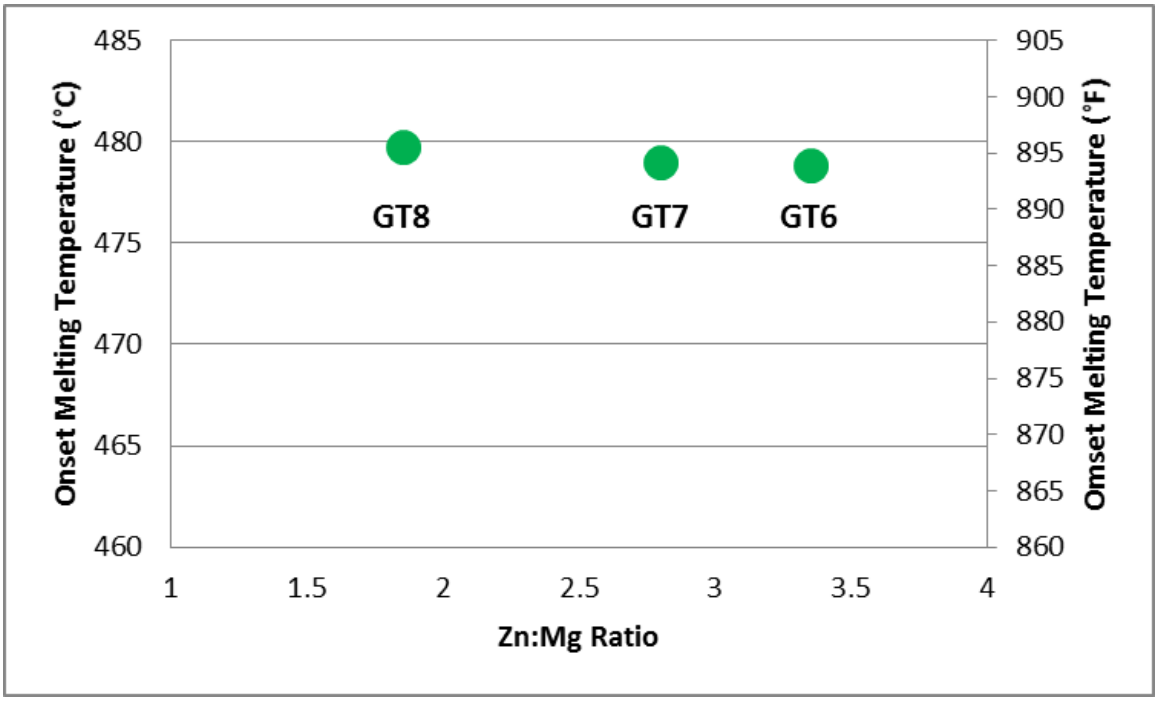


Figure 55 – *Onset melting data gathered by DSC on alloys GT6-8.*

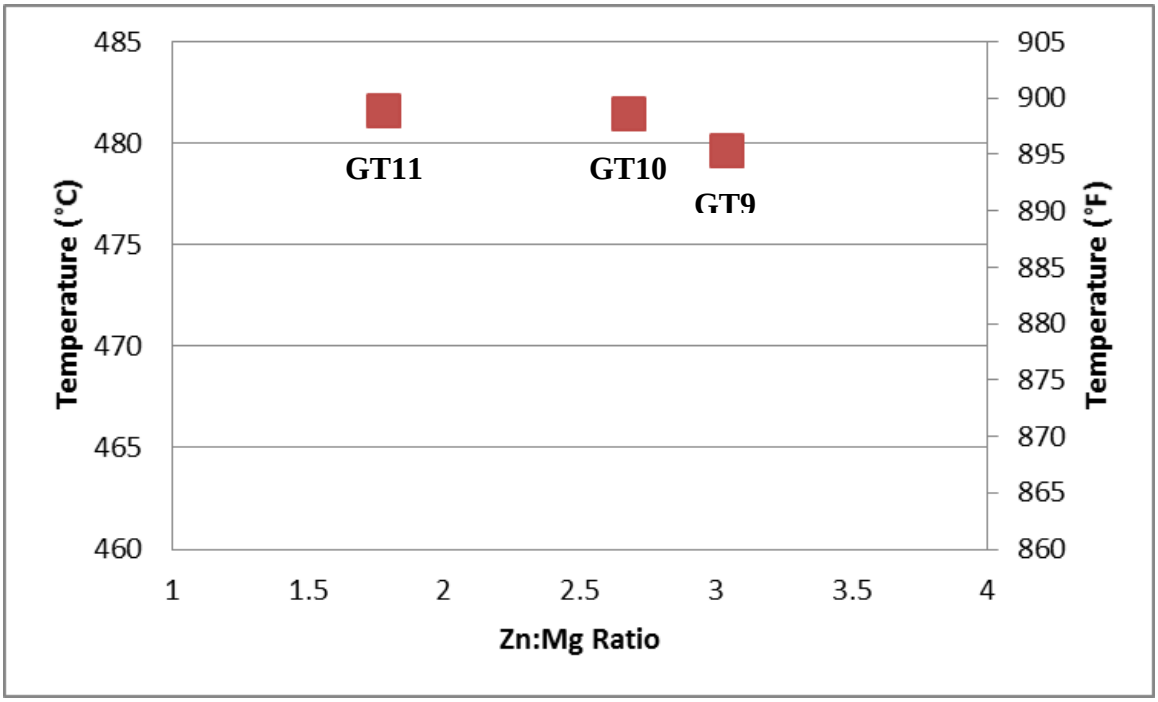


Figure 56 – *Onset melting data gathered by DSC on alloys GT9-11.*

### 10.3 Homogenization

It was decided to homogenize alloys GT1-5 at 440°C (824°F) as this would provide at least a 20°C (68°F) buffer for each of the alloys to avoid localized melting during the homogenization process. Similarly, alloys GT6-8 were homogenized at 450°C (842°F), and alloys GT9-11 were homogenized at 460°C (860°F). It is also important to note that because dispersoids (Zr, Mn, etc.) were not added to the alloys, that a single step homogenization process was effective (i.e. – a lower temperature first step was not necessary to precipitate out stable dispersoids). The homogenization temperatures in conjunction with the average secondary dendrite arm spacing measurements presented in Table 9 were plugged into a Fick's Second Law solution to estimate the homogenization time for each alloy (see Table 10). The prescribed homogenizations can be seen in Table 11.

Table 10 – *Estimated time to homogenize (in hours) for alloys GT1-11 broken down by alloying elements at 460°C.*

| Alloy | Si | Fe | Cu | Mg | Zn |
|---|---|---|---|---|---|
| GT1 | 2.47 | 1.05E6 | 7.68 | 0.52 | 0.12 |
| GT2 | 2.11 | 9.04E5 | 6.55 | 0.44 | 0.10 |
| GT3 | 3.06 | 1.31E6 | 9.51 | 0.64 | 0.14 |
| GT4 | 2.65 | 1.41E6 | 8.23 | 0.56 | 0.12 |
| GT5 | 1.28 | 5.48E5 | 3.98 | 0.27 | 0.06 |
| GT6 | 5.33 | 2.28E6 | 16.53 | 1.12 | 0.25 |
| GT7 | 2.45 | 9.62E5 | 6.98 | 0.47 | 0.11 |
| GT8 | 3.64 | 1.56E6 | 11.32 | 0.77 | 0.17 |
| GT9 | 4.49 | 1.92E6 | 13.95 | 0.94 | 0.21 |
| GT10 | 2.68 | 1.15E6 | 8.33 | 0.46 | 0.13 |
| GT11 | 2.46 | 1.15E6 | 7.64 | 0.52 | 0.11 |

Table 11 – *The prescribed homogenizations for alloys GT1-11.*

| Alloy | Temperature °C (°F) | Time (Hours) |
|---|---|---|
| GT1 | 440 (824) | 24 |
| GT2 | 440 (824) | 24 |
| GT3 | 440 (824) | 24 |
| GT4 | 440 (824) | 24 |
| GT5 | 440 (824) | 24 |
| GT6 | 450 (842) | 24 |
| GT7 | 450 (842) | 24 |
| GT8 | 450 (842) | 24 |
| GT9 | 460 (860) | 24 |
| GT10 | 460 (860) | 24 |
| GT11 | 460 (860) | 24 |

### 10.3.1 The Homogenized Condition

Following the homogenization treatments described above, GT1-11 were re-evaluated using DSC and optical microscopy to determine the rolling temperature and effectiveness of the homogenization process. Optical micrographs of alloys GT1-5 show that the alloys respond well to the assigned homogenization treatment (see Figure 57 – 61). However, it should be noted that due to the gravity casting method all of the alloys tend to contain a high level of porosity. Optical micrographs of alloys GT6-8 (see Figures 62 – 64) appear to show a decrease in the effectiveness of the prescribed

homogenization processes with increasing Mg content. It was decided, however, to continue with the rolling procedure.

GT9-11, which will no longer be discussed, showed a high degree of segregation in the "homogenized" condition. The microstructures of the G9-11 in the "homogenized" condition appear to indicate the segregation was a result of the casting process, and therefore macro-segregation. Therefore, GT9-11 were abandoned.

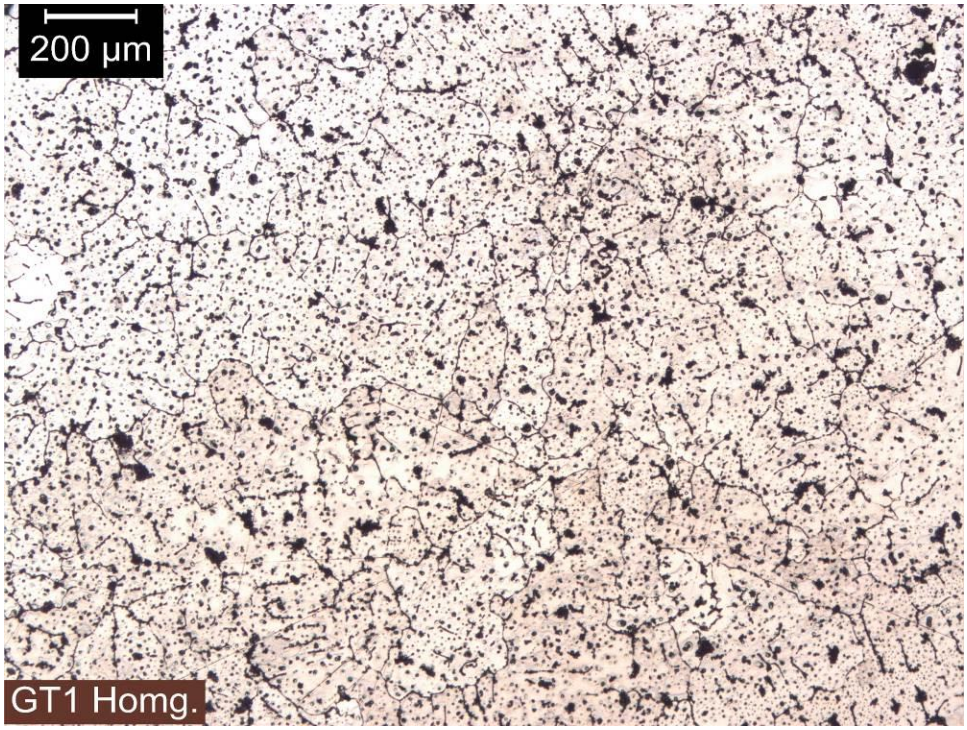


Figure 57 – *GT1 in the homogenized condition (phosphoric acid solution).*

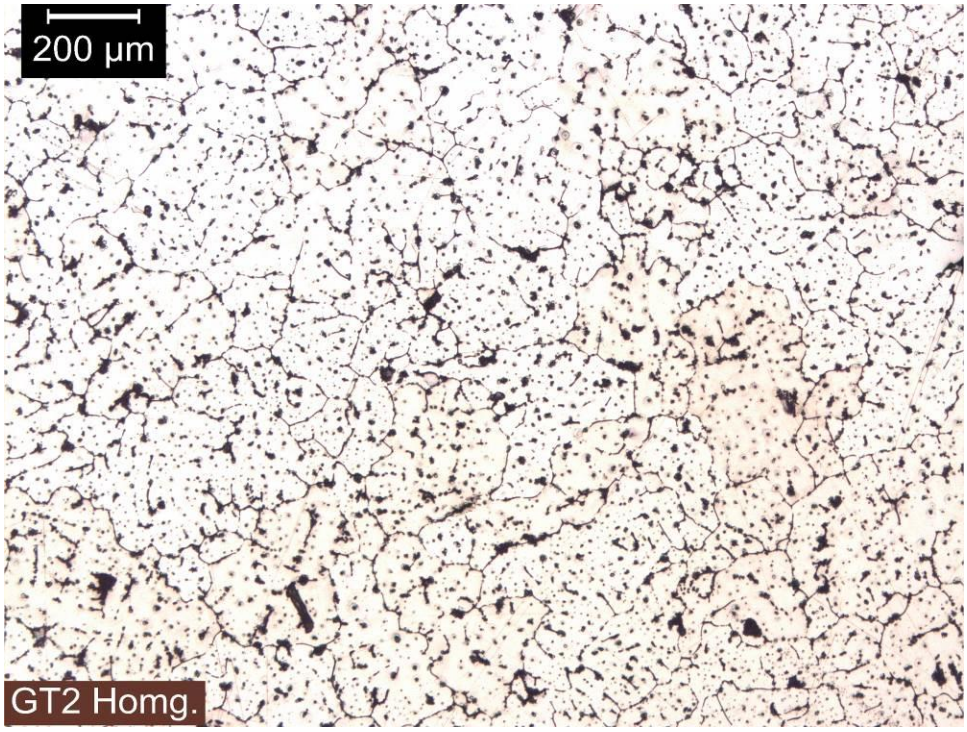


Figure 58 – *GT2 in the homogenized condition (phosphoric acid solution).*

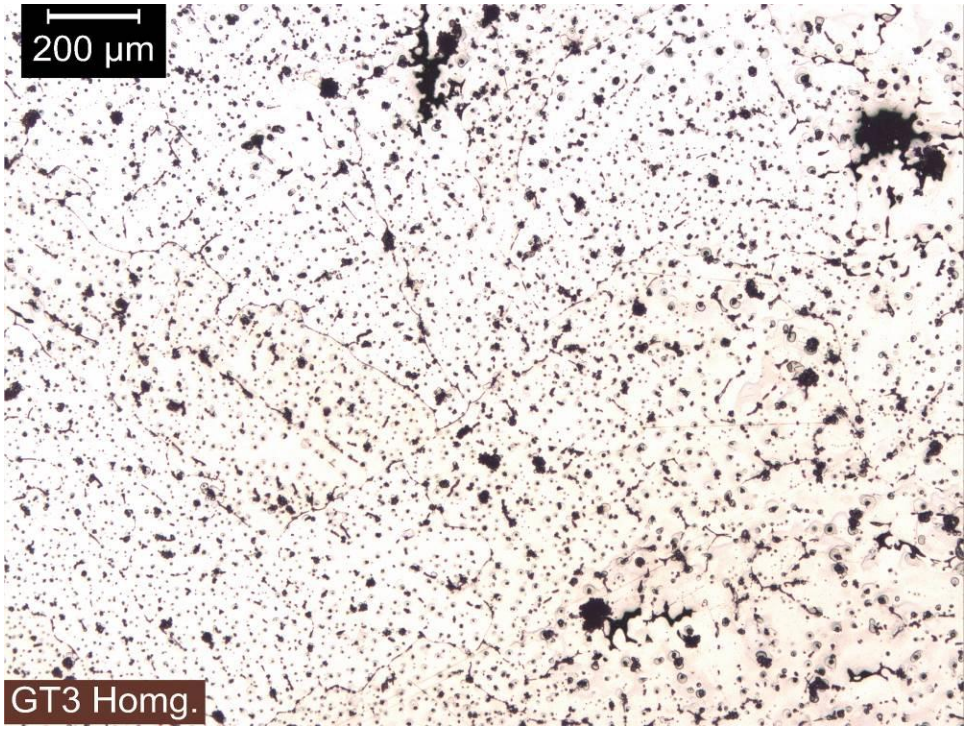


Figure 59 – *GT3 in the homogenized condition (phosphoric acid solution).*

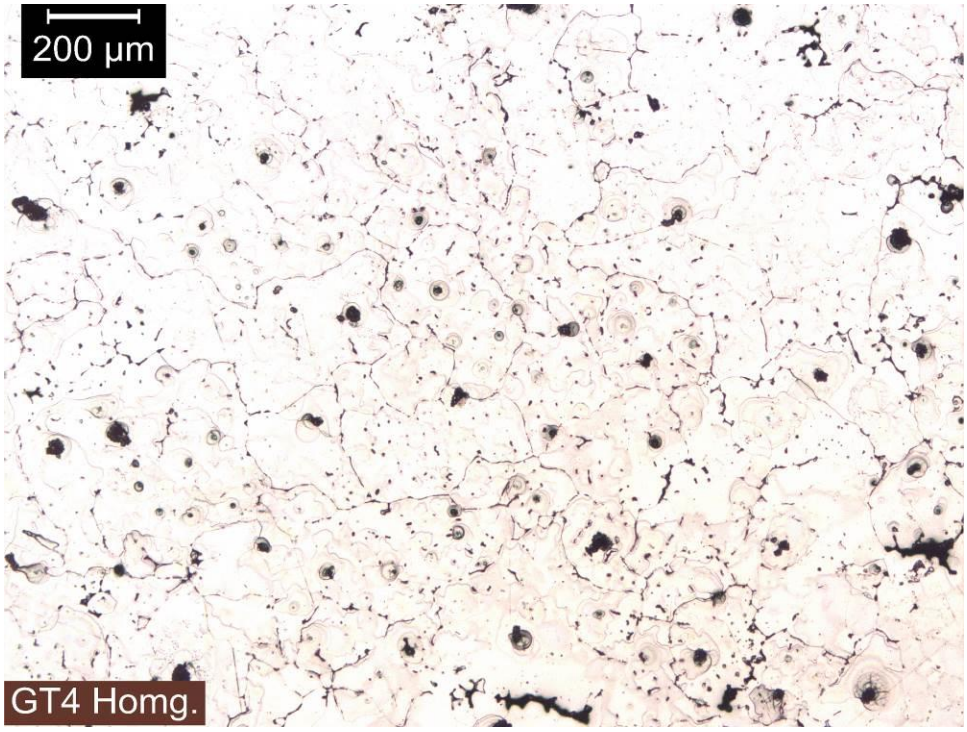


Figure 60 – *GT4 in the homogenized condition (phosphoric acid solution).*

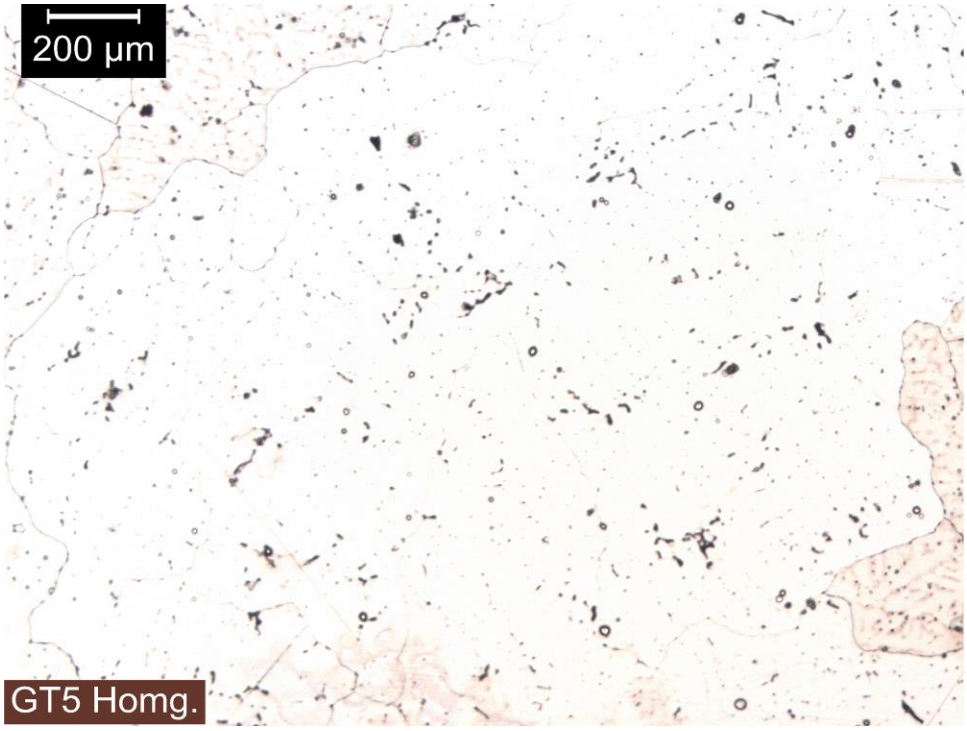


Figure 61 – *GT5 in the homogenized condition (phosphoric acid solution).*

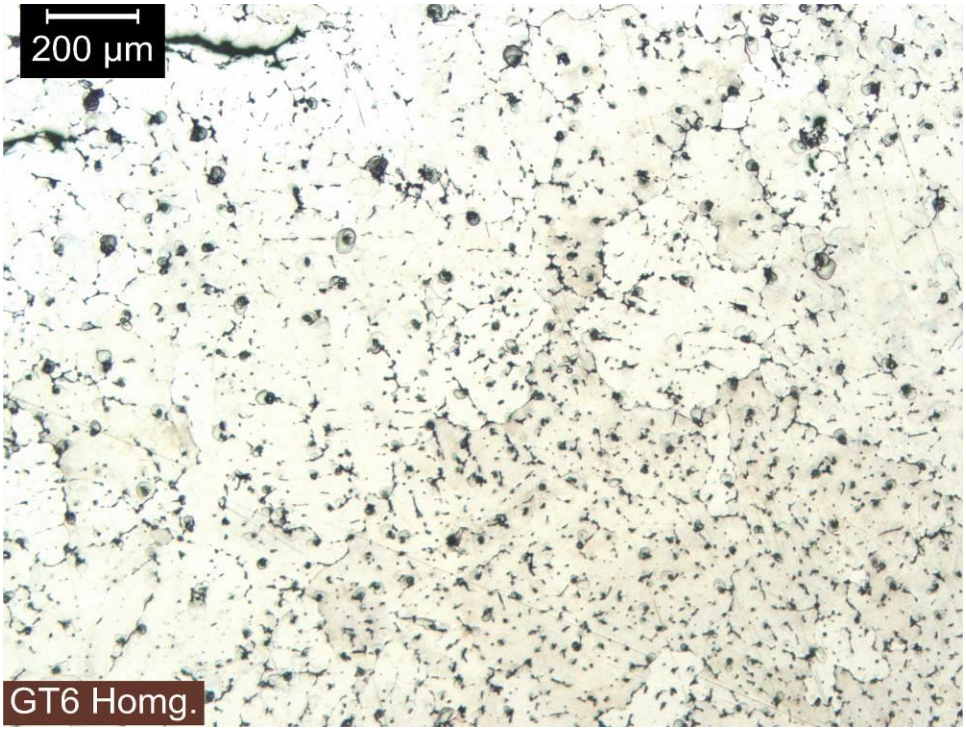

Figure 62 – *GT6 in the homogenized condition (phosphoric acid solution).*

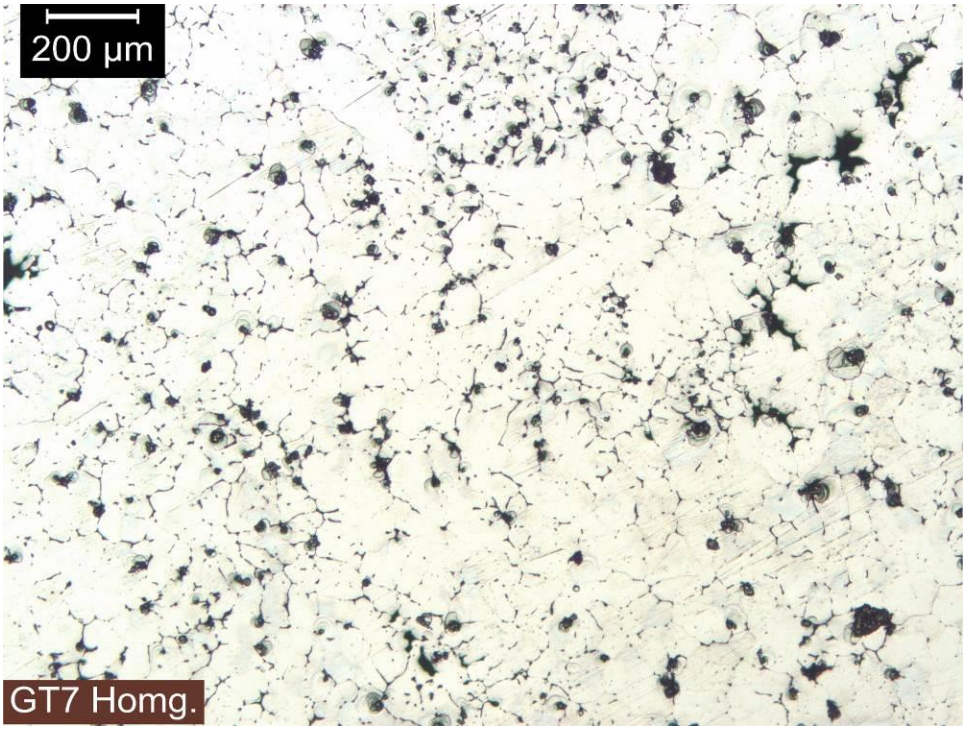

Figure 63 – *GT7 in the homogenized condition (phosphoric acid solution).*

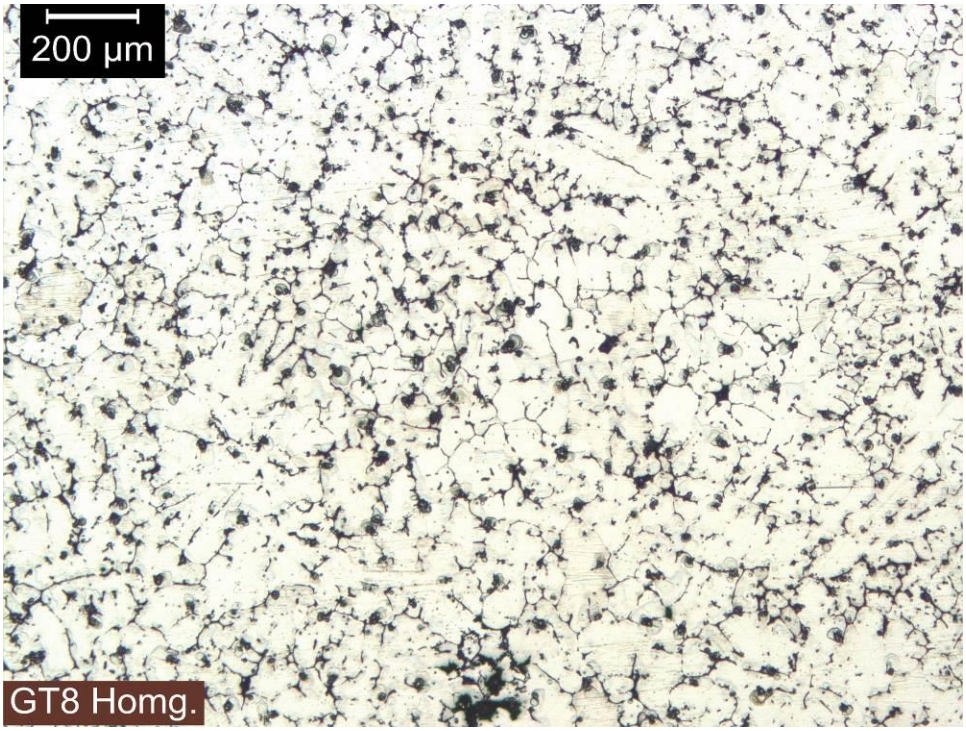

Figure 64 – *GT8 in the homogenized condition (phosphoric acid solution).*

DSC scans of alloys GT1-11 (see Figure 65 for an example) showed that a rolling temperature of 343°C (650°F), a temperature similar to what is generally used in the extrusion industry, was acceptable (i.e. – it was well below any incipient melting). Therefore, the ingots were allowed to soak at 343°C prior to rolling. It is worth noting, however, that the rolls themselves were not heated during the process.

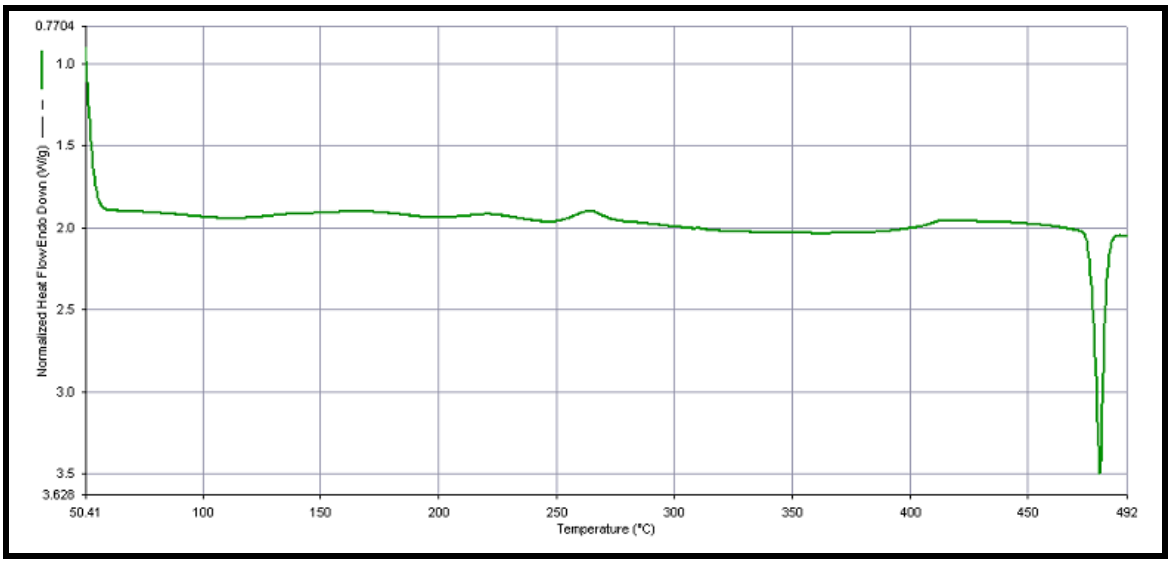


Figure 65 – *DSC scan of GT1 showing the preheat temperature for the rolling process was below the onset melting temperature.*

### 10.4 Conclusions

The compositions of GT1-11 were verified by Vista-Metals and analyzed. It was shown that the onset melting temperature of an alloy in the as-cast condition is heavily dependent on the Cu level in the alloy. Homogenization practices for each alloy were developed based on a Fick's second law estimation utilizing the Cu diffusion coefficient, and the results for each alloy were analyzed. It was determined that GT1-8 were all successfully homogenized, but GT9-11 were not homogenized with the prescribed practice. This may be due to a casting defect as the final composition GT9-11 was not near their target compositions (i.e. – the composition of GT6-8).

# CHAPTER 11

# ROLLING, SOLUTION HEAT TREATMENT, AND STRETCHING

This chapter details the experimental results and observations obtained from the rolling, SHT, and stretching of GT1-8. Optical micrographs of the final grain structure of each alloy are also presented. These operations were performed according to the experimental procedure presented in *Chapter 9 – Materials and Experimental Procedure*.

## 11.1 Rolling

The GT1-8 ingots were preheated to 343°C (650°F) and then rolled to approximately a 60% reduction over the course of three passes (see Table 12) at GT. In between passes the alloys were allowed to soak in the pre-heat furnace for approximately 1 hour to re-gain any heat lost during the rolling process. Following the last pass, the alloys were water quenched and sectioned for differential scanning calorimetry (DSC) analysis to determine the SHT temperature. With respect to liquation cracking, GT1-5 showed almost no liquation cracks in the F-condition (as rolled condition). GT6-8 displayed some liquation cracks indicating the liquation layer was not fully removed prior to rolling. This could be a direct result of the alloys' higher Mg content as an equal amount (~0.25 in) was removed from each ingot prior to rolling. These cracks were removed from the side of each plate prior to SHT.

Table 12 – *Final rolling reductions for alloys GT1-8.*

| Alloy | Starting Thickness (mm) | Final Thickness (mm) | Percent Reduction |
|---|---|---|---|
| **GT1** | 20.6 | 8.97 | 57% |
| **GT2** | 20.6 | 9.08 | 56% |
| **GT3** | 20.6 | 9.08 | 56% |
| **GT4** | 20.6 | 8.97 | 57% |
| **GT5** | 20.6 | 8.90 | 57% |
| **GT6** | 19.5 | 8.53 | 56% |
| **GT7** | 19.5 | 8.75 | 55% |
| **GT8** | 19.5 | 8.63 | 56% |

### 11.2 Solution Heat Treatment

DSC scans were ran on GT1-8 in the F-temper in order to determine a proper SHT for each alloy. The onset melting temperature given by the DSC scans for each alloy can be seen in Table 13. Typically, an alloy's SHT temperature should be as close as possible to the onset melting temperature in order to ensure the alloy has been solutionized. Therefore, alloys GT1-5 were SHT at 470°C (878°F) for 1 hour and GT6-8 were SHT at 472°C (882°F) for 1 hour at UAC-Canton. The alloys were then water quenched and tested for electrical conductivity, which revealed the SHT to be successful.

Table 13 – *Onset melting temperature (°C) post rolling and solution heat treatment temperature (°C) for alloys GT1-5 as determined by DSC.*

| Alloy | Onset Melting (°C) | SHT Temperature (°C) |
|---|---|---|
| **GT1** | 475 | 470 |
| **GT2** | 482 | 470 |
| **GT3** | 481 | 470 |
| **GT4** | 478 | 470 |
| **GT5** | 480 | 470 |
| **GT6** | 477 | 472 |
| **GT7** | 477 | 472 |
| **GT8** | 481 | 472 |

### 11.3 Stretching

Immediately following the SHT, quench, and conductivity tests, alloys GT1-8 were stretched at UAC-Canton using an MTS testing frame. The target stretch percentage for each alloy was 1.5%. Alloys GT6-8, however, cracked into 2 pieces before this percentage was reached. The cracks appeared to have originated on the sides of the GT6-8 indicating they were liquation cracks, suggesting the liquation band on GT6-8 extended further into the ingots than previously thought. The final plastic deformation percentage for each alloy is listed in Table 14. Following the stretch percentage, the alloys were frozen on ice to slow the natural aging process.

Table 14 – *Plastic deformation percentage obtained via stretching for GT1-8. Note: the target stretch percentage was 1.5%.*

| Alloy | Stretch % | Alloy | Stretch % |
|---|---|---|---|
| **GT1** | 1.50 | **GT5** | 1.50 |
| **GT2** | 1.50 | **GT6** | 1.00 |
| **GT3** | 1.50 | **GT7** | 0.73 |
| **GT4** | 1.50 | **GT8** | 0.55 |

### 11.4 Optical Micrographs of GT1-8

Optical micrographs were taken on GT1-8 in the W-condition (SHT and stretched condition), and can be seen in Figured 66 – 73. The micrographs were taken in the L-S (or L-ST) direction at 50x and 100x. The samples were etched using Barker's Reagent (see *Appendix B – Common Etchants*).

a.) b.)

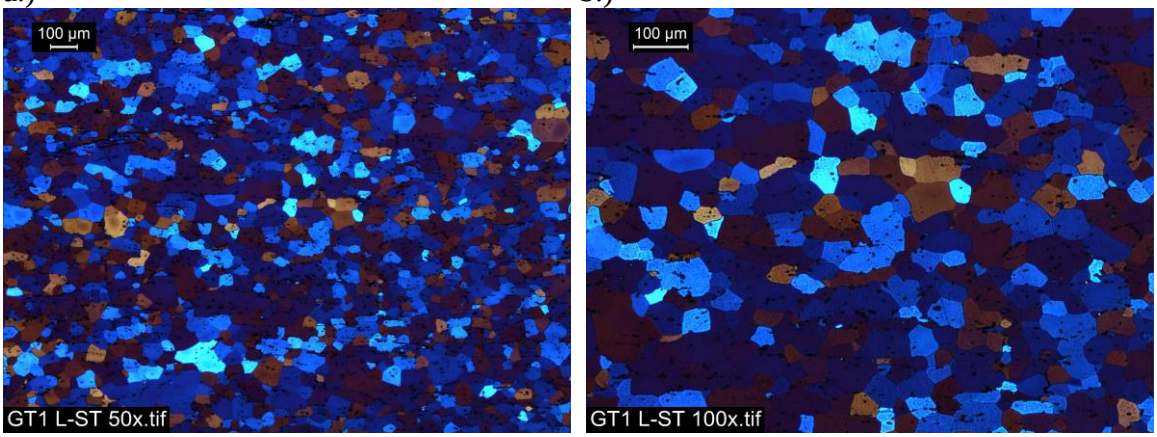


Figure 66 – *Microstructure of GT1 a.) at 50x and b.) at 100x (L-ST, Barker's reagent).*

a.) b.)

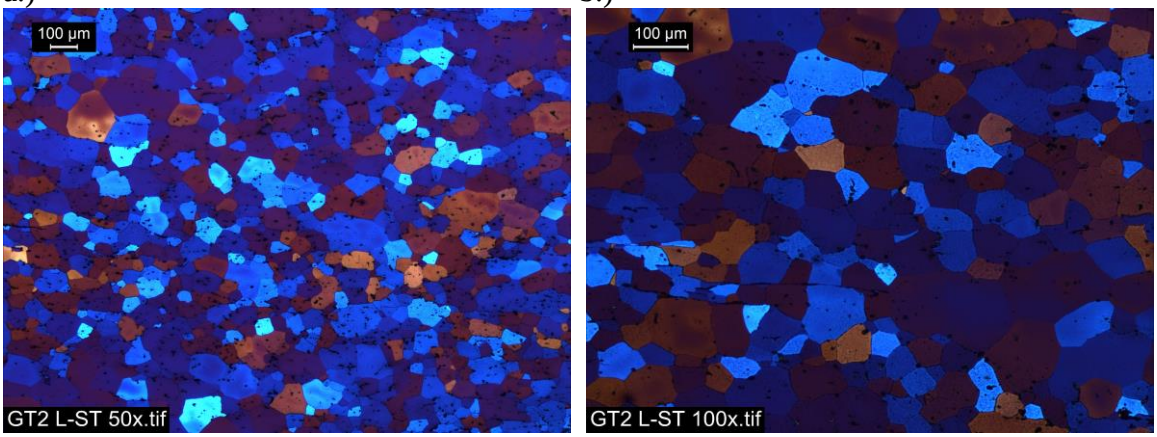


Figure 67 – *Microstructure of GT2 a.) at 50x and b.) at 100x (L-ST, Barker's reagent).*

a.) b.)

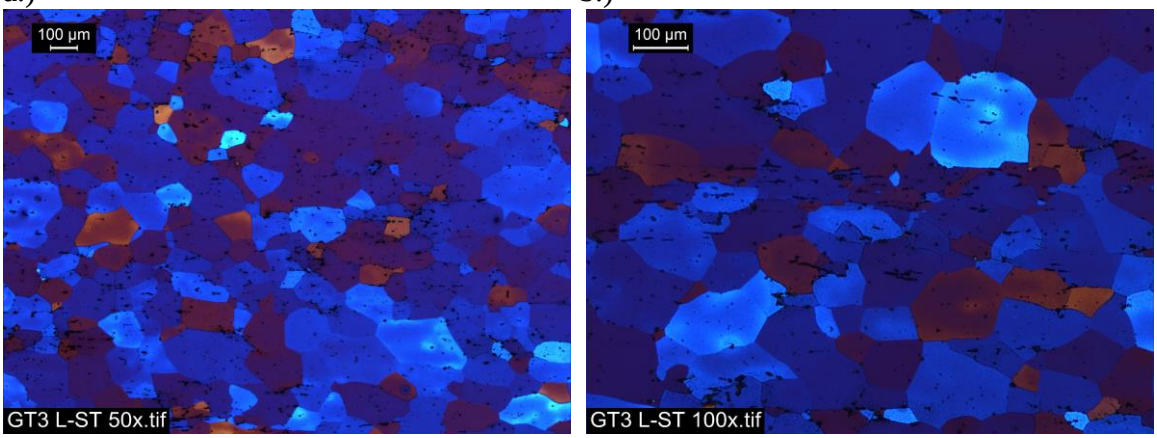


Figure 68 – *Microstructure of GT3 a.) at 50x and b.) at 100x (L-ST, Barker's reagent).*

a.) b.)

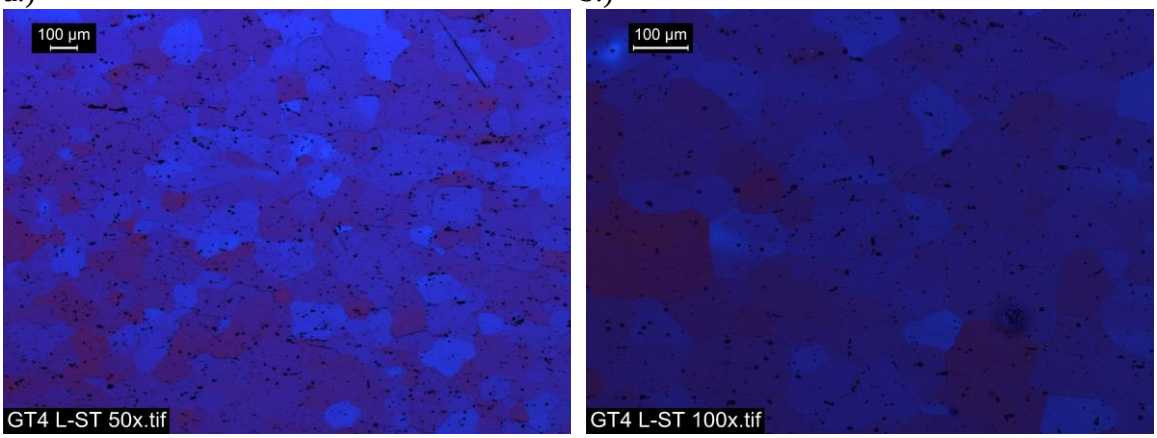


Figure 69 – *Microstructure of GT4 a.) at 50x and b.) at 100x (L-ST, Barker's reagent).*

a.) b.)

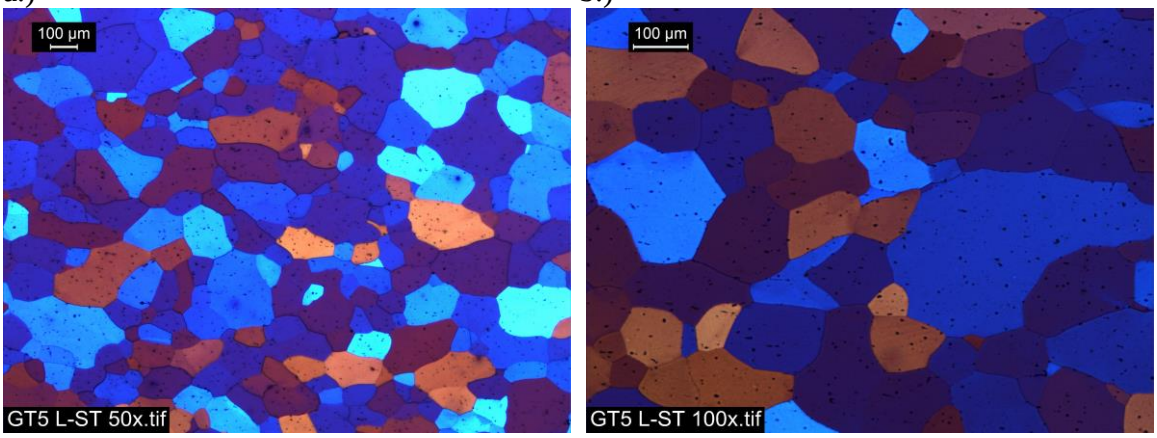


Figure 70 – *Microstructure of GT5 a.) at 50x and b.) at 100x (L-ST, Barker's reagent).*

a.) b.)

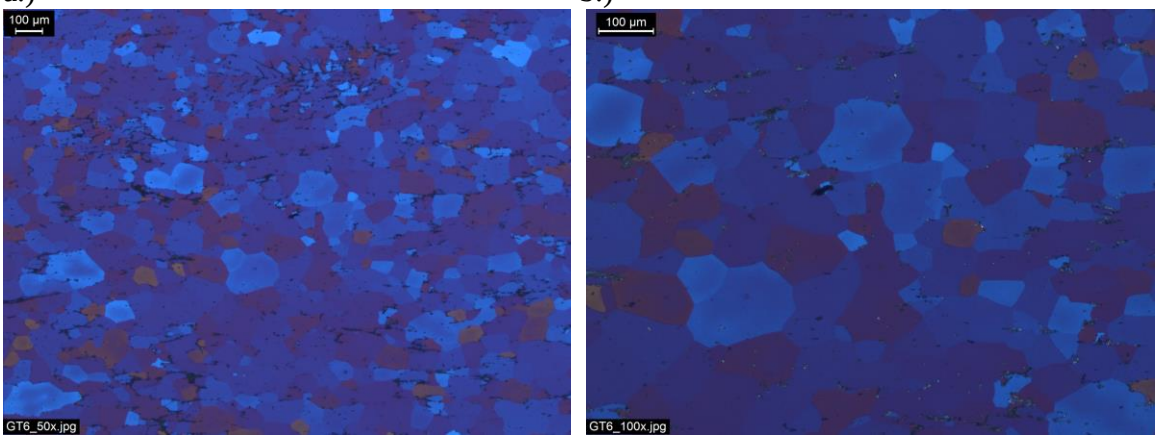


Figure 71 – *Microstructure of GT6 a.) at 50x and b.) at 100x (L-ST, Barker's reagent).*

a.) b.)

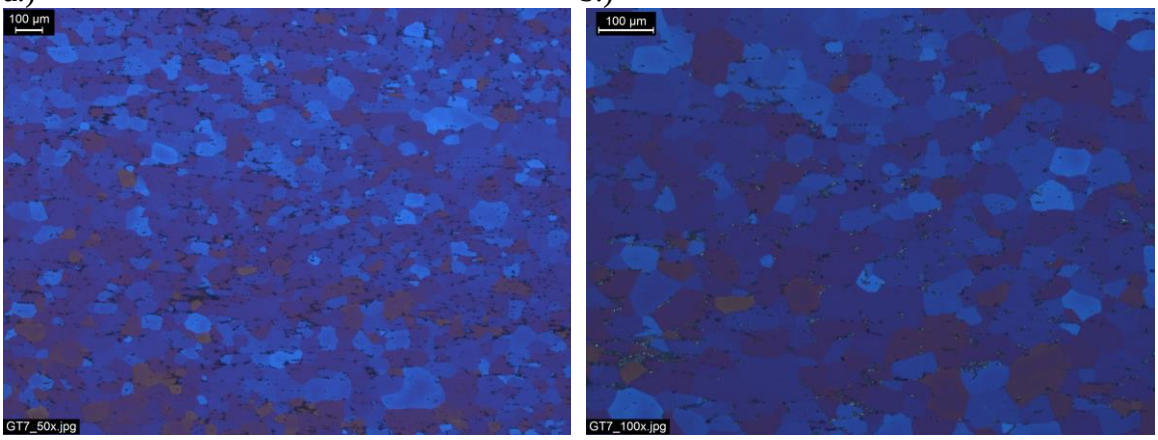


Figure 72 – *Microstructure of GT7 a.) at 50x and b.) at 100x (L-ST, Barker's reagent).*

a.) b.)

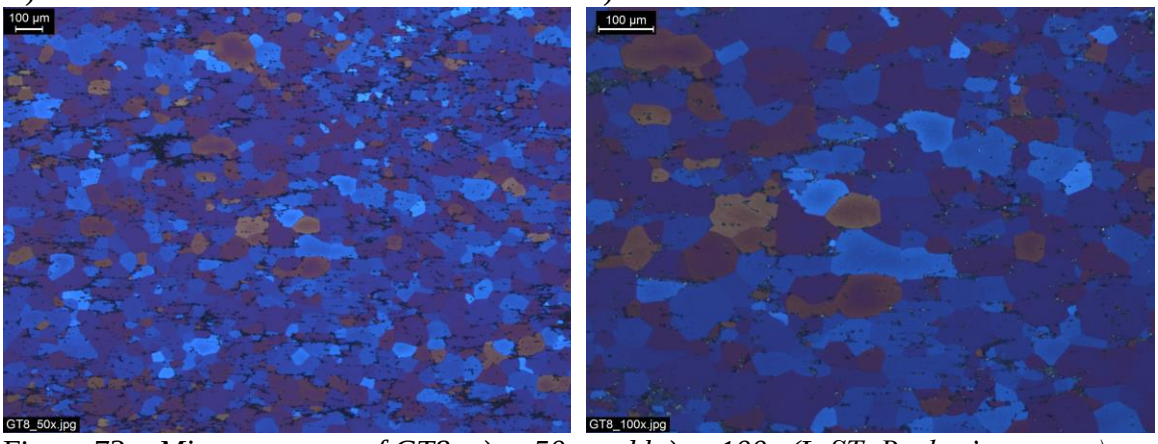


Figure 73 – *Microstructure of GT8 a.) at 50x and b.) at 100x (L-ST, Barker's reagent).*

It is apparent from each of the micrographs that each alloy was fully recrystallized (REX) during the SHT process. This results is not unexpected due the lack of dispersoid forming elements. Therefore, the final microstructure appears to be fairly equiaxed in nature, whereas an un-REX product would exhibit strong rolling textures, especially in the L-S direction. There also appears to be a reduced grain size with increasing Cu content, but this variation could be artifact of slightly different mold temperatures during the casting process (i.e. – the cooling rate of the mold from the pre-heat process may have been different between casts). It should also be noted that GT7 and GT8 appear to have a Mg-phase out of solution, probably $Mg_2Si$.

## 11.5 Conclusions

The results of the rolling, SHT, and stretching process were covered. Alloys GT1-8 were successfully rolled, SHT, and stretched (to varying degrees). Following the stretching process, the alloys were kept at 0°C (32°F) to slow down the natural aging process until each alloy had been fully processed. As expected, each alloy displayed a fully REX microstructure due to a lack of dispersoid forming elements.

# CHAPTER 12

# THE EFFECTS OF NATURAL AGING

The industrial production of 7xxx-series alloys typically contains a natural aging (NA) period between stretching and artificial aging (AA) either intentionally or inadvertently depending upon the alloy. This chapter focuses on the various effects of NA on experimental alloys GT1-8 in the T6 and T7 tempers. The compositions of these alloys allows for a systematic approach to quantifying the effects of NA with respect to the Zn:Mg ratio and the Cu-content.

There is evidence in the literature to suggest that Cu stabilizes GP zones and therefore could stabilize GP-I zones that form during the natural aging process. Low Cu alloys as shown by Hatch [1] should have a positive response to NA in the T6 temper while high Cu alloys like 7075 show a negative response to NA. Alloys GT1-5 will be used to test this theory and determine if the effects are still present in the T7, or over-aged, temper.

Alloys GT6-8 will be used to test the theory that preferred GP zone precipitation can be manipulated by changing the Zn:Mg ratio. In theory, a higher Zn:Mg ratio should inhibit the precipitation of GP-I zones, while a low Zn:Mg ratio should do the reverse. Therefore, their response to NA should may be altered. For example, GT8 may be not be sensitive to NA because it can only form GP-I zones, whereas GT6 may show a negative response to NA.

Following SHT, samples of GT1-8 were quenched and stretched approximately 1.5% (see Table 3-3). The samples were then allowed to NA for various times (2, 4, 5, 6, 8, 24, 48, and 96 hours) before being AA. The T6 temper was achieved by aging the samples for 24 hours at 120°C (248°F). The T7 temper was achieved by aging the samples for 24 hours at 120°C (248°F) followed by 24 hours at 160°C (320°F).

Rockwell hardness B-scale (HRB), electrical conductivity (%IACS), and differential scanning calorimetry (DSC) were then used to quantify and analyze the effects of NA on both tempers.

## 12.1 The Effects of NA on the T6 Temper

Alloys GT1-8 were naturally aged for various times between 0 and 100 hours before being aged for 24 hours at 120°C (248°F). The resulting temper can be viewed as an "equivalent" T6. A true T6 temper usually occurs at the very early stages of the second aging step (i.e. – the 160°C step), but is harder to obtain on a constant basis without industrial computer controls. Therefore, due to the logarithmic nature of the 120°C aging curves, which will be presented in *Chapter 13 – Artificial Aging*, it was decided to use the "equivalent" T6 temper for this study.

It should be noted that references in this section to 7178-, 7075-, and 7079-type behavior refer to the NA behaviors of these alloys as described by Hatch [1]. 7178-T6 shows a linear decrease in tensile and yield strength with increased NA time in the T6 temper; 7075-T6 shows a decrease in tensile and yield strength with increased NA time with a dip in these properties at very short NA times; 7079-T6 shows an increase in tensile and yield strength with increased NA time.

### 12.1.1 Rockwell Hardness and Conductivity

Rockwell hardness B-scale data versus NA time for GT1-8 in the T6 temper can be seen in Figures 74 – 81, respectively. Hardness data for GT1 (see Figure 74) shows a 7075-type behavior with the characteristic drop occurring at approximately 8 hours. The conductivity of GT1-T6 (see Table 15), however, appears relatively unaffected by NA time. The dip present in Figure 74 must therefore be a product of precipitate type or transition instead of reversion. Reversion of precipitates back into solid solution would suggest the conductivity should also drop. The dip is therefore most likely the product of a transition zone between VRC/GP-II zone and GP-I zone dominance in the

microstructure. The effect of prolonged NA leading to an increase in GP-I zones, and therefore a decrease in η', can also be discerned in Figure 74.

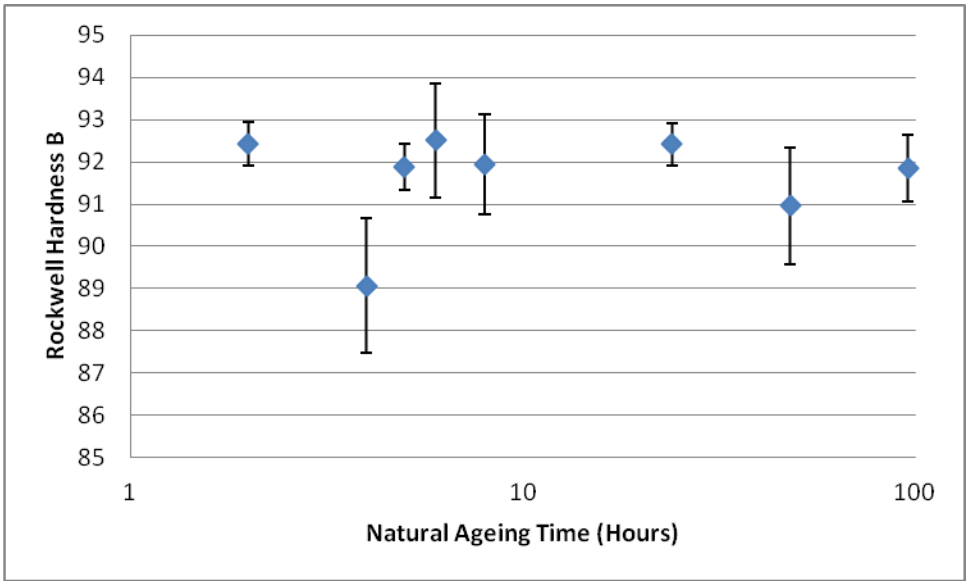


Figure 74 – *Rockwell hardness (B-scale) versus NA time for GT1-T6.*

Table 15 – *Rockwell hardness and conductivity (%IACS) data for several GT1-T6 samples focusing on the low NA times.*

| NA Time (Hours) | Rockwell Hardness B | Conductivity (%IACS) |
|---|---|---|
| 2 | 92.43 ± 0.52 | 31.4 |
| 4 | 89.07 ± 1.59 | 31.6 |
| 6 | 92.51 ± 1.34 | 31.4 |
| 8 | 91.93 ± 1.18 | 33.1 |
| 24 | 92.41 ± 0.51 | 32.7 |

GT2-T6, like GT1-T6, displays a 7075-type behavior with the dip in hardness shifting from 4 to approximately 5 hours (see Figure 75). The dip in GT2-T6 also appears to be wider than the dip in GT1. The conductivity measurements for select NA times for GT2-T6 can be seen in Table 16; however, like GT1-T6, NA appears to have no effect on the electrical conductivity in the T6 temper.

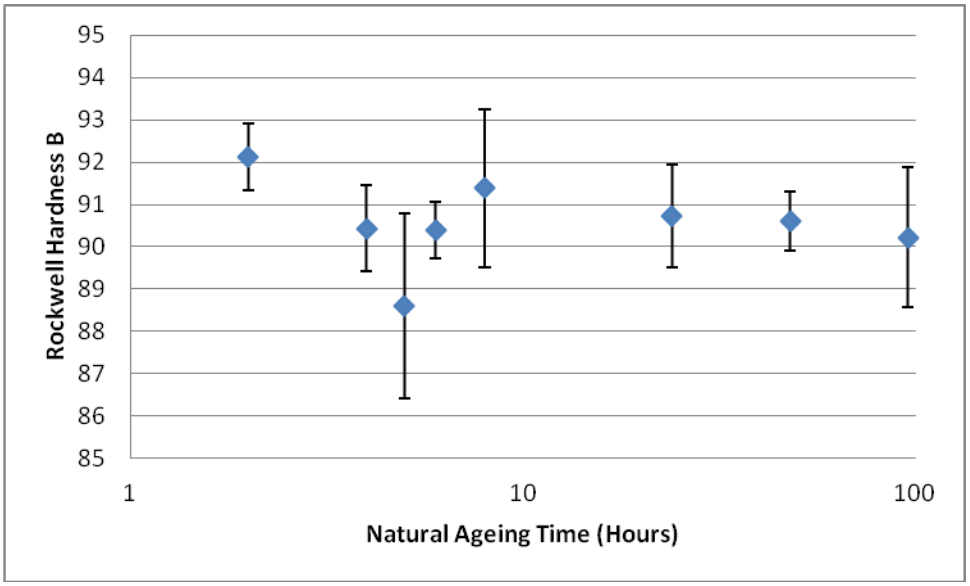


Figure 75 – *Rockwell hardness (B-scale) versus NA time for GT2-T6.*

Table 16 – *Rockwell hardness and conductivity (%IACS) data for several GT2-T6 samples focusing on the low NA times.*

| NA Time (Hours) | Rockwell Hardness B | Conductivity (%IACS) |
|---|---|---|
| 2 | 92.13 ± 0.52 | 32.8 |
| 4 | 90.43 ± 1.02 | 32.7 |
| 6 | 92.51 ± 1.35 | 33.5 |
| 8 | 91.93 ± 1.87 | 32.6 |
| 24 | 92.41 ± 0.51 | 32.3 |

Therefore, it seems likely that the drops in hardness data for GT1-T6 and GT2-T6 are the result of a transition between GP-I or GP-II zone dominance in the microstructure. The data suggests that the high hardness values recorded prior to the dip are due to the formation of GP-II zones upon AA. Likewise, the increased hardness values after the dip could be the result of stabilized GP-I zones transitioning directly into η upon AA. If these two assumptions are correct, the dip would therefore likely be the result of a transition period between GP-zone dominance, where GP-I zones are not large enough to transform to η upon AA, but are stabilized enough to halt the formation of GP-II zones. If this theory is correct, however, the GP-I zones must still be present in the T6 temper and cannot have dissolved back into solid solution because no drop in conductivity was

observed. Therefore, it appears HRTEM or atom probe tomography would be needed to validate this theory.

GT3-T6 displays no correlation between NA time and hardness (see Figure 76), which is most indicative of a 7178-type behavior. The conductivity data presented in Table 17 once more shows no correlation between conductivity and NA. It is worth noting, however, that the conductivity of GT1-3 in the T6 temper is increasing with decreasing Cu-content as expected, and this trend will continue with GT4-T6 and GT5-T6.

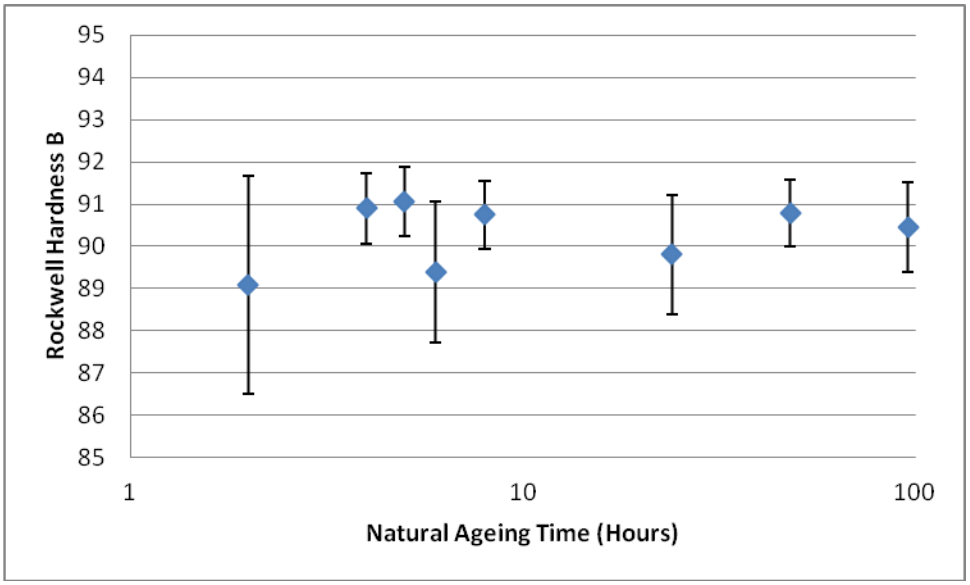


Figure 76 – *Rockwell hardness (B-scale) versus NA time for GT3-T6.*

Table 17 – *Rockwell hardness and conductivity (%IACS) data for several GT3-T6 samples focusing on the low NA times.*

| NA Time (Hours) | Rockwell Hardness B | Conductivity (%IACS) |
|---|---|---|
| 2 | 89.10 ± 2.58 | 33.5 |
| 4 | 90.90 ± 0.83 | 32.7 |
| 6 | 89.39 ± 1.66 | 33.8 |
| 8 | 90.74 ± 0.81 | 33.5 |
| 24 | 89.81 ± 1.41 | 33.6 |

GT4, which is a low Cu alloy, displays a 7079-type behavior with an almost linear increase in hardness with NA time in the T6 temper (Figure 77). Conductivity data for GT4-T6 can be seen in Table 18. It is speculated that in low Cu alloys GP-I zones, which

precipitate in a homogeneous manner, are not stabilized. It is believed that upon heating non-stabilized GP-I zones quickly revert back to solid solution leaving behind a fine dispersion of solute upon which GP-II zones can easily nucleate [2]–[4]. This hypothesis appears to be supported by Figure 77.

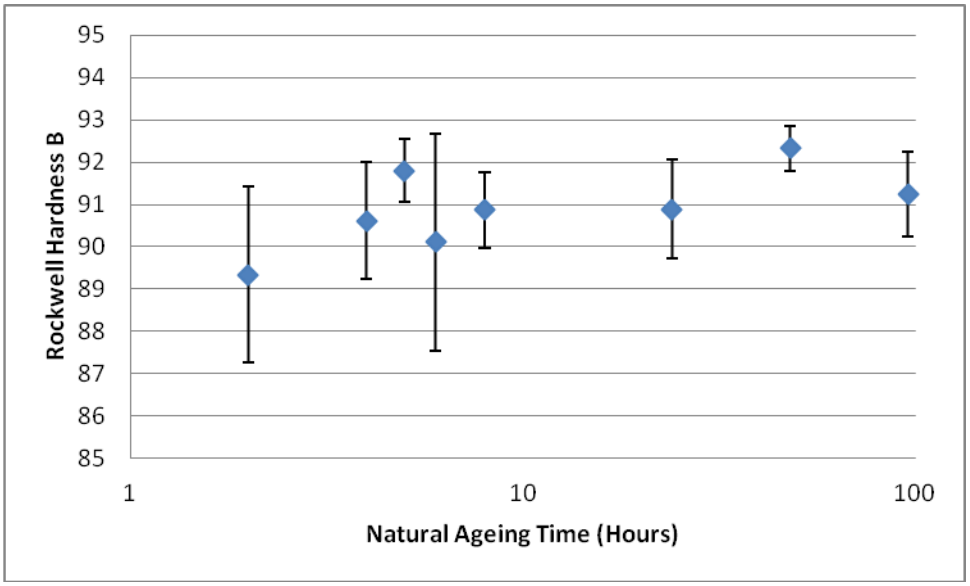


Figure 77 – *Rockwell hardness (B-scale) versus NA time for GT4-T6.*

Table 18 – *Rockwell hardness and conductivity (%IACS) data for several GT4-T6 samples focusing on the low NA times.*

| NA Time (Hours) | Rockwell Hardness B | Conductivity (%IACS) |
|---|---|---|
| 2 | 89.35 ± 2.07 | 35.0 |
| 4 | 90.61 ± 1.38 | 34.9 |
| 6 | 90.12 ± 2.56 | 35.3 |
| 8 | 90.87 ± 0.90 | 34.7 |
| 24 | 90.89 ± 1.18 | 34.5 |

GT5, which contains only trace amounts of Cu, also displays a 7079-type behavior (Figure 78); however instead of a linear trend line the hardness data for GT5-T6 appears to more "logarithmic" in nature. The electrical conductivity data for GT5-T6 (Table 19), as was the case for GT1-4, shows no correlation to NA time. A similar rational behind the increase in hardness with increased NA time in GT4-T6 can be applied to GT5-T6. It should be noted that due to the lack of Cu only one type of GP-zone (GP-I zones) are expected to form in GT5 at any temperature.

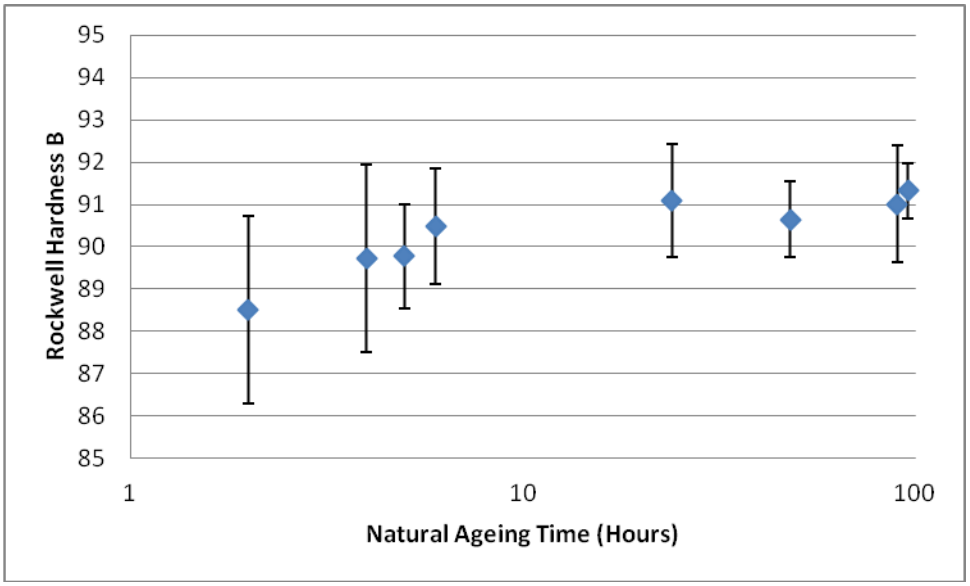


Figure 78 – *Rockwell hardness (B-scale) versus NA time for GT5-T6.*

Table 19 – *Rockwell hardness and conductivity (%IACS) data for several GT5-T6 samples focusing on the low NA times.*

| NA Time (Hours) | Rockwell Hardness B | Conductivity (%IACS) |
|---|---|---|
| 2 | 88.52 ± 2.22 | 37.0 |
| 4 | 89.73 ± 2.23 | 37.8 |
| 6 | 90.49 ± 1.37 | 37.8 |
| 8 | 91.01 ± 1.37 | 38.1 |
| 24 | 91.09 ± 1.34 | 37.1 |

Although the nature of hardness tests make it difficult to draw definite conclusions, it appears that Cu plays a crucial role in determining an alloys response to NA in the T6 temper. In high Cu alloys, NA can be considered deleterious to the alloy's hardness due to the stabilization of GP-I zones. Naturally, this would suggest that as the volume fraction of GP-I zones increase with NA that hardness should drop, and this was shown to be true. Conversely in low Cu alloys, GP-I zones are not stabilized and revert back into solid solution quickly upon heating above the GP-I solvus. Once GP-I zones revert back to solid solution they leave behind a fine, even dispersion of solute, which can serve a nucleation site for GP-II zones.

GT3-T6 provides an interesting case. The Cu content of GT3 (1.25 wt.%) is neither low nor high, and appears to create a smooth transition between GP zone

dominance regimes. This could be a result of the size of GP-I zones forming in the matrix with increased NA times. If the zones are small enough, they maybe following the P6 precipitation sequence (see *Part I – Chapter 6 – The Precipitation Process*). The lack of HRTEM and in-situ characterization techniques, however, means this theory cannot be validated from the data presented.

Alloys GT6-8 contain Cu contents of approximately 2.15-2.25 wt.%, which would suggest the alloys should behave like GT1 and GT2 (i.e. – 7075 behavior); however, as can be seen in Figures 79 – 81 and Tables 20 – 22, no trend can be established for these alloys based on the hardness data with respect to NA time in the T6 temper. As was shown in Figure 75, GT8-T6 is expected to only form GP-I zones due to its high Mg content, and perhaps behave similarly to GT5-T6. However, GT6-T6 should be dominated by GP-II zones and therefore behave similarly to GT1-T6. Even though clear NA trends should be discernable, it appears the substantial amount of solid solution strengthening that occurs from the increased Mg content masks the effects of NA in the alloys. The theory appears well-grounded since there is a general rise in hardness with increasing MG content and a general decrease in conductivity (i.e. – increasing the Mg content increases the strain in the lattice). Therefore, while the effects of NA seen in GT1-5 may still be present in GT6-8, the effects are too subtle to be observed via hardness data.

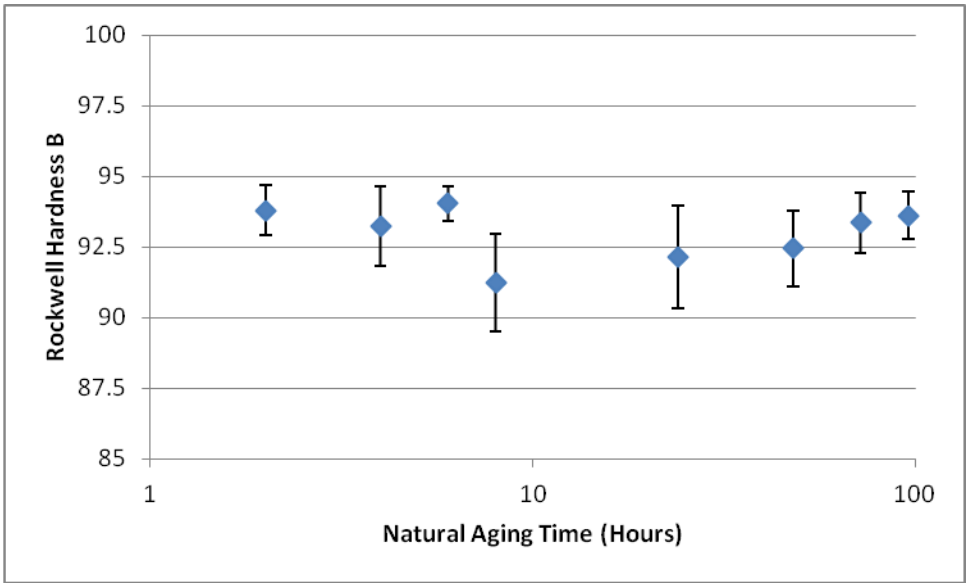


Figure 79 – *Rockwell hardness (B-scale) versus NA time for GT6-T6.*

Table 20 – *Rockwell hardness and conductivity (%IACS) data for several GT6-T6 samples focusing on the low NA times.*

| NA Time (Hours) | Rockwell Hardness B | Conductivity (%IACS) |
|---|---|---|
| 2 | 93.80 ± 0.88 | 29.6 |
| 4 | 93.23 ± 1.41 | 29.9 |
| 6 | 94.03 ± 0.61 | 29.8 |
| 8 | 91.24 ± 1.71 | 29.3 |
| 24 | 92.13 ± 1.81 | 29.6 |
| 48 | 92.45 ± 1.34 | 29.4 |
| 72 | 93.35 ± 1.07 | 29.5 |
| 96 | 93.61 ± 0.84 | 29.7 |

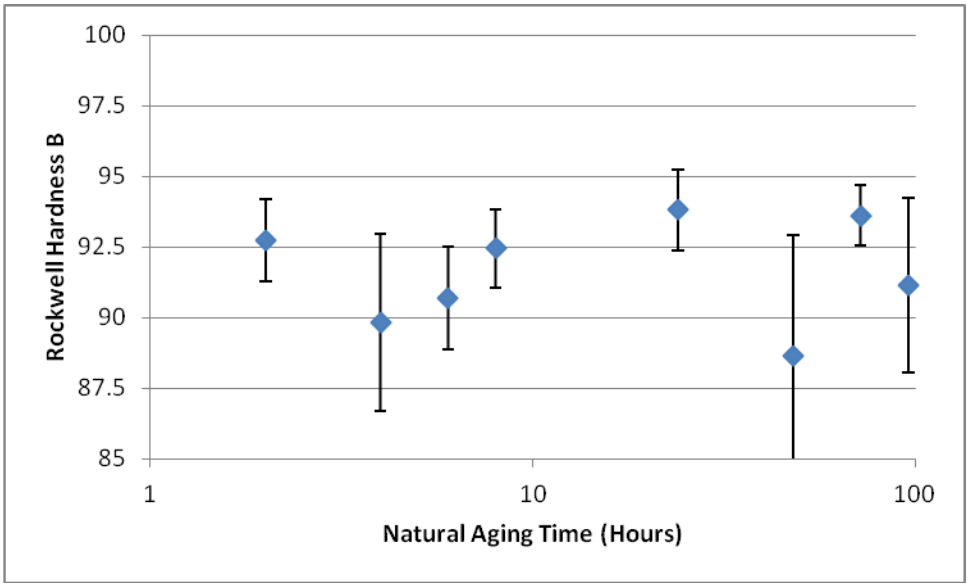


Figure 80 – *Rockwell hardness (B-scale) versus NA time for GT7-T6.*

Table 21 – *Rockwell hardness and conductivity (%IACS) data for several GT7-T6 samples focusing on the low NA times.*

| NA Time (Hours) | Rockwell Hardness B | Conductivity (%IACS) |
|---|---|---|
| 2 | 92.75 ± 1.46 | 29.9 |
| 4 | 89.82 ± 3.12 | 29.8 |
| 6 | 90.68 ± 1.82 | 29.4 |
| 8 | 92.45 ± 1.39 | 29.6 |
| 24 | 93.81 ± 1.45 | 29.3 |
| 48 | 88.67 ± 4.24 | 28.4 |
| 72 | 93.62 ± 1.06 | 28.8 |
| 96 | 91.16 ± 3.09 | 28.5 |

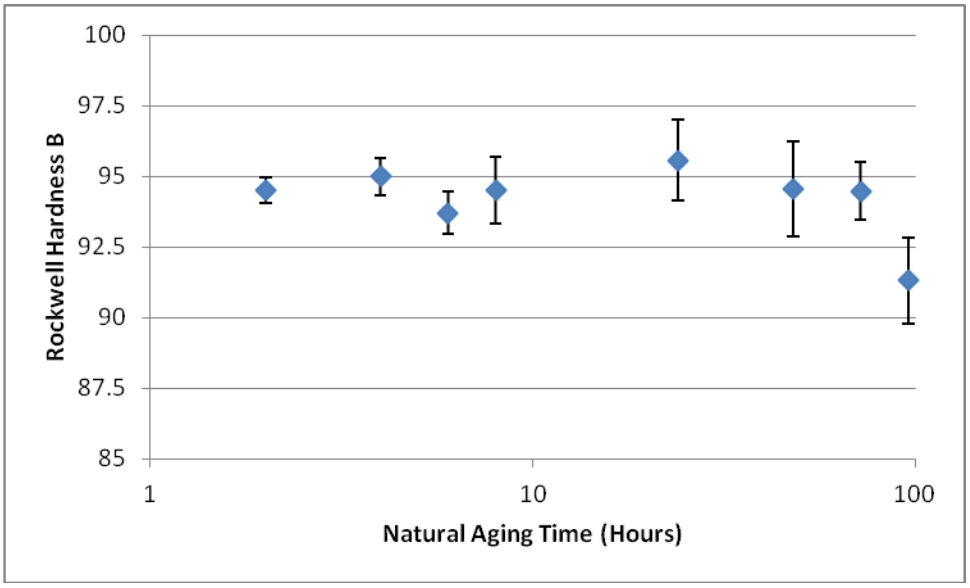


Figure 81 – *Rockwell hardness (B-scale) versus NA time for GT8-T6.*

Table 22 – *Rockwell hardness and conductivity (%IACS) data for several GT8-T6 samples focusing on the low NA times.*

| NA Time (Hours) | Rockwell Hardness B | Conductivity (%IACS) |
|---|---|---|
| 2 | 94.51 ± 0.45 | 27.7 |
| 4 | 94.99 ± 0.67 | 27.9 |
| 6 | 93.71 ± 0.73 | 27.6 |
| 8 | 94.52 ± 1.18 | 27.9 |
| 24 | 95.57 ± 1.45 | 27.8 |
| 48 | 94.55 ± 1.69 | 27.3 |
| 72 | 94.48 ± 1.02 | 27.7 |
| 96 | 91.31 ± 1.52 | 27.5 |

### 12.1.2 DSC

DSC analysis was conducted on GT1-8 in the T6 temper after NA for 2, 8, and 96 hours. Several key observations can be made based on the DSC data in combination with previously presented hardness and conductivity data, especially with respect to GP zone dissolution, η' and η precipitation, and eutectic stabilization. Figures 82 – 84 displays scans on GT1-5-T6 NA for 2, 8, and 96 hours, respectively.

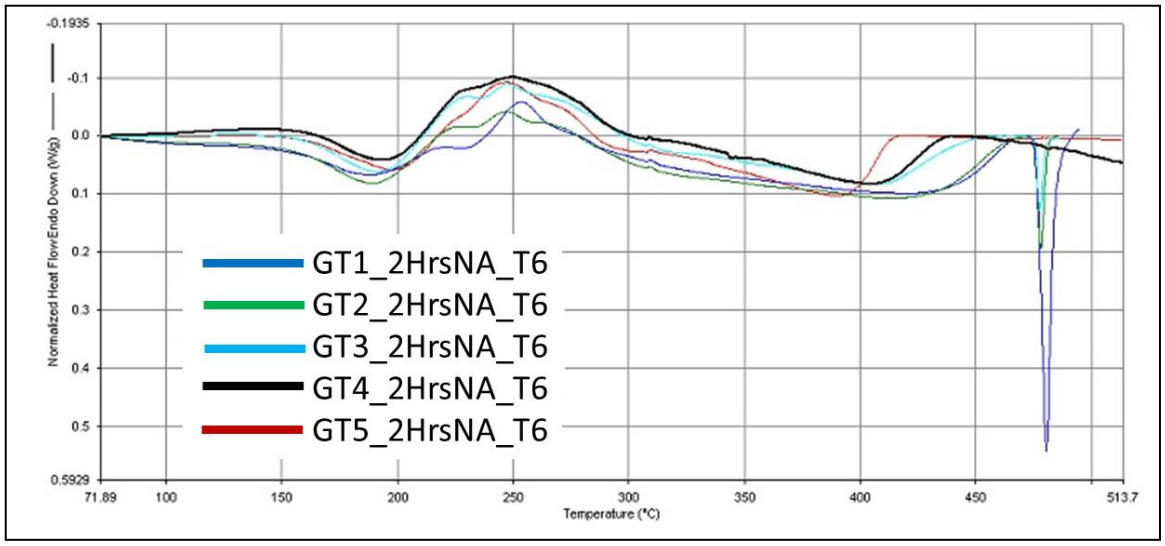


Figure 82 – *DSC analysis of alloys GT1-5 naturally aged for 2 hours prior to being aged to a T6 temper.*

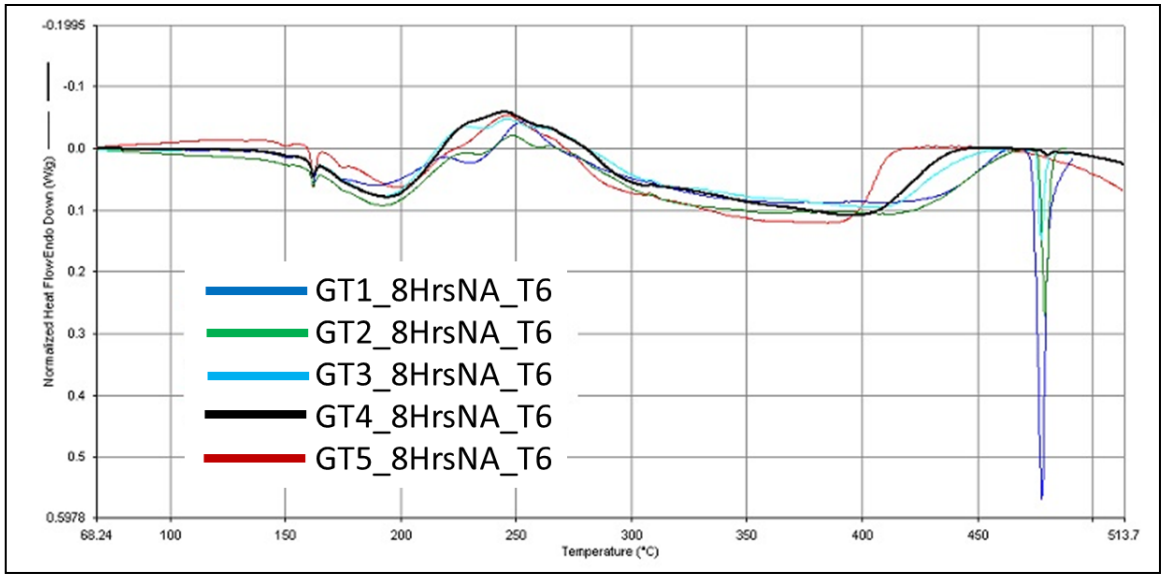


Figure 83 – *DSC analysis of alloys GT1-5 naturally aged for 8 hours prior to being aged to a T6 temper.*

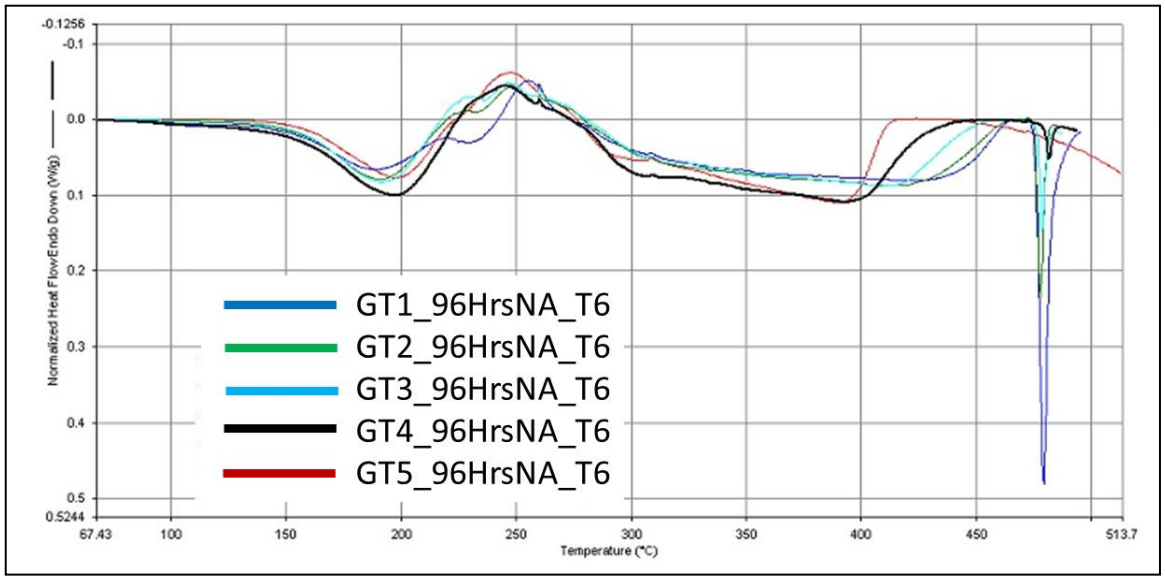


Figure 84 – *DSC analysis of alloys GT1-5 naturally aged for 96 hours prior to being aged to a T6 temper.*

DSC scans on GT1-T6 (Figure 85) display an increase in GP-zone dissolution with increasing NA time, which is due to the formation of GP-I zones. Figure 85 also displays a decrease in η' and η precipitation with increased NA time. These decreases are likely due to the fact that the solute needed for GP-II zone formation is being taken up by GP-I zones. The decrease in η with increased NA time suggests that at least some portion of these GP-I zones are reverting back to solid solution instead of transforming to η as NA time is increased. Due to the nature of the precipitation process of GP-I zones this seems likely to do with the number of GP-I zones present (i.e. – more GP-I zones potentially means smaller GP-I zones, which cannot transform directly to η). Therefore, the DSC data for GT1-T6 correlates to the hardness data presented in Figure 74.

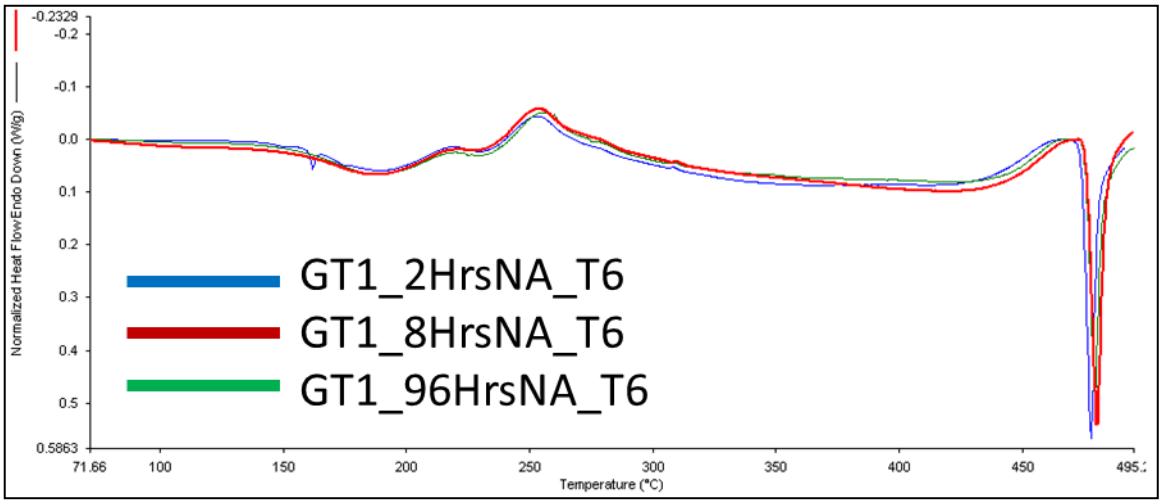


Figure 85 – *DSC analysis of GT1-T6 naturally aged for 2, 8, and 96 hours prior to artificial aging.*

With regard to eutectic melting, as the NA time increases there appears to be a decrease in the onset melting temperature along with a decrease in the area under the peak (Table 23). Generally, this would suggest Cu is being tied up in the system, perhaps in GP-I zone or η' both of which are known to have some solubility for Cu.

Table 23 – *Eutectic melting peak analysis for GT1-5 in the T6 temper after 2, 8, and 96 hours of NA.*

| | Onset Melting (°C) | | | Melting Peak (°C) | | | Area Under Peak (J/g) | | |
|---|---|---|---|---|---|---|---|---|---|
| **Alloy** | **2 Hrs NA** | **8 Hrs NA** | **96 Hrs NA** | **2 Hrs NA** | **8 Hrs NA** | **96 Hrs NA** | **2 Hrs NA** | **8 Hrs NA** | **96 Hrs NA** |
| **GT1** | 476.1 | 473.3 | 475.7 | 480.5 | 477.8 | 479.5 | 8.84 | 7.90 | 7.47 |
| **GT2** | 475.9 | 476.8 | 475.7 | 477.9 | 479.2 | 477.5 | 1.80 | 2.61 | 2.07 |
| **GT3** | 475.7 | 475.8 | 476.8 | 477.9 | 477.5 | 478.5 | 1.05 | 1.51 | 1.11 |
| **GT4** | - | 478.0 | 479.8 | - | 480.2 | 481.9 | - | 0.06 | 0.34 |
| **GT5** | - | - | - | - | - | - | - | - | - |

The DSC data for GT2-T6 (Figure 86) shows a slight decrease in GP zone dissolution with increase NA time, which again correlates to the increased number of GP-I zones present in the matrix. As with GT1-T6, the increased number GP-I zones correlates to a decrease in the η' and η precipitation peaks. There is also evidence of a third unknown phase precipitating out after η, which could be T-phase. Eutectic melting appears to increase initially (2 hours to 8 hours NA) in terms of both temperature and

area under the peak and then decrease (8 hours to 96 hours NA). It should be noted that the 8 hour sample here falls directly in the hardness dip present in Figure 75, suggesting the dip may correlate to a critical time in the development of GP-I zones. It is reasonable to speculate the dip correlates to a period where GP-I zones are too large to quickly dissolve back into solution (and thus act as a nucleation sites for GP-II zones), but are too small to be stable at 120°C thus releasing Cu back into the system.

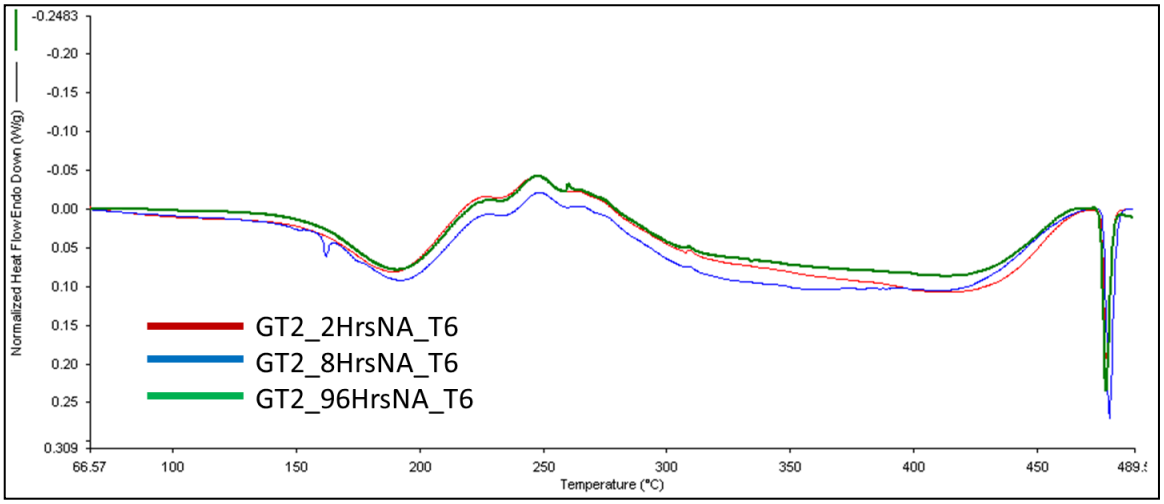


Figure 86 – *DSC analysis of GT2-T6 naturally aged for 2, 8, and 96 hours prior to artificial aging.*

With respect to DSC data many of the observations made on the GT2-T6 data are also applicable to GT3-T6 (see Figure 87). NA time appears to increase GP zone dissolution, decrease η', and decrease η formation. The possible T-phase precipitation peak is also present. However unlike GT1 and GT2, increases in NA time appear to stabilize and promote eutectic melting to some degree. If the theory presented for GT2 holds true, this could suggest that GP-I zones in GT3 are not stable enough to withstand artificial aging at 120°C and therefore dissolve back into solution releasing Cu into the system. The decrease Cu content would suggest this could be possible (i.e. – less Cu, less stable GP zones).

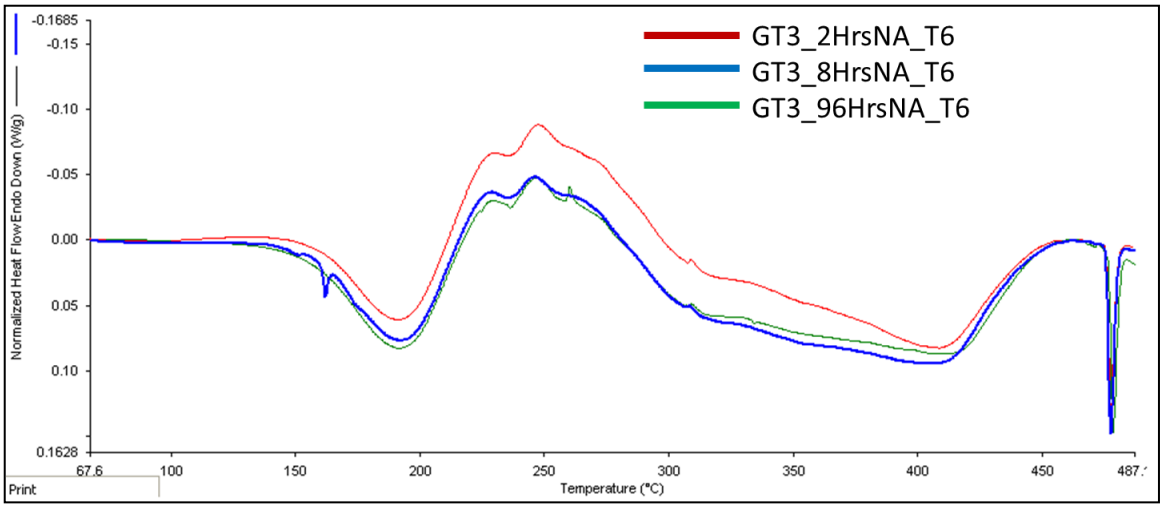


Figure 87 – *DSC analysis of GT3-T6 naturally aged for 2, 8, and 96 hours prior to artificial aging.*

The DSC data for for GT4-T6 (see Figure 88) appears to show a decrease in GP zone formation and an increase in GP zone dissolution with increased NA time. The η' and η precipitation peaks also appear to decrease with NA time, which appears to contradict the hardness data in Figure 77. With regards to the eutectic melting, GT4-T6 shows no sign of eutectic melting in the 2 hours of NA sample, but as NA time increases a peak appears. This peak then continues to grow in magnitude as well as increases in terms of peak and onset melting temperature. GT4 is a low Cu alloy suggesting that, while early stage GP-I zones are not sufficiently stabilized enough to be present at 120°C, as NA time is increased GP-I zones become stabilized past the GP-II zone precipitation temperature due to their size.

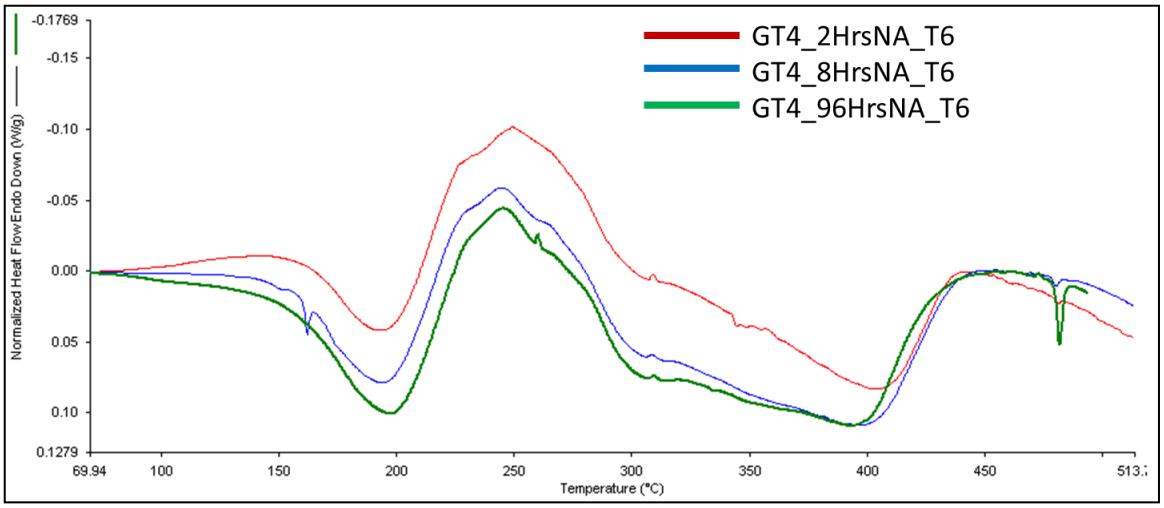


Figure 88 – *DSC analysis of GT4-T6 naturally aged for 2, 8, and 96 hours prior to artificial aging.*

DSC scans on GT5-T6 (Figure 89) show that GP zone formation initially increases and then decreases with NA time. A similar trend can be seen in the GP zone dissolution peak. However, with respect to the η' and η precipitation peaks there appears to be an initial decrease (2 hours to 8 hours of NA) followed by an increase (8 hours to 96 hours NA). This suggests that as GP-I zones continue to precipitate out they become smaller and smaller due to an ever decreasing amount of unused solute. Therefore, upon aging these smaller GP-I zones can follow P6 instead of P2 or P3. However, it should be noted that any GP-I zones precipitating out would be competing with previously precipitated GP-I zones for solute, and could be consumed by the larger GP-I zones. Regardless, the GP-I zones should not be stabilized to any degree and should dissolve readily upon heating and thus creating a fine dispersion of solute upon which GP-II zones can precipitate readily (i.e. – this is why low Cu 7xxx-sereis alloys are generally NA for at least three days). Therefore, the decrease in η' and η observed in the 8 hours of NA sample could be related to an interaction between the two precipitates as the η' solvus should approach the η precipitation temperature in a Cu-free alloy. Interestingly, there appears to be the precipitation of some form of a Cu-free T-phase in a few of the GT5 DSC scans.

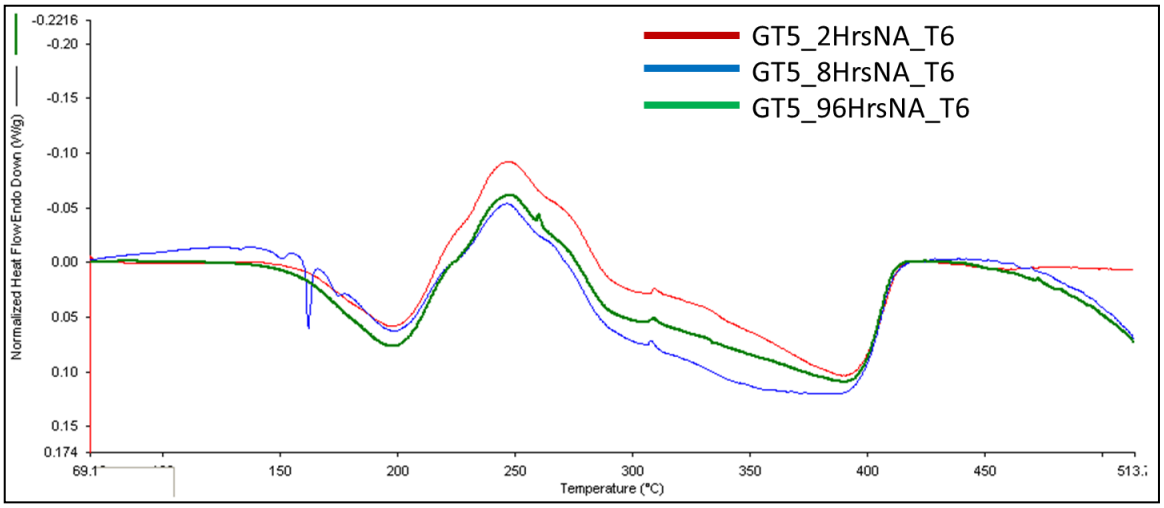


Figure 89 – *DSC analysis of GT5-T6 naturally aged for 2, 8, and 96 hours prior to artificial aging.*

DSC scans were conducted on GT6-8 in the T6 temper can be seen in Figures 90 – 92. Once again the sample were NA for 2, 8, and 96 hours before being AA to a T6 temper. It is interesting to note the change in precipitate type as the Zn:Mg ratio is change. Figures 90 and 91 appear to suggest that as the Mg level is raised the η' and η-peaks are shifted to a higher temperature indicating that a stabilization has occurred of these phases. This could be due to the increased lattice strain spurred by the increased Mg content. However, DSC analysis of GT8 appears to show no η peak. Careful observation of the GT6-8 scans suggests that T-phase is also being stabilized as Mg is increased and therefore it is possible the η-peak in GT8 has merged with the T-phase precipitation peak, or that the η' and η precipitation peaks have merged (which is more likely the case).

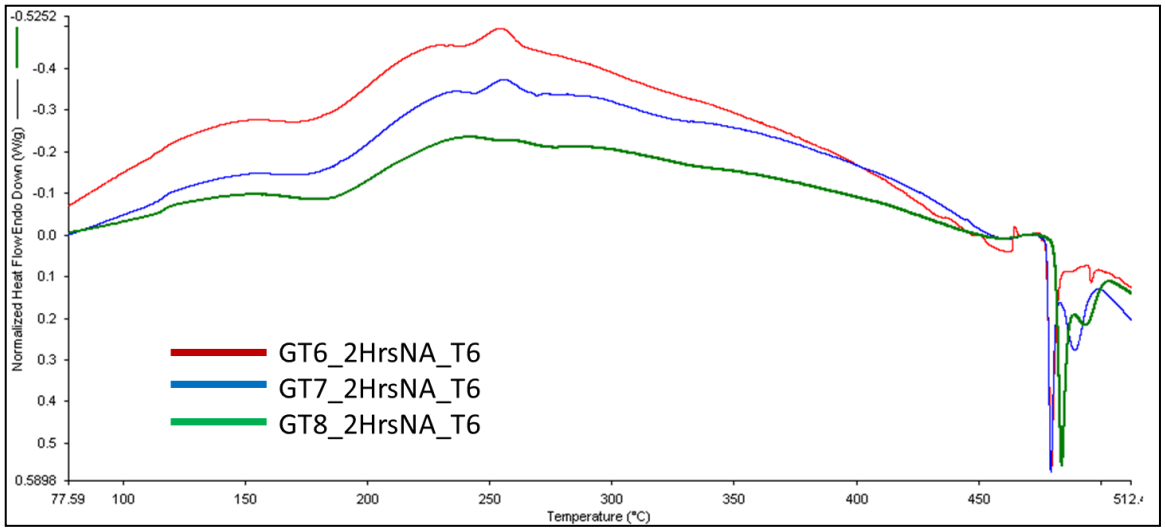


Figure 90 – *DSC analysis of alloys GT6-8 naturally aged for 2 hours prior to being aged to a T6 temper.*

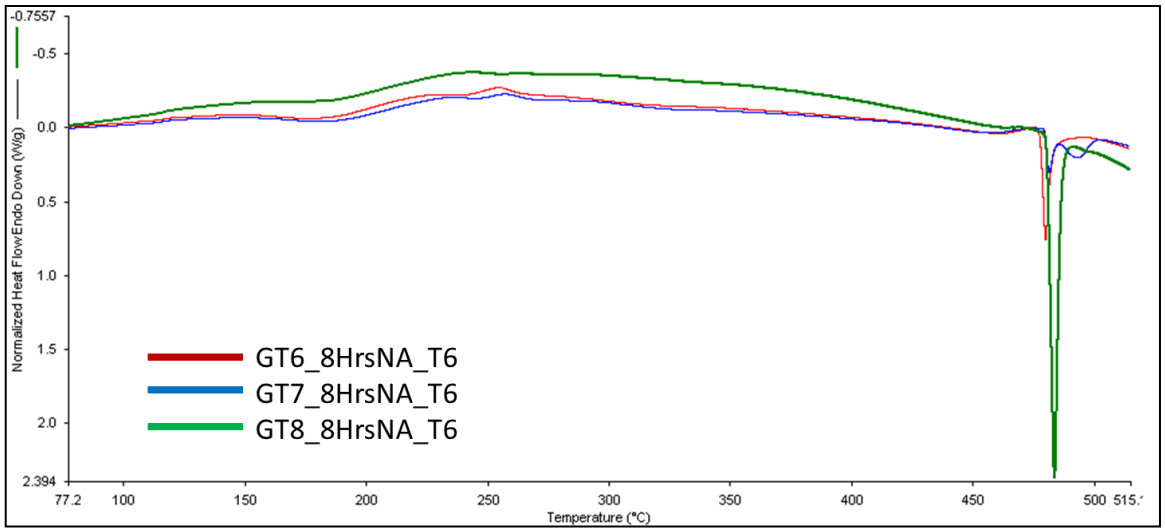


Figure 91 – *DSC analysis of alloys GT6-8 naturally aged for 8 hours prior to being aged to a T6 temper*

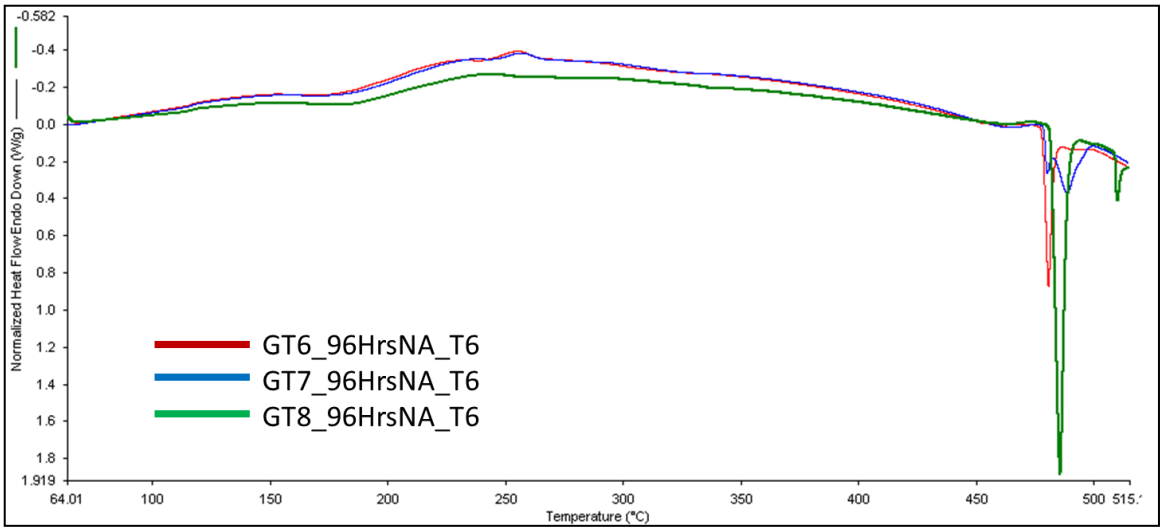


Figure 92 – *DSC analysis of alloys GT6-8 naturally aged for 96 hours prior to being aged to a T6 temper.*

The DSC analysis of GT6-T6 (Figure 93) appear to correlate to the hardness data presented in Figure 79 in that the alloy is relatively unaffected by NA. The GP zone dissolution and the η'/η precipitation peaks appear to be unaffected by NA; however, it should be noted that the T-phase precipitation peak appears to increase with increased NA time.

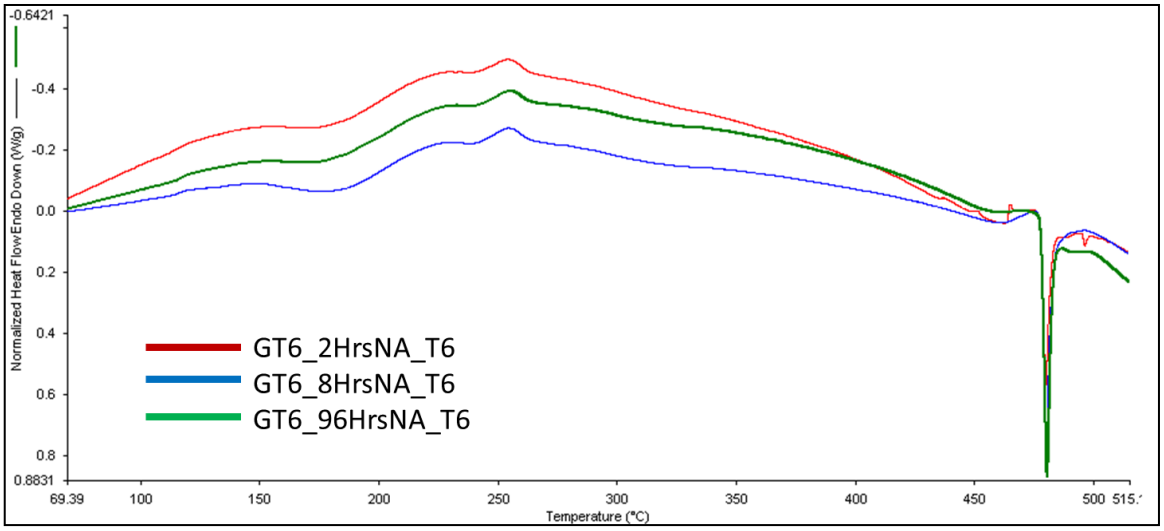


Figure 93 – *DSC analysis of GT6-T6 naturally aged for 2, 8, and 96 hours prior to artificial aging.*

DSC scans on GT7-T6 (Figure 94) appear to show little change in the main precipitation peaks with increased NA time, although the 8 hour sample precipitation

peaks appear to be shifted to a slightly higher temperature. Although the eutectic melting temperature does not appear to be affected by the NA time, the area under the melting peaks does decrease with increased NA time; however, the area under the peaks of the subsequent unknown melting peaks appear to increase with NA time. Similarly to GT6-T6, T-phase can clearly be seen precipitating out in the GT7-T6 DSC scans.

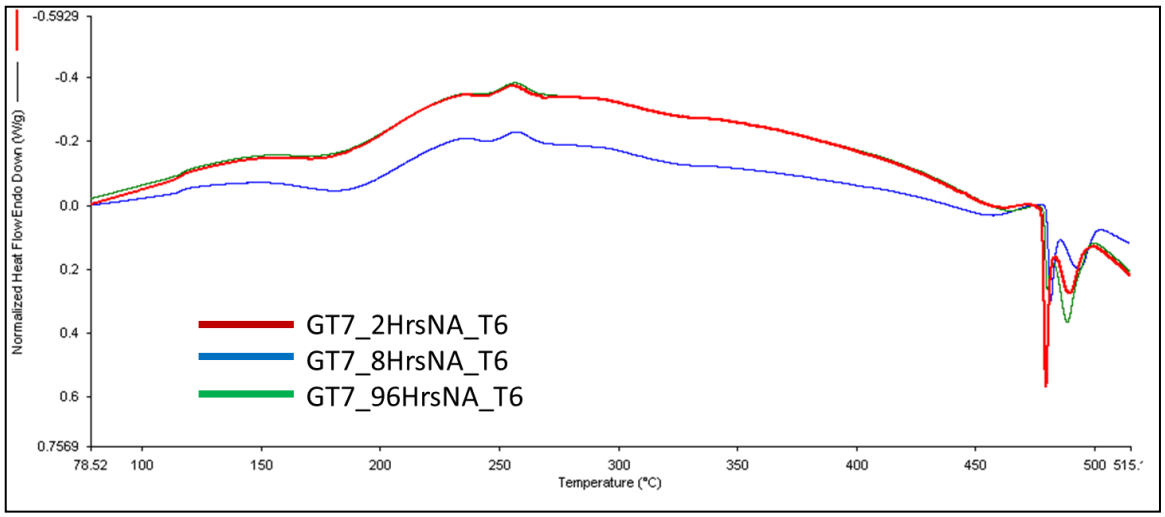


Figure 94 – *DSC analysis of GT7-T6 naturally aged for 2, 8, and 96 hours prior to artificial aging.*

The η' and η precipitation peaks appear to have merged in GT8-T6 (Figure 95), and this effect becomes more pronounced as NA time is increased. This could account for the sudden drop off in strength seen in Figure 81. The η nor the T-Phase peaks in GT8, however, appear to be effected by NA time. Eutectic melting temperature does also not appear to be effect by NA time, but the amount of eutectic in the microstructure appears to be increasing with NA time. It should also be noted that the melting peaks of two unknown phases can also be seen in Figure 95.

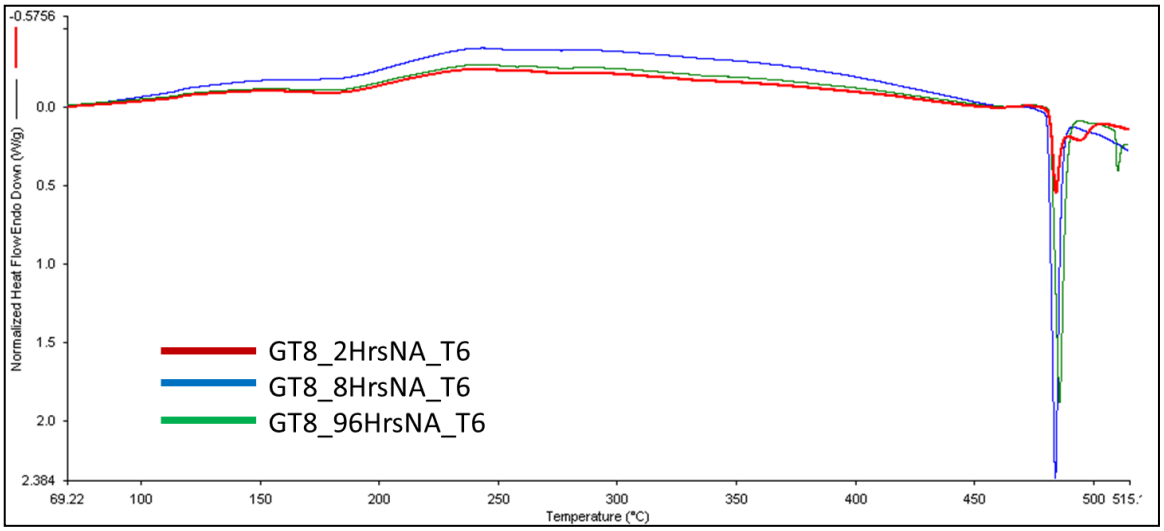


Figure 95 – *DSC analysis of GT8-T6 naturally aged for 2, 8, and 96 hours prior to artificial aging.*

It is obvious from the Rockwell hardness and DSC data that natural aging has a profound effect on the mechanical properties of 7xxx-series alloys in the T6-temper. Furthermore, the degree to which natural aging affects a 7xxx-series alloy and whether it is beneficial or detrimental to an alloy can be directly related to its composition. This is due to the various interactions of solute elements, most notably Cu, to VRCS and GP zones.

## 12.2 The Effects of NA on the T7 Temper

Following testing in the T6 temper, GT1-8 were AA at 160°C (320°F) for 24 hours to produce a T7 temper. The alloys were subsequently tested for hardness and electrical conductivity (%IACS) as well as characterized via DSC technology. It should be noted that due to the small specimen size and the REX nature of GT1-8 that conductivity measurements proved difficult for these alloys. Therefore, any conclusions drawn from conductivity alone are open for deliberation.

### 12.2.1 Rockwell Hardness and Conductivity

Figures 96 – 105 and 106 – 111 contain the results of the hardness and conductivity date for alloys GT1-5-T7 and GT6-8-T7, respectively. All error bars represent one standard deviation. There appears to be little effect of NA on GT1-T7

(Figures 96 and 97) with respect to hardness or conductivity. With respect to hardness, it appears the GT1-T7 sample NA for 24 hours prior to AA is the hardest with the rest of the measurements not following a distinguishable trend. Figure 97 displays hardness versus conductivity for GT1-T7. It can be seen that GT1-T7 (with the notable except of the 2 hours of NA sample) follows a normal 7xxx-T7 trend line (i.e. – there is a semi-linear decrease in mechanical properties as the product is overaged). Structurally, Figures 96 and 97 suggest that GP-I zones stabilized in long NA times have transformed directly to η upon over-aging therefore mitigating the deleterious effects of NA seen in the T6 temper.

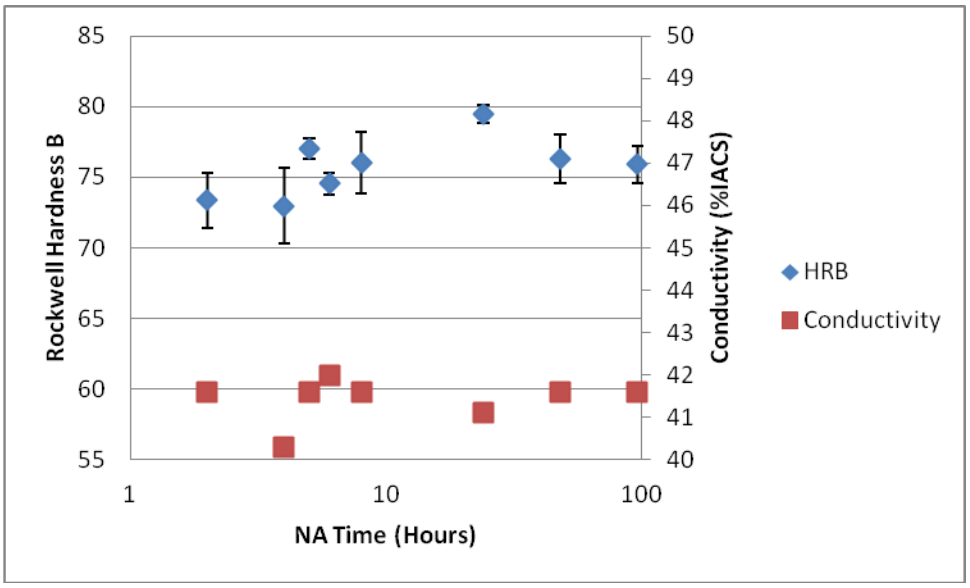


Figure 96 – *Rockwell hardness (B-scale) and conductivity (%IACS) versus NA time for GT1-T7.*

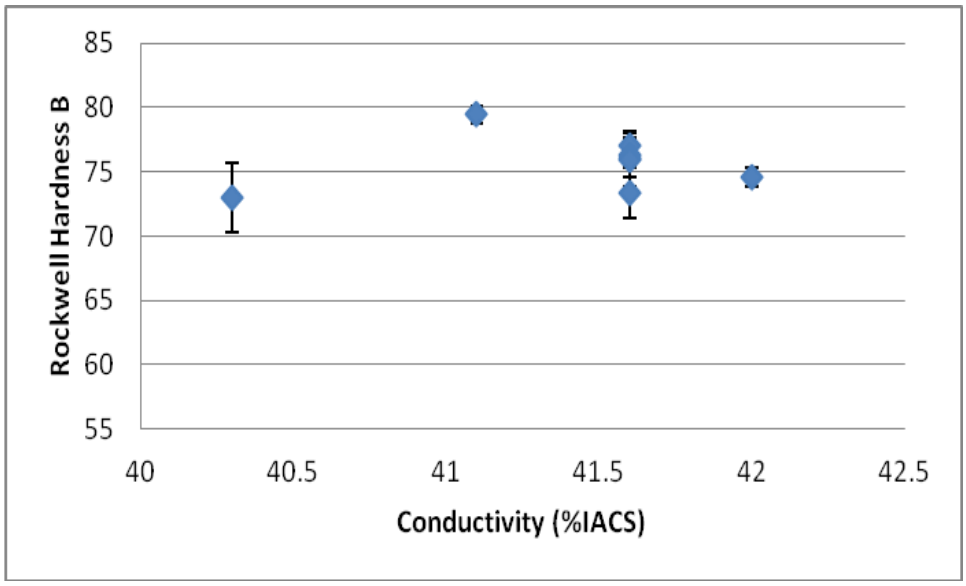


Figure 97 – *Rockwell hardness (B-scale) versus conductivity (%IACS) for GT1-T7.*

Figure 98 displays a decrease in conductivity with increased NA time for GT2-T7, although hardness appears to be unaffected. The decrease in conductivity suggest one of two possibilities suggest that the stabilized GP-I zones formed at long NA reverted back to solid solution and did not transform to η; however, Figure 99 which displays hardness versus conductivity shows a clear linear trend suggesting that the precipitation kinetics have been altered due to the increased NA period (i.e. – the GP-I zone to η transformation has been reduced).

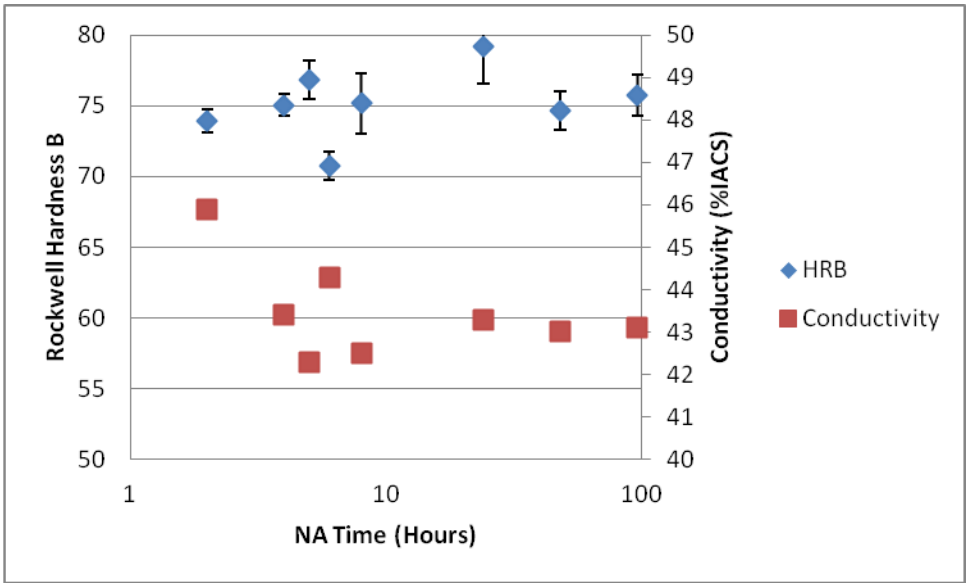


Figure 98 – *Rockwell hardness (B-scale) and conductivity (%IACS) versus NA time for GT2-T7.*

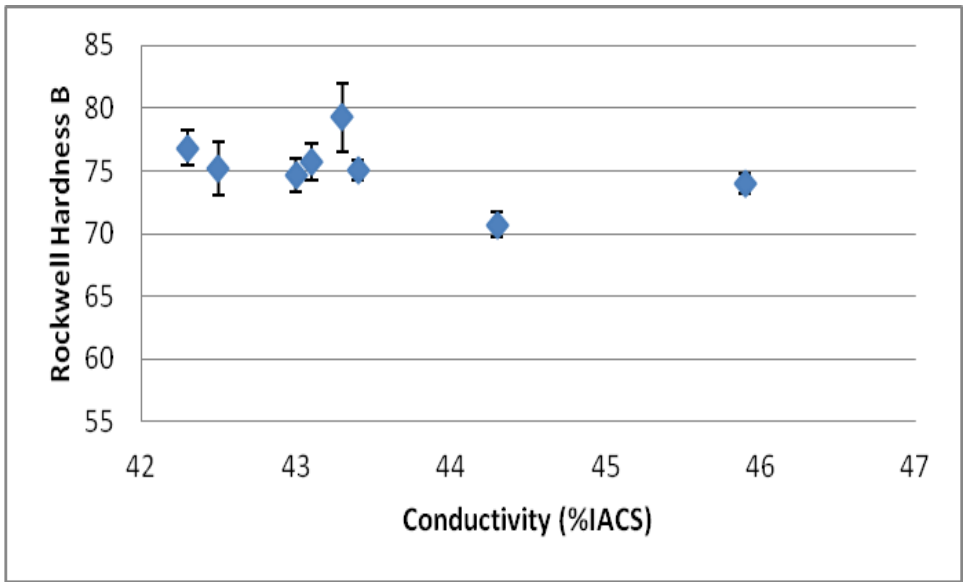


Figure 99 – *Rockwell hardness (B-scale) versus conductivity (%IACS) for GT2-T7.*

GT3-T7 (Figures 100 and 101) appears to act similar to GT1-T7. The hardness and conductivity data do not display a clear trend when plotted against NA time (Figure 100), but do display a linear trend when plotted against each other (Figure 101). It should be noted that 160°C (320°F) is close to the suspected η' to η transformation temperature. Therefore, furnace fluctuations or furnace temperature gradients could be interfering with the results.

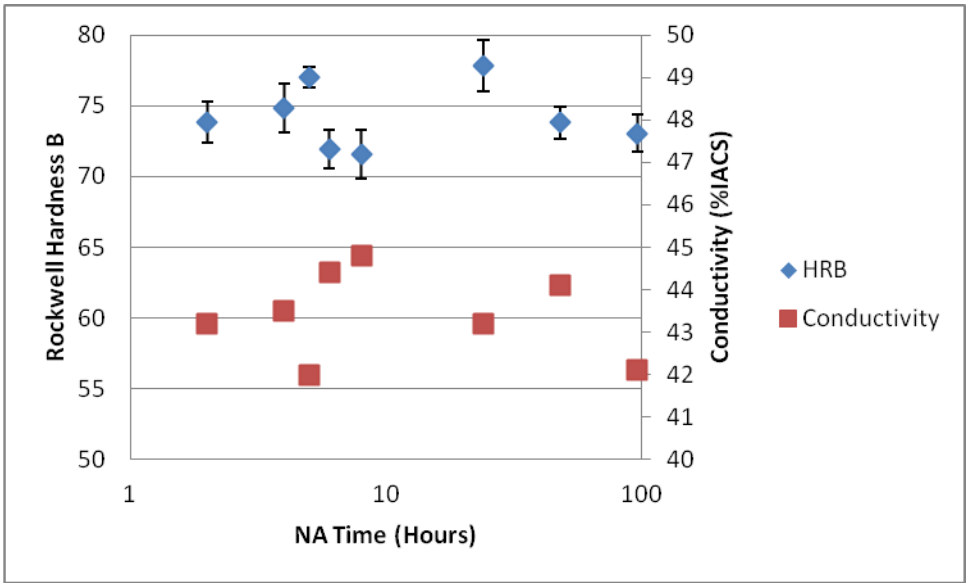


Figure 100 – *Rockwell hardness (B-scale) and conductivity (%IACS) versus NA time for GT3-T7.*

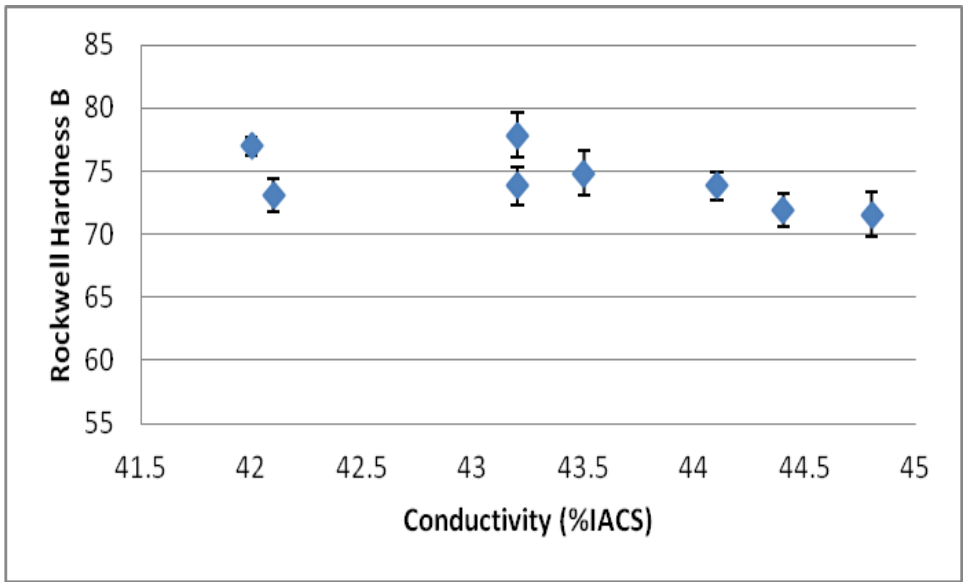


Figure 101 – *Rockwell hardness (B-scale) versus conductivity (%IACS) for GT3-T7.*

GT4-T7 behave similarly to GT2-T7 when hardness and conductivity are plotted against NA time as can be seen in Figures 102 and 103. The hardness of GT4-T7 appears to drop at 8 hours before peaking at 24 hours and then once again appearing to drop; the error of these measurement, however, makes it difficult to draw any definite conclusions. The conductivity of GT4-T7 appears to drop as NA time is increased. As previously mentioned, this suggests that GP-I zones formed during NA did not transform to η, but

dissolved back into solid solution. In the low-Cu GT4, this also suggests one of two possibilities: 1.) the GP-I zones may not have quickly dissolved and created a fine dispersion for GP-II zones to precipitation upon as previously thought, or 2.) the increased number of GP-II zones formed due to the quick dissolution of GP-I zones in the low Cu alloy actually reduces the kinetics of the over-aging process (i.e. – more solute out of solution so diffusion slows down). When combined with the T6 data, it appears that scenario 2 is the more likely mechanism at play in GT4.

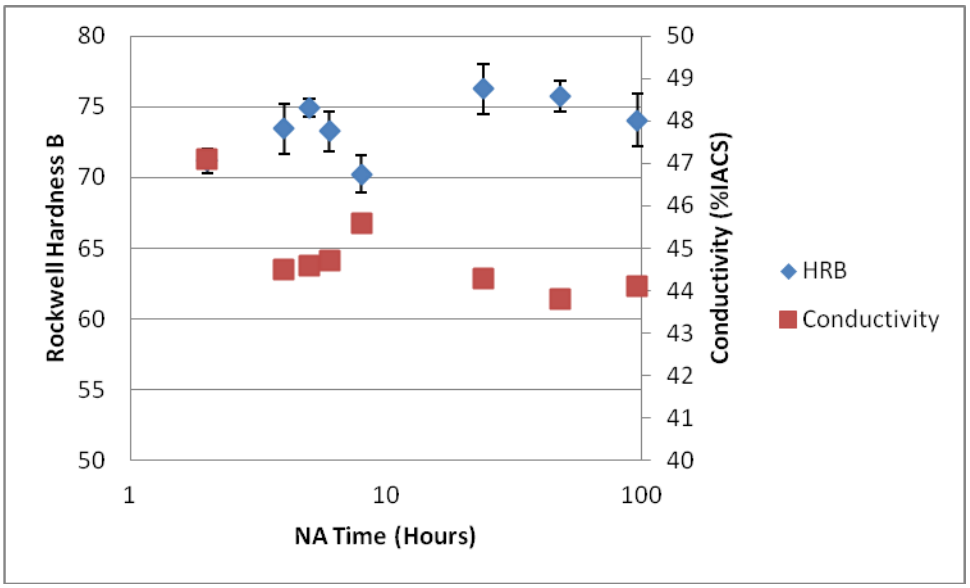


Figure 102 – *Rockwell hardness (B-scale) and conductivity (%IACS) versus NA time for GT4-T7.*

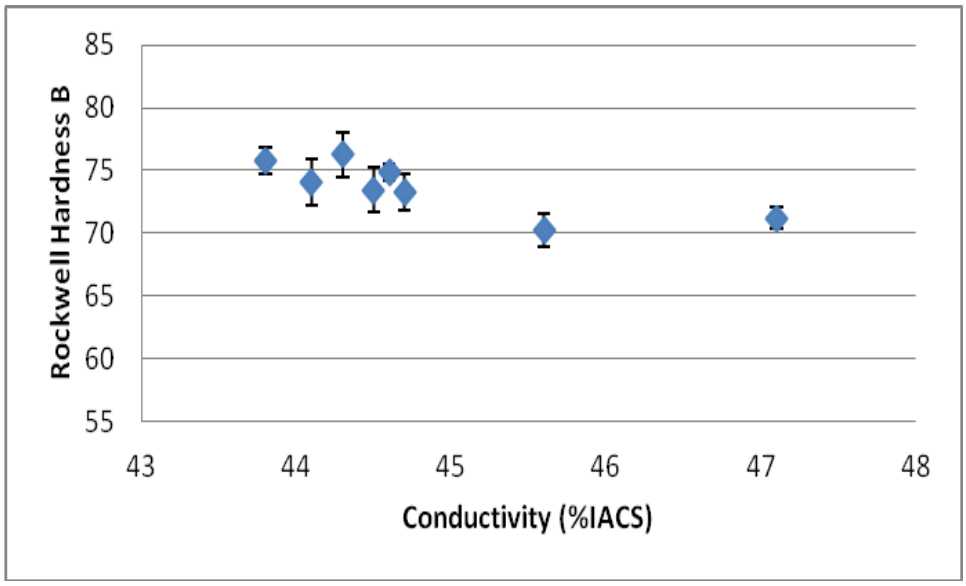


Figure 103 – *Rockwell hardness (B-scale) versus conductivity (%IACS) for GT4-T7.*

Unfortunately, both the hardness and conductivity data for GT5-T7 presented in Figure 104 is too convoluted to discern any trends related to the effects of NA in the T7 temper. Figure 105, which displays hardness versus conductivity data for GT5-T7 suggests that any of the effects seen in Figure 104 are kinetic in nature. Therefore, it is likely that furnace fluctuations and temperature gradients have caused error in the experiment.

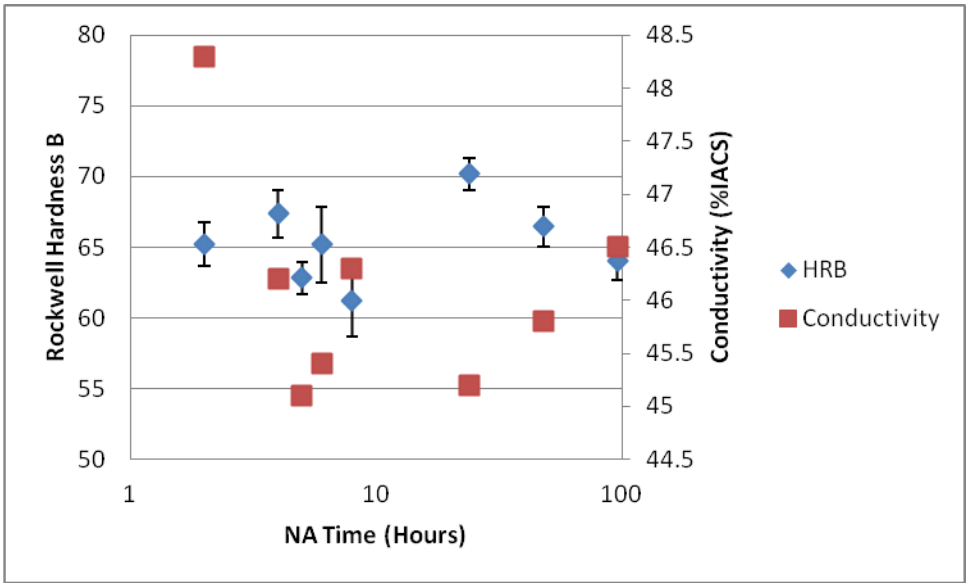


Figure 104 – *Rockwell hardness (B-scale) and conductivity (%IACS) versus NA time for GT5-T7.*

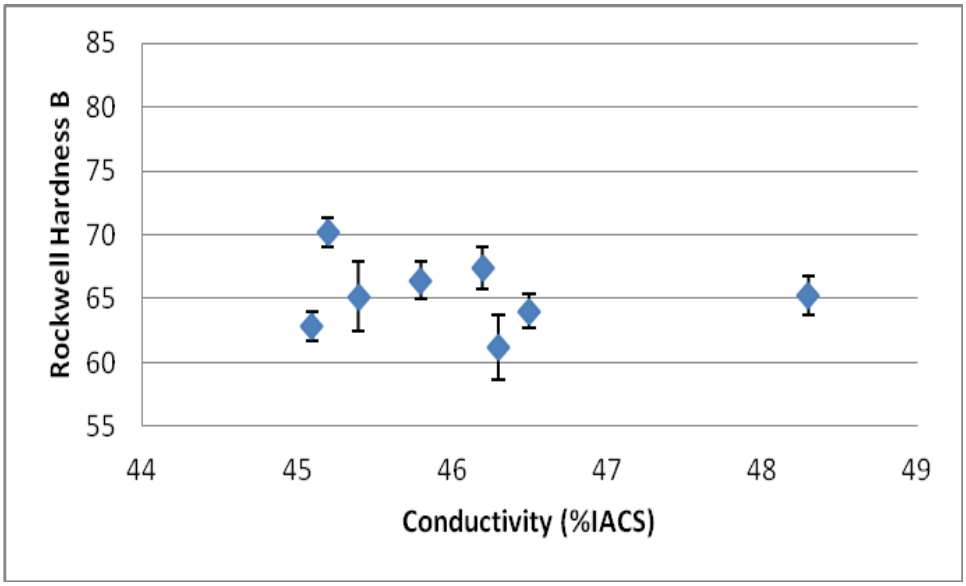


Figure 105 – *Rockwell hardness (B-scale) versus conductivity (%IACS) for GT5-T7.*

GT6-T7 (Figures 106 and 107) appears to show a dip in hardness at 8 hours, much like GT3-T7 and GT4-T7. With respect to conductivity, it appears conductivity goes up with increased NA time, but there is significant scatter in the data. The hardness versus conductivity plot (Figure 107), however, seems to suggest that perhaps there is a trend here although not a conclusive one. Increased conductivity in the sample would suggest that over-aging readily has occurred, but the DSC scans on the GT6-T6 revealed a developed T-phase peak that appeared to stabilize with increased NA time. Therefore, it is possible that T-phase present in GT6-T7 at longer NA times is coarsening faster than that at short NA increasing the conductivity.

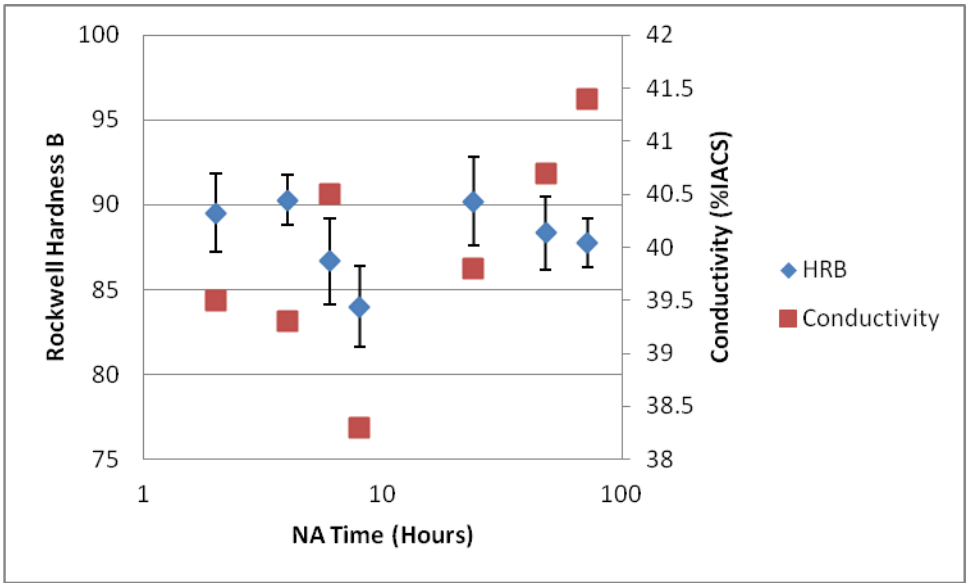


Figure 106 – *Rockwell hardness (B-scale) and conductivity (%IACS) versus NA time for GT6-T7.*

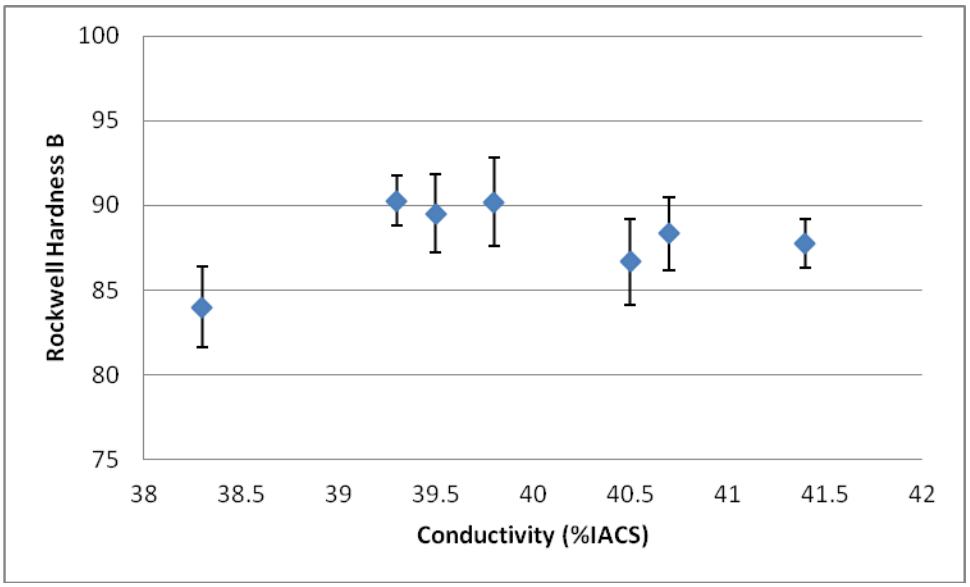


Figure 107 – *Rockwell hardness (B-scale) versus conductivity (%IACS) for GT6-T7.*

Alloys GT7-T7 (Figures 108 and 109) and GT8-T7 (110 and 111) both display trends similar to GT6-T7 indicating the increase in conductivity with increased NA maybe real. GT7-T7 and GT8-T7 also show a slight downward trend with respect to hardness, which would be expected with increased T-phase precipitation and coarsening as previously suggested.

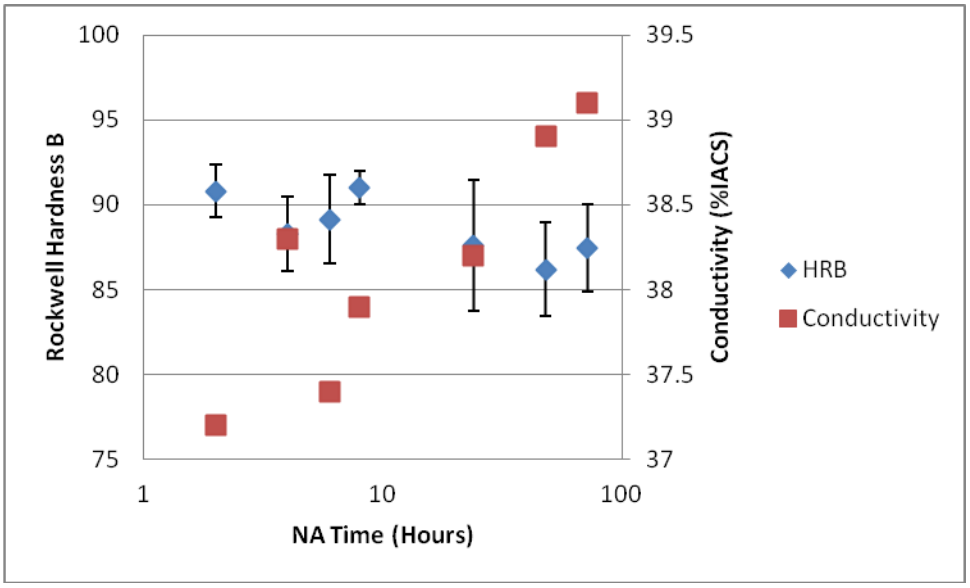


Figure 108 – *Rockwell hardness (B-scale) and conductivity (%IACS) versus NA time for GT7-T7.*

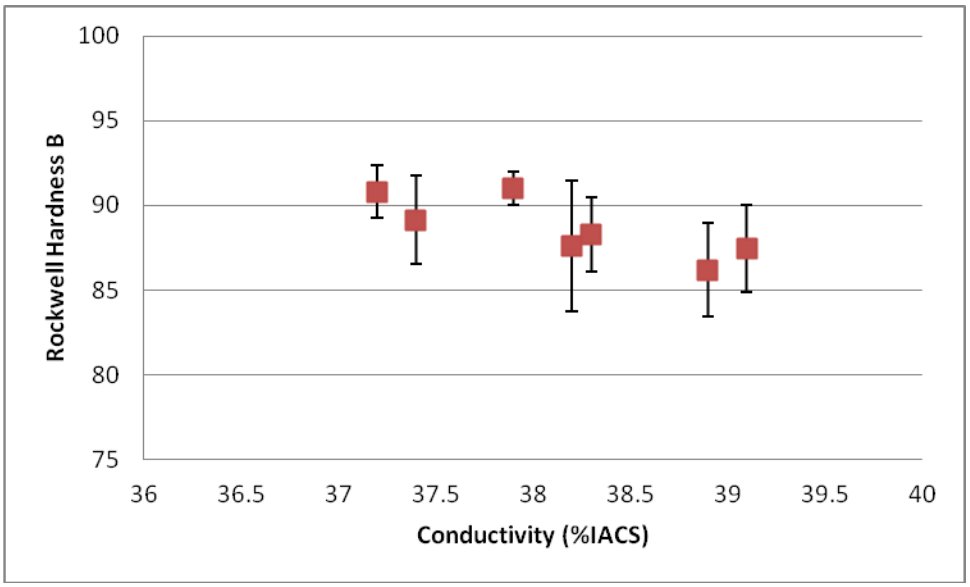


Figure 109 – *Rockwell hardness (B-scale) versus conductivity (%IACS) for GT7-T7.*

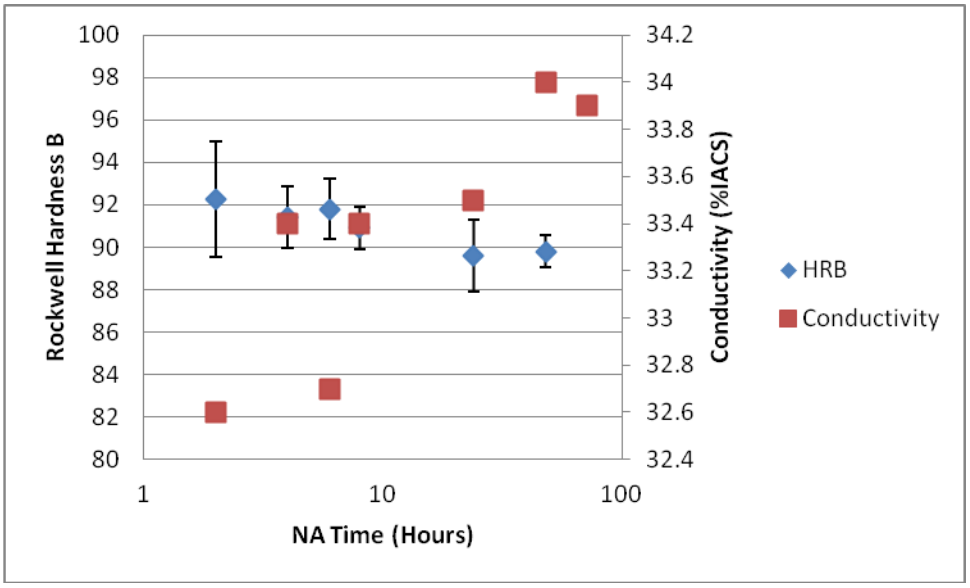


Figure 110 – *Rockwell hardness (B-scale) and conductivity (%IACS) versus NA time for GT8-T7.*

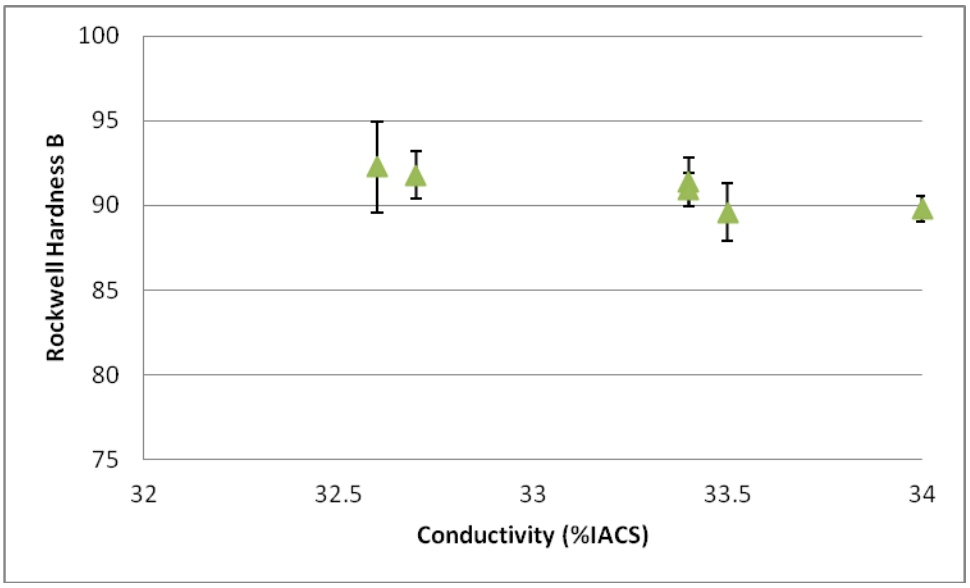


Figure 111 – *Rockwell hardness (B-scale) versus conductivity (%IACS) for GT8-T7.*

With respect to hardness and conductivity, the effects of NA appear to still be present in some cases, but are minimal compared to the effects seen in the T6 temper. Generally, it has been suggested that these effects center on the stability of GP-I zones and the precipitation and subsequent coarsening of T-phase, however these theories based on Rockwell hardness and conductivity measurements alone cannot be considered conclusive due to the inherent error in each method. It is evident that much more

sensitive techniques will be necessary to effectively characterize and quantify the effects of NA on the T7 temper.

### 12.2.2 DSC

Several key observations can be made based on DSC analysis of GT1-8 in the T7 temper, especially when combined with the previously presented hardness and conductivity data. The effects of NA on the T7 temper and the precipitates present which were difficult to distinguish using hardness and conductivity alone are much clearer in the DSC scans.

Figures 112 – 114 display DSC analysis on GT1-5 in the T7 temper after 2, 8, and 96 hours of NA. It is obvious from the Figures that the Cu content plays a vital role in determining location and shape of the η' and η precipitation peaks. For instance as Cu is lowered, the η' precipitation peak moves closer to η peak, which is a known effect. The solutionization temperature also appears to be effected by the Cu content. It appears that low Cu alloys go into solution faster, which is probably due to the fact the precipitates aren't stabilized by Cu in these alloys.

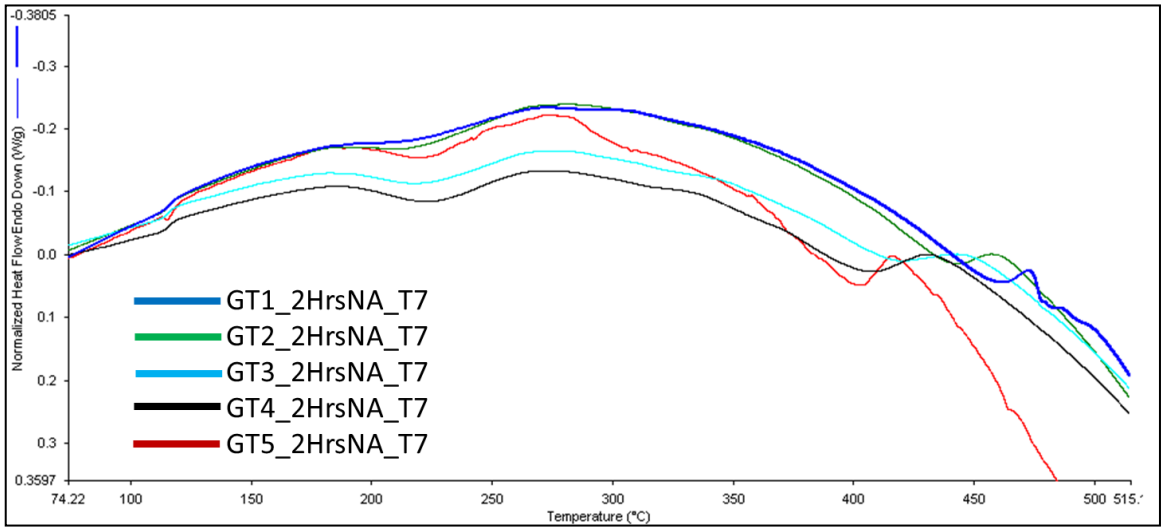


Figure 112 – *DSC analysis of alloys GT1-5 naturally aged for 2 hours prior to being aged to a T7 temper.*

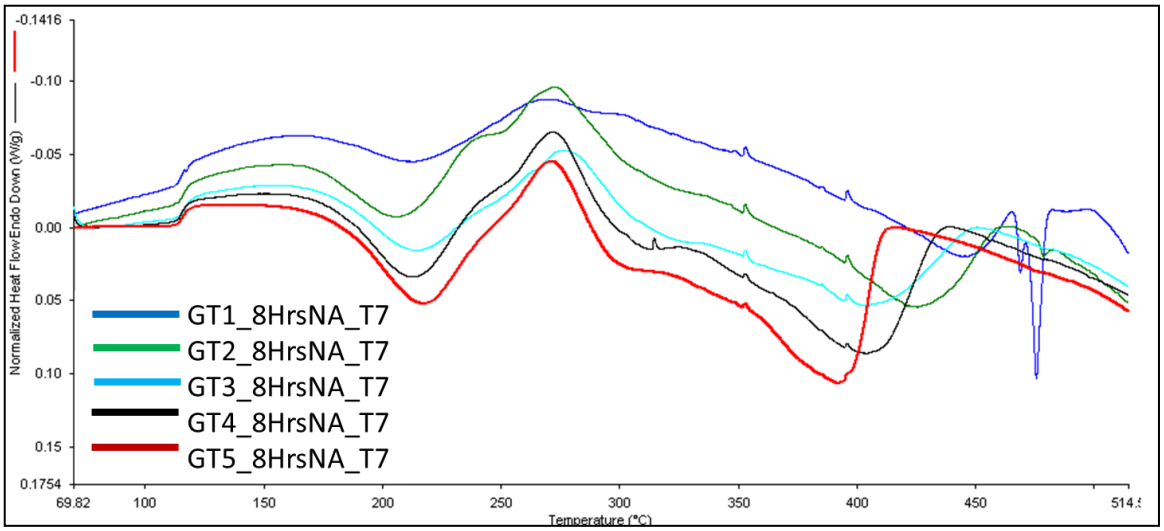


Figure 113 – *DSC analysis of alloys GT1-5 naturally aged for 8 hours prior to being aged to a T7 temper.*

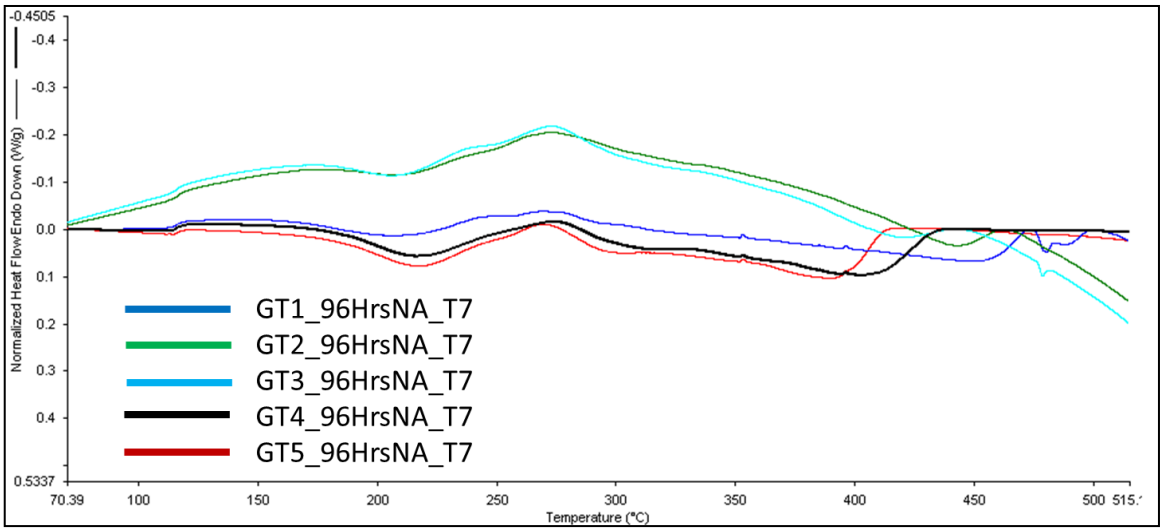


Figure 114 – *DSC analysis of alloys GT1-5 naturally aged for 96 hours prior to being aged to a T7 temper.*

DSC analysis of GT1-T7 appears to show a direct correlation between η' and NA time as can be seen in Figure 115. The other precipitation peaks (i.e. – GP-zones, η-phase, and T-phase) are all present in each sample, but only the 96 hours of NA sample displays a η' precipitation peak. It should also be noted that the η-peak for the 96 hour sample has been shifted to a higher temperature. Although this not expected, it appears to correlate to the hardness data shown in Figure 96 where the 96 hour sample displays a higher hardness then the two or eight hour samples. It is possible that the increased

precipitation of GP-I zones associated with longer NA time has slowed down the coarsening behavior of GT1, or the presence of η' in the T73 temper could be the result of an unknown precipitation mechanism.

GT1-T7 appears to show two sharp exothermic reactions at roughly 300°C and 400°C. These peaks are shown in other alloys as well (see Figures 112 – 114), although a different temperatures. These peaks could not be identified, but the sharpness of the peaks suggests they represent a quick reaction like recrystallization. It should also be mentioned that there appears to be a change in the eutectic melting with NA time, although the various peaks could not be identified (see Table 24).

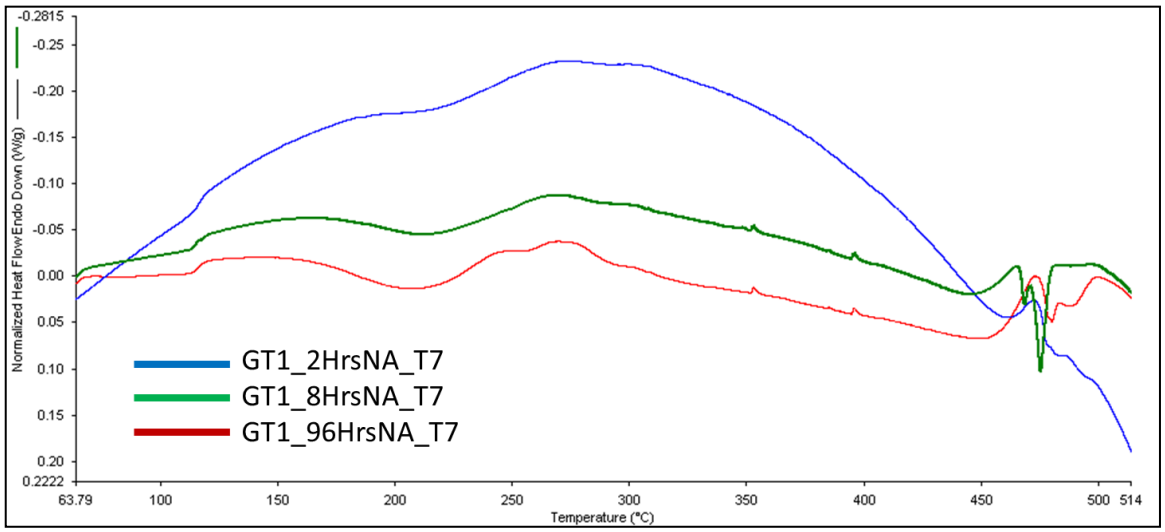


Figure 115 – *DSC analysis of GT1-T7 naturally aged for 2, 8, and 96 hours prior to artificial aging.*

Table 24 – *Eutectic melting peak analysis for GT1-5 in the T7 temper after 2, 8, and 96 hours of NA.*

| | Onset Melting (°C) | | | Melting Peak (°C) | | | Area Under Peak (J/g) | | |
|---|---|---|---|---|---|---|---|---|---|
| **Alloy** | **2 Hrs NA** | **8 Hrs NA** | **96 Hrs NA** | **2 Hrs NA** | **8 Hrs NA** | **96 Hrs NA** | **2 Hrs NA** | **8 Hrs NA** | **96 Hrs NA** |
| **GT1** | 475.8 | 467.5 | 476.3 | 478.1 | 468.7 | 480.0 | 0.54 | 0.08 | 0.41 |
| **GT2** | - | 476.8 | - | - | 478.6 | - | - | 0.08 | - |
| **GT3** | - | - | 476.7 | - | - | 478.4 | - | - | 0.19 |
| **GT4** | - | - | - | - | - | - | - | - | - |
| **GT5** | - | - | - | - | - | - | - | - | - |

Figure 116 displays the DSC analysis of GT2-T7, which appears to be very similar to GT1-T7. Unlike GT1-T7, however, GT2-T7 displays a η' precipitation peak at 8 and 96 hours NA indicating that whatever process is dictating the presence of this precipitation peak is directly affected by the Cu content. This appears to support the proposal that GP-I zones stabilized during the NA stage have slowed down the coarsening kinetics. This theory is also supported by the Rockwell hardness and conductivity data presented in Figure 98 (i.e. – the samples that had been NA longer had a higher hardness and lower conductivity than the shorter NA samples in general). It is important to note that only the 8 hour sample of GT2 displays the sharp exothermic peaks, again at approximately 300°C and 400°C.

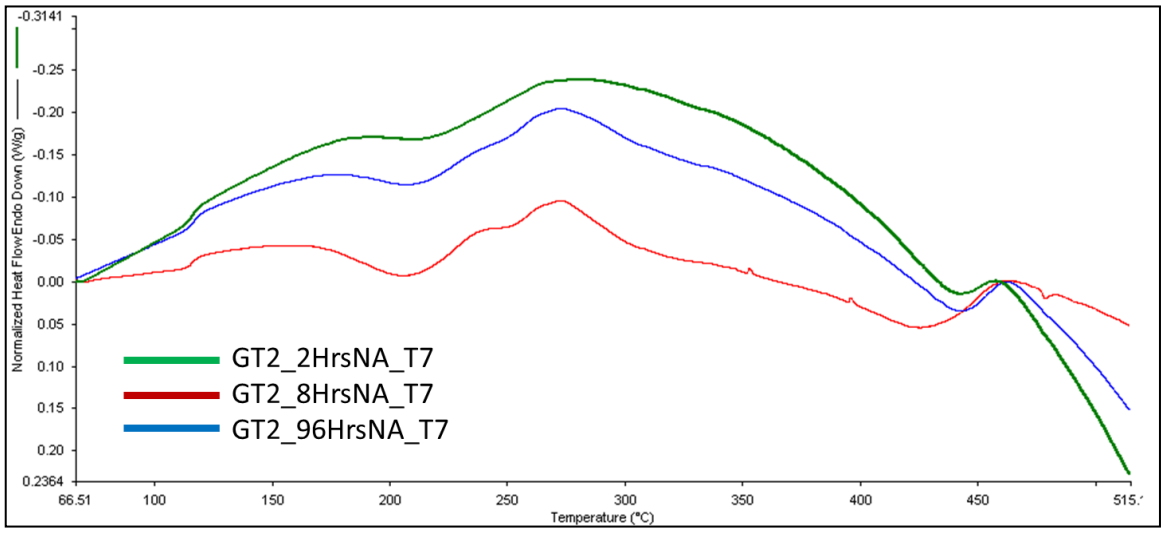


Figure 116 – *DSC analysis of GT2-T7 naturally aged for 2, 8, and 96 hours prior to artificial aging.*

Similarly, GT3-T7 displays the same trend at GT1 and GT2 (see Figure 117). The η' and η precipitation peaks are sharper and more defined in the GT3-T7 96 hours NA sample then they were in the GT1 or GT2 samples. The T-phase peak in the 96 hours is also sharper than in the previous two alloys. The mechanisms causing this reaction to this point has only been hypothesized as slightly stabilized GP-I zones that slow down the coarsening kinetics via complex dissolution and precipitation reactions, however this may not be entirely the case. As has been previously established the

precipitation sequence in 7xxx-series is complex with multiple sub-precipitation sequence culminating in the precipitation of η. The definition of the η-peak in the 96 hours GT3 sample suggests that the larger GP-I zones, which transform directly to η, may do this at a slower rate than their GP-II counterparts.

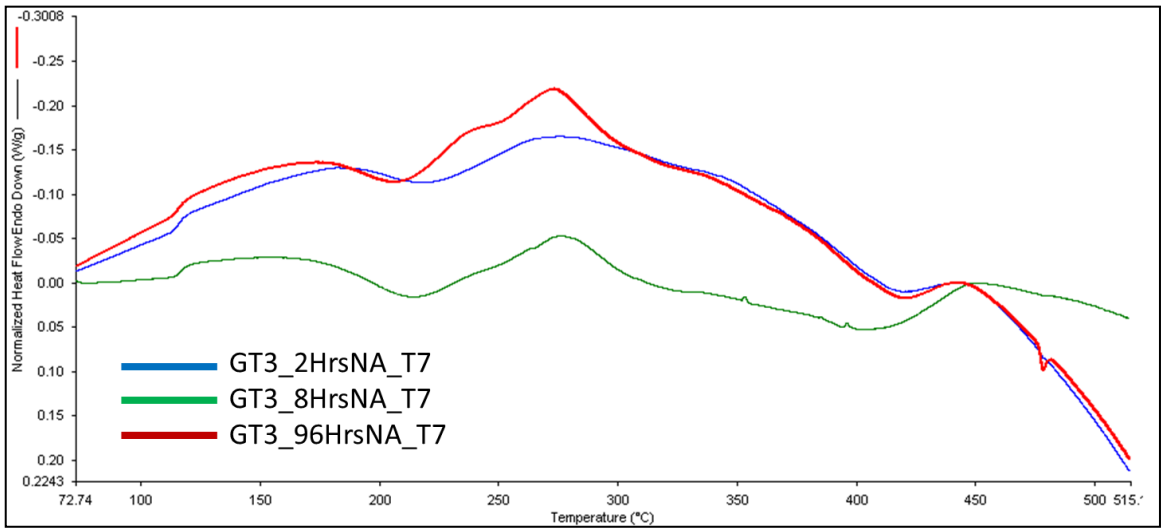


Figure 117 – *DSC analysis of GT3-T7 naturally aged for 2, 8, and 96 hours prior to artificial aging.*

The low-Cu GT4-T7 alloy, however, displays a η' precipitation peak in the 8 hour sample, but then the peak almost disappears in the 96 hour sample (see Figure 118). Likewise, the small exothermic peaks appear to be shifted in the 8 hour sample. GT4-T6 showed a positive response to NA indicating that the GP-I zones which precipitated out during the NA process quickly reverted back into solution and provided a fine dispersion of solute upon which GP-II could precipitate. The similarities between the 2 and 96 hours curves suggest this also to be case, but presence of very distinct η' and η peaks in the 8 hours sample indicates that a slightly different mechanism is at play. One possibility is that the GP-I zones in the 8 hour sample are not stabilized enough to survive the initial artificial aging step and revert back into the solute. This solute is then used to precipitate out GP-II zones/η'/η in a manner described above. Conversely, the 96 hours of NA sample contains stabilized GP-I zones that follow the more rapid direct GP-I to η

transformation. If true, this is important because it serves as a "speed gauge" for two of the relevant precipitation sequences found in the 7xxx-series alloy system.

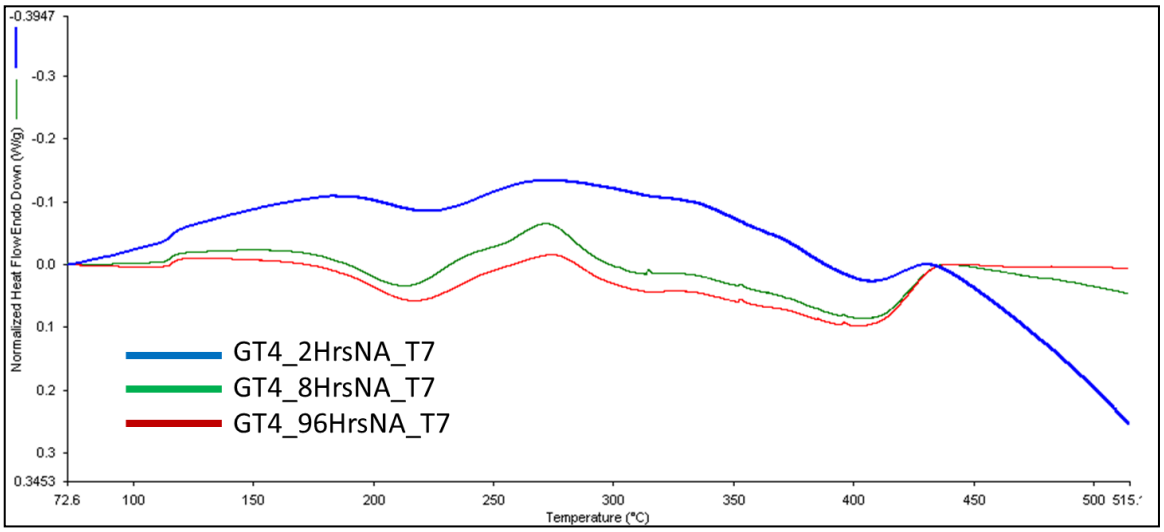


Figure 118 – *DSC analysis of GT4-T7 naturally aged for 2, 8, and 96 hours prior to artificial aging.*

Conversely to GT1-4, NA time prior to aging appears to have little to no effect on the Cu-free GT5 with respect to DSC analysis (see Figure 119). This appears to mimic the hardness and conductivity data presented in Figure 104. This is not unexpected as GT5 should only have one type of GP zone (it takes a Cu-addition to create the "plate-like" GP-II zones). Therefore, it appears reasonable for all three scans on GT5-T7 to display the same precipitation pattern.

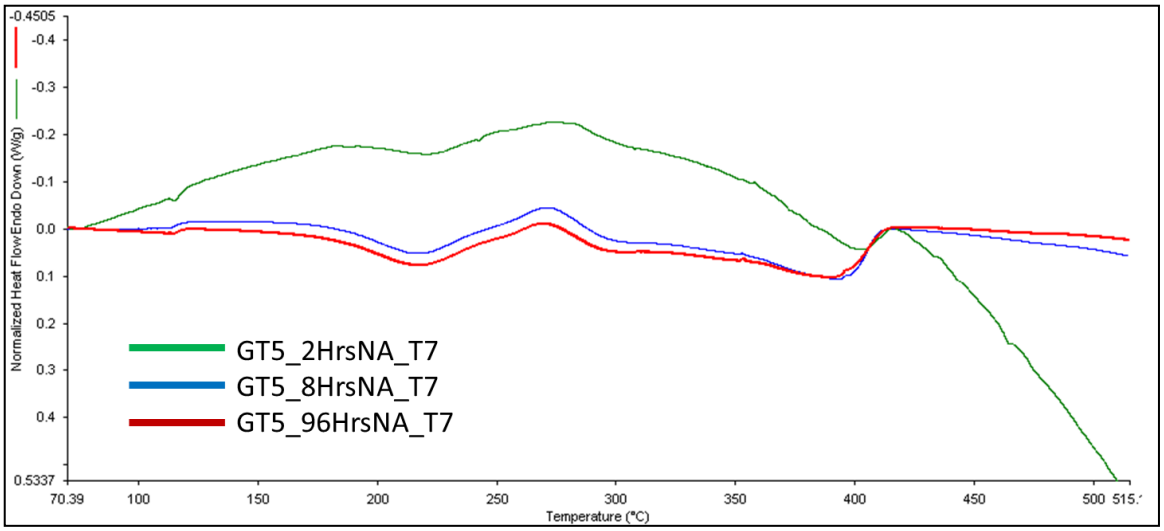


Figure 119 – *DSC analysis of GT5-T7 naturally aged for 2, 8, and 96 hours prior to artificial aging.*

DSC analysis of GT6-8-T7 naturally aged for 2, 8, and 96 hours can be seen in Figured 120 – 122, respectively. These Figures indicate that the Zn:Mg ratio also affects the precipitation sequence and kinetics of 7xxx-series alloys. As was the case with the Cu content, the Zn:Mg ratio also appears to effect the eutectic melting and final solution temperatures (both appear to rise with decreasing Zn:Mg ratio).

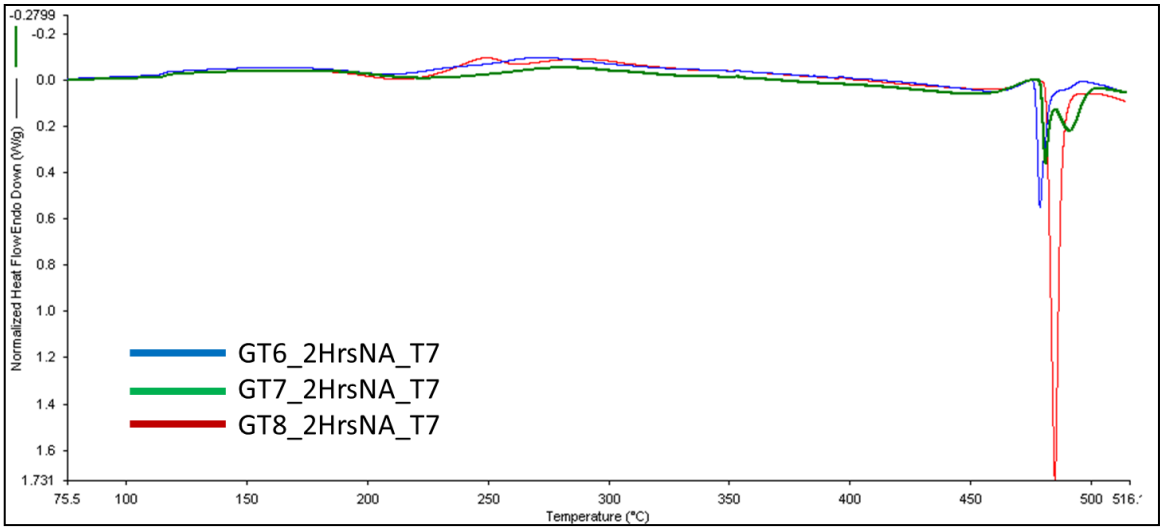


Figure 120 – *DSC analysis of alloys GT6-8 naturally aged for 2 hours prior to being aged to a T7 temper.*

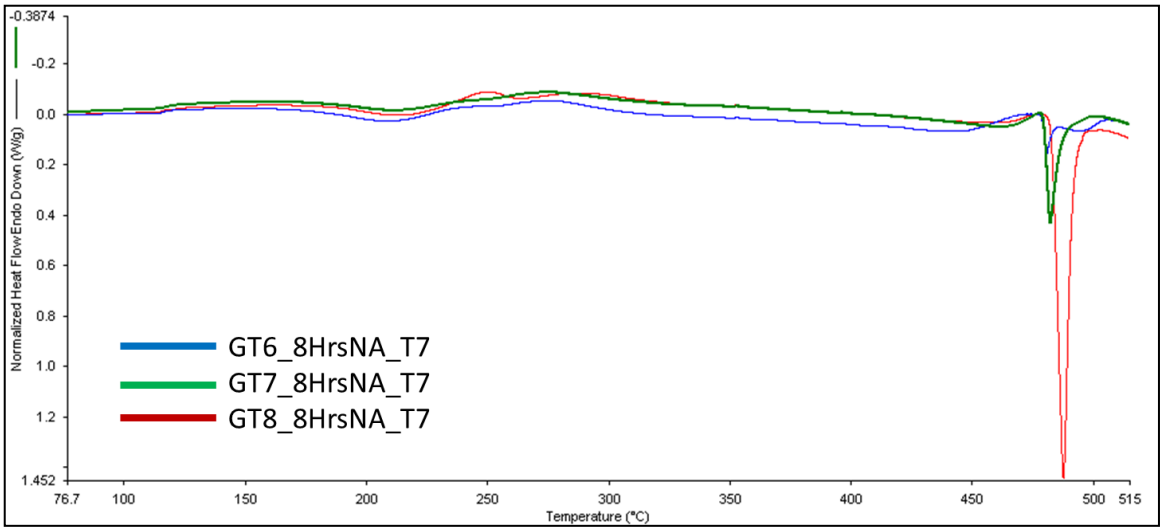


Figure 121 – *DSC analysis of alloys GT6-8 naturally aged for 8 hours prior to being aged to a T7 temper.*

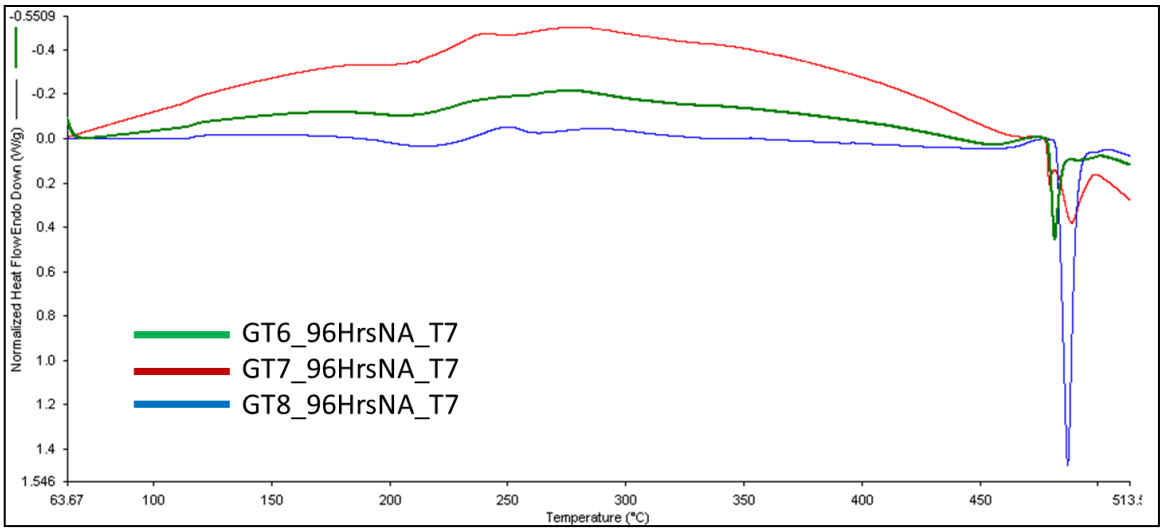


Figure 122 – *DSC analysis of alloys GT6-8 naturally aged for 8 hours prior to being aged to a T7 temper.*

Experimental alloy GT6-T7 appears to show a trend remarkably similar to GT1-3 in the T7 temper (see Figure 123) with respect to the η' and η precipitation peaks. It should be noted, however, that unlike GT1-3 even the 2 hours NA sample displays a small, but distinct η' precipitation peak. GT7-T7, likewise, displays a DSC pattern almost identical to GT3-T7 (see Figure 124). These two alloys appear to indicate that the Zn:Mg ratio may have a similar effect to Cu with respect to slowing down the

kinetics, but GT8-T7 (see Figure 125) breaks this trend (i.e. – GT8-T7 only shows one precipitation peak regardless of NA time).

As was previously presented, lowering the Zn:Mg ratio should increase the precipitation of GP-I zones. If the Zn:Mg ratio of GT8 is such that only the precipitation of GP-I zones is possible (a theory which would also be supported by the DSC scans on GT8-T6), then the previously presented theory about the effect of GP-I zones on the kinetics of the coarsening behavior of 7xxx-series alloys would still hold. Alternatively, however, if GT8 is not mostly comprised of GP-I zones, then theory begins to loose traction. Still, with the data presented it appears that theory is well grounded although future studies should use more sophisticated techniques (i.e. – *in-situ* techniques) to determine if the GP-I zone coarsening theory is truly correct.

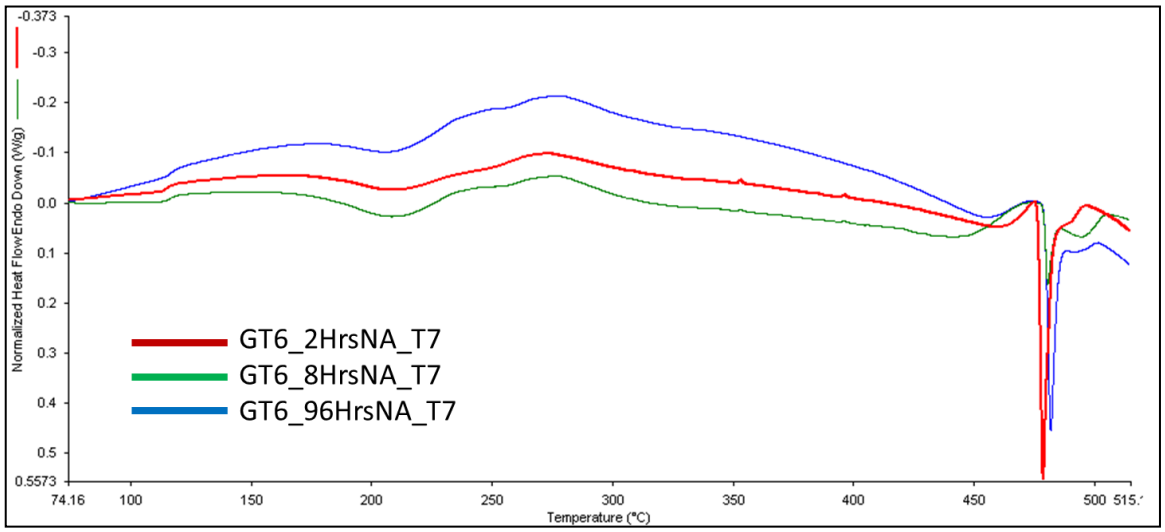


Figure 123 – *DSC analysis of GT6-T7 naturally aged for 2, 8, and 96 hours prior to artificial aging.*

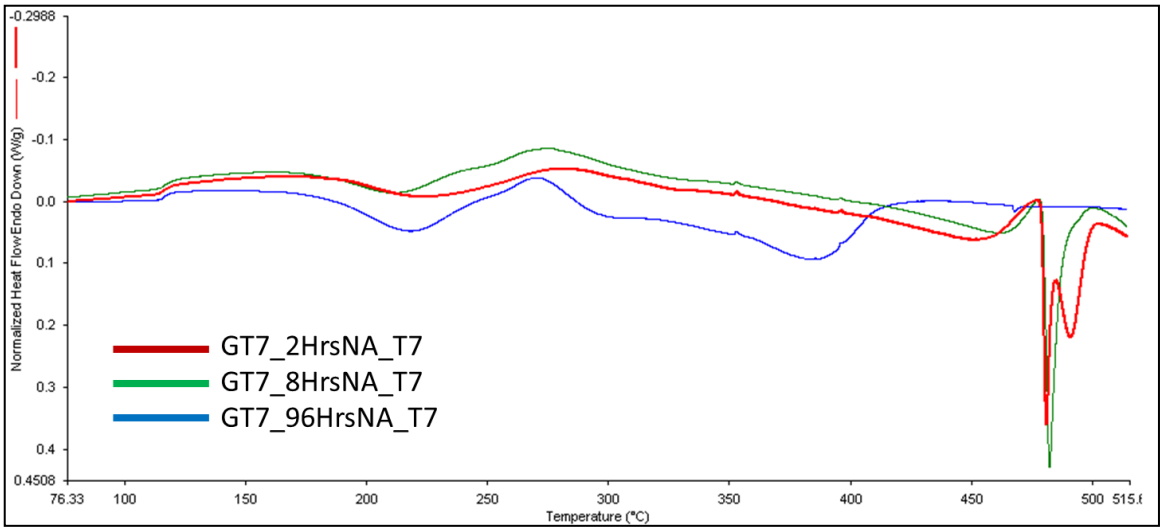


Figure 124 – *DSC analysis of GT7-T7 naturally aged for 2, 8, and 96 hours prior to artificial aging.*

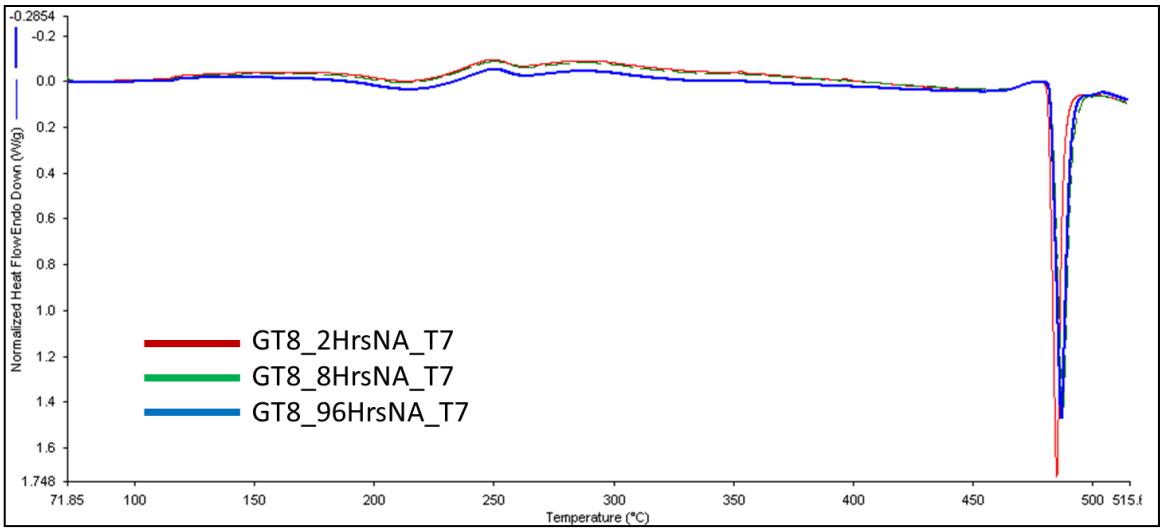


Figure 125 – *DSC analysis of GT8-T7 naturally aged for 2, 8, and 96 hours prior to artificial aging.*

## 12.3 Conclusions

The various effects of NA on GT1-8 in the T6 and T7 tempers were presented, analyzed, and discussed using Rockwell hardness, conductivity, and DSC analysis. It was shown that not only do the NA time, the Cu content, and the Zn:Mg ratio affect the particular precipitation sequences an alloy will undergo, but can also effect the kinetics of these reactions. The fact that these effects were seen even in the extreme overaged

conditions utilized for this study indicates that aluminum manufacturers need to consider the NA process when trying to maximize/alter an alloys properties.

## 12.4 References


[1] J. E. Hatch, *Aluminum: Properties and Physical Metallurgy*. ASM, 1984.

[2] M. R. Clinch, S. J. Harris, W. Hepples, N. J. H. Holroyd, M. J. Lawday, and B. Noble, "Influence of zinc to magnesium ratio and total solute content on the strength and toughness of 7xxx-series alloys," *Mater. Sci. Forum*, vol. 519–521, pp. 339–344, 2006.

[3] L. . Berg, J. Gjønnes, V. Hansen, X. . Li, M. Knutson-Wedel, G. Waterloo, D. Schryvers, and L. Wallenberg, "GP-zones in Al–Zn–Mg alloys and their role in artificial aging," *Acta Mater.*, vol. 49, no. 17, pp. 3443–3451, 2001.

[4] A. Deschamps, Y. Brechet, and F. Livet, "Influence of copper addition on precipitation kinetics and hardening in Al-Zn-Mg alloy," *Mater. Sci. Technol.*, vol. 15, pp. 993–1000, 1999.

# CHAPTER 13

# ARTIFICAL AGING

The artificial aging (AA) behavior of GT1-8 were studied via Rockwell hardness B-scale (HRB) measurements. Single step AA curves were developed and emphasis was placed on determining the η' to η transformation temperature (i.e. – the "cross-over" temperature at which over-aging of the alloy readily occurs). This was accomplished by plotting HRB values versus the AA temperature for the 24 hour samples (ex – 24 hours at 100°C, 120°C, 140°C, etc.). In some cases certain solvus/precipitation temperatures were established.

## 13.1 Single Step Aging Curves

Samples of GT1-8 were solution heat treated (SHT), quenched, and then AA for various times between 0 and 96 hours at 100°C (212°F), 120°C (248°F), 140°C (284°F), 160°C (320°F), 180°C (356°F), and 200°C (392°F). The samples were subsequently tested for Rockwell hardness (B-scale) and conductivity (%IACS). It should be noted, however, that many of the samples proved too small to provide reliable conductivity measurements. Therefore, conductivity was checked to ensure proper SHT and aging had occurred, but the measurements will not be presented here. These AA curves can be seen in Figures 126 – 133. In order to adequately view all of the temperature curves, HRB values below 60 are not presented. Figures 126 – 133 also do not display error bars, however, the individual aging curves with error bars can be seen in *Appendix C – Single Step Aging Curves for GT1-8 with Error Bars* (see Figures 203 – 250).

The aging behavior of GT1 can be seen in Figure 126. For temperatures below 160°C, GT1 displays almost a "logarithmic" aging behavior, which is typical of 7xxx-series alloys at these temperatures. At temperatures equal to or above 160°C, GT1 ages to T6 quickly (i.e. – it hits T6 in under 1 hour) and then begins to overage. As expected,

this coarsening behavior occurs faster as the temperature is increased. The highest hardness valued obtained for GT1 was 93.0 ± 2.0 HRB at 140°C – 24 hours. It should be noted there is a noticeable dip in the 120°C curve at approximately 4 hours, which could be due to a VRC to GP-II zone transformation or a GP-I zone reversion.

Likewise, several dips can be observed at the high aging temperatures (i.e. – temperatures ≥ 160°C) which is not typical of over-aging 7xxx-series alloys. This could indicate the precipitation of another phase, possible T-phase. It should be noted that these over-aging dips disappear from the aging curves of GT2-4, but reappear in the Cu-free GT5. The DSC scans presented in *Chapter 4 – The Effects of Natural Aging* showed an unknown phase precipitating at high temperatures in GT5 indicating that a similar reaction maybe occurring in GT1.

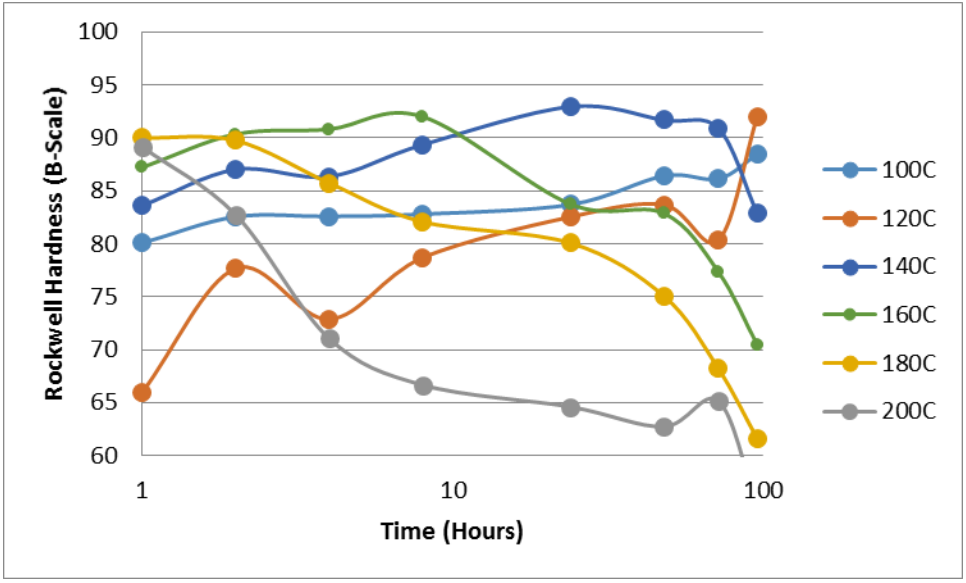


Figure 126 – *Artificial aging behavior, Rockwell hardness (B-scale) vs. time (hours), of GT1.*

The AA behavior of GT2 can be seen in Figure 127. Similar trends as those observed in GT1 can be seen in GT2, including the dip in the 120°C aging curve, although this dip is present at 24 hours rather than 4 hours. It can also be seen that GT2 must be aged longer and at a higher temperature to reach the T6 temper. For example, the highest HRB value observed was 92.9 ± 1.4 HRB at 140°C – 96 hours, but a similar

measurement was obtained at 160°C – 4 Hours (approximately 92.6 HRB). This could be due to η' precipitation temperature approaching the η precipitation temperature at the Cu level is lowered due to the decrease in lattice strain. This effect can be seen in Figures 82 – 84 where the η' precipitation peak in the DSC scans shifts closer to the η precipitation peak in GT2 than in GT1.

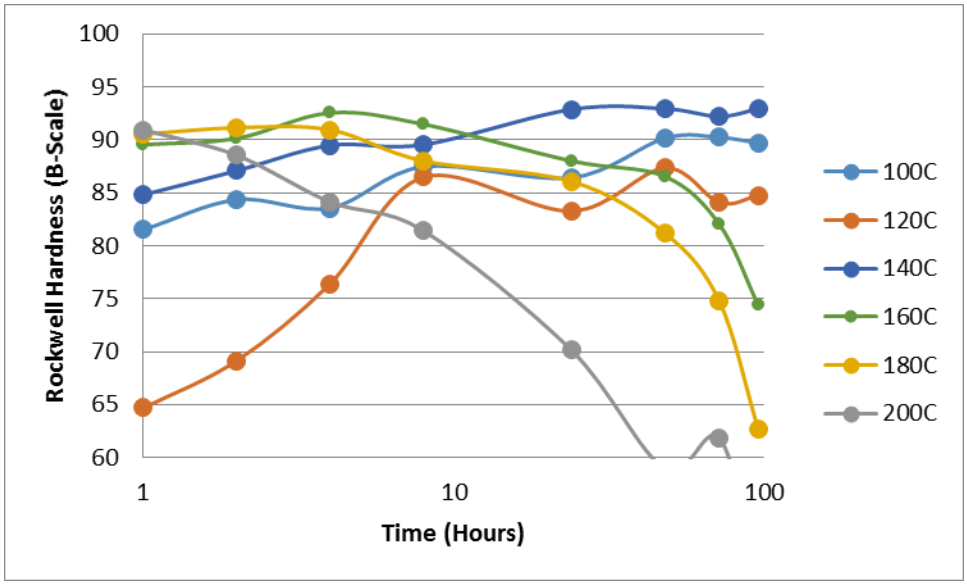


Figure 127 – *Artificial aging behavior, Rockwell hardness (B-scale) vs. time (hours), of GT2.*

While GT3 also displays a similar aging behavior to GT1 and GT2, it should be noted that the dip in hardness associated with low temperature aging is largely reduced, and the highest hardness measurement observed, 94.1 ± 1.1 HRB, occurs at 160°C – 8 hours (see Figure 128). This is significant because at 160°C GT3 overages readily implying that the η' and η precipitation temperatures are close together for this composition. It could also be observed that the previously mentioned low-temperature dip could be present in the 140°C curve implying the GP solvus is also increasing in temperature, but the surrounding measurements are within experimental error. Once more, the various DSC scan in *Part II – Chapter 12 –The Effect of Natural Aging* support this hypothesis.

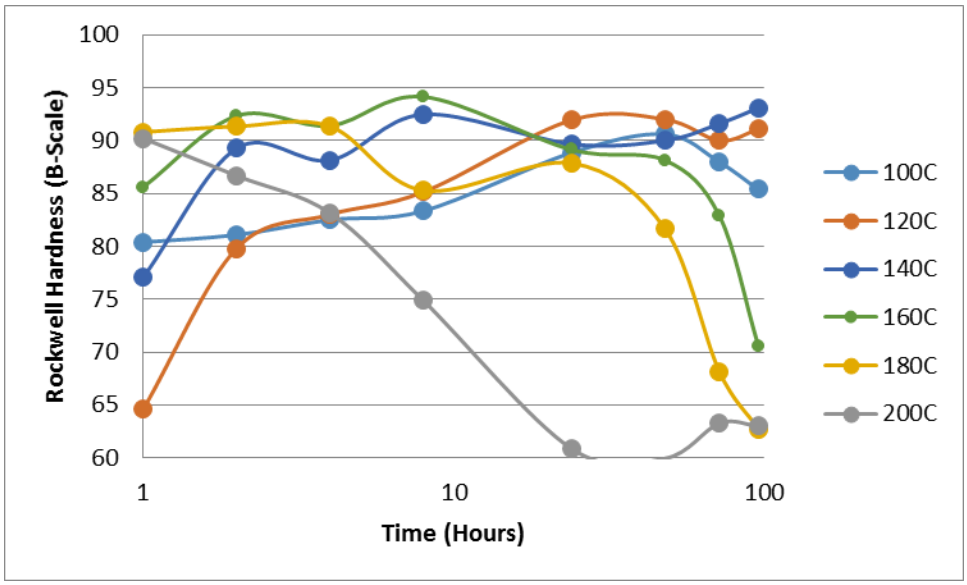


Figure 128 – *Artificial aging behavior, Rockwell hardness (B-scale) vs. time (hours), of GT3.*

Figure 129 displays the artificial aging behavior of GT4. The highest hardness value observed for GT4 was 92.8 ± 1.0 HRB at 140°C – 96 hours. Much like GT1-3, GT4 appears to experience over-aging behavior at temperatures greater than or equal to 160°C, although it could be noted that the over-aging is kinetically slower in GT4. GT4 displays a dip in its 100°C aging curve, which appears to break up the pattern set up by GT1-3 (i.e. – lowering Cu raises the GP solvus temperature), however, it should be noted that the type of GP zone may be different for low Cu 7xxx-series alloys as previously noted in *Part I – Chapter 6 – The Precipitation Process* and *Part II – Chapter 12 – The Effects of Natural Aging*. The argument could also be made that the dip observed is a GP-I solvus, whereas the previous peaks could be associated with a GP-II solvus, although neither claim can be validated via the testing methods utilized (i.e. – hardness and DSC).

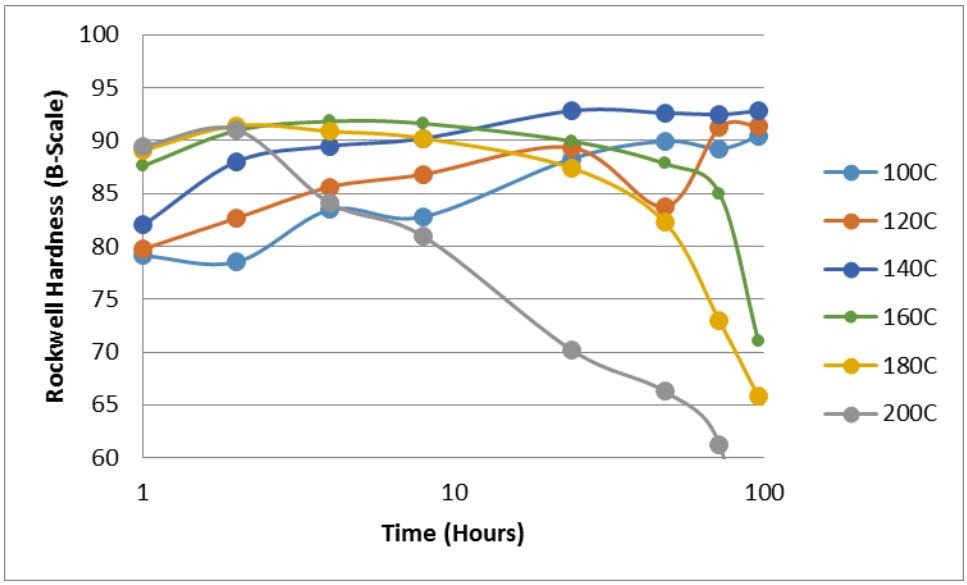


Figure 129 – *Artificial aging behavior, Rockwell hardness (B-scale) vs. time (hours), of GT4.*

The single-step aging curves for the Cu-free GT5 (see Figure 130) appear to show the alloy experiencing over-aging behavior at 140°C suggesting that not only can the Cu content effect the precipitation temperature of η', but of η as well. The highest hardness value obtained for GT5 was 91.1 ± 1.4 HRB and was observed at 160°C – 4 hours, although a similar value was observed at 140°C – 48 hours. The trend of seeing various dips at low aging temperatures is also continued with GT5 with dips being present in both the 100°C and 120°C aging curves. The fact that GP-I zones may not be stabilized in low Cu alloys suggests that they dissolve readily upon heating allowing GP-II zones, η', and η to precipitate on the "freed up" solute in solid solution [1], [2]. Since the hardness trends for GT1-4 seem to suggest that the GP-II solvus, the η' and η precipitation temperatures appear to be approaching each other, this would account for the relativity "smooth" curves and quick over-aging behavior compared to GT1-4. DSC scans on GT5 (see Figure 89) appear to support this claim.

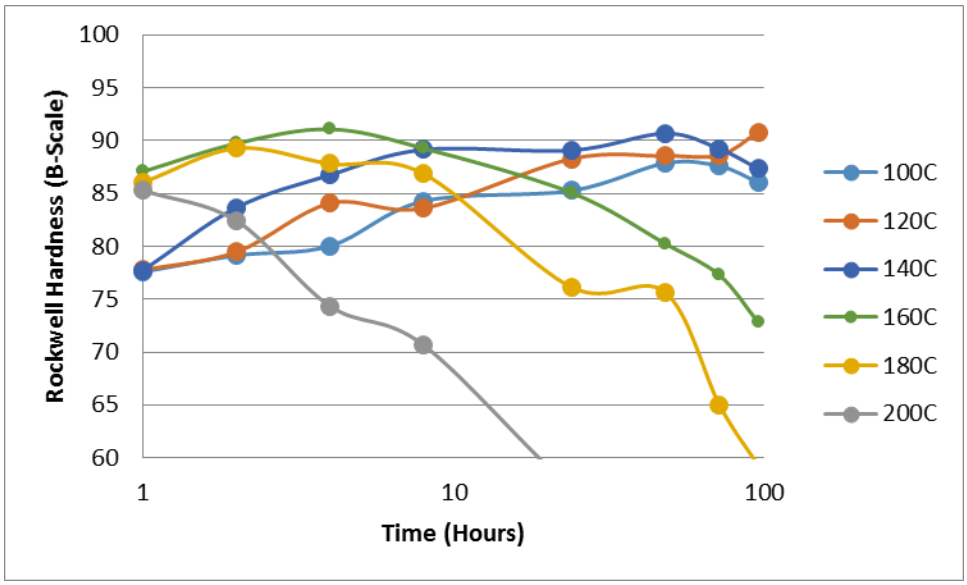


Figure 130 – *Artificial aging behavior, Rockwell hardness (B-scale) vs. time (hours), of GT5.*

The AA behaviors of GT6-8 are more convoluted than those of GT1-5. For example, GT6 (Figure 131) displays over-aging behavior as low as 120°C (248°F) with every curve displaying multiple dips both before and after peak strength is obtained. Similar results can be seen in the AA behaviors of GT7 (Figure 132) and GT8 (Figure 133). This suggests that a complex precipitation sequence is present in these alloys probably comprising various aspects of P1-P7. With respect to the low temperature dips, the stain induced by the high Cu contents of GT6-8 should force the GP-zone, η', and η precipitation peaks to be distinct. Likewise the high temperature dips could be the result of the high Mg and Cu contents of these alloys could be forcing the precipitation of S- or β-phase. The precipitation of S-phase, which follows the precipitation sequence [3]:

$$\alpha_{ssss} \rightarrow \text{GPB zones} \rightarrow S' (Al_2CuMg) \rightarrow S (Al_2CuMg)$$

Could account for the over-aging behavior of these alloys as S-phase is known to over-age readily. However, further research is needed to verify these hypothesis, as the DSC scans presented in *Part II – Chapter 12 – The Effects of Natural Aging* do not necessarily support this possibility. It should be noted that the DSC scans on GT6-8 do show that T-

phase is precipitating out in the alloys and therefore the “dips” present in the HRB curves could be the result of the T-phase precipitation process.

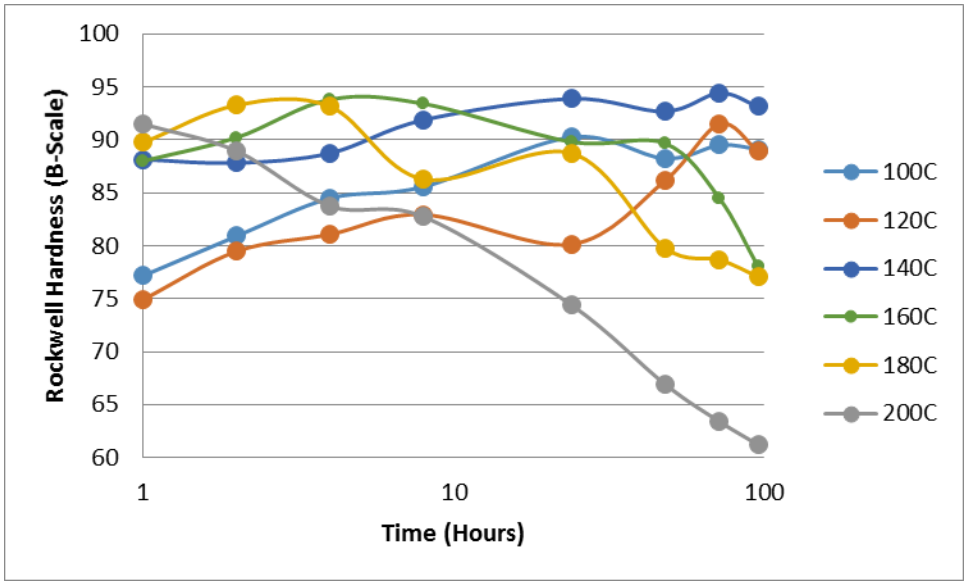


Figure 131 – *Artificial aging behavior, Rockwell hardness (B-scale) vs. time (hours), of GT6.*

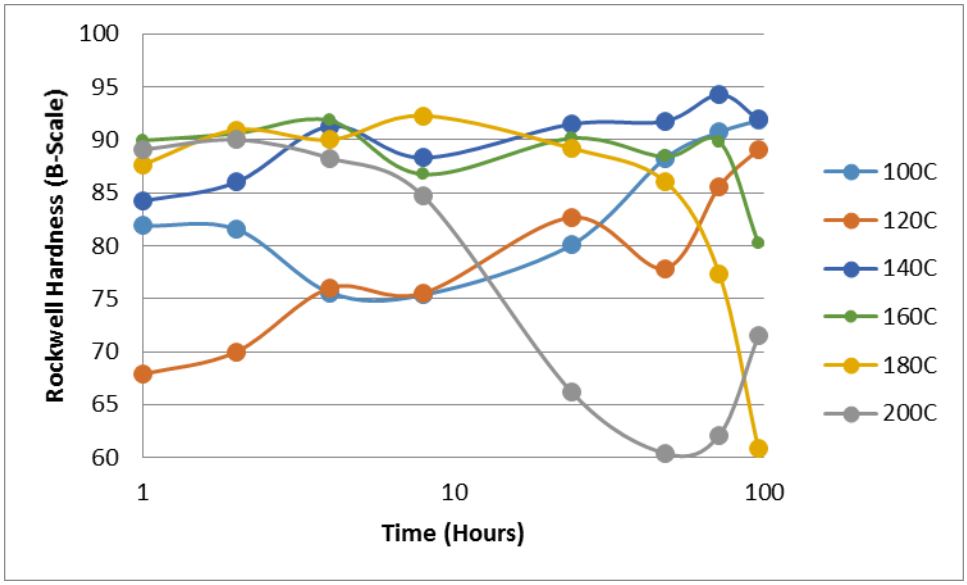


Figure 132 – *Artificial aging behavior, Rockwell hardness (B-scale) vs. time (hours), of GT7.*

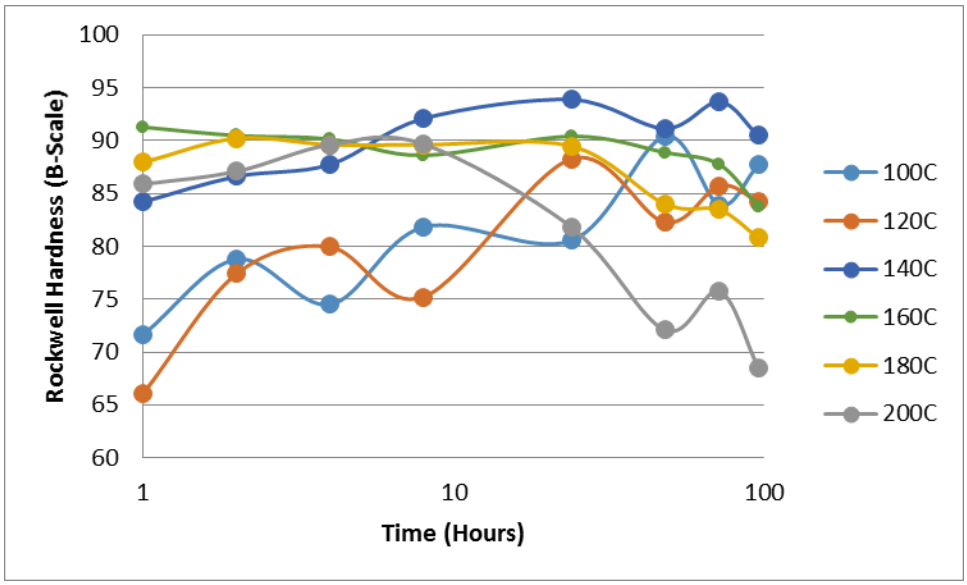


Figure 133 – *Artificial aging behavior, Rockwell hardness (B-scale) vs. time (hours), of GT8.*

In the case of GT1-5 where the Zn:Mg ratio was kept fairly constant, there appears to be a direct correlation between the η' precipitation temperature and Cu content. It was shown, for example, that the η' precipitation temperature approaches the η precipitation temperature with decreasing Cu content. Evidence was also presented that Cu may also effect the different GP zone solvus boundaries (both Type I and II), but more sophisticated characterization work is needed to substantiate these claims. GT1-5 also all displayed over-aging behavior at temperatures equal to or greater than 160°C suggesting 160°C is near to the η' to η transformation temperature, although it should be also noted that GT5 displayed over-aging behavior at 140°C suggesting the η-precipitation temperature can also be altered by Cu content. Possible evidence of T-phase precipitation was also presented, but was not validated.

GT6-8 displayed more convoluted AA behaviors, which could be result of various precipitation sequences (P1-P6) being present in the alloys. Unlike GT1-5, the alloys did not display distinct aging patterns as the Zn:Mg ratio was altered, but did appear to exhibit over-aging behavior at lower temperatures compared to GT1-5.

### 13.2 Determining the η'-η Transformation Temperature

In order to determine the η' to η transformation temperature for GT1-8, the 24 hour samples from each single step aging curve presented in Figures 126 – 133 were plotted against each other for each alloy. HRB measurements for GT1 AA for 24 hours at various temperatures can be seen in Figure 134. There appears to be a distinct GP solvus between 120°C and 140°C where the alloy goes from being under-aged at 120°C (i.e. – GP zone dominant) to near peak hardness at 140°C (i.e. – η' dominant). This suggests that the GP-II zone to η' transformation happens readily near 140°C unlike at lower temperatures. There also appears to be a η' to η transformation occurring between 140°C and 160°C, which matches up well with literatures (see *Part I – Chapter 6 – The Precipitation Process*), as GT1 appears overaged after just 24 hours of AA at 160°C. . As the temperature is further increased, the degree of over-aging increases, which could be attributed to either an increased volume fraction of η or coarser η-precipitates.

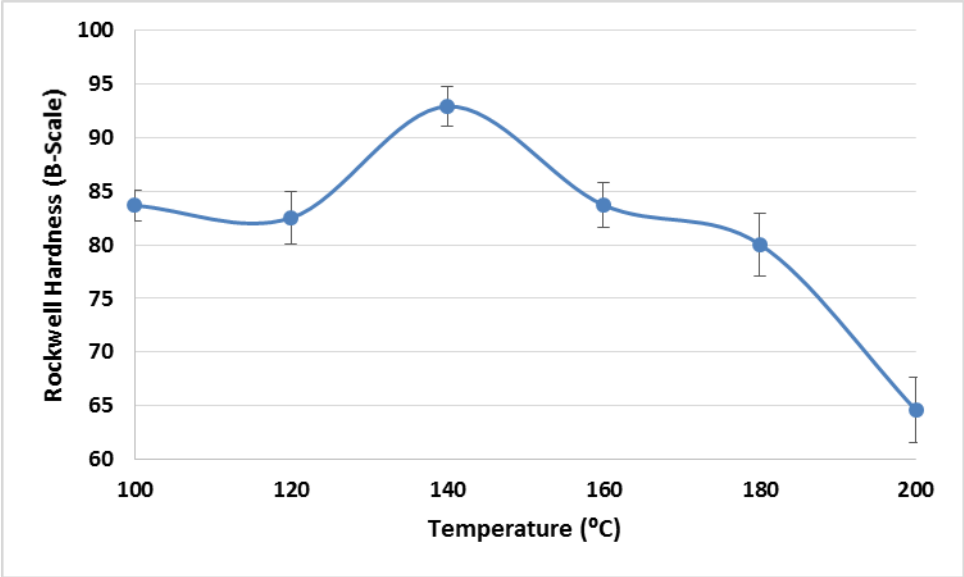


Figure 134 – *Rockwell hardness (B-scale) data for GT1 artificially aged for 24 hours at various temperatures.*

GT2 displays similar results to GT1 (Figure 135), however the curve appears slightly compressed in comparison. This "compression" could be direct result of the lower Cu content compared to GT1, and matches well with the DSC scans for GT2. Cu

additions, as previously noted, can increase the stability of GP-II zones and η' as well as aid the precipitation process by increasing the lattice strain. Therefore, the lower Cu content could affect the stability of GP-II zones (especially at higher temperatures) and slowed down the aging kinetics.

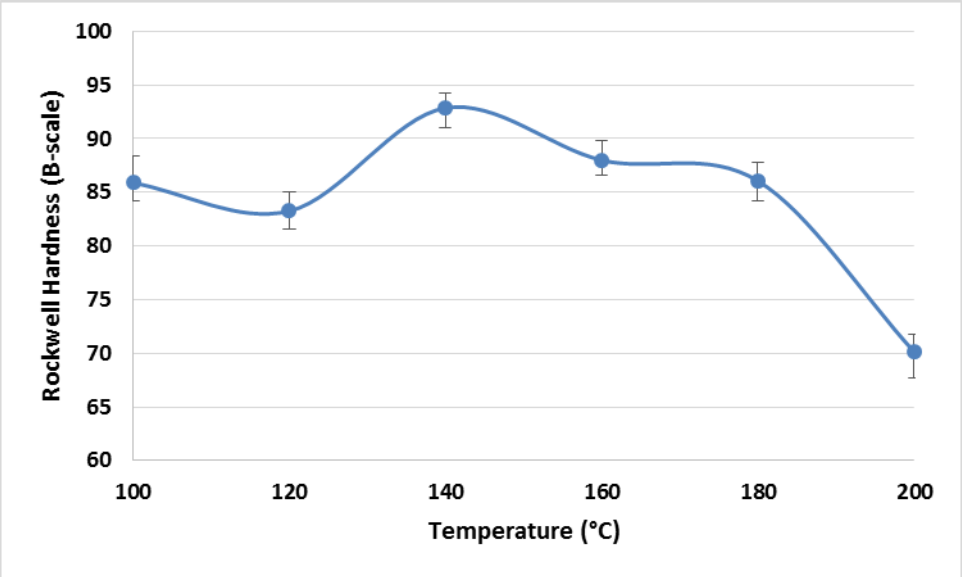


Figure 135 – *Rockwell hardness (B-scale) data for GT2 artificially aged for 24 hours at various temperatures.*

The HRB data for GT3 (Figure 136) does not appear indicative of either a high-Cu or low-Cu alloy, but rather a mixed behavior. At temperatures ≤ 180°C there is no distinction between GP-zone and η' precipitation, but after 24 hours of AA at 200°C over-aging occurs readily. It should be noted that for temperatures between 100°C and 180°C the alloy appears to reach T6 after 24 hours of artificial aging, which was not expected.

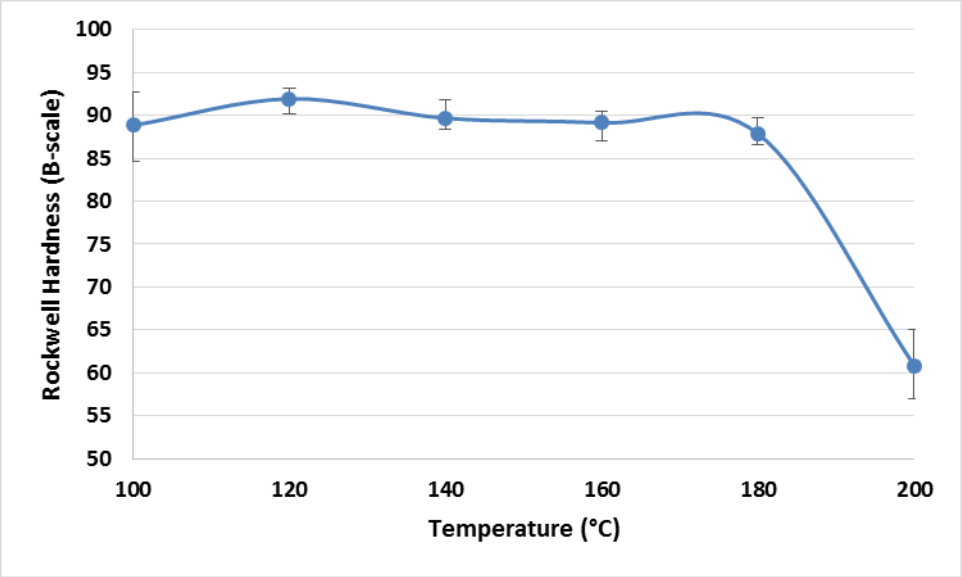


Figure 136 – *Rockwell hardness (B-scale) data for GT3 artificially aged for 24 hours at various temperatures.*

The results of GT4 (Figure 137) continue the trend of solvus temperature "compression" with decreasing Cu-content started with GT1 and GT2. There appears to be a slight GP zone solvus between 120°C and 140°C like GT1 and GT2, and over-aging appears to occur readily at higher temperatures. The compressed curve and the fact that the 160°C sample appears to be within error of the 140°C implies that the η' transformation temperature is approaching the η transformation temperature as Cu is lowered.

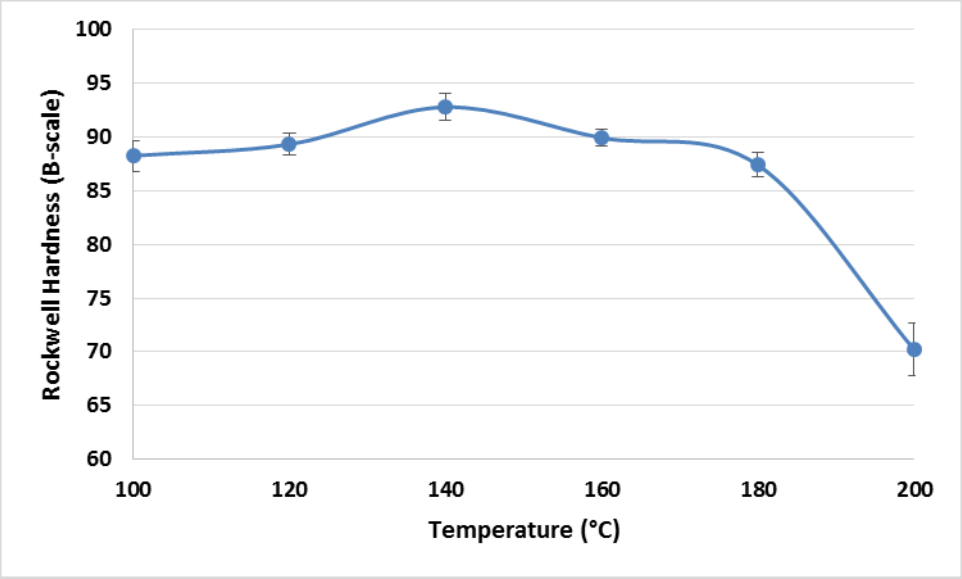


Figure 137 – *Rockwell hardness (B-scale) data for GT4 artificially aged for 24 hours at various temperatures.*

The Cu-free GT5 (Figure 138) does not display any clear precipitation or transformation temperature, but rather a gradual increase in hardness followed by over-aging behavior. It is also worth noting that the GT5 is the weakest alloy studied, which is to be expected as the η' transformation temperature should be equal to that of η in a Cu-free alloy. The single step aging curve for GT5 (Figure 130) implied that the GP-II zone solvus, if present, may be approaching the η'/η precipitation temperature, and this is backed up by Figure 138.

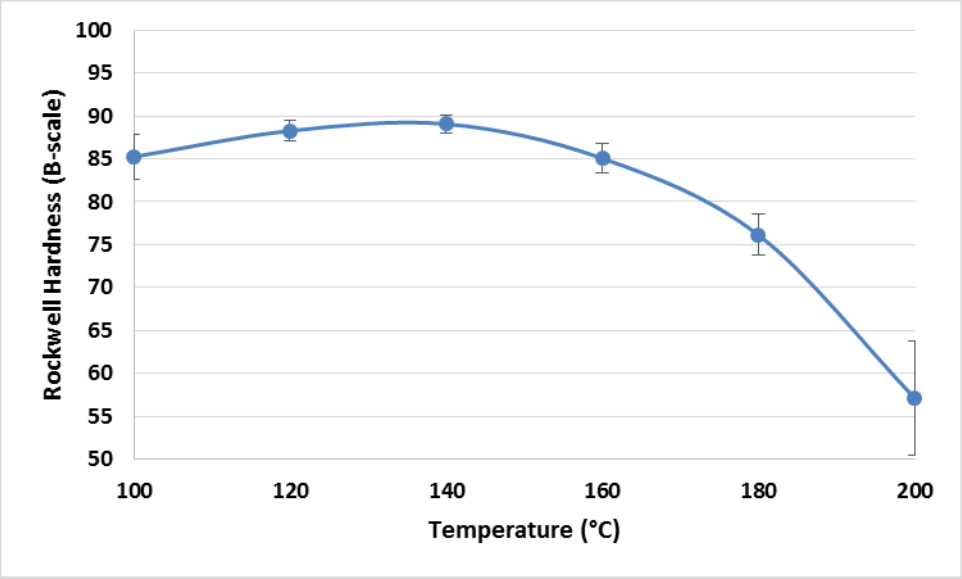


Figure 138 – *Rockwell hardness (B-scale) data for GT5 artificially aged for 24 hours at various temperatures.*

The strange precipitation behavior of GT6-8 observed in Figures 131 – 133 can also be seen in Figures 139 – 141. For example, GT6 (see Figure 139) and GT7 (see Figure 140) both clearly display the η' peak and over-aging behavior typical of GT1 and 2, but the dip associated with GP zone transformation is greater in magnitude in GT6 and 6 than for any previously presented experimental alloy (i.e. – GT1-5). As previously suggested, this suggests the presence of another "semi-dominate" precipitation sequence in the microstructure (i.e. – T-phase). Interestingly, GT8 (see Figure 141) does not display an form of GP solvus even though the relative Cu level would suggest one should be present, but does exhibit a η' and over-aging behavior similar to GT6 and GT7. This could be due to an experimental error or could be attributed to the lower Zn:Mg ratio of GT8 (i.e. – this could be due to T-phase precipitating out at 180°C).

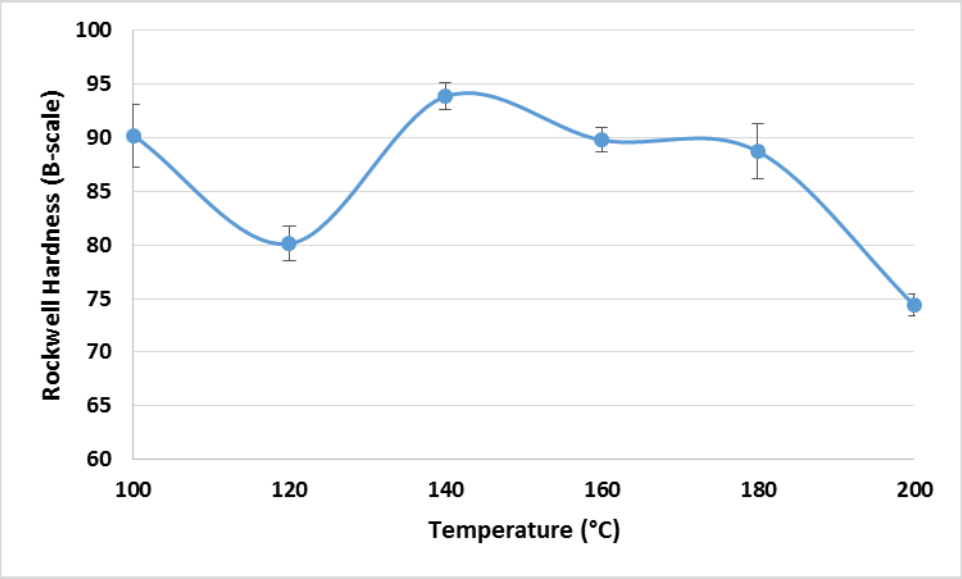


Figure 139 – *Rockwell hardness (B-scale) data for GT6 artificially aged for 24 hours at various temperatures.*

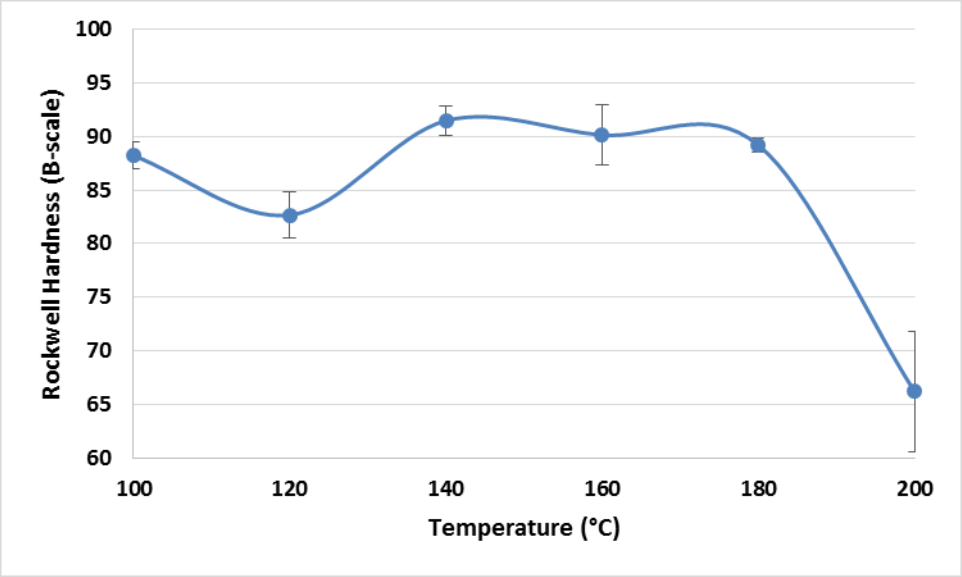


Figure 140 – *Rockwell hardness (B-scale) data for GT7 artificially aged for 24 hours at various temperatures.*

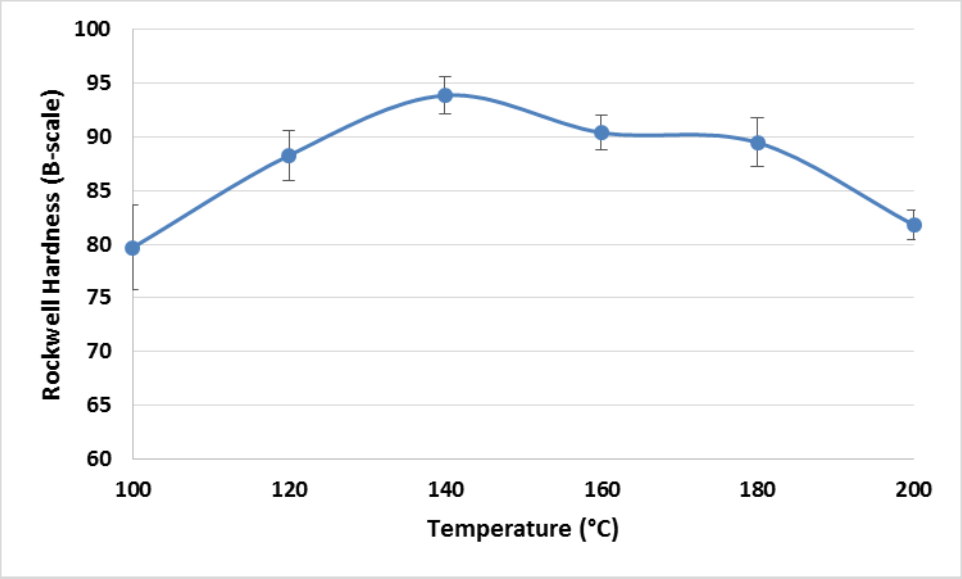


Figure 141 – *Rockwell hardness (B-scale) data for GT8 artificially aged for 24 hours at various temperatures.*

It is clear from Figures 134 – 141 that over-aging begins to readily occur between 140°C and 160°C for each experimental alloy, and as the temperature is increased over-aging occurs at a faster rate. Likewise, the η' precipitation temperature appears to be in the neighborhood of 140°C for the alloys studied. In the cases of GT1-2 and GT6-7 distinct GP solvus temperatures around 120°C could be distinguished. For GT1 and GT2, the sovlus temperature probably represents a transition zone between GP-II and η'; the GP solvus in GT6 and GT7 could be the product of GP-II zone transformation into η' coupled with the dissolution/transformation of GPB zones into S', but that hypothesis is currently untested.

### 13.3 Conclusions

AA curves for GT1-8 were produced for various temperatures between 100°C and 200°C. These curves were then utilized to determine the GP-zone and η' solvus temperatures for the various compositions studied. An understanding of the effects of composition on artificial aging behavior is important in the development of new 7xxx-series aluminum alloys as it allows one to avoid lengthy artificial aging studies by narrowing the "temperatures of interest" gap. If one can understand how an alloy will

behave in a certain temperature range, research can be focused on the kinetic effects of aging rather than determining the appropriate aging temperature.

Although the DSC work presented in *Part II – Chapter 12 – The Effects of Natural Aging* appear to support these conclusions, additional future work needs to focus on completing the characterization study on the observed effects using advanced characterization techniques (i.e. – in-situ SAXS, atom probe, etc.) as well as incorporating the effects of grain refiners and disperoid forming elements. Advanced modeling techniques may also prove useful in characterizing and validating the various solvus temperatures presented.

## 13.4 References


[1] N. Q. Chinh, J. Lendvai, D. H. Ping, and K. Hono, "The effect of Cu on mechanical and precipitation properties of Al–Zn–Mg alloys," *J. Alloys Compd.*, vol. 378, no. 1–2, pp. 52–60, Sep. 2004.

[2] M. E. Fine, "Precipitation hardening of aluminum alloys," *Metall. Trans. A*, vol. 6, no. April, pp. 625–630, 1975.

[3] C. Genevois, D. Fabregue, A. Deschamps, and W. J. Poole, "On the coupling between precipitation and plastic deformation in relation with friction stir welding of AA2024 T3 aluminum alloy," *Mater. Sci. Eng. A*, vol. 441, pp. 39–48, 2006.

# CHAPTER 14

# THE EFFECT OF COMPOSITION ON THE PRECIPITATE FREE ZONE

The 7xxx-series of aluminum alloys is generally susceptible to stress corrosion cracking (SCC), a process which is highly dependent on chemical composition and heat treatment, in the T6 temper. This susceptibility can be mitigated if the alloys are over-aged to a T7 temper at the concession of strength [1]–[3]. Furthermore, it is widely accepted that the main differences between the T6 and T7 tempers are related to the distribution of matrix precipitates; the dislocation density; the composition, size, and distribution of grain boundary phases; and the width of the precipitate free zone (PFZ) [1], [3]–[7].

In order to attempt to correlate the effects of composition, namely the (Zn+Cu):Mg ratio, to the width of the PFZ in 7xxx-series aluminum alloys, transmission electron microscopy (TEM) was utilized to measure the PFZ size of GT1-8 in the T7 temper. Two registered alloys, 7075 and 7136, were also studied in order correlate the results from GT1-8 to commercial aerospace alloys. The TEM samples were prepared at GT, UAC-Canton, and ST2 according to the procedure laid out in *Part II – Chapter 9 Materials and Experimental Procedure*, while the TEM images were taken at GT with assistance from Todd Walters and Judy Dickson. Characterization of grain boundary precipitates in GT4 was performed by Dr. Thomas Dorin (Deakin University) using a field emission gun TEM (FEGTEM) equipped with EDX. These results in conjunction with the DSC scans presented in *Part II – Chapter 12 – The Effects of Natural* Aging and literature searches were utilized to identify the grain boundary precipitates in GT1-8.

## 14.1 Results

The following section is sub-divided into two sections. The first section details TEM work performed at GT, which aimed at measuring the PFZ size. Identification of grain boundary particles was carried out via literature searches and DSC scan analysis. The identification of grain boundary precipitates in this section was then compared to FEGSTEM EDX measurements by Dr. Thomas Dorin on GT4-T7. It was found both identification methods characterized the grain boundary precipitates as the same precipitates.

### 14.1.1 PFZ Measurements and Grain Boundary Precipitate Identification using DSC

TEM images of experimental 7xxx-series alloys GT1-8 can be seen in Figures 142 – 149, and average measurements of the observed PFZ can be seen in Table 25. TEM images of 7136-T73 and 7075-T73 can be seen in Figures 150 and 151 respectively.

Table 25 – *Average PFZ observed in experimental alloys GT1-8 and commercial alloys 7136 and 7075.*

| **Alloy** | **<PFZ>** | **Alloy** | **<PFZ>** |
|---|---|---|---|
| GT1 | 22.94 ± 10.08 nm | GT6 | 18.25 ± 6.60 nm |
| GT2 | 26.02 ± 9.59 nm | GT7 | 22.29 ± 9.08 nm |
| GT3 | 20.00 ± 10.30 nm | GT8 | 19.65 ± 6.76 nm |
| GT4 | 45.68 ± 20.54 nm | 7136 | 14.99 ± 5.09 nm |
| GT5 | 22.43 ± 9.00 nm | 7075 | Not Observed |

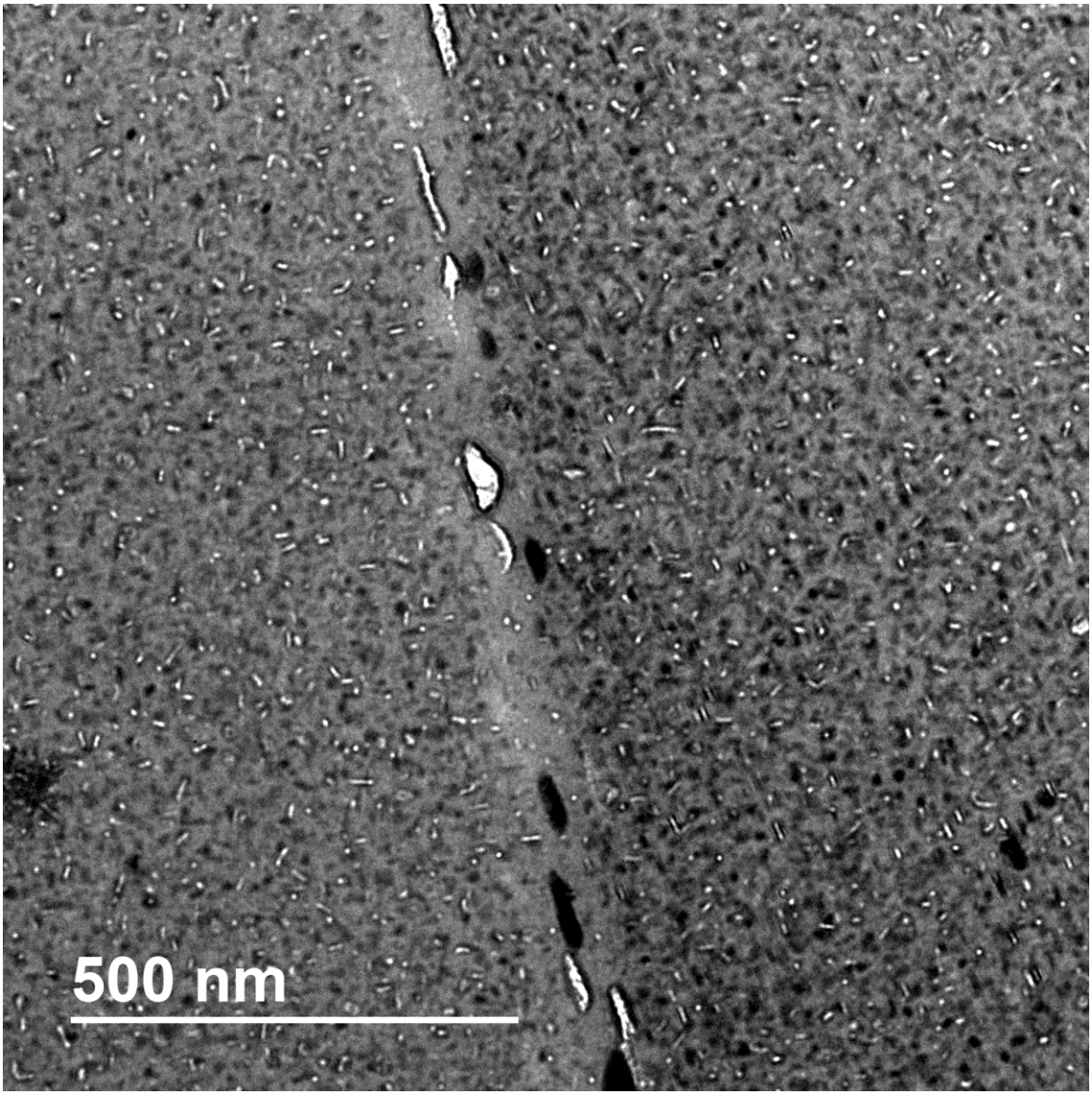

Figure 142 – *TEM image of GT1-T7.*

GT1-T7 (see Figure 142) displays an average PFZ size of 22.94 ± 10.08 nm with two (possibly three) distinct grain boundary precipitates. Although diffraction patterns were unable to be obtained on the grain boundary precipitates, their general contrast with the Al matrix and morphology hint at their composition when compared to other results found in academic literature and the DSC results presented in *Chapter 12 – The Effects of Natural Aging*. For example, the dark lenticular precipitates are most likely η-phase (they appear similar in size, shape, and color to those characterized as such by Embury and Nicholson [8]) and the thin white lenticular precipitates appears similar to those

characterized by Raghaven [9] who identified them as T-phase. The T-phase peak in the GT1 DSC scans is present, but is not a dominate peak hinting that the other light precipitates are most likely Cu- or Si-containing intermetallics (ex. – S-phase, $Al_7Cu_2Fe$, etc.) [10]. The large eutectic melting peaks present in the DSC scans appear to confirm this hypothesis. It should also be noted that various precipitates can be seen within the grain, which are likely smaller variants of the pre-mentioned phases/precipitates along with GP zones and η'.

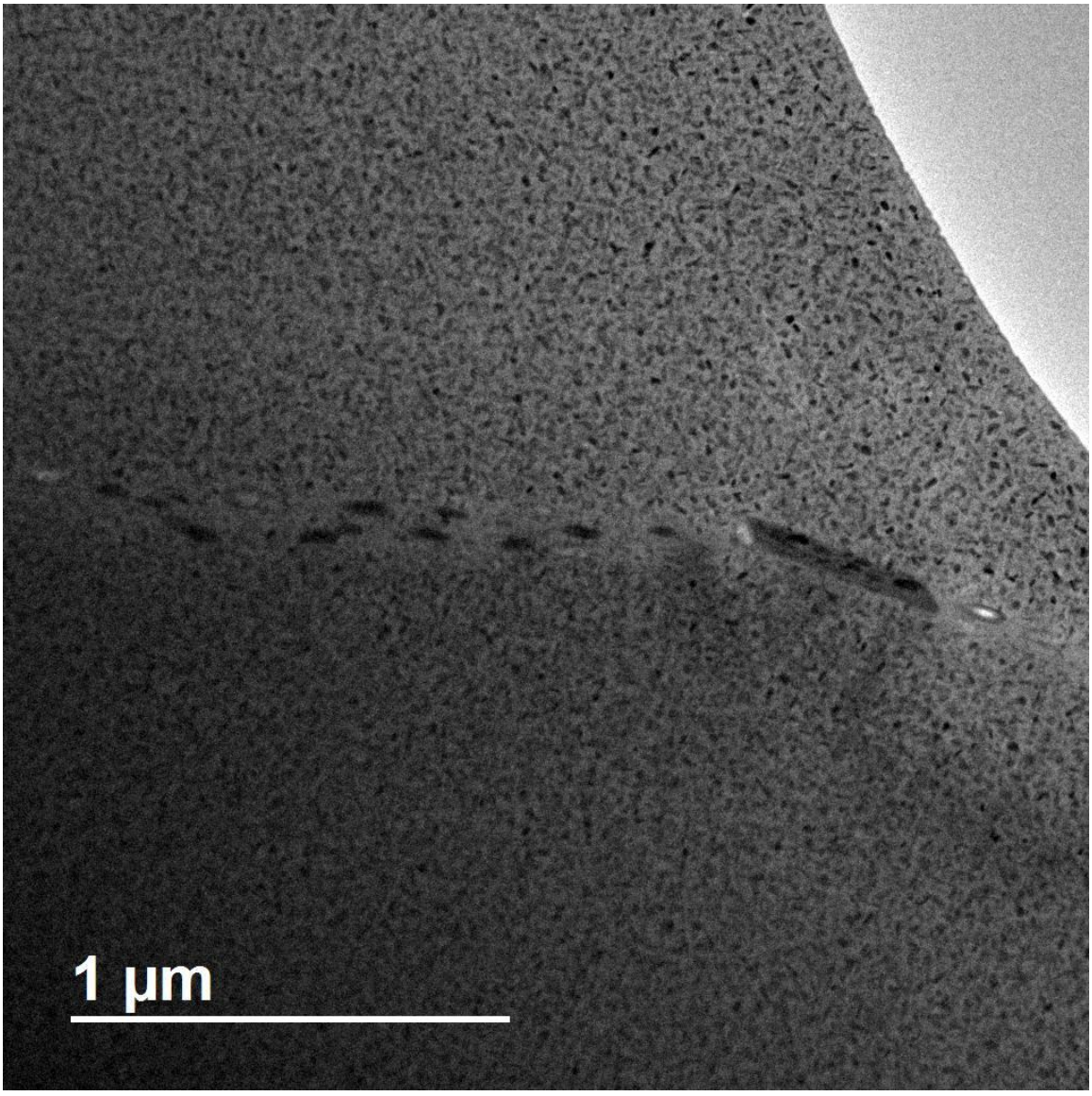


Figure 143 – *TEM image of GT2-T7.*

GT2-T7 (Figure 143) displays an average PFZ size of 26.02 ± 9.59 nm, which is slightly larger than GT1-T7, but not statistically significant. Once again the grain boundary is filled with η-precipitates, but Figure 143 also reveals a large intermetallic particle near the edge of the sample. The number of light colored grain boundary particles is decreased in GT2, although one appears to be joined with the large unknown intermetallic. Unlike GT1, only one type of precipitate appears to be visible within the grain. The presences of T-phase is not seen in Figure 143 despite being present in the DSC scans of GT2 indicating the grain boundary present may not be truly representative of the vast majority of grain boundaries present in the alloy.

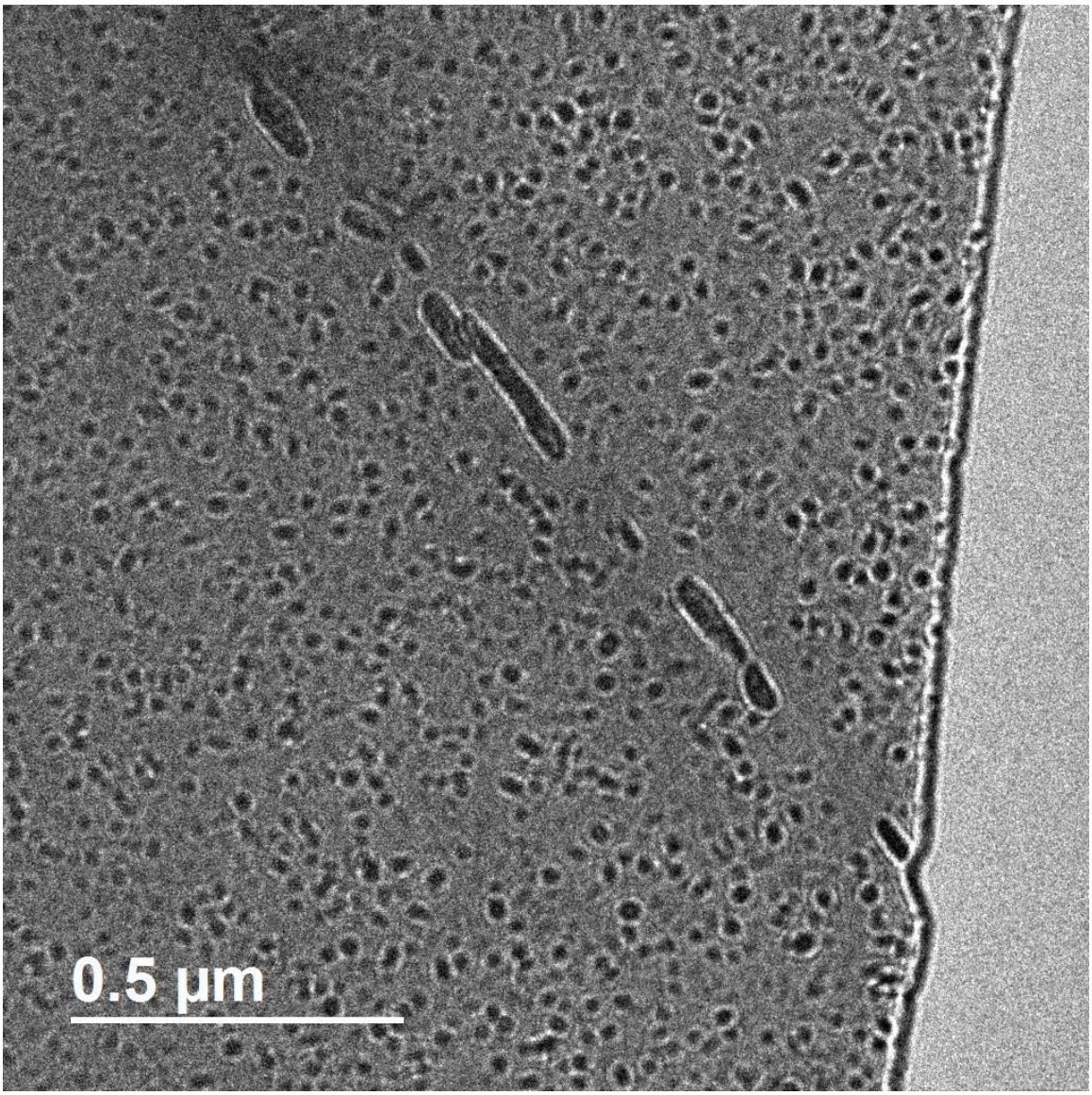

Figure 144 – *TEM image of GT3-T7.*

GT3-T7 (Figure 144) displays an average PFZ size of 20.00 ± 10.30 nm, which is smaller than GT1-T7 or GT2-T7, but again not statistically significant. GT3-T7 appears to only display η precipitates in the grain boundaries, and likewise, appears to only display one type of precipitate inside the grain boundary akin to GT2-T7. While this is not entirely in line with the DSC data, the scans do reveal a strong η-peak indicating that this phase should dominate the microstructure as can be seen in Figure 144.

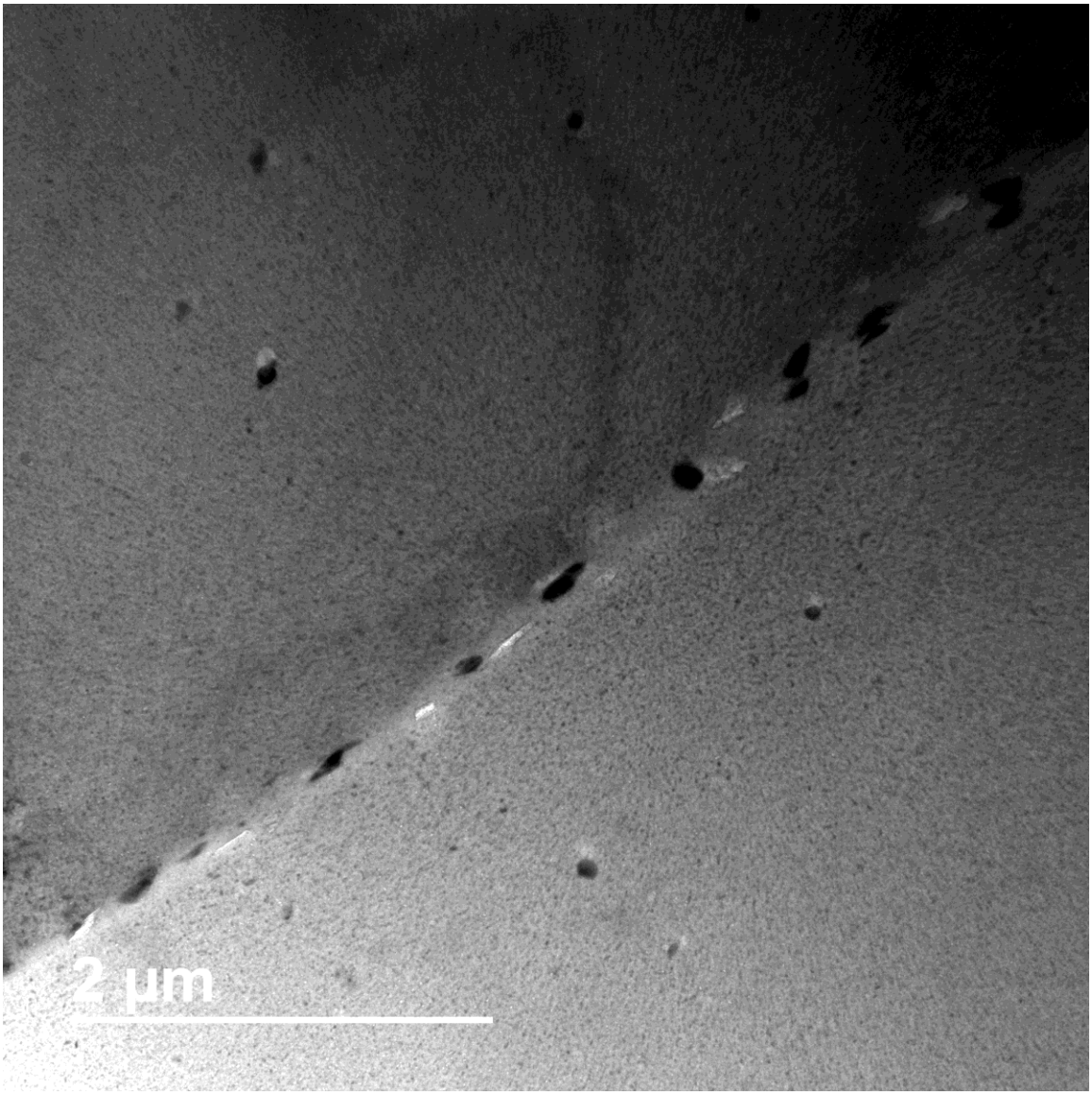


Figure 145 – *TEM image of GT4-T7.*

GT4-T7 (Figure 145) displays an average PFZ size of 45.68 ± 20.54 nm, which is by far the largest PFZ size studied during this investigation. The grain boundary is dotted with η phase, T-phase, and other Cu-containing intermetallics all of which appear in the various DSC scans of GT4. There appears to be a fine dispersion of η in the grain as well, but the presence of several larger unknown, round intermetallics within the grain is noticeable.

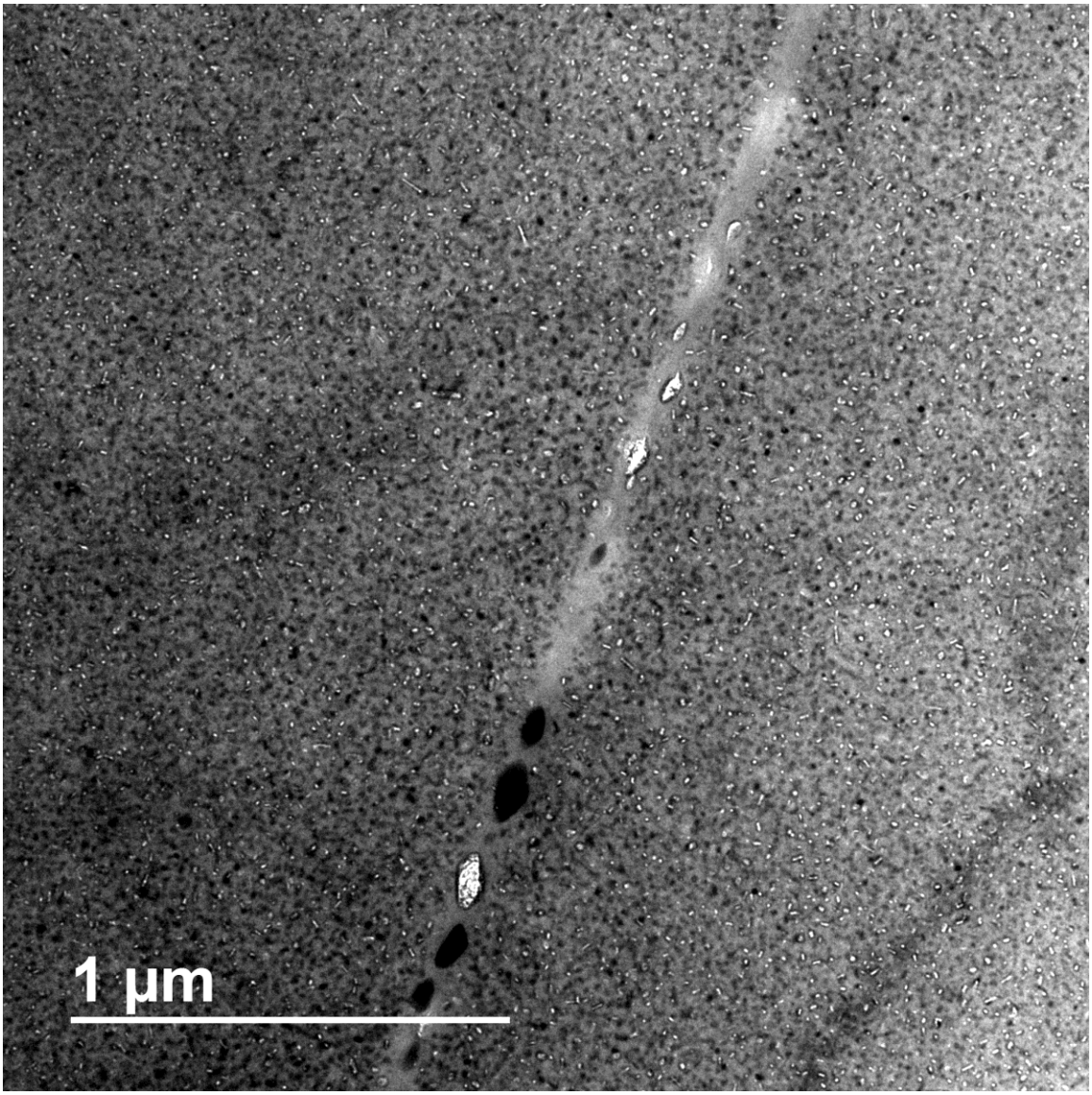

Figure 146 – *TEM image of GT5-T7.*

GT5-T7 (Figure 146) displays an average PFZ size of 22.43 ± 9.00 nm, which is close to that of alloys GT1-3 in the T7 temper. The appearance of the large white precipitates in the grain boundary is noticeable in the Cu-free GT5 indicating they are either Fe- or Si-intermetallics. The grain boundary also shows these dual precipitates. It is possible these phases are a Cu-free form of T-Phase, which did appear to form during the DSC scan of GT5 (see *Chapter 12 – The Effects of Natural Aging)*.

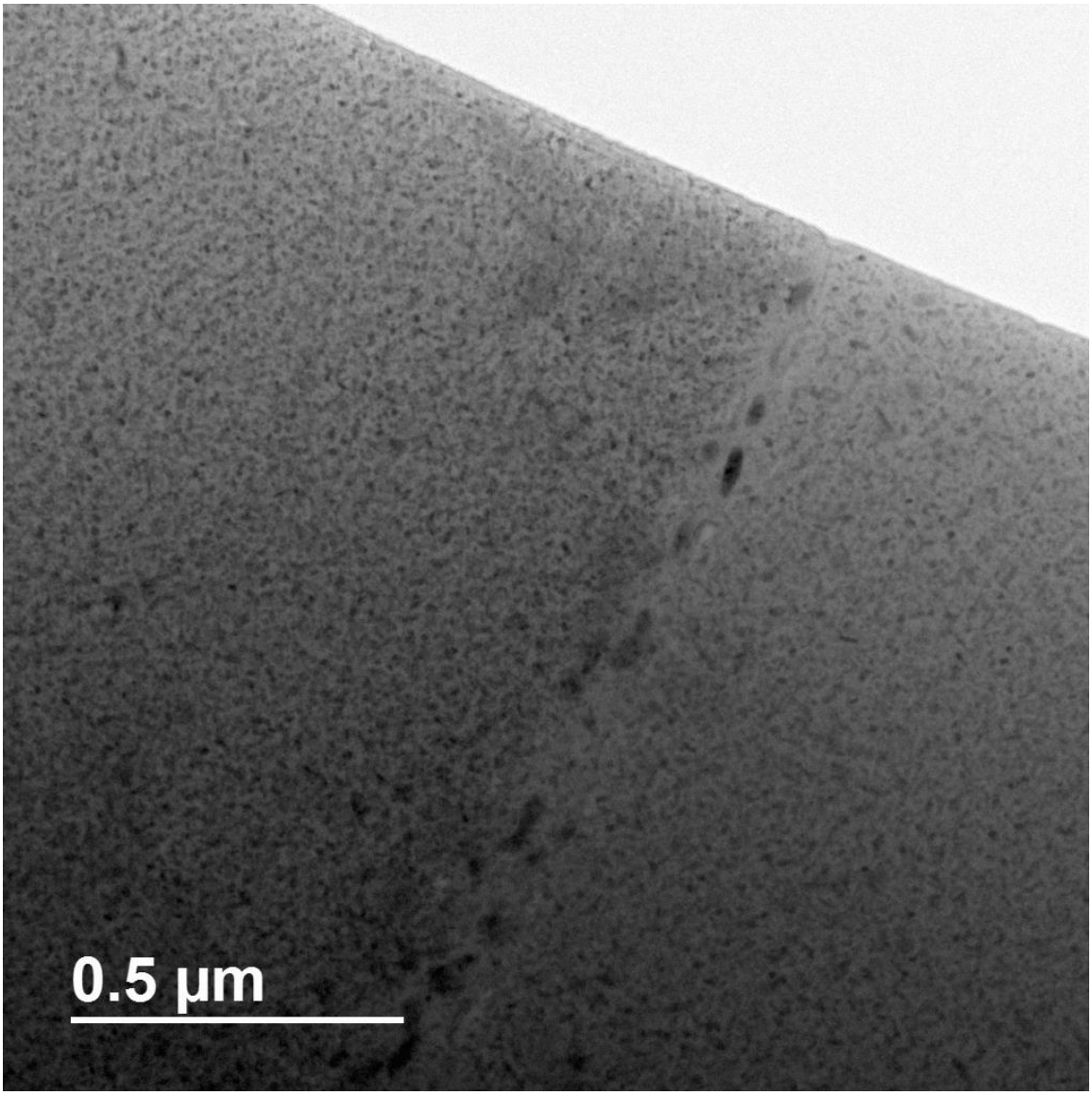

Figure 147 – *TEM image of GT6-T7.*

GT6-T7 (Figure 147) displays an average PFZ size of 18.25 ± 6.60 nm. The grain boundary appears to display a variety of phases and intermetallics similar to those found in GT2-T7. It should be noted that T-phase does appear to be present in the small amounts in the DSC scans, and likewise light colored intermetallics are scattered along the grain boundary of GT6-T7 shown in Figure 147.

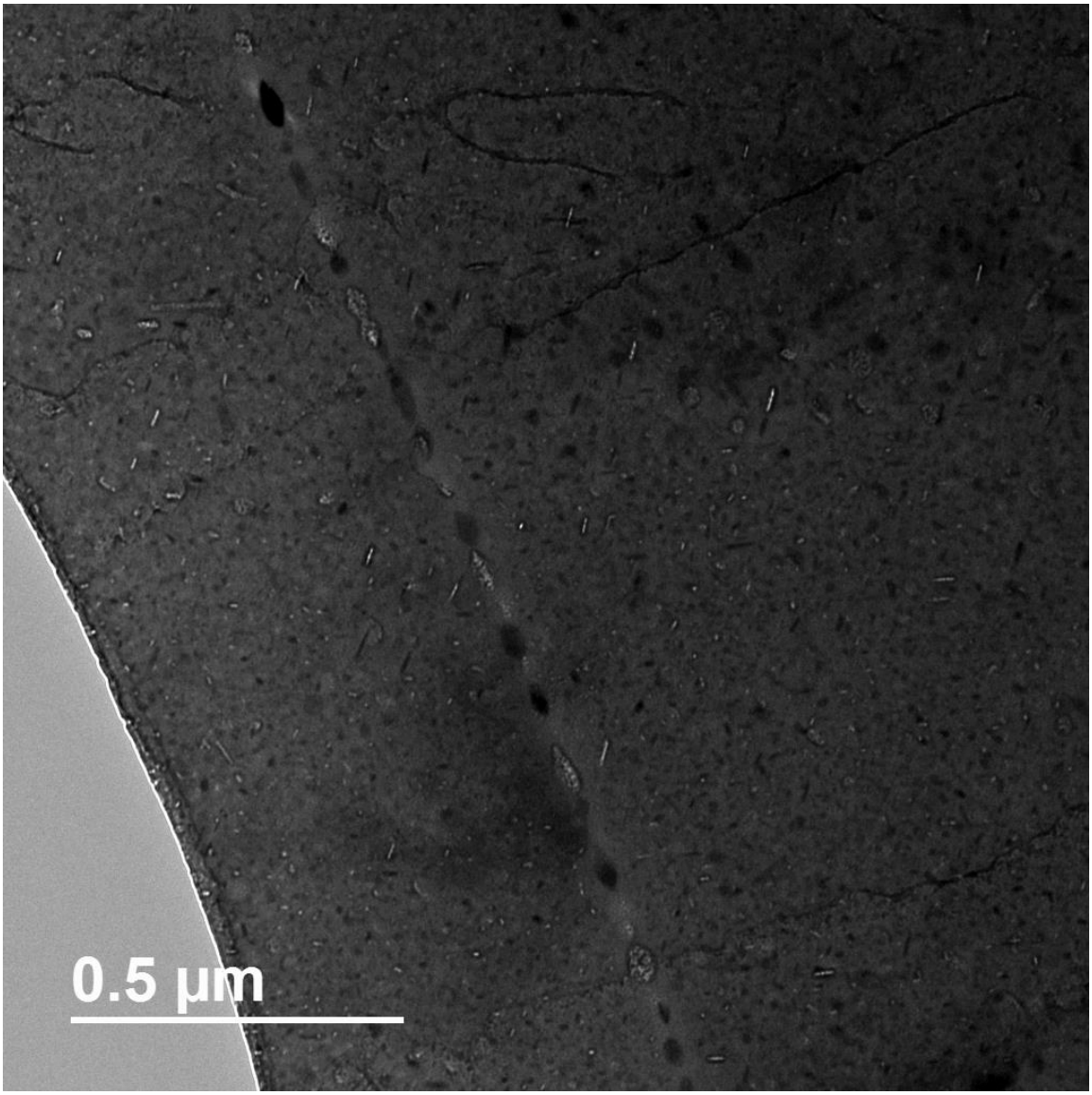

Figure 148 – *TEM image of GT7-T7.*

GT7-T7 (Figure 148) displays an average PFZ size of 22.29 ± 9.08 nm. The presence of T-phase in the grain boundary of GT7 correlates directly to the increase in T-phase precipitation seen in the DSC scans of GT7. The various other types of Cu-containing intermetallics can also be seen in the DSC sans of GT7, especially in the T6 temper, by the dual eutectic melting peaks.

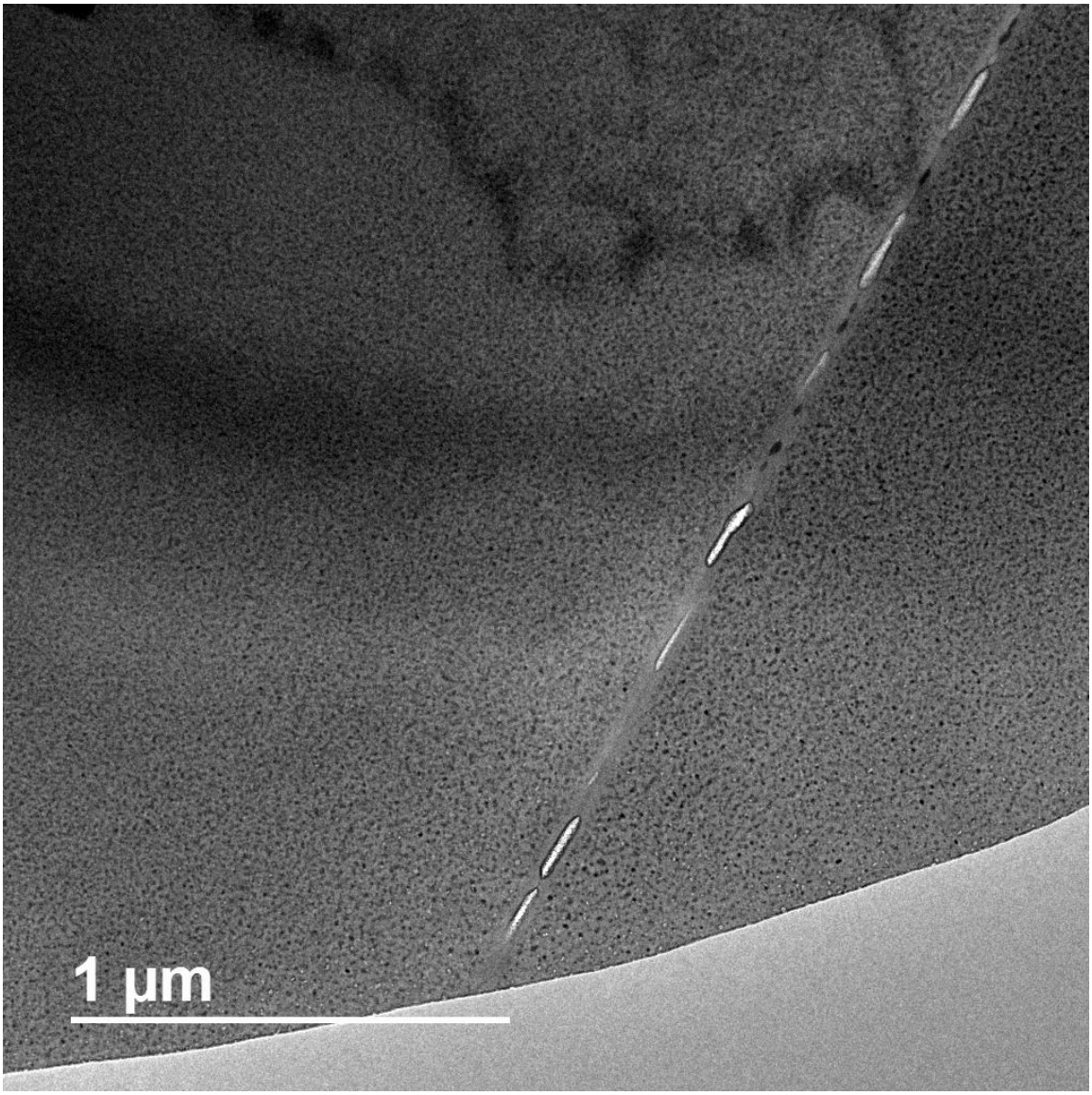

Figure 149 – *TEM image of GT8-T7.*

GT8-T7 (Figure 149) displays an average PFZ size of 19.65 ± 6.76 nm, which is within error of the rest of the other experimental alloys, and contains mostly long white particles in the grain boundaries. These white particles appear close in appearance to the T-phase identified by Raghavan [9]. Furthermore, this assumption is backed up by the DSC scans which showed an increase in T-phase precipitation in GT8 (see *Chapter 12 – The Effects of Natural Aging*). There does appear to be some η-phase in the grain boundary, but the precipitates are small and short. Unfortunately, the precipitates inside

the grain could not be identified as it would be interesting to determine if the precipitation sequence is altered (i.e. – $\alpha_{ssss}$ → GP zones → η → T-phase).

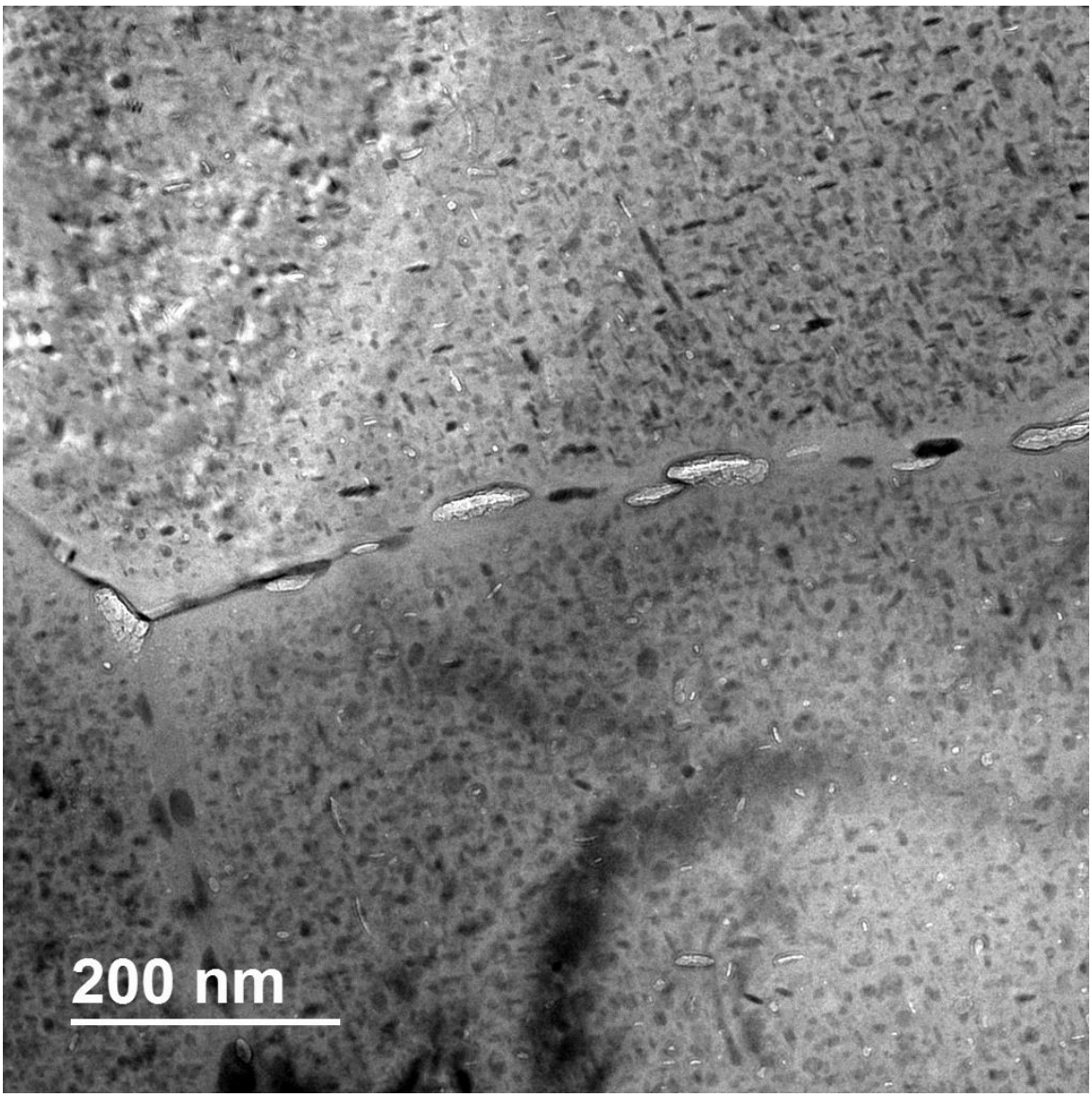


Figure 150 – *TEM image of 7136-T7.*

7136-T7 (Figure 150), which displays an average PFZ size of 14.99 ± 5.09 nm, appears to have grain boundary microstructure similar to GT1-T7. It should be noted however, the grain precipitates appear to be more advanced (i.e. – more lenticular) than those found in GT1. Similarly it is interesting to note the grain precipitates near Cu-containing intermetallics in the grain boundaries appear to be more advanced than those near η in the grain boundaries. This is not surprising as these large Cu-phases (i.e. – S-

phase, $Al_7Cu_2Fe$, etc) would not drain the surrounding matrix of Zn as the grain boundary η precipitates would.

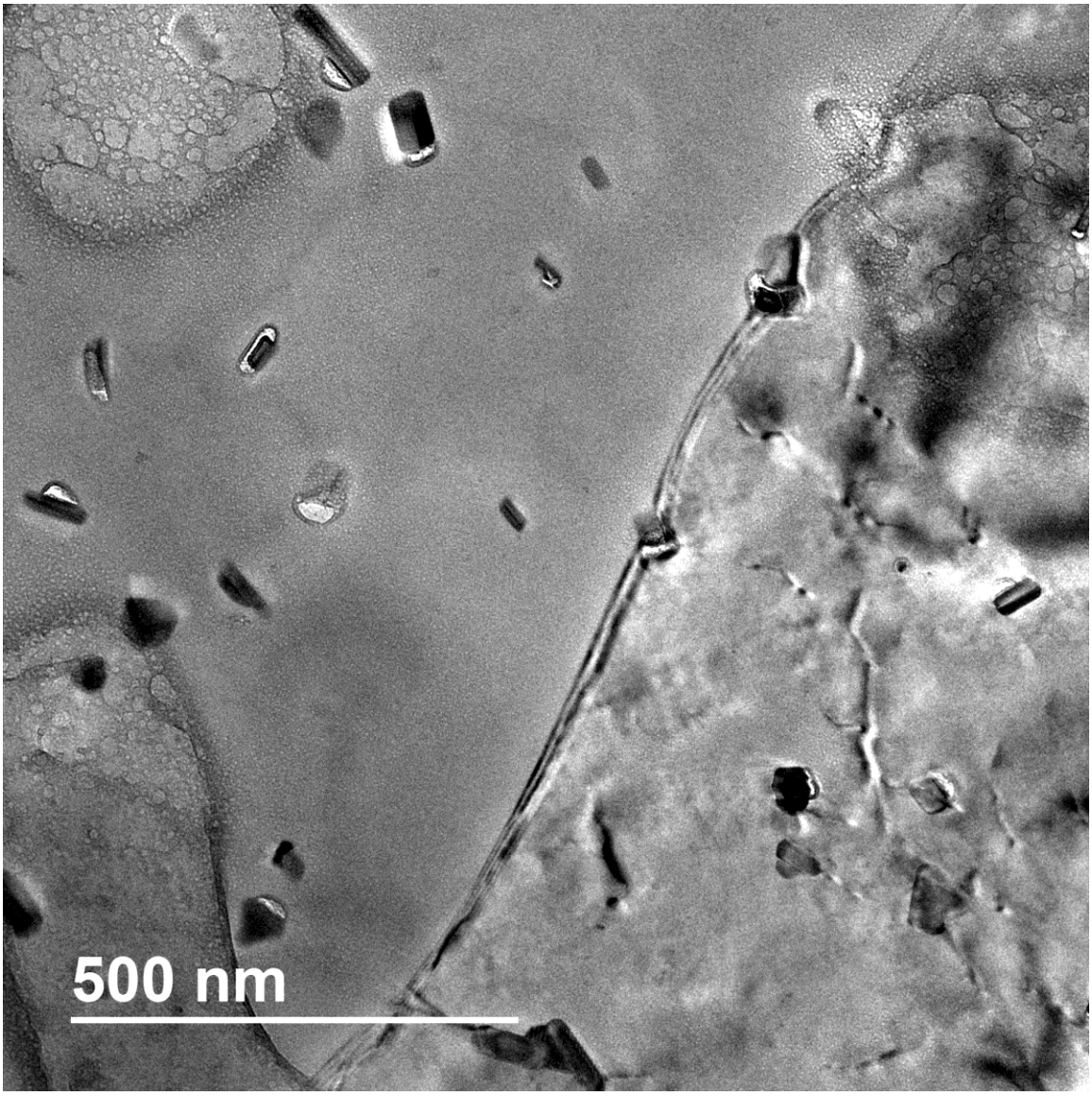


Figure 151 – *TEM image of 7075-T7.*

Interestingly, 7075-T7 (Figure 151) did not display a PFZ, although the grain boundary in Figure 151 appears to contain one solid intermetallic. A PFZ, interestingly enough, does not appear to be seen in around the large grain intermetallics, which are most likely E-phase. A small area of corrosion can be seen in the top left corner of Figure 151 and it is possible the precipitates have corroded away masking the PFZ. Another more unlikely answer is that the quench sensitivity of 7075 has caused the alloy

to form only grain boundary precipitates and precipitates on large dispersoid phases left over from the homogenization process.

### 14.1.2 Conformation of Grain Boundary Precipitates using EDX

Figure 152 displays a bright field TEM image and corresponding EDX maps of Al, Si, Mg, and Zn for GT4-T7. It can be seen from Figure 152 that the larger dark particles on the grain boundary are rich in terms of Mg and Zn indicating either η or T-phase, which matches well with the DSC scans.

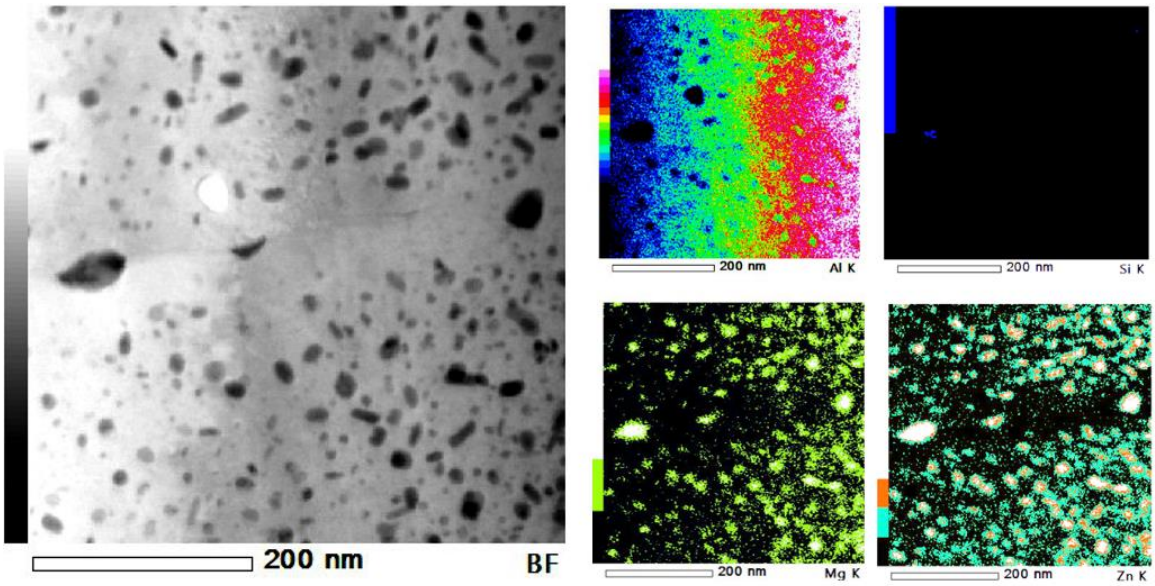


Figure 152 – *Bright field TEM image and corresponding EDS maps of Al, Si, Mg, and Zn for GT4-T7. Courtesy of Dr. Thomas Dorin (Deakin University).*

Figure 153 displays a bright field TEM image and corresponding EDX map of an Fe intermetallic in the GT4-T7 matrix. The Fe intermetallic is surrounded by what appears to be η-precipitates. The intermetallic is surrounding by Al-Zn-Mg particles indicating a high volume fraction of η-type precipitates inside the grains.

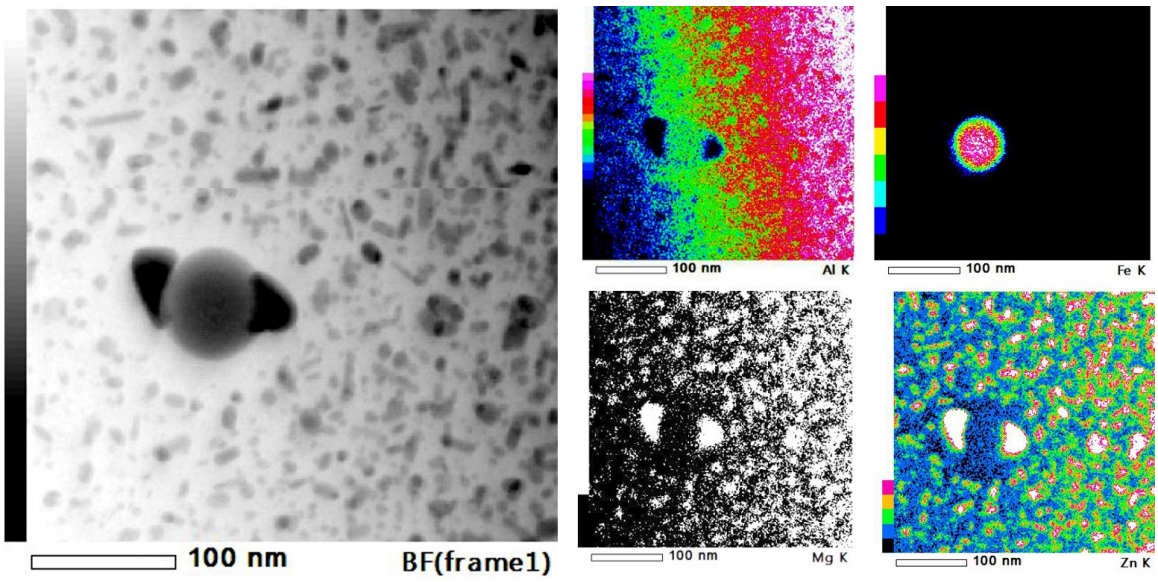


Figure 153 – *Bright field TEM image and corresponding EDC maps of Al, Si, Mg, and Zn of an Fe intermtallic in the GT4-T7 matrix. Courtesy of Dr. Thomas Dorin (Deakin University).*

### 14.2 Discussion

Unfortunately, the role of composition does not appear to effect the width of the PFZ in any statistically significant way. It does, however, effect the types of precipitates in the grain boundary, which is to be expected. For example, it was shown that increasing the Mg content for a given Zn:Mg ratio not only promotes the formation of T-phase, but appears to make it the dominate grain boundary forming precipitate (see Figure 149).

Therefore it appears likely that the width of the PFZ zone is more likely controlled by the quench sensitivity of an aluminum alloy. As will be shown in Part III, this typically is directly related to the type of dispersoid found in an alloy. This correlation may have been hinted at here in Figures 150 and 151 with 7075 and 7136 displaying significantly different grain boundaries. Although, as previously noted, this may be the effects of sample corrosion.

In an attempt to correlate the PFZ findings to the relative corrosion resistance of GT1-8 in the T73 temper exfoliation corrosion (EXCO) and interganular corrosion (IGC) testing was performed. The results of these corrosion tests can be seen in Appendices D

and E, respectively (note: no correlation was found between EXCO and IGC resistance and the observed PFZ size, although compositional correlations were made).

### 14. 3 Conclusions

TEM imaging was utilized in an attempt to correlate the composition of the experimental alloys GT1-8 to with their respect PFZ size. Unfortunately, no clear trend was established with the respect to the Zn, Mg, and Cu levels and PFZ size, but the effect of dispersoid forming elements on grain precipitation is clear (i.e. – there is a noticeable difference in the 7136 and 7075 samples used for reference when compared to GT1-8). The TEM images presented appear to validate the DSC scans found in *Chapter 12 – The Effects of Natural Aging*, especially when compared to those found in academic literature.

Future studies should focus on using advanced TEM techniques to determine if the individual grain boundary precipitates produce different PFZ sizes in any statistically significant systematic manner. If such a correlation could be obtained, then age practices and compositional fluctuations could be used in tandem to improve the SCC resistance of an alloy. It was shown that GB precipitates can alter grain precipitates, so a systematic study of these effects would also be vastly interesting from a pure mechanical properties perspective as well.

### 14.4 References


[1] T. H. Sanders Jr., R. R. Sawtell, J. T. Staley, R. J. Buccie, and A. B. Thakker, "Effect of microstructure on fatigue crack growth of 7xxx aluminum alloys under constant amplitude and spectrum loading," 1978.

[2] R. Rangathan, "Recrystallization resistance in aluminum alloys containing zirconium," Georgia Institute of Technology, 1991.

[3] S. P. Ringer and K. Hono, "Microstructural evolution and age-hardening in aluminum alloys: atom probe, field-ion microscopy, and transmission electron microscopy studies," *Mater. Charact.*, vol. 44, pp. 101–103, 2000.

[4] J. T. Staley, "Aging kinetics of aluminum alloy 7050," *Metall. Trans.*, vol. 5, pp. 929–932, 1974.

[5] T. Ogura, S. Hirosawa, A. Hirose, and T. Sato, “Effects of microalloying tin and combined additions of silver and tin on the formation of precipitate free zones and mechanical properties in Al-Zn-Mg alloys,” *Mater. Trans.*, vol. 52, pp. 900–905, 2011.

[6] T. D. Burleigh, “The postulated mechanisms for stress corrosion cracking of aluminum alloys - a review of literature 1980-1989,” *Corrosion*, vol. 47, pp. 89–98, 1991.

[7] J. F. Nie and B. C. Muddle, “Microstructural design of high-strength aluminum alloys,” *J. Phase Equilibria*, vol. 19, pp. 543–551, 1998.

[8] J. D. Embury and R. B. Nicholson, “The nucleation of precipitates: the system Al-Zn-Mg,” *Acta Metall.*, vol. 13, pp. 403–417, 1965.

[9] M. Raghavan, “Microanalysis of precipitate free zones (PFZ) in Al-Zn-Mg and Cu-Ni-Nb alloys,” *Metall. Trans. A*, vol. 11, pp. 993–999, 1980.

[10] S. Liu, Y. Zhang, W. Liu, Y. Deng, and X. Zhang, “Effect of step-quenching on microstructure of aluminum alloy 7055,” *Trans. Nonferrous Met. Soc. China*, vol. 20, pp. 1–6, 2010.

# PART III

# RESEARCH ON REGISTERED 7XXX-SERIES ALUMINUM ALLOYS

# CHAPTER 15

# INTRODUCTION

The complex nature of registered 7xxx-series aluminum alloys stems from the incorporation of various micro-alloying elements in their compositions. Typically in addition to Zn, Mg, and Cu, these alloys often contain various grain refiners (ex. – TiB, TiC, AlTi) as well as dispersoid forming elements (ex. – Cr, Zr, Sc, Mn, La, etc.). Other common alloy additions include beryllium (Be), which is often added to improve the casting finish, and silver (Ag), which acts as a vacancy sink and reduces the size of the precipitate free zones (PFZ). The effects of these various alloying additions can be far reaching and can affect not only an alloy's final properties, but its processing as well. Therefore, it is necessary to determine if the various effects observed in Part II on the simple quaternary Al-Zn-Mg-Cu alloys still hold true for registered 7xxx-series extruded products.

Several registered 7xxx-series extruded aluminum alloys were studied including 7136, 7075, 7050, 7249, and 7150. The extrusions for this work were either provided by UAC-Canton or obtained from commercial sources. Due to the proprietary nature of the casting, homogenization, extrusion, and post-plastic deformation processes an overall "experimental procedure" will not be covered in this section; however, individual chapters will contain their own relevant experimental procedures as necessary.

This section therefore focuses chiefly on the post-plastic deformation processes: solution heat treatment (SHT) and aging. Chapter 16 briefly introduces the materials used. Chapter 17 attempts to correlate the composition of 7xxx-series alloys to their relative quench sensitivity from SHT. Chapter 18 studies the artificial aging (AA) behavior of a few common 7xxx-series alloys. Lastly, Chapter 19 explores the concept of a true aging curve, which allows one to visualize the entire precipitation process.

# CHAPTER 16

# MATERIALS

Several common 7xxx-series aluminum alloys were provided by the Universal Alloy Corporation and obtained from commercial sources. These alloys, whose partial composition can be seen in Table 26, vary significantly from one other in terms of Zn, Mg, and Cu contents. The alloys also contain different dispersoid forming elements. Each of the alloys in Table 26 were used in their extruded form. Table 27 details which alloys were used in each chapter of this section. Figure 154 displays the average partial composition (i.e. – average Zn, Mg, and Cu contents) for the various registered alloys used in this section alongside the compositions of the experimental alloys used in *Part II – The Quaternary Al-Zn-Mg-Cu system*.

Table 26 – *Major alloying additions ranges in wt.% as well as common dispersoid forming elements for the 7xxx-series alloys used in this work* [1].

| Alloy | Zn | Mg | Cu | Dispersoid |
|---|---|---|---|---|
| **7136** | 8.7-9.4 | 1.8-2.5 | 1.9-2.5 | Zr |
| **7050** | 5.7-6.7 | 1.9-2.6 | 2.0-2.6 | Zr, Cr |
| **7075** | 5.1-6.1 | 2.1-2.9 | 1.2-2.0 | Cr |
| **7150** | 5.6-6.9 | 2.0-2.7 | 1.9-2.5 | Zr |
| **7249** | 7.2-8.4 | 2.0-2.9 | 1.2-1.9 | Cr |
| **7178** | 6.3-7.3 | 2.0-2.7 | 1.6-2.4 | Cr |

Table 27 – *Testing matrix detailing which alloys were utilized in each chapter.*

| | 7136 | 7050 | 7075 | 7150 | 7249 | 7178 |
|---|---|---|---|---|---|---|
| Chapter 17 *Quench Sensitivity and C-Curve Development* | ✓ | ✓ | ✓ | ✓ | ✓ | ✓ |
| Chapter 18 *Artificial Aging* | ✓ | | | ✓ | | |
| Chapter 19 *Development of True Aging Curves* | | ✓ | ✓ | | | |

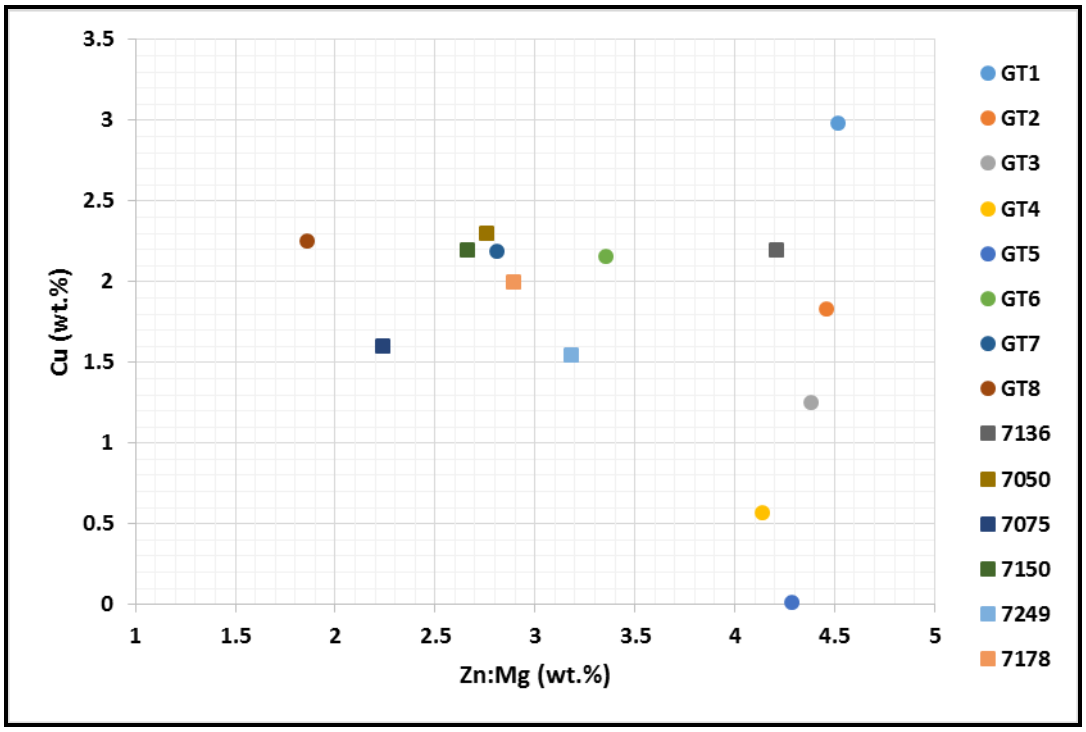


Figure 154 – *The average partial composition of the various registered 7xxx-series aluminum alloys used in this section versus the compositions of the experimental Al-Zn-Mg-Cu alloys used in Part II.*

As can be seen in Figure 154, the experimental alloys used in Part II represent the diversity of the registered 7xxx-series alloys presented here. The extruded products used here were selected due to their similar aspect radios, however some variations did exist. Other factors such as extrusion ratio and extrusion parameters are considered proprietary information and were not used in the selection of extrusions for this study. Other processing parameters including solution heat treatments, stretch percentages, and artificial aging temperatures/times were determined for this study independent of UAC-Canton from academic literature.

## 16.1 References

[1] The Aluminum Association, *International Alloy Designations and Chemical Composition Limits for Wrought Aluminum and Wrought Aluminum Alloys*. Arlington, VA, 2009.

# CHAPTER 17

# QUENCH SENSITIVITY AND C-CURVE DEVELOPMENT

The quench sensitivities of 7136, 7136+Sn, 7050, 7075, 7150, 7249, and 7178 from solution heat treatment (SHT) were determined. The registered compositions of these alloys represent a wide range of Zn:Mg ratios, Cu contents, and dispersoids (see Table 26 in *Part III – Chapter 16 – Materials*). The quench sensitivity for each alloy was tested using a modified Jominy end quench and Rockwell hardness B-scale testing (HRB). The hardness of each alloy was tested in the W and T6 tempers. The hardness data was then in turn utilized to develop generalized C-curves.

## 17.1 Experimental Procedure

Samples measuring 30.48 cm (12 in) x 3.81 cm (1.5 in) x 0.64 cm (0.25 in), an example of which can be seen below in Figure 155, were machined out of various extruded alloys with similar aspect ratios. While an effort was made to test extrusions with similar microstructures, the 7136 and 7136+Sn extrusions did not display a strong fibered grain morphology. Micrographs (Barker's reagent) of the extruded bars can be seen in Figures 156 – 162.

Figure 155 – *Example of a quench test sample (7136, W-temper).*

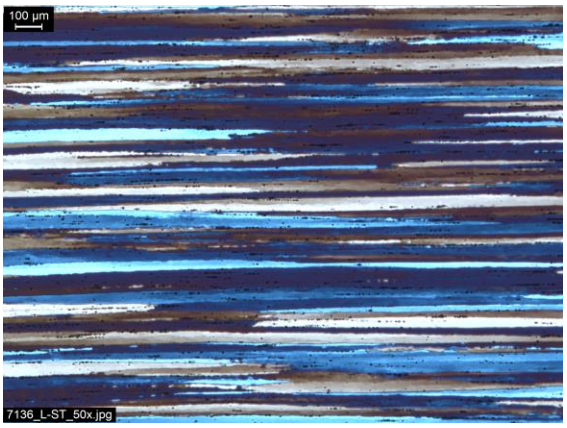


Figure 156 – *7136 quench bar L-S (Barker's Reagent).*

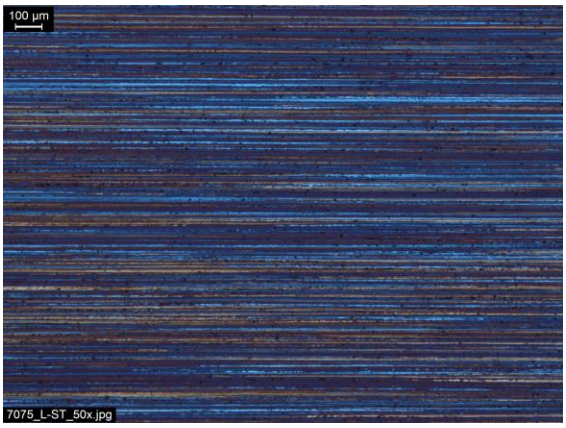


Figure 157 – *7075 quench bar L-S (Barker's Reagent).*


Figure 158 – *7136+Sn bar L-S (Barker's Reagent).*

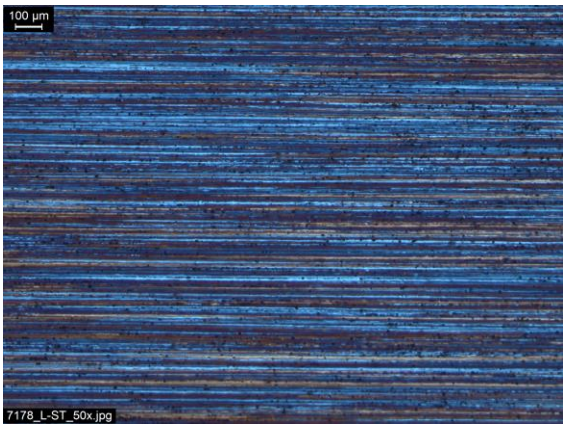


Figure 159 – *7178 quench bar L-S (Barker's Reagent).*

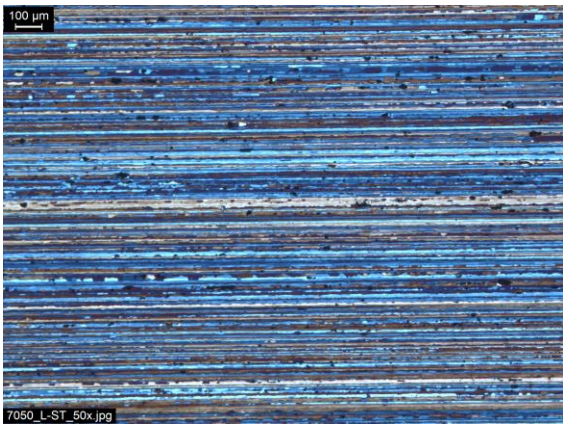


Figure 160 – *7050 quench bar L-S (Barker's Reagent).*

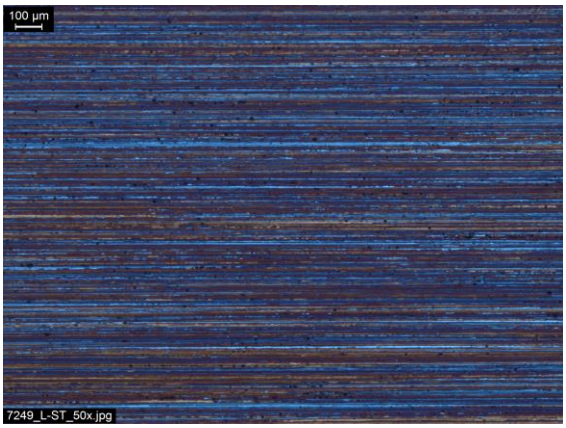


Figure 161 – *7249 quench bar L-S (Barker's Reagent).*

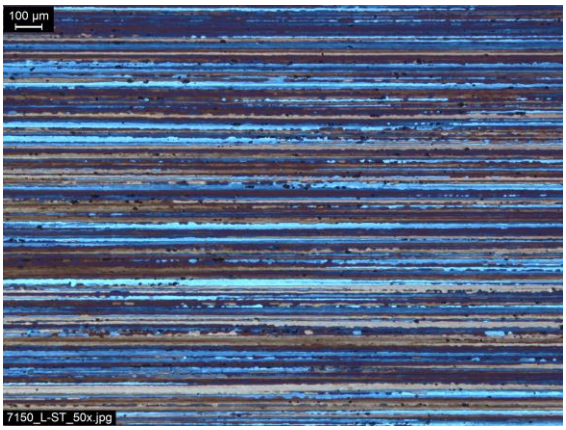

Figure 162– *7150 quench bar L-S (Barker's Reagent).*

The samples were then SHT for approximately 45 minutes before being end quenched in water as shown in Figure 163. During the quenching operation, the samples were suspended such that 3.81 cm (1.50 in) of the samples were below the water line. The samples were allowed to cool for 10 minutes before being fully submerged in the quench tank. Throughout the quenching process the water used for quenching was being circulated and monitored for temperature fluctuations (the water never reached a temperature more than a few degrees above room temperature during the quenching process).

Figure 163 – *Quench rate test set-up. The sample is 30.48 cm (12 in) long with 3.81 cm (1.5 in) submerged below the water line. It was held in the circulated quench tank for 10 minutes before being fully quenched.*

The quench rates assumed for these samples (Table 28) were taken from previous UAC-Canton experiments on 2024. During those experiments, samples of the same dimensions as those studied for this work were fitted with a series of thermocouples to record the various quench rates as a function of distance from the end of the sample (i.e. – the end of the sample in the water). Thermocouples were placed at: 1.91 cm (0.75 in), 3.81 cm (1.5 in), 5.08 cm (2 in), 6.35 cm (2.5 in), 7.62 cm (3 in), 10.16 cm (4 in), 15.24 cm (6 in), and 20.32 cm (8 in). The average quench rates recorded during the UAC trails can be seen in Figure 164 (note: the thermocouple numbers in Figure 164 correspond to those listed in Table 28).

Table 28 – *Quench rates for the samples tested based off the distance from the bottom of the sample (i.e. – the end of the sample in the water). Note: the water line is located 3.81 cm (1.5 in) from the bottom of the samples.*

| **Thermocouple** | **1** | **2** | **3** | **4** | **5** | **6** | **7** | **8** |
|---|---|---|---|---|---|---|---|---|
| **Distance from Quench Media (cm)** | 1.91 | 3.81 | 5.08 | 6.35 | 7.62 | 10.16 | 15.24 | 20.32 |
| **Distance from Quench Media (in)** | 0.75 | 1.50 | 2.00 | 2.50 | 3.00 | 4.00 | 6.00 | 8.00 |
| **Quench Rate (°C/min)** | 8886 | 6519 | 2284 | 678 | 315 | 171 | 91 | 26 |
| **Quench Rate (°F/s)** | 267 | 197 | 69 | 21 | 10 | 6 | 3 | 1 |

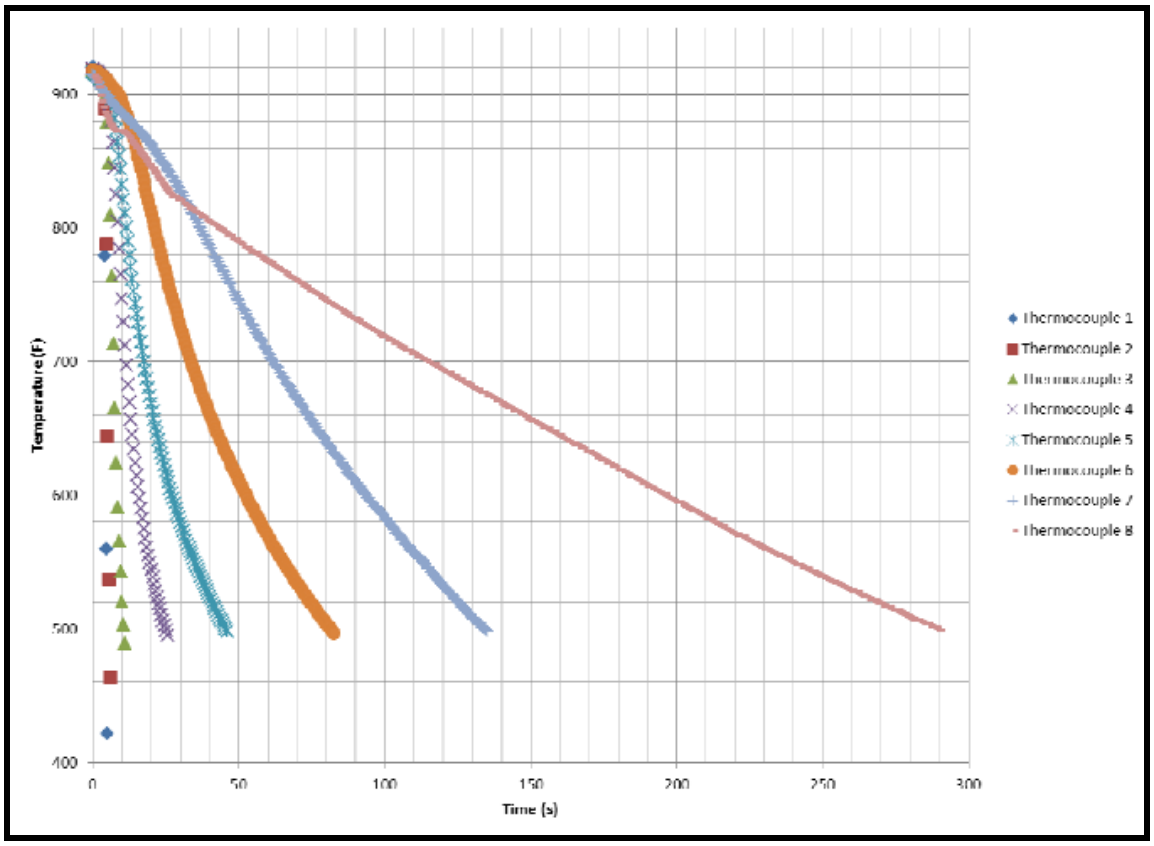


Figure 164 – *Chart displaying the average quench rate per thermocouple.*

Following the quench procedure, the samples were immediately tested for HRB in the resulting W-temper. The samples were then aged for 24 hours at 120°C (248°F) to obtain a T6 temper. Once again, the samples tested for HRB.

### 17.2 Quench Sensitivity

The results of HRB testing on the quench sensitivity samples can be seen below in Figure 165 (W temper), Figure 166 (T6 temper), and Figure 167 (W and T6 tempers). It is interesting to note the appearance of c-curve kinetic reactions taking place as the quench rate is decreased which is to be expected, and whose effect is seen in every alloy to varying degrees in both tempers. The dip in strength seen in the poor quench regions seems to correlate to the quench sensitivity of GP-II zones (i.e. – in the regions where the quench was poor, GP-II zone precipitation is difficult due to a low vacancy concentration). It is therefore likely that the increase in HRB seen in the T6 temper in the

poor quench region is due most likely to either the precipitation of GP-I zones or the emergence of the stable hardening phase η out of the solid solution.

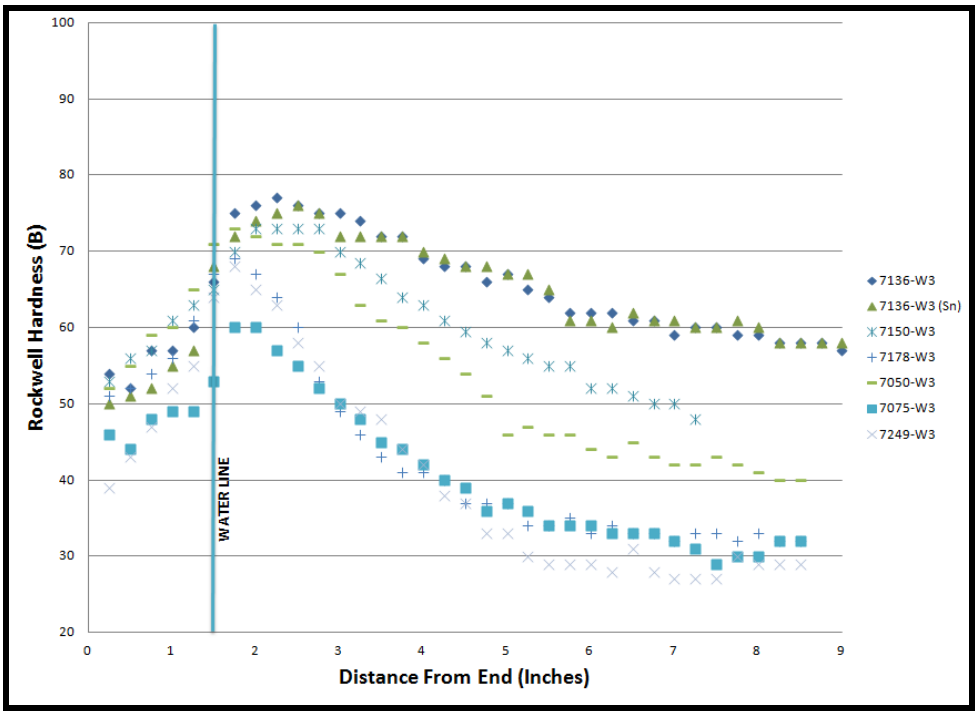


Figures 165 – *Rockwell hardness (B) versus distance from the end of the quench test specimen (inches) for the W temper. Note: all test points below 1.5 inches were submerged during the quench.*

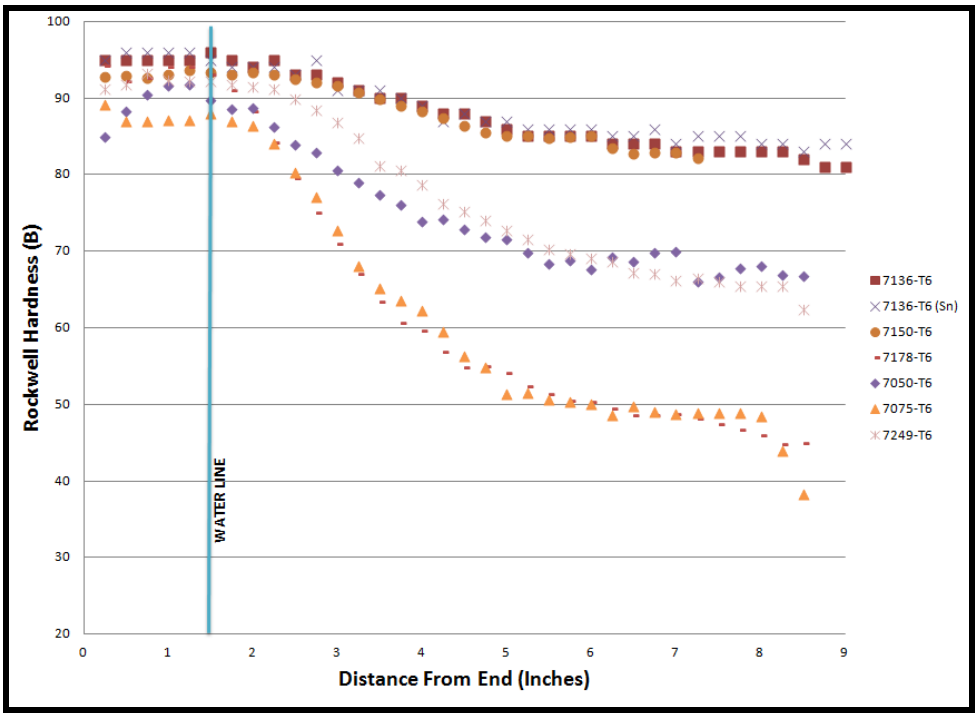


Figure 166 – *Rockwell hardness (B) versus distance from the end of the quench test specimen (inches) for the T6 temper. Note: all test points below 1.5 inches were submerged during the quench.*

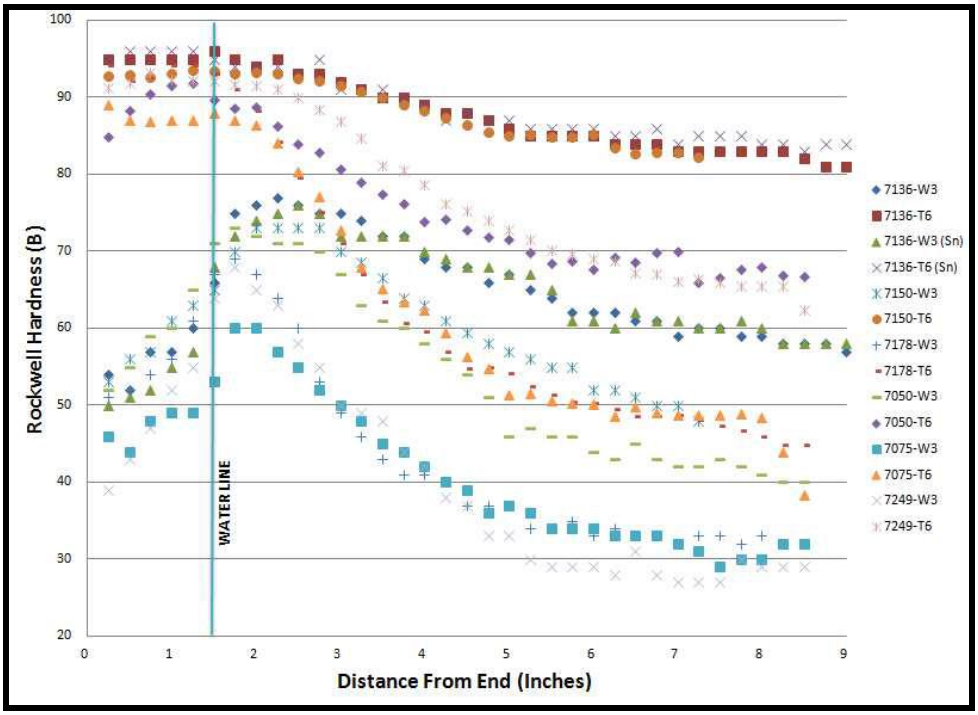


Figure 167 – *Rockwell hardness (B) versus distance from the end of the quench test specimen (inches) for the W and T6 tempers. Note: all test points below 1.5 inches were submerged during the quench.*

Figures 165 – 167 reveal the appearance of three distinct groups of alloys: 7136, 7136+Sn, and 7150 display little to no quench sensitivity, especially in the T6 temper; 7075 and 7178 display a large quench sensitivity in both tempers; 7050 and 729 fall in between the two extremes. A quick look at the compositions of these alloys reveals that the relative quench sensitivities do not correlate to total alloying content (see Table 29) as is usually the case (i.e. – typically alloys with a higher solute content are considered more quench sensitive), but rather to the dispersoid forming elements found in each alloy. 7075 and 7178 are alloyed with Cr, which is known to increase quench sensitivity. 7136, 7136+Sn, and 7150 are alloyed with Zr, which is known to retain vacancies during quenching from SHT thus desensitizing the alloys. The surprising cases are those of 7050 and 7249. Although its registered composition has some tolerance for Cr additions, 7050 chiefly utilized Zr as a dispersoid. Therefore, it should not have been as quench sensitive. Conversely, 7249 appeared to be desensitized to quench rate compared to the other Cr-containing alloys (7075 and 7178). For the case of 7249, this is probably due to its high Zn content.

Table 29 – *Total alloying content for various 7xxx-series alloys based off their registered compositions (wt.%) with quench sensitivity (low, medium, or high) as well as the main dispersoid forming element(s) found in each alloy.*

| Alloy | Total Solute Content (wt.%) | Quench Sensitivity | Dispersoid Elements |
|---|---|---|---|
| **7136** | 15.07 | Low | Zr |
| **7150** | 12.72 | Low | Zr |
| **7050** | 13.06 | Medium | Zr, Cr |
| **7249** | 13.06 | Medium | Cr |
| **7075** | 12.68 | High | Cr |
| **7178** | 14.48 | High | Cr |

The observation that quench sensitivity appears to be more dependent on dispersoid elements rather than the relative Zn, Mg, and Cu contents is not surprising and appears to confirm the findings/conclusions presented in *Part II – Chapter 14 – The Effect of Composition on the Precipitate Free Zone.* In other words, it appears that precipitate forming elements in 7xxx-series (i.e. – Zn, Mg, and Cu) have little-to-no

bearing on the PFZ size, which is a quench dependent property. This is probably due to the fact that dispersoids can act as heterogeneous nucleation sites for the various precipitates found in 7xxx-series alloy thus binding up Zn, Mg, and Cu atoms that would otherwise diffuse to the grain boundary.

### 17.3 C-Curve Development

The c-curves for heat treatable aluminum alloys can be estimated from the quench sensitivity data as proven by Evancho et al. [1] and Bernardin et al. [2]. The c-curve is given by the following mathematical expression:

$$C_t = k_1 k_2 exp\left(\frac{k_3 k_4^2}{RT(k_4 - T)^2}\right) exp\left(\frac{k_5}{RT}\right) \quad (27)$$

Where

$C_t$ = critical time required to precipitate a constant amount.
$k_1$ = constant which equals the natural logarithm of the fraction transformed.
$k_2$ = constant related to the reciprocal of the number of nucleation sites (2.2E-19 for 7050, 4.1E-13 for 7075).
$k_3$ = constant related to the energy required to from a nucleus (5190 for 7050, 1050 for 7075).
$k_4$ = constant related to the solvus temperature (850 for 7050, 780 for 7075).
$k_5$ = constant related to the activation energy for diffusion (180,000 for 7050, 140,000 for 7075).
R = gas constant (8.3143 $JK^{-1}mol^{-1}$)
T = temperature (°K)

The values for the k-coefficients, $k_2$-$k_5$ for aluminum alloys 7075 and 7050 were provided by Evancho et al. [1]. It should be noted that $k_1$ can be estimated by Equation 28:

$$k_1 = -ln\left(\frac{0.995\sigma_{max} - \sigma_{min}}{\sigma_{max} - \sigma_{min}}\right) \quad (28)$$

The HRB quench sensitivity data for the W temper was used to generate c-curves for each alloys which can be seen in Figure 168. It should be noted that the k-coefficients for 7050 and 7075 were taken from Evancho et al. [1]. These coefficients were then applied to the other alloys testes based off whether they displayed a high quench

sensitivity, in which case the 7075 k-coefficients were used, or a low-to-medium quench sensitivity, in which the 7050 k-coefficients were used. Therefore the c-curves below are not absolute and only serve to give a general idea of an alloys true c-curve; however, it should be noted that the c-curves presented for 7075 and 7050 match up well with those found in literature.

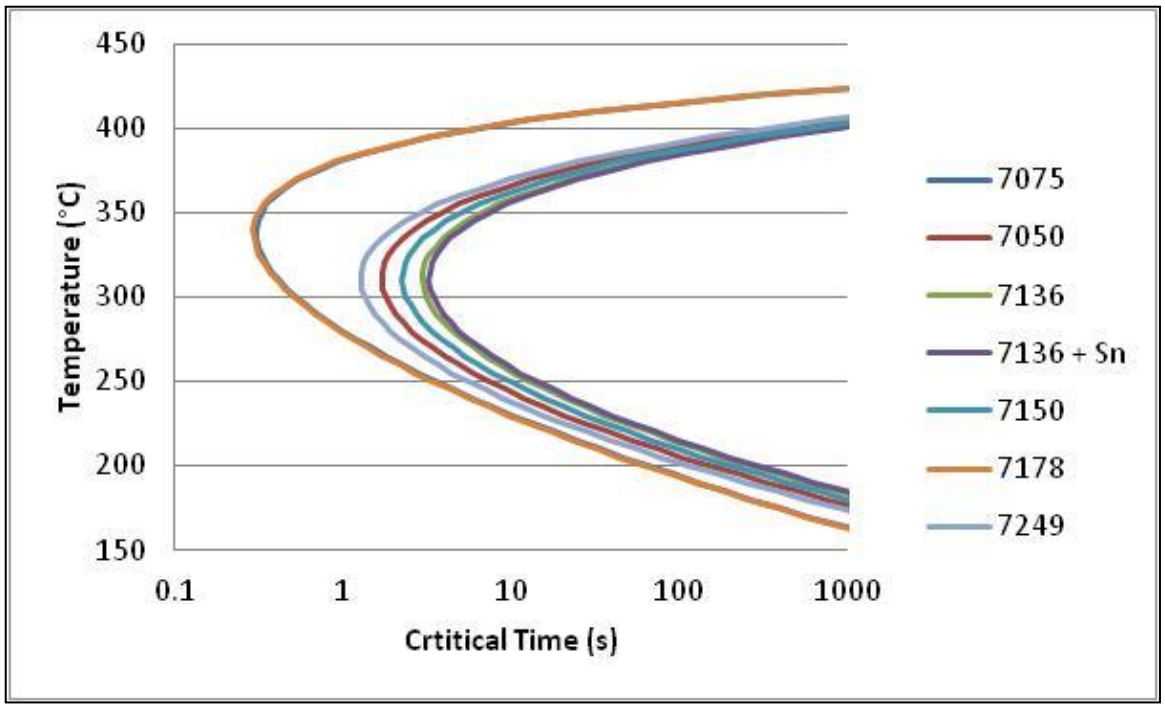


Figure 168 – *C-curves for various 7xxx-series alloys. It should be noted that the k-coefficients were taken from literature sources for 7075 and 7050. These values were then used as the k-coefficients for the other alloys tested.*

### 17. 4 Conclusions

Quench sensitivity charts and C-curves were developed under various assumptions for a variety of 7xxx-series alloys. The dependence of the main precipitation process (P1) on VRC in 7xxx-series alloys was illustrated. The hardening effect in the "poor" quench regions seen in the transition from the W- to the T6-temper is believed to be primarily due to the precipitation of GP-I zones and η-phase. In contrast, the hardening effects seen in the "good" quench regions is due the precipitation of GP-II zones and η' primarily.

It was also shown that the correlation between dispersoid forming elements and quench sensitivity appears to be stronger than that between total alloying content and quench sensitivity. 7075 and 7178 were shown to be highly quench sensitive whereas 7136 and 7150 was shown to be non-quench sensitive. These results match well with those of Nowill [3].

These findings are important because it allows one to alter the main alloying elements of 7xxx-series aluminum alloys (i.e. – Zn, Mg, and Cu) to promote certain mechanical properties via the alteration/control of the precipitation process while not effecting the quench sensitivity of the alloy with respect to hardness. It should be noted, however, that certain alloys like 7150, while shown here not to be quench sensitive with respect to hardness, are known to be quench sensitive with respect to intergranular corrosion (IGC) due to the type of precipitates forming (a factor which is dependent on the Zn, Mg, and Cu contents).

## 17.5 References


[1] J. W. Evancho and J. T. Staley, "Kinetics of precipitation in aluminum alloys during continous cooling," *Metall. Trans.*, vol. 5, pp. 43–47, 1974.

[2] J. D. Bernardin and I. Mudawar, "Validation of the quench factor technique in predicting hardness in heat treatable aluminum alloys," *Int. J. Heat Mass Transf.*, vol. 38, pp. 863–873, 1995.

[3] C. Nowill, "Investigation of the quench and heat rate sensitivities of selected 7000 series aluminum alloys," Worcester Polytechnic Institute, 2007.

# CHAPTER 18

# ARTIFICAL AGING

The 7xxx-series of aluminum alloys are a precipitation hardenable grade of aerospace alloys. Their properties can often times be tailored by utilizing various quenching and aging practices to meet specific application requirements (ex. – high strength, high toughness, increased corrosion resistance, low residual stress, etc.). Generally, 7xxx-series aluminum alloys are subjected to a two-step artificial aging cycle during the industrial process, although other more complex artificial aging practices such as retrogression and re-aging (RRA), or T77 age practices, are sometimes utilized.

The following chapter is a collage of aging studies, which stemmed from the test results garnered on GT1-8, namely those from *Part II – Chapter 12 – The Effects of Natural Aging* and *Part II – Chapter 13 – Artificial Aging*. The topics herein covered are as follows: the development of industrial two-step artificial aging curves on aluminum alloys 7136, 7050, 7075, and 7249; the effect of natural aging; the effects of low temperature aging on 7136; and the effects of stretching on the T7 Temper. These topics are important because they allow one to better translate the aforementioned results to industrial grade alloys.

## 18.1 Experimental Procedure

The basic experimental procedure for each of the following sub-studies on AA was essentially the same. First extrusions provided by UAC-Canton or obtained from commercial sources were SHT and stretched before being macro-etched using a caustic solution followed by a nitric rinse. These macro-graphs ensured that the hardness specimens were taken from a region with no REX grains. Examples of these macrographs can be seen in Figures 169 – 171. Following inspection on macrographs, hardness samples measuring approximately 2.54 cm (1 in) x 2.54 cm (1 in) were cut from

the extrusion prior to aging. The furnaces and characterization equipment used were the same as those in *Part II – The Quaternary Al-Zn-Mg-Cu System*. Any deviations from this general experimental procedure will be noted in the following sections.

a.) b.)

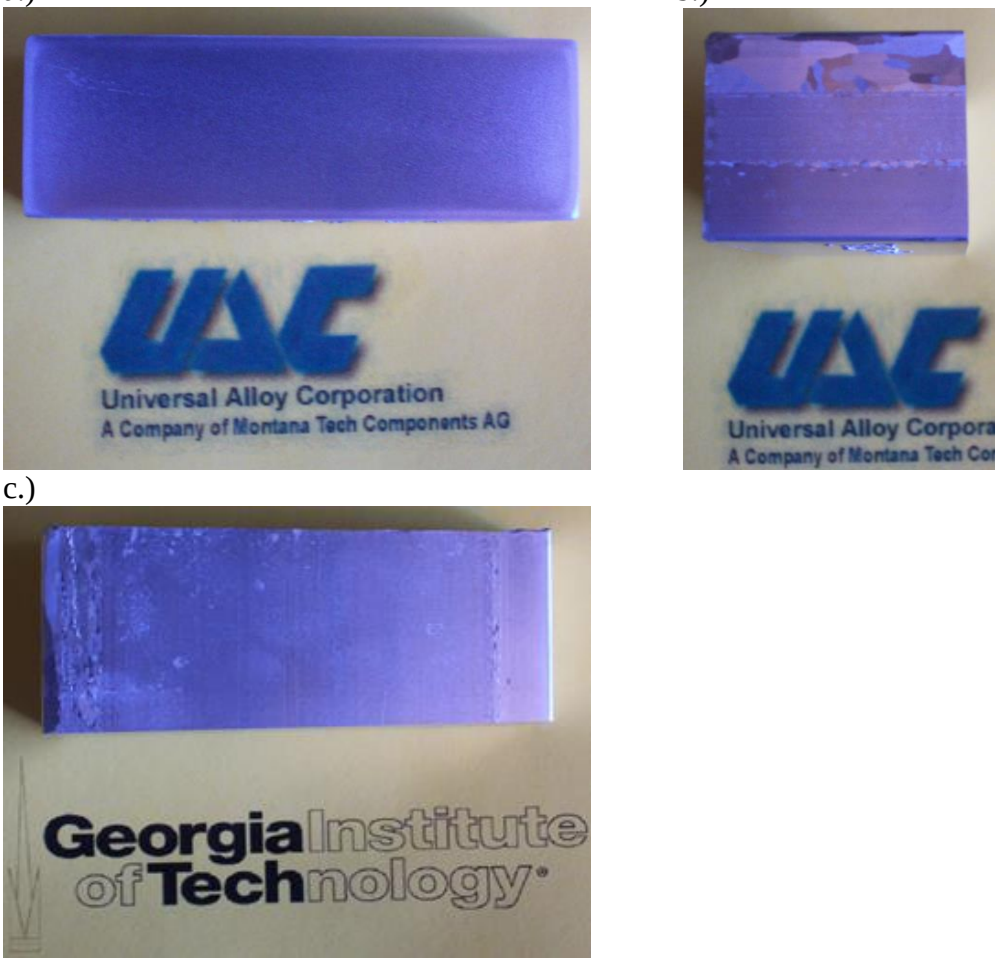


Figure 169 – *Macro etch of 7136 (caustic solution followed by Nitric rinse): a.) LT-ST direction, b.) L-ST direction, c.) L-LT direction.*

a.)


b.)

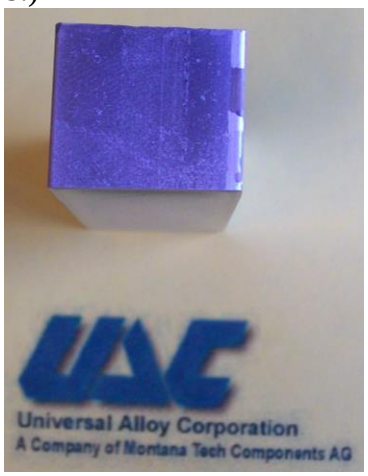


c.)


Figure 170 – *Macro etch of 7136 + Sn (caustic solution followed by Nitric rinse): a.) LT-ST direction, b.) L-ST direction, c.) L-LT direction.*

a.)

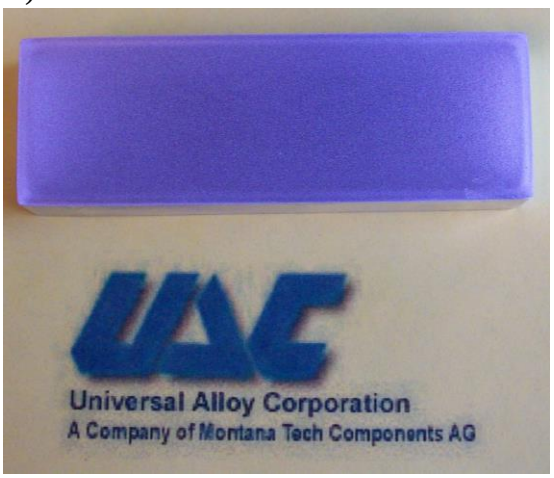


b.)


c.)


Figure 171 – *Macro etch of 7150 (caustic solution followed by Nitric rinse): a.) LT-ST direction, b.) L-ST direction, c.) L-LT direction.*

### 18.2 The Artificial Aging Behaviors of 7136, 7050, 7075, and 7249

Industrial aging practices for 7xxx-series aluminum alloys typically involve two steps: a low temperature step meant to precipitate out a fine dispersion of GP-II zones and η' and a high temperature second step meant to precipitate out η. Typically, the industrial tempers utilized in these products (i.e. – T6, T79, T76, etc.) all occur during the second step, although an "equivalent T6" can sometimes be reached using a single step aging curve (it is equivalent because it is usually within standard error of the true T6 temper).

A common first step aging temperature is 120°C (250°F) due to curve's "logarithmic nature." Figure 172 displays Rockwell hardness (B-scale) for 7136, 7050, 7075, and 7249 aged at 120°C for up to 24 hours. There appears to be a slight dip in hardness around 4-8 hours for each alloy, which most likely corresponds to a transformation temperature (i.e. – VRC → GP-II zones, GP-I reversion, etc.). Likewise, Table 30 displays conductivity data (%IACS) for the alloys during the same aging cycle.

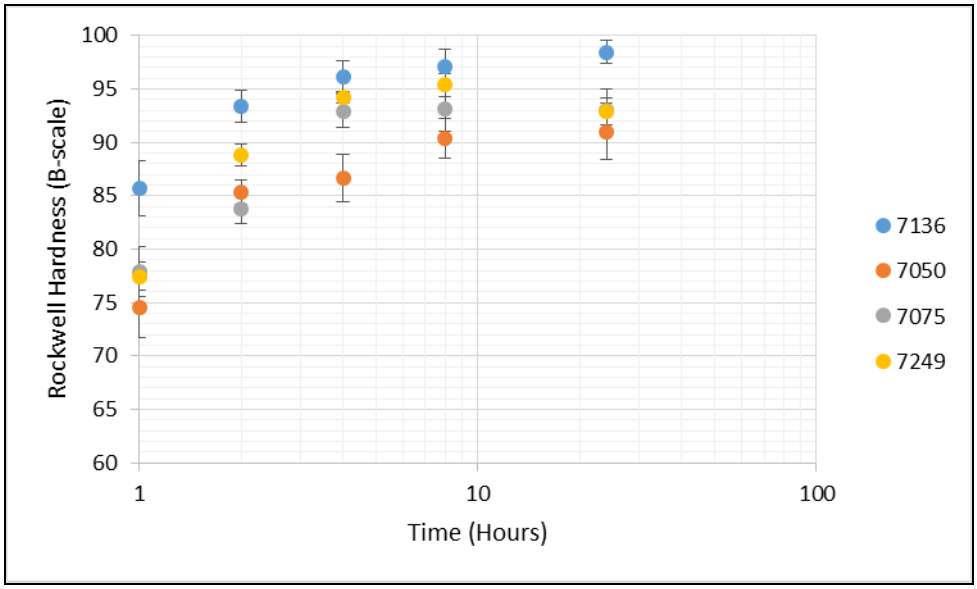


Figure 172 – *Rockwell hardness (B-scale) versus artificial aging time (hours) for various alloys aged at 120°C (250°F).*

Table 30 – *Select conductivity measurements (%IACS) on 7136, 7050, 7075, and 7249 versus artificial aging time at 120°C (250°F).*

| Time (Hours) | 7136 | 7050 | 7075 | 7249 |
|---|---|---|---|---|
| 1 | 26.9 | 29.5 | 28.8 | 29.3 |
| 2 | 28.0 | 31.5 | 29.8 | 29.7 |
| 4 | 29.0 | 32.2 | 31.0 | 31.2 |
| 8 | 31.3 | 33.8 | 32.1 | 31.3 |
| 24 | 32.4 | 34.8 | 33.6 | 32.8 |

The first step AA cures for 7136 at 130°C (266°F) and 140°C (284°F) can be seen in Figures 173 and 174. The curves appear similar to the 120°C curves for 7136 and 7136+Sn indicating that the GP-zone solvus for these alloys is above 140°C. It should be

noted, however, that these curves do not display the dip in hardness seen in the 120°C curve.

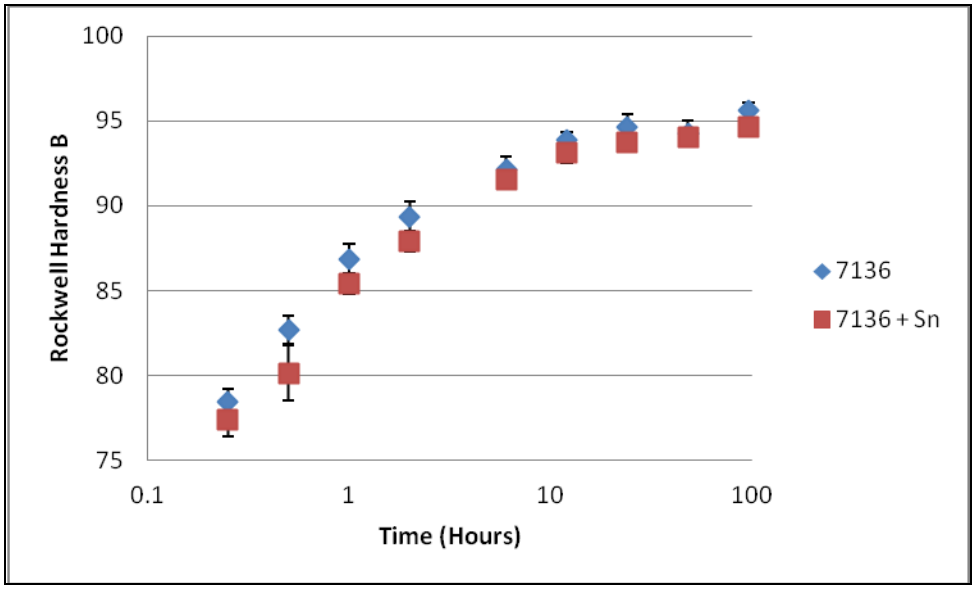


Figure 173 – *Artificial ageing behavior of 7136 and 7136+Sn at 130°C (266°F) showing Rockwell Hardness (B) vs. time (hours).*

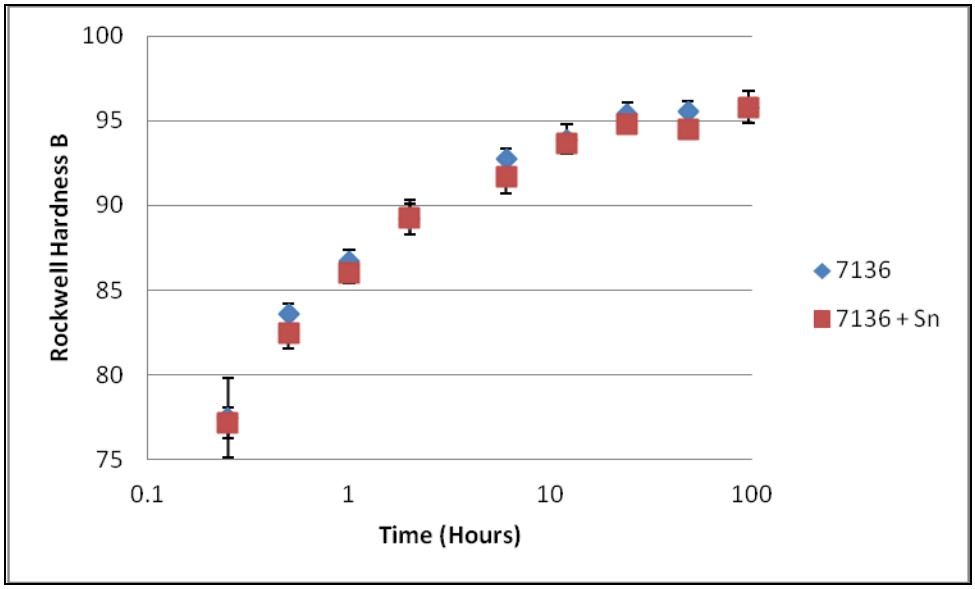


Figure 174 – *Artificial ageing behavior of 7136 and 7136+Sn at 140°C (284°F) showing Rockwell Hardness (B) vs. time (hours).*

After being artificially aged at 120°C for 24 hours, samples of 7136, 7050, 7075, and 7249 were artificially aged at 160°C (320°F) for up to 24 hours to incited over-aging behavior. The hardness measurements (HRB) can be seen in Figure 175 and select

conductivity measurements (%IACS) can be seen in Table 31. As previously stated, the concept of using an "equivalent" T6 in Part II is justified by Figure 175. It should also be noted that once the registered alloys begin to overage that a linear decreasing trend begins to occur for the artificial aging times covered, another assumption which was made in Part II while studying the GT experimental alloys.

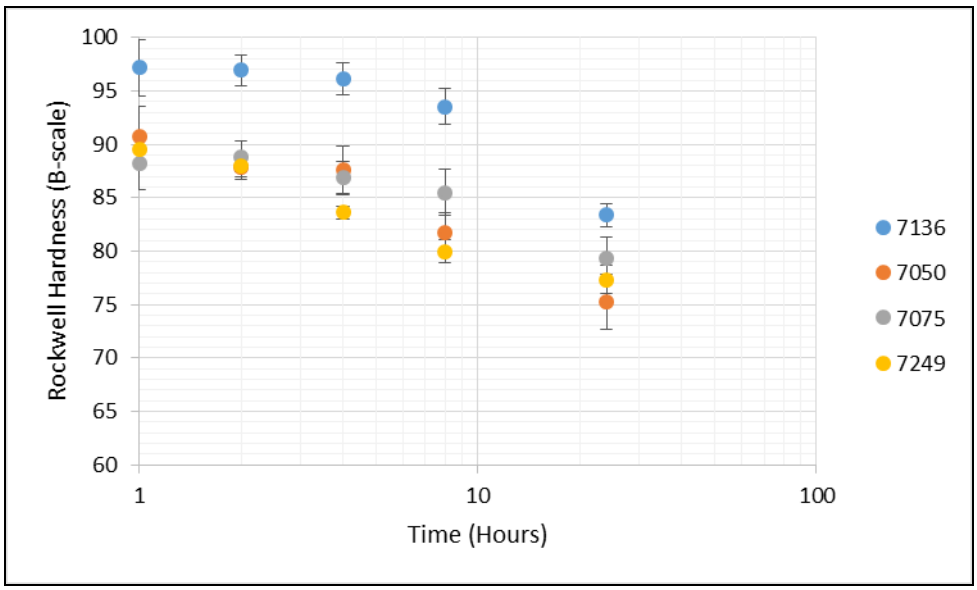


Figure 175 – *Rockwell hardness (B-scale) versus artificial aging time (hours) for various alloys aged at 160°C (320°F) after 24 hours at 120°C (250°F)..*

Table 31 – *Select conductivity measurements (%IACS) on 7136, 7050, 7075, and 7249 versus artificial aging time at 160°C (320°F).*

| Time (Hours) | 7136 | 7050 | 7075 | 7249 |
|---|---|---|---|---|
| 1 | 33.4 | 34.5 | 35.2 | 37.3 |
| 2 | 35.6 | 35.4 | 37.1 | 38.7 |
| 4 | 36.5 | 37.8 | 39.8 | 41.5 |
| 8 | 39.5 | 39.5 | 41.0 | 43.8 |
| 24 | 43.5 | 42.7 | 42.3 | 45.9 |

### 18.3 The Effects of Natural Aging

The effects of natural aging and its effect on the decomposition process was studied in detail in *Part II – The Quaternary Al-Zn-Mg-Cu System*. It was found that increased NA time was detrimental to varying degrees for high-Cu alloys, but beneficial for low-Cu alloys due to Cu's ability to stabilize GP-I zones. For this study, it was

determined to see if these effects still held true for registered 7xxx-series alloys, and to characterize the NA behavior of 7136, 7050, 7075, and 7249 using Rockwell hardness and conductivity measurements. 7136 was then furthered studied using DSC.

### 18.3.1 Hardness Results

Figure 176 displays Rockwell hardness versus NA time for 7136, 7050, 7075, and 7249. Table 32 displays select conductivity measurements on the alloys at various NA times. As can be seen from the Rockwell hardness and conductivity data, the appearance of VRC decreases the conductivity by increasing the lattice strain. At the same time, GP-I zones are forming, which are visible by the dips in the NA curves, causing the hardness to increase. It should be noted that these trends will be made easier to see in *Part III – Chapter 19 – The Development of True Aging Curves*.

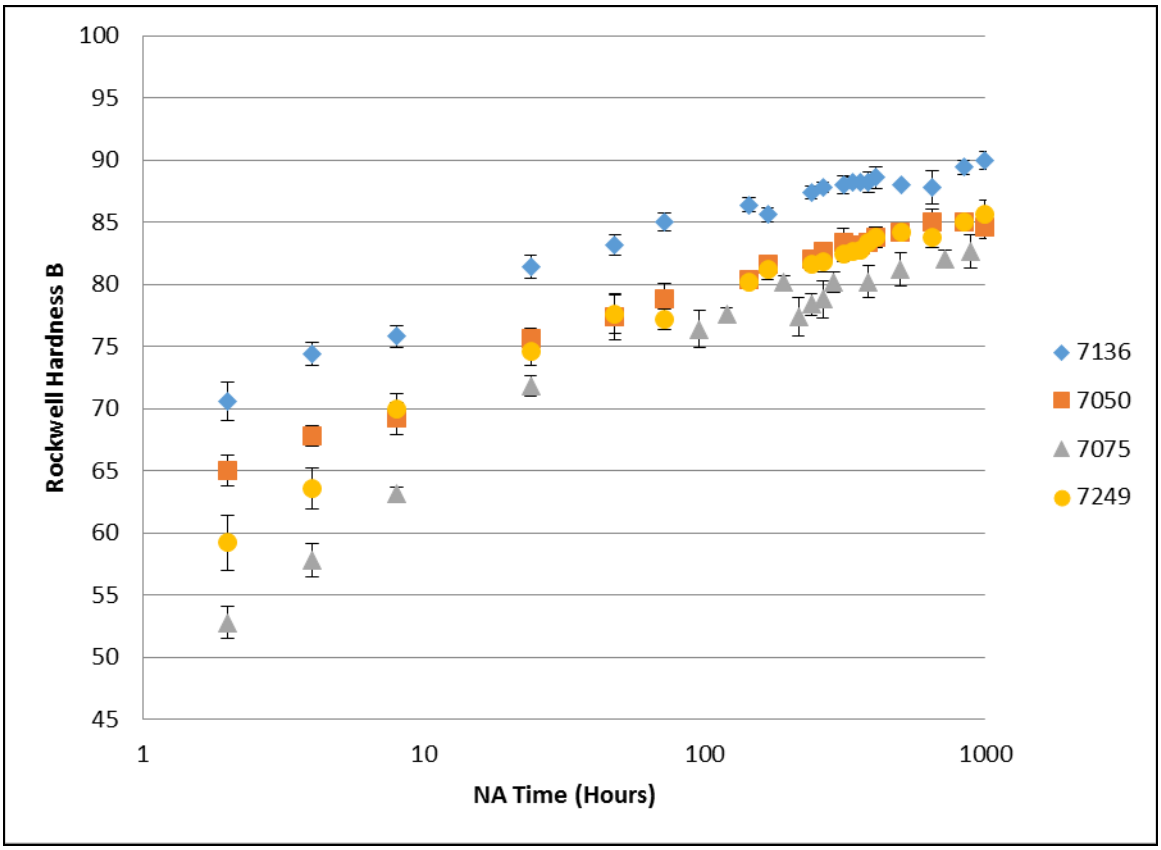


Figure 176 – *Rockwell hardness (B-scale) versus natural aging time for various 7xxx-series aluminum alloys.*

Table 32 – *Conductivity (%IACS) versus natural aging time for various 7xxx-series aluminum alloys.*

| NA Time (Hrs) | 7136 | 7050 | 7075 | 7249 |
|---|---|---|---|---|
| 0 | 28.9 | 29.8 | 32.5 | 31.4 |
| 2 | 27.9 | 28.6 | 31.1 | 30.0 |
| 4 | 27.3 | 28.5 | 30.6 | 29.5 |
| 8 | 26.9 | 28.4 | 29.5 | 28.6 |
| 24 | 26.4 | 27.6 | 28.4 | 28.1 |
| 48 | 26.1 | 27.2 | 28.2 | 27.8 |
| 72 | 26.1 | 27.2 | 28.0 | 27.7 |
| 144 | 26.1 | 27.1 | 28.0 | 27.7 |
| 240 | 26.1 | 27.0 | 28.0 | 27.7 |
| 408 | 26.1 | 27.1 | 27.7 | 27.7 |
| 504 | 26.0 | 26.9 | 27.9 | 27.6 |
| 648 | 26.2 | 27.1 | 27.7 | 27.7 |
| 840 | 26.1 | 27.0 | 27.6 | 27.7 |
| 1000 | 26.0 | 26.9 | 27.6 | 27.7 |

As can be seen in Table 32, the conductivity drops rather quickly upon NA before leveling off, which is to be expected as vacancies begin to cluster in the lattice. It should also be noted that these early NA time correspond to the "dip" times seen in the high-Cu alloys in *Part II – Chapter 12 – The Effects of Natural Aging.* This appears to indicate the observed dips represent a GP-I/GP-II cross over point in which the vacancy concentration is too low for GP-II zones to readily form upon heating, but the NA time is not long enough to create a fine dispersion of GP-I zones either. However, more high-powered characterization studies (i.e. – HRTEM, SAXS, etc.) would be needed to completely validate this hypothesis.

In a manner similar to the experiments conducted on alloys GT1-8, the registered alloys were artificially aged to an equivalent T6 and a T73 temper following various natural aging times. One significant difference, however, was the registered alloys were allowed to NA for up to approximately 1000 hours instead of 96. The results of these tests can be seen in Figures 177 (7136), 178 (7050), 179 (7075), and 180 (7249).

Aluminum alloy 7136 (see Figure 177) appears to show a similar behavior to GT1 and 2 in that there appears to be a decrease in hardness with increased NA time in the T6

temper. This not surprising as 7136 has a similar Cu content and Zn:Mg ratio as GT1 and GT2. For 7136-T7, NA also appears to be detrimental to hardness, but the adverse effects of NA take longer to appear. This is likely due to GP-I zones becoming large enough to follow precipitation sequence P2 instead of P3 (see *Part I – Chapter 6 – The Precipitation Process*), or the ability of Zr-dispersoids to retain vacancies during the quench from SHT.

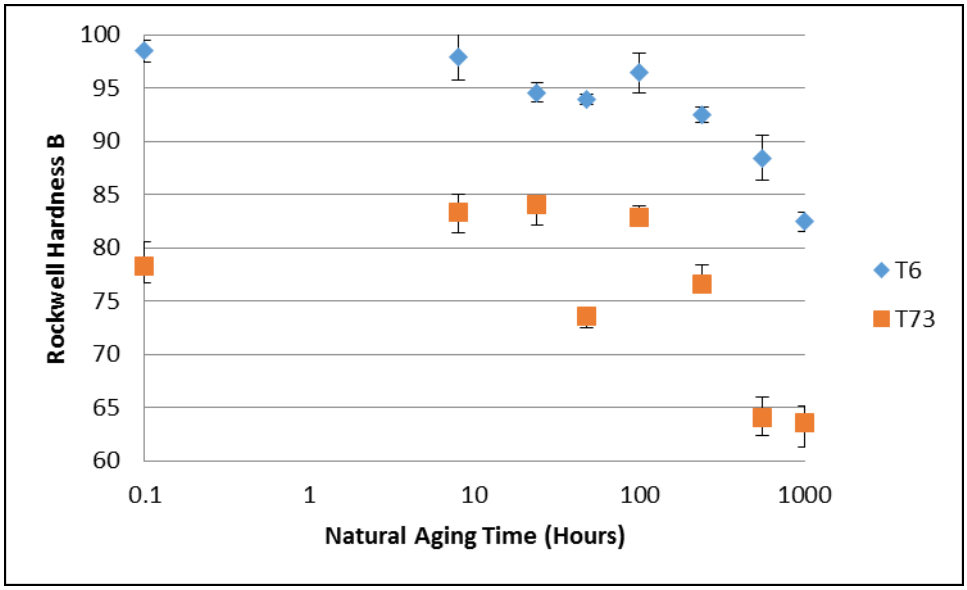


Figure 177 – *The effects of NA on the Rockwell hardness (B-scale) of 7136-T6 and –T73.*

Figure 178 displays the Rockwell hardness data versus natural aging time for aluminum alloy 7050 in the T6 and T7 temper. The high Cu content of 7050 would appear to suggest that natural aging should be detrimental to the properties of 7050-T6, however, no clear trend can be established from the data presented in Figure 178. A similar conclusion can be reached for 7050-T7. When the composition of AA7050 is compared to the experimental alloys, it becomes clear that the alloy should behave most like GT7, which it does.

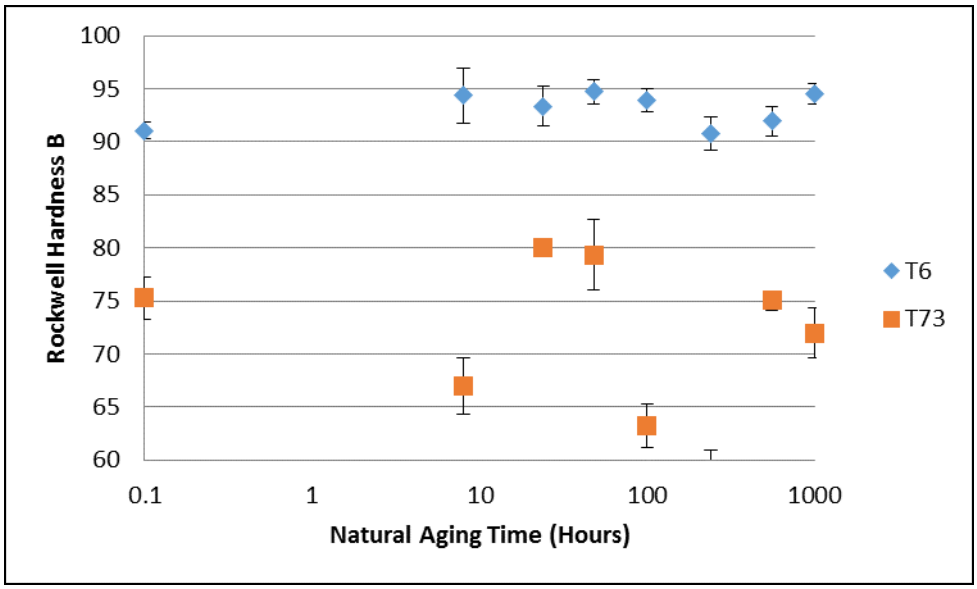


Figure 178 – *The effects of NA on the Rockwell hardness (B-scale) of 7050-T6 and –T73.*

Aluminum alloy 7075 has a Cu content between GT 2 and 4, and a Zn:Mg ratio between GT7 and 8. This would appear to suggest that the alloy should have a detrimental response to increased natural aging times, which is not entirely the case (see Figure 179). The hardness data on 7075-T6 and –T7 appears to suggest the mechanisms governing the precipitation process may have been altered or kinetically slowed down. It appears reasonable that the kinetics may have been altered at some point during the processing of the extrusion (ex. – SHT) because the observation could be made that the curves in Figure 179 appear similar to those presented by Hatch [1] except "stretched out" (i.e. – the dip described by Hatch occurs between 0 and 72 hours below upon which the hardness rises sharply and then begins to decrease with increased natural aging time). If the kinetics have been altered by some compositional or processing step, then the data presented in Figure 179 appears to validate the data on GT2.

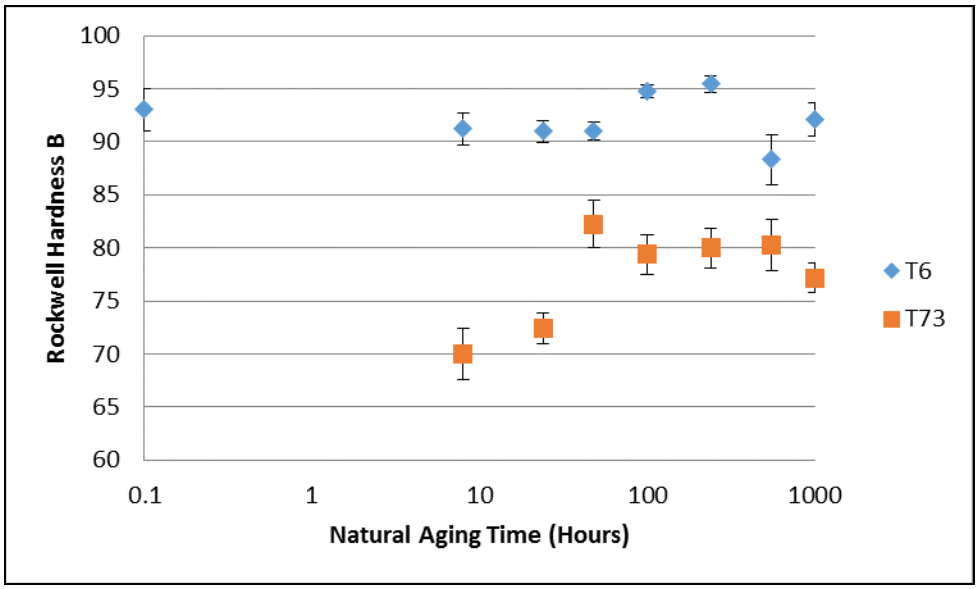


Figure 179 – *The effects of NA on the Rockwell hardness (B-scale) of 7075-T6 and –T73.*

Aluminum alloy 7249 should behave similarly to GT2, 3, 6, and 7 based on its Zn:Mg ratio and Cu content. The alloy appears to have a negative response to natural aging after 96 hours in both the T6 and the T7 temper, although it must be pointed out the T7 data contains a lot of scatter. AA7249 appears to validate the data gathered on GT3 suggesting that if GT3 were naturally aged longer than 96 hours that the hardness would also decrease in the T6 and T7 tempers with increased natural aging time.

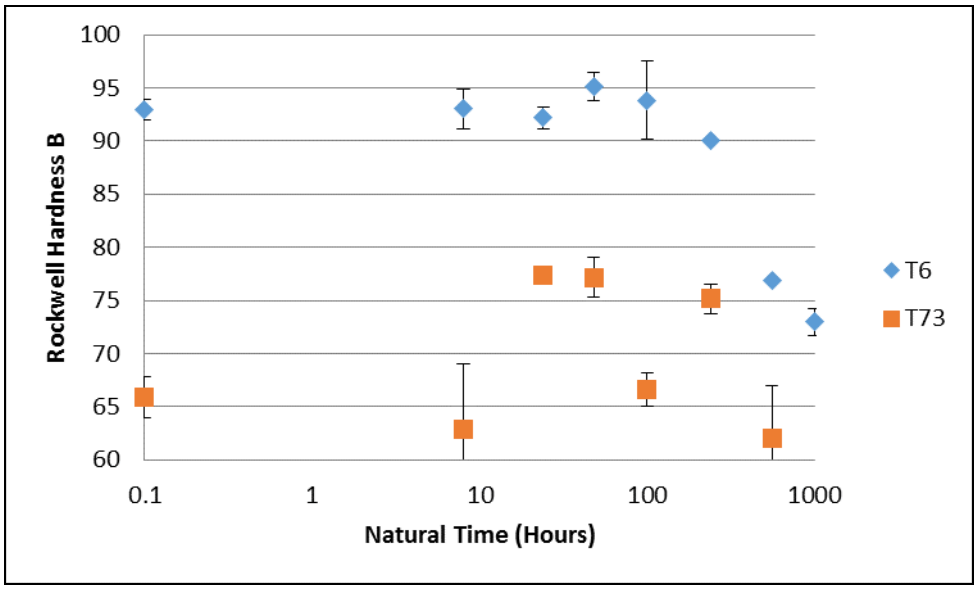


Figure 180 – *The effects of NA on the Rockwell hardness (B-scale) of 7249-T6 and –T73.*

### 18.3.2 AA7136 DSC Results

Figure 181 and Table 33 display a comparison of DSC scans ran on 7136 samples that were stretch 1% plastically before being NA for 2, 24, and 72 hours prior to being AA to a T6 temper.

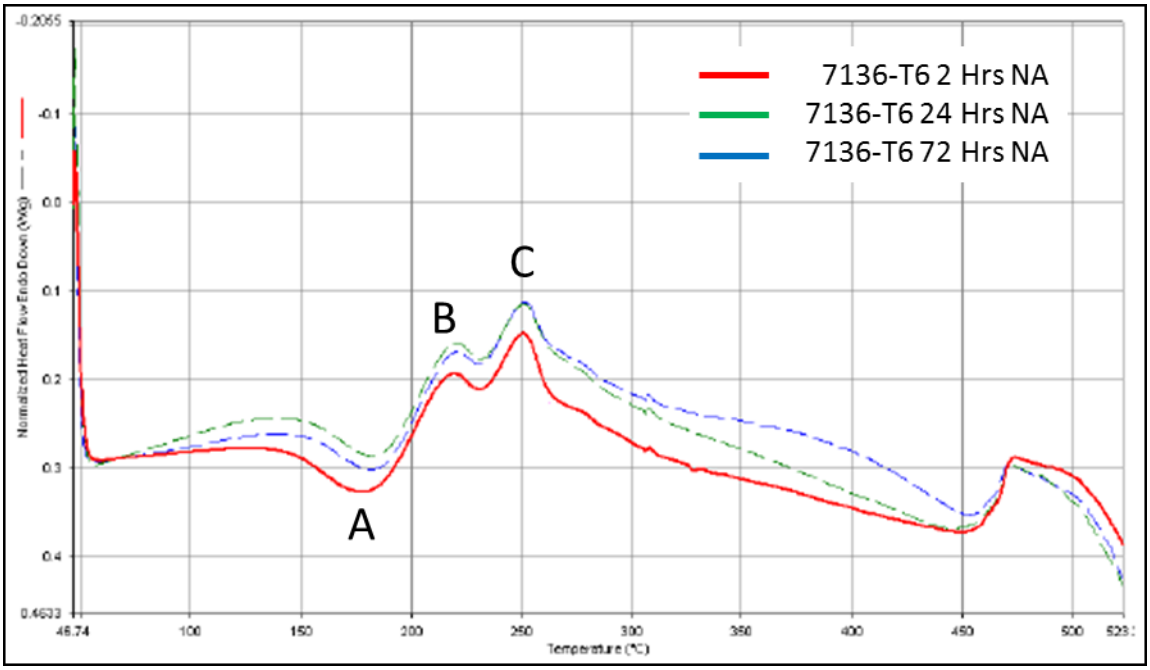


Figure 181 – *DSC scans of 7136 stretched 1% comparing the effect of NA time after stretching in the T6 temper. Peak A represents the reversion of GP zones, while peaks B and C represent the nucleation of η' and η respectively.*

Table 33 – *Comparison of DSC results on three 7136-T6 samples stretched 1% before being NA for various times.*

| NA Time | GP Dissolution Temp. | η' Nucleation Temp | Diff. Between GPD and η' Nucleation | η Nucleation Temp | Diff. Between GPD and η Nucleation |
|---|---|---|---|---|---|
| 2 Hrs. | 178°C | 219°C | 0.12 W/g | 251°C | 0.18 W/g |
| 24 Hrs. | 181°C | 222°C | 0.13 W/g | 252°C | 0.19 W/g |
| 72 Hrs | 184°C | 222°C | 0.13 W/g | 252°C | 0.17 W/g |

Upon inspection it can be seen that GP dissolution peak appears to increase in magnitude and temperature with increasing NA time after stretch. This increase in magnitude is due to an increase in GP-I zones due to the high Cu content of 7136. The DSC scans reveal that the η' and η peaks also increase in magnitude and temperature

between 2 and 24 hours NA, but do not increase further between 24 and 72 hours. It should be noted that as with GT1 a T-phase precipitation peak is present in Figure 181.

### 18.3.3 Conclusions

The natural aging behaviors of several registered 7xxx-series aluminum alloys were tested with respect to Rockwell hardness in a manner similar to the experiments performed on GT1-8. The results garnered appear to validate the results in *Part II – Chapter 12 – The Effects of Natural Aging* in that the trends observed therein also appear in the registered alloy system, although the kinetics of these various reactions appear altered, which could be the results of processing or dispersoid/vacancies interactions. DSC scans on 7136 result in similar to curves to those produced for GT1 and GT2 providing further proof the precipitation process is similar.

## 18.4 The Effects of Low Temperature Aging on 7136

The structure and nature of GP-II zones indicate a high dependence on the mobility of Mg to partially relieve the lattice strain caused by the clustering of Zn atoms. As previously discussed, Mg becomes mobile in Al around 100°C (i.e. – vacancy migration becomes rapid enough for the mass transport of Mg atoms), therefore it was decided to subjugate 7136-W and 7050-W extrusions to a series of low-temperature aging experiments. It should be noted that the low-temperature first step age will be referred to as a "pre-age" (PA) step from this point forth.

It should be noted that the concept of pre-aging had been previously patented by Staley and Sawtell [2] in 1984. However, it was decided to still include the data gathered on the PA material because it makes an important point in that once the precipitation process is fully understood it can then be manipulated.

### 18.4.1 Experimental Procedure

Extrusions of 7136 and 7050 were sectioned to from 1.5 in by 1.5 in hardness specimens. Following sectioning, the samples underwent AA practices at GT before

undergoing hardness and conductivity testing at UAC-Canton. The following AA practices were utilized:

12 hours at 121°C (250°F)
6 hours at 106°C (222°F) → 12 hours at 121°C (250°F)
12 hours at 106°C (222°F) → 12 hours at 121°C (250°F)
24 hours at 121°C (250°F)
6 hours at 106°C (222°F) → 24 hours at 121°C (250°F)
12 hours at 106°C (222°F) → 24 hours at 121°C (250°F)

It should be noted that every sample underwent the same NA time and every sample was aged to a T6 temper. Following testing of the T6 samples, it was determined to evaluate the effects of PA on the T7 temper using the following two AA practices:

6 hours at 106°C → 24 hours at 120°C → 9 hours at 160°C
24 hours at 120°C → 9 hours at 160°C

**18.4.2 Results**

The T6 Temper

The results of the hardness and conductivity tests for the T6 samples can be seen in Figures 182 (7050) and 183 (7136). It becomes apparent that the low temperature aging step promotes the growth of GP zones and therefore later the precipitation of a higher volume fraction of η' creating a stronger alloy at an equivalent conductivity to a non-PA sample. Therefore, Figures 182 and 183 provided definitive proof that an increased number of GP zones leads to an increase in the strength of a 7xxx-series alloy in the T6-temper.

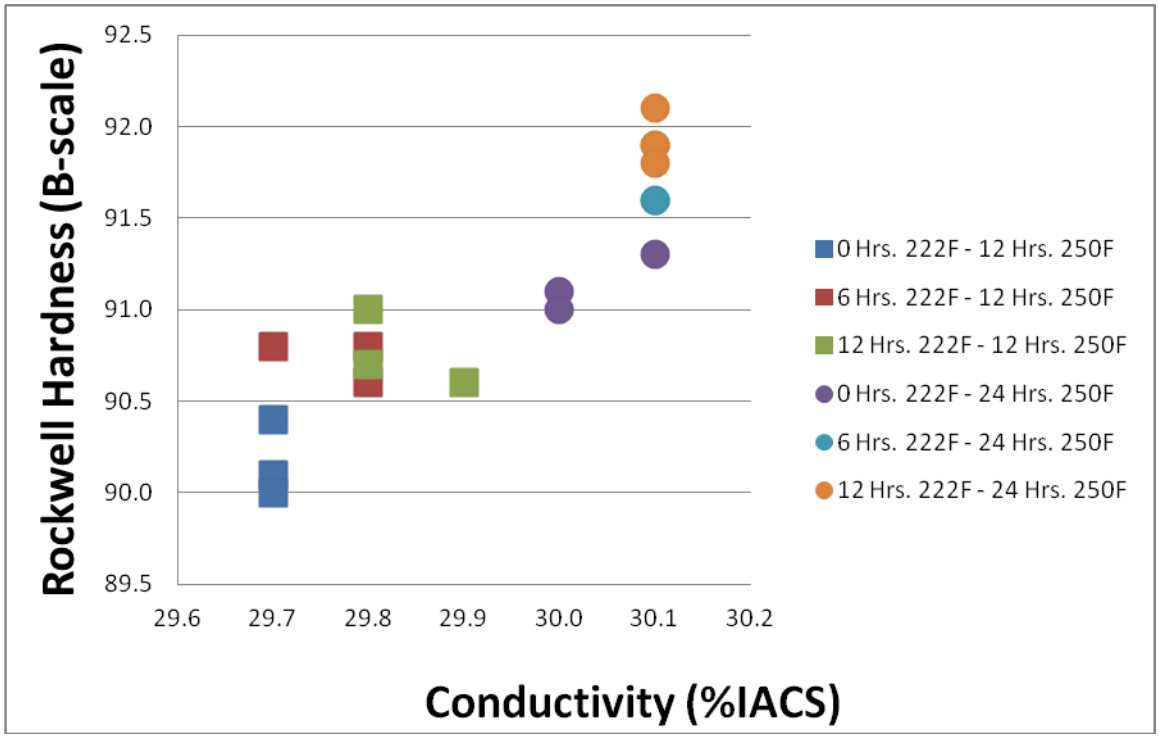


Figure 182 – *Rockwell hardness (B-scale) versus conductivity for 7050-T6511 showing the difference between various aging practices.*

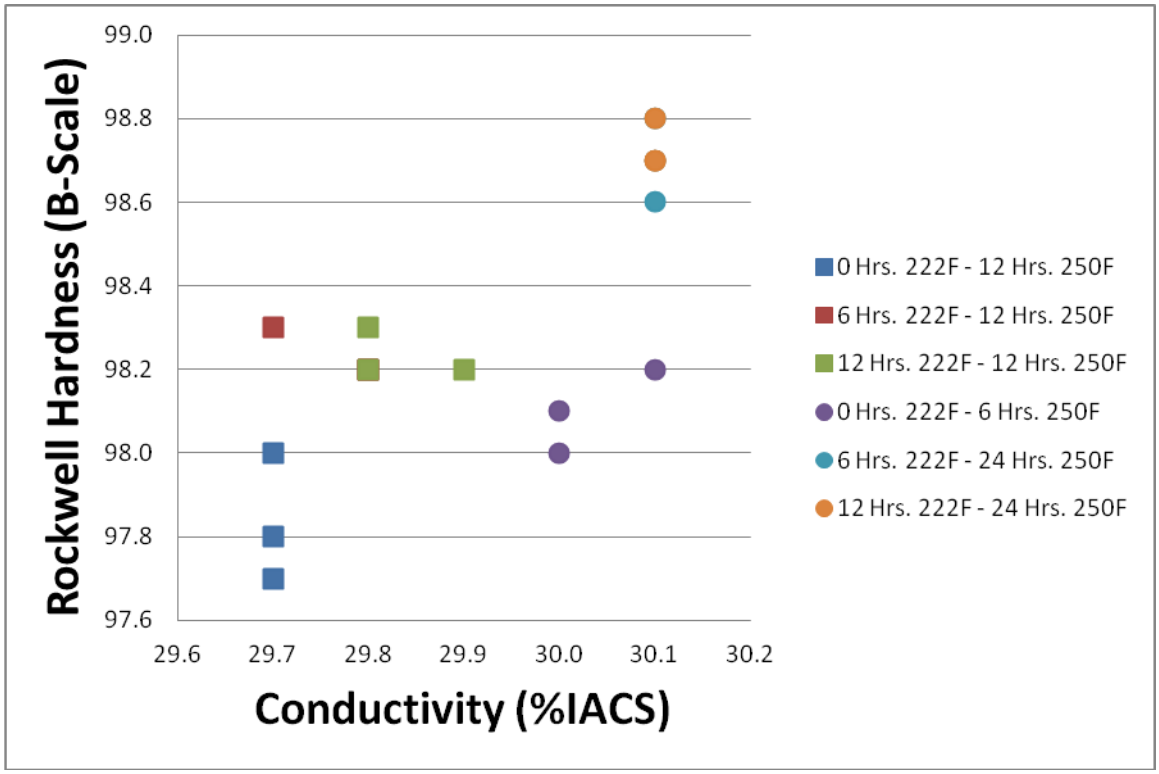


Figure 183 – *Rockwell hardness (B-scale) versus conductivity for 7136-T6511 showing the difference between various aging practices.*

The T7 Temper

The results of the T7 temper tensile tests on 7050 can be seen in Figures 184 – 186. It is interesting to note that although there appears to be a peak difference between the two curves, they appear to follow a similar over-aging path indicating that the select precipitation of GP-II zones has little effect on the bulk precipitation of η. This could be due to the fact that η known to nucleate from numerous other phases, including GP-I zones, and directly from the solid solution whereas η' nucleates almost entirely on GP-II zones. The other possibility is that perhaps GP-II zones cannot nucleate readily at 106°C in 7050, meaning that the increase in strength seen in the T6 temper is the direct result of an increased number of GP-I zones alone.

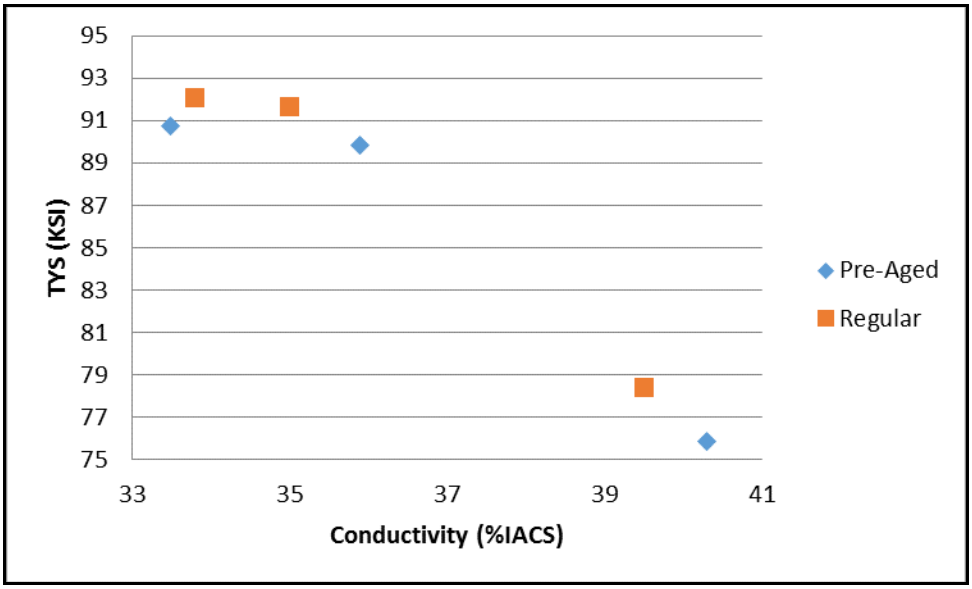


Figure 184 – *Tensile yield strength versus conductivity comparison of a three-step aging process (denoted "Pre-Aged") and a standard industrial aging process (denoted "Regular") for 7050.*

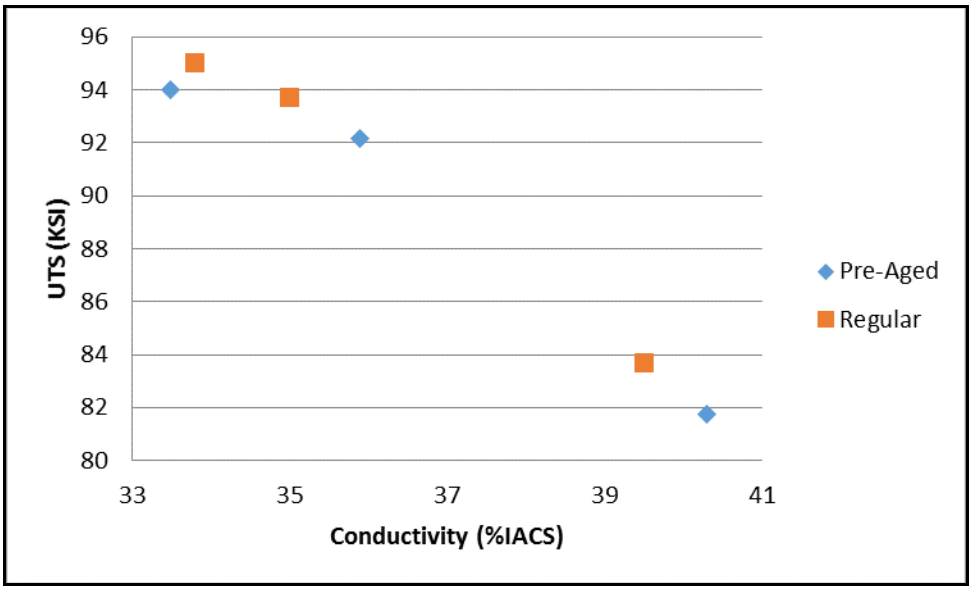


Figure 185 – *Ultimate tensile strength versus conductivity comparison of a three-step aging process (denoted "Pre-Aged") and a standard industrial aging process (denoted "Regular") for 7050.*

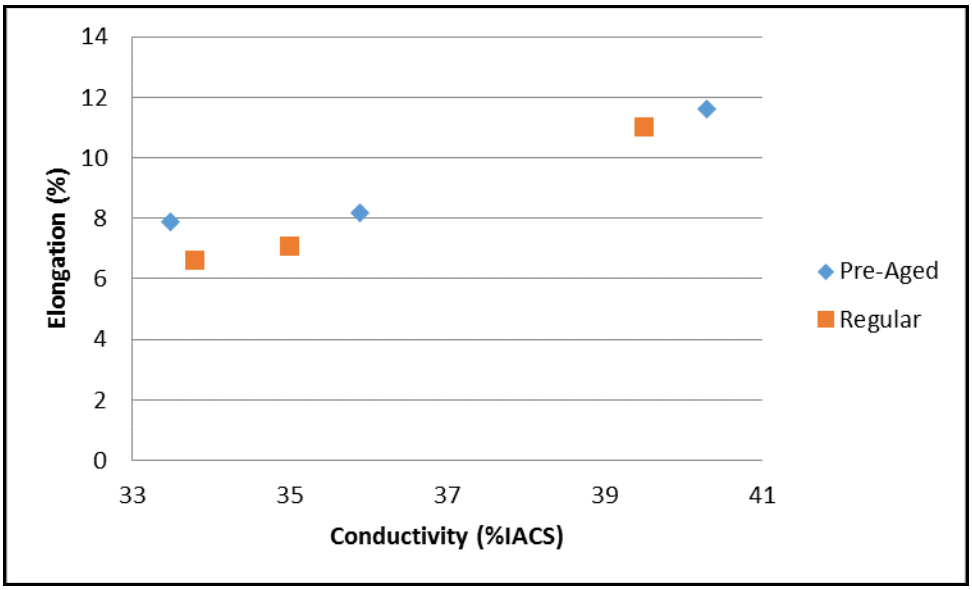


Figure 186 – *Elongation versus conductivity comparison of a three-step aging process (denoted "Pre-Aged") and a standard industrial process (denoted "Regular") for 7050.*

### 18.4.3 Conclusions

The concept of PA as outlined by Staley and Sawtell [2] appears to be of little sue for adequately quenched over-aged (i.e. – T7 products), however, it does appear to increase T6 properties significantly. This is could be due to the processes manipulation

of GP-I zones rather than GP-II zones as previously thought. Future work on the matter should focus on utilizing precise computer control furnaces as the temperatures in question are around the GP transition temperature. Therefore, even slight drops in temperature could results in invalid results.

### 18.5 The Effects of Stretching on the T7 Temper

The ability of η to precipitate directly upon dislocations (i.e. – P5), it was decided to study the effects of stretching on the T7 temper in 7136. It is general knowledge that stretching lowers the strength of 7xxx-series aluminum alloys in the T6 temper and increases the coarsening kinetics by the heterogeneous precipitation of large η precipitates, but the purpose of this study was to quantify these changes and see how they altered the precipitation process, especially the over-aging behavior of the material. Understanding the effects of stretching on the precipitation sequence in registered 7xxx-series aluminum alloys is an important and vital step in being able to translate the results from the experimental alloys, GT1-8, to commercial products.

Figure 187 displays Rockwell hardness data for 7136 for the second step of an industrial two-step artificial aging practice (i.e. – 120°C for 24 hours followed by aging at 160°C) after having been SHT and stretched for various amounts. It should be noted that the samples were NA for 72 hours prior to AA. The effect of stretching in Figure 187 is pronounced, especially with respect to the coarsening kinetics from T6 to T7. It is evident that by increasing the stretch percentage the alloys over-age more rapidly, but there is also a significant loss in strength. This loss of strength is due to the formation of η on dislocations introduced during the stretching process, which coarsen at a high rate due to their size. This in turn voids the matrix of the solute needed to precipitate out GP zones and η'. The changes in conductivity with time for 7136 can be seen in Figure 189.

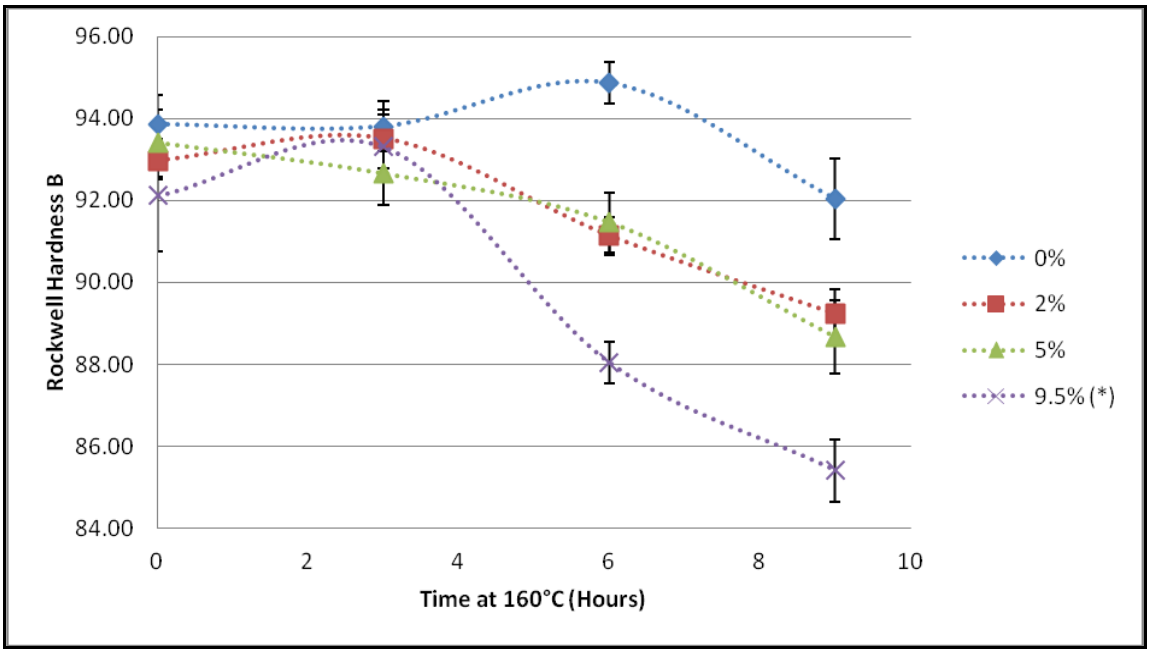


Figure 187 – *Artificial ageing behavior of 7136 showing the effect of stretching on hardness during the transition from T6 to T7.*

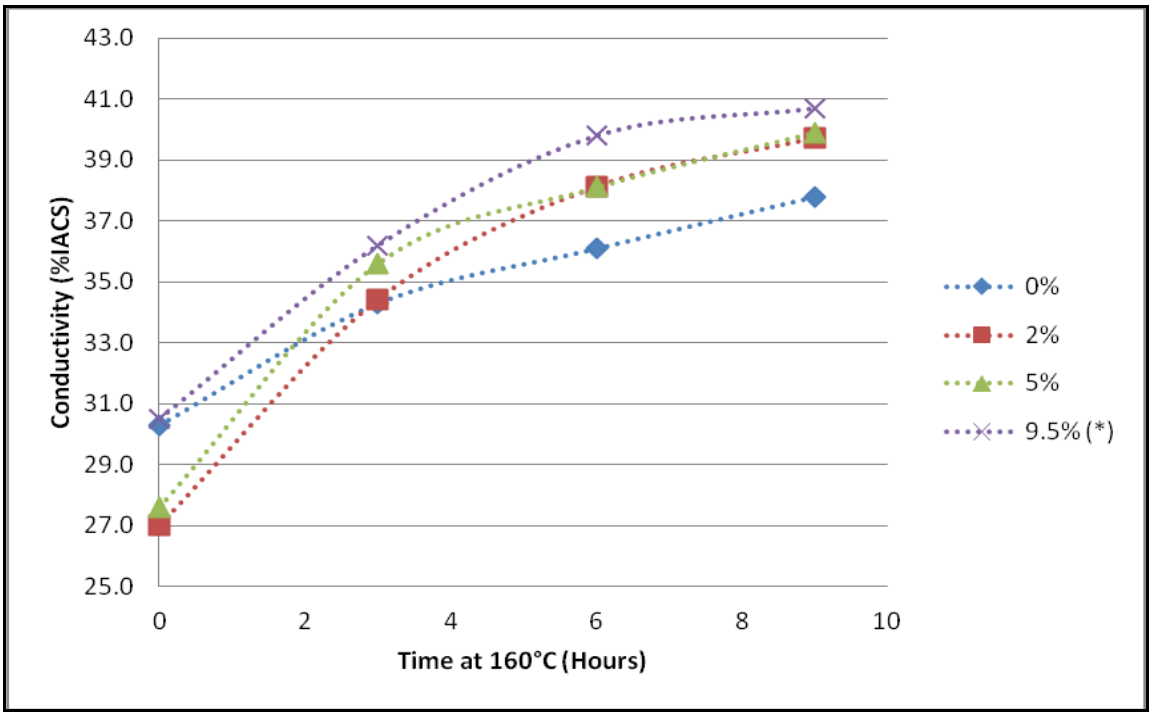


Figure 189 – *Artificial ageing behavior of 7136 showing the effect of stretching on conductivity during the transition from T6 to T7.*

Interestingly, there appears to be a "stretch-window" between 2 and 5% in which 7136 can be stretched without the loss of strength. While not easily explained, this is

important because one function of the stretch process is to elevate residual stretch left from the SHT process, which can cause distortion during the machining process. The fact this "window" appears suggests that 7136 can be stretched up to 5% if needed to elevate residual stress without a significant loss in strength.

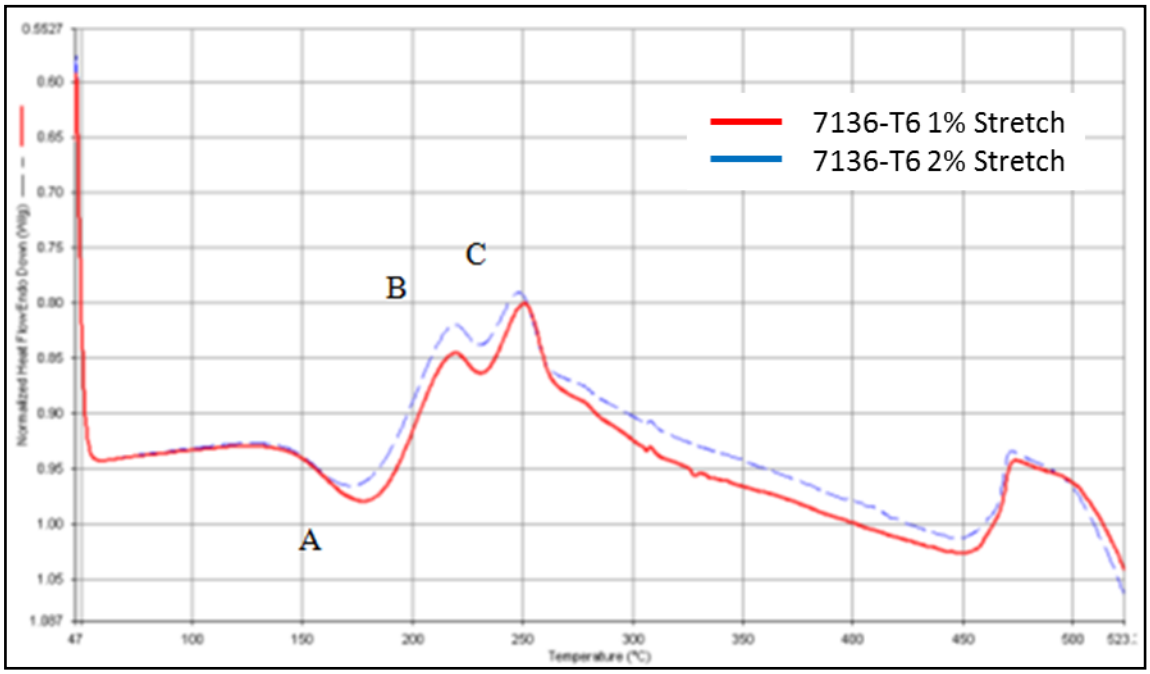


Figure 190 – *DSC scans of 7136-T6 stretched 1% and 2% before being naturally aged for 2 hours following SHT prior to undergoing artificial ageing. Peak A represents the reversion of GP zones, while peaks B and C represent the nucleation of η' and η respectively.*

In conjunction with the hardness tests, DSC scans (see Figure 190) were ran on 7136 samples stretched 1 and 2%. After stretching the samples were NA for 2 hours prior to AA. Upon inspection several key features can be seen regarding the dissolution of GP zones and the nucleation of η' and η:

- The peak of the GP zone dissolution (Peak A in Figure 53) is at a higher temperature for the material stretched 1% as opposed to 2%.
- The η' nucleation temperature does not appear to be effected by the stretch percentage, but the magnitude of the peak is affected with respect to the GP zone dissolution peak.
- The η nucleation temperature shifts with respect to the stretch percentage, but the magnitude of the peak with respect to the GP zone dissolution peak does not.

These results are presented below in Table 34 along with DSC scans ran on 7136-T6 0%. It should be noted that similar results appear when the samples were aged 72 hours naturally before being aged to a T6 temper.

Table 34 – *Comparison of DSC results on the three 7136-T6 samples NA for 2 hours. Note: all temperatures are ± 3°C.*

| Stretch | GP Dissolution Temp. | η' Nucleation Temp | Diff. Between GPD and η' Nucleation | η Nucleation Temp | Diff. Between GPD and η Nucleation |
|---|---|---|---|---|---|
| 0% | 186°C | 220°C | - | 251°C | - |
| 1% | 178°C | 219°C | 0.12 W/g | 251°C | 0.18W/g |
| 2% | 173°C | 219°C | 0.15 W/g | 248°C | 0.18W/g |

Upon inspection it appears that increasing the stretch percentage decreases the temperature of the GP zone dissolution peak (i.e. – GP zones are easier to dissolve/transform) and the η nucleation peak, while the η' appears unchanged with respect to stretch percentage. This result is very much expected as it is known that η readily nucleates on dislocations which are introduced during the stretching process. Therefore, an increase in stretching percentage should result in an increase in dislocations which should lead to an increase in η which is the observed trend.

These results give insight into how the trends established in Part II would translate under industrial conditions where sometimes processing steps like stretch percentage can vary. Future work should focus on studying a Cu-free alloy as well as an alloy with a low Zn:Mg ratio to see the effect of stretching on T-phase.

### 18.6 Summary

Various concepts revolving around natural and artificial aging of registered 7xxx-series aluminum alloys were studied and characterized. These concepts justified assumption made in Part II on alloys GT-8 as well as validated the garnered results (i.e. – showed the results held true for registered 7xxx-series alloys). Two step AA curves were

produced and the concept of low temperature pre-aging was explored. The effects of natural aging and stretching were also characterized.

## 18.7 References


[1] J. E. Hatch, *Aluminum: Properties and Physical Metallurgy*. ASM, 1984.

[2] J. T. Staley and R. R. Sawtell, "Aging process for 7000 series aluminum base alloys," US4,431,467, 1984.

# CHAPTER 19

# DEVELOPMENT OF TRUE AGING CURVES

The perplexing nature of the decomposition process in 7xxx-series alloys can often times be masked by time-at-temperature effects or completely neglected (as in the case of VRCs) when traditional aging curves are utilized. Therefore, a more "thermodynamic" aging curve has been developed in which time is omitted allowing for the contributions of VRCs, GP-I zones, GP-II zones, η', and η can be fully observed and quantified. These aging curves have been coined "True Aging Curves."

In order to elucidate the decomposition process of 7xxx-series alloys, the concept of a true aging curve was developed. Unlike typical aging curves where alloy properties are plotted against time, a true aging curve plots an alloy property such as tensile strength or hardness against conductivity. This allows for a more thermodynamic view of the decomposition process by eliminating time-at-temperature effects, and allows for the effects of various precipitates, especially VRCs, to be discernible in one plot. An example of a true aging curve can be seen in Figure 191. Figure 191 displays the aging behavior of a 7xxx-series alloy during a typical two-step age practice (120°C to 160°C) and the various precipitations responsible for the observed effects in each region.

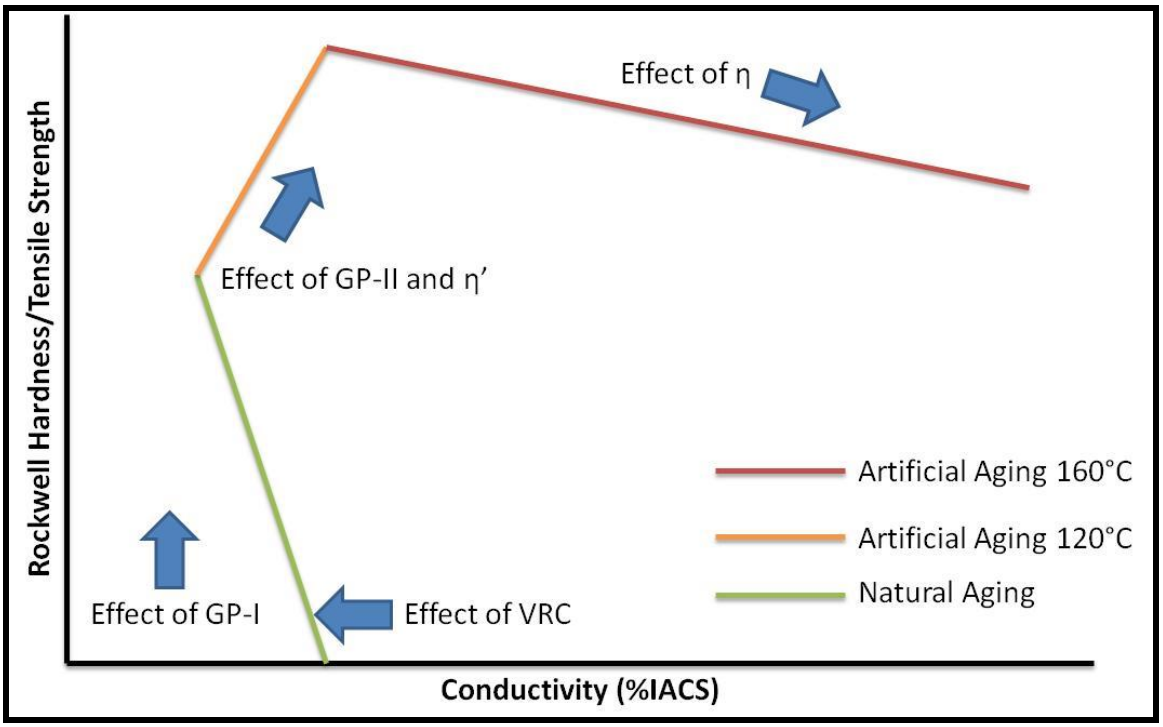


Figure 191 – *Schematic detailing the effects of various precipitates on a true aging curve under the stated two-step aging practice.*

The true aging curve in Figure 191 displays three distinct regions that directly correlate to the three steps, including natural aging, in the aging process. The first region (i.e. – the natural aging region) shows the formation of VRCs following quenching from solution heat treatment and the precipitation of GP-I zones. The decrease in conductivity is the aforementioned 'resistivity anomaly' and is due to an increase in lattice strain caused by the clustering of vacancies. The increase in hardness/strength seen in this region is largely due to the formation of GP-I zones. Region 2 in Figure 191 (i.e. – 'artificial aging at 120°C') correlates to the precipitation of GP-II zones and their subsequent transformation to η'. It is important to note that the peak of this region represents the T6 temper. Likewise, region 3 (i.e. – 'artificial aging at 160°C') reveals the transition from T6 to T7, which correlates to the transformation of GP-I zones and η' into the equilibrium phase, η, and subsequent coarsening of the phase.

### 19.1 Experimental Procedure

Aluminum extrusions of 7050 and 7075 were provided by the UAC-Canton and acquired from other commercial sources. The nominal composition ranges of these alloys along with the main dispersoid forming elements can be seen in Table 35. The 7050 and 7075 extrusions were SHT at 477°C (890°F) and 466°C (870°F) respectively for 1 hour before being water quenched. The alloys were subsequently aged for various times before being subjected to a two-step artificial aging practice of 24 hours at 120°C (248°F) followed by aging at 160°C (320°F). It should be noted that in order to avoid any REX grain issues all measurements and samples were taken sub-surface, and that caustic macro-etches (20g sodium hydroxide per 100 mL distilled water) were used to determine the extent of recrystallization in the extrudes (see Figures 192 and 193).

Table 35 – *The nominal composition ranges in weight percent as well as the main dispersoid forming element for 7050 and 7075 as registered with the Aluminum Association* [1].

| Alloy | Zn | Mg | Cu | Dispersoid |
|---|---|---|---|---|
| **7050** | 5.7-6.7 | 1.9-2.6 | 2.0-2.6 | Zr |
| **7075** | 5.1-6.1 | 2.1-2.9 | 1.2-2.0 | Cr |

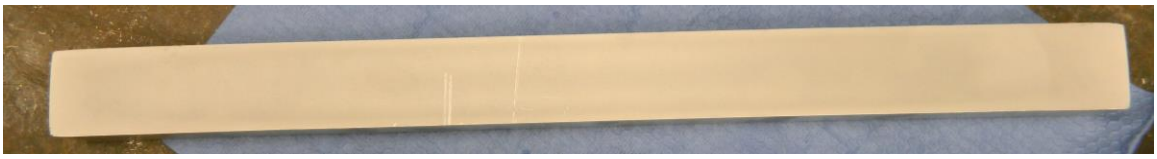

Figure 192 – *Macroscopic etch of the 7050 extrusion used (caustic solution).*

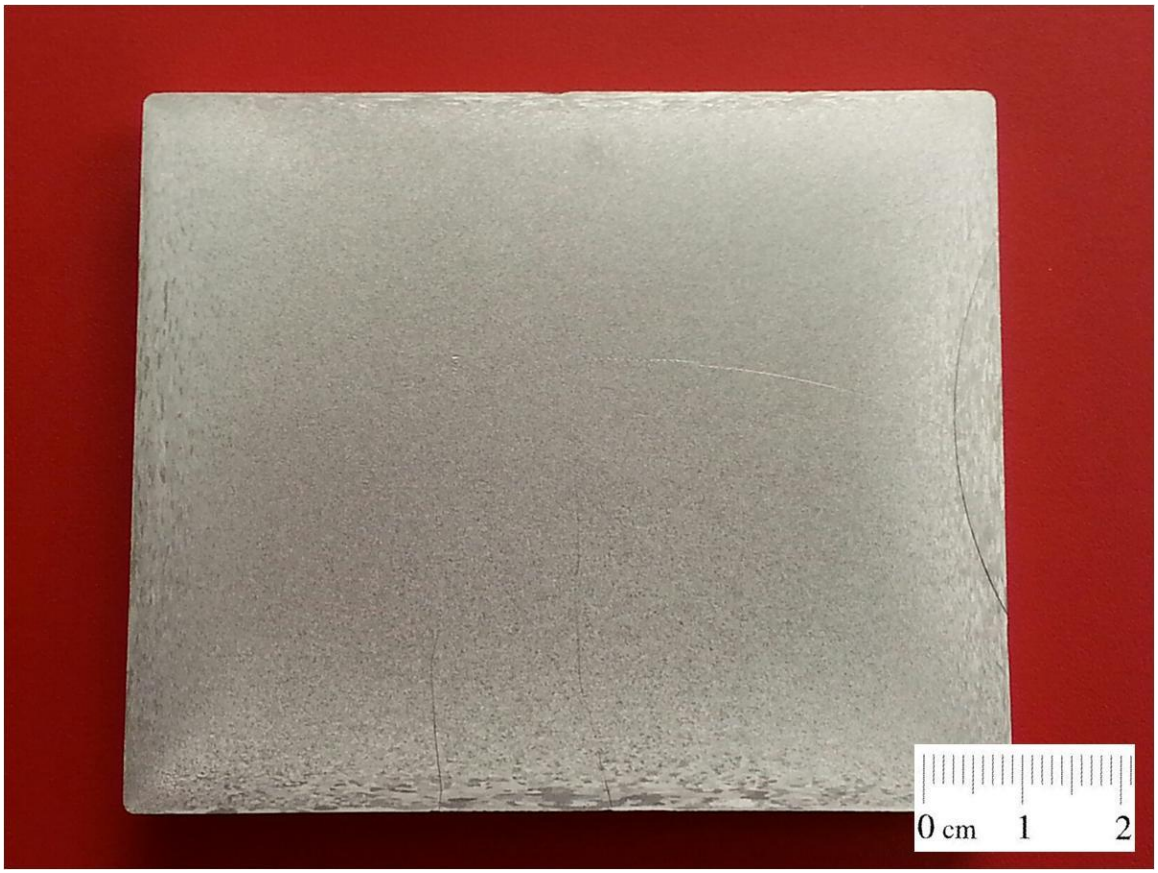

Figure 193 – *Macroscopic etch of the 7075 extrusion used (caustic solution).*

Rockwell hardness (B-scale), conductivity (%IACS), tensile testing, and differential scanning calorimetry were used to produce and test the "true" aging curves. It should be noted that UAC material was only used for Rockwell hardness measurements. All tensile specimens were taken on commercially obtained sources. Rockwell hardness measurements were carried out according to the ASTM E18-14 at GT [2]. Tensile tests were performed at UAC-Canton on a MTS Insight 150 kN load cell. Tensile specimens were taken in the L-direction (i.e. – the extrusion direction). Standard deviation was used to calculate all error bars for hardness, conductivity, and tensile tests.

The grain structure of the tested extrude regions were evaluated via optical microscopy. Micrographs were taken in the L-ST direction and etched using Barker's Reagent (1.8% fluoroboric acid, 98.2% distilled water) and a phosphoric acid solution (10% phosphoric acid, 90% distilled water).

## 19.2 True Aging Curve Development

### 19.2.1 Microstructure

Although the presented concept of a true aging curve does not attempt to correlate texture to an alloy's mechanical properties, micrographs of the extrusions are requisite to ensure the tested material is void of any recrystallized grains, which could introduce unnecessary scatter into the results. Micrographs were taken at the testing location in the L-ST direction and can be seen in Figure 194 (7050) and Figure 195 (7075). The micrographs reveal a fibrous, un-recrystallized microstructure typical of extruded aluminum products.

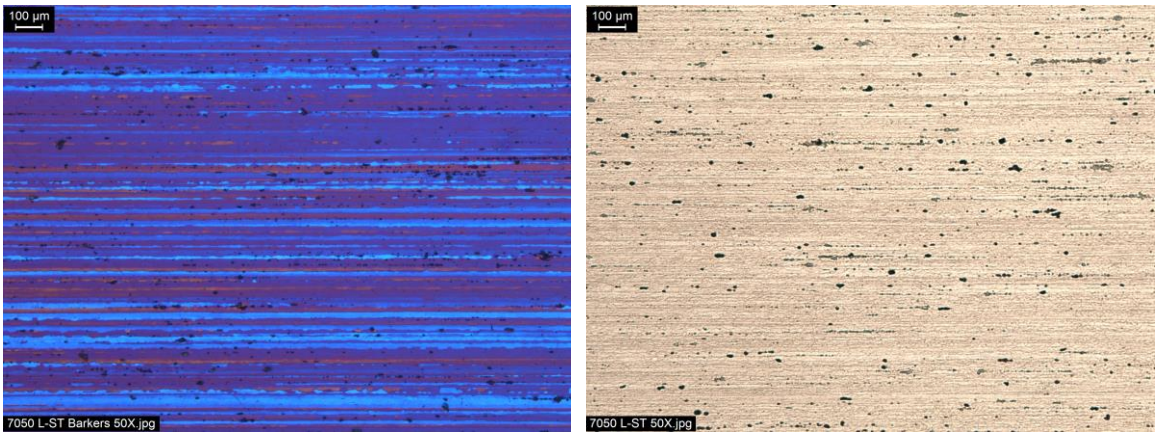


Figure 194 – *Micrographs of the 7050 extrusion (L-ST direction) used: Left.) Barker's Reagent, Right.) Phosphoric Acid Solution.*

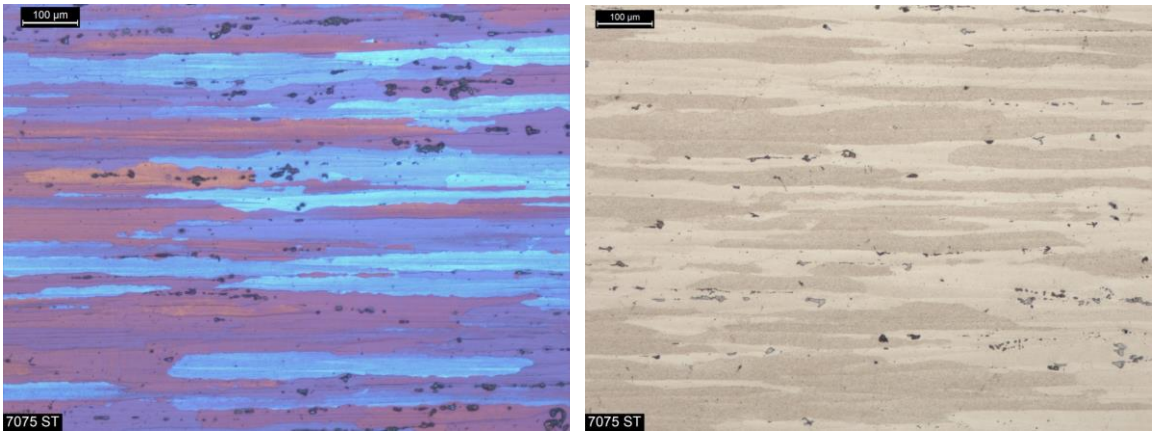


Figure 195 – *Micrographs of the 7075 extrusion (L-ST direction) used: Left.) Barker's Reagent, Right.) Phosphoric Acid Solution.*

### 19.2.2 Rockwell Hardness and Conductivity

Rockwell hardness (B-scale) aging curves for 7050 during the three aging steps (i.e. – natural aging, 120°C, and 160°C) are presented in Figure 196. A true aging curve for 7050 aged using a similar aging practice can be seen in Figure 197. Likewise, Figures 198 and 199 display the hardness data for 7075 accumulated during this study.

a.)

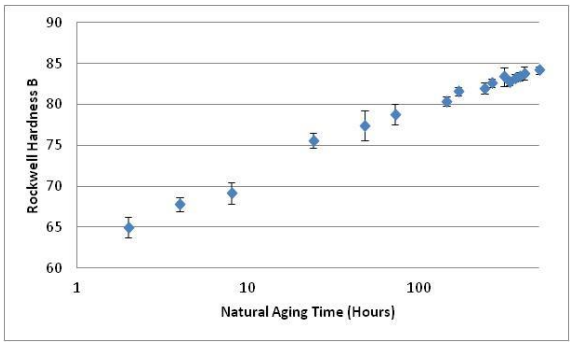


b.)

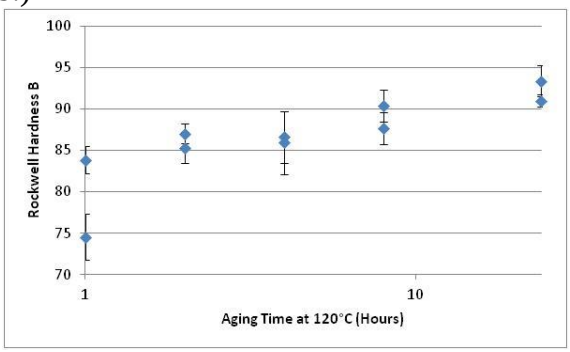


c.)

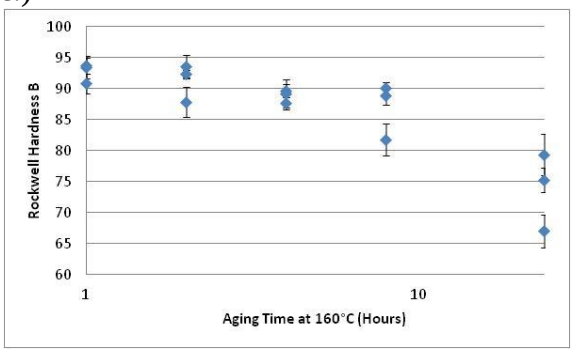


Figure 196 – *Traditional Rockwell hardness (B-scale) aging curves for 7050 along a two-step artificial aging cycle, 120°C → 160°C: a.) natural aging, b.) aging at 120°C after 24 hours of NA, c.) aging at 160°C after 24 hours of artificial aging at 120°C.*

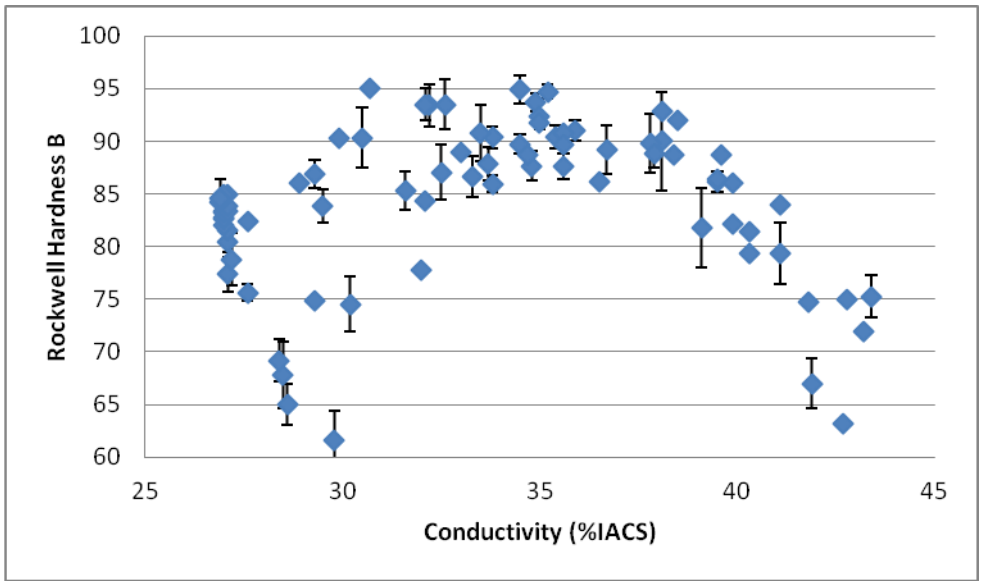


Figure 197 – *Rockwell hardness (B-scale) true aging curve for 7050 along a two-step artificial aging cycle, 120°C → 160°C. Note – in order to capture the effects of VRC formation, the specimens were NA for 500 hours.*

a.)

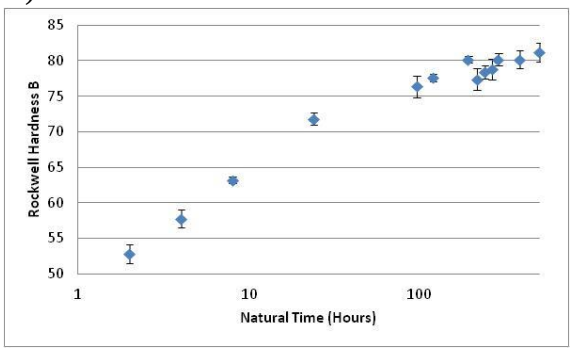


b.)

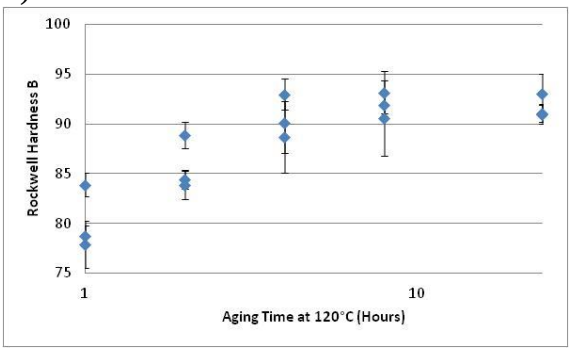


c.)

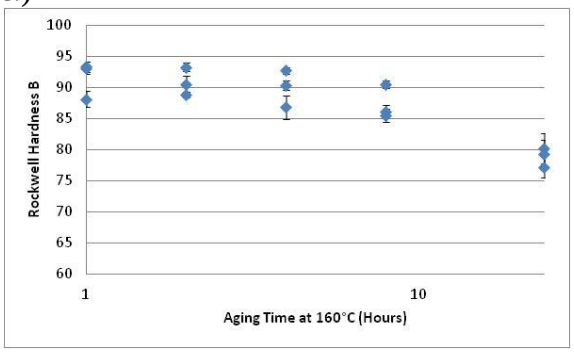


Figure 198 – *Traditional Rockwell hardness (B-scale) aging curves for 7075 along a two-step artificial aging cycle, 120°C → 160°C: a.) natural aging, b.) aging at 120°C after 24 hours of NA, c.) aging at 160°C after 24 hours of artificial aging at 120°C.*

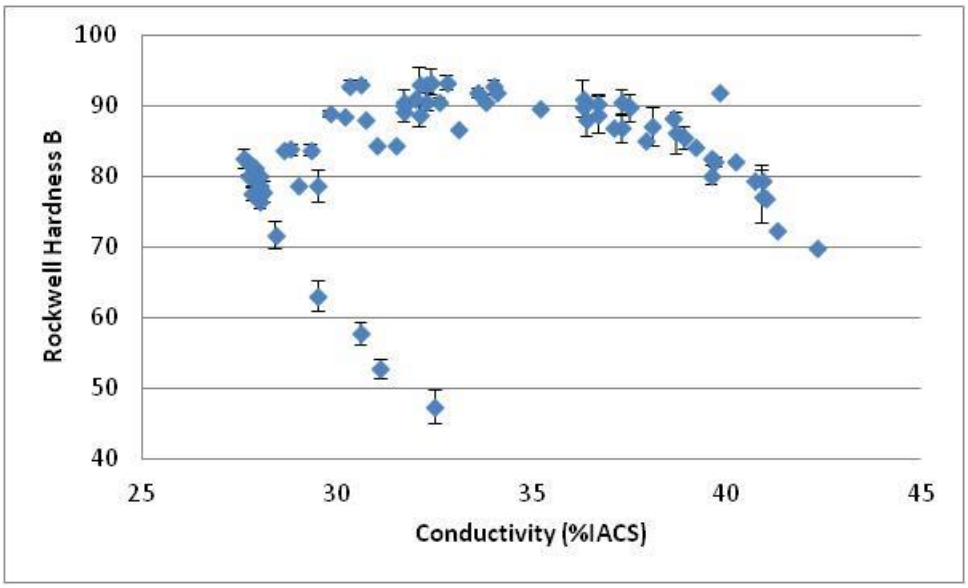


Figure 199 – *Rockwell hardness (B-scale) true aging curve for 7075 along a two-step artificial aging cycle, 120°C → 160°C. Note – in order to capture the effects of VRC formation, the specimens were NA for 500 hours.*

The hardness true aging curves presented in Figures 197 and 199 are analogous to the conceptual true aging curve presented in Figure 191. As with the conceptual curve both curves display three distinct regions: initially both curves display a decrease in conductivity and an increase in hardness during the NA step (i.e. – region 1), and upon AA the curves begin to increase in hardness until the T6 temper is reached (i.e. – region 2). After the T6 temper is reached, the curves display a drop in hardness with increasing conductivity as the samples approach a T7 temper (i.e. - region 3).

**19.2.3 Tensile Tests and Conductivity**

Tensile testing was performed on 7050 and 7075 extrusions obtained from commercial sources and can be seen in Figures 200 and 201, respectively. The curves appear very similar to the Rockwell hardness true ageing curves displayed in Figures 197 and 199.

Aluminum alloy 7050 obtained a maximum strength in region 1 (i.e. – the VRC/GP-I dominate region) of 58 ksi (TYS) at 26 %IACS. In region 2 (i.e. – the GP-

II/η' dominate region), the strength rose to 84 ksi (TYS) at 29 %IACS. Finally, the 7050 extrusion was shown to have a TYS if 80 ksi at 37 %IACS in the η dominate region 3.

Aluminum alloy 7075 obtained a maximum strength in region 1 of 46 ksi (TYS) at 27.5 %IACS. In region 2 the strength jumped to 72.7 ksi (TYS) at 30.9 %IACS. Finally, the 7075 extrusion tested was shown to have a TYS of 56.4 at 40.6 %IACS at the end of region 3.

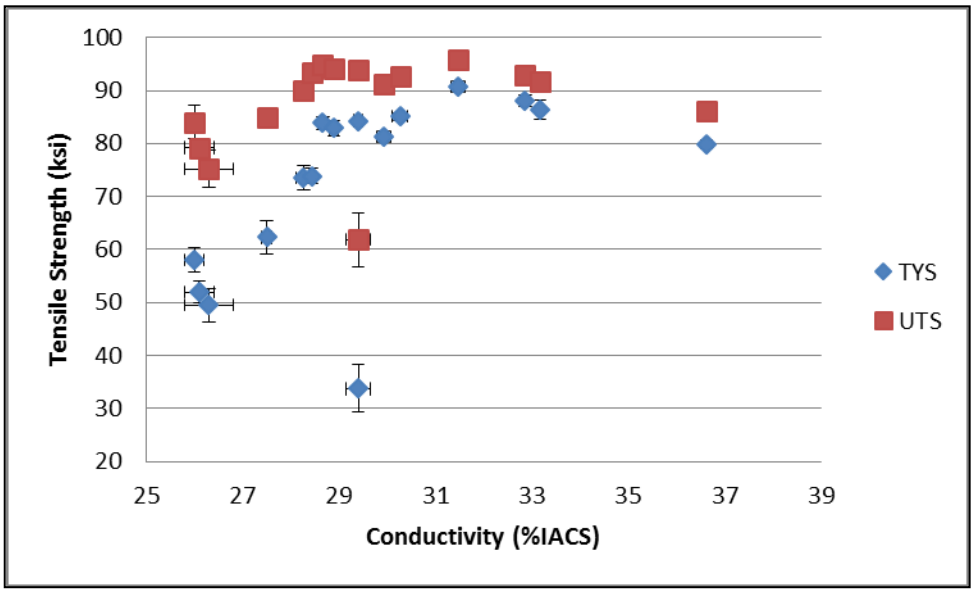


Figure 200 – *True ageing curve for aluminum alloy 7050 (tensile strength versus conductivity).*

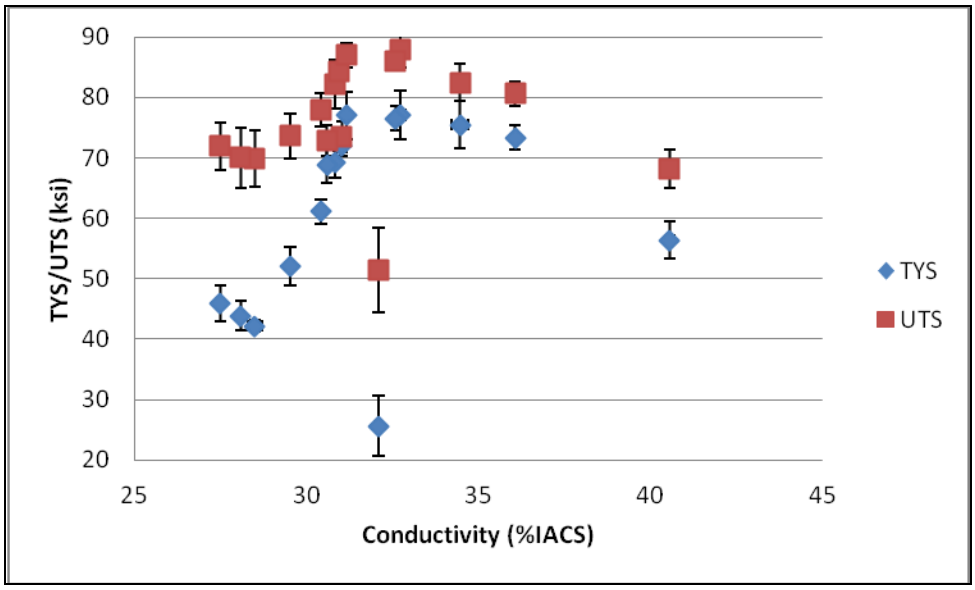


Figure 201 – *True ageing curve for aluminum alloy 7075 (tensile strength versus conductivity).*

The observation could be made that 7050 is more prone to form VRC than 7075 as it obtained a lower conductivity during the NA cycle (i.e. – region 1). This is to be expected as Zr-containing alloys is more prone to retain vacancies during the quench process than Cr-only containing alloys. This was shown in *Part III – Chapter 17 – Quench Sensitivity and C-Curve Development* and is considered "common knowledge" in the aluminum industry.

### 19.3 Discussion

The concept of a true aging curve offers insight into the exact precipitation mechanisms taking place during the various aging steps of 7xxx-series aluminum alloys, especially with respect to compositional variations as can be seen in Figure 202. As previously noted, aluminum alloy 7050 is more prone to form VRC than 7075 and therefore more likely to precipitate GP-II zones than 7075. It is interesting to note, however, that both alloys appear to have a slight increase in conductivity at the onset of aging with little to no hardness gain. This could be due to the rapid dissolution of VRCs or small GP-I zones back into the matrix, but as VRCs have not been observed experimentally, this hypothesis is unconfirmed at this time.

Aluminum alloy 7050 appears to display a GP-II zone to η' transformation in region 2 where there is a slight dip in strenght. Interstingly, aluminum alloy 7075 does not appear to show this transition zone.

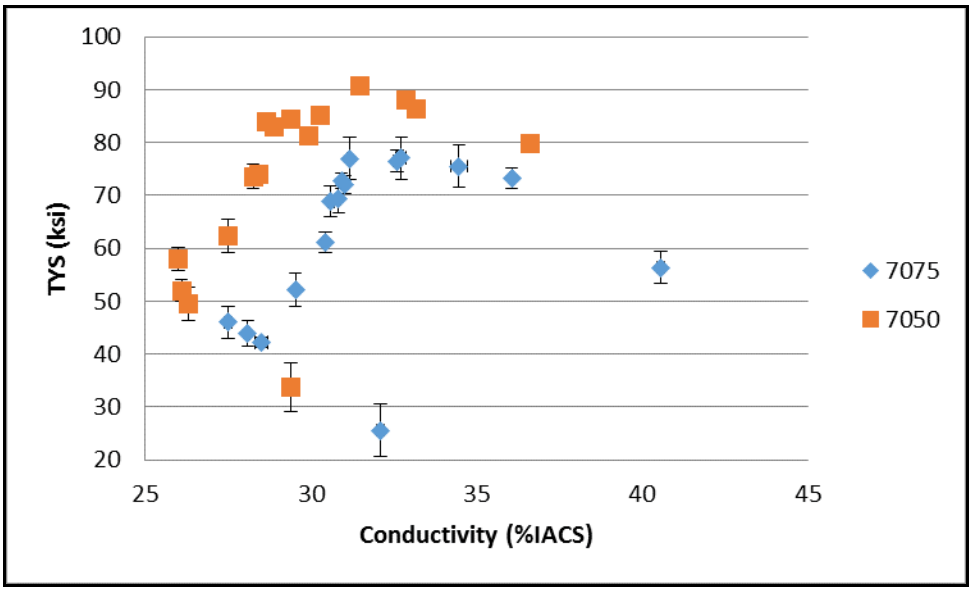


Figure 202 – *True aging curves for 7050 and 7075.*

Further developnment and characterization of true aging curves could offer insights into better ways to quantify the effects of alloying additions such as Ag or Sn, which are thought to retain vacacnies during the quenching process. True aging curves also allow for a thermodynamic view of system, which could be utilized to deteremine if different age practices/processing steps result in a similar products. This could allow for manufactorers to skirt around competitor patents by altering the process, but being able to prove the end-use conditions are equivalent.

## 19.4 Future Work

Future work on developing true aging curves should focus on expanding the concept to include kinetic effects as well as attempt to obtain corrosion resistance data for each region. Advanced characterization techniques could be used to correlation specific features observed in the true aging curves to precipitation events. For example, HRTEM microscopy could provide insight into possible transition zone from GP-II to η' seen in Figure 4-12. Such characterization techniques would also give insight into how

microstructural features such a precipitate size and distribution could affect the strength and conductivity relationship of an alloy.

## 19.5 Conclusions

The concept of a true ageing curve was presented utilizing aluminum alloys 7050 and 7075 procured from various sources. It was shown that true ageing curves can be developed using Rockwell hardness, tensile tests, and conductivity. The benefit of a true ageing curve is it allows for a complete view of the precipitation process as it allows for VRC, GP-zones, η', and η-phase precipitates to be seen and quantified.

Future studies should focus on developing the concept of a true ageing curve to directly relate to more properties including corrosion resistance and toughness. The ability to quantify these properties, along with hardness and tensile strength, in a non-kinetic fashion could be very valuable for alloy development in academic settings were many of the mass production process that affect artificial ageing are not present (ex. – rework).

## 19.6 References


[1] The Aluminum Association, *International Alloy Designations and Chemical Composition Limits for Wrought Aluminum and Wrought Aluminum Alloys*. Arlington, VA, 2009.

[2] ASTM, "E18-14: standard test methods for Rockwell hardness of metallic materials." pp. 1–38, 2014.

# APPENDIX A

# SOLID SOLUBILITY OF COMMON ALLOYING ELEMENTS IN ALUMINUM

The following table is a comprehensive list of the solid solubility of various elements in aluminum. It is important to note that for wrought products the amount of any alloying element is typically far below these compositional limits.

Table 36 – *Maximum solid solubility of elements in aluminum* [1]–[3].

| Element | Temperature (°C) | Temperature (°F) | wt.% | at.% |
|---|---|---|---|---|
| Beryllium (Be) | 644 | 1191 | 0.10 | - |
| Cadmium (Cd) | 649 | 1200 | 0.4 | 0.09 |
| Cobalt (Co) | 657 | 1215 | <0.02 | <0.01 |
| Copper (Cu) | 548 | 1018 | 5.65 | 2.40 |
| Chromium (Cr) | 661 | 1222 | 0.77 | 0.40 |
| Germanium (Ge) | 424 | 795 | 7.2 | 2.7 |
| Iron (Fe) | 655 | 1211 | 0.05 | 0.025 |
| Lithium (Li) | 600 | 1112 | 4.2 | 16.3 |
| Magnesium (Mg) | 450 | 842 | 17.4 | 18.5 |
| Manganese (Mn) | 658 | 1216 | 1.82 | 0.90 |
| Nickel (Ni) | 640 | 1184 | 0.04 | 0.02 |
| Silicon (Si) | 577 | 1071 | 1.65 | 1.59 |
| Silver (Ag) | 566 | 1051 | 55.6 | 23.8 |
| Tin (Sn) | 228 | 442 | ~0.06 | ~0.01 |
| Titanium (Ti) | 665 | 1229 | ~1.3 | ~0.74 |
| Vanadium (V) | 661 | 1222 | ~0.4 | ~0.21 |
| Zinc (Zn) | 443 | 829 | 82.8 | 66.4 |
| Zirconium (Zr) | 660.5 | 1221 | 0.28 | 0.08 |

## A.1 References


[1] I. J. Polmear, *Light Metals*. Arnold, 1995.

[2] J. Murray, A. Peruzzi, and J. P. Abriata, “Alloy Phase Diagrams,” in *ASM Handbook*, 1992, pp. 2.4–2.56.

[3] ASM, “Alloy Phase Diagrams,” in *ASM Handbook*, 2012.

# APPENDIX B

# COMMON ETCHANTS

The following is a table of etchants used in this work. It should be noted that prior to micro-etching samples were polished according the polishing procedure in *Part II – Chapter 9 – Materials and Experimental Procedures*. For macro-etching, a mill finish was utilized.

Table 37 – *Common micro-etchants* [1], [2]**.**

| Etchant Name | Composition | Procedure |
|---|---|---|
| Barker's Reagent | 98.2 mL distilled water<br>1.8 mL fluoroboric acid ($H_3OBF_4$) | 1. Electropolsih for 15s.<br>2. Etch for 45s. |
| Graph-Sargent's Reagent | 84 mL distilled water<br>16 mL nitric acid ($HNO_3$)<br>0.5 mL hydrofluoric acid (HF)<br>3 g chromium trioxide ($CrO_3$) | Immerse sample for 30s. |
| Keller's Reagent | 95 mL distilled water<br>2.5 mL nitric acid ($HNO_3$)<br>1.5 mL hydrogen chloride (HCl)<br>1.0 mL hydrofluoric acid (HF) | Immerse sample for 15s. |
| Phosphoric Acid | 90 mL distilled water<br>10 mL phosphoric acid ($H_3PO_4$) | Immerse samples for 20m. |
| Weck's Reagent | 100 mL distilled water<br>4 g potassium permanganate ($KMnO_4$)<br>1 g sodium hydroxide (NaOH) | Immerse sample for 20s. |

Table 38 – *Common macro-etchants* [1], [2]**.**

| Etchant Name | Composition | Procedure |
|---|---|---|
| Caustic | 100 mL distilled water<br>20 g sodium hydroxide (NaOH) | 1. Etch in caustic for 10m.<br>2. Clean in 50% nitric solution for 5m. |
| Casutic (alt) | 93 mL distilled water<br>5 g sodium fluoride (NaF)<br>2 g sodium hydroxide (NaOH) | 1. Etch in caustic for 10m.<br>2. Clean in 50% nitric solution for 5m. |

## B.1 References


[1] G. Petzow, *Metallographic Etching*, 2nd ed. Materials Park: ASM International, 1999.

[2] K. Mills, J. R. Davis, J. D. Destefani, D. A. Dieterich, G. M. Crankovic, H. J. Frissell, D. M. Jenkins, W. H. Cubberly, R. L. Stedfeld, R. T. Kiepura, and B. R. Sanders, "Metallography and Microstructures," in *ASM Handbook*, 9th ed., Materials Park: ASM International, 2001.

# APPENDIX C

# SINGLE STEP AGING CURVES FOR GT1-8 WITH ERROR BARS

The following appendix displays single step aging curves for GT1-8 for various temperatures between 100°C and 200°C. The error bars present represent one standard deviation.

**GT1**

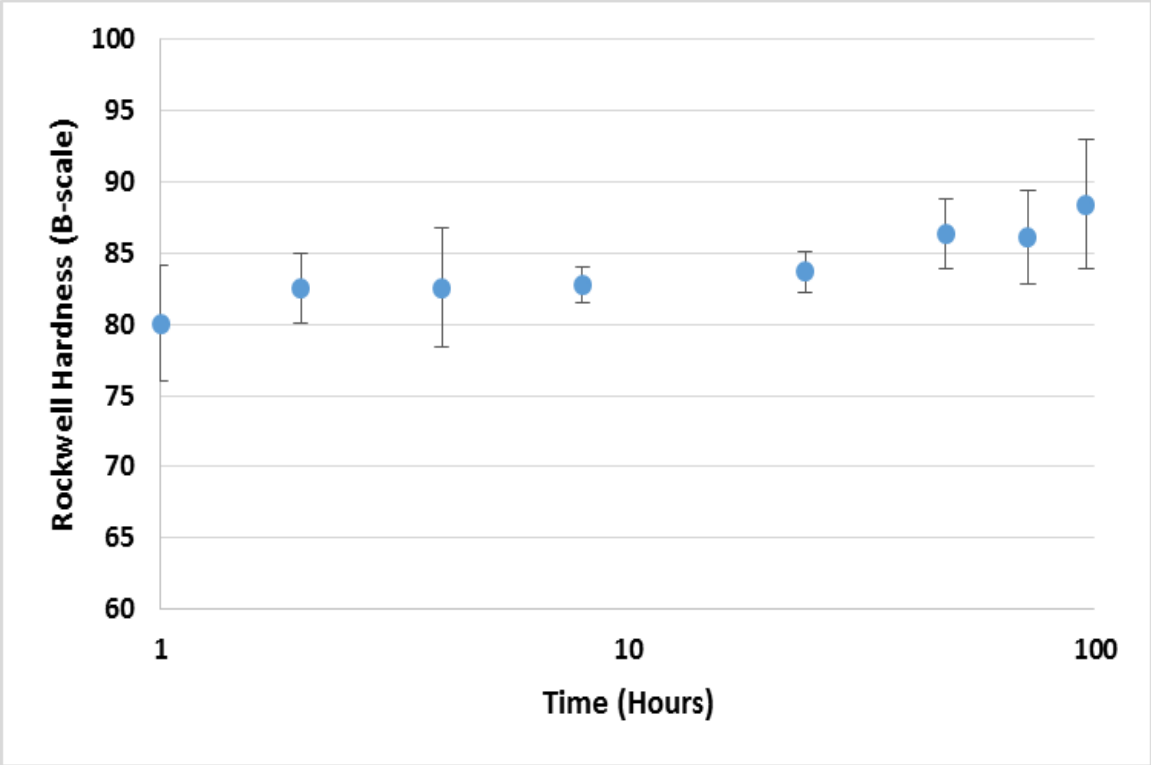


Figure 203 – *Single step aging curve for GT1 at 100°C (212°F).*

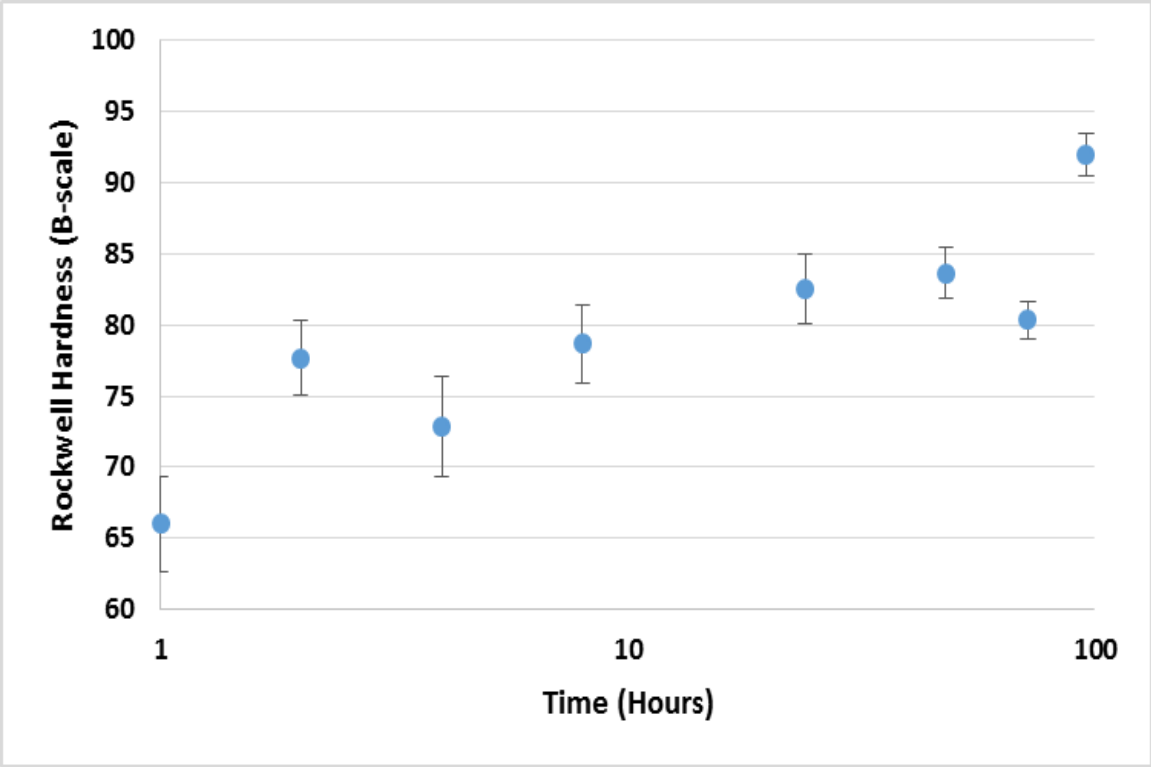


Figure 204 – *Single step aging curve for GT1 at 120°C (248°F).*

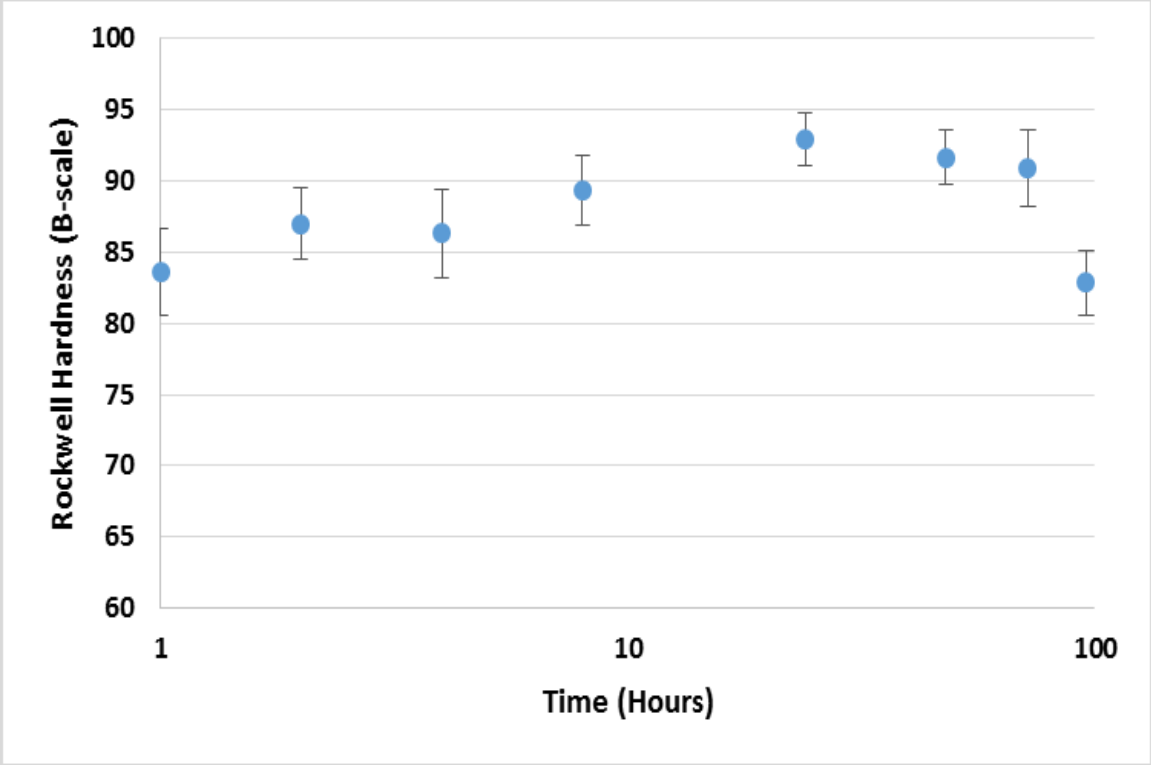


Figure 205 – *Single step aging curve for GT1 at 140°C (284°F).*

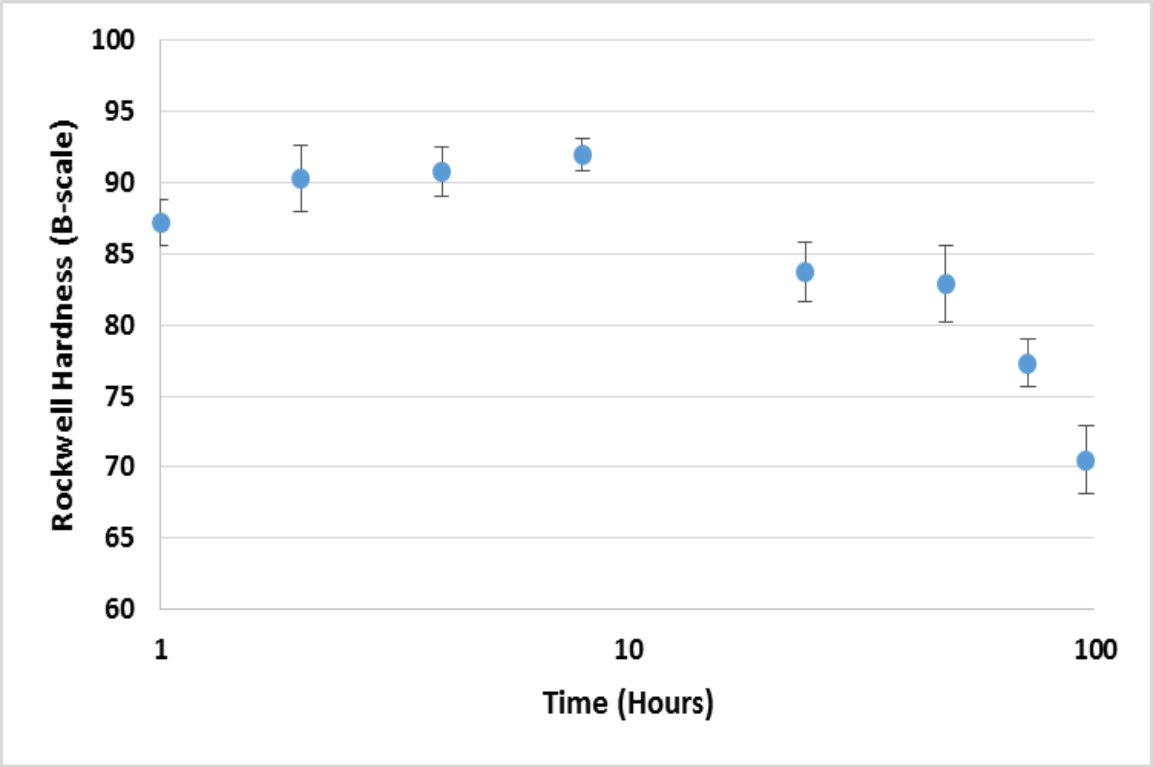


Figure 206 – *Single step aging curve for GT1 at 160°C (320°F).*

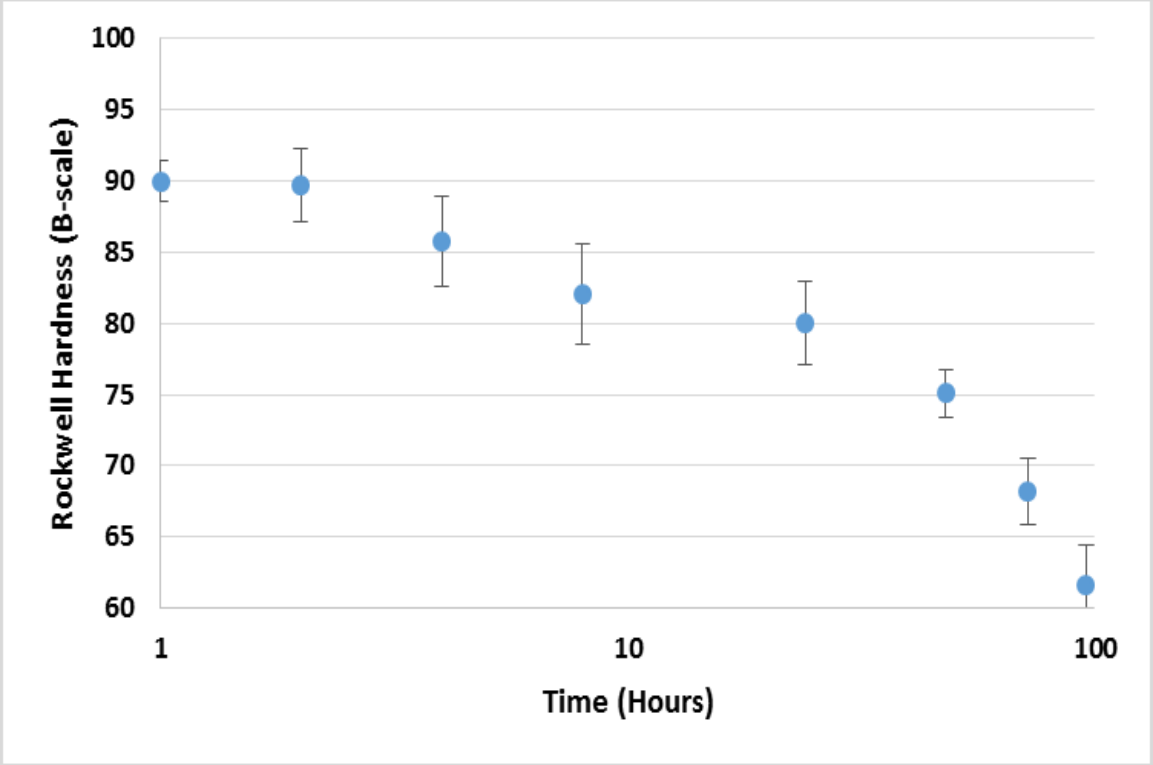


Figure 207 – *Single step aging curve for GT1 at 180°C (356°F).*

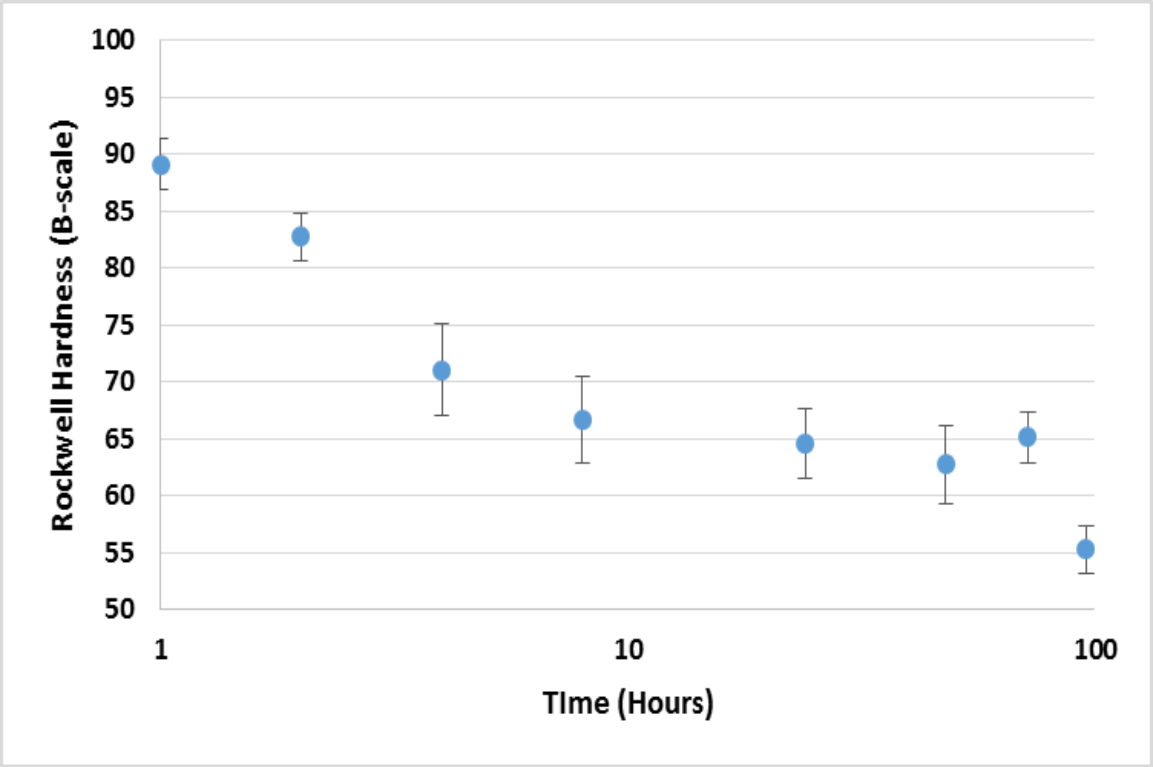


Figure 208 – *Single step aging curve for GT1 at 200°C (392°F).*

**GT2**

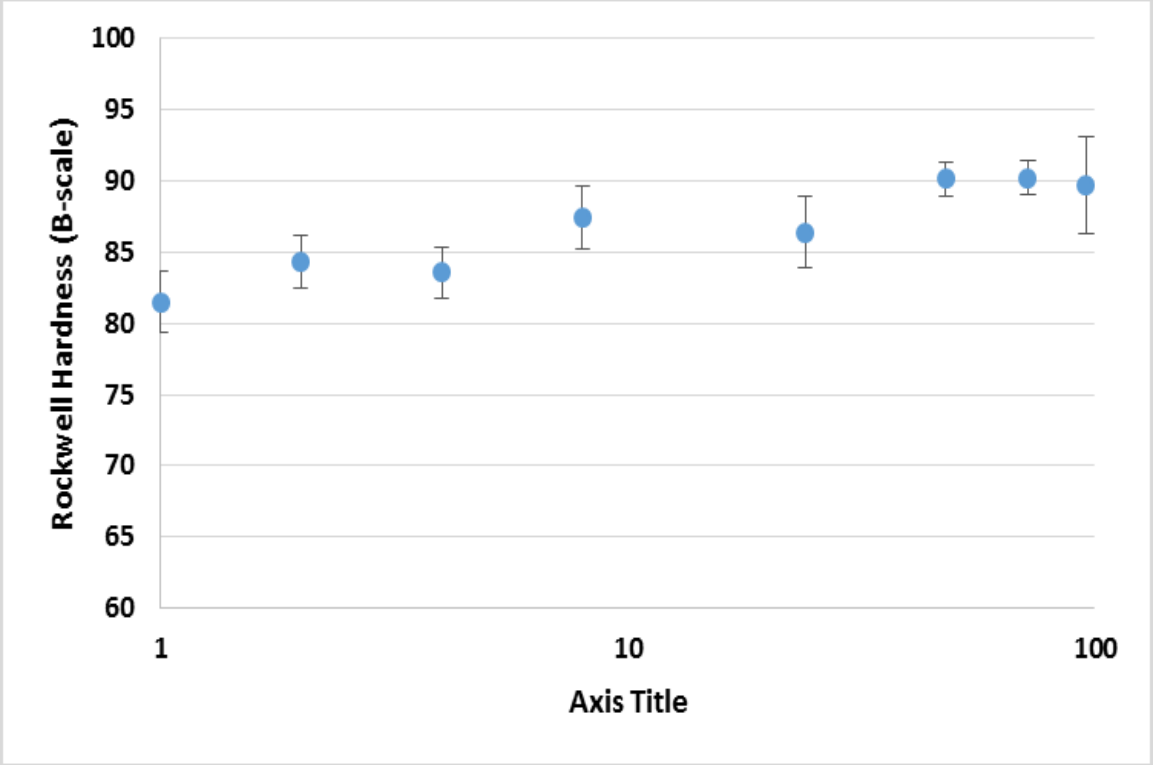


Figure 209 – *Single step aging curve for GT2 at 100°C (212°F).*

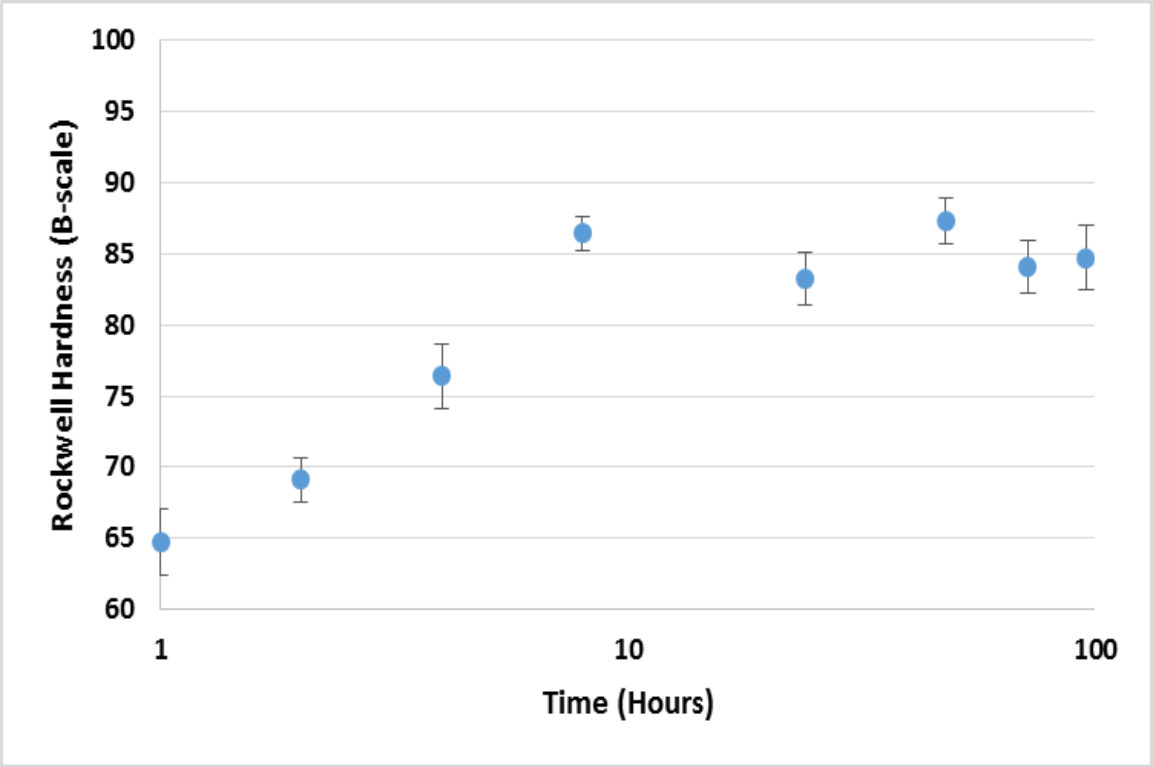


Figure 210 – *Single step aging curve for GT2 at 120°C (248°F).*

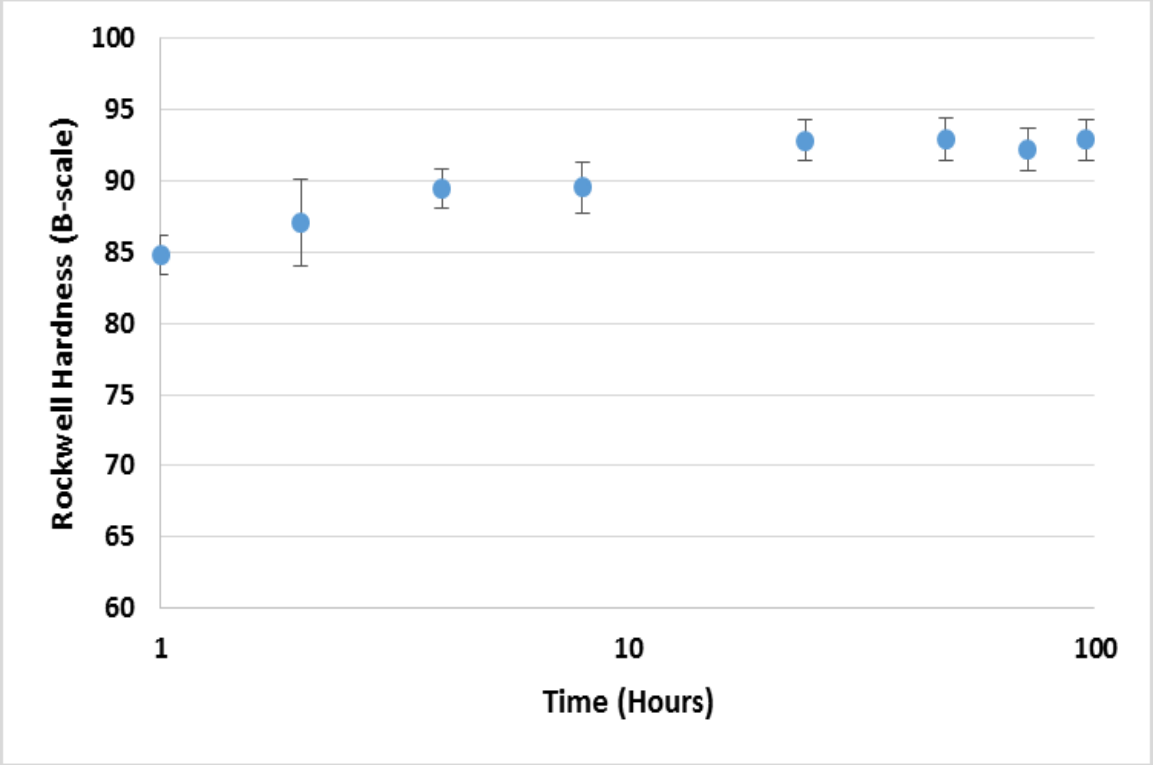


Figure 211 – *Single step aging curve for GT2 at 140°C (284°F).*

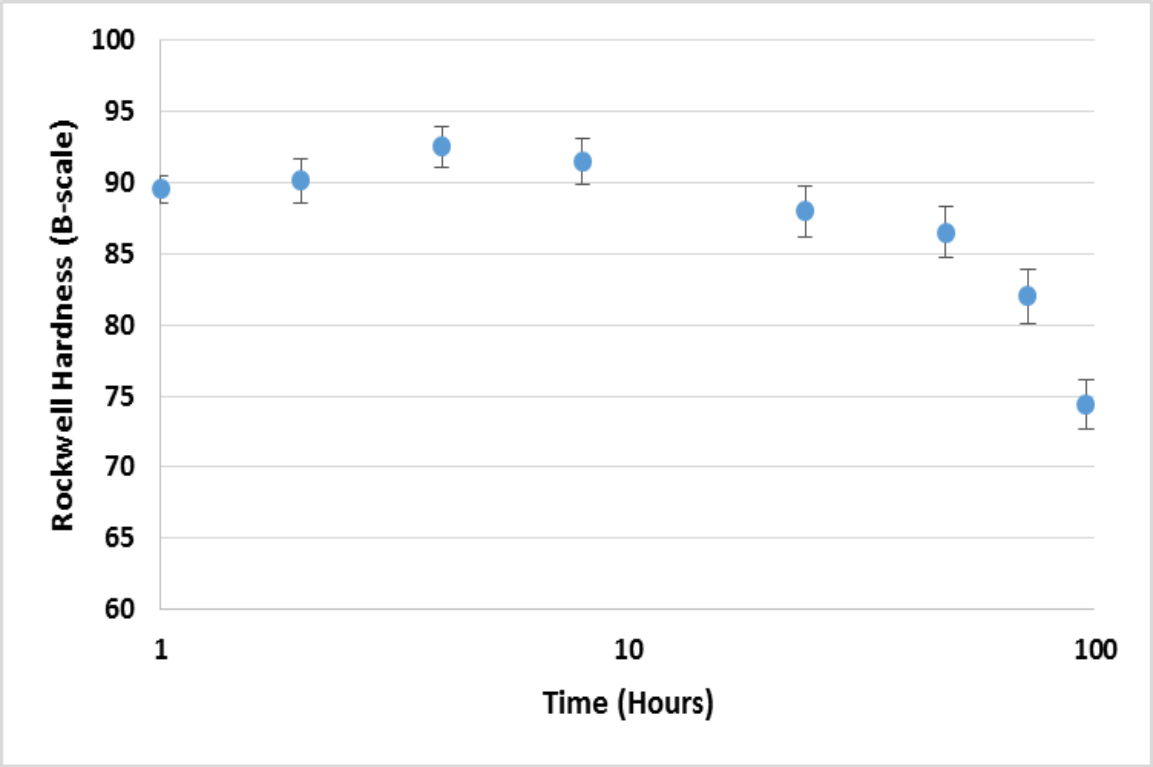


Figure 212 – *Single step aging curve for GT2 at 160°C (320°F).*

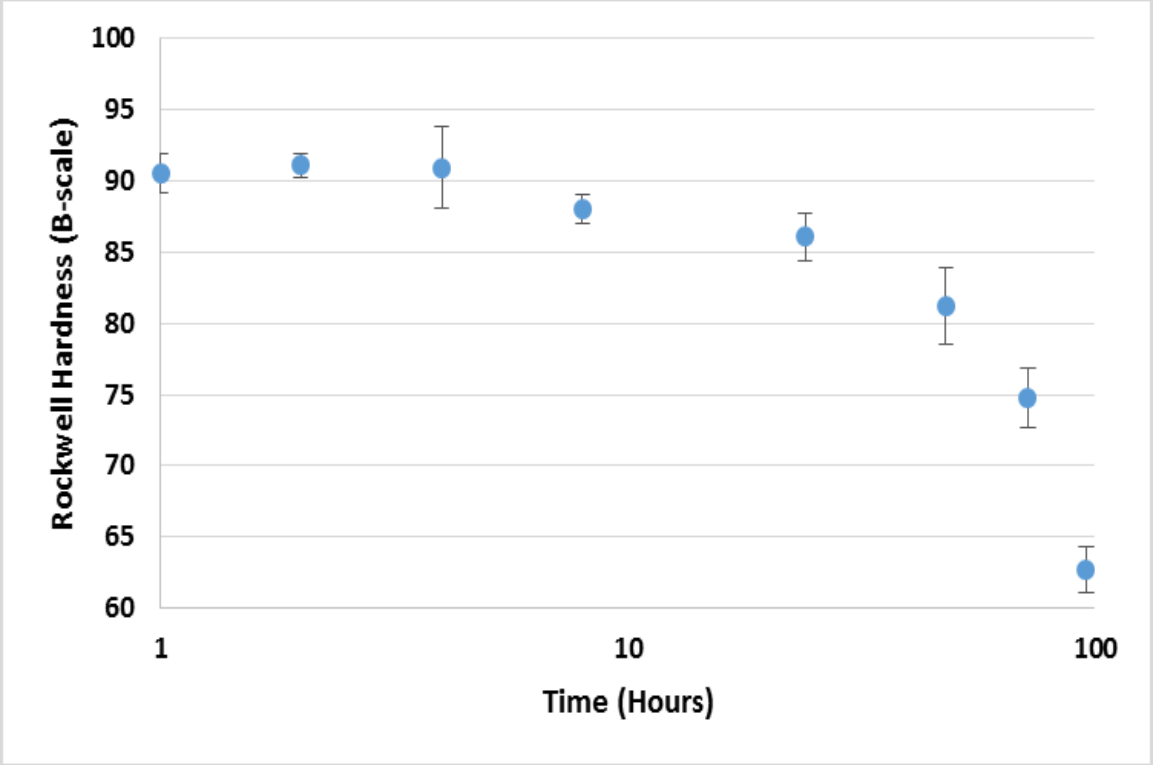


Figure 213 – *Single step aging curve for GT2 at 180°C (356°F).*

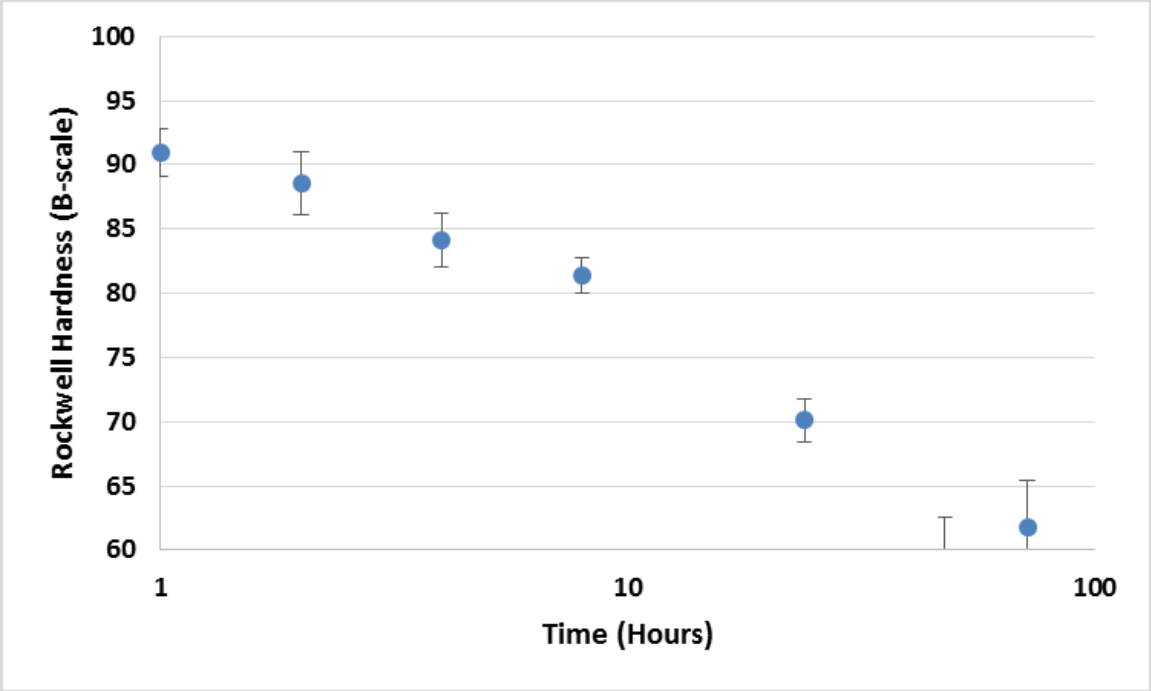


Figure 214 – *Single step aging curve for GT2 at 200°C (392°F).*

**GT3**

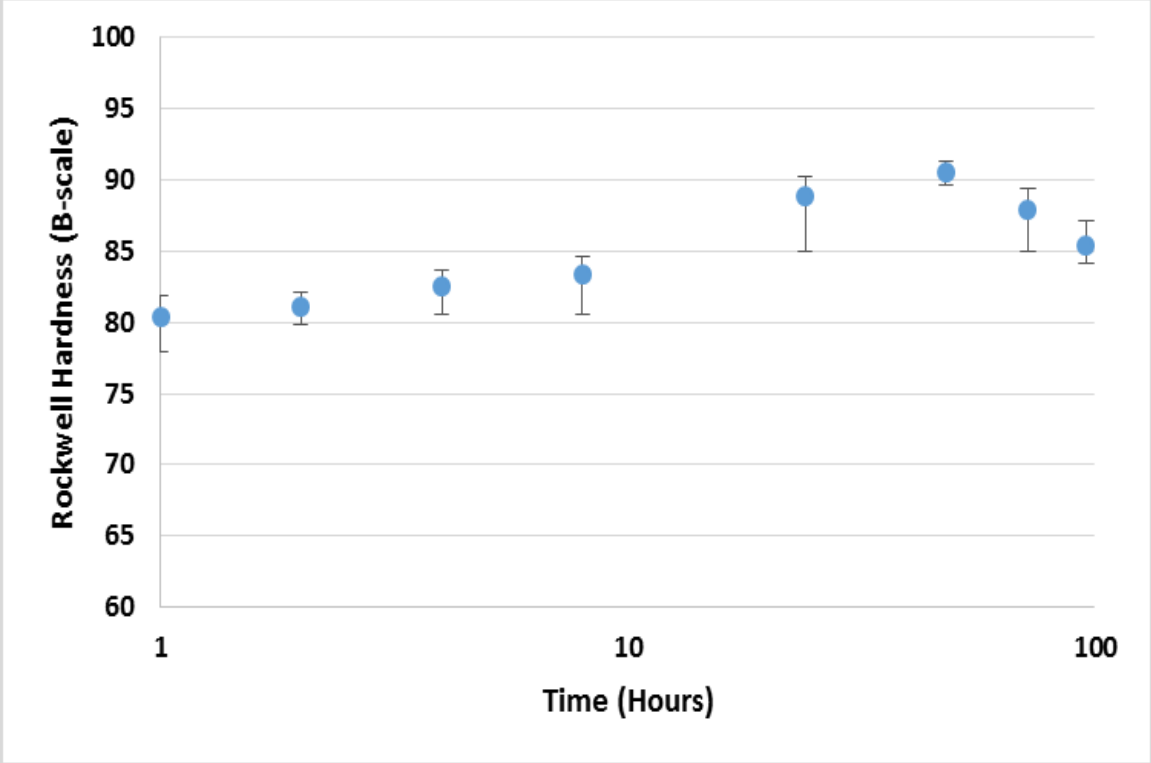


Figure 215 – *Single step aging curve for GT3 at 100°C (212°F).*

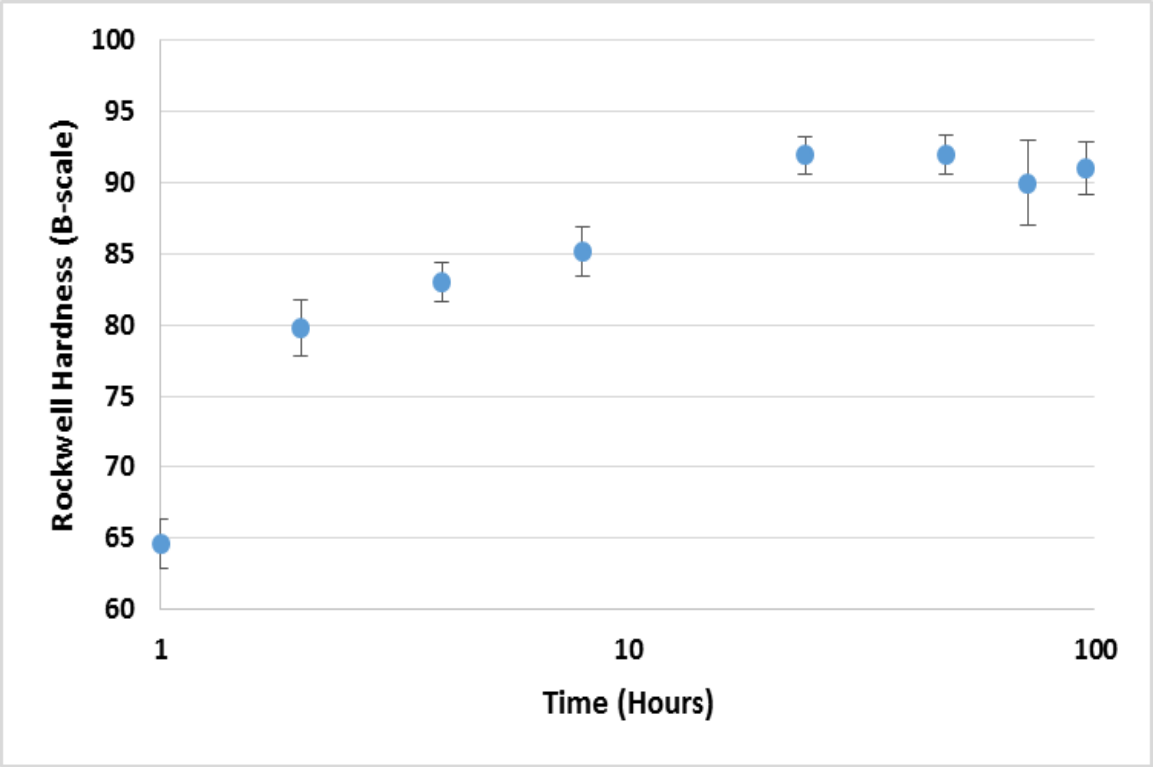


Figure 216 – *Single step aging curve for GT3 at 120°C (248°F).*

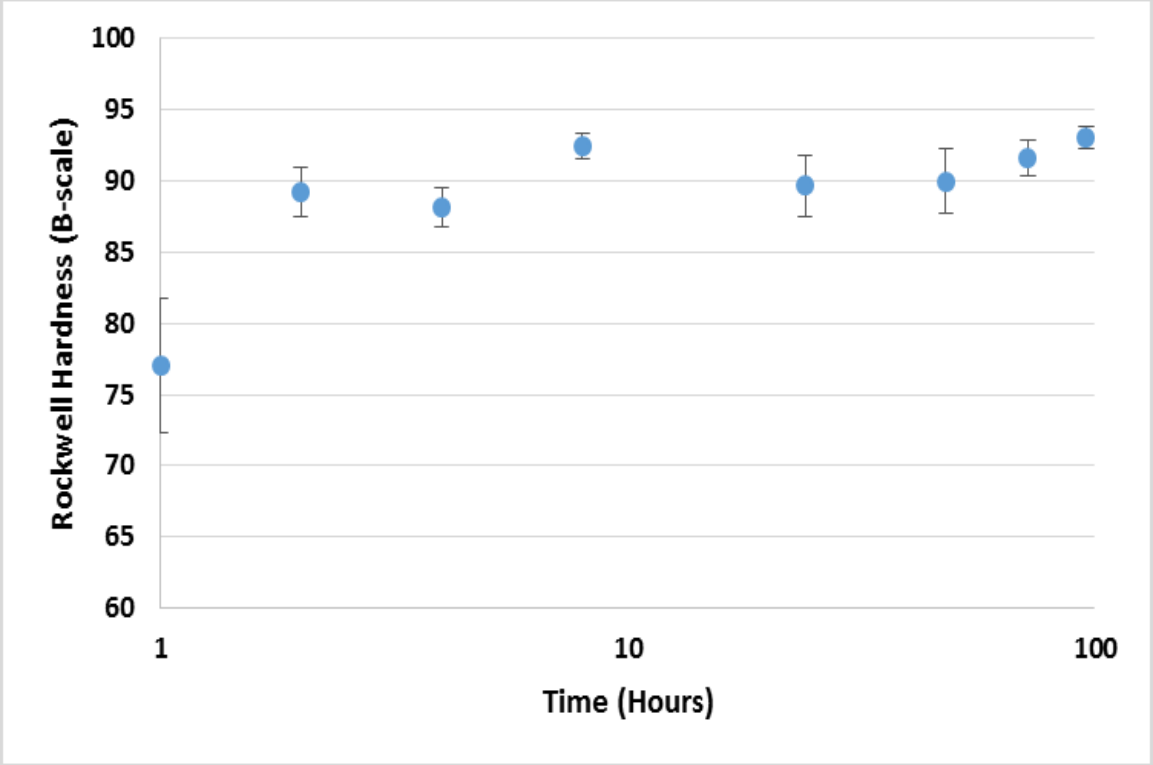


Figure 217 – *Single step aging curve for GT3 at 140°C (284°F).*

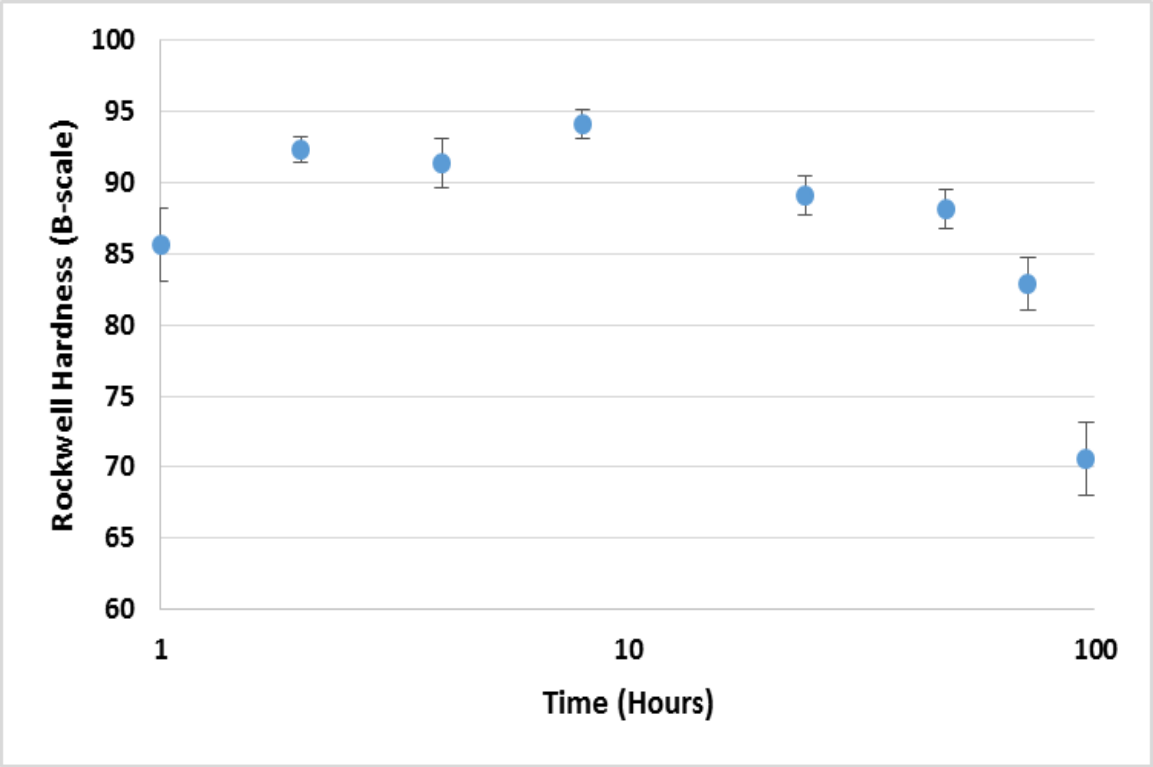


Figure 218 – *Single step aging curve for GT3 at 160°C (320°F).*

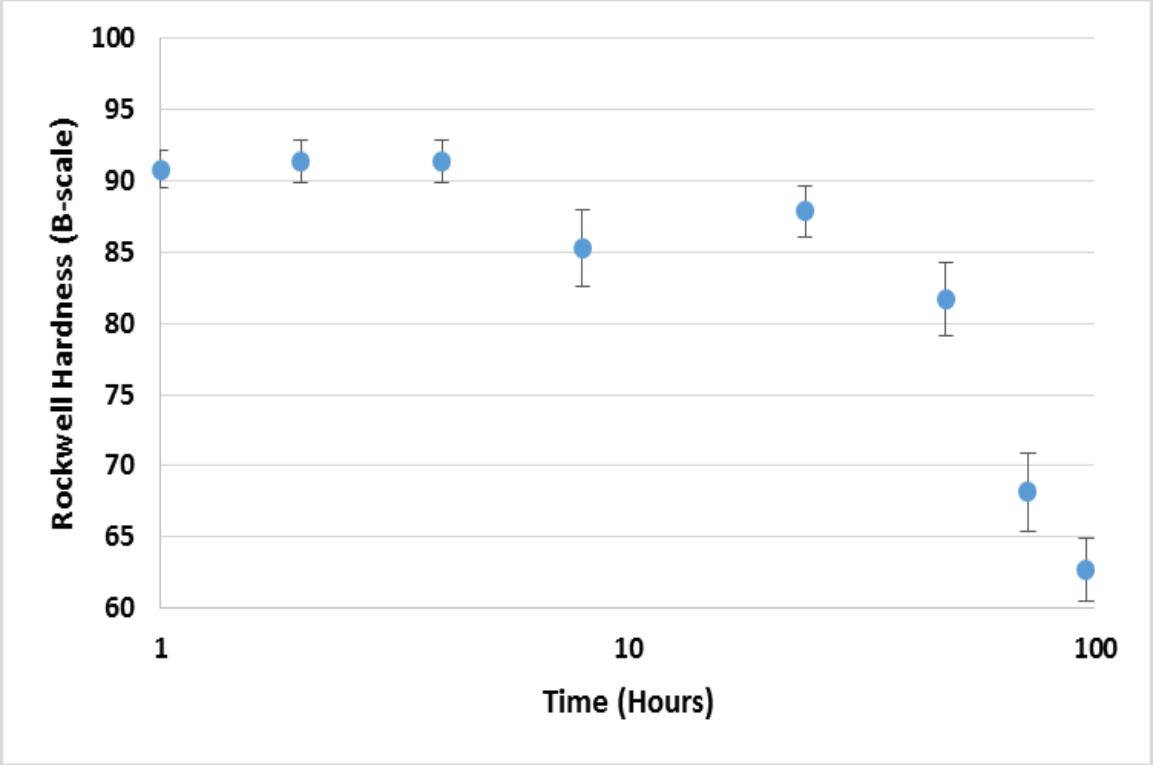


Figure 219 – *Single step aging curve for GT3 at 180°C (356°F).*

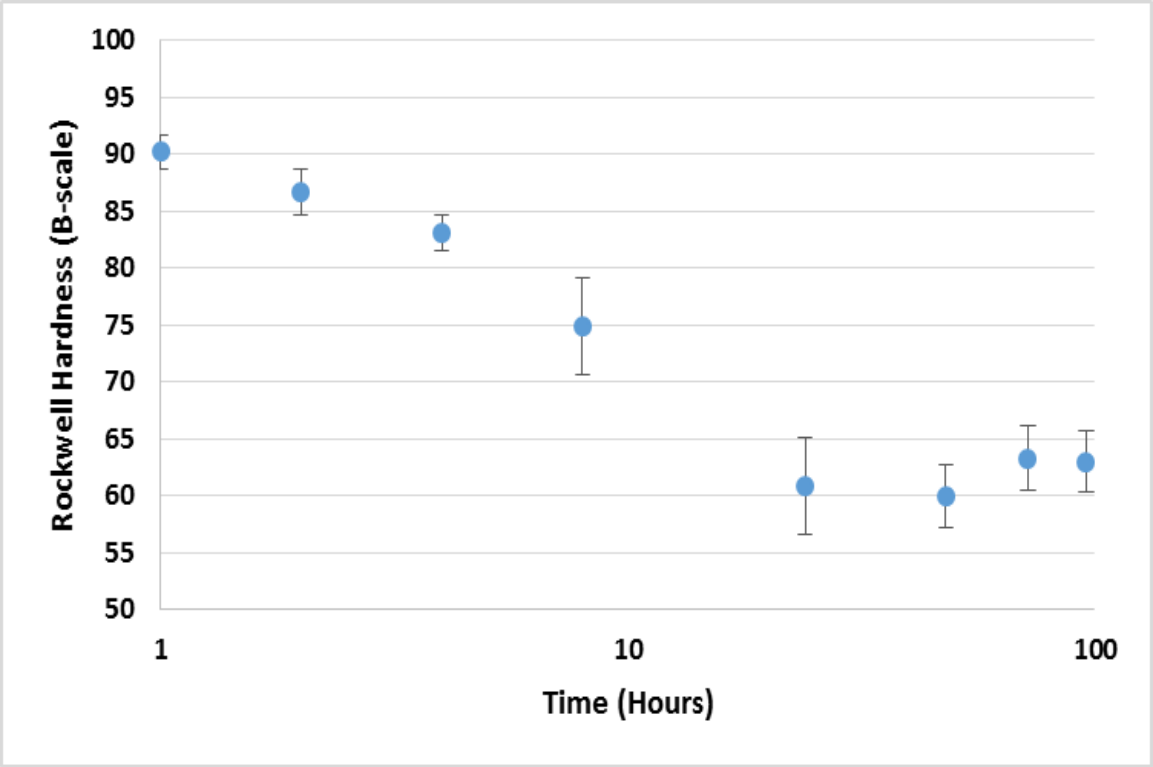


Figure 220 – *Single step aging curve for GT3 at 200°C (392°F).*

**GT4**

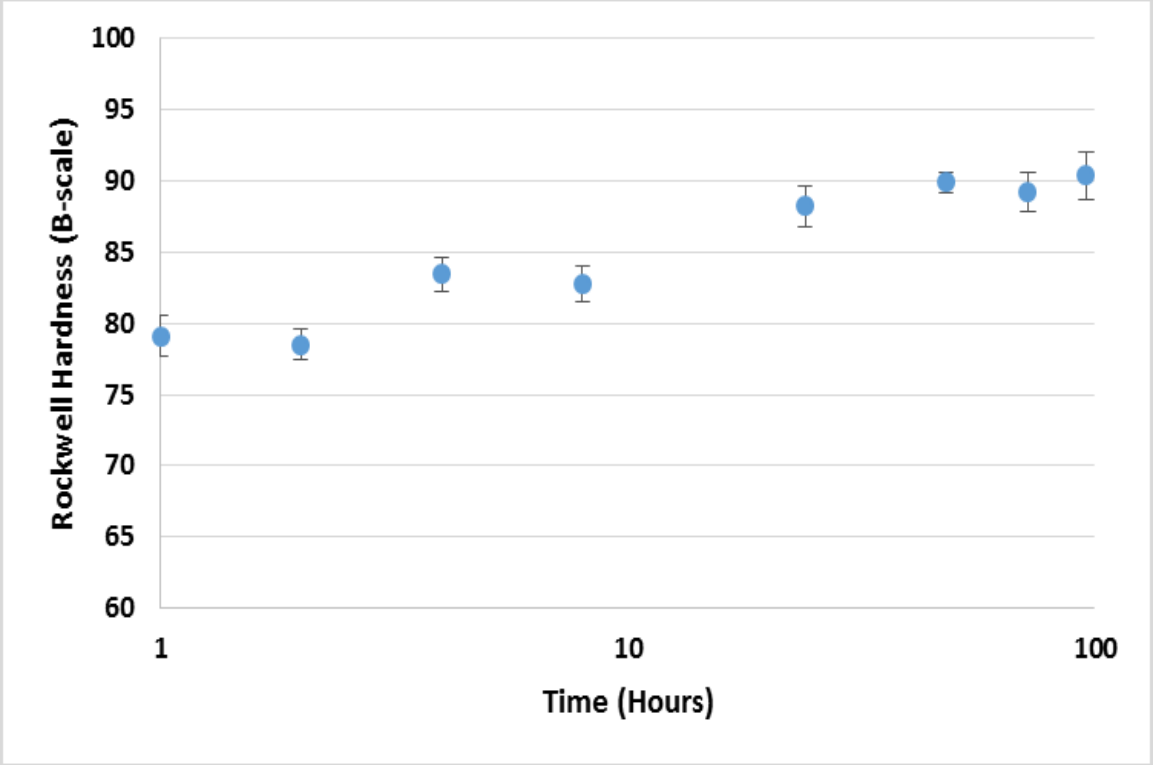


Figure 221 – *Single step aging curve for GT4 at 100°C (212°F).*

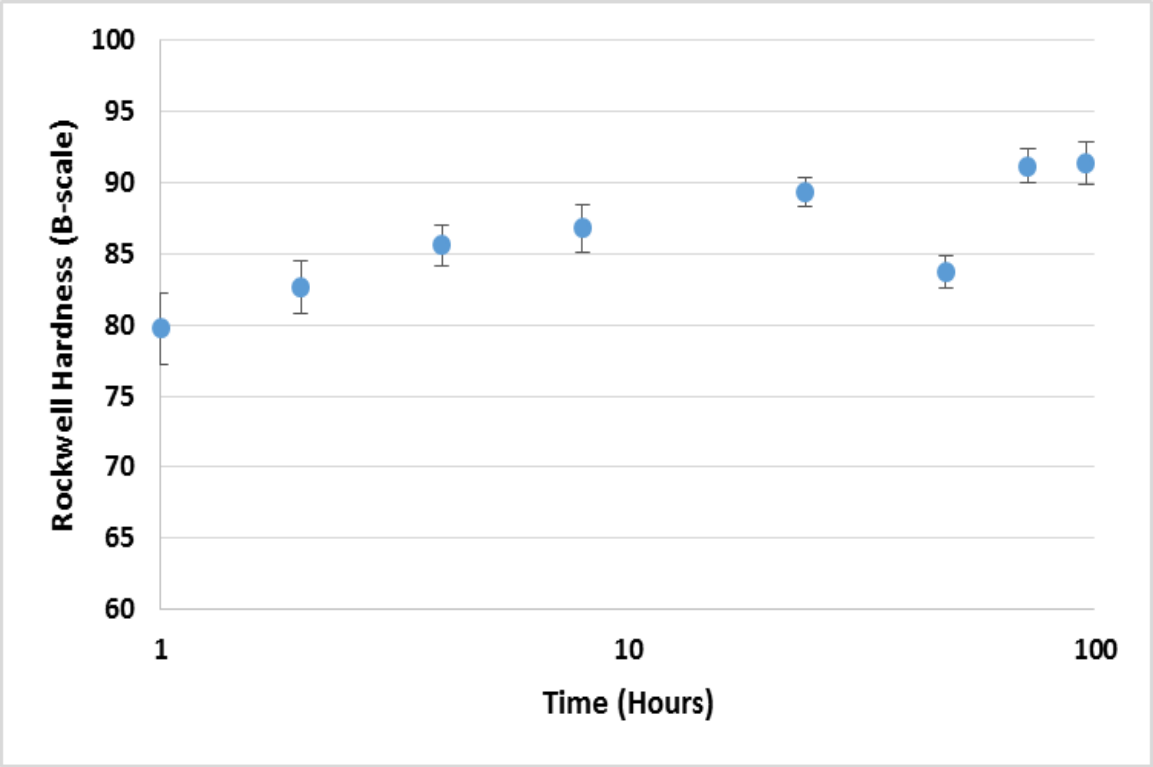


Figure 222 – *Single step aging curve for GT4 at 120°C (248°F).*

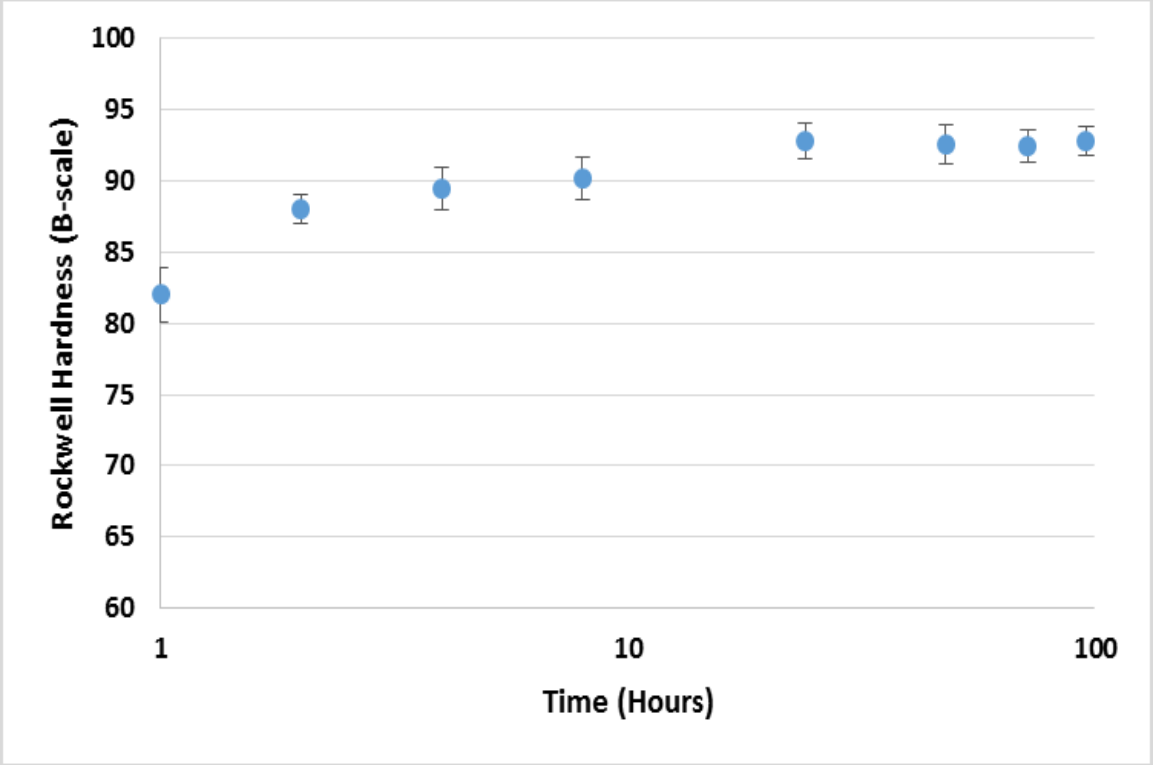


Figure 223 – *Single step aging curve for GT4 at 140°C (284°F).*

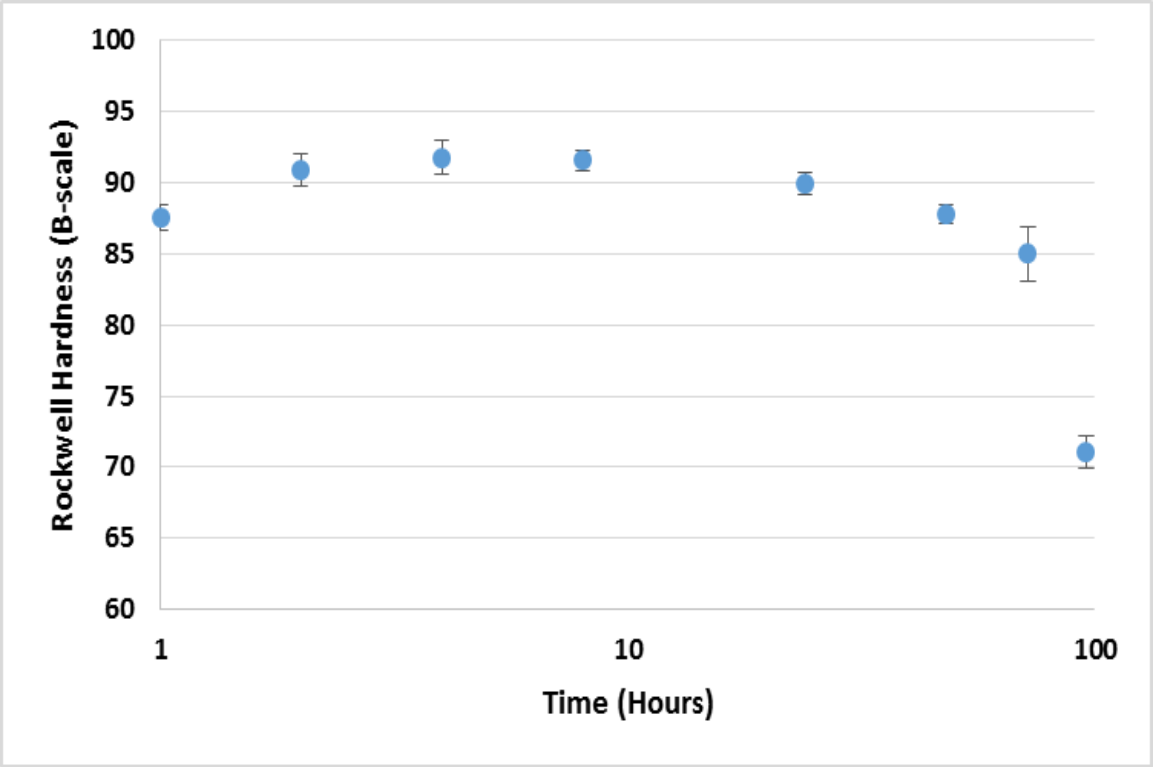


Figure 224 – *Single step aging curve for GT4 at 160°C (320°F).*

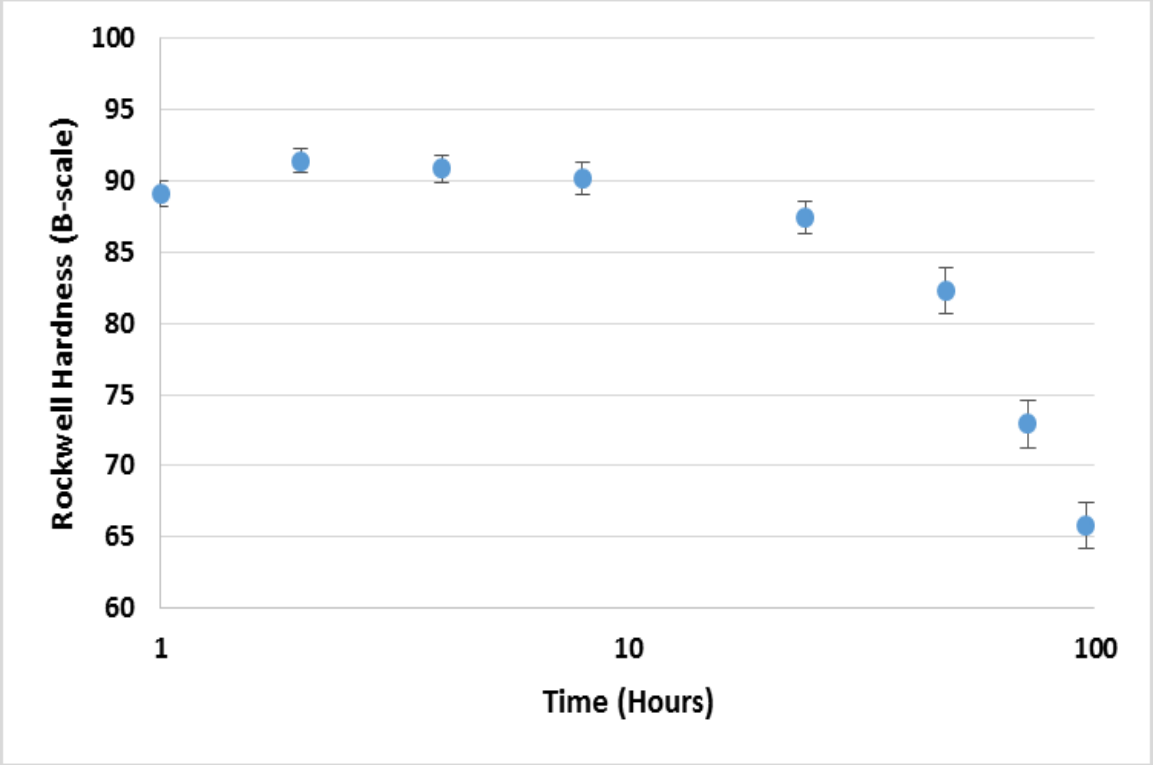


Figure 225 – *Single step aging curve for GT4 at 180°C (356°F).*

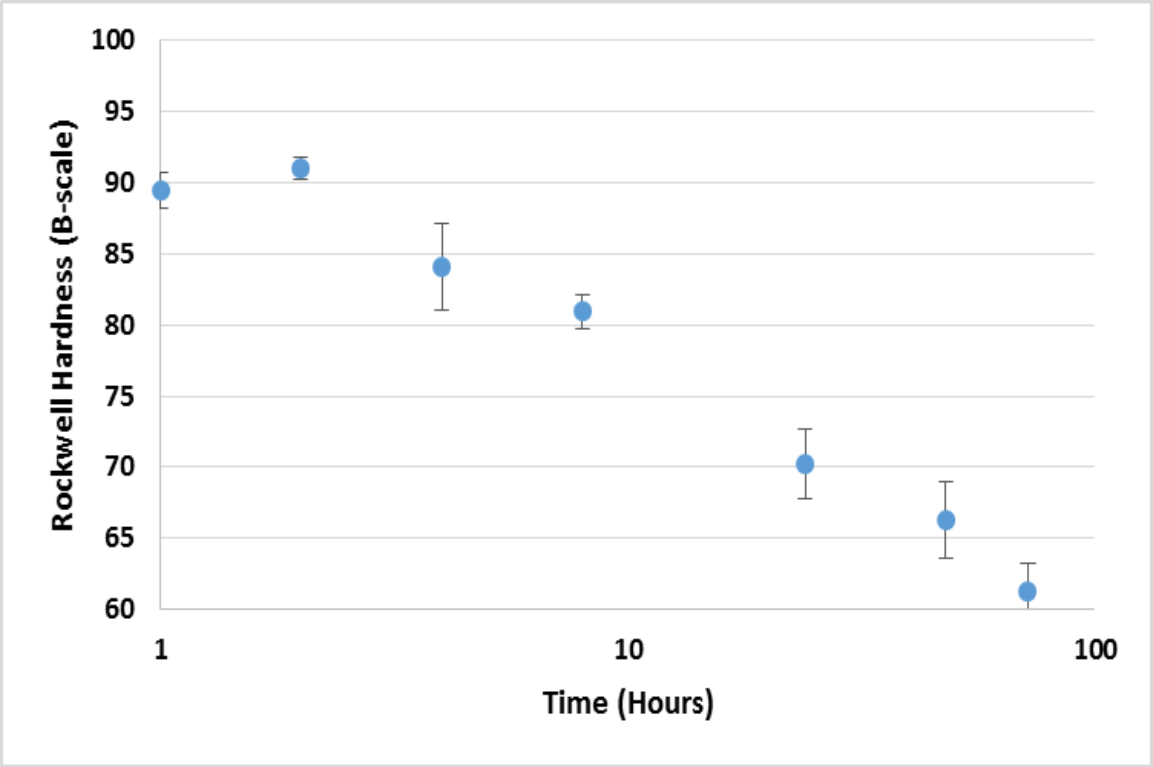


Figure 226 – *Single step aging curve for GT4 at 200°C (392°F).*

**GT5**

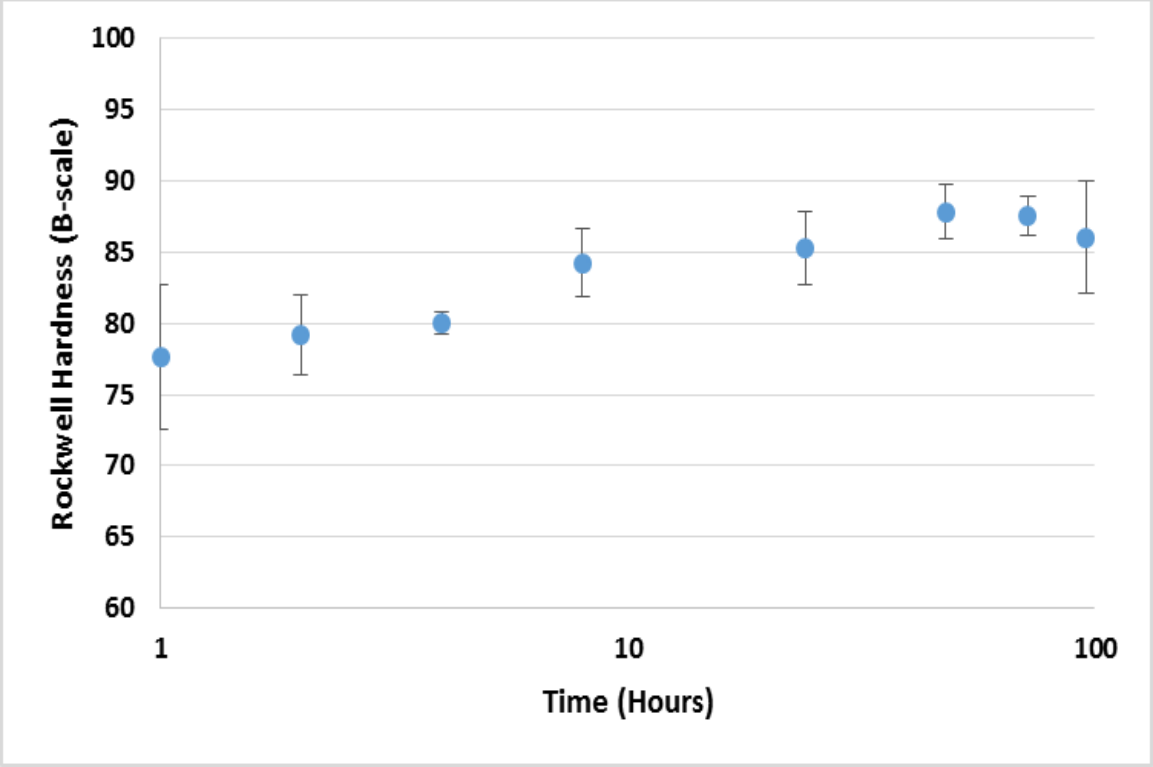


Figure 227 – *Single step aging curve for GT5 at 100°C (212°F).*

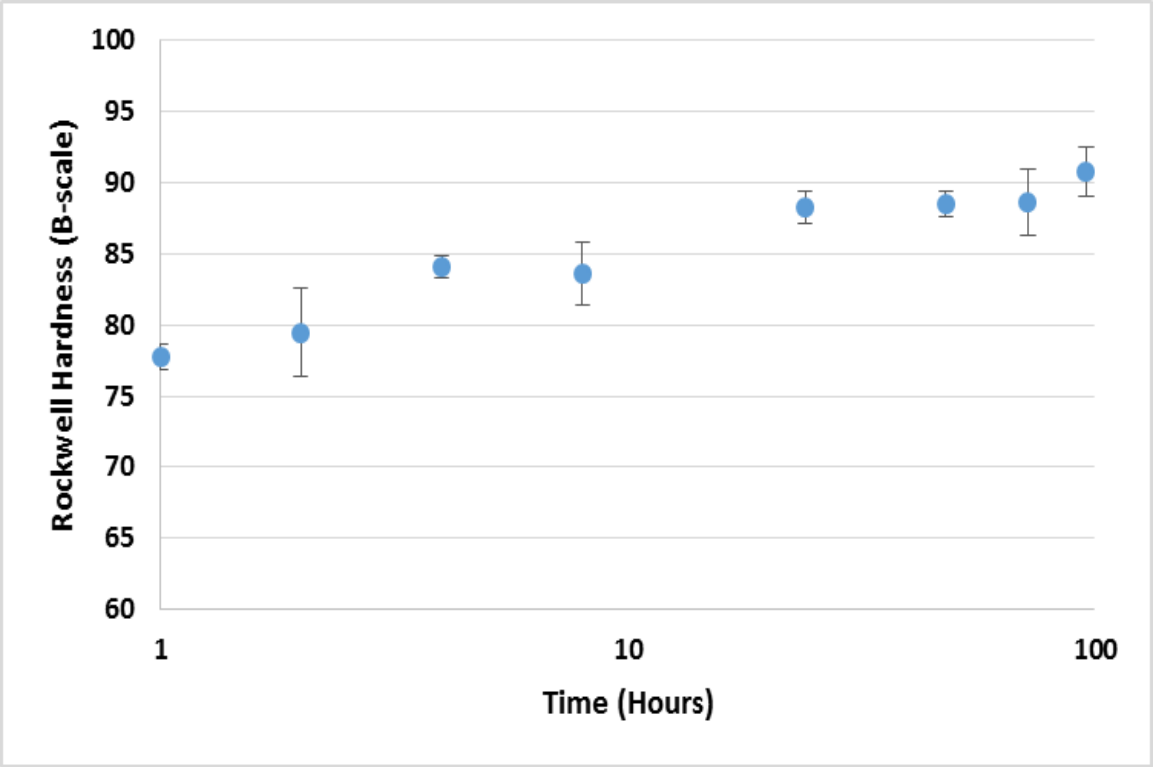


Figure 228 – *Single step aging curve for GT5 at 120°C (248°F).*

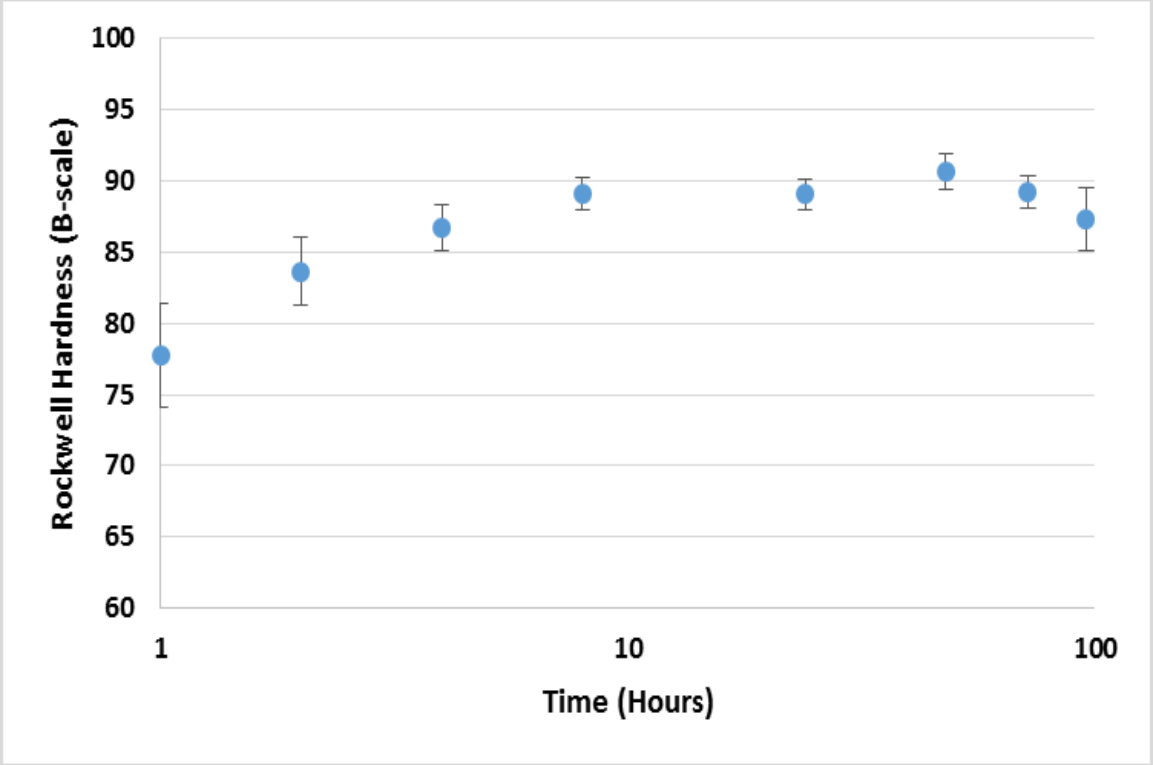


Figure 229 – *Single step aging curve for GT5 at 140°C (284°F).*

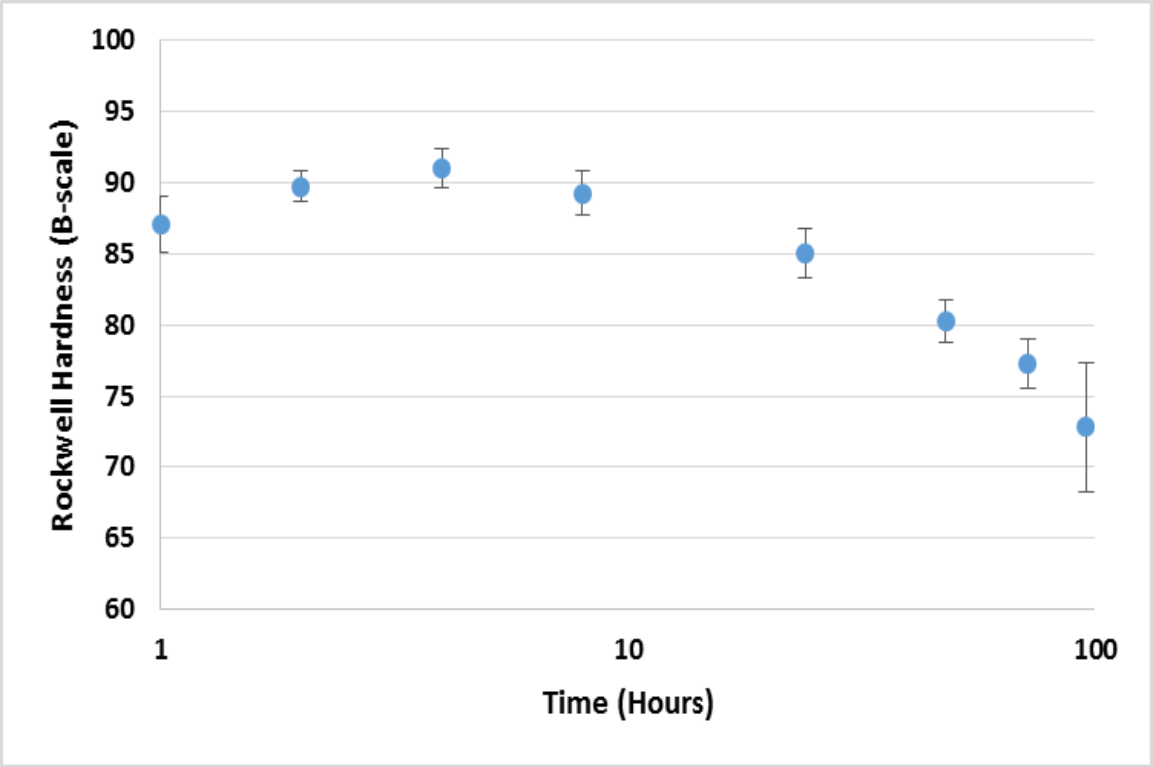


Figure 230 – *Single step aging curve for GT5 at 160°C (320°F).*

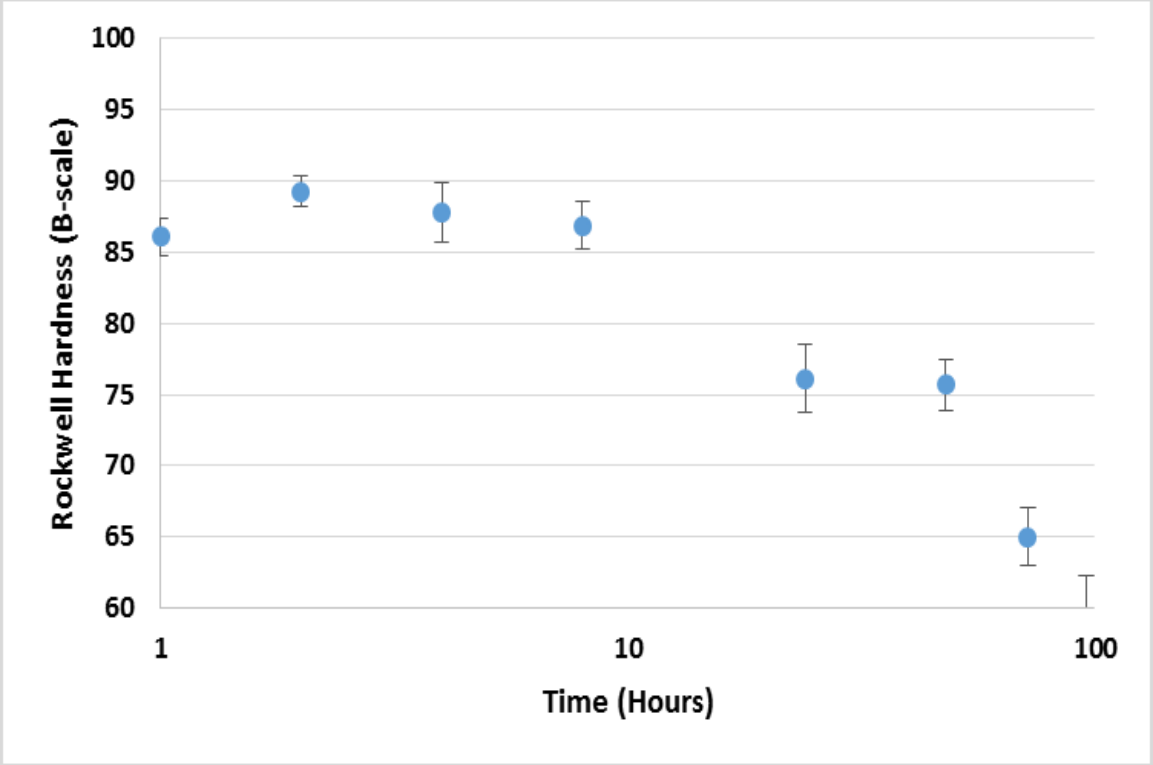


Figure 231 – *Single step aging curve for GT5 at 180°C (356°F).*

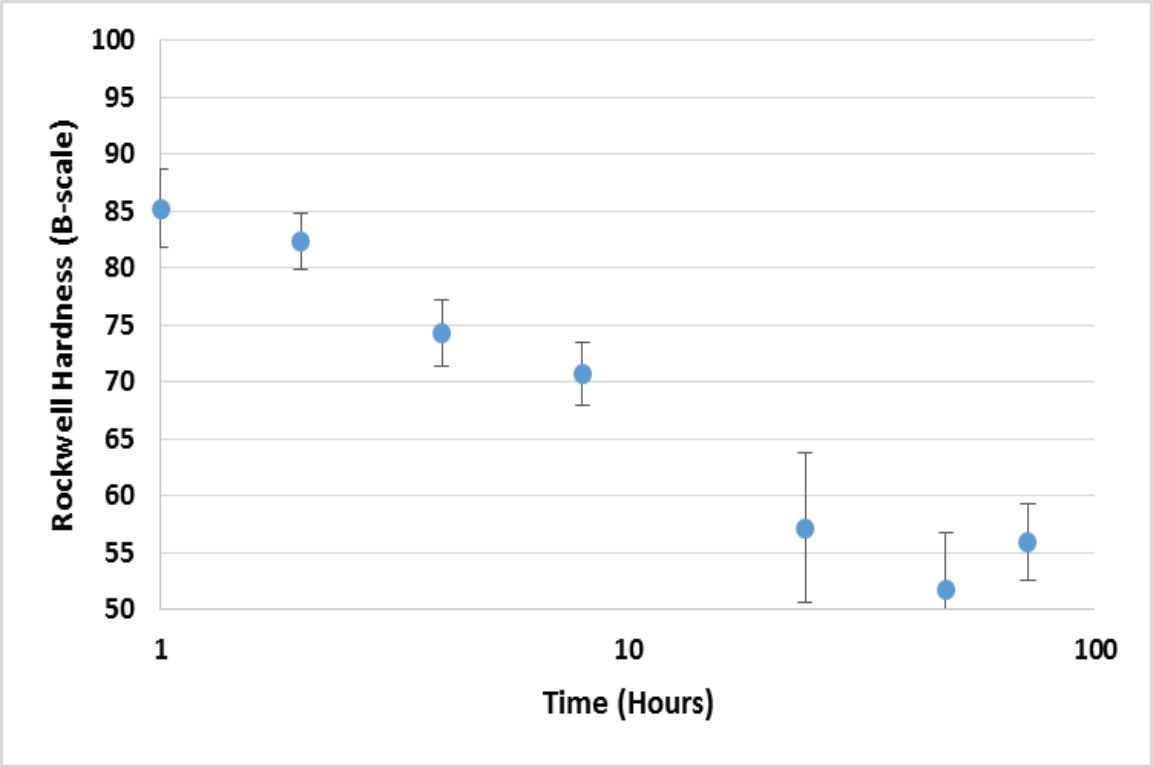


Figure 232 – *Single step aging curve for GT5 at 200°C (392°F).*

**GT6**

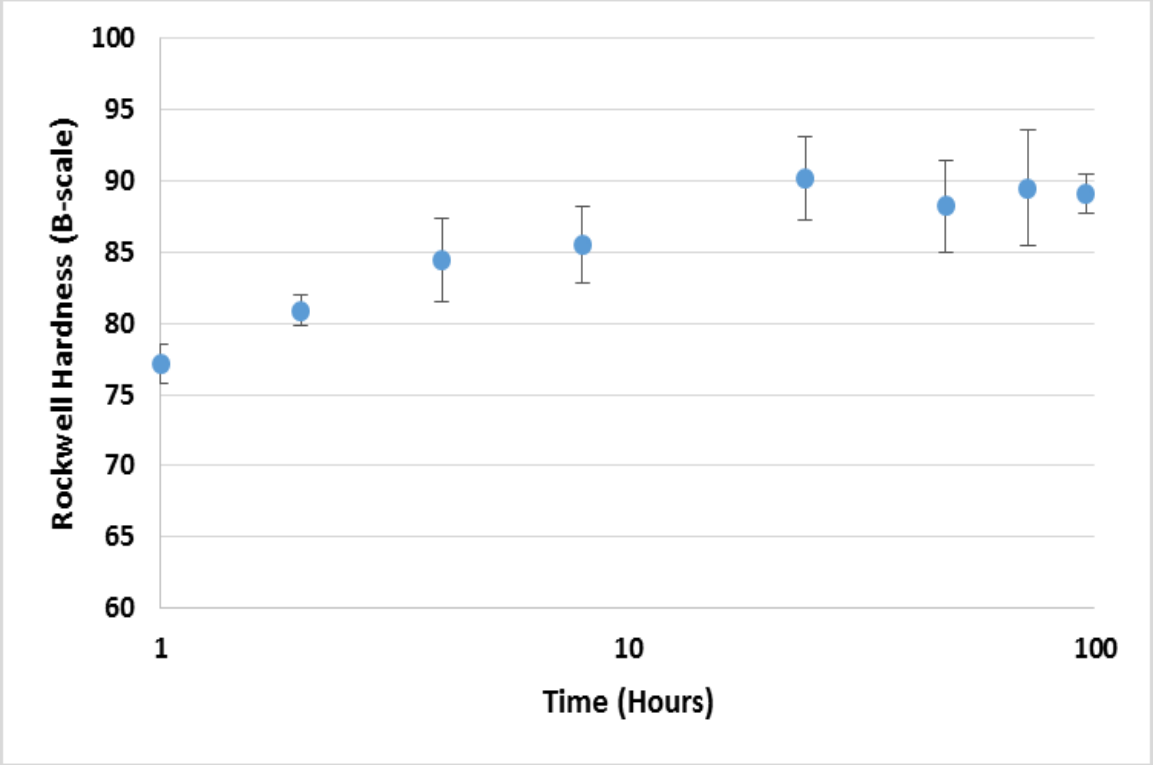


Figure 233 – *Single step aging curve for GT6 at 100°C (212°F).*

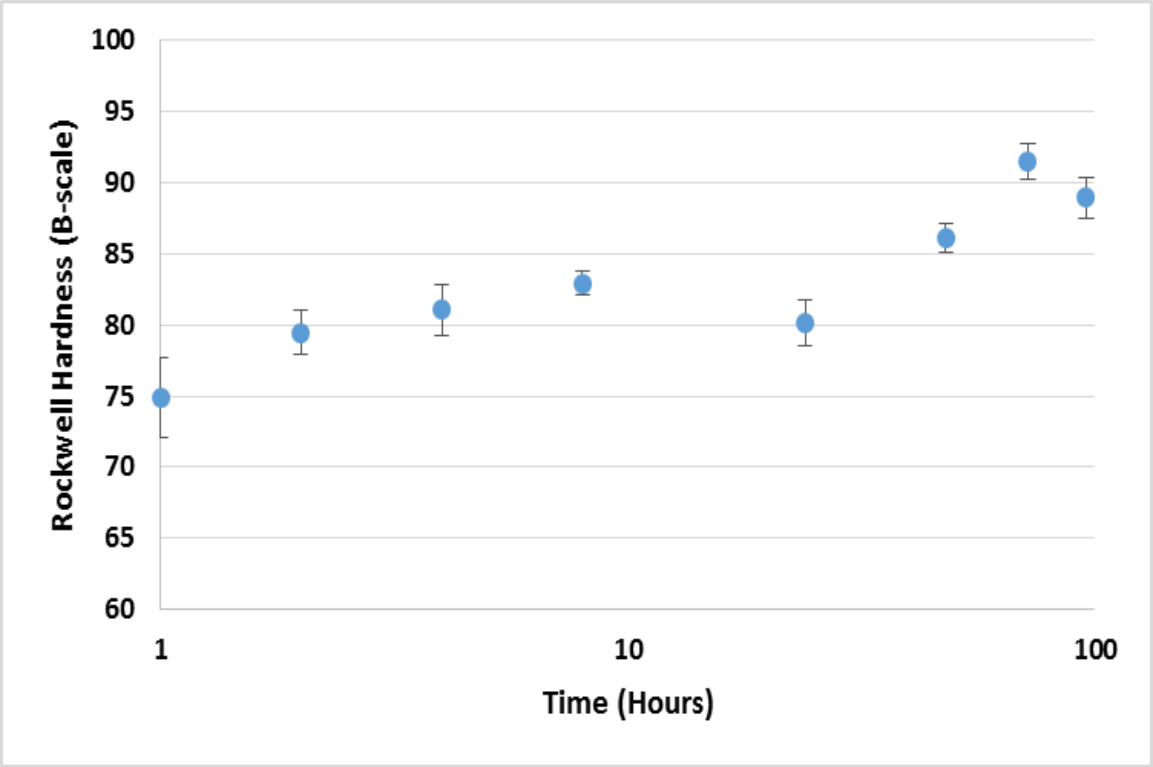


Figure 234 – *Single step aging curve for GT6 at 120°C (248°F).*

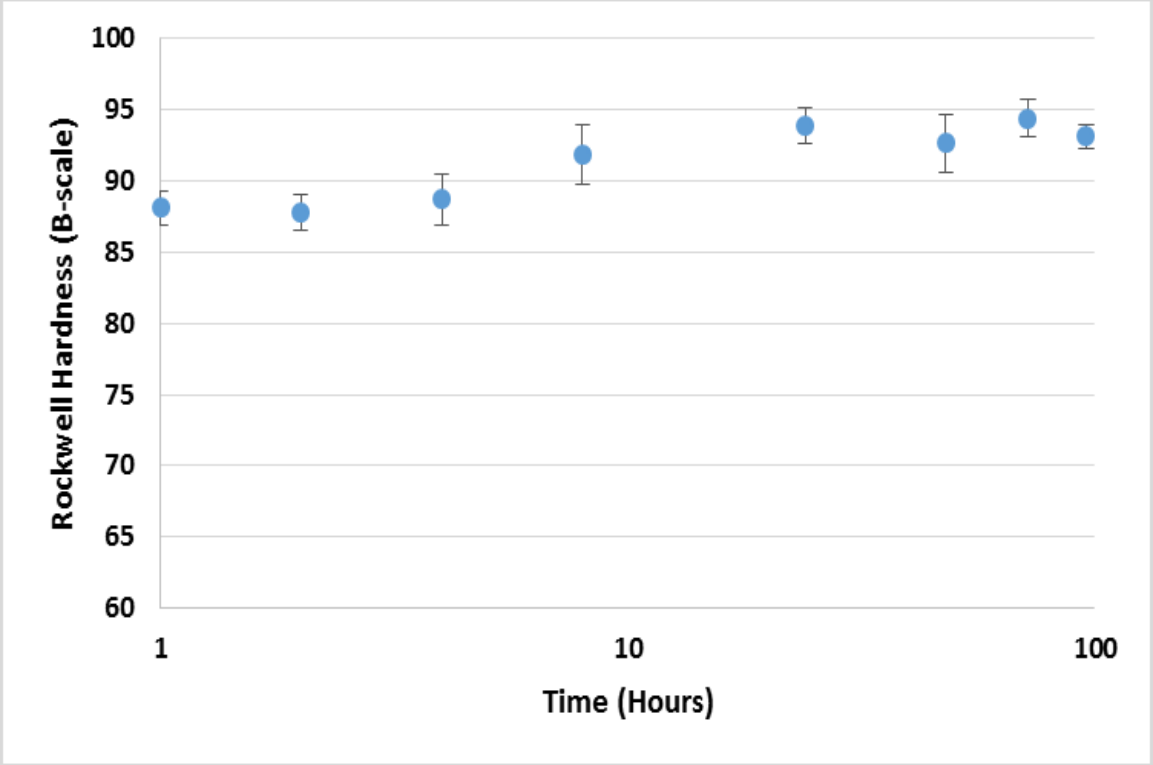


Figure 235 – *Single step aging curve for GT6 at 140°C (284°F).*

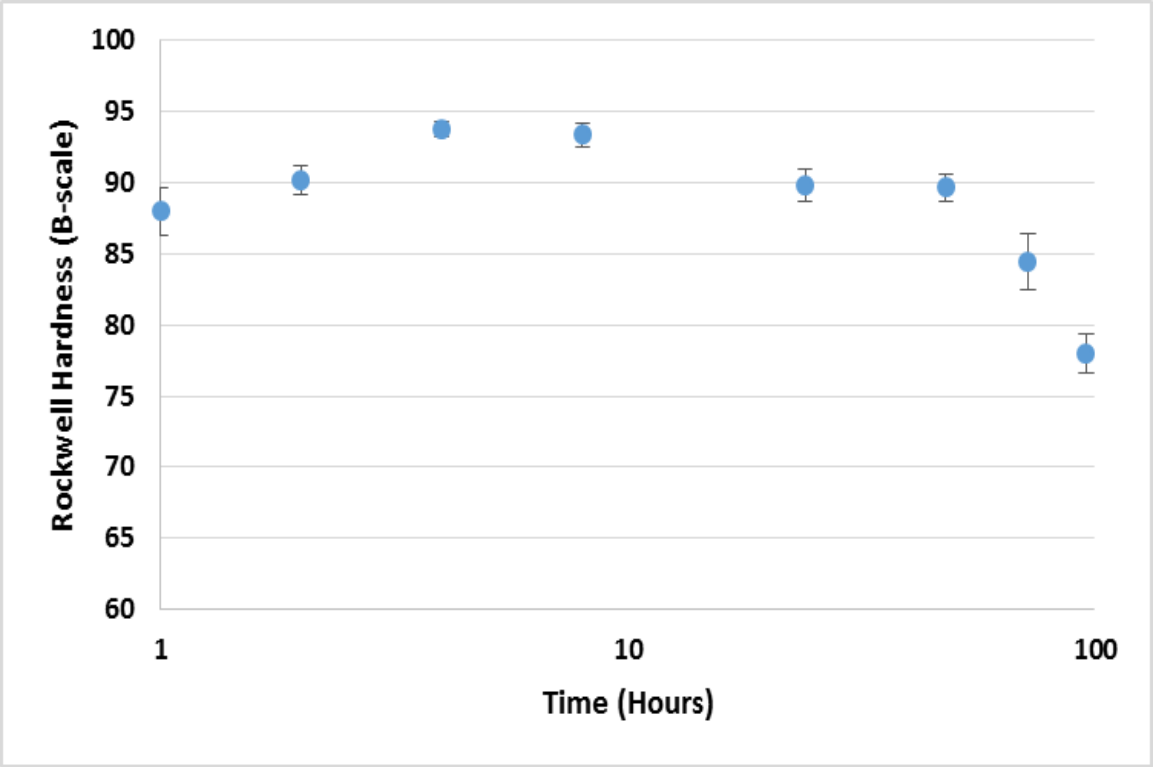


Figure 236 – *Single step aging curve for GT6 at 160°C (320°F).*

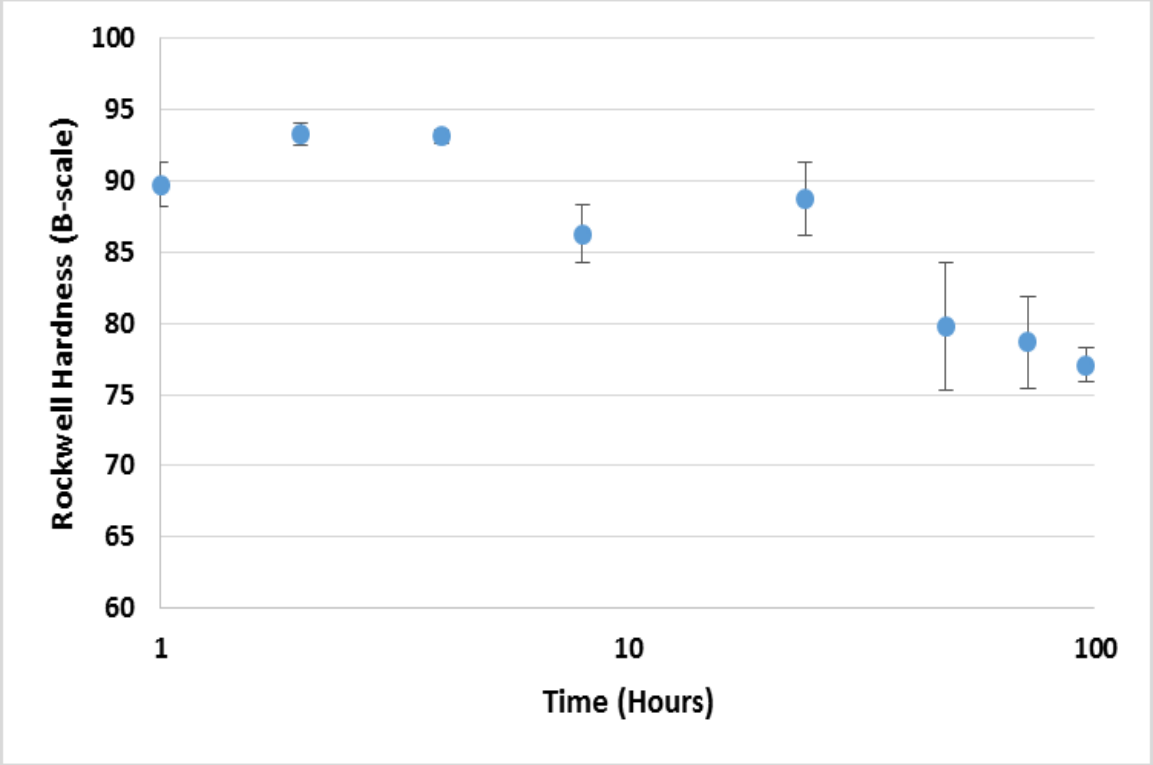


Figure C237 – *Single step aging curve for GT6 at 180°C (356°F).*

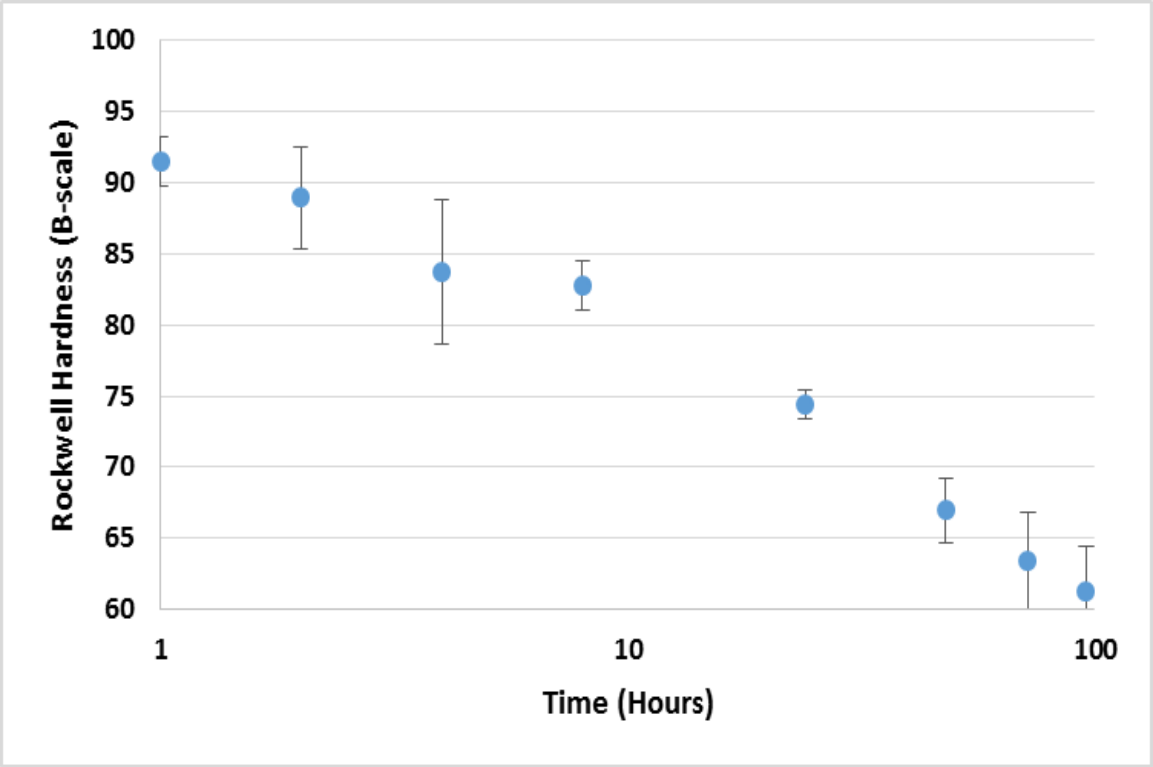


Figure 238 – *Single step aging curve for GT6 at 200°C (392°F).*

**GT7**

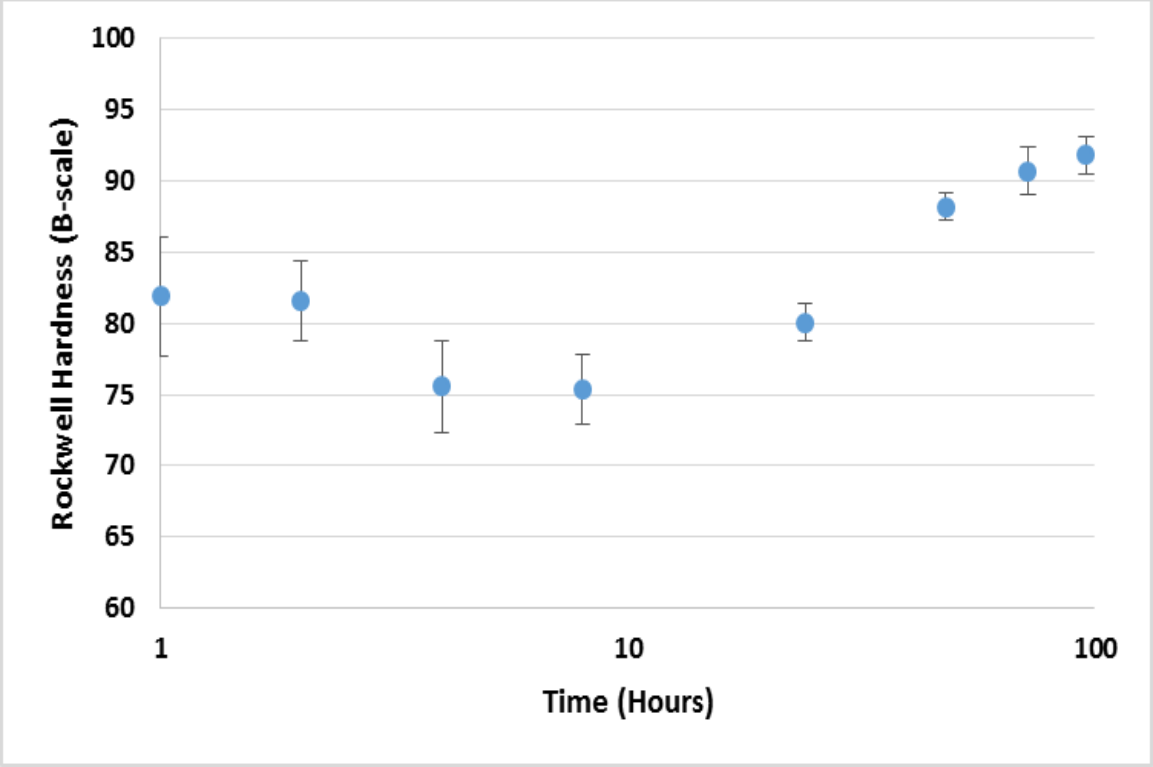


Figure 239 – *Single step aging curve for GT7 at 100°C (212°F).*

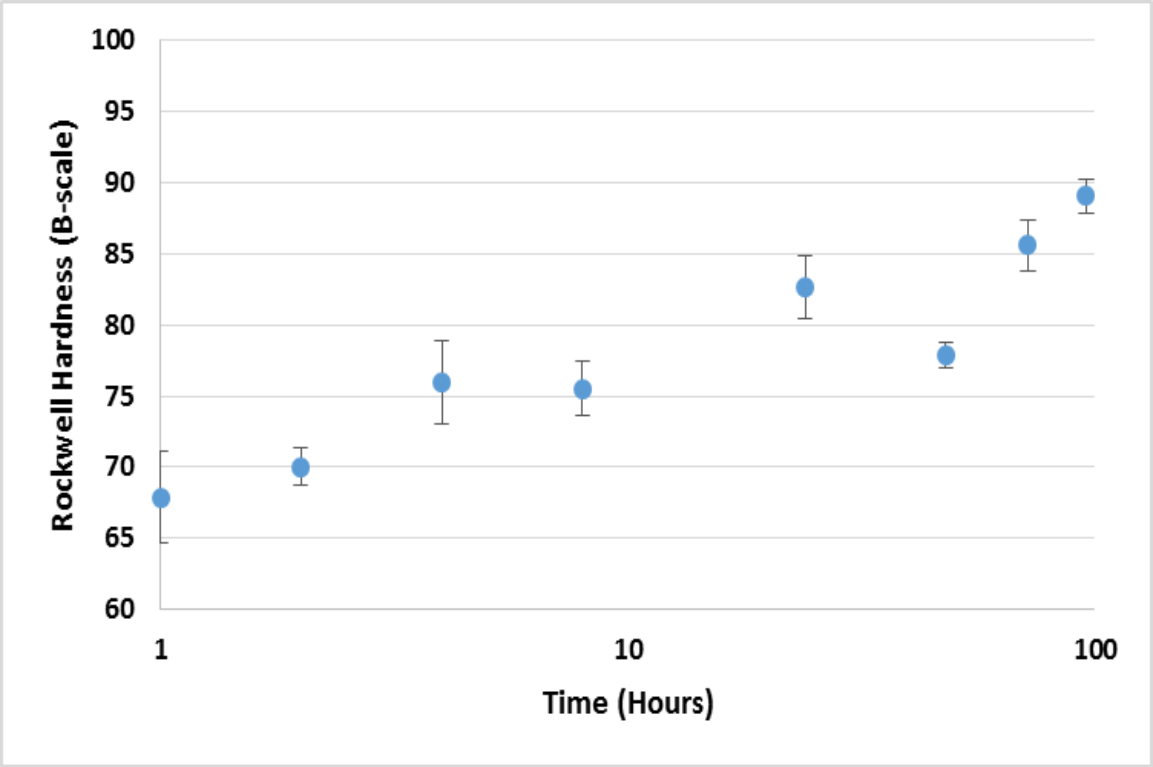


Figure 240 – *Single step aging curve for GT7 at 120°C (248°F).*

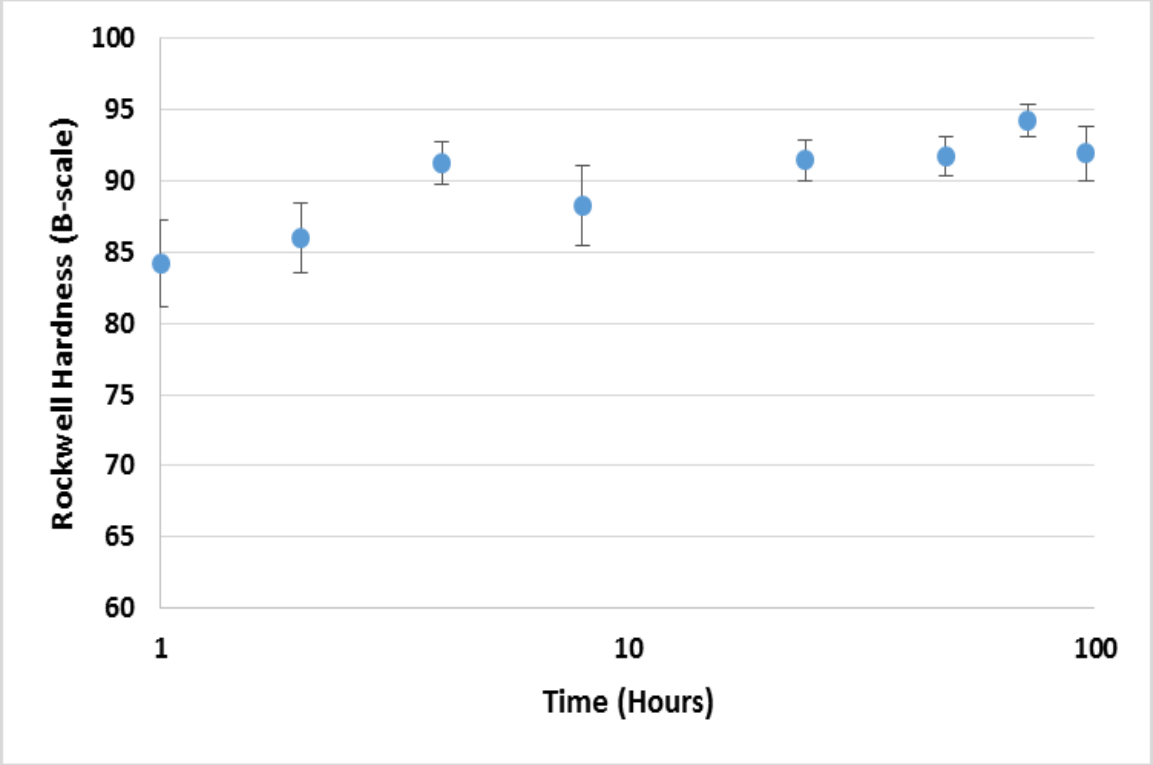


Figure 241 – *Single step aging curve for GT7 at 140°C (284°F).*

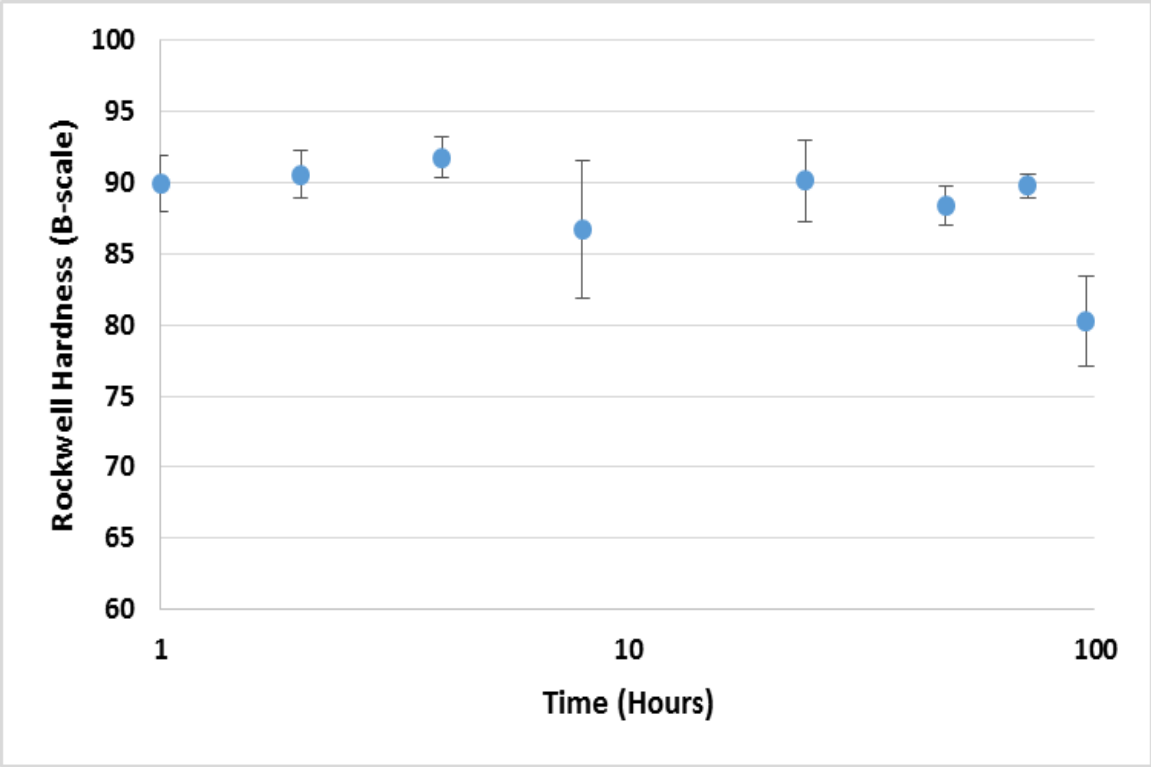


Figure 242 – *Single step aging curve for GT7 at 160°C (320°F).*

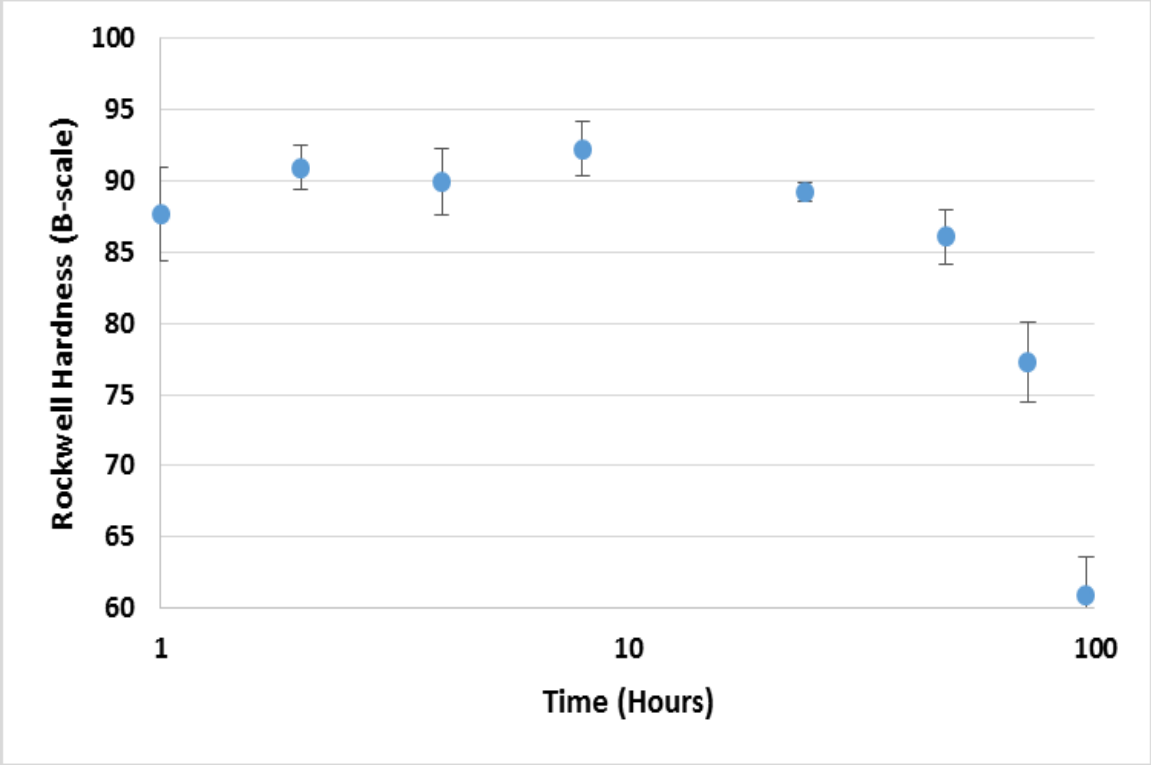


Figure 243 – *Single step aging curve for GT7 at 180°C (356°F).*

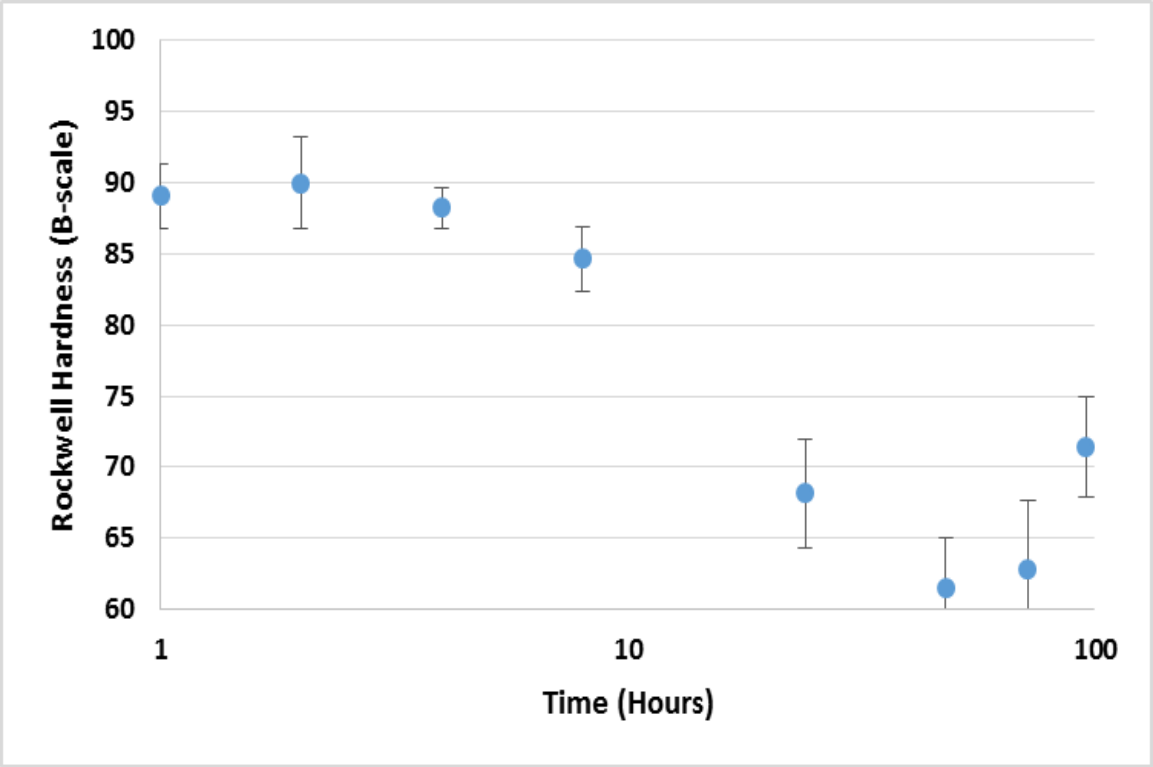


Figure 244 – *Single step aging curve for GT7 at 200°C (392°F).*

**GT8**

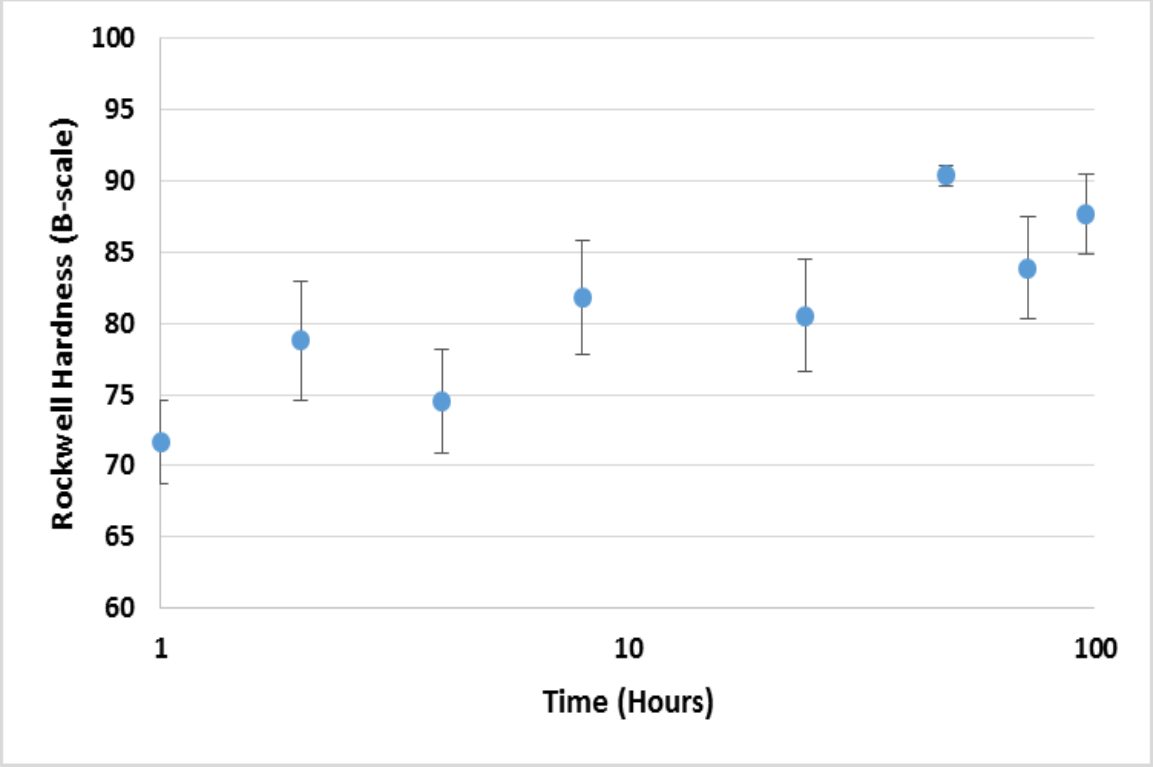


Figure 245 – *Single step aging curve for GT8 at 100°C (212°F).*

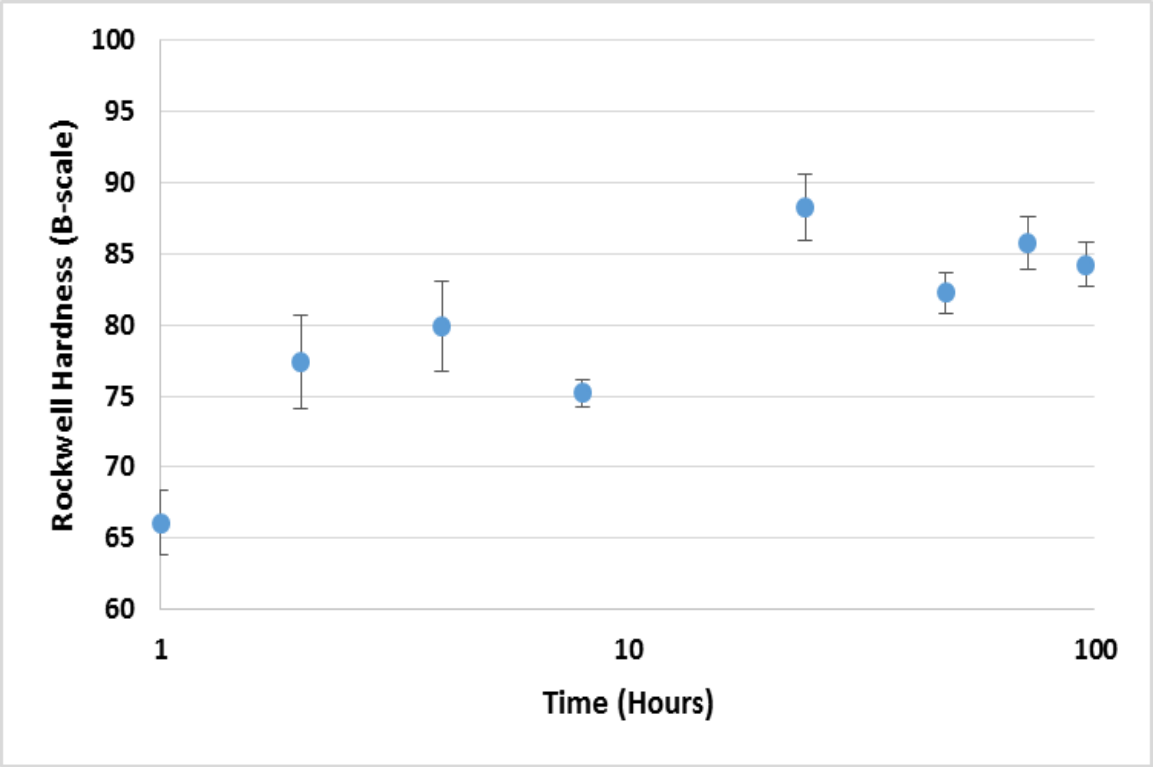


Figure 246 – *Single step aging curve for GT8 at 120°C (248°F).*

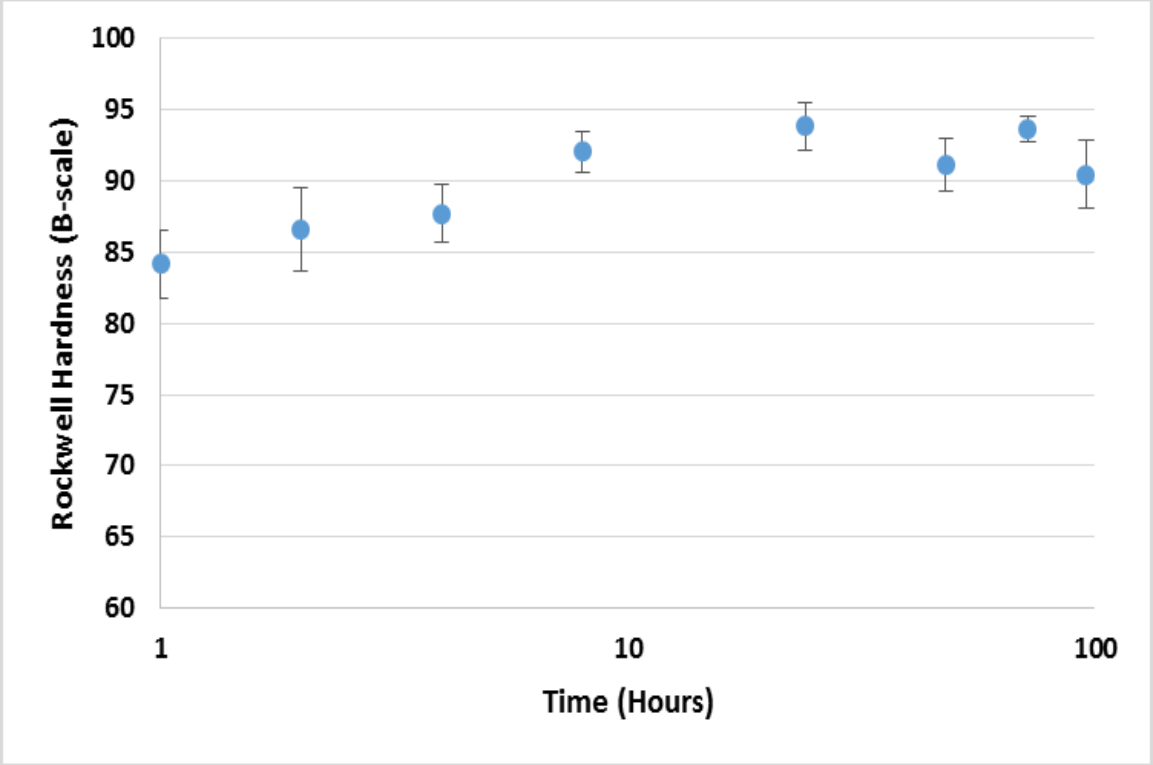


Figure 247 – *Single step aging curve for GT8 at 140°C (284°F).*

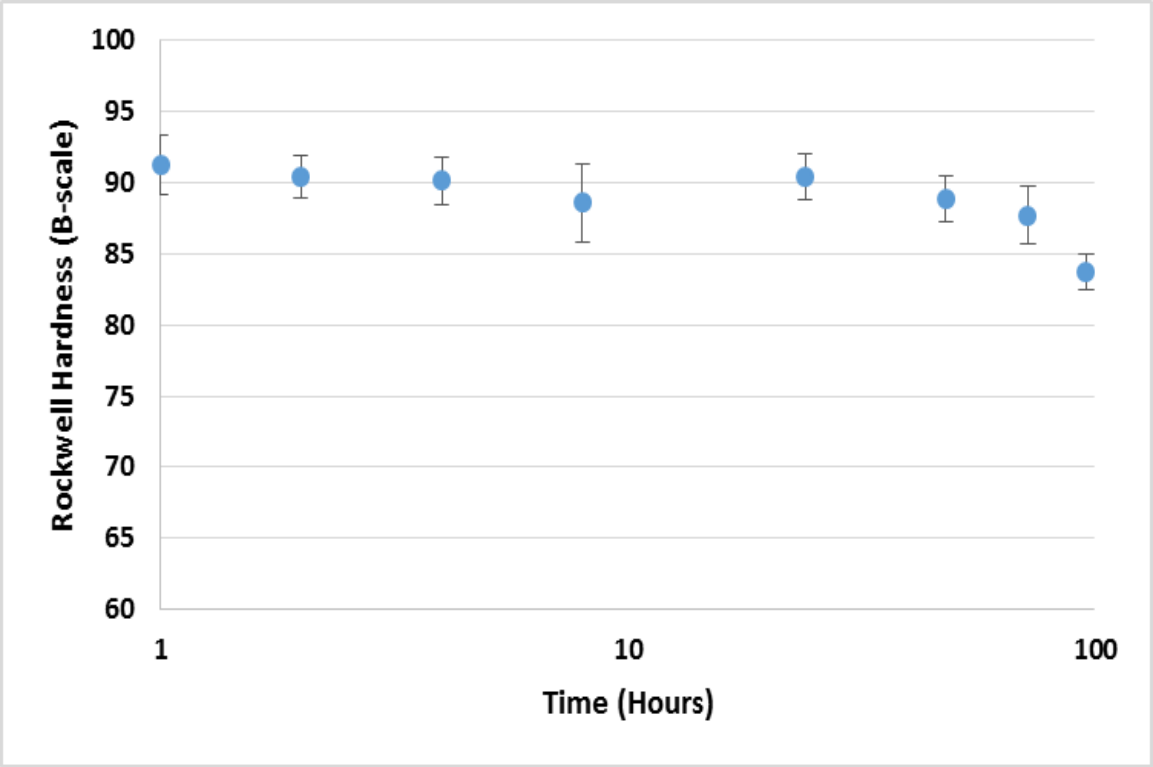


Figure 248 – *Single step aging curve for GT8 at 160°C (320°F).*

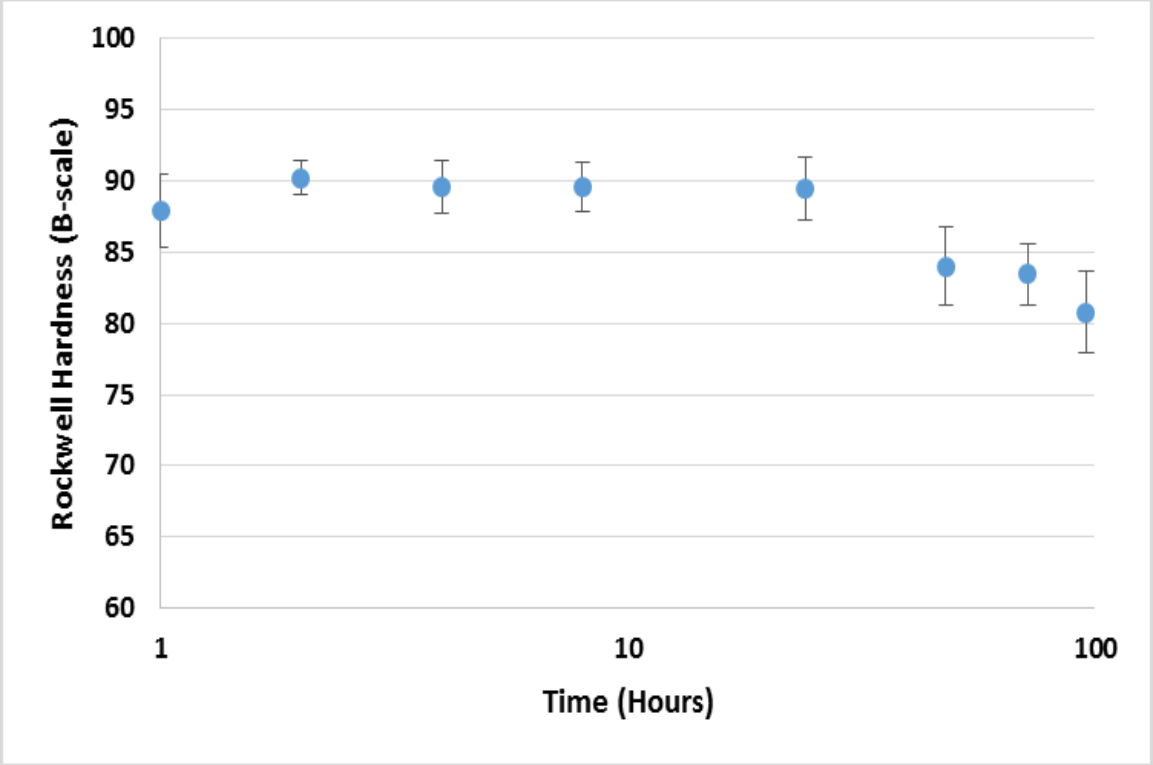


Figure 249 – *Single step aging curve for GT8 at 180°C (356°F).*

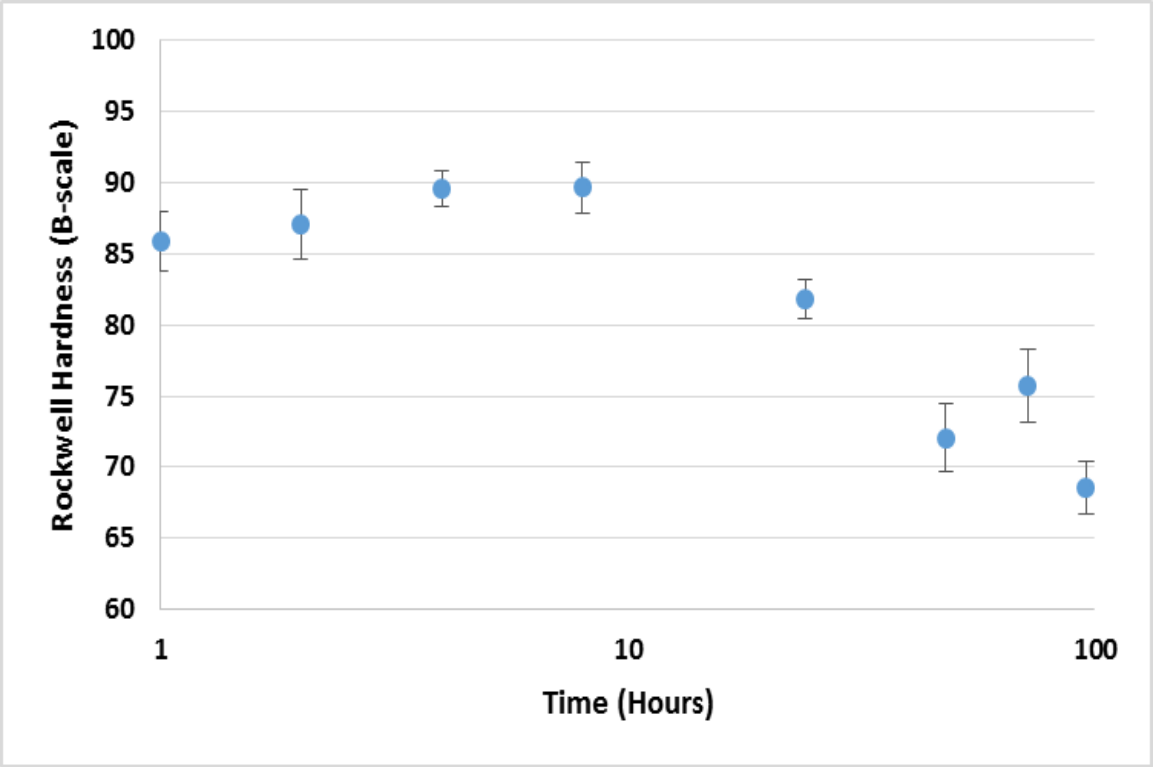


Figure 250 – *Single step aging curve for GT8 at 200°C (392°F).*

# APPENDIX D

# EXFOLIATION CORROSION (EXCO) TESTING OF GT1-8

Exfoliation corrosion (EXCO) is defined by ASTM G34-01[1] as "corrosion that proceeds laterally from the sites of initiation along planes parallel to the surface, generally at grain boundaries, forming corrosion products that force metal away from the body of the material giving rise to a layered appearance." The purpose of this "side work" was to determine the EXCO susceptibility of experimental alloys GT1-8 in the T73 temper and try to correlate them to the PFZ sizes discussed in *Part II – Chapter 14 – The Effect of Composition on the Precipitate Free Zone*.

## D.1 Experimental Procedure

Samples of experimental alloys GT1-8 were overaged to a T73 temper (i.e. – 24 hours at 120°C followed by 24 hours at 160°C) and then milled to reveal the T/10 plane (i.e. – 10% of the material was removed from one of the surfaces). For comparison purposes, a 7136-T73511 sample was also included. The remaining surfaces of the samples were then painted to mitigate corrosion on those surfaces. The samples were then cleaned, dried, measured for dimensions, and weighed before being submerged in the test solution for 48 hours. The EXCO test solution was kept at RT and had the following composition per liter: NaCl 234 g, $KNO_3$ 50 g, $HNO_3$ 6.3 mL, $H_2O$ remainder.

Following submersion, the samples were carefully removed from the solution and photographed after being allowed to air dry and rated according to ASTM G34 (see Figures 251-254) [1]. The samples were then cleaned and re-weighed in order to determine the weight loss per unit area that occurred over the testing process for each sample. It should be noted that the specimen sizes utilized here are not in compliance with the minimum surface area required by ASTM G34 [1].

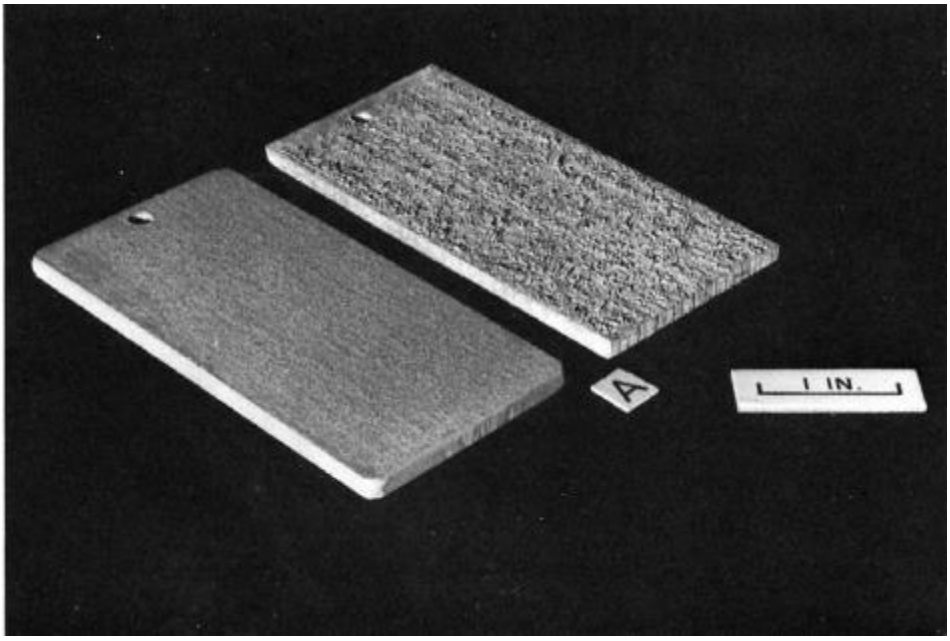


Figure 251 – *Examples of ASTM G34 EXCO rating EA* [1].

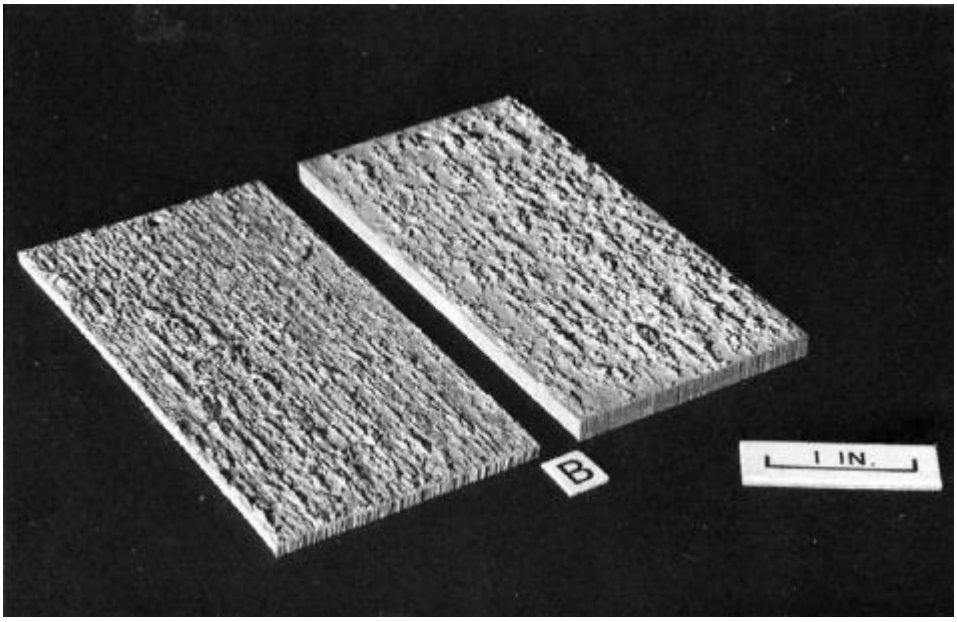


Figure 252 – *Examples of ASTM G34 EXCO rating EB* [1].

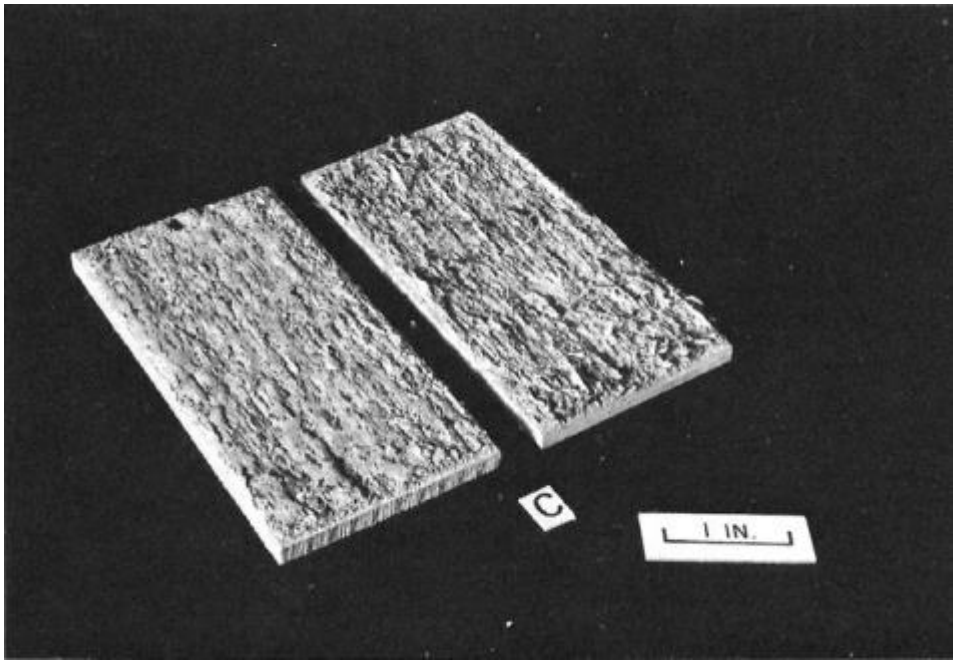

Figure 253 – *Examples of ASTM G34 EXCO rating EC* [1].

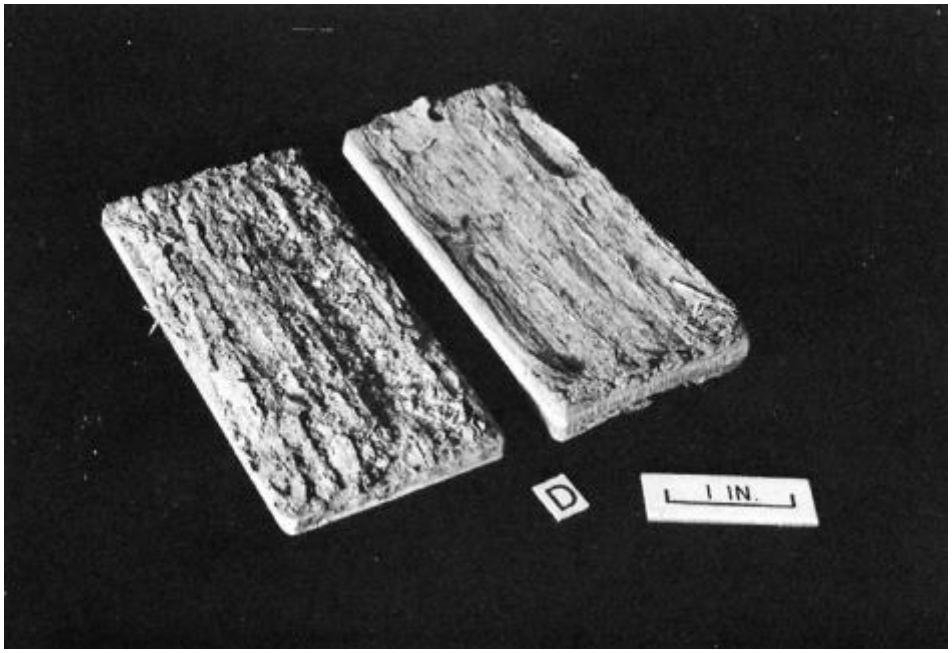

Figure 254 – *Examples of ASTM G34 EXCO rating ED* [1].

## D.2 Results and Discussion

The results of the ASTM G34 tests on GT1-8 and 7136-T73 can be seen in Table 39. Photographs of the samples after testing can be seen in Figures 255 – 262. It should be noted that the G34 rating listed in Table 39 is the mode of three independent classifications by lab technicians at UAC-Canton.

Table 39 – *EXCO results for GT1-8 and 7136 in the T7 temper.*

| Alloy | Test Area ($cm^2$) | Weight (g) | | Loss ($g/cm^2$) | G34 Rating |
|---|---|---|---|---|---|
| | | Before | After | | |
| GT1 | 1.57 | 21.32 | 21.23 | 0.06 | EB |
| GT2 | 1.95 | 25.78 | 25.73 | 0.03 | EA |
| GT3 | 1.16 | 15.54 | 15.53 | 0.01 | EA |
| GT4 | 2.04 | 28.69 | 28.66 | 0.01 | P |
| GT5 | 0.77 | 10.45 | 10.43 | 0.01 | N |
| GT6 | 1.92 | 24.34 | 24.29 | 0.03 | EA |
| GT7 | 1.72 | 22.21 | 22.19 | 0.01 | EA |
| GT8 | 1.57 | 15.73 | 15.57 | 0.10 | EB |
| 7136 | 51.15 | 377.70 | 377.10 | 0.01 | EB |

Figure 255 – *GT1-T73 after 48 hours in EXCO solution.*

Figure 256 – *GT2-T73 after 48 hours in EXCO solution.*

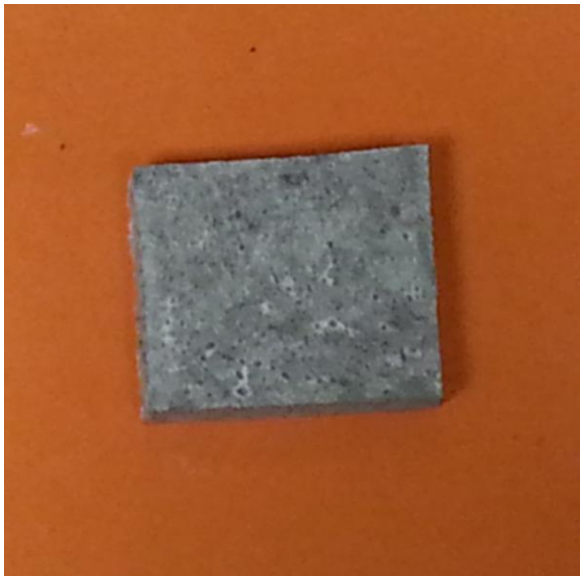

Figure 257 – *GT3-T73 after 48 hours in EXCO solution.*

Figure 258 – *GT4-T73 after 48 hours in EXCO solution.*

Figure 259 – *GT5-T73 after 48 hours in EXCO solution.*

Figure 260 – *GT6-T73 after 48 hours in EXCO solution.*

Figure 261 – *GT7-T73 after 48 hours in EXCO solution.*

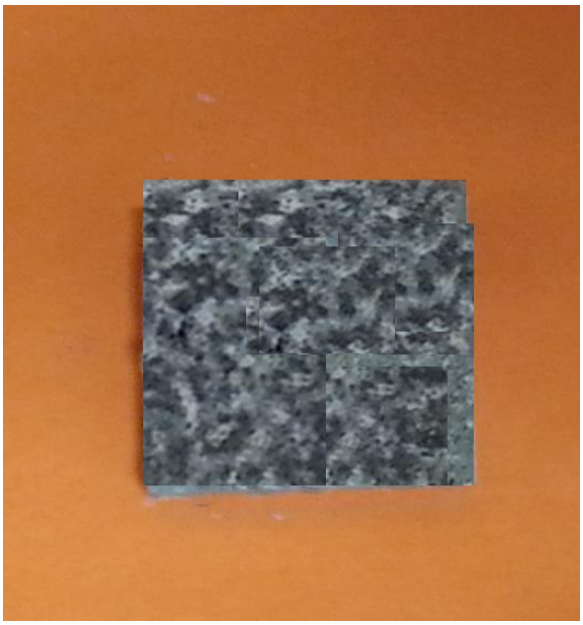

Figure 262 – *GT8-T73 after 48 hours in EXCO solution.*

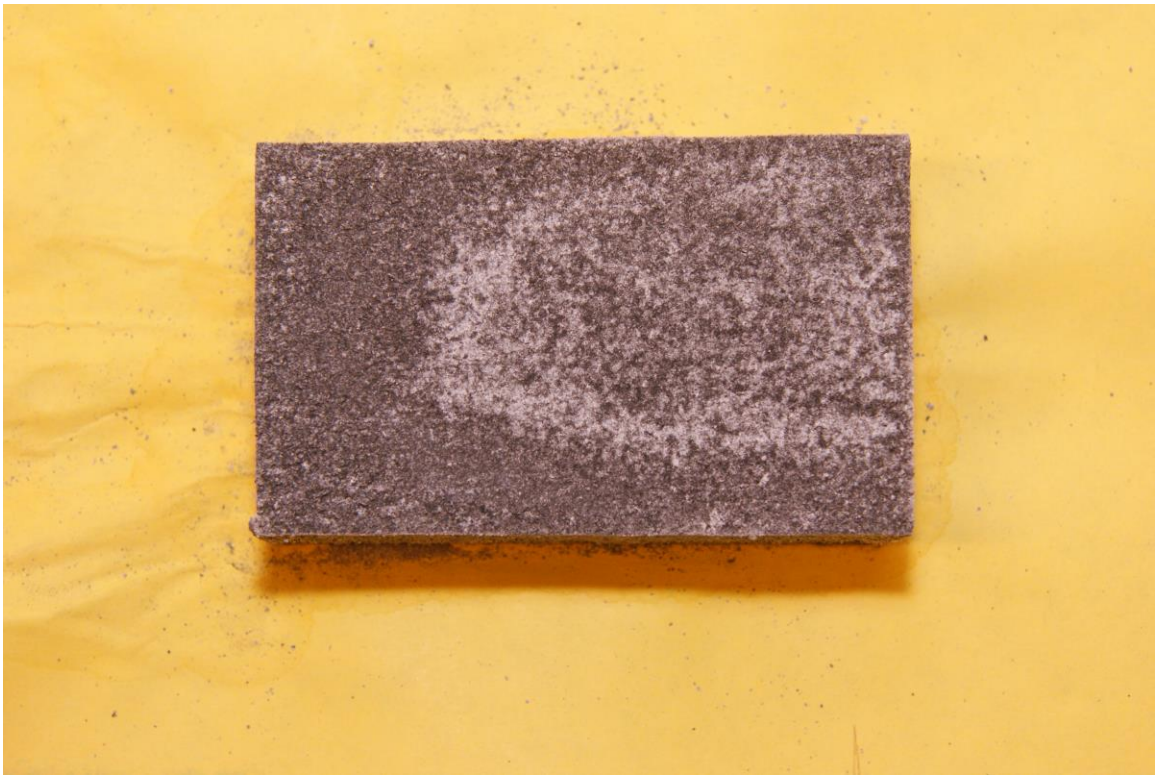

Figure 263 – *7136-T73 after 48 hours in EXCO solution.*

It becomes clear the EXCO data in Table D-1 and from Figures 255 – 263 that the relative susceptibility of a sample to EXCO can be directly related to its Cu content. This

is most evident in GT1-5 and 7136, which has a Cu level approximately around that of GT1 and GT2. This effect of Cu is not unexpected as explained by Hatch [2].

Likewise, with GT6-8 the increasing Mg content also drives down the EXCO resistance. As was shown in *Part II – Chapter 12 – The Effects of Natural Aging* and *Part II – Chapter 14 – The Effect of Composition on the Precipitate Free Zone*, this could be due to the precipitation of T-phase, which is known to be highly corrosive, in the high Mg alloys. GT1-T73, which also displayed T-phase in the grain boundary, also had an EB EXCO rating. Unfortunately, however, no clear trend between PFZ size and EXCO resistance could be established (i.e. – the EXCO resistance appears to relate more to compositional factors than the PFZ size).

It should also be noted that the general resistance to EXCO displayed by GT1-8 (i.e. – every sample was an EB or better) may be partially due to their microstructure being REX [2]. For the 7136-T73511 sample, where little-to-no REX grains exist at the T/10 plane, the resistance is probably due to myriad of factors all of which relate to the over-aged nature of the material.

### D.3 Summary

The resistance to EXCO for GT1-8 in the T73 temper and 7136-T73511 was determined. It was shown that EXCO resistance can be directly related to the Cu content of an aluminum alloy, and the type of precipitates in the grain boundaries (i.e. – T-phase in GT8-T73). No clear link between PFZ size and EXCO resistance could be established.

### D.4 References

[1] ASTM, *G34-01 - Standard test method for exfoliation corrosion susceptibility in 2xxx and 7xxx series aluminum alloys (EXCO Test)*. 2013.

[2] J. E. Hatch, *Aluminum: Properties and Physical Metallurgy*. ASM, 1984.

# APPENDIX E

# INTERGRANULAR CORROSION (IGC) TESTING OF GT1-8

Intergranular corrosion (IGC) is defined as: "the selective attack of grain boundaries with little to no appreciable attack of the grain body" [1], [2]. Typically, the path of corrosion can be seen starting from pitting cavities and the surface and progressing into the metal. Hatch [1] states that IGC resistance in 7xxx-series alloys is directly affected by thermal treatments and can be directly correlated to the types of intermetallic phases present in the grain boundaries. The purpose of this "side work" is to determine the IGC susceptibilities of experimental alloys GT1-8 in the T73 temper and try to correlate them to the PFZ sizes discussed in *Part II – Chapter 14 – The Effect of Composition on the Precipitate Free Zone*. The method used is in compliance with ASTM G110 [2].

## E.1 Experimental Procedure

Samples of GT1-8 were SHT and aged to a T73 temper (120°C – 24 hours → 160°C – 24 hours). It should noted that some of the samples used did not meet the 4 $in^2$ of total surface area minimum ASTM requirement. The samples were then milled to a T/10 thickness (i.e. – 10% of the sample was removed).

In order to remove the sample of all foreign matter, the sample was immersed in a cleaning solution (945 mL reagent water, 50 mL nitric acid, 5 mL hydrofluoric acid) at 93°C (200°F) for 1 minute, and subsequently rinse with reagent water. The sample was immediately then immersed in concentrated nitric acid (70%) for 1 min before being washed with reagent water and air dried.

Once dry, the specimens were placed upon a plastic grating in the test solution (57 g sodium chloride, 1 L reagent water, 10 ml hydrogen peroxide), which was being held at

30°C (86°F), for 6 hours. After being exposed to the test solution, the samples were removed and cleaned using a reagent water and a soft bristle brush.

Metallographic mounts were then made from GT1-8 in the L-ST direction. The samples were then polished and viewed at 200x. Micrographs of the samples taken along the length of the specimen of each IGC attack. These micrographs were then analyzed using FIJI software to calculate the maximum, average, and frequency of the IGC attacks.

### E.2 Results

A typical IGC attack for each experimental alloy can be seen in Figures 264 – 271, and the results of the testing are summarized in Table 40. As can be seen in Figures 264 – 268 as the Cu level is lowered the type of attack and the depth of the attack are generally changed with GT4 displaying only surface pits. Figure 268 (GT5) displays a large prototypical IGC attack, but this was the only such attack observed. The rest of GT5 did not even contain surface pits. For alloys GT6-8, as the Zn:Mg ratio is lowered the type of attack appears to change from vertical to almost horizontal in nature, however the number of attacks greatly increases. Figure 269 displays these trends graphically.

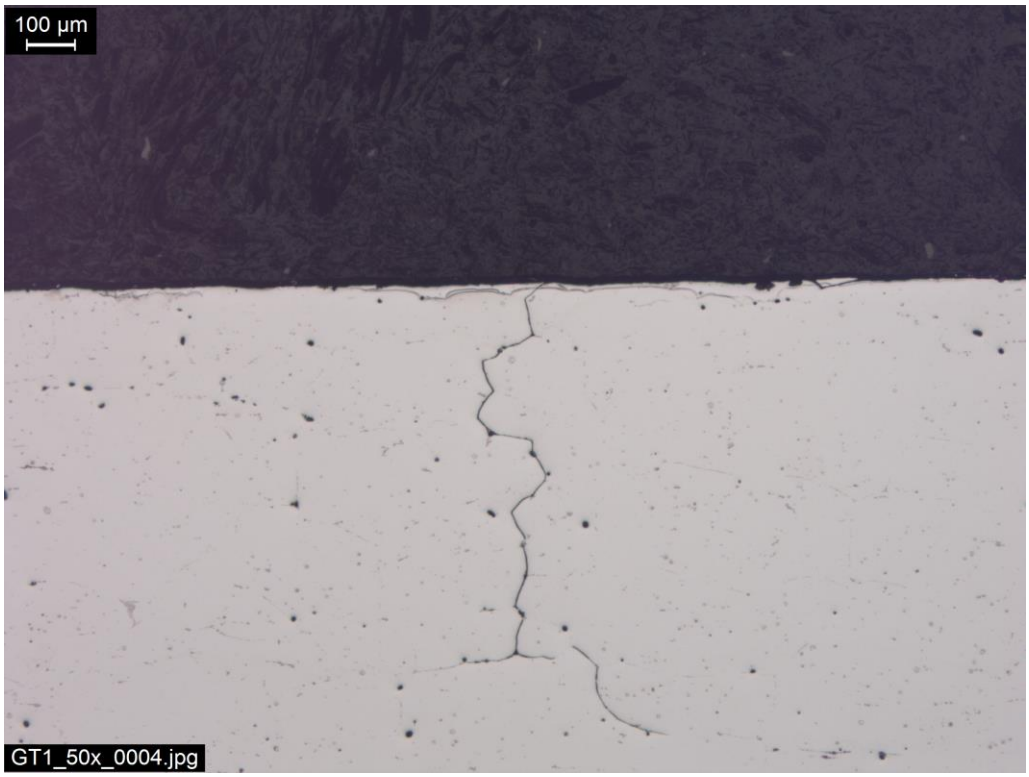

Figure 264 – *A typical IGC attack on GT1-T73 at 50x.*

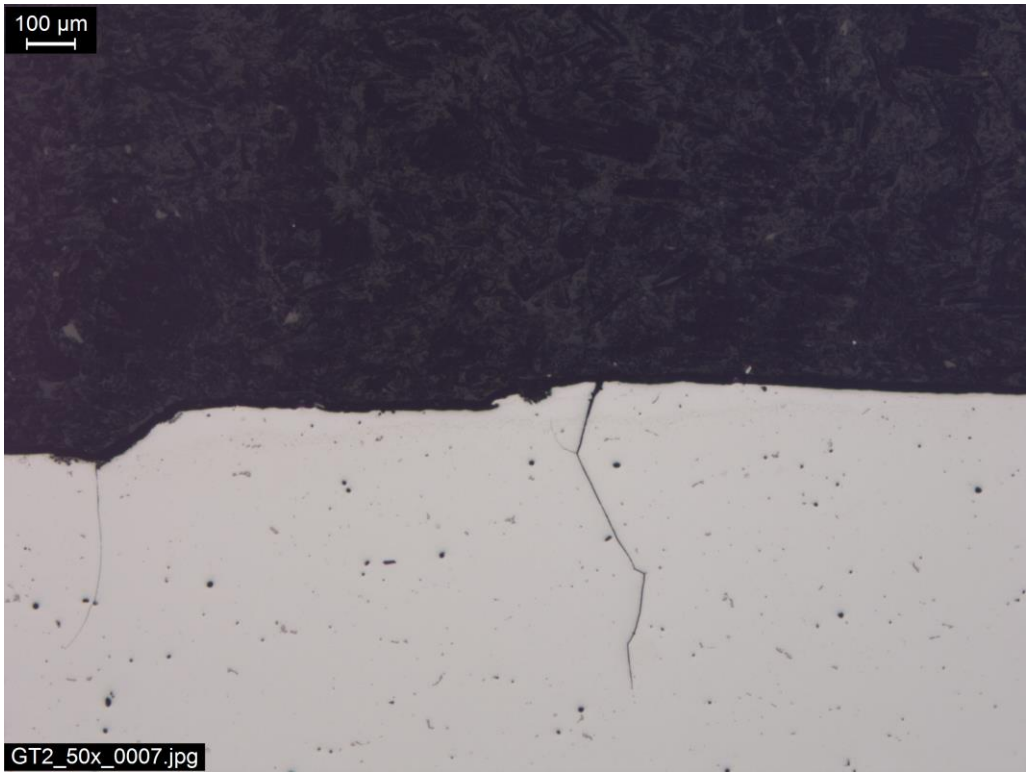

Figure 265 – *A typical IGC attack on GT2-T73 at 50x.*

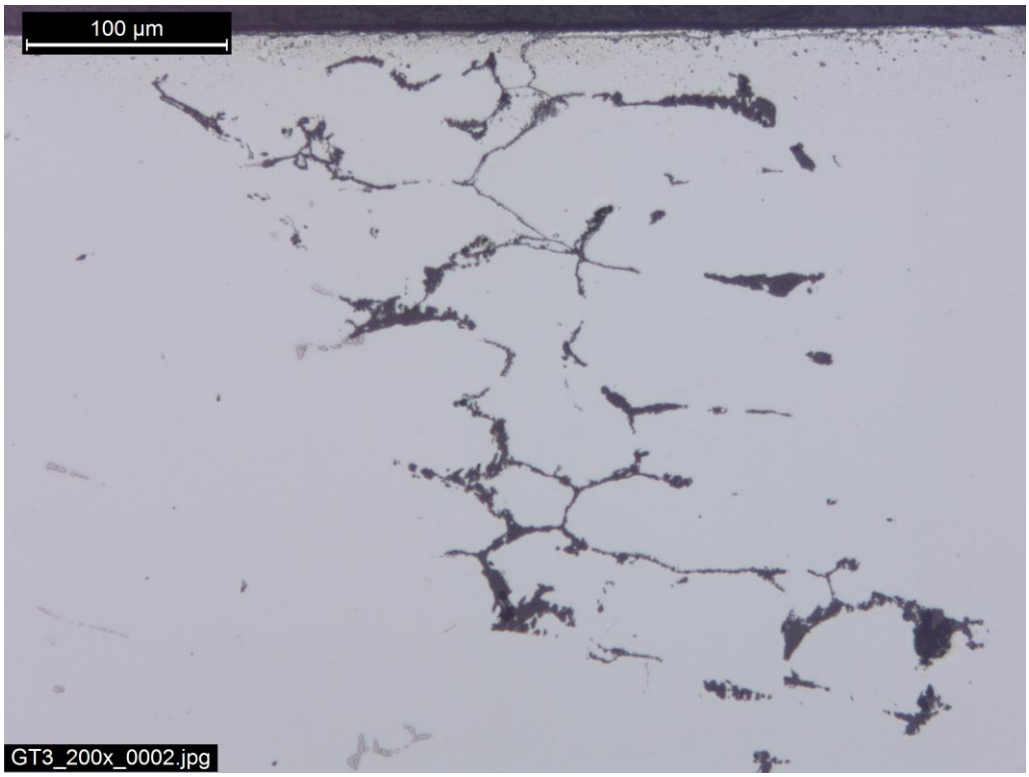

Figure 266 – *A typical IGC attack on GT3-T73 at 200x.*

Figure 267 – *A typical IGC attack on GT4-T73 at 200x.*

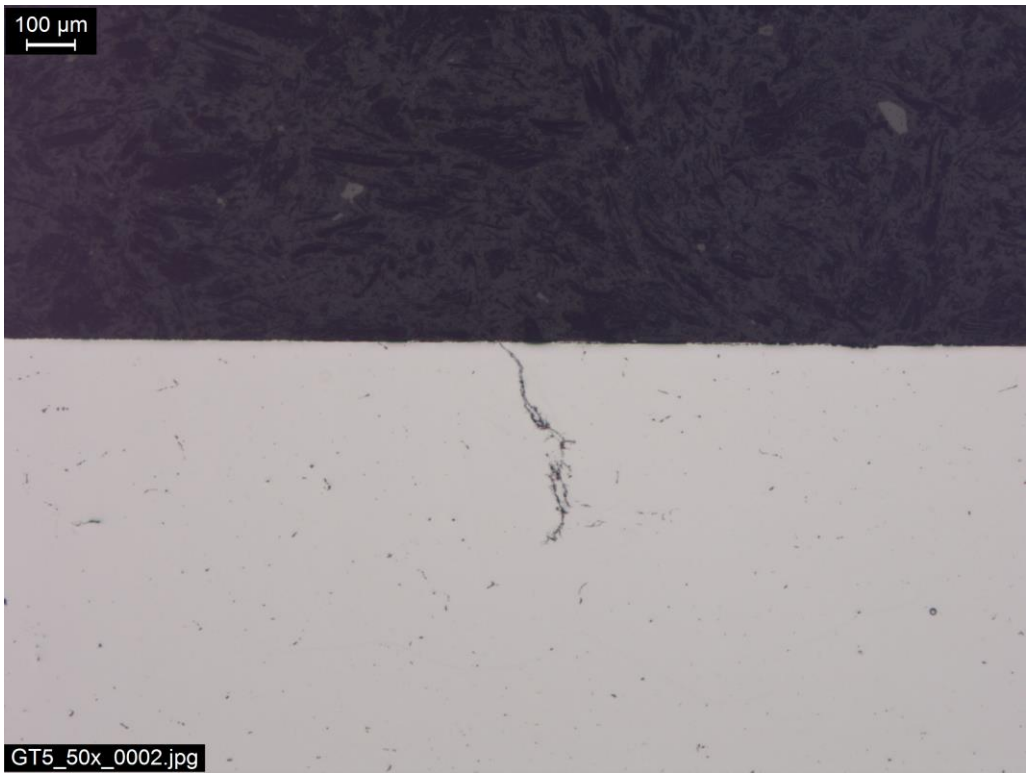

Figure 268 – *A typical IGC attack on GT5-T73 at 50x.*

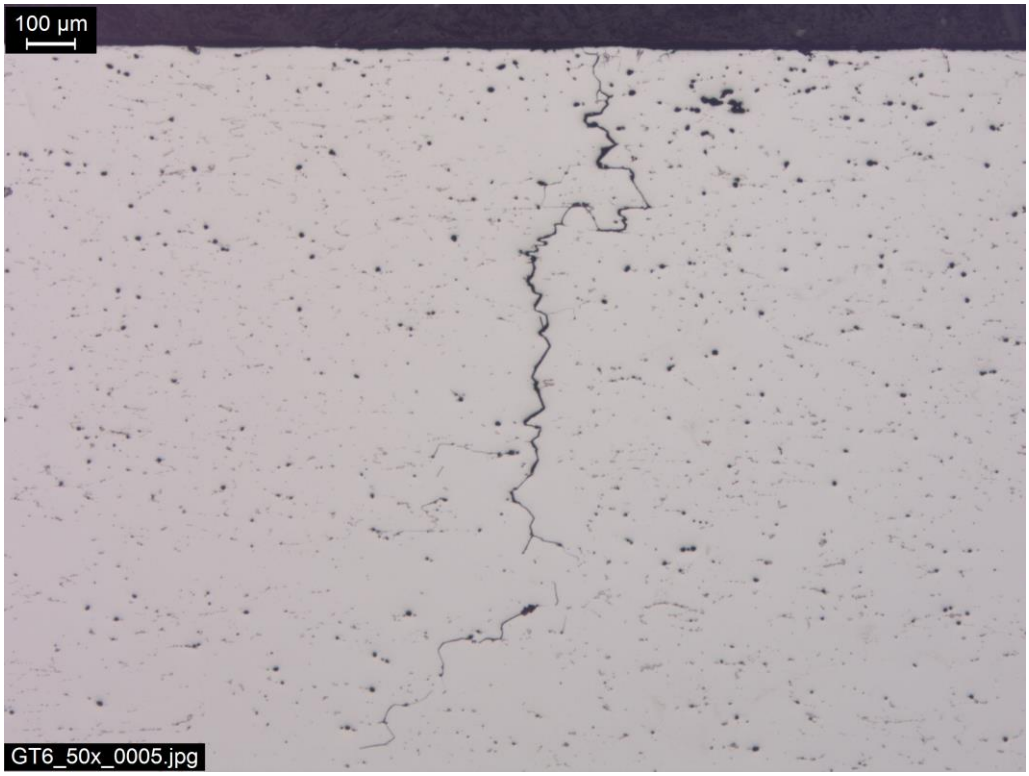

Figure 269 – *A typical IGC attack on GT6-T73 at 50x.*

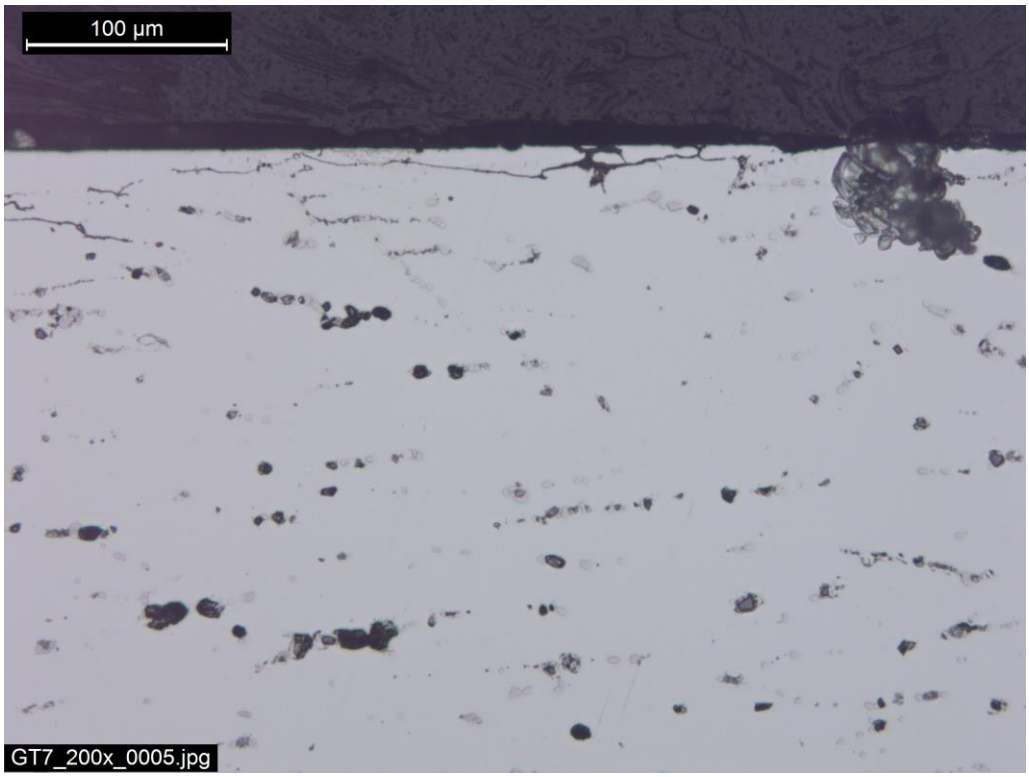

Figure 270 – *A typical IGC attack on GT7-T73 at 200x.*

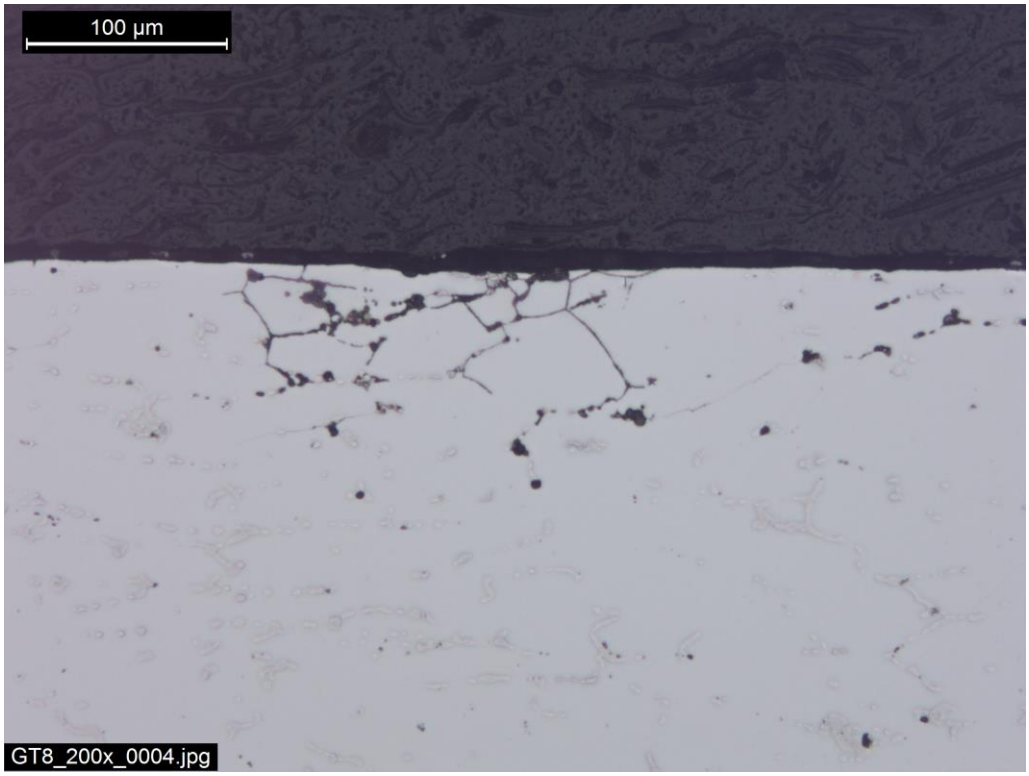

Figure 271 – *A typical IGC attack on GT8-T73 at 200x.*

Table 40 – *IGC testing results for GT1-8 in the T7 temper.*

| Alloy | Average Depth (µm) | Max. Depth (µm) | Attacks per cm |
|---|---|---|---|
| GT1 | 620 | 2,953 | 8.44 |
| GT2 | 651 | 2,574 | 5.90 |
| GT3 | 169 | 439 | 2.81 |
| GT4 | 5 | 11 | 4.50 |
| GT5 | 221 | 436 | 1.15 |
| GT6 | 435 | 2,603 | 7.65 |
| GT7 | 30 | 60 | 15.5 |
| GT8 | 88 | 231 | 24.8 |

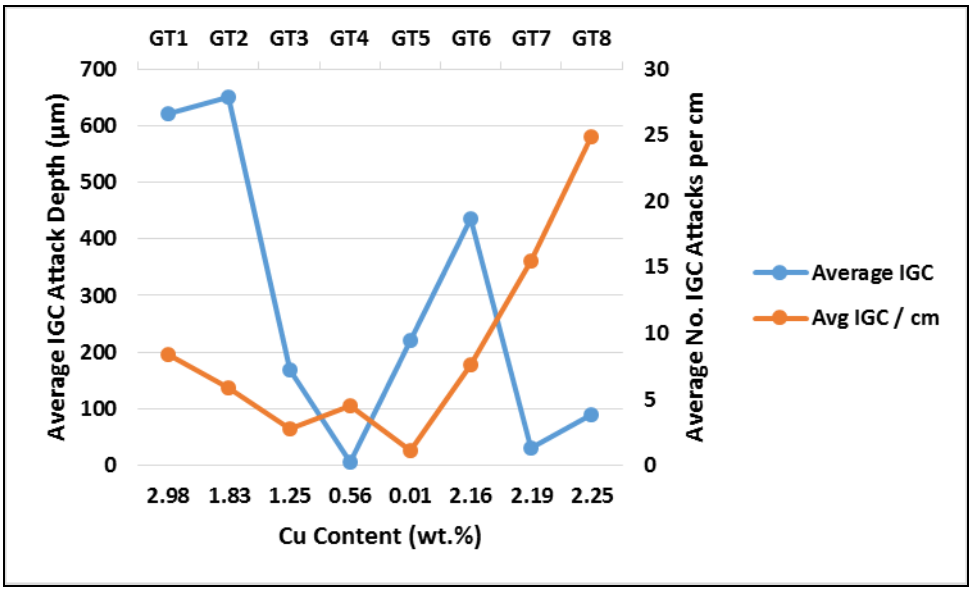


Figure 272 – *Average IGC attack depth and number of attacks per cm versus the alloy Cu content of GT1-8 (wt.%).*

Unfortunately, no correlation between maximum IGC attack (a property usually used for the certification of parts in the extrusion industry) and Cu content could be made due to the Cu-free GT5. However, if GT5 is ignored (as previously mentioned only one IGC attack was observed) then it appears the average IGC attack directly correlates to the Cu content. GT6-8 appear to show that the average depth of attack can also be modified by the Mg content, which cause the attacks to become shallower, although more numerous.

Figure 273 displays the max and average IGC attack depths versus the PFZ size. Interesting, the sample with the largest PFZ (GT4) appears the least prone to IGC;

however, it should be noted that due to the nature of TEM these findings may not be statically significant. The other alloys, GT1-3 and GT5-8, do not display any correlation between PFZ size and IGC attack. Therefore, it is logical to conclude that, like EXCO (see *Appendix D – Exfoliation corrosion (EXCO) testing of GT1-8*), composition plays more of a role in an alloys resistance to IGC than PFZ size. This would seemingly explain the increase in IGC attack in GT5, which displayed large Fe and Si intermetallics as well as T-phase in the grain boundary even though it was Cu-free.

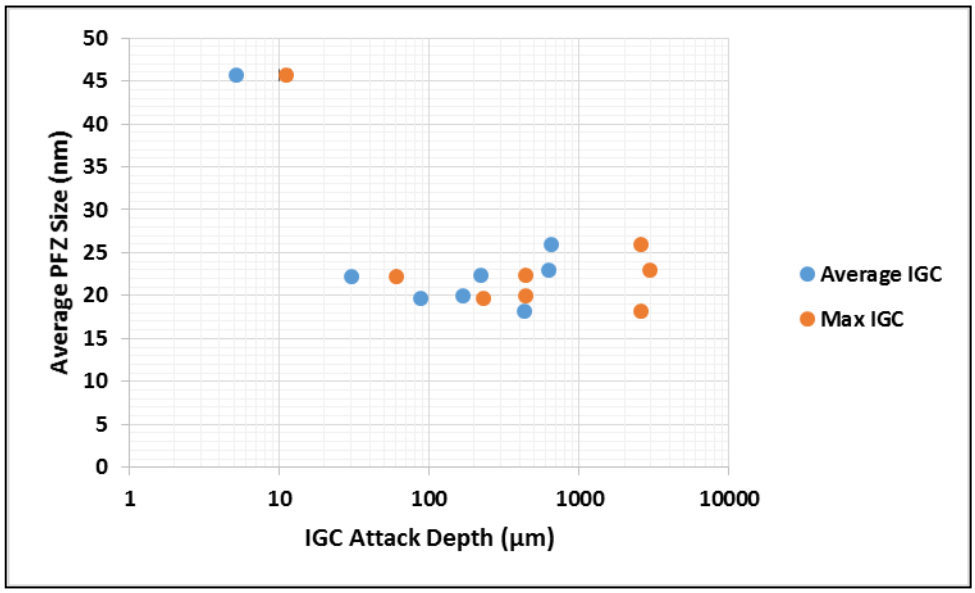


Figure 273 – *Average PFZ size (nm) versus average and max IGC attack depth (µm) for GT1-8.*

## E.3 Summary

IGC testing was performed on samples GT1-8. Unfortunately, no direct correlation could be found between the average PFZ size and the susceptibility to IGC attack. Conversely, the susceptibility to IGC appears to directly correlate to the composition of the phases present in the grain boundary, which is not unexpected.

## E.4 References

[1] J. E. Hatch, *Aluminum: Properties and Physical Metallurgy*. ASM, 1984.

[2] ASTM, *G110 - Standard practice for evaluating intergranular corrosion resistance of heat treatable aluminum alloys by immersion in sodium chloride and hydorgen peroxide solution*. 1992.

# SUMMARY

Various properties of 7xxx-series aluminum alloys can be directly correlated to their respected compositions including, but not limited to: aging behavior, quench sensitivity, and precipitate composition. It should be noted that with respect to the phenomena evaluated that the (Zn+Cu):Mg, or the Zn:Mg, ratio and the dispersoid forming elements appear to have the largest effects. It appears that for high Zn:Mg ratios that the (Zn+Cu):Mg ratio provides a better correlation to properties due to the fact that the main hardening precipitates in Al-Zn-Mg-Cu alloys, η'/η, have an extended composition range, which allows for the substitution of Cu for Zn. Conversely, for systems with excess Mg (i.e. – low Zn:Mg ratios) it appears that the Zn:Mg ratio provides a better fit, which could be directly correlated to a shift in the composition of η' and η.

With respect to the as-cast condition it was shown that the Cu content could be directly correlated to the onset melting temperature and therefore directly influences the homogenization temperature of an alloy. It was shown that although Zn and Cu appears to have little effect on the effectiveness of the homogenization, high Mg alloys proved to be less responsive to homogenizations tailored for the Cu and therefore may require multi-step homogenization practices.

The effects of natural aging and the artificial aging behavior of 7xxx-series alloys was shown to be directly dependent on the (Zn+Cu):Mg ratio, especially the relative Cu content with its ability to alter to GP-zone precipitation process. The systematic approach presented, which mirrors the industrial process for extrusion at each step, provides valuable insights into the aging behaviors of 7xxx-series alloys. Using the information provided herein, one could establish new aging practices for developed 7xxx-series alloys (whether to improve upon existing practices or skirt patients) or one could determine a "best guess" aging practice for new 7xxx-series alloys were the artificial

aging behavior has not be evaluated yet. The natural aging information provided is also valuable with respect to secondary forming operations (ex. – stretch forming) on 7xxx-series aluminum alloys.

Unfortunately, the PFZ size could not be directly correlated to the (Zn+Cu):Mg ratio, although the grain boundary precipitates were shown to be directly affected. Future studies should focus on determining if the PFZ around individual precipitates varies instead of the grain boundary on the whole. If such a correlation could be established, the (Zn+Cu):Mg ratio could be altered to influence the type of grain boundary precipitate formed and therefore the PFZ size.

# REFERENCES

The following is a compiled list of the references used in order of appearance.

Chapter 1 – Introduction


1. A. Wilm, “Metallurgical invesitgations of aluminum alloys containing magneisum,” *Metallurgie*, vol. 8, p. 225, 1911.
2. P. D. Merica, R. G. Waltenberg, and H. Scott, “Heat treatment of Duralumin,” *Sci. Pap.*, pp. 271–315, 1919.
3. M. E. Fine, “Precipitation hardening of aluminum alloys,” *Metall. Trans. A*, vol. 6, no. April, pp. 625–630, 1975.
4. JAA, “Chronology,” *Japan Aluminum Assocatiation*, 2002. [Online]. Available: http://www.aluminum.or.jp/basic/alumi-sangyo/hf00.html. [Accessed: 24-Apr-2014].
5. I. J. Polmear, “Aluminium alloys – a century of age hardening,” *Mater. Forum*, vol. 28, pp. 1–14, 2004
6. The Aluminum Association, *International Alloy Designations and Chemical Composition Limits for Wrought Aluminum and Wrought Aluminum Alloys*. Arlington, VA, 2009.


Part I – A Review of Literature

Chapter 2 – Introduction

Chapter 3 – Solidification of Al-Zn-Mg-Cu Alloys


1. I. J. Polmear, *Light Metals*, Arnold, 1995.
2. E. P. Degarmo, J. T. Black, and R. A. Kohser, *Materials and Processes in Manufacturing*, 9th ed. 2003.
3. S. Kalpakjan and S. Schmid, *Manufactoring Engineering and Techonology*, 5th ed. Pearson, 2006.
4. J. R. Davis, *Aluminum and Aluminum Alloys*. ASM International, 1993.
5. V. S. Zolotorevsky, N. A. Belov, and M. V. Glazoff, *Casting Aluminum Alloys*. Pittsburgh, 2007.
6. D. Mortensen, “A mathematical model of the heat and fluid flows in direct-chill casting of aluminum sheet ingots and billets,” *Metall. Mater. Trans. B*, vol. 30, pp. 119–133, 1999.
7. H. G. Fjaer and A. Mo, “ALSPEN - a mathematical model for thermal stresses in direct chill casting of aluminum billets,” *Metall. Trans. B*, vol. 21, pp. 1049–1061, 1990.
8. J.-M. Drezet and M. Rappaz, “Modeling of ingot distortions during direct chill casting of aluminum alloys,” *Metall. Mater. Trans. A*, vol. 27, pp. 3214–3225, 1996.

9. N. Pourkia, M. Emamy, H. Farhangi, and S. H. Seyed Ebrahimi, “The effect of Ti and Zr elements and cooling rate on the microstructure and tensile properties of a new developed super high-strength aluminum alloy,” *Mater. Sci. Eng. A*, vol. 527, pp. 5318–5325, 2010.
10. E. Lavernia, G. Rai, and N. J. Grant, “Rapid solidification processing of 7xxx aluminium alloys: a review,” *Mater. Sci. Eng.*, vol. 79, pp. 211–221, 1986.
11. Y. Birol, “The performance of Al-Ti-C grain refiners in twin-roll casting of aluminum foilstock,” *J. Alloys Compd.*, vol. 430, pp. 179–187, 2007.
12. L. Yu, X. Liu, Z. Wang, and X. Bian, “Grain refinement of A356 alloy by AlTiC/AlTiB master alloys,” *J. Mater. Sci. Lett.*, vol. 40, pp. 3865–3867, 2005.
13. H. T. Kim and S. W. Nam, “Solidification cracking susceptibility of high strength aluminum alloy weldment,” *Scr. Mater.*, vol. 34, no. 7, pp. 1139–1145, 1996.
14. J. E. Hatch, *Aluminum: Properties and Physical Metallurgy*. ASM, 1984.
15. T. Sheppard, *Extrusion of Aluminium Alloys*. Kluwer Academic Publishers Group, 1999.
16. X. M. Li and M. J. Starink, “Identification and analysis of intermetallic phases in overaged Zr-containing and Cr-containing Al-Zn-Mg-Cu alloys,” *J. Alloys Compd.*, vol. 509, pp. 471–476, 2011.
17. S. H. Seyed Ebrahimi, M. Emamy, N. Pourkia, and H. R. Lashgari, “The microstructure, hardness, and tensile properties of a new super high strength aluminum alloy with Zr addition,” *Mater. Des.*, vol. 31, pp. 4450–4456, 2010.
18. C. Mondal and A. K. Mukhopadhyay, “On the nature of T (Al2Mg3Zn3) and S (Al2CuMg) phases present in as-cast and annealed 7055 aluminum alloy,” *Mater. Sci. Eng. A*, vol. 391, pp. 367–376, 2005.
19. L. Hai, C. Dahu, W. Zhixiu, and Z. Ziqiao, “High-pressue homogenization treatment of Al-Zn-Mg-Cu aluminum alloy,” *J. Mater. Sci.*, vol. 43, pp. 1583–1586, 2008.
20. K. Chen, H. Liu, Z. Zhang, S. Li, and R. I. Todd, “The improvement of constituent dissolution and mechanical properties of 7055 aluminum alloy by stepped heat treatments,” *J. Mater. Process. Technol.*, vol. 142, no. 1, pp. 190–196, Nov. 2003.
21. J. P. Schaffer, A. Saxena, S. D. Antolovich, T. H. Sanders Jr., and S. B. Warner, *The Science and Design of Engineering Materials*. Atlanta, GA: WCB/McGraw-Hill, 1999.
22. R. Nadella, D. G. Eskin, Q. Du, and L. Katgerman, “Macrosegregation in direct-chill casting of aluminum alloys,” *Prog. Mater. Sci.*, vol. 53, pp. 421–480, 2008.

Chapter 4 – The Homogenization of Al-Zn-Mg-Cu Alloys

1. J. T. Staley, “Properties related to fracture toughness,” *Am. Soc. Test. Mater.*, 1976.

2. I. J. Polmear, *Light Metals*. Arnold, 1995.
3. T. Sheppard, *Extrusion of Aluminium Alloys*. Kluwer Academic Publishers Group, 1999.
4. T. S. Srivatsan, S. Anand, S. Sriram, and V. K. Vasudevan, "The high-cycle fatigue and fracture behavior of aluminum alloy 7055," *Mater. Sci. Eng. A*, vol. 281, pp. 292–304, 2000.
5. T. S. Srivatsan and V. K. Vasudevan, "Temperature and the ductility, deformation, and fracture of Al 7055," *J. Met.*, vol. 1, p. 42, 1999.
6. J. Champlin, J. Zakrajsek, T. S. Srivatsan, P. C. Lam, and M. Manoharan, "Influence of notch severity on the impact fracture behavior of aluminum alloy 7055," *Mater. Des.*, vol. 20, p. 331, 1999.
7. L. Hai, C. Dahu, W. Zhixiu, and Z. Ziqiao, "High-pressue homogenization treatment of Al-Zn-Mg-Cu aluminum alloy," *J. Mater. Sci.*, vol. 43, pp. 1583–1586, 2008.
8. J. E. Hatch, *Aluminum: Properties and Physical Metallurgy*. ASM, 1984.
9. J. Dickson, L. Zhou, a. Paz y Puente, M. Fu, D. D. Keiser, and Y. H. Sohn, "Interdiffusion and reaction between Zr and Al alloys from 425° to 625 °C," *Intermetallics*, pp. 1–9, Feb. 2014.
10. X. Fan, D. Jiang, Q. Meng, and L. Zhong, "The microstructural evolution of an Al – Zn – Mg – Cu alloy during homogenization," vol. 60, pp. 1475–1479, 2006.
11. S. . Lim, S. . Yun, and S. . Nam, "Improved quench sensitivity in modified aluminum alloy 7175 for thick forging applications," *Mater. Sci. Eng. A*, vol. 371, no. 1–2, pp. 82–90, Apr. 2004.
12. H. P. Degischer, G. Rumplmair, W. Lacom, and F. Kutner, "Distribution of Al3Zr precipitates in AlZn4.5Mg," in *Proc. Int. Electron Microscopy*, 1984, p. 753.
13. O. Engler, E. Sachot, J. C. Ehrstrom, A. Reeves, and R. Shahani, "Recrystallization and texture in hot deformed aluminum alloy 7010 thick plates," *Mater. Sci. Technol.*, vol. 12, pp. 717–729, 1996.
14. J. D. Robson, "Optimizing the homogenization of zirconium containing commercial aluminium alloys using a novel process model," vol. 338, no. v, pp. 219–229, 2002.
15. J. Murray, A. Peruzzi, and J. P. Abriata, "Alloy Phase Diagrams," in *ASM Handbook*, 1992, pp. 2.4–2.56.
16. J. D. Robson and P. B. Prangnell, "Dispersoid precipitation and process modelling in zirconium containing commerical aluminum alloys," vol. 49, pp. 599–613, 2001.
17. C. S. Smith, "Grains, phase, and interphase: An interpretation of the microstructure," *Trans. Met. Soc. AIME*, vol. 175, pp. 15–51, 1948.
18. E. E. Underwood, *Quantitative Stereology*. Addison-Wesley, 1970.
19. X. Lü, E. Guo, P. Rometsch, and L. Wang, "Effect of one-step and two-step homogenization treatments on distribution of Al3Zr dispersoids in commercial AA7150 aluminium alloy," *Trans. Nonferrous Met. Soc. China*, vol. 22, no. 11, pp. 2645–2651, Nov. 2012.

20. Y.-L. Deng, L. Wan, L.-H. Wu, Y.-Y. Zhang, and X. M. Zhang, "Microstructural evolution of Al-Zn-Mg-Cu Alloy during homogenization," *J. Mater. Sci.*, vol. 46, pp. 875–881, 2011.
21. X. Fan, D. Jiang, Q. Meng, B. Zhang, and T. Wang, "Evolution of eutectic structures in Al-Zn-Mg-Cu alloys during heat treatment," *Trans. Met. Soc. AIME*, vol. 16, pp. 577–581, 2006.
22. Y. Deng, Z. Yin, and F. Cong, "Intermetallic phase evolution of 7050 aluminum alloy during homogenization," *Intermetallics*, vol. 26, pp. 114–121, 2012.
23. Y. D. Li and W. L. Wu, "Microstructural evolution of Al – Zn – Mg – Cu alloy during homogenization," pp. 875–881, 2011.
24. M. S. Zedalis and M. E. Fine, "Precipitation and ostwald ripening in dilute Al base-Zr-V alloys," *Metall. Trans. A*, vol. 17, pp. 2187–2198, 1986.
25. S. H. Seyed Ebrahimi, M. Emamy, N. Pourkia, and H. R. Lashgari, "The microstructure, hardness, and tensile properties of a new super high strength aluminum alloy with Zr addition," *Mater. Des.*, vol. 31, pp. 4450–4456, 2010.
26. J. T. Staley, "Microstructure and toughness of high-strength aluminum alloys," in *Properties Related to Fracture Toughness*, 1976, pp. 71–96.
27. A. R. Eivani, H. Ahmed, J. Zhou, and J. Duszczyk, "An experimental and theoretical investigation of the formation of Zr-containing dispersoids in Al-4.5Zn-1Mg aluminum alloys," *Mater. Sci. Eng. A*, vol. 527, pp. 2418–2430, 2010.
28. U. M. Iqbal and V. S. S. Kumar, "Effect of Process Parameters on Microstructure and Mechanical Properties on Severe Plastic Deformation Process of Aa7075-T6 Aluminum Alloy," vol. 623, pp. 705–709, 2013.
29. H. Yongdong, Z. Xinming, and C. Zhiqiang, "Effect of minor Sc and Zr addition on grain refinement of as-cast Al-Zn-Mg-Cu alloys," *China Foundary*, vol. 6, pp. 214–218, 2009.
30. Y. W. Riddle and T. H. Sanders, "A study of coarsening , recrystallization , and morphology of microstructure in Al-Sc- ( Zr ) - ( Mg ) alloys," *Metall. Mater. Trans. A*, vol. 35, no. 1, pp. 341–350, 2004.
31. A. K. Mukhopadhyay, "Microstructure and properties of high strength aluminium alloys for structural applications," *Trans. Indian Inst. Met.*, vol. 62, no. 2, pp. 113–122, 2009.
32. X. M. Li and M. J. Starink, "Identification and analysis of intermetallic phases in overaged Zr-containing and Cr-containing Al-Zn-Mg-Cu alloys," *J. Alloys Compd.*, vol. 509, pp. 471–476, 2011.
33. A. K. Mukhopadhyay, Q. B. Yang, and S. R. Singh, "The influence of zirconium on the early stages of aging of a ternary Al-Zn-Mg alloy," *Acta Metall.*, vol. 42, no. 9, pp. 3083–3091, 1994.
34. S. Liu, J. You, X. Zhang, Y. Deng, and Y. Yuan, "Influence of cooling rate after homogenization on the flow behavior of aluminum alloy 7050 under hot compression," *Mater. Sci. Eng. A*, vol. 527, no. 4–5, pp. 1200–1205, Feb. 2010.

35. K. Chen, H. Liu, Z. Zhang, S. Li, and R. I. Todd, “The improvement of constituent dissolution and mechanical properties of 7055 aluminum alloy by stepped heat treatments,” vol. 142, pp. 190–196, 2003.
36. The Aluminium Development Association, *Equilibrium Diagrams of Aluminium Alloy Systems*. London: The Aluminium Development Association, 1961.
37. J. D. Robson and P. B. Prangnell, “Modelling Al 3 Zr dispersoid precipitation in multicomponent aluminium alloys,” vol. 352, pp. 240–250, 2003.
38. J. D. Robson, “A new model for prediction of dispersoid precipitation in aluminium alloys containing zirconium and scandium,” vol. 52, pp. 1409–1421, 2004.
39. B. Ou, J. Yang, and M. Wei, “Effect of Homogenization and Aging Treatment on Mechanical Properties and Stress-Corrosion Cracking of 7050 Alloys,” 2007.

Chapter 5 – Plastic Deformation of Wrought Aluminum Alloys

1. T. Sheppard, *Extrusion of Aluminium Alloys*. Kluwer Academic Publishers Group, 1999.
2. G. E. Dieter, H. A. Kuhn, and S. L. Semiatin, *Handbook of Workability and Process Design*. ASM, 2003.
3. J. G. Kaufman, *Introduction to Aluminum Alloys and Tempers*. ASM, 2000.
4. J. Hirsch, B. Skrotzki, and G. Gottstein, *Aluminum Alloys: Their Physical and Mechanical Properties*. Aachen, Germany: International Conference on Aluminum Alloys, 2008.
5. J. E. Hatch, *Aluminum: Properties and Physical Metallurgy*. ASM, 1984.
6. H. J. McQueen, S. Spigarelli, M. E. Kassner, and E. Evangelista, *Hot Deformation and Processing of Aluminum Alloys*. CRC Press, 2011.
7. The Aluminum Association, *Rolling Aluminum: From the Mine through the Mill*. Aluminum Association, 1990.
8. P. K. Saha, *Aluminum Extrusion Technology*. Metals Park, Ohio: ASM, 2000.
9. T. Sheppard, “The modern extrusion process: temperature and speed,” in *Modern Extrusion: plant, tooling, processing, and products*, University of Aston - Birmingham, 1980.
10. S. H. Seyed Ebrahimi, M. Emamy, N. Pourkia, and H. R. Lashgari, “The microstructure, hardness, and tensile properties of a new super high strength aluminum alloy with Zr addition,” *Mater. Des.*, vol. 31, pp. 4450–4456, 2010.
11. T. Udomphol, “Extrusion.” Suranaree University of Technology, 2007.
12. T. Sheppard and E. P. Wood, “Effect of section geometry on extrudability of Al-Cu-Mn alloy,” *Met. Technol.*, vol. 7, pp. 58–66, 1980.
13. V. I. Johannes and C. W. Jowett, “Temperature distribution in aluminum extrsuion billets,” in Six International Aluminum Extrusion Technology Seminar, 1996.

14. C. Zener and J. H. Hollomon, “Effect of strain rate upon plastic flow of steel,” *J. Appl. Phys.*, vol. 15, no. 1, pp. 22–32, 1944.
15. H. Zhang, N. Jin, and J. Chen, “Hot deformation behavior of Al-Zn-Mg-Cu-Zr aluminum alloys during compression at elevated temperature,” *Trans. Nonferrous Met. Soc. China*, vol. 21, no. 3, pp. 437–442, Mar. 2011.
16. C. M. Sellars and W. J. McTegart, “On the mechanisms of hot deformation,” *Acta Metall.*, vol. 14, no. 3, pp. 1136–1138, 1966.
17. Y. D. Li and W. L. Wu, “Microstructural evolution of Al – Zn – Mg – Cu alloy during homogenization,” pp. 875–881, 2011.
18. T. Sheppard, N. Parson, and M. Zaidi, “Dynamic recrystallization in Al-7Mg alloy,” *Met. Sci.*, vol. 17, no. 10, pp. 481–490, 1983.
19. E. P. Degarmo, J. T. Black, and R. A. Kohser, *Materials and Processes in Manufacturing*, 9th ed. 2003.
20. J. Polmear, *Light Metals*. Arnold, 1995.
21. R. Rangathan, “Recrystallization resistance in aluminum alloys containing zirconium,” Georgia Institute of Technology, 1991.
22. R. A. Petkovic, M. J. Luton, and J. J. Jonas, “Recovery and recrystallization of polycrystalline copper after hot working,” *Acta Metall.*, vol. 27, pp. 1633–1648, 1979.
23. R. D. Doherty, D. a. Hughes, F. J. Humphreys, J. J. Jonas, D. J. Jensen, M. E. Kassner, W. E. King, T. R. McNelley, H. J. McQueen, and A. D. Rollett, “Current issues in recrystallization: a review,” *Mater. Sci. Eng. A*, vol. 238, pp. 219–274, Nov. 1997.
24. Y. W. Riddle and T. H. Sanders, “A study of coarsening, recrystallization, and morphology of microstructure in Al-Sc-(Zr)-(Mg) alloys,” *Metall. Mater. Trans. A*, vol. 35, pp. 341–350, 2004.
25. K. C. Kim and S. W. Nam, “Effects of Mn-dispersoids on the fatigue mechanism in an Al–Zn–Mg alloy,” *Mater. Sci. Eng. A*, vol. 244, pp. 257–262, 1998.
26. Z.-C. Sun, L.-S. Zheng, and H. Yang, “Softening mechanism and microstructure evolution of as-extruded 7075 aluminum alloy during hot deformation,” *Mater. Charact.*, vol. 90, pp. 71–80, Apr. 2014.

Chapter 6 – The Precipitation Process

1. N. Luiggi, J. P. Somon, and P. Guyot, “Residual resistivity of clusters in solid solutions,” *J. Phys. F Met. Phys.*, vol. 10, pp. 865–872, 1980.
2. J. T. Staley, “Aging kinetics of aluminum alloy 7050,” *Metall. Trans.*, vol. 5, pp. 929–932, 1974.
3. L. . Berg, J. Gjønnes, V. Hansen, X. . Li, M. Knutson-Wedel, G. Waterloo, D. Schryvers, and L. . Wallenberg, “GP-zones in Al–Zn–Mg alloys and their role in artificial aging,” *Acta Mater.*, vol. 49, no. 17, pp. 3443–3451, 2001.
4. M. R. Clinch, S. J. Harris, W. Hepples, N. J. H. Holroyd, M. J. LAWDAY, and B. Noble, “Influence of zinc to magnesium ratio and total solute content on the strength and toughness of 7xxx-series alloys,” *Mater. Sci. Forum*, vol. 519–521, pp. 339–344, 2006.

5. A. Deschamps, F. Livet, and Y. Brechet, “Influence of predeformation on ageing in an Al-Zn-Mg Alloy-I: microstructure evolution and mechanical properties,” *Acta Mater.*, vol. 47, pp. 281–292, 1998.
6. A. Deschamps and Y. Brechet, “Influence of predeformation on ageing in an Al-Zn-Mg Alloy - II: modeling precipitation kinetics and yield stress,” *Acta Mater.*, vol. 47, pp. 293–305, 1998.
7. G. Waterloo, V. Hansen, J. Gjønnes, and S. R. Skjervold, “Effect of predeformation and preaging at room temperature in Al – Zn – Mg –( Cu , Zr ) alloys,” *Mater. Sci. Eng.*, vol. 303, pp. 226–233, 2001.
8. C. Panseri and T. Federighi, “Ischronal annealing of vacancies in aluminum,” *Philos. Mag.*, vol. 3, no. 35, pp. 1223–1240, 1958.
9. J. D. Embury and R. B. Nicholson, “The nucleation of precipitates: the system Al-Zn-Mg,” *Acta Metall.*, vol. 13, pp. 403–417, 1965.
10. N. Z. Ryum, *Z. Met.*, vol. 66, pp. 338–344, 1975.
11. Z. Katz and N. Z. Ryum, “Precipitation kinetics in Al-alloys,” *Scr. Metall.*, vol. 15, no. 3, pp. 265–268, 1980.
12. P. Curratis, R. Kroggel, and R. Wolter, *Z. Met.*, vol. 78, p. 268, 1987.
13. H. Loffler, I. Kovacs, and J. Lendvai, “Decomposition processes in Al-Zn-Mg alloys,” *J. Mater. Sci.*, vol. 18, pp. 2215–2240, 1983.
14. G. Dlubek, R. Krause, O. Brummer, and G. Plazaola, “Study of formation and reversion of guinier-preston zones in Al-4.5at%Zn-xat%Mg alloys by positrons,” *J. Mater. Sci.*, vol. 21, pp. 853–858, 1986.
15. R. Ferragut, A. Somoza, and A. Dupasquier, “On the two-step ageing of a commercial Al-Zn-Mg Alloy: a study by positron lifetime spectroscopy,” *J. Phys. Condens. Matter*, vol. 8, pp. 8945–8952, 1996.
16. S. P. Ringer and K. Hono, “Microstructural evolution and age-hardening in aluminum alloys: atom probe, field-ion microscopy, and transmission electron microscopy studies,” *Mater. Charact.*, vol. 44, pp. 101–103, 2000.
17. T. H. Sanders Jr., R. R. Sawtell, J. T. Staley, R. J. Buccie, and A. B. Thakker, “Effect of microstructure on fatigue crack growth of 7xxx aluminum alloys under constant amplitude and spectrum loading,” 1978.
18. H. Schmalzried and V. Gerold, “Rontgenographische untersucugen urberdie ausartung einer aluminum-madnesiu-zink-legiergung,” *Z. Met.*, vol. 49, pp. 291–301, 1957.
19. P. N. Andler and R. Delasi, “Calorimeteric studies of 7000 series aluminum alloys - II: comparision of 7075, 7050, RX720,” *Met. Trans. A*, vol. 8, pp. 1185–1190, 1977.
20. G. Sha and A. Cerezo, “Early-stage precipitation in Al–Zn–Mg–Cu alloy (7050),” *Acta Mater.*, vol. 52, no. 15, pp. 4503–4516, Sep. 2004.
21. N. Q. Chinh, J. Lendvai, D. H. Ping, and K. Hono, “The effect of Cu on mechanical and precipitation properties of Al–Zn–Mg alloys,” *J. Alloys Compd.*, vol. 378, no. 1–2, pp. 52–60, Sep. 2004.
22. R. Rangathan, “Recrystallization resistance in aluminum alloys containing zirconium,” Georgia Institute of Technology, 1991.

23. J. H. Auld and S. M. Cousland, “The structure of the metstable h’ phase in aluminum-zinc-magnesium alloys,” *J. Aust. Inst. Met.*, vol. 19, pp. 194–201, 1974.
24. X. . Li, V. Hansen, J. Gjønnes, and L. . Wallenberg, “HREM study and structure modeling of the n’ phase, the hardening precipitates in commerical Al-Zn-Mg alloys,” *Acta Mater.*, vol. 47, no. 9, pp. 2651–2659, 1999.
25. A. Deschamps and Y. Brechet, “Influence of quench and heating rates on the ageing response of an Al-Zn-Mg-(Zr) alloy,” *Mater. Sci. Eng.*, vol. A251, pp. 200–207, 1998.
26. J. Gjønnes and C. J. Simensen, “An electron microscope investigation of the mircostructures in an aluminum-zinc-magnesium alloy,” *Acta Mater.*, vol. 18, pp. 871–890, 1970.
27. H. Y. Hunsicker, “Development of Al-Zn-Mg-CU alloys for aircraft,” in *Proc. Rosehain Centenary Conf. on the Contribution of Physical Metallurgy to Engineering Practice*, 1976, pp. 359–376.
28. A. Yamaoto, K. Minami, U. Ishihara, and H. Tsubakino, “Calorimetric and resistivity study on the formation and redissolution of precipitates in 7050 aluminum alloys,” *Mater. Trans. JIM*, vol. 39, pp. 69–74, 1998.
29. A. K. Mukhopadhyay, “Microstructure and properties of high strength aluminium alloys for structural applications,” *Trans. Indian Inst. Met.*, vol. 62, no. 2, pp. 113–122, 2009.
30. J. Lendvai, “Precipitation and strengthening in aluminium alloys,” *Mater. Sci. Forum*, vol. 217–222, pp. 43–56, 1996.
31. G. Sha and A. Cerezo, “Characterization of precipitates in an aged 7xxx series Al alloy,” *Surf. Interface Anal.*, vol. 36, pp. 564–568, 2004.
32. T. Sheppard, *Extrusion of Aluminium Alloys*. Kluwer Academic Publishers Group, 1999.
33. The Aluminum Association, *International Alloy Designations and Chemical Composition Limits for Wrought Aluminum and Wrought Aluminum Alloys*. Arlington, VA, 2009.
34. B. Sarkar, M. Marek, and E. A. Stark Jr., “The effect of Cu content and heat treatment on the stress corrosion characteristics of Al-6Zn-2Mg-XCu alloys,” *Met. Mater. Trans. A.*, vol. 12, pp. 1939–1943, 1981.

Chapter 7 – Post Processing Factors

1. C. Nowill, “Investigation of the quench and geating rate sensitivities of selected 7000 series aluminum alloys,” Worcester Polytechnic Institute, 2007.
2. J. E. Hatch, *Aluminum: Properties and Physical Metallurgy*. ASM, 1984.
3. A. Deschamps and Y. Bre, “Nature and distribution of quenched-induced precipitation in an Al-Zn-Mg-Cu alloy,” *Scr. Mater.*, vol. 39, no. 11, pp. 1517–1522, 1998.
4. K. Chen, H. Liu, Z. Zhang, S. Li, and R. I. Todd, “The improvement of constituent dissolution and mechanical properties of 7055 aluminum alloy by stepped heat treatments,” vol. 142, pp. 190–196, 2003.

5. S. . Lim, S. . Yun, and S. . Nam, “Improved quench sensitivity in modified aluminum alloy 7175 for thick forging applications,” *Mater. Sci. Eng. A*, vol. 371, no. 1–2, pp. 82–90, Apr. 2004.
6. S. D. Liu, X. M. Zhang, M. a. Chen, and J. H. You, “Influence of aging on quench sensitivity effect of 7055 aluminum alloy,” *Mater. Charact.*, vol. 59, no. 1, pp. 53–60, Jan. 2008.
7. T. Sheppard, *Extrusion of Aluminium Alloys*. Kluwer Academic Publishers Group, 1999.
8. A. Deschamps and Y. Brechet, “Influence of quench and heating rates on the ageing response of an Al-Zn-Mg-(Zr) alloy,” *Mater. Sci. Eng.*, vol. A251, pp. 200–207, 1998.
9. A. J. Bryant, “The effect of composition upon the quench-sensitivity of some Al-Zn-Mg alloys,” *J. Inst. Met.*, vol. 94, pp. 94–99, 1966.
10. C. Garcia-Cordovilla and E. Louis, “Investigation of the decomposition of the solid solution of a commerical Al-Zn-Mg alloy (7015), by means of DTA, hardness and conductivity measurements,” in *Thermal Analysis*, H. G. Wideman, Ed. Birkhauser Verlag, 1980, pp. 421–426.
11. L. F. Mondolfo, *Aluminium Alloys: Structure and Properites*. London: Butterworths, 1976.
12. H. Loffler, I. Kovacs, and J. Lendvai, “Decomposition processes in Al-Zn-Mg alloys,” *J. Mater. Sci.*, vol. 18, pp. 2215–2240, 1983.
13. G. Dlubek, R. Krause, O. Brummer, and G. Plazaola, “Study of formation and reversion of guinier-preston zones in Al-4.5at%Zn-xat%Mg alloys by positrons,” *J. Mater. Sci.*, vol. 21, pp. 853–858, 1986.
14. R. Ferragut, A. Somoza, and A. Dupasquier, “On the two-step ageing of a commercial Al-Zn-Mg Alloy: a study by positron lifetime spectroscopy,” *J. Phys. Condens. Matter*, vol. 8, pp. 8945–8952, 1996.
15. A. Deschamps, F. Livet, and Y. Brechet, “Influence of predeformation on ageing in an Al-Zn-Mg Alloy-I: microstructure evolution and mechanical properties,” *Acta Mater.*, vol. 47, pp. 281–292, 1998.
16. R. N. Allen and J. B. Vander Sande, “The oriented growth of precipitates on dislocations in Al-Zn-Mg,” *Acta Mater.*, vol. 28, no. 9, pp. 1185–1189, 1980.
17. S. Cersesara and P. Fiorini, *Mater. Sci. Eng.*, vol. 10, pp. 205–210, 1972.
18. G. Waterloo, V. Hansen, J. Gjønnes, and S. R. Skjervold, “Effect of predeformation and preaging at room temperature in Al – Zn – Mg –( Cu , Zr ) alloys,” *Mater. Sci. Eng.*, vol. 303, pp. 226–233, 2001.
19. A. Deschamps and Y. Brechet, “Influence of predeformation on ageing in an Al-Zn-Mg Alloy - II: modeling precipitation kinetics and yield stress,” *Acta Mater.*, vol. 47, pp. 293–305, 1998.
20. J. Lamb, V. Dangerfield, and T. H. Sanders Jr., “The effect of natural aging on 7xxx-series alloys,” Canton, GA, 2013.
21. J. T. Staley, “Aging kinetics of aluminum alloy 7050,” *Metall. Trans.*, vol. 5, pp. 929–932, 1974.
22. H. Y. Hunsicker, “Development of Al-Zn-Mg-Cu alloys for aircraft,” in *Proc. Rosehain Centenary Conf. on the Contribution of Physical Metallurgy to Engineering Practice*, 1976, pp. 359–376.

23. M. R. Clinch, S. J. Harris, W. Hepples, N. J. H. Holroyd, M. J. Lawday, and B. Noble, “Influence of zinc to magnesium ratio and total solute content on the strength and toughness of 7xxx-series alloys,” *Mater. Sci. Forum*, vol. 519–521, pp. 339–344, 2006.
24. G. Sha and A. Cerezo, “Early-stage precipitation in Al–Zn–Mg–Cu alloy (7050),” *Acta Mater.*, vol. 52, no. 15, pp. 4503–4516, Sep. 2004.
25. N. Q. Chinh, J. Lendvai, D. H. Ping, and K. Hono, “The effect of Cu on mechanical and precipitation properties of Al–Zn–Mg alloys,” *J. Alloys Compd.*, vol. 378, no. 1–2, pp. 52–60, Sep. 2004.
26. B. Cina, “Retrogression and Reaging and the Role of Dislocations in the Stress Corrosion of 7000-Type Aluminum Alloys,” vol. 20, no. October, pp. 2087–2092, 1989.
27. D. K. Xu, N. Birbilis, and P. A. Rometsch, “The effect of pre-ageing temperature and retrogression heating rate on the strength and corrosion behaviour of AA7150,” vol. 54, pp. 17–25, 2012.
28. J. T. Staley and R. R. Sawtell, “Aging process for 7000 series aluminum base alloys,” US4,431,4671984.
29. J. Buha, R. N. Lumley, and a. G. Crosky, “Secondary ageing in an aluminium alloy 7050,” *Mater. Sci. Eng. A*, vol. 492, no. 1–2, pp. 1–10, Sep. 2008.

Part II – The Quaternary Al-Zn-Mg-Cu System

Chapter 8 – Introduction

Chapter 9 – Materials and Experimental Procedure

1. H. Last, “Precipitation of dispersoids in aluminum alloys,” Georgia Institute of Technology, 1991.
2. R. Rangathan, “Recrystallization resistance in aluminum alloys containing zirconium,” Georgia Institute of Technology, 1991.
3. ASTM, “E18-14: standard test methods for Rockwell hardness of metallic materials.” pp. 1–38, 2014.

Chapter 10 – The As-Cast Condition and Homogenization

Chapter 11 – Rolling, Solution Heat Treatment, and Stretching

Chapter 12 – The Effects of Natural Aging

1. J. E. Hatch, *Aluminum: Properties and Physical Metallurgy*. ASM, 1984.

Chapter 13 – Artificial Aging

1. N. Q. Chinh, J. Lendvai, D. H. Ping, and K. Hono, “The effect of Cu on mechanical and precipitation properties of Al–Zn–Mg alloys,” *J. Alloys Compd.*, vol. 378, no. 1–2, pp. 52–60, Sep. 2004.

2. M. E. Fine, “Precipitation hardening of aluminum alloys,” *Metall. Trans. A*, vol. 6, no. April, pp. 625–630, 1975.
3. C. Genevois, D. Fabregue, A. Deschamps, and W. J. Poole, “On the coupling between precipitation and plastic deformation in relation with friction stir welding of AA2024 T3 aluminum alloy,” *Mater. Sci. Eng. A*, vol. 441, pp. 39–48, 2006.

Chapter 14 – The Effect of Composition on the Precipitate Free Zone

1. T. H. Sanders Jr., R. R. Sawtell, J. T. Staley, R. J. Buccie, and A. B. Thakker, “Effect of microstructure on fatigue crack growth of 7xxx aluminum alloys under constant amplitude and spectrum loading,” 1978.
2. R. Rangathan, “Recrystallization resistance in aluminum alloys containing zirconium,” Georgia Institute of Technology, 1991.
3. S. P. Ringer and K. Hono, “Microstructural evolution and age-hardening in aluminum alloys: atom probe, field-ion microscopy, and transmission electron microscopy studies,” *Mater. Charact.*, vol. 44, pp. 101–103, 2000.
4. J. T. Staley, “Aging kinetics of aluminum alloy 7050,” *Metall. Trans.*, vol. 5, pp. 929–932, 1974.
5. T. Ogura, S. Hirosawa, A. Hirose, and T. Sato, “Effects of microalloying tin and combined additions of silver and tin on the formation of precipitate free zones and mechanical properties in Al-Zn-Mg alloys,” *Mater. Trans.*, vol. 52, pp. 900–905, 2011.
6. T. D. Burleigh, “The postulated mechanisms for stress corrosion cracking of aluminum alloys - a review of literature 1980-1989,” *Corrosion*, vol. 47, pp. 89–98, 1991.
7. J. F. Nie and B. C. Muddle, “Microstructural design of high-strength aluminum alloys,” *J. Phase Equilibria*, vol. 19, pp. 543–551, 1998.
8. J. D. Embury and R. B. Nicholson, “The nucleation of precipitates: the system Al-Zn-Mg,” *Acta Metall.*, vol. 13, pp. 403–417, 1965.
9. M. Raghavan, “Microanalysis of precipitate free zones (PFZ) in Al-Zn-Mg and Cu-Ni-Nb alloys,” *Metall. Trans. A*, vol. 11, pp. 993–999, 1980.
10. S. Liu, Y. Zhang, W. Liu, Y. Deng, and X. Zhang, “Effect of step-quenching on microstructure of aluminum alloy 7055,” *Trans. Nonferrous Met. Soc. China*, vol. 20, pp. 1–6, 2010.

Part III – Registered 7xxx-Series Aluminum Alloys

Chapter 15 – Introduction

Chapter 16 – Materials

1. The Aluminum Association, *International Alloy Designations and Chemical Composition Limits for Wrought Aluminum and Wrought Aluminum Alloys*. Arlington, VA, 2009.

Chapter 17 – Quench Sensitivity and C-Curve Development

1. J. W. Evancho and J. T. Staley, “Kinetics of precipitation in aluminum alloys during continous cooling,” *Metall. Trans.*, vol. 5, pp. 43–47, 1974.
2. J. D. Bernardin and I. Mudawar, “Validation of the quench factor technique in predicting hardness in heat treatable aluminum alloys,” *Int. J. Heat Mass Transf.*, vol. 38, pp. 863–873, 1995.
3. C. Nowill, “Investigation of the quench and heat rate sensitivities of selected 7000 series aluminum alloys,” Worcester Polytechnic Institute, 2007.

Chapter 18 – Artificial Aging

1. J. E. Hatch, *Aluminum: Properties and Physical Metallurgy*. ASM, 1984.
2. J. T. Staley and R. R. Sawtell, “Aging process for 7000 series aluminum base alloys,” US4,431,467, 1984.

Chapter 19 – Development of True Aging Curves

1. The Aluminum Association, *International Alloy Designations and Chemical Composition Limits for Wrought Aluminum and Wrought Aluminum Alloys*. Arlington, VA, 2009.
2. ASTM, “E18-14: standard test methods for Rockwell hardness of metallic materials.” pp. 1–38, 2014.

Summary

Appendix A – Solid Solubility of Common Elements in Aluminum

1. I. J. Polmear, *Light Metals*. Arnold, 1995
2. J. Murray, A. Peruzzi, and J. P. Abriata, “Alloy Phase Diagrams,” in *ASM Handbook*, 1992, pp. 2.4–2.56.
3. ASM, “Alloy Phase Diagrams,” in *ASM Handbook*, 2012.

Appendix B – Common Etchants

1. G. Petzow, *Metallographic Etching*, 2nd ed. Materials Park: ASM International, 1999.
2. K. Mills, J. R. Davis, J. D. Destefani, D. A. Dieterich, G. M. Crankovic, H. J. Frissell, D. M. Jenkins, W. H. Cubberly, R. L. Stedfeld, R. T. Kiepura, and B. R. Sanders, “Metallography and Microstructures,” in *ASM Handbook*, 9th ed., Materials Park: ASM International, 2001.

Appendix C – Single Step Aging Curves for GT1-8 with Error Bars

Appendix D – Exfoliation Corrosion (EXCO) Testing of GT1-8

1. ASTM, *G34-01 - Standard test method for exfoliation corrosion susceptibility in 2xxx and 7xxx series aluminum alloys (EXCO Test)*. 2013.
2. J. E. Hatch, *Aluminum: Properties and Physical Metallurgy*. ASM, 1984.

Appendix E – Intergranular Corrosion (IGC) of GT1-8

1. J. E. Hatch, *Aluminum: Properties and Physical Metallurgy*. ASM, 1984.
2. ASTM, *G110 - Standard practice for evaluating intergranular corrosion resistance of heat treatable aluminum alloys by immersion in sodium chloride and hydorgen peroxide solution*. 1992.

VITA

**JUSTIN DALE LAMB**

Justin Lamb was born in Hendersonville, North Carolina. He attended public school at North Henderson High School in Hendersonville, North Carolina. He received a B.S. in Physics and Mathematics from Emory & Henry College in Emory, Virginia in 2010 where he played NCAA division III football before coming to Georgia Tech to pursue a doctorate in Materials Science and Engineering. Lamb also attended the University of Wollongong, Wollongong, Australia in 2009 as part of study abroad program focusing on mathematics.